

Giovanni Seminara
Stefano Lanzoni
Nicoletta Tambroni

Theoretical Morphodynamics: Straight Channels

STUDIES IN SCIENCES AND TECHNOLOGY

- 1 -

STUDIES IN SCIENCES AND TECHNOLOGY

Editor-in-Chief

Paolo Maria Mariano, University of Florence, Italy

Scientific Board

Michele Benzi, Scuola Normale of Pisa, Italy

Kaushik Bhattacharya, California Institute of Technology, United States

John Dainton, University of Liverpool, United Kingdom

Marc Geers, Eindhoven University of Technology, Netherlands

Krishna Kannan, Indian Institute of Technology Madras, India

Martin Kruzik, Institute of Information Theory and Automation Czech Academy of Sciences,, Slovakia

Xanthippi Markenscoff, University of California, United States

Fabrizio Mollaioli, Sapienza University of Rome, Italy

Domenico Mucci, University of Parma, Italy

Maria Patrizia Pera, University of Florence, Italy

Anja Schlömerkemper, University of Würzburg, Germany

Reuven Segev, Ben-Gurion University of the Negev, Israel

Giovanni Seminara, University of Genoa, Italy

Marco Spadini, University of Florence, Italy

David John Steigmann, University of California Berkeley, United States

Paolo Vannucci, University of Versailles Saint-Quentin-en-Yvelines, France

Giovanni Seminara, Stefano Lanzoni, Nicoletta Tambroni

Theoretical Morphodynamics: Straight Channels

FIRENZE UNIVERSITY PRESS
2023

Theoretical Morphodynamics: Straight Channels / Giovanni Seminara, Stefano Lanzoni, Nicoletta Tambroni. – Firenze : Firenze University Press, 2023.

(Studies in Sciences and Technology ; 1)
<https://books.fupress.com/isbn/9791221502138>

ISBN 979-12-215-0212-1 (Print)
ISBN 979-12-215-0213-8 (PDF)
ISBN 979-12-215-0214-5 (XML)
DOI 10.36253/979-12-215-0213-8

Graphic design: Alberto Pizarro Fernández, Lettera Meccanica SRLs
Front cover image: © azmansinoby|123rf.com

Volume published with the support of Università degli studi di Padova - Dipartimento di Ingegneria civile, edile ed ambientale – ICEA. (University of Padua - Department of Civil, Environmental and Architectural Engineering.)

Peer Review Policy

Peer-review is the cornerstone of the scientific evaluation of a book. All FUP's publications undergo a peer-review process by external experts under the responsibility of the Editorial Board and the Scientific Boards of each series (DOI 10.36253/fup_best_practice.3).


Referee List

In order to strengthen the network of researchers supporting FUP's evaluation process, and to recognise the valuable contribution of referees, a Referee List is published and constantly updated on FUP's website (DOI 10.36253/fup_referee_list).

Firenze University Press Editorial Board

M. Garzaniti (Editor-in-Chief), M.E. Alberti, F. Vittorio Arrigoni, E. Castellani, F. Ciampi, D. D'Andrea, A. Dolfi, R. Ferrise, A. Lambertini, R. Lanfredini, D. Lippi, G. Mari, A. Mariani, P.M. Mariano, S. Marinai, R. Minuti, P. Nanni, A. Orlandi, I. Palchetti, A. Perulli, G. Pratesi, S. Scaramuzzi, I. Stolzi.

FUP Best Practice in Scholarly Publishing (DOI 10.36253/fup_best_practice)

 The online digital edition is published in Open Access on www.fupress.com.

Content license: except where otherwise noted, the present work is released under Creative Commons Attribution 4.0 International license (CC BY 4.0: <http://creativecommons.org/licenses/by/4.0/legalcode>). This license allows you to share any part of the work by any means and format, modify it for any purpose, including commercial, as long as appropriate credit is given to the author, any changes made to the work are indicated and a URL link is provided to the license.

Metadata license: all the metadata are released under the Public Domain Dedication license (CC0 1.0 Universal: <https://creativecommons.org/publicdomain/zero/1.0/legalcode>).

© 2023 Author(s)

Published by Firenze University Press
Firenze University Press
Università degli Studi di Firenze
via Cittadella, 7, 50144 Firenze, Italy
www.fupress.com

*This book is printed on acid-free paper
Printed in Italy*

Contents

Acknowledgements	7
<i>Giovanni Seminara, Stefano Lanzoni, Nicoletta Tambroni</i>	
1. Introduction	9
1.1 Rationale behind the present Monograph	9
1.2 Plan of the Monograph	11
2. Incompressible hydrodynamics in straight channels	15
2.1 The motion of viscous incompressible fluids	15
2.1.1 Stress	15
2.1.2 Constitutive law	16
2.1.3 Governing equations	16
2.1.4 Boundary and initial conditions	18
2.2 Turbulent flows	19
2.2.1 General features of turbulence	19
2.2.2 The energy cascade	21
2.2.3 Investigating turbulent flows	22
2.2.4 The Reynolds averaged formulation for turbulent flows	26
2.2.5 The RANS equations	26
2.2.6 Boundary conditions for the RANS equations	27
2.2.7 Transport equation for the mean vorticity	29
2.2.8 The closure problem	29
2.2.9 Wall-bounded flows: plane uniform turbulent flow	32
2.3 Turbulent flow in straight cylindrical open channels	37
2.3.1 Geometrical preliminaries	37
2.3.2 Formulation	38
2.3.3 Uniform steady (normal) flow.	39
2.3.4 The case of infinitely wide rectangular channels.	41
2.3.5 The case of channels with finite width and arbitrary shape	43
2.3.6 Turbulence driven secondary flows in channels	46
2.4 Depth averaged formulation: the shallow water approximation	48

CONTENTS

2.4.1	Pressure is hydrostatically distributed	49
2.4.2	Derivation of the shallow water equations	50
2.4.3	Closures	53
2.4.4	Boundary conditions	54
2.5	One-dimensional formulation: de Saint-Venant equation	54
2.5.1	Derivation of the 1D governing equations	55
2.5.2	Closures	57
2.5.3	Boundary conditions	57
3.	The sediment transport capacity of open channel flows	59
3.1	The motion of an isolated heavy particle in viscous fluids	59
3.1.1	Small particles: The equation of Maxey-Riley-Gatignol	60
3.1.2	The particle response time and the Stokes number	62
3.1.3	Larger particles	63
3.1.4	An important application: Settling of a sphere in a fluid at rest at moderate-large Reynolds numbers	64
3.2	The modes of sediment motion	65
3.2.1	Transport mode versus sheet/debris mode	65
3.2.2	Transport mode: bedload versus suspended load	67
3.2.3	The modern view: coherent turbulent structures and their role in particle entrainment	67
3.3	Bedload transport	69
3.3.1	Threshold conditions for particle entrainment as bedload	69
3.3.2	Bedload transport capacity of homogeneous sediments in uniform open channel flow	72
3.3.3	The recent contribution of computational fluid dynamics (CFD) to modeling sediment transport in open channels.	78
3.4	Threshold conditions for particle entrainment in suspension	82
3.4.1	The entrainment mechanism	82
3.4.2	Incipient particle entrainment	83
3.5	Modeling the dynamics of suspensions	85
3.5.1	Modeling techniques	85
3.5.2	The Eulerian approach: governing equations of sediment mixtures	87
3.5.3	Governing equations of the dynamics of suspensions of uniform sediments in the dilute approximation	90
3.5.4	Equilibrium transport of dilute turbulent suspensions of small particles in open channel flows: the equilibrium Eulerian approach	93
4.	Sediment transport in natural channels	101
4.1	The evolution equation of the bed interface	101

4.2	Bedload transport of homogeneous sediments in non-uniform flows	103
4.2.1	Spatial non uniformities	103
4.2.2	Temporal non uniformities	103
4.3	Non uniform dilute suspensions of homogeneous sediments	103
4.3.1	The 3D Reynolds averaged advection-diffusion equation	103
4.3.2	Depth averaged model of transport in suspension	105
4.3.3	Analytical relationship for the depth integrated suspended sediment flux per unit width appropriate to slowly varying flows	111
4.4	Bedload transport of homogeneous sediments on sloping beds	113
4.4.1	Threshold conditions for the inception of sediment motion on sloping beds	113
4.4.2	Bedload transport on sloping beds: dimensional arguments	118
4.4.3	Bedload transport on sloping beds: Theoretical and experimental estimates	119
4.5	Flow resistance in natural channels	123
4.5.1	Small scale fluvial bedforms	123
4.5.2	Bedform regime	124
4.5.3	Bedform characteristics at equilibrium	126
4.5.4	Bedforms and flow resistance	128
4.5.5	Bedforms and sediment transport	132
4.5.6	Small scale fluvial bank-forms	132
4.6	Summary of the mathematical formulation for homogeneous sediments	135
4.7	Extensions to heterogeneous sediments	137
4.7.1	Threshold for particle entrainment of heterogeneous sediments: Hiding	137
4.7.2	Evaluation of grain size specific bed load transport capacity	139
4.7.3	Grain size specific formulation of Exner equation: Hirano's approach	142
4.7.4	Grain size specific formulation of Exner equation: The missing role of vertical sorting	144
4.8	Appendix: Bedload transport of homogeneous sediments on finite slopes	146
5.	The basic state: Straight channels at equilibrium	153
5.1	The basic <i>equilibrium</i> profile of straight channels	153
5.1.1	The notion of morphodynamic equilibrium	153
5.1.2	Mathematical formulation of 1D morphodynamic equilibrium	156
5.1.3	The case of cylindrical channels	156
5.1.4	The case of non cylindrical channels: rectangular channels with variable width	159
5.1.5	The case of non cylindrical channels: natural rivers	165
5.1.6	Additional effects	168
5.2	The basic <i>equilibrium</i> cross-section of straight channels	168

CONTENTS

5.2.1	The early field observations	168
5.2.2	The equilibrium shape of channels unable to transport sediments	169
5.2.3	The equilibrium shape of channels able to transport sediments: solution of the stable channel paradox for gravel rivers	172
5.2.4	The equilibrium shape of channels able to transport sediments: sand rivers	176
6.	Free and forced bars in straight channels	181
6.1	Free and forced bars in the laboratory	182
6.2	Bars: The simplest theoretical framework.	184
6.3	The formation of free bars: Linear stability analysis	189
6.3.1	Bar formation under bedload dominated conditions	189
6.3.2	Free bar formation: the effect of suspended load	199
6.3.3	Convective versus absolute instability	200
6.3.4	A conceptual digression: is 2D morphodynamics a well-posed problem?	201
6.4	Forced bars in straight channels	201
6.4.1	Excitation of non migrating spatial modes in straight rectangular channels	201
6.4.2	Bars forced by channel width variations	205
6.5	The development of free and forced bars of finite amplitude: weakly nonlinear theories	212
6.5.1	Weakly nonlinear free bars	212
6.5.2	Weakly nonlinear forced bars	219
6.6	Fully nonlinear free and forced bars	220
6.6.1	Numerical simulations of finite amplitude free bars	220
6.6.2	Numerical simulations of finite amplitude forced bars	227
6.6.3	Interaction between free and forced bars in straight cohesionless channels	228
6.7	Bars in the field: additional complexities of bar morphodynamics	230
6.7.1	The effect of flow unsteadiness	230
6.7.2	Recent field observations of alternate bar migration	236
6.7.3	The role of sediment heterogeneity: sorting patterns	240
6.7.4	The role of insufficient sediment supply	248
6.7.5	Further effects that influence the development of alternate bars in the field	249
7.	Introduction to the morphodynamics of mixed alluvial-bedrock straight channels	251
7.1	Detachment limited versus transport limited	251
7.2	Mechanisms of bedrock erosion	252
7.3	Morphology of bedrock channels	253
7.3.1	Large scale morphological features of bedrock channels	254
7.3.2	Small scale morphological features of bedrock channels	254
7.4	Early morphological models of the reach-basin scale	257

7.5	Mechanistic models of bedrock erosion	259
7.5.1	The saltation-abrasion model	260
7.5.2	Developments of Sklar-Dietrich model	263
7.5.3	Extension of the saltation-abrasion model to total load	268
7.6	Mechanics of bedrock channel incision	273
7.6.1	Insight on the bedrock incision process from laboratory observations	273
7.6.2	1D incision models	278
7.6.3	Stability of the longitudinal bed profile and autogenic development of knickpoints	282
7.6.4	The interplay of incision and alluviation in shaping the cross section of bedrock channels	283
7.7	Towards a theoretical framework for the morphodynamics of mixed bedrock-alluvial channels	287
7.7.1	Particle entrainment in mixed bedrock-alluvial channels	287
7.7.2	Modeling bedload transport in mixed bedrock-alluvial channels	289
7.7.3	Bed evolution equations for mixed bedrock-alluvial rivers	290
7.7.4	Consistency of the theoretical framework: Free bars in mixed bedrock-alluvial channels	291
7.7.5	The effect of macro-roughness	294
8.	Epilogue	297
8.1	Achievements and limits of recent developments	297
8.2	Final warning	301
9.	Mathematical Appendix	303
9.1	Asymptotic expansions	303
9.1.1	A simple example of asymptotic representation	303
9.1.2	Asymptotic expansions	305
9.1.3	The asymptotic forms of some integrals: method of steepest descents	306
9.2	Elements of perturbation methods	308
9.2.1	Weakly damped linear oscillator: exact solution	308
9.2.2	Perturbation solution based on a straightforward expansion	309
9.2.3	Dealing with non-uniformities: The method of multiple scales	311
9.3	An introduction to stability theory	315
9.3.1	The general notion of stability	315
9.3.2	The toy model	317
9.3.3	The base state	318
9.3.4	Linear stability analysis: Temporal normal modes	318
9.3.5	The initial value problem for linear perturbations and the convective-absolute nature of the instability	321

CONTENTS

9.3.6 Weakly nonlinear stability analysis	326
10. Bibliography	337
11. Notations	363

Acknowledgements

Giovanni Seminara, Stefano Lanzoni, Nicoletta Tambroni

Our attempt to build a rational theory of morphodynamics has developed through the years, starting from the early 1980's, when the senior Author (GS) took part in a memorable conference on River Meandering held in New Orleans (Blondeaux and Seminara, 1983). That meeting was a rare chance to meet some of the giants of geomorphology (Luna Leopold and J. C. Brice) together with some of the rising stars of the fluvial engineering community (most notably Gary Parker and Huib de Vriend). The first seeds of the contents of the present Monograph and its companion (Seminara *et al.*, 2023) may be traced back to that meeting.

In the following 40 years we have interacted with a number of colleagues to whom we are indebted. Firstly, to all the members of the *enlarged Genoa group*, with whom we spent some very enlightening and productive time and, most importantly, had a lot of fun. Some of them are coauthors of our papers, others have shared ideas, feelings and enthusiasm with us. Let us mention each of them. The older ones: Paolo Blondeaux, Marco Colombini, Marco Tubino and Giovanna Vittori; the middle generation: Michele Bolla Pittaluga, Alessandro Cantelli, Bianca Federici, Enrico Foti, Michele Guala, Brad Murray, Paola Passalacqua, Rodolfo Repetto, Luca Solari, Nunzio Siviglia, Yasuharu Watanabe, Peter Whiting, Dino Zardi, Guido Zolezzi; last, but not least, the young generation: Manuel Bogoni, Alessandro Frascati, Sergio Lopez Dubon, Rossella Luchi, Marco Mazzuoli and Peter Nelson.

We are also indebted to further outstanding colleagues with whom we have also had deep human relationships. Gary Parker, an explosive personality, has been a continuous source of inspiration for generations of researchers in the field, with whom he has generously shared ideas and knowledge. Chris Paola deserves an equally prominent place in our heart for his deep and original thinking and his quiet and warm personality which has made our long friendship a great privilege. Syunsuke Ikeda warmly welcomed us in the Japanese community under his undisputed leadership. We also acknowledge enjoyable scientific conversations with Bill Dietrich, a master in capturing the physics of complex natural phenomena and asking difficult provocative questions and Marcelo Garcia, the 'most Italian' of our foreign coworkers, still remembered in our laboratory for his overwhelming energy. Finally, we acknowledge fruitful interactions with many members of the Dutch scientific community, notably Erik Mosselman, Ralph Schielen, Nico Struiksmma and Huib de Vriend.

We are particularly grateful to several scientists who granted us permission to use figures contained in their dissertations or provided us with modified versions of figures contained in their published material. Let us list them.

- Paul Carling and Keith Richardson kindly made available Figures 147, 148 and 149;
- Phairot Chatanantavet kindly granted his permission to use Figures 144 and 165;
- Alessandra Crosato kindly made available data to plot Figures 119, 120 and 121;
- Andrea Defina kindly made available Figure 114;

- Joris Eekhout kindly granted his permission to use Figures 3.3, 3.6 and 3.7 of his PhD Dissertation;
- Noah Finnegan kindly granted his permission to use Figures 4, 7, 10, 13 and 19 of his PhD Dissertation;
- Simona Francalanci kindly granted her permission to use Figures 2.18 and 2.21 of her PhD Dissertation;
- Shahan Ahmed Huda kindly granted his permission to use Figures 2.2, 3.1 and 3.4 of his MSc Dissertation;
- Jason William Kean kindly granted his permission to use Figures 2.2 and 2.10 of his PhD Dissertation;
- Michael Lamb kindly granted his permission to use Figure 1 (p. 249), Figure 4 (p. 264) and Figure 6 (p. 268) of his PhD Dissertation;
- Suzanne Leclair and Gary Parker kindly made available Figure 59;
- Marco Mazzuoli kindly made available Figure 6;
- Peter Nelson read Chapter 7, pointed out an error in the text and provided some very useful references. Peter has also made available Figures 135 and 141;
- Yarko Nino kindly granted his permission to reproduce Figure 8.19 of his PhD Dissertation;
- Jeff Nittrouer kindly granted his permission to use Figure 2.1 of his PhD Dissertation;
- Gary Parker read Chapter 8, made useful comments and kindly provided Figure 137;
- Rodolfo Repetto kindly granted his permission to use Figures 3.2, 3.3, 3.6 and 4.3 of his PhD Dissertation;
- Joel Scheingross kindly granted his permission to use Figures 6.3 and 6.10 of his PhD Dissertation;
- Ralph Schielen kindly granted his permission to use Figures 2.5, 2.6 and 2.10 of his PhD Dissertation;
- Alyssa Jennifer Serlet kindly granted her permission to use Figure 3.19 of her PhD Dissertation;
- Guglielmo Stecca kindly granted his permission to use Figure 7.10 of his PhD Dissertation;
- Peter Whiting kindly made available Figure 134;
- Miguel Wong kindly made available Figure 26;
- Scott Wright kindly made available the data to reproduce Figure 51.

The Department of Civil Chemical and Environmental Engineering (formerly Istituto di Idraulica) of the University of Genova has provided, thanks to the early leadership of Enrico Marchi, an environment with sufficient intellectual freedom to allow GS and NT to fully express their potentialities. A similar intellectual freedom has inspired Luigi D'Alpaos who encouraged SL to start what would become a longstanding collaboration with the Genoa group.

Thanks are also due to the anonymous Referees for their careful reviews of our manuscript. Finally, our families have carried much of the burden. This book is dedicated to them.

1. Introduction

In 2018 the senior members of the Genoa group of Morphodynamics (Blondeaux *et al.*, 2018) published an introductory Monograph to the subject of Morphodynamics of Sedimentary Patterns. The idea was that a series of such Monographs focusing on specific topics in the wide area of fluvial, tidal, coastal and submarine Morphodynamics would follow in the next years. The present one and the companion Monograph (Seminara *et al.*, 2023) are indeed the first two on fluvial subjects, while two Monographs on coastal subjects (Blondeaux and Vittori, 2023; Blondeaux *et al.*, 2023) are forthcoming.

1.1. Rationale behind the present Monograph

In Blondeaux *et al.* (2018) it has been clarified that river planforms can be classified into two main classes: meandering and braiding, a straight river alignment being a rather exceptional case. This notwithstanding, the present Monograph restricts its attention to the Morphodynamics of straight channels. Why?

The mechanistic approach to fluvial morphodynamics, developed in the last few decades, has clarified that the formation of meandering as well as braiding patterns in alluvial channels are the consequences of a simple fact: the uniform flow of water and the equilibrium configuration of bed topography in an ideal perfectly straight channel with cohesionless granular bed is unstable to various classes of perturbations of the bottom pattern and/or channel alignment. Hence, in order to investigate meandering and braiding rivers, one must explore the nature of such instabilities. It turns out that a class of perturbations plays a major role in the formation of large scale fluvial sedimentary patterns: they are called *bars*.

Indeed, the ubiquitous nature of the 'bar' unit has been known since the cornerstone field observations of Leopold and Wolman (1957), which may be seen as the starting point of the modern fluvial morphodynamics. Soon, bars were recognized as the fundamental building block of both meandering and braiding patterns. A bar unit consists of a sequence of a riffle and a pool, separated by an oblique sharp front (Figure 1). Except for the case of very narrow channels, bars are invariably present in both sandy and gravel rivers. A major feature of the bar unit is that it gives rise to an *oscillatory topographic forcing*. By simple continuity requirements, this forcing generates a topographically driven secondary flow whose ultimate expression is the winding of the thread of high velocity (Figure 1). Note, that the tendency of the stream to follow a meandering path is an ubiquitous feature of fluvial patterns in nature, but it also occurs in artificially straightened channels, i.e. channels confined by artificial straight banks. However, the way these sinuous courses are organized depends on a further major feature of bars, namely that they form rows and the number of rows accommodated in a channel depends on the channel width. In fairly narrow channels, a single row of bars (called *alternate bars*) forms and the river alignment is either (nearly) straight (e.g. the artificial course of the Rhine River constrained within in-erodible banks depicted in Figure 2a) or meandering. In wide channels, *multiple row bars* develop and the river is defined as 'braiding' (Figure 2b).

Leopold and Wolman (1957) also found that the wavelength of the pool-riffle unit is a function of channel width. Figure 3 reproduces the celebrated original plot presented in that paper,

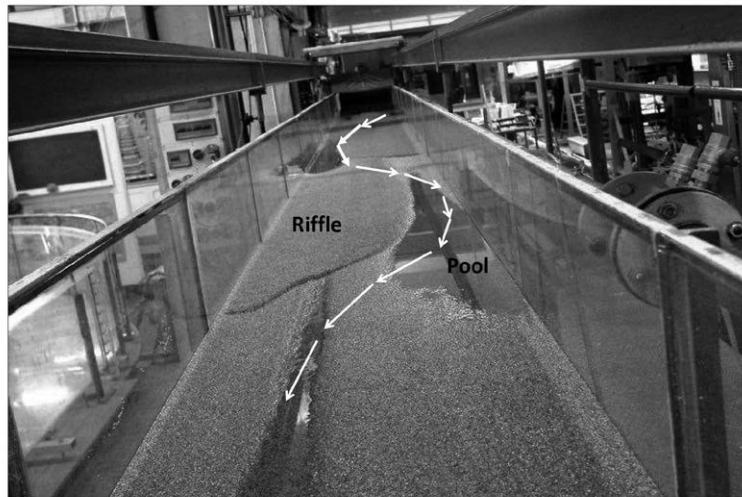
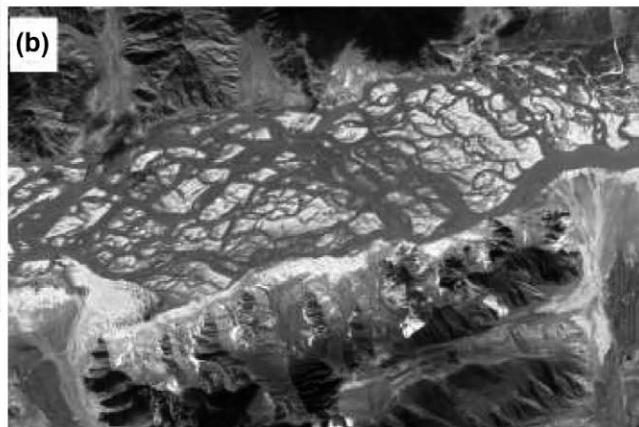


Figure 1. Photo of alternate bars generated in the Genoa lab, showing a sequence of riffles and pools separated by oblique fronts which forces the flow to follow a winding path.



The braided Bramaputra River in the vicinity of Arunachal Pradesh, India.
Source: Google Maps
(27°42'56.44" N 94°40'02.29" E)



The single row of bars displayed by the Rhine river in the vicinity of Vaduz (Liechtenstein)

Source: Google Maps (47°07'51.19" N 9°29'20.24" E)

Figure 2. Examples of single (a) and multiple (b) row bars displayed by an artificially straightened river (a) and a natural braiding river (b) respectively (credit: Google Earth (a) GoogleGeoBasis-DE/BKG (©2009) 47°09'05"N, 9°30'07"E dates:7/22/2022–newer; (b) Landsat/Copernicus, 27°19'19"N, 94°46'35"E dates: 1/7/2022–newer)

reporting data for both meandering rivers and straight channels measured in the field or in the

laboratory. Having established a correlation between pool-riffle wavelength and channel width may be considered a first major achievement in the development of morphodynamics. Our analysis

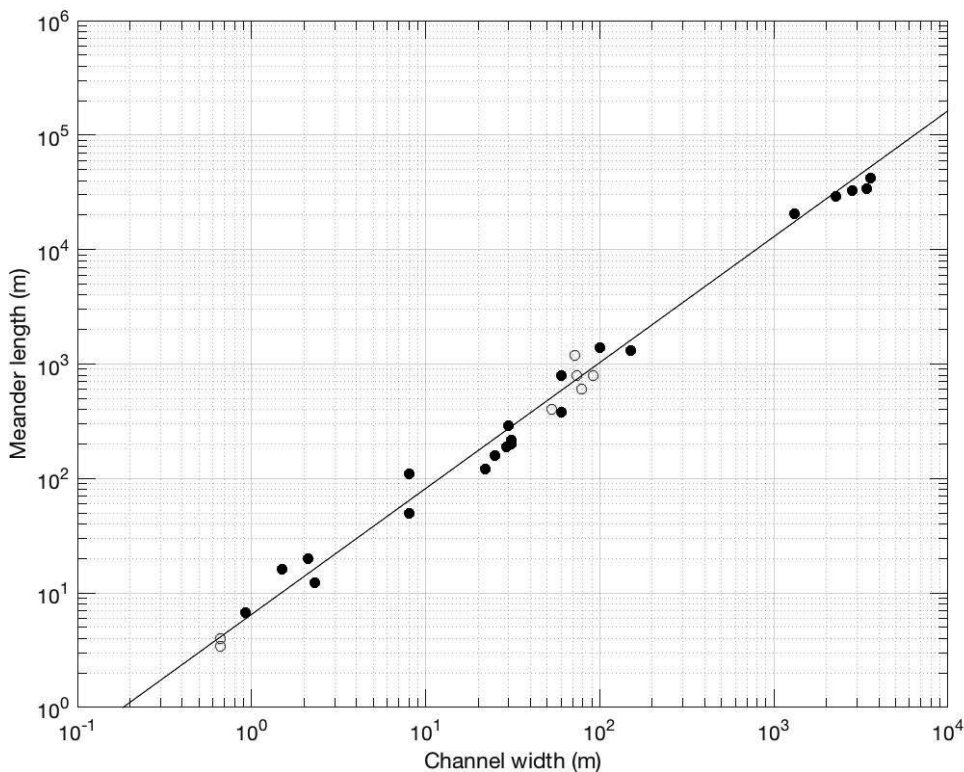


Figure 3. The celebrated plot of Leopold and Wolman (1957) where the cartesian wavelength of meanders (\bullet) and of the pool-riffle sequences in straight channels (\circ) is plotted versus the channel width. Data refer to both flume and field observations of Leopold and Wolman (1957) and further Authors (data extracted from Leopold and Wolman, 1957, Fig. 45).

will show that alternate (as well as multiple row) bars observed in nature indeed arise from an 'intrinsic' instability mechanism whereby an initially flat bottom topography in a straight cohesionless channel is unable to keep flat: the flow and bottom topography respond to arbitrary small perturbations of their initial state allowing for their selective amplification and migration. This is a 'free' process in that it arises spontaneously, i.e. in the absence of any forcing effect. For this reason Seminara and Tubino (1989) have coined the term '*free bars*' for alternate and multiple row bars.

We will also show that *forced bars* are similar bottom features that do not migrate and arise when some local or distributed perturbation of bank alignments or bottom topography are forced by permanent external causes. An important class of forced bars is driven by channel curvature and are called *point bars*. They are investigated in the companion Monograph (Seminara *et al.*, 2023), where it will be clarified that meander formation is a process apparently similar but conceptually distinct from bar formation.

1.2. Plan of the Monograph

The program we have in mind is intended for a reader at the postgraduate level with some background in Maths (elementary calculus), in Fluid Mechanics (elementary) and in Sediment

Transport (elementary).

The first part of the Monograph is thus devoted to build up some more advanced knowledge of the two basic tools required to investigate Fluvial Morphodynamics, namely the Mechanics of Turbulent Flows and The Mechanics of Sediment Transport in straight open channels. This is a huge task which could easily require entire books to be fulfilled. We will restrict the treatment to the main topics required to construct the foundations of Morphodynamics.

We start, in Chapter 2, recalling the governing equations of incompressible flows of Newtonian fluids in the general Navier-Stokes formulation. We then outline turbulent flow modeling, present the so called RANS (Reynolds Averaged Navier Stokes) equations, and discuss some of the closure models appropriate to open channel flows. Next, we derive in a systematic manner the depth averaged model (sometimes called *shallow water* or *2D de Saint Venant equations*) and the *cross sectionally averaged* model of flow in open channels (*1D de Saint Venant equations*). Applications of each of these models will be needed in order to analyze the various morphodynamic patterns at different spatial and temporal scales.

The goal of Chapter three is to introduce the reader to the variety of mechanisms whereby a unidirectional turbulent stream acting on a flat cohesionless granular bed can entrain solid particles and transport them downstream until they settle on the bed. A rigorous solution of this problem is not available yet, in spite of longstanding attempts of many scientific communities, encompassing geomorphology, fluid mechanics and general physics. In the last decade, significant progress has been made with the help of increasingly powerful CFD and experimental techniques. This notwithstanding a variety of semi-empirical approaches have played and continue to play a fundamental role. We start assessing the state of the art on the motion of an isolated heavy particle in viscous fluids. Next, we outline the various modes whereby sediment particles lying on the cohesionless bed of a straight channel may be destabilized when a strictly uniform turbulent open channel flow acts on them. These modes range between two limit conditions described as *transport mode* and *debris (or sheet) mode*. We focus on the transport mode, and investigate the two distinct mechanisms of transport, namely *bed load*, associated with low stresses acting on the bottom and *suspended load* experienced for relatively high stresses. The configuration analyzed in this chapter is fairly idealized, channel alignment is straight, the flow is plane and uniform, sediment particles are equally sized spheres and the amount of sediments supplied upstream equals the transport capacity of the channel.

In the next chapter we extend the analysis of sediment transport such to encompass the *spatially and temporally varying* characteristics encountered in nature. A crucial role in this respect is played by the sloping character of the bed. We then complete our formulation of the general problem of morphodynamics. We first recall the evolution equation of the bed interface derived in the first Monograph of the present series (Blondeaux *et al.* (2018)) for the case of homogeneous sediments. Next, we derive appropriate formulations for the depth integrated sediment flux per unit width, able to account for the sloping character of the bed interface and for the spatial-temporal dependence of the flow. Finally, we deal with the last source of complexity, which is associated with the heterogeneous character of fluvial sediments. In the absence of a rigorous formulation of the Mechanics of Sediment Transport, analysis must again rely mostly on experimental observations and physically based reasoning. We then review grain size specific formulations for the transport of sediment mixtures accounting for the phenomenon of *hiding* whereby finer grains, protruding in the turbulent boundary layer less than larger grains, feel fluid drag less intensely than larger grains.

Next, we take advantage of the body of knowledge established in the previous chapters and proceed to construct a *theory of straight fluvial morphodynamics*. The approach we follow is mechanistic.

We then start (Chapter 5) identifying the ideal channel configuration that plays the role of the

basic state for the whole theory of River Morphodynamics. Essentially, we seek the conditions required for a straight channel with uniform cross section to be in *morphodynamic equilibrium*. The latter condition essentially implies that the bed interface keeps flat and the channel banks are not eroded. Such an ideal state exists: flow discharge must be constant, uniform sediments must be supplied to the channel at constant rate, while channel slope and channel width must attain appropriate 'equilibrium' values with some 'equilibrium cross-sectional shape'. Ideal equilibrium implies that neither bed aggradation nor bed degradation may occur as the rate of sediment supply exactly meets the sediment transport capacity of the stream at any cross section. Needless to say, nature is more complex as rivers undergo spatial and temporal fluctuations of both flow discharge and sediment supply. We then complete the chapter reviewing the various attempts to interpret the quasi-equilibrium states displayed by rivers in nature.

Obviously, the existence of an equilibrium configuration does not insure that such an equilibrium is stable. And, indeed, one hardly encounters in nature a straight channel with the characteristics established in Chapter 5. It is then necessary to ascertain how an ideal equilibrium channel responds to perturbations. Chapter 6 investigates the origin and the characteristics of *bars*. As already pointed out, it turns out that *free bars* (both single and multiple row bars) result from a spontaneous instability of the basic state. The linear analysis of such an instability is quite successful in predicting wavelength and migration speed of these features, while a nonlinear analysis is needed to predict their amplitudes. We then present analytical solutions for the weakly nonlinear instability case, showing that bar instability leads to a so called *supercritical bifurcation*. Numerical solutions as well as laboratory observations are also discussed. They confirm the significance of analytical results.

Next, we investigate *forced bars*, focusing, in particular, on spatial oscillations of channel width which give rise to the development of central bars, frequently observed in nature. We then review further effects that influence the development of bars in the field, including the *unsteady character of the basic state* and the *role of an insufficient sediment supply*.

Finally, we devote specific attention to the role of *sediment heterogeneity*, which leads to the appearance of so called *sorting patterns*. Sorting is essentially a process whereby, starting from a spatially uniform grain size distribution, the distinct motion of different grain sizes leads to clearly identifiable, *organized non uniformities* of the grain size distribution in the horizontal and/or in the vertical directions. We will distinguish sorting patterns in straight channels into two classes: patterns originating mostly from a rearrangement of the grain size distribution of the surface layer (*bedload sheets, longitudinal streaks*) and patterns undergoing vertical sorting where the grain size distribution is rearranged in both horizontal and vertical directions (*bars*).

In Chapter 7 we relax the alluvial constraint and discuss the morphodynamics of bedrock channels. This is a broad subject that has been widely explored recently and will deserve a Monograph of its own in the future. We will limit ourselves to outlining some of the novelties brought up when morphodynamic patterns develop in the (complete or partial) absence of an alluvial cover of river beds. After a brief overview of the large and small scale morphological patterns observed in bedrock channels, we present the main tool of bedrock morphodynamics, namely the 'detachment limited' version of the evolution equation of the bed interface. This equation involves a major unknown quantity, the absolute *erosion rate* \mathcal{E} , i.e. the local net variation of bed elevation.

Hence, any further development of the analysis calls for some understanding of the physical mechanisms of bedrock erosion and the construction of suitable physically based models of the erosion process. In the early literature, a power law closure relationship was proposed for \mathcal{E} as a function of drainage area of the basin and local channel slope. Models based on such a closure have enjoyed some popularity as they can successfully predict the occurrence of a transition from bedrock to alluvial and its dependence on the history of tectonic uplift. They also allow one to evaluate the response of a bedrock channel to changes in tectonic and climatic conditions, such as the formation and upstream migration of a *knickpoint* in response to a base level drop at some initial cross section. Recently, a real breakthrough in the development of the subject has arisen

from a successful attempt to construct a physically based model for \mathcal{E} in the major case of bedrock abrasion driven by saltating bed load. Here, the two main effects controlling the rate of erosion are found to be the so called *tool effect* (i.e. the availability of bed load) and the *cover effect*, controlling what fraction of the bed surface is free of alluvial cover and thus available for erosion. This model has generated a flow of research contributions that, on one hand extended the latter approach to account for further mechanisms contributing to the erosion process, on the other hand applied erosion models to simulate 1-D and 2-D channel incision processes.

We conclude the chapter reviewing some of the recent attempts to provide a general formulation for the morphodynamics of mixed alluvial-bedrock channels and their tentative applications to the formation of bars under mixed conditions.

The final Chapter of the Monograph is devoted to a glance at the future. Although the body of knowledge established in the last few decades has led to the satisfactory rational framework discussed in this Monograph, some features of straight morphodynamics are as yet unclear or have received attention from the scientific community only recently. Most notable in this respect is the new branch of morphodynamics, called *eco-morphodynamics*, which investigates the interaction of sedimentary patterns with ecological processes. This allows to widen the perspective of the river, which is no longer seen only as a mechanical system, with the main function to transport water and sediments, but also as the host of rich biota components. This raises a bunch of interesting novel problems, like the effects of vegetation on sedimentary patterns, the contribution of rivers to the carbon cycle and the role of river networks as ecological corridors, encompassing the positive aspects connected with river restoration as well as the ability of rivers to act as vectors of pathogens. These topics are likely to develop further in the near future.

2. Incompressible hydrodynamics in straight channels

We start our journey recalling some fundamental notions on turbulent flow of incompressible fluids in straight open channels with a fixed bed. In other words, in this Chapter we ignore the presence of a solid phase carried by the stream. This assumption will be relaxed in the following Chapters.

2.1. The motion of viscous incompressible fluids

Let us consider a viscous incompressible fluid flowing under gravity in a domain \mathbb{V} bounded by a bed interface, Γ_η , a free surface, Γ_H , and some inflow, Γ_{in} , and outflow, Γ_{out} , open boundaries (i.e., boundaries permeable to fluid motion). The flow is referred to a cartesian reference frame (x_1, x_2, x_3) which is assumed to be at rest (Figure 4). It is convenient to assume the x_3 axis aligned with the vertical direction and pointing upwards.

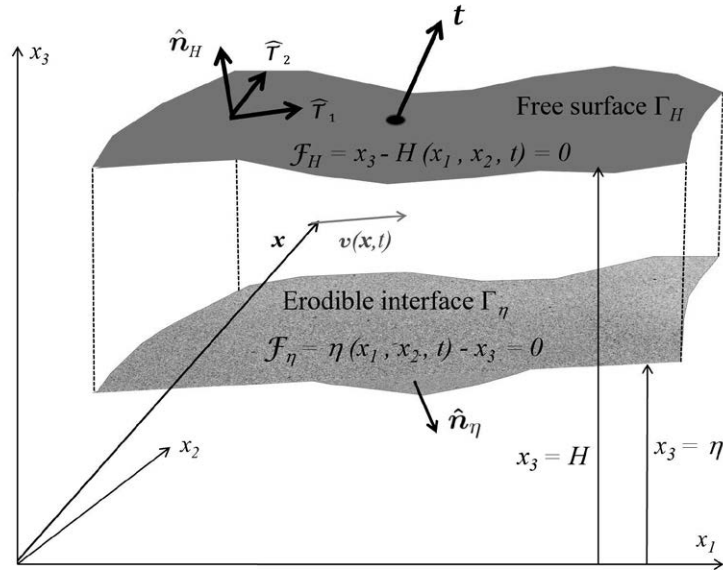


Figure 4. Sketch of the flow domain, a region bounded by a bed interface, a free surface and some open boundaries.

2.1.1 Stress

We take an Eulerian viewpoint and assume that quantities describing the motion of fluid particles are functions of position \mathbf{x} and time t . In particular, $\mathbf{v}(\mathbf{x}, t)$ denotes the local instantaneous fluid velocity while $\mathbf{t}(\mathbf{x}, t; \hat{\mathbf{n}})$ is the instantaneous stress vector acting on a surface element of fluid

located at \mathbf{x} . The unit vector $\hat{\mathbf{n}}$ normal to the element will be taken as oriented in the outward direction. In any continuum in motion, local dynamic equilibrium implies that the stress vector \mathbf{t} is obtained from the stress tensor $\mathbf{T}(\mathbf{x}, t)$ through the relationship (see, e.g. Batchelor, 1967, pg. 9):

$$\mathbf{t} = \mathbf{T} \cdot \hat{\mathbf{n}}, \quad (1a)$$

or, in scalar form,

$$t_i = T_{ij} \hat{n}_j \quad (i = 1, 2, 3), \quad (1b)$$

where T_{ij} is the j -component of the stress vector acting on a fluid surface element with unit normal parallel to the x_i axis and Einstein summation rule is adopted¹.

2.1.2 Constitutive law

In viscous incompressible Newtonian fluids, such as pure water, stresses arise in response to the strain rate and are linearly proportional to it. The relationship between the stress tensor \mathbf{T} and the strain rate tensor \mathbf{D} is called *constitutive law* because it sets the foundations of the theoretical framework on which the mechanics of fluid motion stands. The constitutive law of viscous incompressible Newtonian fluids reads:

$$\mathbf{T} = -p \mathbf{I} + 2 \mu \mathbf{D}, \quad (2a)$$

or, in scalar form

$$T_{ij} = -p \delta_{ij} + 2 \mu D_{ij} = -p \delta_{ij} + \mu \left(\frac{\partial v_i}{\partial x_j} + \frac{\partial v_j}{\partial x_i} \right). \quad (2b)$$

Here $p(\mathbf{x}, t)$ is pressure, \mathbf{I} is the unit tensor² and μ is dynamic viscosity, a fluid property weakly dependent on temperature for Newtonian liquids under ordinary conditions.

2.1.3 Governing equations

The governing equations of motion of a viscous incompressible fluid express in differential form the principle of mass conservation and Newton law.

Mass conservation: the continuity equation

Due to the restriction of fluid incompressibility, mass conservation also implies volume conservation which reduces to a pure kinematical constraint on the velocity field. It reads (Batchelor, 1967):

$$\nabla \cdot \mathbf{v} = \frac{\partial v_i}{\partial x_i} = 0. \quad (3)$$

The equation of continuity (3) simply states that, in order for a velocity field to satisfy mass conservation, it must be *divergence free (or solenoidal)*.

The equations of motion: Navier Stokes equations

¹ Einstein summation rule states that any repeated index symbol is summed over, i.e. if the index i is used twice in a given term of a tensor expression, then the term is to be summed for all i . The rule applies to any distinct pair of indices. For example, equation (1)b is a concise version of the following equation:

$$t_i = T_{i1} \hat{n}_1 + T_{i2} \hat{n}_2 + T_{i3} \hat{n}_3 \quad (i = 1, 2, 3)$$

² The diagonal components of the unit tensor \mathbf{I} are equal to one. The remaining components vanish. The unit tensor in scalar form is also denoted by δ_{ij} and is called *Kronecker index*.

The equations of motion for a viscous incompressible fluid with constant properties subject to gravity take the form of the Navier-Stokes equations:

$$\frac{d\mathbf{v}}{dt} = -g \hat{\mathbf{x}}_3 - \frac{1}{\rho} \nabla p + \nu \nabla^2 \mathbf{v}, \quad (4a)$$

or, in scalar form

$$\frac{dv_i}{dt} = -g \delta_{i3} - \frac{1}{\rho} \frac{\partial p}{\partial x_i} + \nu \nabla^2 v_i, \quad (4b)$$

where ρ is density, $\nu (\equiv \mu/\rho)$ is kinematic viscosity and d/dt is the material derivative defined as

$$\frac{d}{dt} = \frac{\partial}{\partial t} + v_j \frac{\partial}{\partial x_j}. \quad (5)$$

The Navier-Stokes equations express in differential form a balance between the effects of inertia, gravity and viscous stress acting on fluid particles.

The vorticity equation

Vorticity $\boldsymbol{\omega}$ is an important property of fluid flows. Physically, it is a *vectorial measure of the local fluid rotation rate*, a concept that may be visualized thinking of a microscopic paddle wheel placed into the flow: its spinning rate would be twice the modulus of vorticity.

Mathematically, vorticity is defined as the curl of the velocity field, hence:

$$\boldsymbol{\omega} = \nabla \times \mathbf{v}, \quad \omega_i = \delta_{ijk} \frac{\partial v_k}{\partial x_j}, \quad (6)$$

where δ_{ijk} is Ricci tensor³.

The reader will readily show that incompressible fluids satisfy a continuity equation for $\boldsymbol{\omega}$ that is identical with the continuity equation for the velocity field, hence:

$$\nabla \cdot \boldsymbol{\omega} = 0. \quad (7)$$

The vorticity equation is obtained taking the curl of the Navier Stokes equations. Recalling that $(\nabla \times) \nabla f \equiv 0$ for any scalar field f , it immediately follows that both *pressure and gravity do not affect the vorticity dynamics* and the vorticity equation has the form:

$$\frac{\partial \boldsymbol{\omega}}{\partial t} + \nabla \times (\mathbf{v} \cdot \nabla \mathbf{v}) = \nu \nabla^2 \boldsymbol{\omega}. \quad (8)$$

Some algebra⁴ then allows to prove the following identity:

$$\nabla \times (\mathbf{v} \cdot \nabla \mathbf{v}) = \nabla \times \left[\nabla \frac{\mathbf{v}^2}{2} - \mathbf{v} \times \boldsymbol{\omega} \right] = -\nabla \times (-\mathbf{v} \times \boldsymbol{\omega}) = \mathbf{v} \cdot \nabla \boldsymbol{\omega} - \boldsymbol{\omega} \cdot \nabla \mathbf{v}. \quad (9)$$

Substituting from (9) into (8) one ends up with the following form of the vorticity equation for viscous incompressible fluids:

$$\frac{d\boldsymbol{\omega}}{dt} = \frac{\partial \boldsymbol{\omega}}{\partial t} + \underbrace{\mathbf{v} \cdot \nabla \boldsymbol{\omega}}_{\text{convection}} = \underbrace{\boldsymbol{\omega} \cdot \nabla \mathbf{v}}_{\text{distortion}} + \underbrace{\nu \nabla^2 \boldsymbol{\omega}}_{\text{diffusion}}. \quad (10)$$

³ The components of Ricci tensor are defined as follows: $\delta_{ijk} = 0$ if at least two of the indices i, j, k are equal; $\delta_{ijk} = 1$ if ijk is an even permutation of 123; $\delta_{ijk} = -1$ if ijk is an odd permutation of 123. It follows that if one performs an even number of permutations on the indices of the tensor δ_{ijk} the tensor is unaffected (e.g. $\delta_{ijk} = \delta_{jki}$) whilst an odd number of permutations changes its sign (e.g. $\delta_{ijk} = -\delta_{jik}$).

Hence, vorticity is convected by the velocity field, a process simply leading to vorticity being redistributed throughout the flow domain without affecting its intensity. Intensification of vorticity is known to be associated with distortion, i.e. twisting and extension of the vortex tubes (see Batchelor, 1970, Section 5.2). Finally, vorticity is dissipated by molecular viscosity.

2.1.4 Boundary and initial conditions

The mathematical problem described by the unsteady system of quasi-linear partial differential equations (3) and (4), in order to be well posed, needs to be complemented by suitable initial and boundary conditions (e.g. Fletcher, 1991).

For unsteady flows, the initial condition consists of specifying a divergence free velocity field \mathbf{v}_0 everywhere in the flow domain at the initial time $t = 0$:

$$\mathbf{v}(\mathbf{x}, 0) = \mathbf{v}_0(\mathbf{x}), \quad \nabla \cdot \mathbf{v}_0 = 0 \quad \mathbf{x} \in \mathbb{V}. \quad (11)$$

At the solid-liquid interface Γ_η , describing the channel bed assumed to be fixed ($x_3 = \eta(x_1, x_2)$), we impose the conditions of vanishing normal velocity, i.e., a no flux condition (*boundary impermeability*) as well as vanishing tangential velocity (*no slip*), hence we write:

$$\mathbf{v}|_\eta = 0, \quad (12)$$

where the notation $f|_\eta$ implies that the quantity $f(x_3)$ is computed in $x_3 = \eta$. Furthermore, the free surface Γ_H is defined by the equation

$$\mathcal{F}_H = x_3 - H(x_1, x_2, t) = 0 \quad (13)$$

and must be a *material surface*. This kinematical constraint leads to the following boundary condition:

$$\left. \frac{d\mathcal{F}_H}{dt} \right|_H = \left[-\frac{\partial H}{\partial t} - v_1 \frac{\partial H}{\partial x_1} - v_2 \frac{\partial H}{\partial x_2} + v_3 \right]_H = 0, \quad (14)$$

This constraint is equivalent to stating that:

$$\mathbf{v}|_H \cdot \hat{\mathbf{n}}_H = V_H. \quad (15)$$

⁴ Let us first prove the identity:

$$[\mathbf{v} \cdot \nabla \mathbf{v}]_i = v_l v_{i,l} = \left[\nabla \frac{\mathbf{v}^2}{2} - \mathbf{v} \times \boldsymbol{\omega} \right]_i = v_m v_{m,i} - \delta_{ijk} v_j \omega_k = v_m v_{m,i} - \delta_{ijk} \delta_{kmn} v_j v_{n,m}$$

where we have employed the notation: $f_{,i} \equiv \partial f / \partial x_i$. The two Ricci tensors appearing in this expression satisfy a very important identity that proves useful at this stage:

$$\delta_{ijk} \delta_{kmn} = \delta_{kij} \delta_{kmn} = \delta_{im} \delta_{jn} - \delta_{in} \delta_{jm}$$

Substituting the latter identity into the previous relationship one finds:

The second step consists of proving the second identity:

$$\begin{aligned} [\mathbf{v} \cdot \nabla \mathbf{v}]_i &= v_m v_{m,i} - v_n v_{n,i} + v_m v_{i,m} = v_m v_{i,m} \\ \nabla \times (\mathbf{v} \cdot \nabla \mathbf{v}) &= -\nabla \times (\mathbf{v} \times \boldsymbol{\omega}) = \mathbf{v} \cdot \nabla \boldsymbol{\omega} - \boldsymbol{\omega} \cdot \nabla \mathbf{v} \end{aligned}$$

In scalar terms we need to show that:

$$[\nabla \times (\mathbf{v} \cdot \nabla \mathbf{v})]_i = -\delta_{imn} [-\mathbf{v} \times \boldsymbol{\omega}]_{n,m} = -\delta_{imn} \delta_{njk} (v_j \omega_k)_{,m}$$

Using the previous identity on products of Ricci tensors and the continuity equations for incompressible fluids ($v_{m,m} = \omega_{m,m} \equiv 0$), one finds:

$$[\nabla \times (\mathbf{v} \cdot \nabla \mathbf{v})]_i = -v_i \omega_{m,m} - v_{i,m} \omega_m + v_{m,m} \omega_i + v_m \omega_{i,m} = -v_{i,m} \omega_m + v_m \omega_{i,m} = [\mathbf{v} \cdot \nabla \boldsymbol{\omega} - \boldsymbol{\omega} \cdot \nabla \mathbf{v}]_i$$

This completes the proof.

Here, V_H is the velocity of the free surface that is defined as follows:

$$V_H = -\frac{\frac{\partial \mathcal{F}_H}{\partial t}}{|\nabla \mathcal{F}_H|}, \quad (16)$$

and $\hat{\mathbf{n}}_H$ is the unit vector locally normal to the free surface, which reads:

$$\hat{\mathbf{n}}_H = \frac{\nabla \mathcal{F}_H}{|\nabla \mathcal{F}_H|}. \quad (17)$$

Hence, (14) is physically equivalent to the continuity requirement that the free surface must be impermeable to fluid particles such that *the normal component of the fluid velocity at the free surface equals the velocity of the free surface*.

The free surface is also stress-free to the extent that air motion has negligible effects, hence:

$$\hat{\boldsymbol{\tau}}_1 \cdot \mathbf{t}|_H = \hat{\boldsymbol{\tau}}_2 \cdot \mathbf{t}|_H = \hat{\mathbf{n}}_H \cdot \mathbf{t}|_H = 0. \quad (18)$$

Here, $\mathbf{t}|_H$ is the stress vector acting at the free surface ($\equiv \mathbf{T}|_H \cdot \hat{\mathbf{n}}_H$). Moreover, $\hat{\boldsymbol{\tau}}_1$ and $\hat{\boldsymbol{\tau}}_2$ are unit vectors in the plane locally tangent to the free surface orthogonal to each other. Finally, curvature of the free surface is assumed small enough for surface tension to have negligible effect.

A prescribed velocity vector is usually imposed at the inflow boundary Γ_{in} :

$$\mathbf{v}|_{\Gamma_{in}} = \mathbf{v}_{in}. \quad (19)$$

Exact conditions to be applied at an outflow planar boundary Γ_{out} have been derived by Gresho (1991) and Sani and Gresho (1994). However these conditions are expressed in terms of the distributions of the forces acting on the outflow surface. As such information is usually unavailable, those conditions can hardly be implemented.

Alternatively, the so called natural outflow or *do nothing* boundary conditions (Heywood *et al.*, 1994) can be used, as well as periodic conditions as discussed in John (2016).

The above initial-boundary value formulation poses a formidable mathematical problem for which no general solution is known. Even its existence and uniqueness have not been mathematically ascertained in general (www.claymath.org/millennium-problems). In particular, the difficulty arises for relatively low viscosity fluids (for water $\nu \simeq 10^{-6} \text{ m}^2/\text{s}$) flowing with large speeds. Exact solutions of the Navier Stokes equations have been found for simple or idealized geometries of the flow domain and strictly unidirectional flow conditions (e.g. ducts, channels, half-space bounded by a wall). However, even these solutions have limited use as they are stable only under relatively slow flow conditions. As the velocity exceeds some threshold value, the exact solution becomes unstable and a sequence of increasingly irregular flow patterns develop, until the flow regime changes from laminar to turbulent.

2.2. Turbulent flows

Fluid flows of relevance to engineering and geophysics are most often *turbulent*. In particular, fluvial streams are typically characterized by values of the mean longitudinal velocity $u \sim \mathcal{O}(1 \text{ m/s})$ and characteristic length scales ℓ (say the flow depth) falling in the range 1 – 10 m. Hence, the Reynolds number

$$R_\ell = \frac{u \ell}{\nu} \quad (20)$$

attains typical values in the range $10^6 - 10^7$, for which flow conditions are invariably *turbulent*.

2.2.1 General features of turbulence

Turbulence is a major ubiquitous feature of fluid motions characterized by at least one of the following properties: high fluid speed, low fluid viscosity, large spatial scale of the flow region. All

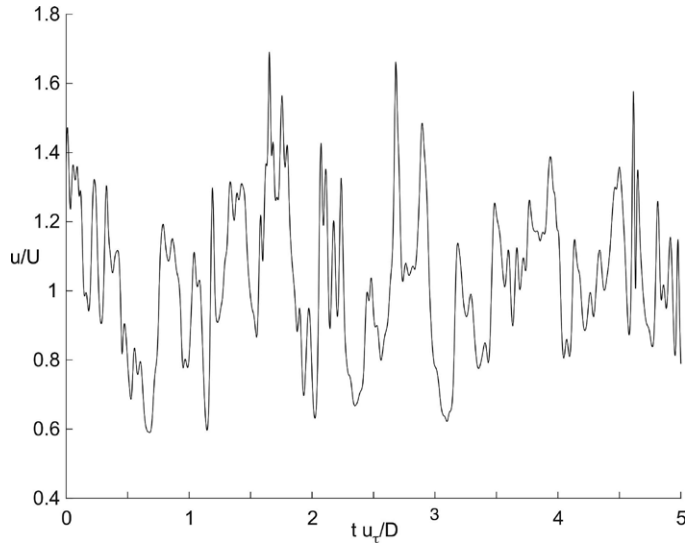


Figure 5. A typical turbulent signal.

these features are typical of the flow of water in a fluvial stream.

Turbulence can be superficially associated with disorder or irregularity of the flow characteristics both in time and in space (see a typical turbulent signal in Figure 5). More precisely, the turbulent syndrome displays itself through a number of typical features: unpredictability, a wide range of spatial scales and an enhancement of exchange processes (Lesieur, 1997).

- *Unpredictability*

This property arises from the fact that two flows starting from initial conditions very close to each other exhibit quite distinct temporal evolutions. Hence, a small uncertainty in the initial conditions is so strongly amplified as to render detailed predictions unfeasible.

- *Wide range of spatial scales*

The second distinct feature of turbulent motions is the presence of a wide range of spatial and temporal scales and leads to the classical picture of turbulent flows as the superposition of ‘eddies’ of variable sizes (see, e.g. Figure 6), defining a continuous distribution of scales of motion. The largest eddies have sizes comparable with the characteristic length scale ℓ of the flow (e.g. the average depth in open channel flows).

- *Enhancement of exchange processes*

The third feature is the strong *enhancement of exchange processes*: turbulent flow exchange matter, momentum and heat at a much faster rate than viscous flows. Increased rate of momentum exchange leads to enhanced dissipation of turbulent flows but it also delays separation of boundary layers, thus decreasing drag of bluff bodies. Similarly, increased rate of heat exchange enhances heat loss but it also makes heat transfer more efficient.

The latter feature may be conveniently interpreted in terms of a comparison between molecular and eddy diffusivities. Let u be a velocity scale characteristic of large eddies (say the root mean square amplitude of the velocity fluctuations in the flow). We can then define a time scale of large eddies as ℓ/u and a scale for the *eddy diffusivity* of turbulent flows as $u\ell$. The effectiveness of large turbulent eddies in enhancing exchange processes may be appreciated noting that the time required for molecular transport processes to spread over a region of spatial scale ℓ is of order ℓ^2/\mathfrak{D} , where \mathfrak{D} denotes the kinematic molecular diffusivity of the

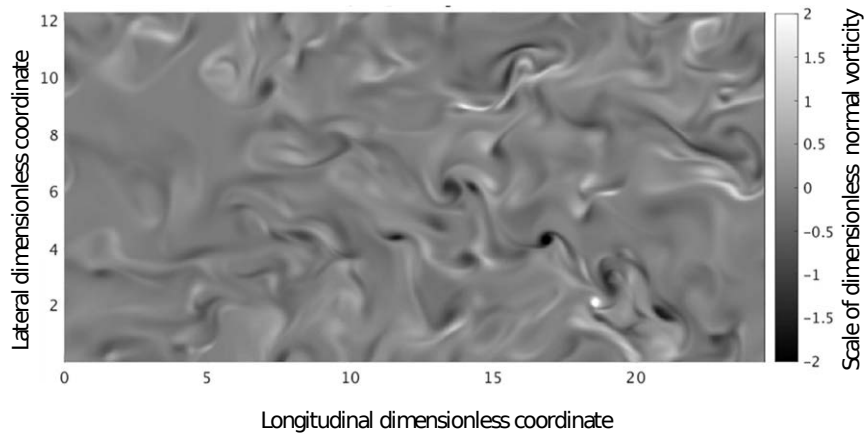


Figure 6. Coherent structures in a turbulent flow. The image refers to an oscillatory flow, approximating the flow generated by a small amplitude sea wave close to a bottom consisting of spherical particles free to move (Mazzuoli *et al.*, 2019). Coherent structures are visualized on a horizontal plane at a small distance from the bottom, by the normal component of the flow vorticity. The snapshot is taken at an instant close to the peak of the wall velocity. Coordinates are scaled by $\sqrt{\nu T/\pi}$, with T wave period (courtesy of Marco Mazzuoli).

transported quantity, i.e. the kinematic viscosity ν for momentum transport or the thermal diffusivity \mathfrak{D}_t for heat transport. Hence, the Reynolds number $R_\ell \equiv u\ell/\nu$ may be interpreted as the ratio between eddy and molecular diffusivities or between the time scales of turbulent and molecular transport of momentum. In rivers and estuaries, typical values for u and ℓ are around 0.1 m/s and 10 m respectively, hence a typical scale for the eddy diffusivity $u\ell$ is 10^6 times larger than the kinematic viscosity ν , i.e. turbulent exchange processes occur at a rate which is roughly 6 orders of magnitude larger than molecular processes.

2.2.2 The energy cascade

We have seen that one striking feature of turbulence is its dissipative nature. But what mechanism controls the rate of energy dissipation? The answer to this important question came from the notion of *energy cascade* put forward by Richardson (1922) and developed twenty years later in the fundamental work of Andrei Kolmogorov (Kolmogorov, 1941), an outstanding Russian mathematician.

The picture arisen from those investigations (and a number of later works) may be summarized as follows. Essentially, one must recognize that eddies do not live independently of each other. Nonlinear interactions due to convective inertia lead to a continuous interaction among eddies of all scales, whereby energy is statistically directed from the nearly inviscid largest scales, which store energy extracted from the mean flow, towards the smallest scales which adjust their sizes so as to make viscous effects effective in dissipating energy into heat.

The 'width' of the range of scales characterizing a specific turbulent flow and the size of the smallest eddies were estimated by Kolmogorov by means of a theory based on few assumptions valid at large Reynolds numbers.

The first assumption states that the motion at the microscale is *statistically isotropic*: hence, the memory of large scale features is lost along the cascade process.

The second assumption postulates that the statistics of the small-scale motion has 'universal' features, determined only by the rate ϵ at which energy is dissipated per unit fluid mass and by the fluid kinematic viscosity ν . On purely dimensional grounds, the sizes of the smallest scales, called *Kolmogorov microscales*, are then found to read (Kolmogorov, 1941):

$$\ell_k = (\nu^3/\epsilon)^{1/4}, \quad \tau_k = (\nu/\epsilon)^{1/2}, \quad v_k = (\nu\epsilon)^{1/4}, \quad (21a,b,c)$$

where ℓ_k, τ_k and v_k define spatial, temporal and velocity microscales, respectively. Under the additional assumption that production balances dissipation, we can relate ℓ_k, τ_k and v_k to the corresponding scales of large eddies (also called *integral scales*) by estimating the rate of energy dissipation per unit mass ϵ as the ratio between a measure of kinetic energy of large scale motion (say u^2 per unit mass) and a measure of the lifetime of large eddies (say ℓ/u). Hence:

$$\epsilon \sim \frac{u^3}{\ell}, \quad (22)$$

resulting in the scalings

$$\frac{\ell_k}{\ell} \sim R_\ell^{-3/4}, \quad \frac{\tau_k}{\ell/u} \sim R_\ell^{-1/2}, \quad \frac{v_k}{u} \sim R_\ell^{-1/4}. \quad (23a,b,c)$$

The latter relations suggest that the smallest eddies increasingly reduce their sizes as the Reynolds number of the flow increases. In natural streams with $R_\ell \sim 10^6$, ℓ_k is typically smaller than 1 mm, τ_k ranges about 0.1 s and v_k does not exceed a few mm/s. Note that ℓ_k is comparable with the typical size of particles that are carried in suspension by river flow.

Finally, the third assumption concerns the statistics of motions of eddies of scale ℓ_i in the so called *inertial subrange* such that $\ell_k \ll \ell_i \ll \ell$: Kolmogorov (1941) assumed that this statistics has a universal form determined only by ϵ and ℓ_i , i.e. is independent of ν . We do not derive here the consequences of the latter assumption, and refer the interested reader to standard textbooks on turbulence (Monin and Yaglom, 1971; Frisch, 1995; Pope, 2000).

2.2.3 Investigating turbulent flows

The two major techniques employed to investigate the complex spatial-temporal structure of turbulent flows have relied on some important modern technological developments. On one hand, physical experiments have become feasible with the tremendous development of experimental techniques evolved from hot wire anemometry (around 1970) to hot film and, more recently, laser doppler anemometry and acoustic doppler velocimeters, which enable one to measure high frequency turbulent fluctuations with great accuracy and efficiency. On the other hand, numerical simulations have progressively acquired an increasing role owing to the fast and huge development of computational facilities. *Direct Numerical Simulation* (DNS), *Large Eddy Simulation* (LES) and numerical computations based on the *Reynolds Averaged Navier-Stokes* (RANS) equations are widespread tools presently used to study turbulent flows at the various scales. More recently, an attempt has also been made to combine LES and RANS, through the so called *Detached eddy simulation* (DES) approach, aimed at treating efficiently problems in which the boundary layer separates massively. We refer the interested reader to Spalart (2009) and Keylock *et al.* (2012) for thorough reviews of the latter subject. Below, we limit ourselves to outline the other three approaches commonly used to investigate turbulent flows.

- *Direct numerical simulation* is a deterministic approach that consists of solving numerically the full time-dependent Navier-Stokes equations with appropriate initial and boundary conditions (see, e.g. Hirsch, 2007). Averaging the numerical output then allows one to obtain the mean

quantities (fluid velocity, fluid stresses, etc.) of direct practical relevance. This technique is increasingly employed in the literature, though the enormous computational effort it requires limits its applicability to simple geometries and flows at relatively low Reynolds numbers, far from the range significant for geophysical applications. This limitation is a direct consequence of the wide range of scales present in turbulent motions (Moin and Mahesh, 1998). Since DNS solves all scales of motion, the number of grid points in each direction is proportional to the ratio between the largest and the smallest eddy in the flow. This ratio is proportional to the Reynolds number $R_\ell^{3/4}$ based on the integral scale ℓ . Thus, the number of points in three dimensions is $\propto R_\ell^{9/4}$. Although it is hard to expect that, in the near future, DNS will become a feasible practical tool at the values of R_ℓ characteristic of natural flows, however DNS is an important research tool, helping to gain insight into turbulence physics and improve simplified models of practical relevance. It is essentially a numerical experiment with no limitation of the kind present in laboratory experiments, where the probe has a finite size, measurements cannot be performed too close to a wall, etc.

- *Large Eddy simulation* is a technique intermediate between DNS and RANS. It represents a weaker form of DNS, whereby the large, energy-carrying eddies are simulated deterministically while the small sub-grid scales are modelled and, hence, influence statistically the large-scale motion (see, e.g. Lesieur and Metais, 1996; Metais, 2002). In particular, the evolution equations for the large scales are obtained by filtering the Navier-Stokes equations through a proper low-pass filter that eliminates the small scales (Figure 7). As a consequence, large scales are still characterized by an intense spatio-temporal variability. Note that the small sub-grid scales tend to be more isotropic and homogeneous than the large scales, thus justifying the use of more general closure models. Furthermore, the stresses modeled at the sub-grid scale provide a relatively small contribution to the total turbulent stresses. Despite the filtering of small scales, the computational costs are still quite high. In these types of flows the coherent structures that arise close to a solid wall are of fundamental importance for turbulence dynamics and methods to bypass the problem of fully resolving these eddies at a reasonable cost are thus required (see, e.g. Piomelli and Balaras, 2002). Attempts in this direction have recently appeared (see the reviews by Stoesser, 2014; Sotiropoulos, 2019).

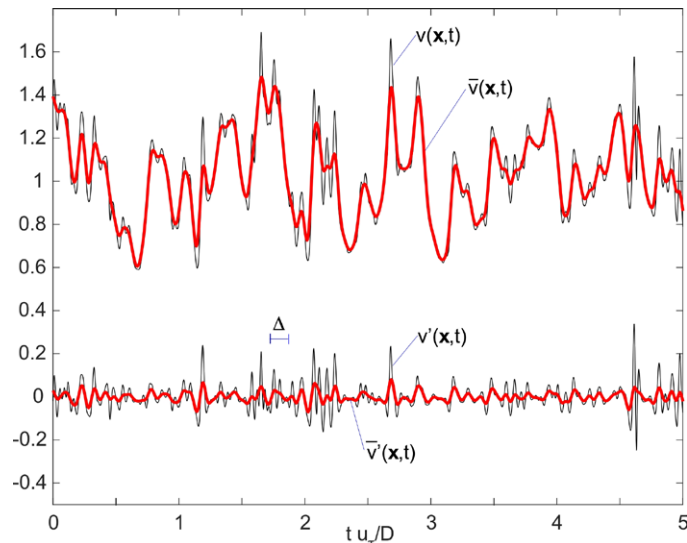


Figure 7. An example of 1D instantaneous velocity field $v(x;t)$ (thin, black) and its 1D filtered form $\bar{v}(x;t)$ (bold, red) obtained with the help of a Gaussian filter are plotted and compared with the associated residual field $v'(x;t)$ (thin, black) and its filtered form $\bar{v}'(x;t)$ (bold, red).

- *The Reynolds Averaged Navier-Stokes Equations* are obtained by averaging over the turbulence

the Navier-Stokes equations (see Section 2.2.4) to yield a set of transport equations for the averaged momentum. This fundamental idea stems from the cornerstone approach originally proposed by Reynolds (1895) and has produced a widespread body of knowledge. As discussed in the next Section, averaging generates a set of new unknowns that require a *closure* able to account in some parametric form for the effects of the flow scales that have been removed by averaging. In principle, the effects of all the scales of motion are modelled, but no universal model has been found for all types of flows: suitable adjustments of the model constants are needed, depending on the specific features of the flow field to be simulated (Wilcox, 1993). In general, RANS are effective in simulating statistically steady flows or flows characterised by statistical properties which vary slowly with time (i.e., on a characteristic time scale much larger than the turbulent time scale). Since RANS equations involve statistical quantities, their solution requires temporal and spatial discretizations much coarser than those necessary for DNS or even LES. They are therefore applicable to extended flow domains with complex geometries, as those typical of rivers. We will thus base our treatment of open channel morphodynamics on the information provided by the RANS approach.

The *complementary nature* of experiments and computations in turbulence research is clearly exemplified by the study of *coherent structures* characterizing wall turbulence. The idea of the existence of distinctly recognizable organized motions in wall turbulence was first suggested by Theodorsen (1952), followed by Townsend (1976). The presence of fundamental turbulent structures as hairpin vortices was later on confirmed by detailed experimental observations and DNS simulations (Figure 8). These coherent structures are strictly linked to the so called *bursting cycle*, whereby *ejections* of low-speed fluid outward from the wall are followed by *sweep* of high-speed fluid toward the wall (see, e.g. Pope, 2000). In particular, experimental observations (Head and Bandyopadhyay, 1981), LES simulations (Moin and Kim, 1982) and DNS simulations (Kim *et al.*, 1987) have clearly shown that each bursting process arises from the roll up of initial structures consisting of sheets of transverse vorticity and leads to the formation of a hairpin vortex.

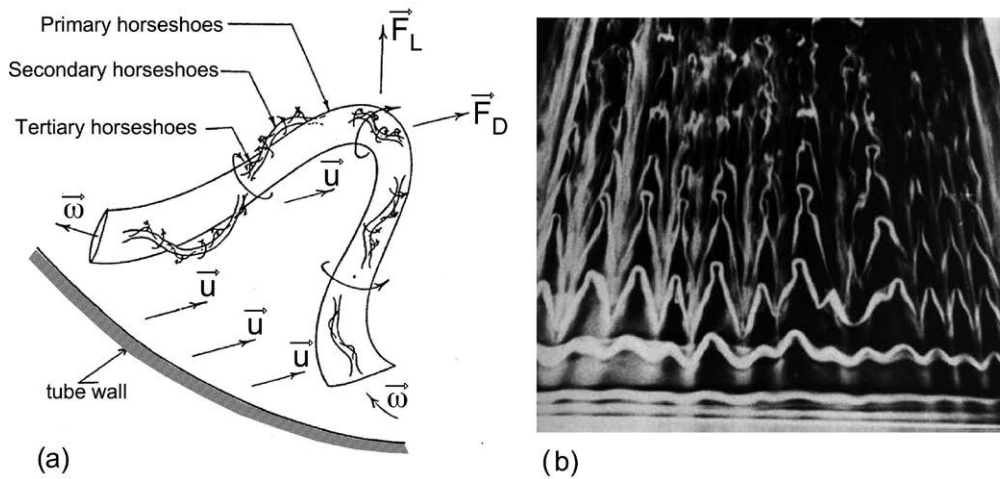


Figure 8. (a) The sketch of Theodorsen (1952), suggesting that the fundamental structure of wall turbulence consists of horseshoe (hairpin) vortices (modified from Panton, 2001); (b) Hairpin vortices created by a boundary layer trip wire using smoke in air, flow is from bottom to top (reproduced from Figure 3 of Perry *et al.*, 2007, accessed under the terms of the Creative Commons CC BY license).

The burst cycle, in turn reflects the statistical distribution of velocity fluctuations. Indeed, sweep events are characterized by positive values of the fluctuation of longitudinal velocity (v'_x) and negative values of the fluctuation of vertical velocity (v'_z), i.e. they are events of the fourth quadrant in the (v'_x, v'_z) plane, while ejections belong to the second quadrant ($v'_x < 0, v'_z > 0$), as represented schematically in Figure 9.

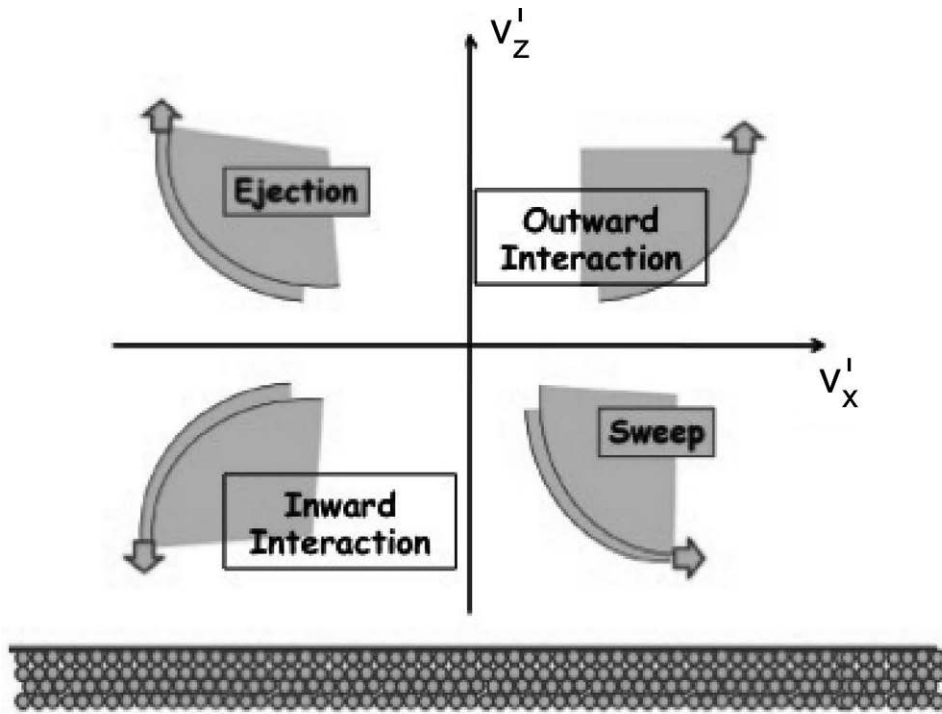


Figure 9. Sketch describing the various types of wall events in the plane of horizontal (v'_x) and vertical (v'_z) turbulent velocity fluctuations.

The sign of the product ($v'_x v'_z$) plays a major role in wall turbulence, as turbulent fluctuations contribute significantly to momentum exchange. A positive v'_z associated with a negative v'_x identifies the transport of negative momentum from a lower layer to a faster upper layer and vice versa. As it will be explained in Section 2.2.4, when averaging the momentum equation over the turbulence, momentum exchange driven by turbulent fluctuations is a mechanism that produces additional effective stresses, known as *Reynolds stresses*, which sum to viscous stresses generated by molecular diffusion. Both sweeps and ejections contribute to generating positive Reynolds stresses, implying increasing turbulence production and drag, whereas first and third quadrant events contribute to negative Reynolds stresses. Importantly, most of the production of turbulent energy near the wall (nearly 70%), is strictly correlated with the bursting process (Kim *et al.*, 1971; Wallace, 1985). Also, note that, very close to the wall, sweep events prevail over ejection events, while farther from the wall ejections dominate.

Wall roughness may clearly exert a significant role on bursting dynamics. The experimental measurements carried out by Nezu and Nakagawa (1993) revealed the persistence of high and low speed structures also in the presence of hydraulically rough wall conditions. On the other hand, the numerical calculations of Choi *et al.* (1993), referring to the role of riblets in drag reduction, showed that the effect of the roughness may be strictly dependent on the size of roughness elements compared with the size of wall longitudinal vortices.

The above picture immediately suggests the relevance of turbulent coherent structures for a deep understanding of the mechanics of sediment transport. Attempts to extend the use of numerical simulations to include the presence of solid particles transported by the turbulent flow stream have been proposed in the recent literature (Schmeeckle, 2014). As it will be discussed in Chapter 3, these analyses suffer from obvious restrictions due to a number of difficulties encountered when one attempts to simulate particle motion in a neighbourhood of walls, including the need to

account for the effects of particle-particle and particle wall interactions. This notwithstanding, this research tool may help assessing the limits of the available semi-empirical approaches to sediment transport widely employed by engineers and geomorphologists.

The morphodynamic problems we are going to treat in this Monograph invariably involve wall bounded turbulent flows with complex geometries and large spatial domains. Moreover, they refer to statistically steady flows or flows varying on a time scale much larger than that of turbulence. As discussed above, under these conditions, the RANS approach provides sufficiently robust information with reasonable mathematical and computational efforts. In the remaining of this chapter we will use the RANS approach to derive the depth-averaged shallow water equations and the cross-sectionally averaged de Saint-Venant equation which will be extensively exploited throughout this Monograph to investigate the morphodynamics of river meandering.

2.2.4 The Reynolds averaged formulation for turbulent flows

The rationale behind a statistically averaged approach to Navier-Stokes equations is the assumption that a turbulent flow field can be treated as a *stochastic process*. Hence, the problem of predictability takes a weaker form: one simply assumes that the *probability distributions* of quantities which characterize turbulent motions are *predictable* once the external controllable parameters of the flow are fixed. The knowledge of only few average properties of the flow field, namely the *mean* and the *second moments* (also called *correlations*) are usually sufficient for most practical purposes.

We define the *mean* velocity $\langle v_j \rangle$ at location (\mathbf{x}, t) in the form of the probabilistic average:

$$\langle v_j \rangle = \int_{-\infty}^{\infty} v_j p(v_j) dv_j \quad (j = 1, 2, 3), \quad (24)$$

where $p(v_j)$ is the probability density function of the variable v_j .

Similarly, the spatial-temporal second-order correlation between v_i at (\mathbf{x}, t) and v_j at $(\mathbf{x} + \delta\mathbf{x}, t + \delta t)$ reads

$$R_{ij}(\mathbf{x}, t; \delta\mathbf{x}, \delta t) = \langle v_i(\mathbf{x}, t) v_j(\mathbf{x} + \delta\mathbf{x}, t + \delta t) \rangle. \quad (25)$$

The correlation (24) becomes a purely spatial correlation if δt vanishes and a temporal correlation if $\delta\mathbf{x}$ vanishes.

The stochastic approach is further simplified if one assumes that the process is *stationary* and *ergodic*. The former condition implies that all the statistical properties of the stochastic process do not change if the initial time is changed. Ergodicity of a stationary process implies that one can safely replace the probabilistic average of any quantity (e.g. $\langle v_j \rangle$) with a corresponding time average, hence:

$$\langle v_j \rangle = \lim_{T \rightarrow \infty} \frac{1}{T} \int_{-T/2}^{T/2} v_j(\mathbf{x}, t) dt. \quad (26)$$

The so called *ergodic theorem* (Monin and Yaglom, 1971, pg. 251) establishes a necessary and sufficient condition for ergodicity which, in physical terms, is equivalent to the requirement that the characteristics of the process at two instants t and $t + \tau$ become progressively less correlated as τ tends to infinity. In other words the flow must lose memory of its past as time progresses. The above condition is assumed to be valid for turbulent flows on a purely intuitive basis.

The latter assumption is at the base of the so called *Reynolds averaging* models. At each point and time instant the flow is described in terms of first and second order moments, i.e. the mean velocity, the mean pressure and the so-called Reynolds stresses, as discussed below. This type of models is widely adopted in the study of strongly inhomogeneous, high Reynolds number, turbulent flows confined by rough walls with fairly complex geometries. This is the case of the natural environments of interest for the present Monograph. We then proceed to formulate the Reynolds averaged form of the governing equations.

2.2.5 The RANS equations

Following Reynolds (1895) let us decompose the local instantaneous flow field as follows

$$v_i = u_i + v'_i \quad (i = 1, 2, 3), \quad p = P + p', \quad (27a,b)$$

where

$$u_i = \langle v_i \rangle, \quad \langle v'_i \rangle = 0, \quad (28a,b)$$

$$P = \langle p \rangle, \quad \langle p' \rangle = 0. \quad (29a,b)$$

The equations governing the mean flow field (\mathbf{u}, P) are then readily derived by applying the averaging procedure to the Navier-Stokes and continuity equations (3), (4). The averaging operator satisfies the following conditions

$$\langle \mathcal{L}f \rangle = \mathcal{L}\langle f \rangle, \quad \langle fg \rangle = \langle f \rangle \langle g \rangle + \langle f'g' \rangle, \quad (30a,b)$$

where \mathcal{L} is any linear differential operator (e.g. $\frac{\partial}{\partial t}$, $\frac{\partial}{\partial x_j}$, $\frac{\partial^2}{\partial x_j \partial x_j}$). Note that (30) follow immediately from (27, 28, 29).

Using (30) the continuity equation (3) can be averaged to give

$$\nabla \cdot \mathbf{u} = \frac{\partial u_j}{\partial x_j} = 0. \quad (31)$$

Hence, the mean velocity vector is divergence free (i.e. solenoidal). It follows from (3), (31) and (28) that the instantaneous velocity fluctuations must also be divergence free.

Averaging the Navier-Stokes equations leads to the so called *Reynolds equations*, which read:

$$\frac{D\mathbf{u}}{Dt} = \frac{\partial \mathbf{u}}{\partial t} + \mathbf{u} \cdot \nabla \mathbf{u} = -\frac{1}{\rho} \nabla P - g \hat{\mathbf{x}}_3 + \nu \nabla^2 \mathbf{u} + \frac{1}{\rho} \nabla \cdot \mathbf{T}^t, \quad (32a)$$

or, in scalar form

$$\frac{\partial u_i}{\partial t} + u_j \frac{\partial u_i}{\partial x_j} = -\frac{1}{\rho} \frac{\partial P}{\partial x_i} - g \delta_{i3} + \nu \frac{\partial^2 u_i}{\partial x_j^2} + \frac{\partial}{\partial x_j} (-\langle v'_i v'_j \rangle). \quad (32b)$$

In (32a) we denote by D/Dt the material derivative associated with the mean flow, while \mathbf{T}^t is the Reynolds stress tensor defined in the form

$$T_{ij}^t = -\rho \langle v'_i v'_j \rangle. \quad (33)$$

Reynolds stresses arise from the nonlinearity of convective terms of Navier-Stokes equations. The exchange of momentum due to turbulent fluctuations is effectively a diffusion process (turbulent diffusion) similar to molecular diffusion, but with a much larger rate (see, e.g. Fisher *et al.*, 1979).

In conclusion, Reynolds equations involve the mean components of the flow field which exhibit a behavior far more regular than their instantaneous components. However, they also involve a new set of unknowns, the six components of the symmetric Reynolds tensor, which pose the well known *closure problem*, namely the need to derive further equations relating the new unknowns to the mean flow field (see, e.g. Wilcox, 1993).

2.2.6 Boundary conditions for the RANS equations

Reynolds averaging the boundary conditions and ignoring the turbulent fluctuations of free surface elevation ($\langle H \rangle = H$), the following averaged forms of conditions (14) and (18) are obtained.

- *Kinematic boundary conditions.*

At the free surface:

$$\left. \frac{D\mathcal{F}_H}{Dt} \right|_H = \left[\frac{\partial \mathcal{F}_H}{\partial t} + \mathbf{u} \cdot \nabla \mathcal{F}_H \right]_H = 0, \quad (34)$$

or, recalling the definition (13):

$$\left[-\frac{\partial H}{\partial t} - u_1 \frac{\partial H}{\partial x_1} - u_2 \frac{\partial H}{\partial x_2} + u_3 \right]_H = 0. \quad (35)$$

Close to solid boundaries the complexity of turbulent flows is circumvented by imposing the *no slip condition* at some conventional distance ($x_3 = \eta_0$) empirically defined (see Section 2.3.4). Hence:

$$u_1|_{\eta_0} = u_2|_{\eta_0} = u_3|_{\eta_0} = 0. \quad (36)$$

- *Dynamic boundary conditions.*

The dynamic boundary condition at the free surface states that the stress vector must vanish (in the absence of any external stress, e.g. forced by wind action):

$$\mathbf{t}|_H = [(-P \mathbf{I} + \mathbf{T}^t + \mathbf{T}^\mu)_H \cdot \hat{\mathbf{n}}_H] = 0, \quad (37)$$

where $\mathbf{T}^\mu = 2\mu\langle \mathbf{D} \rangle$ are the turbulence averaged viscous stresses. Recalling (17) one finds:

$$\hat{n}_{H1} = -\frac{\partial H / \partial x_1}{|\nabla \mathcal{F}_H|}, \quad \hat{n}_{H2} = -\frac{\partial H / \partial x_2}{|\nabla \mathcal{F}_H|}, \quad \hat{n}_{H3} = \frac{1}{|\nabla \mathcal{F}_H|}, \quad (38a,b,c)$$

where

$$|\nabla \mathcal{F}_H| = \sqrt{1 + \left(\frac{\partial H}{\partial x_1} \right)^2 + \left(\frac{\partial H}{\partial x_2} \right)^2}. \quad (39)$$

Noting that far from solid boundaries viscous stresses are in general much smaller than turbulent stresses, the dynamic boundary conditions in scalar form are eventually written as:

$$t_1|_H = \left[(P - T_{11}^t) \frac{\partial H}{\partial x_1} - T_{12}^t \frac{\partial H}{\partial x_2} + T_{13}^t \right]_H = 0, \quad (40a)$$

$$t_2|_H = \left[-T_{21}^t \frac{\partial H}{\partial x_1} + (P - T_{22}^t) \frac{\partial H}{\partial x_2} + T_{23}^t \right]_H = 0, \quad (40b)$$

$$t_3|_H = \left[-T_{31}^t \frac{\partial H}{\partial x_1} - T_{32}^t \frac{\partial H}{\partial x_2} + (-P + T_{33}^t) \right]_H = 0. \quad (40c)$$

The conditions to be applied at open inflow/outflow boundaries are in principle similar to those discussed for the Navier-Stokes equations. A velocity profile is usually defined at the inlet to provide a certain inflow discharge, while natural outflow (i.e. do nothing) conditions can be applied at the outlet. However, the presence of additional Reynolds stresses implies that turbulent quantities have also to be prescribed at open boundaries, depending on the closure model adopted to express them as a function of turbulence averaged velocities.

Finally, the initial state of the system must be prescribed:

$$(u_1, u_2, u_3, P) = (u_{10}, u_{20}, u_{30}, P_0)(x_1, x_2, x_3), \quad H = H_0(x_1, x_2) \quad (t = 0). \quad (41a,b)$$

2.2.7 Transport equation for the mean vorticity

We have seen that one of the distinctive features of turbulent flows is to enhance the exchange processes. Transport equations must then be available to assess the dynamics of the various quantities characterizing a turbulent flow. A special role is played by the transport equations of turbulent kinetic energy as well as energy dissipation and Reynolds stresses. We do not pursue their derivation here, but the reader must be aware that those transport equations are major ingredients of advanced turbulent modeling (see, e.g. Wilcox, 1994) that may be needed in some morphodynamic problems. Here, we limit ourselves to the transport equation for the mean vorticity, that will be seen to help understanding the mechanism of generation of secondary flows in curved channels.

Let us perform the Reynolds decomposition of vorticity:

$$\boldsymbol{\omega} = \boldsymbol{\Omega} + \boldsymbol{\omega}'. \quad (42)$$

Reynolds averaging the vorticity equation (10) then allows us to derive a transport equation for the mean vorticity, that reads:

$$\frac{D\Omega_i}{Dt} = \frac{\partial\Omega_i}{\partial t} + \underbrace{u_j \frac{\partial\Omega_i}{\partial x_j}}_{\text{mean transport}} = \underbrace{\Omega_j \frac{\partial u_i}{\partial x_j}}_{\text{mean distortion}} + \underbrace{\nu \nabla^2 \Omega_i}_{\text{viscous diffusion}} - \underbrace{\frac{\partial\langle v'_j \omega'_i \rangle}{\partial x_j} + \frac{\partial\langle v'_i \omega'_j \rangle}{\partial x_j}}_{\text{turbulent transport}}. \quad (43)$$

Hence, changes of the local value of the mean vorticity arise from its transport by the mean velocity field as well as by the average effect of the transport of vorticity fluctuations by the fluctuations of the velocity field. The mean vorticity intensifies as the vortex lines of the mean vorticity field undergo extension and twisting. Finally, the mean vorticity is dissipated by molecular viscosity.

2.2.8 The closure problem

Reynolds stresses T_{ij}^t may be considered as generally determined by the global history of the mean-velocity field with assigned initial and boundary conditions. However, seeking a closure relationship fully accounting for the latter feature is not feasible.

Some progress is made adopting the fundamental simplifying assumption of the so called *one point closure schemes*: the turbulence at each location (in space and time) may be characterized by a *single spatial and temporal scale*. This is an obvious simplification, given the wide spectrum of scales which is known to be excited by turbulence. However, in spite of their strongly simplified nature, these closures prove quite useful: indeed, all such models are semi-empirical in nature and may be described as 'post-dictive' in that their success is ultimately determined by the 'ad hoc' tuning of empirical ingredients such to reproduce accurately particular classes of turbulent flows.

The origin of one point closure schemes may be traced back to Boussinesq (1877), who suggested the idea that a turbulent flow may be interpreted as a laminar flow with a greatly enhanced viscosity, called *eddy viscosity*. This idea was further pursued by Prandtl (1925), who introduced the concept of *mixing length*, i.e. the single spatial scale characteristic of turbulence at local level. Prandtl work represents the first successful attempt to predict the average properties of a turbulent shear flow on the basis of a phenomenological closure assumption. Various developments of the latter ideas arose from phenomenological, dimensional and statistical arguments through the work of great scientists, including Von Karman and Kolmogorov. But it was not until after 1970 that modeling could slowly develop into an actual computational tool. Closure models were then refined through the interaction of experimental and numerical investigations. A new line of thought was also pursued through the derivation of closure models on a rational basis (Lumley, 1970, 1978; Speziale, 1985, 1987, 1991), i.e. analyzing the formal consequences of various general constraints that any closure relationship must satisfy.

Boussinesq linear closure

A major outcome of these investigations was to provide some substantiation to the classical Boussinesq closure relationship which reads:

$$\frac{T_{ij}^t}{\rho} = 2\nu_T \langle D_{ij} \rangle - \frac{2}{3} \mathcal{K} \delta_{ij}, \quad (44)$$

where:

- $\nu_T(\mathbf{x}, t)$ is the so called (kinematic) *eddy viscosity*;
- $\langle D_{ij} \rangle$ is the Reynolds averaged *strain rate tensor* defined as follows:

$$\langle D_{ij} \rangle = \frac{1}{2} \left[\frac{\partial u_i}{\partial x_j} + \frac{\partial u_j}{\partial x_i} \right]; \quad (45)$$

- $\mathcal{K} = \langle v_i'^2 \rangle / 2$ is the *turbulent kinetic energy per unit mass*.

The reader will immediately recognize that the isotropic contribution $-\frac{2}{3} \rho \mathcal{K} \delta_{ij}$ may be regarded as a small correction of the mean pressure P needed in order to satisfy the identity $T_{ii}^t = -2\rho \mathcal{K}$. A strict analogy is thus established between the constitutive law of viscous incompressible fluids (2) and (44). However, differently from ν , that is a fluid property, the eddy viscosity is a flow property which characterizes the turbulence at the given location and at the given time.

In order to make any progress with (44) one needs to formulate an appropriate model to evaluate $\nu_T(\mathbf{x}, t)$. A large number of such models of increasing complexity has been developed in the engineering literature (Pope, 2000). A distinction can be made between *zero-equation models*, whereby ν_T is estimated on the basis of algebraic relations, and *N-equation models*, in which N additional equations are introduced to eventually estimate ν_T .

Zero-equation models

The simplest closure model for the eddy viscosity consists of simply assigning an appropriate algebraic expression to it. As already pointed out, the origin of this approach goes back to the classical notion of mixing length put forward by Prandtl (1925). For a two-dimensional shear flow, on pure dimensional ground one may write:

$$\nu_T = u_\tau \ell, \quad (46)$$

where u_τ is the *friction velocity* defined in terms of some relevant flow shear stress τ and ℓ is the mixing length scale.

Algebraic expressions for the length scale ℓ have been tested for a variety of free shear layers and wall bounded shear flows. In the former case a constant value of ℓ is found to be a good first approximation (Tennekes and Lumley, 1972; Wilcox, 1994). In the latter case, the length scale is in general a function of the distance from the wall, z . The simplest choice is to assume $\ell = kz$, as firstly proposed by Prandtl (1925), where k is known as *Von Karman constant*. Improvement of this relation includes the introduction of a multiplying function that damps the length scale as the wall is approached, yielding a better description of the Reynolds stresses in this region (Van Driest, 1956).

Generalizations of (46) to complex flow configurations have been proposed. In particular, the generalization of Smagorinsky (1963) has been widely employed for subgrid modeling in the context of large eddy simulation.

One- and two-equation models

The advantage of zero equation models is their numerical simplicity. Their drawbacks are the facts that the friction velocity is determined by the mean flow only and the mixing length scale is given a priori rather than being flow-dependent.

The former limit is overcome by one-equation models in which, taking advantage of the Kolmogorov-Prandtl relationship (Kolmogorov, 1942; Prandtl, 1945), the friction velocity is related linearly to the square root of the turbulent kinetic energy

$$u_\tau \propto \mathcal{K}^{1/2}. \quad (47)$$

Hence, according to relation (46), the local eddy viscosity ν_T becomes a function of a priori-assigned mixing length and of the local value of \mathcal{K} . The latter quantity is computed through the transport equation for the turbulent kinetic energy. This equation can be obtained by multiplying the Navier-Stokes equations by u'_j , taking the time average of all terms, and subtracting the equation which governs the kinetic energy of the mean flow (see, e.g. Tennekes and Lumley, 1972). The resulting partial differential equation states that the turbulent kinetic energy is produced by Reynolds stresses that extract energy from the mean flow, is dissipated by viscous stresses and transported by the mean flow and the turbulent fluctuations themselves (turbulent diffusion). A pressure-strain correlation also arises, which however does not contribute to variations of the turbulent kinetic energy, it simply leads to directional redistribution of Reynolds stresses. As for the Reynolds equations, nonlinear terms eventually arise that needs to be suitably expressed in terms of known quantities. Specifically, the production term is closed using the Boussinesq assumption for T_{ij}^t , the flux term is assumed to be proportional to the gradient of \mathcal{K} while the dissipation term is expressed algebraically in terms of \mathcal{K} and ℓ (see, e.g. Wilcox, 1994). Clearly, the resulting one-equation model has still a strong limitation: it is incomplete as the mixing length still needs to be assigned a-priori. As a consequence, one-equation models do not usually perform much better than zero equation models and are mainly suitable for shear layers.

Two equation models are still based on the Boussinesq assumption and express the eddy viscosity in terms of two turbulent quantities for which transport equations are derived. The advantage is that both the friction velocity and the turbulent length scale arise from the solution of the transport equations. Two of such models have enjoyed great popularity, namely the so-called \mathcal{K} - ε model (Launder and Spalding, 1974) and the \mathcal{K} - ω model (Kolmogorov, 1942; Saffman, 1970; Saffman and Wilcox, 1974), with its later modification (Wilcox, 2008). Here, ε is the rate of dissipation of turbulent kinetic energy per unit mass while the pseudo-vorticity ω has been interpreted as either "the rate of dissipation of energy in unit volume and time" (Kolmogorov, 1942) or "a frequency characteristic of the turbulence decay process under its self-interaction" (Saffman, 1970).

For the \mathcal{K} - ε model, dimensional arguments indicate that

$$\nu_T \propto \frac{\mathcal{K}^2}{\varepsilon}. \quad (48)$$

Transport equations are then needed for \mathcal{K} and ε . The transport equation for turbulent kinetic energy is identical with that employed in one-equation models. The exact transport equation for the specific turbulent dissipation rate is quite complex and poses a number of difficult closure problems. The classical approach is rather to conceive an artificial equation for a pseudo-dissipation rate, formulated in perfect analogy with the equation for \mathcal{K} , such to include convection, diffusion, production and dissipation terms. Experimental data and DNS simulations have been used to set the various proportionality coefficients appearing in the model. The reader interested in the details of the models are referred to Wilcox (1994), where appropriate boundary conditions are also discussed.

For the \mathcal{K} - ω model, dimensional arguments allow one to express the eddy viscosity as

$$\nu_T \propto \frac{\mathcal{K}}{\omega}. \quad (49)$$

Unlike the equation for the turbulent kinetic energy, that can be derived directly from the Reynolds equations, the equation for ω is only postulated by analogy with the turbulent kinetic energy equation. Also, in this model various supposedly universal constants appear. Some of them have been estimated using remarkably simple theoretical arguments (Saffman, 1970), while others rely on experimental data and/or the results of DNS simulations (see, e.g. Wilcox, 2008).

In general, the performance of the \mathcal{K} - ε closure model is qualitatively satisfactory for unseparated shear layers and high Reynolds number flows, even though extensions to the case of low Reynolds number have also been proposed (see, e.g. Rodi and Mansour, 1993). An important distinctive feature of the \mathcal{K} - ω model is that it allows for integration through the viscous sublayer to the wall. On the other hand, the \mathcal{K} - ω model turns out to be strongly sensitive to free-stream boundary conditions in free shear flows whereas the \mathcal{K} - ε model is insensitive.

A number of further two-equation models have been proposed both before and after the two most popular models discussed above. The reader is referred to specialized books (e.g. Wilcox, 1993; Pope, 2000; Durbin and Petterson Reif, 2011) for exhaustive reviews.

2.2.9 Wall-bounded flows: plane uniform turbulent flow

Understanding the nature of wall turbulence is a fundamental prerequisite of any morphodynamic theory. The relevant physical mechanisms whereby sediment particles are continuously transported by a fluvial stream and exchanged with the bed are in fact controlled by the fluid motion in the vicinity of the bed. Before we devote some specific attention to open channel flows, it is thus instructive to analyze the simplest, yet fundamentally important, case of plane uniform turbulent flow.

Let us consider the uniform turbulent flow in an open channel of infinite length and width (Figure 10), inclined by an angle θ to the horizontal. The uniform character of the turbulent flow

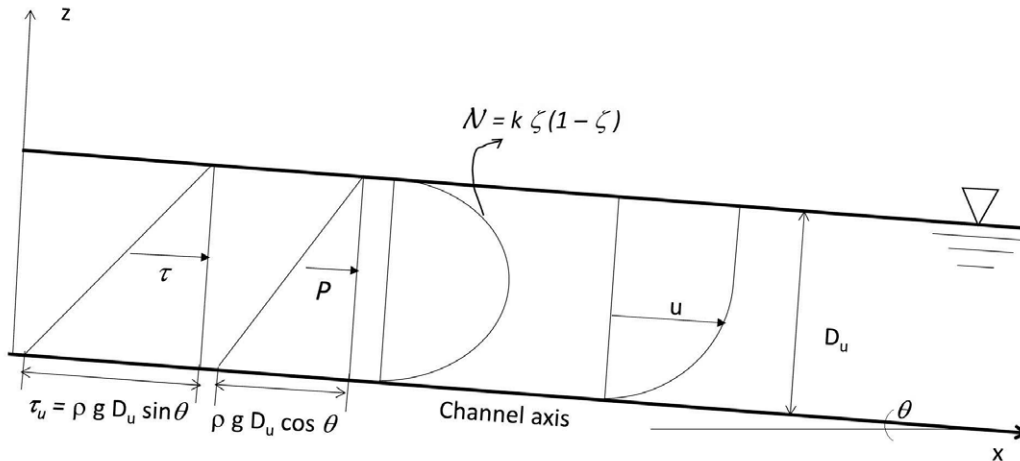


Figure 10. Sketch of a plane uniform turbulent flow and distributions of relevant flow quantities. ζ is the dimensionless coordinate z/D_u .

implies that it is statistically stationary and longitudinally homogeneous. The turbulence averaged flow is thus uni-directional ($\langle \mathbf{u} \rangle = u \hat{\mathbf{x}}$), with statistical properties depending only on the cartesian coordinate normal to the wall z ($u = u(z)$). As a consequence, mean inertial terms are identically zero.

The RANS equations take the following form

$$\frac{\partial P}{\partial z} = -\rho g \cos \theta - \rho \frac{d\langle v_z'^2 \rangle}{dz}, \quad (50)$$

$$-\frac{d}{dz}\langle v'_x v'_z \rangle + \nu \frac{d^2 u}{dz^2} = -g \sin\theta. \quad (51)$$

Equation (50) simply shows that the mean pressure is hydrostatic but for a small deviation associated with the normal stress $\rho \langle v_z'^2 \rangle$. Also, longitudinal homogeneity implies that pressure is independent of x .

From (51) the mean motion appears to be determined by a balance between the z -component of the shear stress gradient and gravity: the shear stress comprises both a Reynolds stress contribution $-\rho \langle v'_x v'_z \rangle$ and a viscous contribution that will be seen to play a negligible role except in an immediate neighborhood of the solid boundary.

Integrating (51) and imposing that the free surface is stress free (condition (37)), one finds the following linear distribution of the total stress, τ :

$$\tau = T_{zx}^t + T_{zx}^\mu = -\langle v'_x v'_z \rangle + \nu \frac{du}{dz} = -g \sin\theta (z - D_u) = u_{\tau_u}^2 \left(1 - \frac{z}{D_u}\right), \quad (52)$$

where u_{τ_u} is the friction velocity of uniform flow, defined as $\sqrt{\tau_u/\rho}$ with τ_u equal to the bottom value of the total shear stress τ . Hence, from (52):

$$u_{\tau_u}^2 = g D_u \sin\theta. \quad (53)$$

Equation (52) indicates that at a *perfectly smooth wall*, where the no slip and impermeability conditions apply, Reynolds stresses are identically zero and, hence, the shear stress is wholly viscous. This suggests that, close to the wall, the important physical parameters are the kinematic viscosity of the fluid ν and the wall shear stress τ_u and, consequently, the appropriate length scale is $\delta_\nu = \nu/u_{\tau_u}$. This scale, called *viscous length scale*, controls the thickness of the region ($z u_{\tau_u}/\nu \lesssim 50$) where molecular viscosity directly affects the flow. In this region, called *inner layer*, the total shear stress can be taken approximately equal to τ_u .

On the other hand, for $z u_{\tau_u}/\nu \gg \sim 50$ viscous effects become negligible. In this region, called *outer layer*, turbulent stresses prevail over viscous stresses and decrease linearly, as prescribed by relation (52). The relevant length scale is D_u .

DNS simulations of fully developed turbulent flow in closed plane channels and experimental observation confirm the above picture (Figure 11). Below, we analyse the velocity distribution within each of the above identified layers.

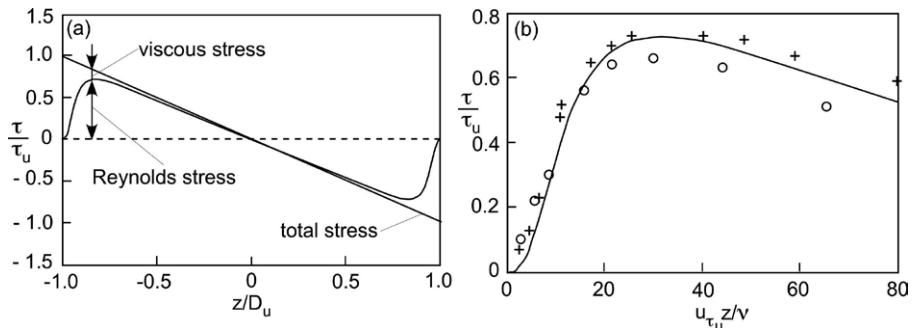


Figure 11. Viscous and turbulent contributions to the shear stress distribution in fully developed turbulent flow in closed plane channels: results of DNS carried out by Kim *et al.* (1987) for $R_\tau = 180$. In this case D_u is half the distance between the channel walls. Symbols represent the experimental data of Eckelmann (1974) for $R_\tau = 142$ (\circ) and $R_\tau = 208$ ($+$).

Inner layer: the law of the wall

The velocity distribution in the inner layer is usually denoted as *law of the wall*. Using as relevant scales the viscous length scale δ_ν and the friction velocity u_{τ_u} , the dimensionless form of equation (52) reads:

$$-\frac{\langle v'_x v'_z \rangle}{u_{\tau_u}^2} + \frac{1}{u_{\tau_u}} \frac{du}{dz^+} = \left(1 - \frac{z^+}{R_\tau}\right), \quad (54)$$

where:

$$z^+ = \frac{z u_{\tau_u}}{\nu}, \quad R_\tau = \frac{u_{\tau_u} D_u}{\nu}. \quad (55a,b)$$

It immediately appears that, for high values of the *friction Reynolds number* R_τ typical of fluvial streams, the dimensionless total stress is equal to unity. In addition, two different behaviours arise: viscous stress dominates over turbulent stress in the limit of small z^+ (i.e. in the *viscous sublayer*); both viscous and turbulent stresses play a role for large z^+ (in the so called *inertial sublayer*).

- The linear law in the *viscous sublayer* ($z^+ \ll 1$).

At the wall ($z^+ = 0$) the stress is purely viscous and equation (54) becomes:

$$\frac{1}{u_{\tau_u}} \frac{du}{dz^+} = 1. \quad (56)$$

Expanding u in powers of z^+ in the vicinity of the wall, it follows that:

$$\frac{u}{u_{\tau_u}} = z^+ + H.O.T. \quad (57)$$

and further analysis would show that the first of the higher order terms (H.O.T.) is $\mathcal{O}(z^+)^4$. Hence, the velocity distribution in the viscous sublayer is approximately linear. Figure 12a confirms the validity of (57). Departures from the linear relation are indeed negligible in the viscous sublayer ($z^+ < 5$), and increase up to 25% as z^+ exceeds 12. Note that, for perfectly smooth wall surfaces, such that the roughness height e_s does not occur as an additional parameter, the viscous sublayer exists independently of the value attained by R_τ . What varies is the dimensional thickness of this layer, that is of the order $(10^{-3} - 10^{-5}) D_u$.

- The law of the wall ($z^+ \gg 1$).

For large values of z^+ , both viscous and turbulent stresses have to be retained in (54). For perfectly smooth wall surfaces, solutions of equation (54) may be expected to be of the form:

$$\frac{u}{u_{\tau_u}} = f(z^+), \quad \frac{\langle v'_x v'_z \rangle}{u_{\tau_u}^2} = \varphi(z^+), \quad (58a,b)$$

and have to satisfy the boundary conditions $f(0) = \varphi(0) = 0$.

These relations are called the *law of the wall* and may be determined experimentally or through DNS. Nevertheless, as it will be shown below, some insight on their shape is obtained in the limit of $z^+ \rightarrow \infty$ and for high enough values of the friction Reynolds number R_τ .

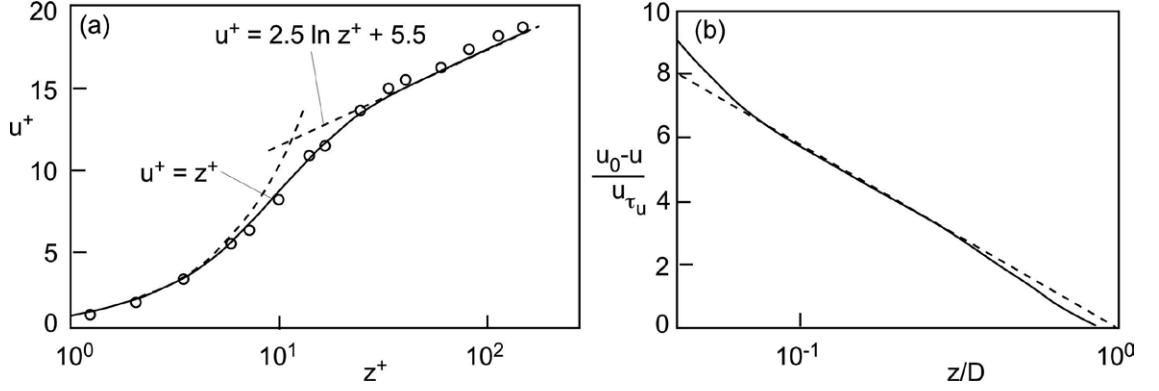


Figure 12. (a) The linear velocity distribution in the viscous sublayer of fully developed turbulent flow in closed plane channels predicted by (57) and the log law predicted by (65) (dotted line) are compared with results of DNS of Kim *et al.* (1987) for $R_\tau = 180$ (solid line) and experimental data of Eckelmann (1974) for $R_\tau = 142$ (\circ) (modified from Kim *et al.*, 1987). (b) The velocity defect law obtained by DNS of channel flow for $R_\tau = 180$ (Kim *et al.*, 1987) is compared with the log law (modified from Pope, 2000, Figure 7.9).

Outer layer: the velocity-defect law

The outer layer is defined by the assumption that the mean velocity profile is independent of the viscous scale. The appropriate length scale is the flow depth while the velocity scale is still u_τ . The dimensionless form of equation (52) then reads:

$$-\frac{\langle v'_x v'_z \rangle}{u_{\tau_u}^2} + \frac{1}{R_\tau} \frac{1}{u_{\tau_u}} \frac{du}{d\zeta} = (1 - \zeta), \quad (59)$$

where:

$$\zeta = \frac{z}{D_u}, \quad (60)$$

For large values of R_τ , equation (59) implies that turbulent stresses dominate and decrease linearly away from the wall. However, no explicit information is given about the mean velocity profile $u^+(\zeta)$. In order to make any progress a turbulent closure model is needed. Using a zero-order closure of the form (46) in conjunction with the Boussinesq linear closure (44) leads to:

$$\frac{1}{u_{\tau_u}} \frac{du}{d\zeta} = \frac{(1 - \zeta)D_u}{\ell(\zeta)} = \frac{dF}{d\zeta}. \quad (61)$$

Integrating the latter equation between ζ and the free surface ($\zeta = 1$) one finds the so called *velocity-defect law*:

$$\frac{u(\zeta) - u(1)}{u_{\tau_u}} = F(\zeta) - F(1). \quad (62)$$

Inertial sublayer: the logarithmic velocity profile

The inertial sublayer is the region where the inner and outer layers merge. The existence of this region is possible only for large enough values of R_τ , such that the limits of $z^+ \rightarrow \infty$ and $\zeta \rightarrow 0$ can be taken simultaneously (Figure 13). It allows the matching of the velocity profiles of the inner and outer layers.

Specifically, it is convenient to match the inner and outer velocity gradient. We then impose that:

$$\frac{du}{dz} = \frac{u_{\tau_u}^2}{\nu} \frac{df}{dz^+} = \frac{u_{\tau_u}}{D_u} \frac{dF}{d\zeta} \quad (63)$$

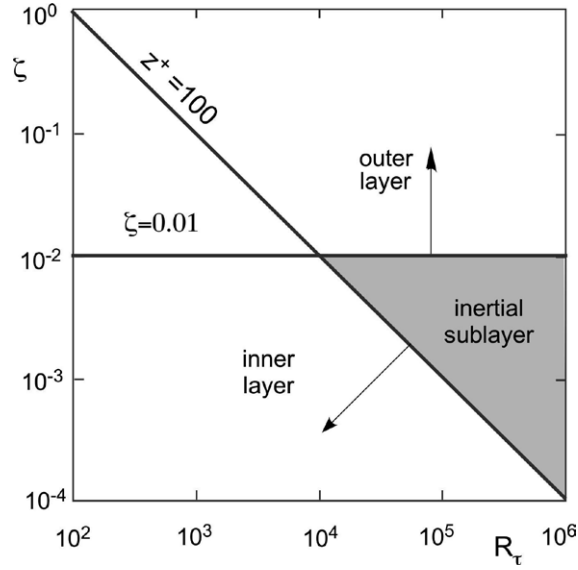


Figure 13. Range of existence of the inertial sublayer in the plane R_τ - ζ according to Tennekes and Lumley (1972).

and eventually find:

$$z^+ \frac{df}{dz^+} = \zeta \frac{dF}{d\zeta} = \frac{1}{k}, \quad (64)$$

where the von Von Kàrmàn constant k takes the value 0.41. It then immediately follows that, in the inertial sublayer, the velocity profile is of logarithmic type:

$$f(z^+) = \frac{1}{k} \ln(z^+) + b_{in}, \quad F(\zeta) = \frac{1}{k} \ln(\zeta) + b_{out}, \quad (65a,b)$$

with b_{in} and b_{out} suitable integration constants. For perfectly smooth walls, both experimental data and DNS indicate that $b_{in} = 5.5$. The value of b_{out} is instead subject to some uncertainty, as DNS suggest a value of 0.2 whilst measurements support the higher value 0.7 (Dean, 1978).

Figure 12a shows that the logarithmic distribution (65) is in excellent agreement with DNS data for values of z^+ larger than 30. Experimental data of Eckelmann (1974), corrected as discussed by Kim *et al.* (1987), also agree with DNS data. This agreement has been further supported by several later observations (see, e.g. Pope, 2000). The transitional region between the viscosity-dominated viscous sublayer ($z^+ < 5$) and the turbulence-dominated log-law region ($z^+ > 30$) is called *buffer layer*.

Figure 12b shows results for the velocity defect obtained by DNS of Kim *et al.* (1987). Agreement with the log law is quite strong in the range 0.08 – 0.3 for z/D . Small deviations are observed in the upper portion of the outer layer, where it tends to deviate from the velocity defect law. The difference between these two profiles:

$$\frac{\Pi}{k} W_f(\zeta) = F(\zeta) - \frac{1}{k} \ln \zeta - b_{out} \quad (66)$$

is called *law of the wake*, with W_f the *wake function* and Π the wake strength (Coles, 1956). For open channel flows, Π tends to be about zero for $R_\tau < 500$, increases rapidly for $500 < R_\tau < 2000$ and attains the almost constant value 0.2 for $R_\tau > 2000$ (Nezu and Nakagawa, 1993).

The effect of wall roughness

Wall surfaces are usually characterized by a distribution of irregular roughness elements, with mean height e_s . The velocity profile is found to be affected by the additional parameter e_s when

the thickness of the viscous sublayer, which we have seen to decrease for increasing values of the friction Reynolds number, becomes of the same order or smaller than e_s . Depending on the ratio $e_s u_{\tau_u}/\nu$ walls may be then classified as follows:

- *Hydraulically smooth* ($e_s u_{\tau_u}/\nu \leq 5$). Roughness does not play any appreciable role. Under such conditions the smooth law (65) is recovered.
- *Hydraulically rough* ($e_s u_{\tau_u}/\nu \geq 70$). In this case, viscous effects do not directly affect the mean velocity distribution and the relevant inner scale is the size of wall roughness e_s . The law of the wall is then found to read:

$$\frac{u}{u_{\tau_u}} = \frac{1}{k} \ln \frac{z}{e_s} + 8.5, \quad (67)$$

where the value of the constant 8.5 has been determined on the basis of experimental data of Nikuradse (1933).

- *Transitional regime* ($5 \leq e_s u_{\tau_u}/\nu \leq 70$). In this regime, both viscous effects and roughness do affect the mean velocity distribution, that may be given the general form:

$$\frac{u}{u_{\tau_u}} = \frac{1}{k} \ln \frac{z}{e_s} + b_t \left(\frac{k u_{\tau_u}}{\nu} \right), \quad (68)$$

where the function $b_t(e_s u_{\tau_u}/\nu)$ has been experimentally determined by various Authors and is found to generally depend on the shape of the roughness elements (Jimenez, 2004).

Note that the characteristic roughness height e_s is often expressed in terms of equivalent sand roughness, defined as the roughness of a uniform sand which, if artificially attached to an otherwise perfectly smooth wall, gives rise to the same law of the wall as the actual irregular roughness of the wall.

2.3. Turbulent flow in straight cylindrical open channels

In fluvial contexts, when dealing with large scale processes like those of interest for the present Monograph, it is often (though not always) sufficient to rely on a *slowly varying assumption* whereby the flow may be treated as a slowly varying sequence of locally uniform flow fields. The uniform turbulent flow in open channels thus plays a fundamental role in the whole theory of Morphodynamics and deserves a thorough attention.

2.3.1 Geometrical preliminaries

Consider the turbulent flow of an incompressible fluid in a straight open channel and assume that the channel boundary is a generalized *cylinder*. This mathematical surface is identified by a curved line (*directrix*), coinciding with the perimeter of the channel cross section, and a straight line (*generatrix*), orthogonal to the channel cross section and tangent to its boundary. The cylinder surface is generated by letting the generatrix translate along the directrix (Figure 14). We choose as *channel axis* the lowest generatrix of the channel boundary, which thus coincides with the *thalweg*, defined as the line connecting the lowest points of successive cross-sections along the river. Needless to say, a cylindrical surface is an obvious idealization of any real channel boundary. This notwithstanding, it is a convenient choice as it allows to build a rigorous theoretical framework for the so called *uniform* open channel flow.

Let us refer the flow to a cartesian system (x, y, z) , with x *longitudinal coordinate* associated with the channel axis, y *lateral coordinate* associated with a horizontal axis normal to the x -axis and lying on the initial channel cross section and the z -axis orthogonal to the x - y plane (Figure 14). Within the present simplified scheme, the *valley plain* is the planar surface parallel to the x - y plane, bounded by the highest generatrices of the cylinder. A distinct *slope* is associated with the channel axis.

Fluvial channels are typically characterized by slope values sufficiently small that the z -axis may be safely confused with *the vertical* axis used to express height above a given level. We

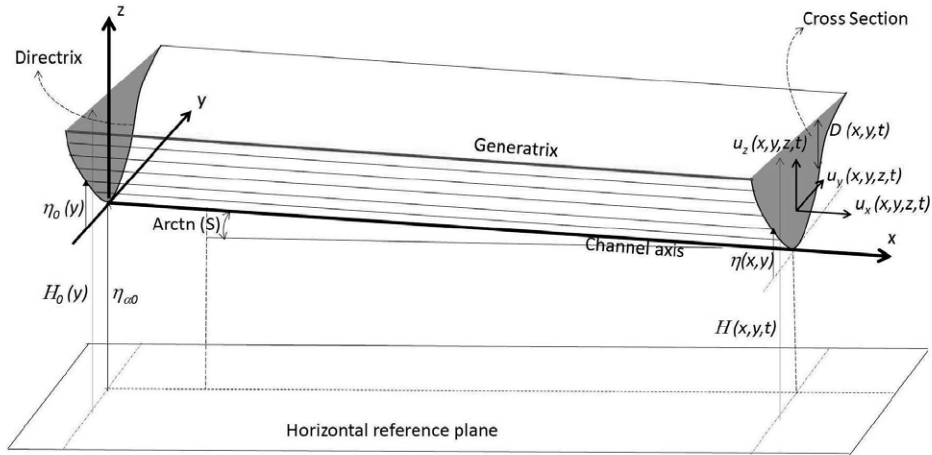


Figure 14. Sketch of a cylindrical open channel and notations.

then define the local instantaneous values of the *free surface elevation* $H(x, y, t)$, the *bed elevation* $\eta(x, y, t)$ and the *flow depth* $D(x, y, t)$ such that (Figure 14):

$$D(x, y, t) = H(x, y, t) - \eta(x, y). \quad (69)$$

Let η_a denote the local *elevation of the channel axis*. We can then write

$$\eta_a = \eta_{a0} - \sin \theta x \simeq \eta_{a0} - S x, \quad (70)$$

with η_{a0} a constant setting the reference value of the elevation of the channel axis at the initial cross section ($x = 0$) and θ the angle that the channel axis forms with the horizontal (see Figure 14). Moreover, we have denoted by S the *channel slope* and assumed θ sufficiently small to allow for the approximation $\sin(\theta) \simeq \tan(\theta)$. Note that, provided the channel cuts the valley plain along its steepest direction, the channel slope coincides with the *valley slope*.

At this stage of our analysis, the solid boundary of the channel is assumed to be fixed, i.e. the bed elevation η is taken to be independent of time. The real boundaries of fluvial channels are erodible, hence, in due course, the latter assumption will have to be relaxed allowing for the spatial-temporal evolution of the solid boundary.

2.3.2 Formulation

The mathematical formulation of the hydrodynamic problem is immediately obtained from the general treatment presented in Section 2.2.4.

Below we refer to the cartesian system introduced in the previous Section and denote by $u_x(x, y, z, t)$, $u_y(x, y, z, t)$, $u_z(x, y, z, t)$ and $P(x, y, z, t)$ the longitudinal, lateral and vertical component of the mean velocity vector and the mean pressure, respectively, averaged over turbulence. Note that the temporal dependence of mean velocity and mean pressure is preserved in order to account for possible flow unsteadiness associated with phenomena (e.g. flood propagation) involving temporal scales much larger than the characteristic period of turbulent fluctuations.

With the latter notations and neglecting the contribution of viscous stresses, as appropriate throughout most of the flow depth (see Section 2.2.9), the dimensional form of the *Reynolds*

averaged conservation equations for the fluid phase reads:

$$\frac{\partial u_x}{\partial x} + \frac{\partial u_y}{\partial y} + \frac{\partial u_z}{\partial z} = 0, \quad (71a)$$

$$\rho \left(\frac{\partial u_x}{\partial t} + u_x \frac{\partial u_x}{\partial x} + u_y \frac{\partial u_x}{\partial y} + u_z \frac{\partial u_x}{\partial z} \right) = -\frac{\partial P}{\partial x} + \frac{\partial T_{xx}^t}{\partial x} + \frac{\partial T_{yx}^t}{\partial y} + \frac{\partial T_{zx}^t}{\partial z} + \rho g S, \quad (71b)$$

$$\rho \left(\frac{\partial u_y}{\partial t} + u_x \frac{\partial u_y}{\partial x} + u_y \frac{\partial u_y}{\partial y} + u_z \frac{\partial u_y}{\partial z} \right) = -\frac{\partial P}{\partial y} + \frac{\partial T_{xy}^t}{\partial x} + \frac{\partial T_{yy}^t}{\partial y} + \frac{\partial T_{zy}^t}{\partial z}, \quad (71c)$$

$$\rho \left(\frac{\partial u_z}{\partial t} + u_x \frac{\partial u_z}{\partial x} + u_y \frac{\partial u_z}{\partial y} + u_z \frac{\partial u_z}{\partial z} \right) = -\frac{\partial P}{\partial z} + \frac{\partial T_{xz}^t}{\partial x} + \frac{\partial T_{yz}^t}{\partial y} + \frac{\partial T_{zz}^t}{\partial z} - \rho g. \quad (71d)$$

The boundary conditions to be associated with the above conservation equations are those presented in Section 2.2.6, namely the kinematic condition (35) at the free surface which is also assumed to be stress free (equation 37), and the no slip condition (36) at a given distance η_0 from the channel bed, depending on the model used to close the turbulence. Finally, in this type of flow, the open boundaries are the upstream and downstream end cross-sections of the channel reach under consideration.

The above system of partial differential equations can be closed with the help of Boussinesq relationship (44). Including into the mean pressure P the minor correction associated with the turbulent kinetic energy \mathcal{K} , one readily finds:

$$\frac{T_{zx}^t}{\rho} = \nu_T \left(\frac{\partial u_x}{\partial z} + \frac{\partial u_z}{\partial x} \right); \quad \frac{T_{yx}^t}{\rho} = \nu_T \left(\frac{\partial u_x}{\partial y} + \frac{\partial u_y}{\partial x} \right); \quad \frac{T_{yz}^t}{\rho} = \nu_T \left(\frac{\partial u_y}{\partial z} + \frac{\partial u_z}{\partial y} \right); \quad (72a)$$

$$\frac{T_{xx}^t}{\rho} = 2\nu_T \frac{\partial u_x}{\partial x}; \quad \frac{T_{yy}^t}{\rho} = 2\nu_T \frac{\partial u_y}{\partial y}; \quad \frac{T_{zz}^t}{\rho} = 2\nu_T \frac{\partial u_z}{\partial z}. \quad (72b)$$

2.3.3 Uniform steady (normal) flow.

As seen in Section 2.2.9, a *uniform turbulent flow* is statistically independent of time and homogeneous in the longitudinal direction. In the case of an open channel, flow uniformity requires the following conditions:

- the channel geometry must not vary in the longitudinal direction, i.e. the channel surface must be cylindrical;
- the flow properties must also be constant in the longitudinal direction: for this condition to be satisfied, the channel reach considered must be sufficiently far from any 'end' conditions which may drive backwater effects.

Under steady, uniform flow conditions (called also normal conditions) it can be easily demonstrated that the following relationships hold:

$$H(x) = H_0 - Sx, \quad \eta(x, y) = \eta_0(y) - Sx, \quad u_x = u(y, z), \quad u_y = u_z = 0, \quad (73)$$

where the function $\eta_0(y)$ defines the shape of the cross section and H_0 is the constant free surface elevation at the initial cross section $x = 0$.

As Reynolds stresses are also independent of the longitudinal coordinate x , the governing

Reynolds equations become:

$$\frac{\partial u}{\partial x} = 0, \quad (74a)$$

$$\frac{\partial T_{yx}^t}{\partial y} + \frac{\partial T_{zx}^t}{\partial z} = -\varrho g S, \quad (74b)$$

$$\frac{\partial T_{yy}^t}{\partial y} + \frac{\partial T_{zy}^t}{\partial z} = \frac{\partial P}{\partial y}, \quad (74c)$$

$$\frac{\partial T_{yz}^t}{\partial y} + \frac{\partial T_{zz}^t}{\partial z} = \frac{\partial P}{\partial z} + \varrho g. \quad (74d)$$

The *dynamic boundary conditions* at the free surface (40) reduce to the simplest form:

$$T_{zx}^t|_H = 0, \quad T_{zy}^t|_H = 0, \quad -P + T_{zz}^t|_H = 0, \quad (75)$$

while the *no slip condition* (36) at the solid boundary will be specified according to the turbulence closure scheme employed. Given the steady character of the flow field initial conditions are not required. Moreover, the only condition needed at open boundaries consists of assigning the flow discharge Q .

Using the Boussinesq closure (44) and accounting for uniformity (equation (73)), one readily finds:

$$T_{xx}^t = T_{yy}^t = T_{zz}^t = 0, \quad T_{zy}^t = T_{yz}^t = 0, \quad (76a)$$

$$\frac{T_{yx}^t}{\varrho} = \frac{T_{xy}^t}{\varrho} = \nu_T \frac{\partial u}{\partial y}, \quad \frac{T_{zx}^t}{\varrho} = \frac{T_{xz}^t}{\varrho} = \nu_T \frac{\partial u}{\partial z}. \quad (76b)$$

The governing equations (74) thus become:

$$\frac{\partial u}{\partial x} = 0, \quad (77a)$$

$$\frac{\partial}{\partial y} \left(\nu_T \frac{\partial u}{\partial y} \right) + \frac{\partial}{\partial z} \left(\nu_T \frac{\partial u}{\partial z} \right) = -g S, \quad (77b)$$

$$\frac{\partial P}{\partial y} = 0, \quad (77c)$$

$$\frac{\partial P}{\partial z} = -\varrho g. \quad (77d)$$

while the dynamic boundary conditions at the free surface (75) simplifies to:

$$\left. \frac{\partial u}{\partial z} \right|_H = 0, \quad P|_H = 0. \quad (78)$$

Equation (77d) is immediately solved to give a hydrostatic distribution of the mean pressure:

$$P = \varrho g (H - z), \quad (79)$$

while equation (77c) implies that the free surface is horizontal in the lateral direction:

$$H = H(x) = H_0 - S x. \quad (80)$$

Hence, under uniform conditions, the free surface is plane with longitudinal slope equal to the channel slope, independently of the shape of the cross-section.

The solution for the flow speed u is obtained integrating the longitudinal momentum equation (77b) along the flow depth and across the section once a closure is assumed for the kinematic eddy viscosity ν_T . Before tackling this problem for prismatic sections with arbitrary shape, it is instructive to consider the case of an infinitely wide rectangular channel.

2.3.4 The case of infinitely wide rectangular channels.

Let us now consider the uniform turbulent flow in a channel with a rectangular and very wide (strictly infinitely wide) cross-section. This problem has been already analyzed in Section 2.2.9. Here, we specifically focus on adequate representations of the eddy viscosity in the context of a zero-order closure model. We only recall that, owing to the plane character of the flow, all partial derivatives along the transverse direction y vanish. The longitudinal momentum equation (77b) then simplifies to:

$$\frac{d}{dz} \left(\nu_T \frac{du}{dz} \right) = -g S. \quad (81)$$

Integration of (81) leads to the following linear distribution of shear stresses:

$$T_{zx}^t = \tau(z) = \varrho \nu_T \frac{du}{dz} = \tau_u \left(1 - \frac{z}{D_u} \right), \quad (82)$$

where D_u is the uniform flow depth while

$$\tau_u = \varrho g D_u S \quad (83)$$

is the shear stress at the channel bed. Note that, differently from relation (52), here only the turbulent stress is considered, owing to its dominance across most of the flow depth.

Experimental observations and dimensional arguments suggest for ν_T a structure of the form

$$\nu_T = \nu_{Tu} = u_{\tau_u} D_u \mathcal{N}(\zeta), \quad (84)$$

where we recall that $u_{\tau_u} = (\tau_u/\varrho)^{1/2}$ is the friction velocity and ζ is the normalized vertical coordinate z/D_u . The mixing length (see equation (46)) is thus taken to scale with the flow depth and has a vertical distribution described by the shape function $\mathcal{N}(\zeta)$. Substituting (84) into equation (82) and integrating one finds:

$$\frac{u}{u_{\tau_u}} = \int_{\zeta_0}^{\zeta} \frac{(1 - \zeta')}{\mathcal{N}(\zeta')} d\zeta', \quad (85)$$

where $\zeta_0 = z_0/D_u$ is the dimensionless elevation where no-slip is imposed at the wall. Once the velocity distribution has been derived, the depth averaged flow velocity U_u is obtained by integrating (85) throughout the flow depth:

$$U_u = \frac{u_{\tau_u}}{1 - \zeta_0} \int_{\zeta_0}^1 d\zeta \int_{\zeta_0}^{\zeta} \frac{(1 - \zeta')}{\mathcal{N}(\zeta')} d\zeta'. \quad (86)$$

Note that the normalized coordinate ζ_0 at which the no slip bed condition is imposed is strictly associated with relative bed roughness, which is typically much smaller than one. Hence, below, we set $(1 - \zeta_0) \simeq 1$.

The choice of an appropriate form for the function $\mathcal{N}(\zeta)$ has been the subject of extensive investigations, reviewed, e.g. by Nezu and Nakagawa (1993).

The simplest option is to assume a constant distribution as suggested by Engelund (1964) to reduce the calculation of turbulent flows to a form amenable to analytical treatment. This choice

provides a useful tool for rough engineering calculations and for gaining qualitative understanding of the mechanisms which control the formation of some river and estuarine bedforms. The idea is to select a constant value \mathcal{N}_0 that produces the mean velocity distribution which fits the experimental data at best. The disadvantage of this approach is its inability to impose the no slip condition at the wall. Indeed, setting $\mathcal{N} = \mathcal{N}_0$, into (85) gives:

$$\frac{u}{u_{\tau_u}} = \frac{1}{\mathcal{N}_0} \left(\zeta - \frac{\zeta^2}{2} \right) + \frac{u_p}{u_{\tau_u}}, \quad (87)$$

with u_p the slip velocity at the bed. According to Engelund (1964) the value $\mathcal{N}_0 = 1/13$ is the one which fits the experimental points better than the logarithmic distribution over 90% of the profile. An expression for the slip velocity u_p is then found by fitting the theoretical value of the surface velocity predicted by (87) to the value obtained from the logarithmic distribution. For rough walls Engelund (1964) finds:

$$\frac{u_p}{u_{\tau_u}} = 2 + 2.5 \ln \frac{D_u}{e_s}. \quad (88)$$

The depth averaged value of U_u predicted by substituting (88) into (87) reads

$$U_u = u_{\tau_u} \left[6.33 + 2.5 \ln \left(\frac{D_u}{e_s} \right) \right]. \quad (89)$$

Depth averaging (67) the reader will find a relationship identical with (89) except for the constant 6.33, which becomes 6.

The next simplest choice for $\mathcal{N}(\zeta)$ is to adopt the linear distribution ($k\zeta$), with k Von Karman constant. This eddy viscosity distribution leads to the classical logarithmic distribution for the flow speed, that we have seen (Section 2.2.9) to apply in the inertial sublayer. Refinements of the linear distribution are then needed in order to reproduce deviations from the logarithmic law observed in the outer layer, where the velocity defect law holds (Figure 12b).

Various corrections to the linear distribution have been proposed in the literature. Nezu and Nakagawa (1993) suggest the following general form for $\mathcal{N}(\zeta)$:

$$\mathcal{N}(\zeta) = \frac{k\zeta(1-\zeta)}{1+w_f(\zeta)}, \quad (90)$$

where $w_f(\zeta)$ is the so called *wake correction*. This latter quantity is associated with the function W_f appearing in the law of the wake (66) through the relation:

$$W_f(\zeta) = \frac{1}{\Pi} \int_{\zeta_0}^{\zeta} \frac{w_f(\zeta')}{\zeta'} d\zeta', \quad (91)$$

with Π the wake strength.

An alternative relatively simple form of $\mathcal{N}(\zeta)$, appropriate to uniform open channel flow, was proposed by Rattray and Mitsuda (1974). It reads:

$$\mathcal{N}(\zeta) = k\zeta(1-\zeta) = k\zeta \frac{\tau(\zeta)}{\tau_u} \quad (\zeta < 0.2), \quad (92a)$$

$$\mathcal{N}(\zeta) = 0.16k \quad (\zeta \geq 0.2). \quad (92b)$$

Finally note that from (86) one may immediately derive an expression for the *flow conductance* χ_u of uniform flows in terms of the relative roughness ζ_0 :

$$\chi_u = \frac{U_u}{u_{\tau_u}} = \int_{\zeta_0}^1 d\zeta \int_{\zeta_0}^{\zeta} \frac{1-\zeta'}{\mathcal{N}(\zeta')} d\zeta'. \quad (93)$$

As an example, adopting for $\mathcal{N}(\zeta)$ the general form (90) in its the simplest form with $w_f(\zeta) = 0$ and using (93), one finds:

$$\zeta_0 = \exp(-1 - k \chi_u). \quad (94)$$

The reader should observe that this relationship allows one to calculate the effective relative elevation ζ_0 at which no slip occurs once the flow conductance χ_u is known. Also, we note that (93), along with (83), lead to the well known Chézy relationship (Chézy, 1776):

$$U_u = \chi_u \sqrt{g D_u S}, \quad (95)$$

valid for uniform open channel flows.

With the help of the above relationships, the vertical distribution of the flow speed may finally be expressed in the form:

$$u(\zeta) = U_u \mathcal{F}_0(\zeta), \quad (96)$$

with

$$\mathcal{F}_0(\zeta) = \frac{\int_{\zeta_0}^{\zeta} \frac{1 - \zeta'}{\mathcal{N}(\zeta')} d\zeta'}{\int_{\zeta_0}^1 d\zeta \int_{\zeta_0}^{\zeta} \frac{1 - \zeta'}{\mathcal{N}(\zeta')} d\zeta'}. \quad (97)$$

The specific expression for $\mathcal{F}_0(\zeta)$ is obtained once the shape function $\mathcal{N}(\zeta)$ is chosen.

To conclude this section, we note that the considered zero-order closure models do not consider viscous effects in the near wall. This is not a severe drawback in the field of river morphodynamics as river boundaries are most commonly hydraulically rough. However, in laboratory observations, smooth and intermediate regimes are not uncommon. Also, some fluvial bedforms (ripples) are typically observed under hydraulically smooth conditions. An empirical tool to account for viscous effects in the *viscous sublayer* within the framework of a zero-order closure was proposed by Van Driest (1956). It consists of correcting the structure of the eddy viscosity in the near wall region as follows:

$$\nu_T = u_{\tau_u} D \mathcal{N}(\zeta) \Gamma(u_{\tau_u} z / \nu), \quad (98)$$

where:

$$\Gamma(u_{\tau_u} z / \nu) = 1 - \exp\left(-\frac{u_{\tau_u} z / \nu}{b_{vd}}\right), \quad b_{vd} = 26, \quad (99)$$

is a *damping function*. For $u_{\tau_u} z / \nu \gg b_{vd}$ the correction becomes ineffective and one recovers the usual logarithmic law, whilst for $u_{\tau_u} z / \nu \ll b_{vd}$, $\Gamma \rightarrow (u_{\tau_u} z / \nu) / b_{vd}$ and $\nu_T \rightarrow 0$, hence Reynolds stresses become negligible and the viscous law $u / u_{\tau_u} = u_{\tau_u} z / \nu$ is recovered.

As a final remark, we note that even though one-equation closure models are sufficient for the purposes of the present Monograph, higher order closure models may be also employed. Applications of the \mathcal{K} - ε model to uniform turbulent flow in open channels first appeared in the literature in the 1980's in the context of investigations concerning the transport of suspended sediments in open channels (Celik and Rodi, 1984, 1988). Since then, this type of models have often been employed in morphodynamic studies and have been implemented in popular codes as DELFT3D (Lesser *et al.*, 2004) and ROMS (Warner *et al.*, 2005). However, the \mathcal{K} - ε model, being based on the linear isotropic Boussinesq closure, is unable to reproduce the observed normal stress anisotropy. To overcome the above deficiency, one must resort to nonlinear closures (Speziale, 1987) or to Reynolds stress models. The reader is referred to specialized books (e.g. Pope, 2000; Wilcox, 2006; Durbin and Pettersson Reif, 2011) for exhaustive reviews.

2.3.5 The case of channels with finite width and arbitrary shape

Wide channels with arbitrary shape

The most obvious extension of results obtained in the previous Section concerns the case of 'wide' channels with arbitrary shape, assuming that the variation of the flow properties in the lateral direction is sufficiently 'slow', to neglect the lateral derivatives in the governing equation (74b). With this assumption, the flow field is treated as a sequence of locally uniform flows, each referring to a vertical strip of infinitesimal thickness (dy), with properties that vary slowly in the lateral direction (Figure 15).

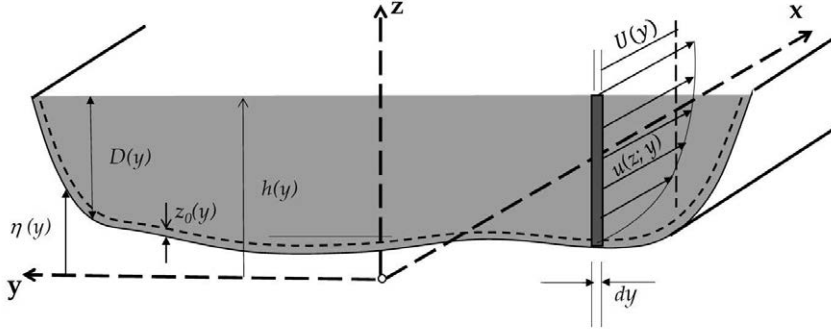


Figure 15. Sketch of a wide cross section with the flow treated as a sequence of locally uniform flows, each referring to a vertical strip of infinitesimal thickness.

Let $D(y)$ be the local flow depth. With the same notations of the previous Section, the solution for the bottom stress and the average pressure associated with each vertical strip reads:

$$\tau(y) = \tau_0(y)(1 - \zeta), \quad P = \rho g D(y) (1 - \zeta), \quad (100)$$

where

$$\tau_0(y) = \rho g D(y) S, \quad \zeta = \frac{z}{D(y)}. \quad (101)$$

The closure for the eddy viscosity, for each vertical strip, is now:

$$\nu_T = u_\tau(y) D(y) \mathcal{N}(\zeta), \quad (102)$$

with $u_\tau(y) = \sqrt{\tau_0(y)/\rho}$. The following vertical distribution for the flow speed then arises:

$$u = U(y) \mathcal{F}_0(\zeta). \quad (103)$$

Here $U(y)$ is the depth averaged flow speed, related to the local values of the flow conductance $\chi(y)$ and friction velocity $u_\tau(y)$ as follows:

$$U(y) = \chi(y) u_\tau(y), \quad (104)$$

where

$$u_\tau(y) = \sqrt{\frac{\tau_0(y)}{\rho}} = \sqrt{g D(y) S}, \quad (105)$$

and $\chi(y)$ is obtained from (93) adopting the local value of $\zeta_0(y)$.

The case of narrow channels

For narrow channels the *slowly varying approximation* is no longer valid as the presence of the channel banks affects the flow field quite significantly. Hence, the full momentum equation (74b) must be solved numerically. This is not a difficult job, once an appropriate closure for the eddy viscosity is assumed. And, as mentioned in Section 2.2.8, a number of increasingly refined models are available in the literature.

However, for the present purposes, a lot can be learnt using a relatively simple closure, still based on Boussinesq assumption, known as the 'isovel method', which was originally empirically proposed by Leighly (1932) and later developed by Houjou *et al.* (1990), Kean and Smith (2004) and Kean *et al.* (2009).

Essentially, the relationship (102) is modified referring to a non cartesian orthogonal system consisting of *isovels*, namely lines of equal longitudinal speed, and *rays*, i.e. lines orthogonal to isovels. We then write:

$$\nu_T = u_\tau(n) D(n) \mathcal{N} \left[\frac{\zeta}{D(n)} \right], \quad (106)$$

where n is the curvilinear coordinate defined along the isovel coinciding with the channel boundary, ζ is the curvilinear coordinate defined along the central ray, $u_\tau(n) \equiv \sqrt{\tau_0(n)/\rho}$ is the friction velocity along the wet boundary and $D(n)$ is the length of the ray (Figure 16 top). The value of

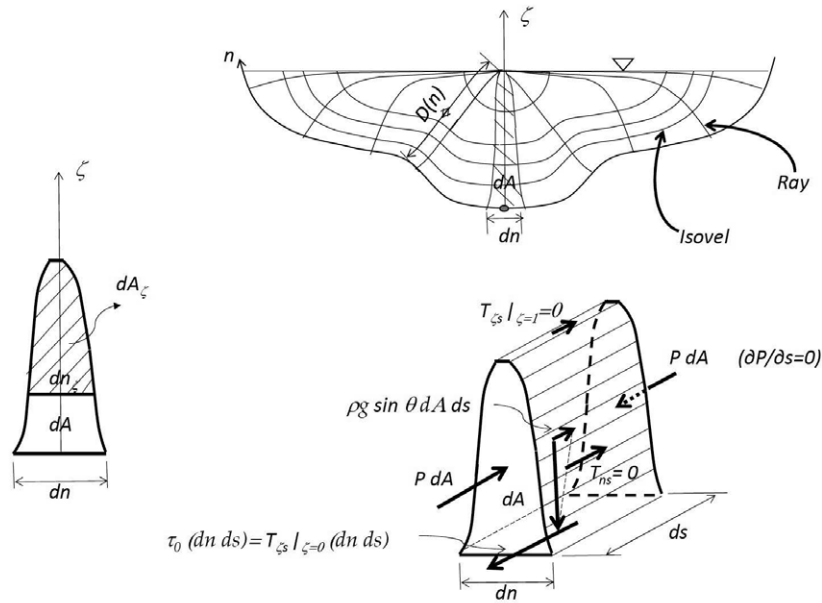


Figure 16. The upper plot shows a sketch of a narrow cross section with the orthogonal network of rays and isovels. The lower plot depicts the forces acting on the boundary of a control volume consisting of an infinitesimal cylinder bounded by two adjacent cross sections at an infinitesimal distance ds , two adjacent ray surfaces at an infinitesimal distance dn , the bottom and the free surface.

$\tau_0(n)$ is determined imposing the dynamic equilibrium of an infinitesimal volume of water bounded by two adjacent ray surfaces, the bottom, the free surface and two channel cross sections at a distance ds (Figure 16 bottom). We note that, within the framework of Boussinesq closure, the stress T_{ns}^t on the ray surfaces vanishes. Indeed, shear on ray surfaces is driven by variations of flow

speed in the normal n -direction, i.e. along isovels. Moreover, the dynamic boundary condition requires that the stress $T_{\zeta s}^t$ on the free surface must also vanish. At last, the pressures acting on two adjacent cross sections are identical due to the constraint of uniformity. Hence, one finds:

$$\tau_0 (ds dn) = \varrho g S dA(n) ds \quad \Rightarrow \quad \tau_0 = \varrho g S \frac{dA}{dn}, \quad (107)$$

having denoted by dA the infinitesimal area of the surface bounded by the two adjacent rays, the bottom line and the free surface (Figure 16).

In order to complete the analysis, we must extend the latter relationship such to calculate the shear stress $\tau \equiv T_{\zeta s}^t$ at any location (ζ, n) in the cross section. A force balance similar to (107) leads to the following relation:

$$\tau = \varrho g S \frac{dA_\zeta}{dn_\zeta}, \quad (108)$$

where dA_ζ is the area of the surface element bounded by the two adjacent rays, the element of the isovel of length dn_ζ through the point (ζ, n) and the free surface.

In order to model the eddy viscosity ν_T , we exploit the *slowly varying assumption* and use the uniform form of ν_T expressed in terms of the local flow field. Hence, we write:

$$\nu_T = u_\tau(n) D(n) \mathcal{N}(\zeta). \quad (109)$$

Here, $\mathcal{N}(\zeta)$ is a function describing the shape of the radial distribution of the eddy viscosity expressed in terms of the normalized radial coordinate ζ .

In particular, recalling (106) and (92), the eddy viscosity may be given the following structure:

$$\nu_T = u_\tau(n) D(n) \left[k \zeta \frac{\tau(\zeta)}{\tau_0} \right] = k \zeta u_\tau(n) \frac{\frac{dA_\zeta}{dn_\zeta}}{\frac{dA}{dn}} \quad (\zeta < \zeta_l), \quad (110a)$$

$$\nu_T = 0.16 k D(n) \sqrt{g D(n) S} \quad (\zeta \geq \zeta_l). \quad (110b)$$

where ζ_l is the value of ζ at which ν_T obtained from (110a) reaches the constant value (110b) describing mixing in the central region of the flow field.

Finally, appropriate boundary conditions must be imposed. At the water surface the tangential stress $T_{\zeta s}^t$, hence $\partial u / \partial \zeta$, must vanish. Moreover, no slip must be imposed at the roughness height ζ_0 . Most often, in order to reduce the computational effort, the latter constraint is replaced by the condition that the velocity a short distance above the boundary must satisfy the law of the wall, namely $u(\zeta) = (u_\tau(n)/k) \ln(\zeta/\zeta_0)$.

2.3.6 Turbulence driven secondary flows in channels

The expression *secondary flow* refers to flow fields that may be conceptually decomposed into a *primary flow*, i.e. a prevailing motion, and a weaker flow field occurring in planes orthogonal to the direction of the primary flow. The first thorough definition of secondary flows goes back to Prandtl (1927). Investigating experimentally the turbulent flow in straight ducts with non-circular cross-sections Prandtl (1927) measured carefully the distribution of mean longitudinal velocity in the cross section and drew the associated isovels (Figure 17a). It clearly appears that the speed increases at corners and decreases near the adjacent walls. Prandtl suggested that this distortion arose from the occurrence of a secondary flow, i.e. an additional circulatory motion which develops in the cross section of channels with uniform but non circular cross sections.

Prandtl makes a further fundamental distinction between secondary flows *of the first kind*, which are driven by the effect of centrifugal forces and the associated pressure gradient and secondary flows *of the second kind*, which are driven by turbulence. The former ones occur in

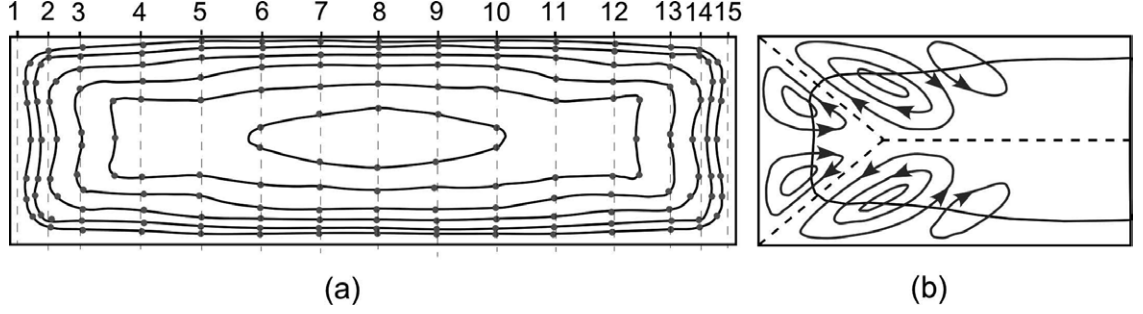


Figure 17. (a) Pattern of isovels measured in the cross section of a rectangular duct subject to a steady uniform turbulent flow. (b) Near corner secondary flows according to Prandtl (1927).

both laminar and turbulent flows in curved open channels or curved ducts. They will be widely investigated in the present Monograph, where we study the morphodynamics of meandering rivers. On the contrary, secondary flows of the second kind are only observed in turbulent flows in non circular channels. Below, we discuss how they are generated.

The mechanism of generation of secondary flows of the second kind

In order to clarify the mechanism of generation of secondary flows of the second kind, let us refer to flow in straight ducts (Figure 18) and consider the mean vorticity equation (43). The aim is to show that secondary flows can be generated by turbulence anisotropy, that gives rise to lateral gradients of the normal Reynolds stresses. In the case of uniform turbulent flow conditions, the equation for the mean streamwise vorticity simplifies to:

$$u_y \frac{\partial \Omega_x}{\partial y} + u_z \frac{\partial \Omega_x}{\partial z} - \nu \nabla^2 \Omega_x = - \frac{\partial \langle v'_y \omega'_x \rangle}{\partial y} - \frac{\partial \langle v'_z \omega'_x \rangle}{\partial z} + \frac{\partial \langle v'_x \omega'_y \rangle}{\partial y} + \frac{\partial \langle v'_x \omega'_z \rangle}{\partial z}, \quad (111)$$

where we have taken into account the fact that, as a result of the uniform character of the mean flow, $\Omega_y = \partial u_x / \partial z$ and $\Omega_z = -\partial u_x / \partial y$, hence the quantity $(\Omega_y \partial u_x / \partial y + \Omega_z \partial u_x / \partial z)$ vanishes.

This equation suggests that, if turbulent fluctuations were not present, as in laminar flows, no secondary flow would develop. Indeed, the only solution of the turbulent uniform flow within the duct would be $\Omega_x = 0$. On the contrary, turbulent fluctuations on the right hand side of (111) generate mean streamwise vorticity.

The physical mechanism underlying this process is better clarified if the right hand side of (111) is expressed in terms of Reynolds stresses. Using the definition of the vorticity fluctuation and the continuity equation for the velocity fluctuations, some algebraic work eventually leads to the following alternative form of the streamwise vorticity equation:⁵

$$u_y \frac{\partial \Omega_x}{\partial y} + u_z \frac{\partial \Omega_x}{\partial z} - \nu \nabla^2 \Omega_x = \frac{\partial^2}{\partial y \partial z} \left(\frac{T_{zz}^t - T_{yy}^t}{\rho} \right) + \left(\frac{\partial^2}{\partial y^2} - \frac{\partial^2}{\partial z^2} \right) \frac{T_{yz}^t}{\rho}. \quad (112)$$

The right hand side of (112) shows that a first contribution to the generation of secondary flow is due to normal stress anisotropy. A second contribution is provided by the Reynolds shear stress

⁵ Using the definition of the vorticity fluctuation, we may write:

$$\begin{aligned} - \frac{\partial \langle v'_y \omega'_z \rangle}{\partial y} - \frac{\partial \langle v'_z \omega'_x \rangle}{\partial z} &= - \frac{\partial}{\partial y} \left\langle v'_y \left(\frac{\partial v'_z}{\partial y} - \frac{\partial v'_y}{\partial z} \right) \right\rangle - \frac{\partial}{\partial z} \left\langle v'_z \left(\frac{\partial v'_z}{\partial y} - \frac{\partial v'_y}{\partial z} \right) \right\rangle \\ &= - \frac{\partial^2}{\partial y \partial z} \frac{\langle v'_z \rangle - \langle v'_y \rangle}{2} - \frac{\partial}{\partial y} \langle v'_y \frac{\partial v'_z}{\partial y} \rangle + \frac{\partial}{\partial z} \langle v'_z \frac{\partial v'_y}{\partial z} \rangle \\ &= - \frac{\partial^2}{\partial y \partial z} \frac{\langle v'_z \rangle - \langle v'_y \rangle}{2} - \left(\frac{\partial^2}{\partial y^2} + \frac{\partial^2}{\partial z^2} \right) \langle v'_y v'_z \rangle + \frac{\partial}{\partial y} \langle v'_z \frac{\partial v'_y}{\partial y} \rangle - \frac{\partial}{\partial z} \langle v'_y \frac{\partial v'_z}{\partial z} \rangle \end{aligned}$$

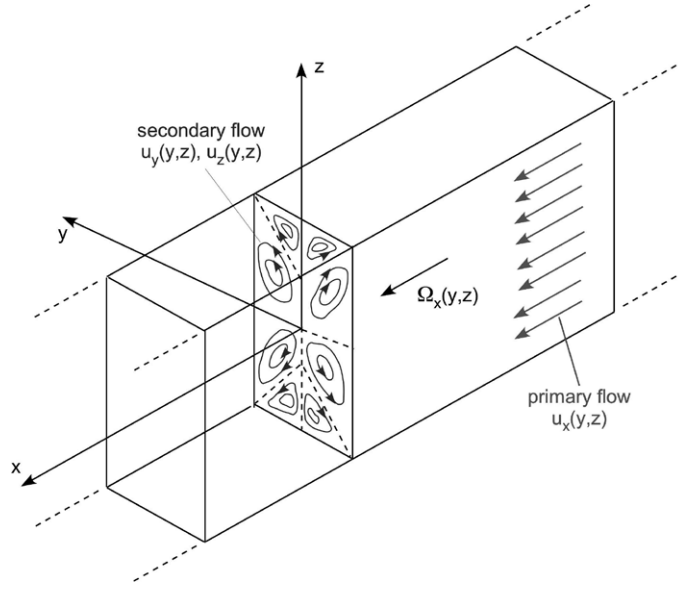


Figure 18. Sketch of secondary flow in a rectangular duct and notations (modified from Speziale, 1987).

associated with the secondary flow. Numerical simulations based on RANS nonlinear closures suggest that the latter contribution may be dominant, an observation that, as pointed out by Durbin and Petterson Reif (2011) (pg. 208), is in contrast with the common belief that normal stress anisotropy would be the origin of secondary flows. Normal stress anisotropy is indeed crucial for their initial formation, but the secondary shear stress then becomes the dominant mechanism responsible for maintaining the secondary flow once it is created.

In the context of Morphodynamics, the formation of turbulent secondary flows has been extensively investigated also for wide open channels (Colombini, 1993; Colombini and Parker, 1995; Yang *et al.*, 2012).

2.4. Depth averaged formulation: the shallow water approximation

Various river and estuarine patterns are characterized by horizontal scales which exceed their vertical scale by more than one order of magnitude. Under these conditions it proves convenient to describe the flow field in terms of depth averaged properties (see the Figure 19 for notations employed in this Section). The advantage of this approach is twofold:

- the number of dependent variables in the depth averaged formulation is reduced from four (the three components of the mean velocity vector and the mean pressure) to three (the depth averaged components of longitudinal and transverse velocity and the free surface elevation);

and

$$\begin{aligned} \frac{\partial \langle v'_x \omega'_y \rangle}{\partial y} + \frac{\partial \langle v'_x \omega'_z \rangle}{\partial z} &= \frac{\partial}{\partial y} \left\langle v'_x \left(-\frac{\partial v'_z}{\partial x} + \frac{\partial v'_x}{\partial z} \right) \right\rangle + \frac{\partial}{\partial z} \left\langle v'_x \left(-\frac{\partial v'_x}{\partial y} + \frac{\partial v'_y}{\partial x} \right) \right\rangle \\ &= -\frac{\partial^2}{\partial x \partial y} \langle v'_x v'_z \rangle + \frac{\partial^2}{\partial x \partial z} \langle v'_x v'_y \rangle + \frac{\partial}{\partial y} \left\langle v'_z \frac{\partial v'_x}{\partial x} \right\rangle - \frac{\partial}{\partial z} \left\langle v'_y \frac{\partial v'_x}{\partial x} \right\rangle \end{aligned}$$

Summing up these equations, noting that mean quantities do not vary in the longitudinal direction owing to flow uniformity, and using the continuity equation for the velocity fluctuations we eventually find:

$$-\frac{\partial \langle v'_y \omega'_x \rangle}{\partial y} - \frac{\partial \langle v'_z \omega'_x \rangle}{\partial z} + \frac{\partial \langle v'_x \omega'_y \rangle}{\partial y} + \frac{\partial \langle v'_x \omega'_z \rangle}{\partial z} = -\frac{\partial^2}{\partial y \partial z} (\langle v_z'^2 \rangle - \langle v_y'^2 \rangle) - \left(\frac{\partial^2}{\partial y^2} - \frac{\partial^2}{\partial z^2} \right) \langle v'_y v'_z \rangle.$$

- the number of independent variables is reduced from four (the longitudinal coordinate x , the lateral coordinate y , the vertical coordinate z and time t) to three (x, y and t).

Let us then denote by L_0 the smaller horizontal scale of the mean flow, i.e. the minimum length over which significant spatial variations of the mean flow occur. Moreover, let D_0 denote a typical value of the flow depth. We then assume:

$$\delta \equiv \frac{D_0}{L_0} \ll 1. \quad (113)$$

Furthermore let us assume the flow to be either steady or slowly varying in time in that the time scale T_0 over which significant variations of the mean flow occur at a fixed location must not be smaller than L_0/U_0 , where U_0 denotes a typical velocity characteristic of the flow in the reach under consideration. The above assumptions are appropriate to investigate a number of river and

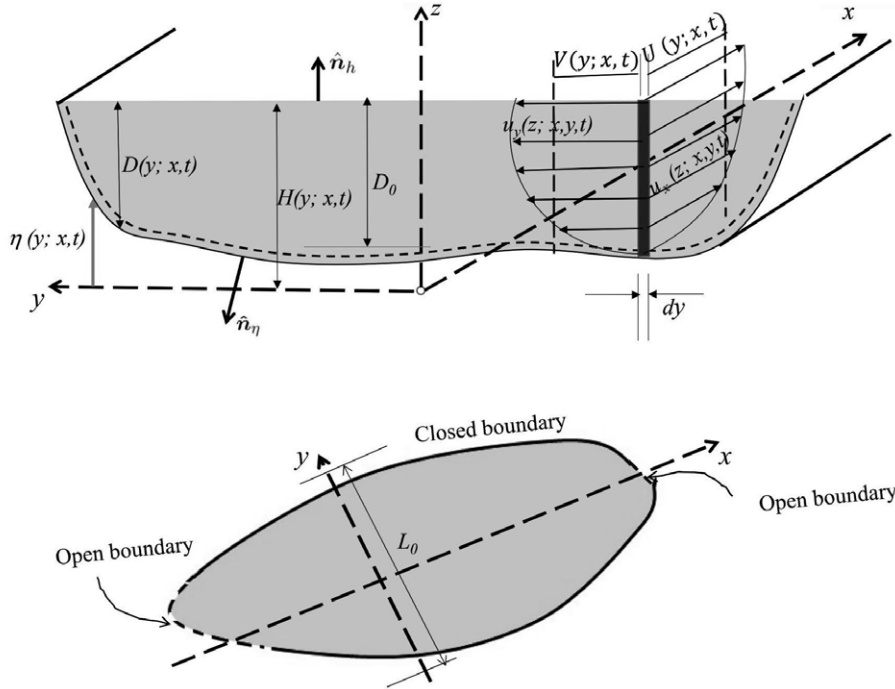


Figure 19. Sketch of the channel and notations for 2D modeling.

estuarine processes. For example, the typical length L_0 of fluvial bars scales with channel width; values of δ based on such length typically range about 10^{-2} - 10^{-3} . In addition, the time scales of both flood propagation in rivers and tidal phenomena are typically much larger than L_0/U_0 , a quantity which ranges about 10^2 - 10^3 s.

2.4.1 Pressure is hydrostatically distributed

We now show that, under the above conditions and recalling that we can approximate the normal to the bed with the vertical axis (Section 2.3.1), the mean pressure is hydrostatically distributed in the vertical direction. In fact, the z -component of the Reynolds equations (see equation (32)) and the continuity equation read:

$$-\frac{\partial P}{\partial z} - \rho g = \rho \left(\frac{\partial u_z}{\partial t} + u_x \frac{\partial u_z}{\partial x} + u_y \frac{\partial u_z}{\partial y} + u_z \frac{\partial u_z}{\partial z} \right) - \frac{\partial T_{zx}^t}{\partial x} - \frac{\partial T_{zy}^t}{\partial y} - \frac{\partial T_{zz}^t}{\partial z}, \quad (114)$$

$$\frac{\partial u_z}{\partial z} = -\frac{\partial u_x}{\partial x} - \frac{\partial u_y}{\partial y}. \quad (115)$$

We can roughly estimate the orders of magnitude of various contributions to (114) and (115) by replacing derivatives with ratios between typical scales of variations of dependent and independent variables. Hence, we take $\partial u_z/\partial z \sim \mathcal{O}(W_0/D_0)$ where W_0 denotes a typical scale for the vertical velocity (say its typical depth-averaged value). Since $\partial u_x/\partial x \sim \mathcal{O}(U_0/L_0)$, continuity implies that W_0 is $\mathcal{O}(\delta)$ smaller than U_0 .

The z -momentum equation suggests that the vertical variation of the mean pressure has a dominant gravitational contribution of order $(\rho g D_0)$, whilst the contribution due to inertia is at most $\mathcal{O}(\rho U_0^2 \delta^2)$. Hence, inertia is $\mathcal{O}(U_0^2/gD_0)\delta^2 = \mathcal{O}(F_{r0}^2)\delta^2$ smaller than gravity, where $F_{r0} = U_0/\sqrt{gD_0}$ is an $\mathcal{O}(1)$ quantity, representing a typical value of the Froude number in the flow reach examined.

On the other hand, the contribution due to the divergence of Reynolds stresses can be estimated recalling that $u_z = \mathcal{O}(\delta U_0)$. Given the slowly varying character of the flow in space and time, and using a Boussinesq type closure for T_{zx}^t , we thus find:

$$T_{zx}^t \sim \mathcal{O}\left(\rho \nu_T \frac{\partial u_x}{\partial z}\right). \quad (116)$$

Recalling (84), we may then assume that ν_T scales with the product between the macro scale of turbulence D_0 and a typical value of the friction velocity $u_{\tau 0}$, which measures the intensity of turbulent velocity fluctuations. Hence:

$$T_{zx}^t \sim \mathcal{O}\left(\rho u_{\tau 0} D_0 \left(\frac{U_0}{D_0}\right)\right). \quad (117)$$

Noting that $u_{\tau 0} \ll U_0$, it is readily seen that the order of magnitude of the ratio between Reynolds stress contribution and gravitational contribution is much smaller than $(U_0^2/gD_0)\delta = F_0^2 \delta$, having set $u_{\tau 0}/U_0 \sim \mathcal{O}(\delta)$.

In conclusion, we may neglect both inertial and Reynolds stress contributions in equation (114) and integrate it at once to give:

$$\frac{P}{\rho} = g(H - z). \quad (118)$$

From (118), it follows that the pressure gradient terms in the x - and y -components of Reynolds equations take the forms:

$$\frac{1}{\rho} \left(\frac{\partial P}{\partial x}, \frac{\partial P}{\partial y} \right) = g \left(\frac{\partial H}{\partial x}, \frac{\partial H}{\partial y} \right). \quad (119)$$

From equation (119) one thus replaces mean pressure P with free surface elevation H as a dependent variable in the governing equations of a 2D scheme.

2.4.2 Derivation of the shallow water equations

The shallow water equations are formally derived by depth integrating the 3D Reynolds averaged forms of the continuity equation and of the x, y -components of the momentum equation.

Consider first the x -component of the Reynolds equations. Using the continuity equation (31) we may rewrite the convective terms as follows:

$$u_x \frac{\partial u_x}{\partial x} + u_y \frac{\partial u_x}{\partial y} + u_z \frac{\partial u_x}{\partial z} = \frac{\partial u_x^2}{\partial x} + \frac{\partial (u_x u_y)}{\partial y} + \frac{\partial (u_x u_z)}{\partial z}. \quad (120)$$

With the help of (120), we now depth integrate the x -component of the momentum equation (32). Using Leibnitz rule, we find:

$$\begin{aligned}
 & \int_{\eta}^H \left\{ \frac{\partial u_x}{\partial t} + \frac{\partial}{\partial x}(u_x^2) + \frac{\partial}{\partial y}(u_x u_y) + \frac{\partial}{\partial z}(u_x u_z) \right\} dz = \\
 & = \frac{\partial}{\partial t} \int_{\eta}^H u_x dz - u_x|_H \frac{\partial H}{\partial t} + u_x|_{\eta} \frac{\partial \eta}{\partial t} \\
 & + \frac{\partial}{\partial x} \int_{\eta}^H u_x^2 dz - u_x^2|_H \frac{\partial H}{\partial x} + u_x^2|_{\eta} \frac{\partial \eta}{\partial x} \\
 & + \frac{\partial}{\partial y} \int_{\eta}^H u_x u_y dz - [u_x u_y]_H \frac{\partial H}{\partial y} + [u_x u_y]_{\eta} \frac{\partial \eta}{\partial y} \\
 & + [u_x u_z]_H - [u_x u_z]_{\eta}.
 \end{aligned} \tag{121}$$

We next define the depth averaged values of the longitudinal and lateral components of the Reynolds averaged velocity vector:

$$U = \frac{1}{D} \int_{\eta}^H u_x dz, \quad V = \frac{1}{D} \int_{\eta}^H u_y dz. \tag{122}$$

Moreover, let us recall the kinematic boundary conditions at the free surface and at the bed interface, which read:

$$\frac{\partial H}{\partial t} + u_x|_H \frac{\partial H}{\partial x} + u_y|_H \frac{\partial H}{\partial y} - u_z|_H = 0, \quad (u_x|_{\eta}, u_y|_{\eta}, u_z|_{\eta}) = 0. \tag{123}$$

With the help of (122) and (123) the left hand side of (121) becomes:

$$\frac{\partial}{\partial t}(DU) + \frac{\partial}{\partial x}(DU^2) + \frac{\partial}{\partial y}(DUV) + \frac{\partial}{\partial x} \int_{\eta}^H (u_x - U)^2 dz + \frac{\partial}{\partial y} \int_{\eta}^H (u_x - U)(u_y - V) dz. \tag{124}$$

Note that we have employed the following decompositions:

$$u_x = U + (u_x - U), \quad u_y = V + (u_y - V). \tag{125}$$

Let us next perform the depth averaging of the Reynolds stress flux to find:

$$\begin{aligned}
 & \int_{\eta}^H \left(\frac{\partial T_{xx}^t}{\partial x} + \frac{\partial T_{xy}^t}{\partial y} + \frac{\partial T_{xz}^t}{\partial z} \right) dz = \frac{\partial}{\partial x} \int_{\eta}^H T_{xx}^t dz + \frac{\partial}{\partial y} \int_{\eta}^H T_{xy}^t dz \\
 & - T_{xx}^t|_H \frac{\partial H}{\partial x} - T_{xy}^t|_H \frac{\partial H}{\partial y} + T_{xz}^t|_H + T_{xx}^t|_{\eta} \frac{\partial \eta}{\partial x} + T_{xy}^t|_{\eta} \frac{\partial \eta}{\partial y} - T_{xz}^t|_{\eta}.
 \end{aligned} \tag{126}$$

Let us now simplify (126) defining the depth averaged values of the T_{xx}^t and T_{xy}^t components of Reynolds stresses as follows:

$$\mathcal{T}_{xx} = \frac{1}{D} \int_{\eta}^H T_{xx}^t dz, \quad \mathcal{T}_{xy} = \frac{1}{D} \int_{\eta}^H T_{xy}^t dz, \tag{127}$$

and recalling that the components of the unit vectors normal to the free surface and bed interface (equation (38)), positive in the outer direction, read:

$$\hat{n}_x|_H = -\frac{\partial H/\partial x}{|\nabla \mathcal{F}_H|}, \quad \hat{n}_y|_H = -\frac{\partial H/\partial y}{|\nabla \mathcal{F}_H|}, \quad \hat{n}_z|_H = \frac{1}{|\nabla \mathcal{F}_H|}, \tag{128a}$$

$$\hat{n}_x|_{\eta} = \frac{\partial \eta/\partial x}{|\nabla \mathcal{F}_{\eta}|}, \quad \hat{n}_y|_{\eta} = \frac{\partial \eta/\partial y}{|\nabla \mathcal{F}_{\eta}|}, \quad \hat{n}_z|_{\eta} = -\frac{1}{|\nabla \mathcal{F}_{\eta}|}. \tag{128b}$$

where $|\nabla\mathcal{F}_H| = \sqrt{1 + (\partial H/\partial x)^2 + (\partial H/\partial y)^2}$ and $|\nabla\mathcal{F}_\eta| = \sqrt{1 + (\partial\eta/\partial x)^2 + (\partial\eta/\partial y)^2}$. With the help of the definition of stress vector (1), we may then write:

$$\left[-T_{xx}^t \frac{\partial H}{\partial x} - T_{xy}^t \frac{\partial H}{\partial y} + T_{xz}^t \right]_H = t_x|_H |\nabla\mathcal{F}_H| \simeq t_x|_H, \quad (129a)$$

$$\left[-T_{xx}^t \frac{\partial \eta}{\partial x} - T_{xy}^t \frac{\partial \eta}{\partial y} + T_{xz}^t \right]_\eta = -t_x|_\eta |\nabla\mathcal{F}_\eta| \simeq -t_x|_\eta, \quad (129b)$$

where we have neglected the quantities $[(\partial H/\partial x)^2 + (\partial H/\partial y)^2]$ and $[(\partial\eta/\partial x)^2 + (\partial\eta/\partial y)^2]$ related to the local bed and surface slopes, which are $O(\delta^2)$ in the light of the assumption (113). Also note that the latter approximation fails close to the banks, where this assumption is no longer satisfied. Moreover, with the same restrictions, the x -components of the stress vector acting on the free surface $t_x|_H$ and on the bed interface $t_x|_\eta$ may be replaced by the x -components of the tangential stress vector acting on the free surface and bed interface respectively: indeed, the local slopes of the free surface and bed interface are $O(\delta)$, hence $n_z \simeq 1$ and

$$t_x|_H \cong \tau_{Hx}, \quad t_x|_\eta \cong \tau_{\eta x}. \quad (130)$$

The reader is warned that the quantities τ_{Hx} and $\tau_{\eta x}$ are the stresses that the air exerts on the free surface and the bed exerts on the bed interface respectively. Hence, they are positive (negative) if directed like (opposite to) the x -axis.

We follow the same steps to depth average continuity equation and the y -component of the Reynolds equations. The following 2D formulation of the governing equations is eventually obtained:

$$\frac{\partial D}{\partial t} + \frac{\partial}{\partial x}(DU) + \frac{\partial}{\partial y}(DV) = 0, \quad (131)$$

$$\begin{aligned} \frac{\partial}{\partial t}(DU) + \frac{\partial}{\partial x}(DU^2) + \frac{\partial}{\partial y}(DUV) + gD \frac{\partial H}{\partial x} - \frac{1}{\rho}(\tau_{Hx} + \tau_{\eta x}) = \\ \frac{1}{\rho} \frac{\partial}{\partial x}(D\mathcal{T}_{xx}) + \frac{1}{\rho} \frac{\partial}{\partial x}(DT_{xx}^{(disp)}) + \frac{1}{\rho} \frac{\partial}{\partial y}(D\mathcal{T}_{xy}) + \frac{1}{\rho} \frac{\partial}{\partial y}(DT_{xy}^{(disp)}), \end{aligned} \quad (132)$$

$$\begin{aligned} \frac{\partial}{\partial t}(DV) + \frac{\partial}{\partial x}(DUV) + \frac{\partial}{\partial y}(DV^2) + gD \frac{\partial H}{\partial y} - \frac{1}{\rho}(\tau_{Hy} + \tau_{\eta y}) = \\ \frac{1}{\rho} \frac{\partial}{\partial x}(D\mathcal{T}_{xy}) + \frac{1}{\rho} \frac{\partial}{\partial x}(DT_{xy}^{(disp)}) + \frac{1}{\rho} \frac{\partial}{\partial y}(D\mathcal{T}_{yy}) + \frac{1}{\rho} \frac{\partial}{\partial y}(DT_{yy}^{(disp)}), \end{aligned} \quad (133)$$

where we have introduced the so called *dispersive stresses*, defined as follows:

$$T_{xx}^{(disp)} = -\frac{\rho}{D} \int_\eta^H (u_x - U)^2 dz, \quad (134a)$$

$$T_{xy}^{(disp)} = -\frac{\rho}{D} \int_\eta^H (u_x - U)(u_y - V) dz, \quad (134b)$$

$$T_{yy}^{(disp)} = -\frac{\rho}{D} \int_\eta^H (u_y - V)^2 dz. \quad (134c)$$

Dispersive stresses are sort of *macro Reynolds stresses* associated with the deviations of the distribution along z of the local mean velocity from its depth averaged value.

Substituting from (131) into (132, 133) the momentum equations in depth averaged form can be rewritten as:

$$\begin{aligned} \frac{\partial U}{\partial t} + U \frac{\partial U}{\partial x} + V \frac{\partial U}{\partial y} + g \frac{\partial H}{\partial x} - \frac{\tau_{Hx} + \tau_{\eta x}}{\rho D} = \\ \frac{1}{\rho D} \left\{ \frac{\partial}{\partial x} [D (\mathcal{T}_{xx} + T_{xx}^{(disp)})] + \frac{\partial}{\partial y} [D (\mathcal{T}_{xy} + T_{xy}^{(disp)})] \right\}, \end{aligned} \quad (135a)$$

$$\begin{aligned} \frac{\partial V}{\partial t} + U \frac{\partial V}{\partial x} + V \frac{\partial V}{\partial y} + g \frac{\partial H}{\partial y} - \frac{\tau_{Hy} + \tau_{\eta y}}{\rho D} = \\ \frac{1}{\rho D} \left\{ \frac{\partial}{\partial x} [D (\mathcal{T}_{xy} + T_{xy}^{(disp)})] + \frac{\partial}{\partial y} [D (\mathcal{T}_{yy} + T_{yy}^{(disp)})] \right\}. \end{aligned} \quad (135b)$$

In order to complete the formulation of the 2D model, appropriate closure relationships are needed.

2.4.3 Closures

The structure of the equations (135a, 135b) suggests that, as a result of depth averaging, the Reynolds stresses present in the 3D form of the momentum equations involve two types of contributions :

- shear stresses acting on the bed and on the free surface (possibly driven by wind action);
- depth averaged longitudinal and lateral stresses acting on the stream cross section.

In order to estimate the former contribution, closure relationships expressing the bottom stress τ_{η} as a function of the depth averaged flow field and the stress at the free surface τ_H as a function of wind velocity, are needed. To achieve this goal it is customary to take advantage of the slow spatial and temporal variation assumed for the flow field, such that the friction stresses may be taken as due to a sequence of quasi-steady and quasi-uniform flows associated with the local values of flow velocity and roughness. One then writes:

$$\tau_{\eta x} = -\rho C_f U \sqrt{U^2 + V^2}, \quad \tau_{\eta y} = -\rho C_f V \sqrt{U^2 + V^2}, \quad (136a)$$

$$\tau_{Hx} = \rho_a C_{fw} U_w \sqrt{U_w^2 + V_w^2}, \quad \tau_{Hy} = \rho_a C_{fw} V_w \sqrt{U_w^2 + V_w^2}. \quad (136b)$$

Here, $C_f = (\chi^{-2})$ is the friction coefficient associated with a uniform flow characterized by the local values of flow depth and roughness, C_{fw} is the friction coefficient associated with the wind action on the free surface, U_w and V_w are longitudinal and lateral components of the wind velocity and ρ_a is the air density. The value of C_f is determined employing classical relationships established for uniform open channel flows. For fixed bed conditions C_f is generally dependent on the local values of relative roughness and Reynolds number. In particular, for hydraulically rough walls, we may write:

$$\chi = C_f^{-1/2} = 6 + 2.5 \ln \frac{D}{e_s}, \quad (137)$$

with e_s the *local* value of the equivalent roughness. The wind friction coefficient C_{fw} takes typical values around 1.5×10^{-3} .

In order to estimate the contribution of the depth averaged longitudinal and lateral stresses acting on the stream cross section one should depth average a 3D closure relationship. However, it is easy to show that this contribution is negligible unless the flow contains layers where shear is intense, as found in separated flows. Indeed, using a Boussinesq type closure and assuming horizontal variations to occur over the large scale L_0 (no separation), one finds:

$$\frac{1}{\rho D} \frac{\partial}{\partial x} (D \mathcal{T}_{xx}) \sim \mathcal{O}\left(\frac{u_{\tau 0} U_0 D_0}{L_0^2}\right). \quad (138)$$

The latter contribution is to be compared with the bottom stress contribution which may be estimated as follows:

$$\frac{|\tau_{\eta x}|}{\rho D_0} \sim \mathcal{O}\left(\frac{C_{f0} U_0^2}{D_0}\right). \quad (139)$$

The ratio between the two is then readily seen to scale with the quantity $\delta^2/C_{f0}^{1/2}$ which is definitely quite small.

The effect of dispersive stresses is also typically small in straight channels but may be significant in curved channels due to the development of a secondary flow which gives rise to a net *dispersive* transfer of longitudinal momentum in the transverse direction. This will be discussed in the companion Monograph, where we will also learn how the shallow water equations can be modified to account for the effects of channel curvature without losing the *dispersive* effect mentioned above.

Including only the effects of bottom and wind stresses and adopting the closure relationships (136), we end up with the classical form of the shallow water equations:

$$\begin{aligned} \frac{\partial D}{\partial t} + \frac{\partial(DU)}{\partial x} + \frac{\partial(DV)}{\partial y} &= 0, \\ \frac{\partial U}{\partial t} + U \frac{\partial U}{\partial x} + V \frac{\partial U}{\partial y} + g \frac{\partial h}{\partial x} - \frac{\rho_a}{\rho} C_{fw} \frac{U_w \sqrt{U_w^2 + V_w^2}}{D} + C_f \frac{U \sqrt{U^2 + V^2}}{D} &= 0, \\ \frac{\partial V}{\partial t} + U \frac{\partial V}{\partial x} + V \frac{\partial V}{\partial y} + g \frac{\partial h}{\partial y} - \frac{\rho_a}{\rho} C_{fw} \frac{V_w \sqrt{U_w^2 + V_w^2}}{D} + C_f \frac{V \sqrt{U^2 + V^2}}{D} &= 0. \end{aligned} \quad (140a,b,c)$$

This formulation may need some modification if applied in a context where secondary flows occur and are such that the flow velocity undergoes spatial variations which are not sufficiently slow.

2.4.4 Boundary conditions

The partial differential system (140) can be shown to be quasi-linear and hyperbolic (Vreugdenhil, 1994). This implies that some surfaces exist in the (x, y, t) plane on which the set of partial differential equations (140) can be formulated in terms of only two independent variables and, hence, transformed into a system of ordinary differential equations. These surfaces are called characteristics and consist of two families of planes. Disturbances that propagate within these planes may loosely be considered as waves moving with given celerities. The boundary conditions needed to render the mathematical problem *well posed* is strictly linked to these celerities and require special attention.

One needs distinguish between closed and open boundaries. At a closed boundary the normal velocity must vanish. In the case of open boundaries, the number of conditions to be prescribed is given by the number of characteristic planes entering the flow domain. This number depends on whether the local Froude number, expressed in terms of the local flow depth and the velocity component U_n normal to the boundary ($Fr = U_n/\sqrt{gD}$), is lower than unity (*sub-critical flow conditions*) or larger than unity (*super-critical flow conditions*). The reader interested in the mathematical derivation of the theory of characteristics for the shallow water equations and in the appropriate boundary conditions is referred to Vreugdenhil (1994).

2.5. One-dimensional formulation: de Saint-Venant equation

Some processes of interest in river morphodynamics, such as long term river aggradation and degradation or selective sorting, develop significantly along channel reaches with longitudinal scale much larger than channel width. Furthermore, their temporal scales far exceed the time scales associated with growth and migration of smaller scale bedforms like dunes or bars. In order to investigate such processes, it is then convenient to average out smaller scale effects and employ a one-dimensional (1D) formulation of the hydrodynamic problem.

This approach is appropriate provided it is possible to identify a *dominant flow direction* in the fluid system (the *stream*) under investigation. Let x be a *longitudinal* axis aligned with the flow

direction: note that the axis may be curvilinear in general but, in the context of a 1D formulation, the hydrodynamic effects of curvature of the channel axis are ignored. Let us call *cross sections* of the channel the intersections of the stream with planes orthogonal to the x -axis (see Figure 20 for notations employed in this Section). One-dimensional modeling employs flow properties that are averaged over the cross section. Hence, mean velocity, momentum flux, discharge and energy flux of the stream will at most be functions of x and t . Before we proceed to formulate the problem in

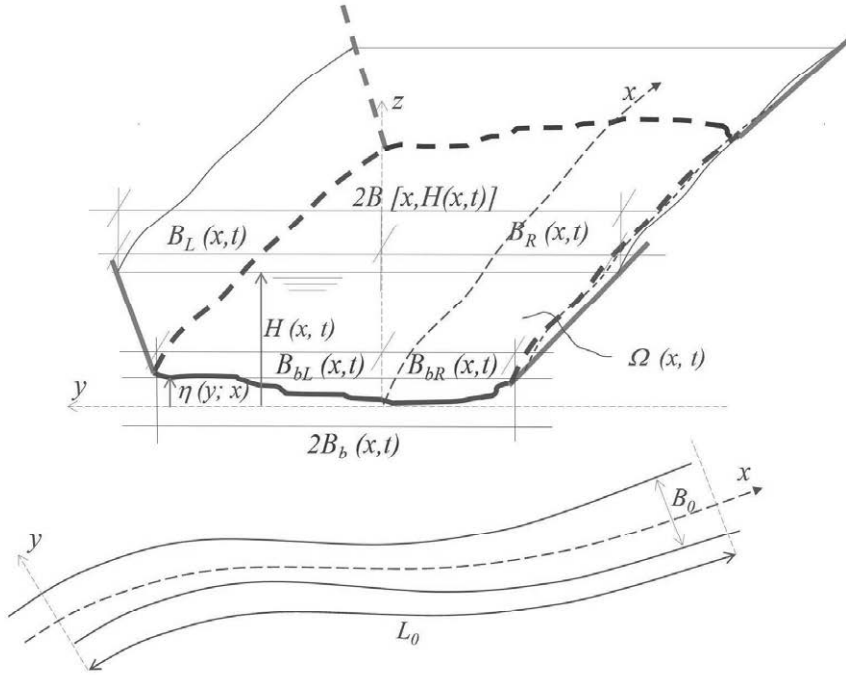


Figure 20. Sketch of the channel and notations for 1D modeling.

terms of cross sectionally averaged quantities we point out that the basic assumption underlying the validity of the 1D approach may be written in the form:

$$\epsilon = \frac{B_0}{L_0} \ll 1, \quad (141)$$

where B_0 and L_0 are typical spatial scales on which the flow quantities exhibit $\mathcal{O}(1)$ (relative) variations in the transverse and longitudinal directions.

Indeed, if (141) is satisfied, the continuity equation (140a) suggests that the transverse component of the depth averaged velocity is at least $\mathcal{O}(\epsilon)$ smaller than the longitudinal component: in other words, the streamlines of the depth averaged flow deviate weakly from the longitudinal direction. Similarly, the transverse component of the shallow water equations (140c) can be employed to estimate the transverse component of ∇H . One readily finds that $\partial H / \partial y$ is at least $\mathcal{O}(\epsilon)$ smaller than $\partial H / \partial x$, hence at the lowest order of approximation the free surface may be assumed horizontal at each cross section ($H = H(x, t)$).

2.5.1 Derivation of the 1D governing equations

The one-dimensional equations are readily obtained by averaging in the transverse direction the shallow water equations.

Let us start with the continuity equation (131). We find:

$$\int_{-B_R}^{B_L} \left[\frac{\partial D}{\partial t} + \frac{\partial}{\partial x}(DU) + \frac{\partial}{\partial y}(DV) \right] dy = \frac{\partial}{\partial t} \int_{-B_R}^{B_L} D dy + \frac{\partial}{\partial x} \int_{-B_R}^{B_L} (DU) dy + (DV)|_{B_L} - (DV)|_{B_R}, \quad (142)$$

where we have not included terms deriving from the application of Leibnitz rule because the flow depth vanishes at $y = -B_R$ and $y = B_L$. Using the boundary conditions $V|_{B_L} = V|_{-B_R} = 0$ and noting that:

$$\int_{-B_R}^{B_L} D dy = \Omega(x, t), \quad \int_{-B_R}^{B_L} (DU) dy = \mathcal{Q}(x, t), \quad (143)$$

with Ω cross sectional area and \mathcal{Q} flow discharge, we end up with the following *1D form of the continuity equation*:

$$\frac{\partial \Omega}{\partial t} + \frac{\partial \mathcal{Q}}{\partial x} = 0. \quad (144)$$

As mentioned above, analysis of the y -component of the shallow water equations (133) is only needed to show that the free surface elevation is constant in the y -direction. We leave this simple exercise to the reader.

Next, let us average the x -component of the momentum equation (132). We find:

$$\int_{-B_R}^{B_L} \left[\frac{\partial}{\partial t}(DU) \right] dy = \frac{\partial \mathcal{Q}}{\partial t}, \quad (145a)$$

$$\int_{-B_R}^{B_L} \left[\frac{\partial}{\partial x}(DU^2) + \frac{1}{\rho} \frac{\partial}{\partial x}(DT_{xx}^{(disp)}) \right] dy = \frac{\partial}{\partial x} \left[\int_{-B_R}^{B_L} dy \int_{\eta}^H u_x^2 dz \right] = \frac{\partial}{\partial x} (\beta_{cor} \mathcal{U}^2 \Omega), \quad (145b)$$

$$\int_{-B_R}^{B_L} \left[\frac{\partial}{\partial y}(DUV) + \frac{1}{\rho} \frac{\partial}{\partial y}(DT_{xy}^{(disp)}) + \frac{1}{\rho} \frac{\partial}{\partial y}(D\mathcal{T}_{xy}) \right] dy = 0, \quad (145c)$$

$$\int_{-B_R}^{B_L} \left[g D \frac{\partial H}{\partial x} \right] dy = g \Omega \frac{\partial H}{\partial x}, \quad (145d)$$

$$\int_{-B_R}^{B_L} \left[-\frac{1}{\rho} (\tau_{Hx} + \tau_{\eta x}) \right] dy = -\frac{1}{\rho} (2B \bar{\tau}_w + \mathcal{P}_w \bar{\tau}_0), \quad (145e)$$

$$\int_{-B_R}^{B_L} \left[\frac{1}{\rho} \frac{\partial}{\partial x}(D\mathcal{T}_{xx}) \right] dy = \frac{1}{\rho} \frac{\partial \Omega \mathcal{T}}{\partial x}, \quad (145f)$$

where an overbar denotes an average along the wetted perimeter ($\bar{\tau}_0$) or across the water surface ($\bar{\tau}_w$), $2B$ is the width of the free surface, \mathcal{P}_w is the wetted perimeter and \mathcal{U} , \mathcal{T} are the cross sectionally averaged flow speed and Reynolds stress T_{xx} , respectively. Moreover, β_{cor} is a correction coefficient which represents the ratio between the actual momentum flux of the stream and the momentum flux of a stream characterized by the same cross sectional area and a constant velocity distribution equal to the cross sectionally averaged speed \mathcal{U} of the actual stream. Hence:

$$\beta_{cor} = \frac{\int_{-B_R}^{B_L} dy \int_{\eta}^H u_x^2 dz}{\Omega \mathcal{U}^2}. \quad (146)$$

Usually, $\beta_{cor} \simeq 1$ provided the cross section is sufficiently regular, whereas it may be significantly different from one in composite sections treated as a single section.

In conclusion, the averaging process leads to the following form of the momentum equation:

$$\frac{\partial \mathcal{Q}}{\partial t} + \frac{\partial}{\partial x} \left(\frac{\beta_{cor} \mathcal{Q}^2}{\Omega} \right) + g \Omega \frac{\partial H}{\partial x} - \frac{1}{\varrho} (2B \bar{\tau}_w + \mathcal{P}_w \bar{\tau}_0) - \frac{1}{\varrho} \frac{\partial(\Omega \mathcal{T})}{\partial x} = 0. \quad (147)$$

The latter equation has been proposed in 1871 by Adh emar Barr e de Saint-Venant (de Saint-Venant, 1871) (but see Hager *et al.* (2019) for a historical account of its relationship to the work of Boussinesq (Boussinesq, 1877)). This equation poses a closure problem similar to those discussed for the 2D case.

2.5.2 Closures

To complete the formulation of the momentum equation (147) the following closure relationships are required.

- *Closure for the average bottom stress $\bar{\tau}_0$ and the average wind stress $\bar{\tau}_w$.*

Closure is achieved using the 1D version of (136). Denoting by \bar{C}_f the cross sectionally averaged value of the friction coefficient of the water stream and by \bar{C}_{fw} the wind friction coefficient, we write:

$$\bar{\tau}_0 = -\varrho \bar{C}_f \mathcal{U} |\mathcal{U}|, \quad \bar{\tau}_w = \varrho_a \bar{C}_{fw} U_w |U_w|. \quad (148)$$

- *Closure for the average Reynolds stress.*

Typically, this contribution is neglected. Semiempirical closures are necessary only when the 1D formulation is employed to investigate processes characterized by fairly short spatial scales.

With the latter assumptions, we end up with the following 1D form of the momentum equation:

$$\frac{\partial \mathcal{Q}}{\partial t} + \frac{\partial}{\partial x} \left(\frac{\beta_{cor} \mathcal{Q}^2}{\Omega} \right) + g \Omega \frac{\partial H}{\partial x} + 2B \frac{\varrho_a}{\varrho} \bar{C}_{fw} U_w |U_w| + \mathcal{P}_w \bar{C}_f \mathcal{U} |\mathcal{U}| = 0. \quad (149)$$

A simplified version of (149) often employed in fluvial contexts is obtained setting $\beta_{cor} = 1$, introducing the hydraulic radius $R_h = \Omega/\mathcal{P}_w$, neglecting the wind contribution and using the continuity equation (144), to find:

$$\frac{\partial \mathcal{U}}{\partial t} + \mathcal{U} \frac{\partial \mathcal{U}}{\partial x} + g \frac{\partial H}{\partial x} + \bar{C}_f \frac{\mathcal{U} |\mathcal{U}|}{R_h} = 0. \quad (150)$$

2.5.3 Boundary conditions

The equations (144) and (149) (or 150) can be shown to form a quasi-linear hyperbolic system of partial differential equations (Whitham, 1974). They must be supplemented with boundary conditions, consisting of known time dependent relationships between H and \mathcal{U} (or H and \mathcal{Q}) at the end sections of the channel reach. Theory of characteristics shows that the number of boundary conditions should be equal to the number of characteristics pointing into the flow domain. Specifically (see, e.g. Whitham, 1974), two of such relationships must be assigned at the upstream boundary under supercritical conditions ($F_r > 1$), whilst one relationship must be assigned at each boundary under subcritical conditions ($F_r < 1$), where the Froude number is now defined as $F_r = \sqrt{\mathcal{Q}^2 2B / (g \Omega^3)}$. Finally, an initial condition for H and \mathcal{U} (or H and \mathcal{Q}) at each cross section within the reach considered must also be assigned.

3. The sediment transport capacity of open channel flows

In this Chapter, we provide some elementary knowledge needed to evaluate the *sediment transport capacity* of turbulent flows in open alluvial channels.

However, before we proceed, we wish to warn the reader: in spite of the longstanding efforts of several communities (engineers, geomorphologists, geophysicists, applied mathematicians and physicists) which have been involved in various aspects of the subject, the available knowledge on the mechanics of sediment transport is as yet largely empirical. For this reason, we will not engage ourselves in an attempt to provide a comprehensive survey of the contributions available in the literature. We will just provide the reader with a physical description of the main aspects of the subject, along with the least amount of analysis useful to give some conceptual interpretation of observations. Recent developments on detailed simulations of the Mechanics of Sediment Transport will deserve a separate thorough assessment in a future Monograph. A brief account will be given in Section 3.3.3.

In this Chapter the mechanisms of sediment transport are analyzed in the context of the simplest hydrodynamic conditions, namely a plane uniform (i.e., longitudinally and laterally homogeneous) turbulent free surface flow on a flat bed made of cohesionless sediments. Moreover, sediment transport is taken to be statistically uniform. In other words, we assume the existence of *equilibrium conditions* such that *the supply of sediments balances exactly the transport capacity of the stream*. Under these conditions, neither net erosion nor net deposition occurs and the bed maintains its initial plane configuration. Needless to say, the latter conditions are never exactly met in reality. In fact, on one hand, the bottom of rivers most commonly exhibits *deviations from the flat configuration* which may take the variety of forms exhibited by the sedimentary patterns described in the introductory Monograph of the present series (Blondeaux *et al.*, 2018). Moreover, the *supply of sediments generally varies in time and space*, depending on the characteristics of the basin as well as on the intensity of single hydrodynamic events. Some of the required extensions of the treatment developed for the uniform case, such to account for the variety of circumstances occurring in nature are presented in the next Chapter. In particular, we will investigate the effects of slow spatial/temporal variations of the local and instantaneous hydrodynamic conditions, as well as of bottom geometry.

Finally, in this Chapter we restrict our attention to cohesionless sediment consisting of sediment particles modeled as solid spheres with the same *diameter*. This is an obvious (albeit widely employed) simplification: natural sediments have shapes rather flatter than the shape of a sphere and their grain size distributions may depart significantly from uniformity. Various interesting consequences arise from the heterogeneous character of natural sediments as particles of different sizes have different mobilities. As a result, sediment transport must be distinctly evaluated for each grain size. Moreover, particles tend to rearrange themselves developing so called *sorting patterns*.

3.1. The motion of an isolated heavy particle in viscous fluids

The fundamental process which needs to be preliminarily understood is the dynamic response of a single particle to the highly irregular turbulent motion of water in natural environments. As

pointed out in Chapter 2, the size of the smallest eddies in natural streams is comparable with the typical size of sand particles. However, the spectrum of grain sizes mobilized by water flow in the natural environment encompasses smaller particles (clay, silt and fine sand) as well as larger particles (coarse sand and gravel). Hence, a variety of regimes may be encountered in particle dynamics and different tools must be adopted in each regime.

3.1.1 Small particles: The equation of Maxey-Riley-Gatignol

Let us introduce the notion of the *undisturbed ambient flow*, namely the flow of the carrier fluid that would exist in the absence of the solid particle. Let $\mathbf{v}^0(\mathbf{x}, t)$ be the Eulerian field defining the spatially and temporally varying undisturbed velocity of the ambient fluid referred to a Cartesian coordinate system x_j ($j = 1, 2, 3$). As already pointed out, we restrict our attention to the case of spherical particles. Let us then consider a sphere of diameter d translating with speed $\mathbf{v}_P(t)$ and rotating with angular velocity $\boldsymbol{\Omega}_P(t)$ in the carrier fluid. Moreover, let $\mathbf{x}_0(t)$ denote the location of the center of the sphere at time t . The presence of the particle modifies the flow field. Let $\mathbf{v}(\mathbf{x}, t)$ denote the modified Eulerian velocity field. The governing equations for the motion of the fluid phase are the Navier-Stokes equations that must be solved with the boundary conditions of no slip at the surface of the sphere and vanishing perturbations sufficiently far from the sphere. Once pressure and velocity fields are known, the fluid stress tensor $\mathbf{T}(\mathbf{x}, t)$ is readily calculated from the constitutive relationship. Finally, the stress vector \mathbf{t} ($\equiv \mathbf{T} \cdot \hat{\mathbf{n}}$) at the surface of the sphere and the hydrodynamic actions on the sphere are obtained by integration over the particle surface. The output of this analysis depends on the regime of particle motion, i.e. on whether the relative Reynolds number of particle motion is small or moderate-large. This is a huge effort that is assessed in a number of textbooks (e.g. Clift *et al.*, 1978; Crowe *et al.*, 2012; Michaelides, 2006). Below, we outline few major achievements of direct interest to sediment transport.

Let us first consider the case of 'small' particles, in the sense clarified below. Maxey and Riley (1983) and, independently, Gatignol (1983), were able to determine an asymptotic approximation for the hydrodynamic force \mathbf{F} on small particles, subject to the following assumptions:

- the particle diameter d is much smaller than the scale of spatial variations of the ambient flow L_0 , with L_0 falling in the range $[\ell_k, \ell]$:

$$\frac{d}{L_0} \ll 1; \quad (151)$$

- the typical Reynolds number R_e of the relative motion of the fluid is small:

$$R_e = \frac{(U_0 - V_P) d}{\nu} \ll 1, \quad (152)$$

with U_0 and V_P scales for the fluid and particle velocity, respectively;

- the fluid shear, of scale U_0/L_0 , is weak, i.e. such that the *shear Reynolds number* R_k is also small:

$$R_k = \frac{U_0 d^2}{L_0 \nu} \ll 1. \quad (153)$$

Physically, this requirement implies that the convective time scale L_0/U_0 , namely the time the fluid takes to move over a distance of the order of L_0 , must be large compared with the viscous time scale d^2/ν , namely the time viscous effects take to diffuse over a distance of the order of particle size;

- the particle rotation is weak, i.e. the *rotational Reynolds number* R_Ω is small.

Under the above conditions, it is convenient to decompose the flow velocity \mathbf{v} into an *ambient* component \mathbf{v}^0 plus a *perturbation* \mathbf{v}^1 , associated with the modification of the undisturbed ambient flow due to the presence of the particle. Correspondingly, the hydrodynamic force on the particle may be decomposed into an *ambient* component \mathbf{F}^0 , i.e. the force that the ambient flow would exert on a fluid sphere instantaneously coincident with the solid sphere and a *perturbation* component \mathbf{F}^1 .

The *equation of motion of a small sphere in a temporally and spatially varying unbounded ambient flow* thus reads:

$$\varrho_s \mathcal{V}_P \frac{d\mathbf{v}_P(t)}{dt} = \mathbf{F}^0 + \mathbf{F}^1, \quad (154)$$

where ϱ_s is the particle density and \mathcal{V}_P is the particle volume. Expressions for \mathbf{F}^0 and \mathbf{F}^1 have been derived by Maxey and Riley (1983) and Gatignol (1983). With the help of these expressions and denoting by \mathbf{w}_P the velocity of the particle relative to the *ambient* component of the fluid velocity:

$$\mathbf{w}_P(t) = \mathbf{v}_P(t) - \mathbf{v}^0(t), \quad (155)$$

one ends up with the *equation of Maxey-Riley-Gatignol* (1983) (hereafter referred to as MRG) in the form:

$$\begin{aligned} s \frac{d\mathbf{w}_P}{dt} &= (s-1)\mathbf{g} + \frac{D\mathbf{v}^0}{Dt} - \frac{3}{4} \frac{c_D}{d} \mathbf{w}_P |\mathbf{w}_P| - c_a \frac{d\mathbf{w}_P}{dt} \\ &\quad - \frac{9\nu}{d} \int_0^t K(t-\tau) \frac{d\mathbf{w}_P}{d\tau} d\tau, \end{aligned} \quad (156)$$

where \mathbf{g} is the gravity vector and $s = \varrho_s/\varrho$ is the relative particle density. Moreover, D/Dt is the material derivative for fluid particles evaluated at the center \mathbf{x}_o of the sphere in motion,

$$\frac{Dv_i^0}{Dt} = \left(\frac{\partial v_i^0}{\partial t} + v_j^0 \frac{\partial v_i^0}{\partial x_j} \right) \Big|_{\mathbf{x}_o(t)}, \quad (157)$$

whilst d/dt denotes a material derivative associated with an observer moving with the particle, so that

$$\frac{dv_i^0}{dt} = \left(\frac{\partial v_i^0}{\partial t} + v_{Pj} \frac{\partial v_i^0}{\partial x_j} \right) \Big|_{\mathbf{x}_o(t)}. \quad (158)$$

In the right hand side of (156) one recognizes various contributions to the force acting on the sphere, scaled by the particle mass $\varrho\mathcal{V}_P$. The first term $(s-1)\mathbf{g}$ is the *submerged particle weight*, whilst $D\mathbf{v}^0/Dt$ is the contribution to the ambient component of the *hydrodynamic action due to fluid acceleration*.

The term $(3c_D \mathbf{w}_P |\mathbf{w}_P|/4d)$ is the *Stokes drag*. Here c_D is the *drag coefficient* related to the drag force F_D through the classical relationship:

$$F_D = \frac{1}{2} c_D \varrho \left(\pi \frac{d^2}{4} \right) |\mathbf{w}_P|^2. \quad (159)$$

The low Reynolds number form of c_D for a sphere reads $(24/R_e)$, with $R_e = |\mathbf{w}_P|d/\nu$ particle Reynolds number based on the instantaneous value of the relative particle velocity.

The term $c_a d\mathbf{w}_P/dt$ is the *added mass force*, with c_a added mass coefficient which takes the value 1/2 for a sphere. Note that the added mass force originates from the relative acceleration of the particle. Indeed, when the translation velocity of a body moving in an unbounded fluid varies, the kinetic energy of the fluid motion also varies. Hence, in order to be able to accelerate and to vary its kinetic energy, the body has to overcome an acceleration reaction responsible for the work done by the body on the fluid. In other words, the presence of the fluid acts such to increase the effective mass of the body.

Finally, the last term is the so called *history term* and $K(t - \tau)$ is the kernel of the convolution integral, which reads $[\pi \nu (t - \tau)]^{-1/2}$. Basset (1888) is usually credited with the original derivation of the history effect for a rigid sphere settling in a fluid that was otherwise at rest, though Boussinesq (1885) did obtain the same result three years before, in a paper apparently not known to Basset.

Note that various higher order contributions to the hydrodynamic force exerted on the particle are not included in the above relationships. They include the effects of *non uniformity of the ambient flow*, a *correction of the Stokes drag*, a *side force* driven by particle rotation and a *lift force* driven by the combined effects of translation and shear of the undisturbed ambient fluid.

3.1.2 The particle response time and the Stokes number

It is of particular interest to estimate how fast the particle is able to adjust its motion to the ambient flow. The simplest way to obtain this estimate is to calculate the time a small sphere released from rest in a quiescent fluid ($\mathbf{v}^0 = 0$, $\mathbf{w}_P = \mathbf{v}_P$) takes to reach its asymptotically steady settling speed. Under these conditions, neglecting for the sake of simplicity the effect of the history term (that usually plays a minor role), the equation (156) reduces to a simple balance between submerged weight of the sphere, Stokes drag and particle inertia:

$$(s + c_a) \frac{dv_P}{dt} = (s - 1)g - 18 \frac{\nu}{d^2} v_P. \quad (160)$$

Here, v_P is the modulus of particle velocity which, in the present case, coincides with $|\mathbf{w}_P|$. This equation is immediately solved with the initial condition $v_P|_{t=0} = 0$ and gives:

$$v_P = w_s \left[1 - \exp\left(-\frac{t}{t_R}\right) \right], \quad (161)$$

where the quantity $t_R = (s + c_a) d^2 / (18 \nu)$ is the *particle response time* and w_s is the asymptotic steady value of the *settling speed*, which reads:

$$w_s = \frac{(s - 1)g d^2}{18 \nu}. \quad (162)$$

The quantity t_R is precisely the sought estimate of the time required by a solid sphere to adjust its motion to the ambient flow. The ratio between t_R and the convective time scale of the ambient velocity field, L_0/U_0 , is a dimensionless parameter called *Stokes number* (S_t). It reads:

$$S_t = (s + c_a) \frac{d^2 / (18 \nu)}{L_0 / U_0}. \quad (163)$$

For *small* particles, say $d = 100 \mu\text{m}$, the value of t_R is approximately equal to $1.5 \cdot 10^{-3}$ s. In turbulent flows the smallest temporal scale is the Kolmogorov microscale τ_k that in river flows is around $5 \cdot 10^{-2}$ s. Hence, for particles in the fine sand range, the Stokes number is very small, $\mathcal{O}(3 \cdot 10^{-2})$. This feature turns out to be quite useful to investigate the dynamics of dilute suspensions in fluvial and tidal environments. Indeed, in the low S_t limit, the following simple asymptotic solution for particle velocity is readily derived:

$$\mathbf{v}_P = \mathbf{v}^0 + w_s \frac{\mathbf{g}}{g}. \quad (164)$$

Hence, *at the leading order of approximation, small particles behave as passive tracers except for their tendency to settle, which makes their trajectories deviate from fluid trajectories.*

The solution (164) is obtained from the dimensionless form of (156). Let us then set:

$$(\tilde{\mathbf{v}}^0, \tilde{\mathbf{v}}_P) = \frac{(\mathbf{v}^0, \mathbf{v}_P)}{U_0}, \quad (\tilde{t}, \tilde{\tau}) = \frac{(t, \tau)}{L_0 / U_0}, \quad (165)$$

having denoted by U_0 and L_0 the flow velocity and length scales, respectively, and used a tilde to denote dimensionless quantities. Substituting from (165) into (156), and recalling that for low particle Reynolds number $c_D = 24\nu/(|\mathbf{w}_P|d)$, with the help of some algebra one finds:

$$\tilde{\mathbf{w}}_P = \tilde{w}_s \frac{\mathbf{g}}{g} - S_t \left[\frac{d\tilde{\mathbf{w}}_P}{d\tilde{t}} + \frac{s}{s+c_a} \frac{d\tilde{\mathbf{v}}^0}{d\tilde{t}} - \frac{1}{s+c_a} \frac{D\tilde{\mathbf{v}}^0}{D\tilde{t}} \right] - \frac{1}{2\delta} \int_0^{\tilde{t}} \frac{d\tilde{\mathbf{w}}_P}{\sqrt{\pi(\tilde{t}-\tilde{\tau})}} d\tilde{\tau}. \quad (166)$$

Besides the Stokes number, two further dimensionless parameters appear. The first is $\tilde{w}_s \equiv w_s/U_0$, namely the settling speed of a spherical particle in the limit of vanishing Reynolds number normalized by the flow velocity scale. The second is the parameter $\delta = \sqrt{\nu L_0/U_0}/d$ which measures the ratio between the distance from the sphere where viscous diffusion is able to spread in a time of the order of the convective time scale and the sphere diameter. In open channel flows, for particles in the fine sand range, δ is an $\mathcal{O}(1)$ parameter.

Analytic solutions of the Maxey-Riley-Gatignol equation valid in the limit of small particle inertia (small S_t) have been obtained by a variety of Authors. For the present purposes, it proves sufficient to present the simplest version of this asymptotic solution (Maxey, 1987). Assume:

$$S_t \ll 1, \quad (167)$$

and expand $\tilde{\mathbf{w}}_P$ in the form:

$$\tilde{\mathbf{w}}_P = \tilde{\mathbf{w}}_{P0} + S_t \tilde{\mathbf{w}}_{P1} + \mathcal{O}(S_t^2). \quad (168)$$

Substituting from (168) into (166) and equating likewise powers of S_t , at the leading order ($\mathcal{O}(S_t^0)$) one finds:

$$\tilde{\mathbf{w}}_{P0} = \tilde{w}_s \frac{\mathbf{g}}{g}. \quad (169)$$

Returning to dimensional variables one immediately recovers the solution (164).

3.1.3 Larger particles

Determining the flow field induced by the unsteady translation and rotation of a particle transported at moderate-large relative Reynolds numbers in a sheared ambient fluid is a fundamental, yet unresolved, problem of Fluid Mechanics. Hence, a rigorous extension of the Maxey-Riley-Gatignol equation to the moderate-large Reynolds number regime is not available. An overview of the history of recent attempts performed to achieve this ambitious goal can be found in Michaelides (2006). A semiempirical general form for the particle equation of motion at moderate R_e has been proposed by Bagchi and Balachandar (2002) for solid spheres and Magnaudet and Eames (2000) for bubbles. It may be written in the general form:

$$(s+c_a) \frac{d\mathbf{v}_P}{dt} = (s-1)\mathbf{g} - \frac{18\nu}{d^2} \mathbf{w}_P (1+0.15R_e^{0.687}) + c_a \frac{d\mathbf{v}^0}{dt} + \frac{D\mathbf{v}^0}{Dt}. \quad (170)$$

The various contributions to (170) are forces per unit mass of the fluid phase. The first term on the right-hand side is the submerged gravity. The second term is the viscous drag, evaluated in terms of the local instantaneous relative particle velocity \mathbf{w}_P and including the finite R_e correction of Schiller and Neumann (1933), which is known to be valid for $R_e < 800$. The third term is the added mass force: for a sphere the added mass coefficient c_a keeps the value 1/2 also in the finite R_e regime. The fourth term is the force due to the pressure gradient in the undisturbed fluid. A last minor contribution, the history term, is not included in (170). Further minor (or insufficiently understood) effects are ignored in (170). Firstly, the strain rate $\nabla\mathbf{v}^0$ of the ambient fluid that modifies the drag force in a complex way is neglected. Shear induced lift and Magnus force driven by particle rotation are usually smaller than the drag force, hence are not included in equation (170). Moreover, when the particle diameter d is comparable with the characteristic length scale of the ambient flow, corrections of the drag force associated with flow non uniformity are likely

to be required, but a suitable form for such corrections at moderate R_e has not been proposed yet. Finally, for particles larger than Kolmogorov scale, particle-turbulence interaction becomes complex and the contribution of smaller-scale eddies is hardly captured by equation (170).

The picture of the dynamics of an isolated particle in turbulent flow emerging from the overview presented in this Section, points at a complex problem that is still far from being complete. A variety of further effects of relevance to morphodynamics would deserve attention.

Firstly, in natural settings sediment particles do not move in an unconfined environment, they interact with boundaries. In particular, natural streams exchange sediments with their cohesionless boundaries through two fundamental mechanisms which will be discussed in the next Section: *entrainment from* and *deposition onto* the bed. Moreover, particles may *collide* either physically or hydrodynamically with boundaries, a process which affects particle trajectory and, in the long term, may also lead to reduction of the particle mass (*abrasion*) as well as *erosion of the channel boundary*.

Moreover, sediment particles are not isolated: clouds of particles are typically transported by the stream near the bed and in the bulk of the flow. In the presence of sediment transport, the nature of the stream turns into that of a *mixture* of two distinct phases, whose motion may occur in a variety of regimes depending on the concentration of the solid phase and the size of sediment particles. In particular, as the concentration increases, particles do no longer behave as isolated: *hydrodynamic and possibly collisional interactions* occur. Moreover, the collective motion of sediment particles may affect the turbulence of the ambient fluid inducing a so called *turbulence modulation*. Accounting for all these features is a formidable task. Some progress has been recently made with the help of modern measuring techniques and computational fluid dynamics, as briefly outlined in the following Sections.

3.1.4 An important application: Settling of a sphere in a fluid at rest at moderate-large Reynolds numbers

The settling speed of a solid sphere in an unbounded fluid at rest is determined imposing a dynamic balance between the submerged weight of the sphere and the drag force expressed in the form of (159) with the drag coefficient c_D a function of the Reynolds number $R_e \equiv w_s d / \nu$. The reader will readily show that this balance leads to the following dimensionless relationship for the settling speed:

$$\tilde{w}_s = \sqrt{\frac{4}{3c_D}}, \quad (171)$$

where:

$$\tilde{w}_s = \frac{w_s}{\sqrt{(s-1)gd}}. \quad (172)$$

An important limit of (171) deserves special attention. At low Reynolds numbers, using the Stokes form for the drag coefficient ($c_D = 24/R_e$), the relationship (171) becomes:

$$\tilde{w}_s = \frac{R_p}{18} \quad (S_t \ll 1), \quad (173)$$

where R_p is a *particle Reynolds number* which plays an important role in sediment transport and reads:

$$R_p = \frac{\sqrt{(s-1)gd^3}}{\nu}. \quad (174)$$

In the intermediate range of values of R_e , employing the standard curve for the drag coefficient (Clift *et al.*, 1978) one may calculate a standard curve for the settling speed of a sphere. This is plotted in dimensionless form in Figure 21. The error associated with the latter estimate does not exceed 4%. Also shown in Figure 21 is the empirical relationship proposed by Dietrich (1982), which reads:

$$\log_{10} \frac{w_s d}{\nu} = -1.2557 + 1.95296 \ell_R - 0.13086 \ell_R^2 - 0.01533 \ell_R^3 + 0.00298 \ell_R^4, \quad (175)$$

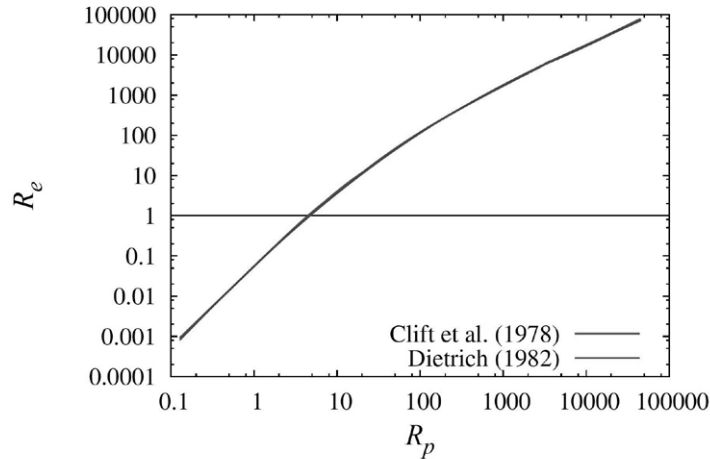


Figure 21. The Reynolds number of a settling sphere $R_e (= w_s d/\nu)$ is plotted versus the particle Reynolds number $R_p (= \sqrt{(s-1)g} d^3/\nu)$. The red line is the standard curve reported in (Clift *et al.*, 1978, p. 114). The blue line is the empirical approximation (175) proposed by Dietrich (1982).

with $\ell_R = \log_{10} R_p$.

Note that solid spheres settling at moderate-large Reynolds numbers are also subject to lateral forces which are associated with vortex shedding: as a result they follow a spiral motion. These lateral oscillations produce a small retardation of the settling process, with reductions of the terminal velocity which, for sand particles, do not reach 1%. A further note of caution is required when the above theoretical arguments are applied to the natural environment as real sediments are hardly spherical. The settling process of particles of arbitrary shape may display a quite complex behavior. Even at low Reynolds numbers, the force experienced by the particle may exhibit a lift component at right angle to particle velocity, which may cause the particle to drift laterally settling along a curved path. The rotational response of particles may also be complicated in general. If particles have a skew shape, i.e. if they do not exhibit suitable symmetries, one cannot define a center of hydrodynamic stress, hence particles rotate while settling and the resulting motion may be spiral or even wobbling if particles change orientation while settling (Happel and Brenner, 1965, Chapter 5). On the contrary, symmetric particles eventually reach a pure translatory motion, hence for such particles one can unambiguously define a terminal settling speed.

3.2. The modes of sediment motion

3.2.1 Transport mode versus sheet/debris mode

There are various modes whereby sediment particles lying on the bed of a natural stream may be destabilized. They range between two limit conditions that will be described as *transport mode* and *debris (or sheet) mode*. These two limit mechanisms are respectively associated with *fairly low* and *fairly high* values of the shear stress transmitted by the stream to a cohesionless bottom.

This can be readily illustrated considering the equilibrium of a plane granular bed, composed of grains of uniform size d , and density ρ_s . The bed is subject to a turbulent uniform free surface flow determining a uniform distribution of the mean shear stress (averaged over turbulence) τ_0 at the bed-fluid interface. Let θ be the inclination angle of the bed, ϕ the angle of repose of the granular medium and c_M its volumetric concentration.

Let us consider a sediment layer of thickness l , bounded by the bed interface and a planar surface parallel to it (Figure 22). This layer will experience destabilizing actions arising from the shear stress exerted by the flowing stream as well as from the down-slope component of the

submerged weight of the granular mixture contained in the layer. The overall destabilizing stress per unit area is then equal to $[\tau_0 + (\rho_s - \rho) c_M l g \sin \theta]$. Contacts among grains provide the stabilizing stress acting on the planar surface. Under conditions of limit equilibrium, the latter may be written in the Coulomb form, $[(\rho_s - \rho) c_M l g \cos \theta \tan \phi]$. The threshold conditions for the granular layer lying above the planar surface to be mobilized are then immediately derived by equating the above stresses. One finds:

$$\frac{l}{d} = \frac{\tau_*}{c_M \cos \theta (\tan \phi - \tan \theta)}, \quad (176)$$

where τ_* is a dimensionless quantity, the *Shields stress*, which will be seen to play an important role in the theory of sediment transport:

$$\tau_* = \frac{\tau_0}{(\rho_s - \rho) g d}. \quad (177)$$

Values of τ_* typically encountered in sand and gravel bed rivers will be presented later on (Figure 24).

The equation (176) immediately suggests that, in order for the thickness of the mobilized layer to be large relative to particle size, at least one of the following conditions must be satisfied:

- the Shields stress τ_* must be large enough;
- the bed inclination θ must be close to the angle of repose of the mixture.

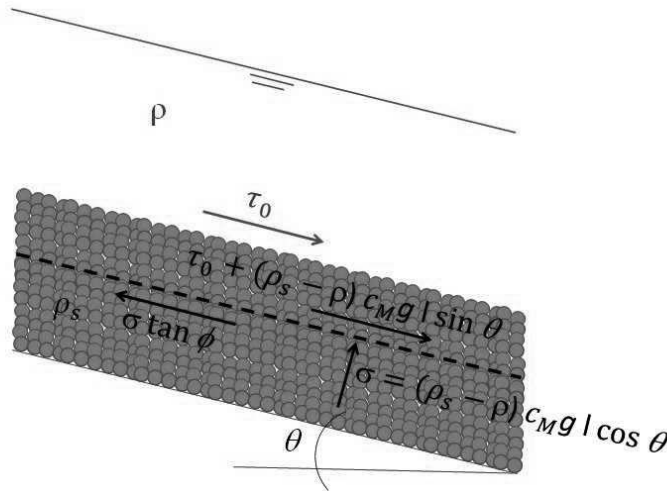


Figure 22. Sketch of the balance of destabilizing versus stabilizing forces acting on a layer of granular mixture

The former condition is characteristic of intense flows and/or fine sediments: this is the so called *sheet mode*, experienced in lowland rivers as well as in coastal areas subject to intense currents generated by tides and wind waves. The latter condition is typical of the massive motion of sediments on high slopes: the so called *debris mode*. However, when the bed inclination is small and the Shields stress takes the fairly small values (most often much smaller than one) typically encountered in fluvial streams, the relationship (176) predicts that the thickness of the destabilized layer does not exceed one particle diameter: the Coulomb type approach is then no longer significant. In fact, under these conditions, the major destabilizing forces are those acting on individual particles lying on the surface layer (hydrodynamic drag and lift), while submerged gravity plays a stabilizing role, allowing for the generation of contact forces between a given

particle and its neighbours. This regime is called *sediment transport mode*. Below, we concentrate on the transport mode. The study of debris flows requires distinct techniques that will deserve a Monograph of its own.

3.2.2 Transport mode: bedload versus suspended load

The traditional view of geomorphologists and engineers has been to establish a relationship between the shear stress, averaged over turbulence, acting on the erodible bed interface and the intensity of sediment transport. Indeed, it has long been recognized that, increasing the flow discharge, a uniform free surface flow over an erodible bed interface undergoes a sequence of stages which are commonly classified as follows.

- *Immobile bed*. If the turbulent intensity is sufficiently weak and/or sediment particles are large enough, particles lying on a cohesionless sediment bed keep immobile (Figure 23a).
- *Incipient particle motion*. Increasing the flow discharge, the shear stress τ_0 acting on the bed also increases. As soon as τ_0 exceeds some threshold value τ_c depending on the sediment characteristics, particles lying on the cohesionless bed are entrained and set in motion.
- *Bedload transport*. Provided the bottom stress (hence the turbulent intensity) keeps sufficiently low ($\tau_c < \tau_0 < \tau_s$) and/or particles are not too small, sediment transport occurs in a thin layer (of the order of few grain diameters) adjacent to the bed, with particles sliding, rolling or saltating, i.e. making small jumps, on the bottom (Figure 23b). This mode of transport is conventionally called *bedload transport*.
- *Transport in suspension*. For larger values of the bottom stress ($\tau_s < \tau_0 < \tau_{sd}$) and/or small enough particles, sediments escape from the bottom layer and are entrained in the bulk of the flow. They are then transported by the fluid behaving as passive tracers except for their tendency to settle as a result of their excess density (Figure 23c). This mode of transport is conventionally called *transport in suspension* as long as the suspension keeps sufficiently dilute that particle interactions (hydrodynamic, frictional and collisional) may safely be neglected.
- *Transition to sheet-debris mode*. This transition occurs for $\tau_0 > \tau_{sd}$, as a result the suspension becomes highly concentrated and particle interactions play a dominant role.

As a final note of caution, the threshold values τ_c , τ_s and τ_{sd} can only be defined in statistical sense as the transition between adjacent transport modes is smooth rather than abrupt.

3.2.3 The modern view: coherent turbulent structures and their role in particle entrainment

As discussed in Section 2.2.3, since the early works of Theodorsen (1952) and Kline and Runstadler (1959), developed and extended by Kline *et al.* (1967), experimental investigations on the detailed structure of the turbulence field in boundary layers and channels have revealed the existence of distinctly recognizable organized motions referred to as 'coherent structures'.

The discovery of coherent structures has had some impact also on the understanding of sediment transport. Indeed, in a laboratory investigation appeared shortly after the discovery of wall structures, Sutherland (1967) clearly observed that bedload particles move collectively "*in a series of short intermittent bursts, each of which is confined to a small area*" which then "*remains relatively undisturbed for a period until another short burst occurs*". The mechanism envisaged by Sutherland (1967), namely an eddy impact onto a sediment bed able to produce a horizontal drag force on the grain large enough to give rise to rolling of the particle about its point of support, already contained the essential features of the process which have later emerged from more detailed investigations.

However, it was only in the 80's that these inspiring ideas were more clearly related to the structure of near wall flow events. In a series of important papers (Heathershaw and Thorne, 1985;

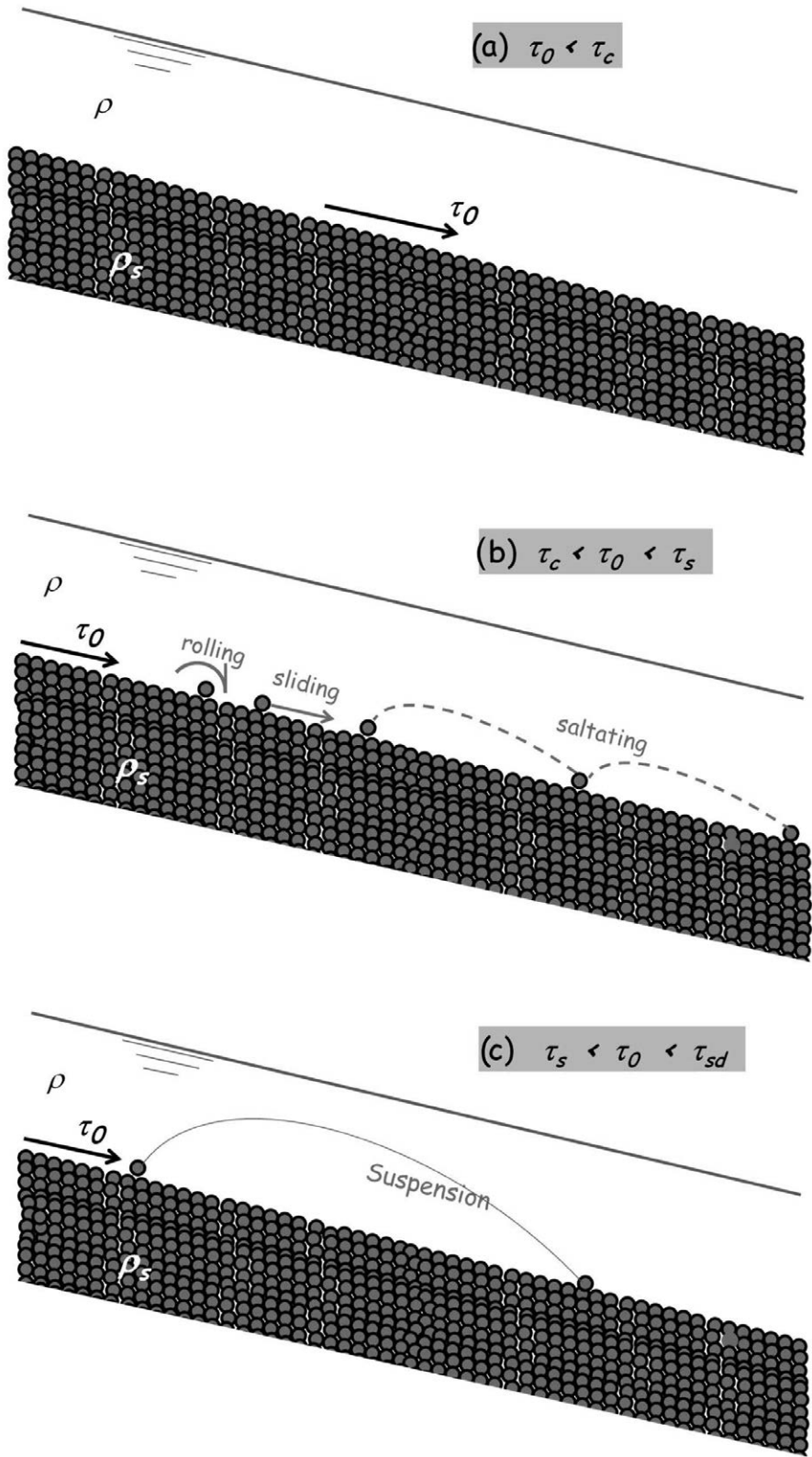


Figure 23. Sketch of the various modes of sediment transport (a) no transport; (b) bedload transport; (c) transport in suspension

Thorne *et al.*, 1989) a technique was developed to measure simultaneously flow field and bedload transport in a shallow tidal channel, with bed composed of a bimodal sand-gravel mixture with dominant content of gravel. An analysis of the experimental results revealed the following facts.

- The bulk of bedload gravel transport was associated with events of the bursting cycle classified as *sweeps*.
- A significant role was also played by so called *outward interactions* ($v'_x > 0, v'_z > 0$), though their relatively low frequency and amplitude gave rise to a fairly small overall effect.
- On the contrary, *ejections* ($v'_x < 0, v'_z > 0$) and *inward interactions* ($v'_x < 0, v'_z < 0$) produced very little transport.

Field observations of bedload transport of gravel in fluvial alluvial streams performed by Drake *et al.* (1988) and later detailed laboratory measurements (Nelson *et al.*, 1995) confirmed the general ideas discussed above.

In order to transform the above observations into modeling capabilities, one should compute the unsteady response of a single particle to the action of organized wall structures. However, this is a formidable problem as a number of difficulties are encountered when one attempts to model the actual process occurring in nature. Firstly, the flow Reynolds number of fluvial and tidal streams is typically very large (say $10^6 - 10^7$), hence outside the range of Reynolds numbers that can be reached by DNS. Rough wall conditions add a further source of difficulty for numerical modeling. Finally, particle-particle and wall-particle interactions pose a formidable hydrodynamic problem, the more so if the wall is irregular. This notwithstanding, considerable progress has been made recently, considering turbulent flows at low Reynolds numbers and restricting the analysis to collections of a relatively small number of spherical particles. Results of these efforts are briefly discussed in Section 3.3.3.

3.3. Bedload transport

3.3.1 Threshold conditions for particle entrainment as bedload

It is hard to trace the earliest known contribution to the problem of defining threshold conditions for the initiation of sediment motion in turbulent streams. However, the first systematic approach to the problem was apparently pursued by Shields (1936). This author was already aware of the highly unsteady and spatially non uniform character of the process of initiation of motion, which is statistical in nature and requires some averaged definition of the critical conditions. The actual approach employed by Shields (1936) to define the critical (mean) bed shear stress for sediment motion is not quite clear. The interested reader may refer to Buffington (1999) and the discussions which followed, for a thorough analysis of the historical developments of the interpretation of Shields work¹. His experiments were performed in flumes with a fully developed uniform turbulent stream flowing on an initially flattened bed of cohesionless natural sediments. Nevertheless, the bed did not keep plane throughout the experiment and the grain size distribution was not uniform.

In principle, entrainment occurs when the static equilibrium of a grain lying on the bed surface is lost. Equilibrium obviously depends on the forces acting on the particle, namely submerged gravity, hydrodynamic forces and contact forces with neighboring grains. Hence, on purely physical ground, the mean critical bed shear stress for the incipient motion of uniform sediments lying at the bottom of a uniform turbulent stream may be assumed to be a function of: i) fluid properties (density ρ and kinematic viscosity ν); ii) particle properties (size d , submerged specific weight $g(\rho_s - \rho)$, shape, grain size distribution); iii) local geometrical arrangement of the cohesionless

¹ In Shields (1936) paper the critical stress was defined as the value of the mean bottom stress below which the average volumetric bedload flux vanishes. Its value was apparently obtained by extrapolating a plot of observed sediment fluxes as a function of the average bottom shear stress. However, it has been argued (Kennedy, 1995) that visual observations might have actually been employed by Shields (1936).

bed, notably the degree of exposure of the particle to the flow; iv) gravity, acting on sediment particles lying on sloping beds.

Ignoring, for the moment, the effects of sediment heterogeneity and particle shape, we can write

$$\tau_c = \tau_c(d, \varrho, \nu, g(\varrho_s - \varrho); e, \tan \theta), \quad (178)$$

where $\tan \theta$ is the bed slope and e is a dimensionless parameter measuring the degree of particle exposure. The application of Buckingham theorem to (178) implies:

$$\tau_{*c} = \tau_{*c}(R_p; e, \tan \theta), \quad (179)$$

where τ_{*c} is the critical value of the Shields stress τ_* (recall the equation 177), while R_p is the particle Reynolds number defined by (174). Essentially, R_p is a dimensionless measure of particle size and turns out to be a convenient alternative to the particle Reynolds number R_τ based on the friction velocity u_τ originally employed by Shields (1936) and defined in the form:

$$R_\tau = \frac{u_\tau d}{\nu}. \quad (180)$$

The use of R_p was apparently first suggested by Yalin (1972). Such a choice avoids the presence of the friction velocity in both sides of (179) and simplifies the actual calculation of the critical Shields stress. Also note that R_p , R_τ and τ_* satisfy the following simple relationship:

$$R_p = \frac{R_\tau}{\sqrt{\tau_*}}. \quad (181)$$

Shields (1936) original results did not consider the effect of bed slope nor the role of particle exposure as natural sediments were employed and the spatial arrangement of particles was random. The critical conditions were identified through a plot in the plane (R_τ, τ_*) based on experimental observations performed by a number of previous Authors along with some observations performed by Shields himself. The plot was later fit by a curve proposed by Rouse (1939). A close analytical approximation of this curve was obtained by Brownlie (1981) and reads:

$$\tau_{*co} = 0.22 R_p^{-0.6} + 0.06 \exp(-17.77 R_p^{-0.6}), \quad (182)$$

where the subscript o is introduced to recall that the above relationship refers to conditions of nearly vanishing bed slope. Brownlie relationship is plotted in the plane (R_p, τ_*) of Figure 24. Also shown are experimental data referring to bankfull conditions for a variety of rivers. They suggest that the threshold conditions for both bedload and suspended load are typically exceeded in the field although Shields criterion clearly overestimates the critical value of the Shields stress for gravel bed river. The above plot also underlines the level of uncertainty that unavoidably characterizes the definition of a threshold which is statistical in nature.

Various later experimental works pointed out the *difficulty to give a precise definition of threshold conditions* for particle motion. In particular, Taylor (1971) showed that the definition of critical conditions depends on the choice of the accuracy of the condition of *vanishing bedload transport*. For large particle Reynolds numbers, the critical value of the Shields parameter may roughly decrease from 0.06 to 0.03 as the dimensionless sediment flux per unit width (scaled by the flow discharge per unit width) decreases from 10^{-2} to 10^{-6} . Similarly, Fenton and Abbott (1977) showed that the value of τ_{*co} decreases as the *degree of exposure of individual grains to the flow* e increases (the lowest value of τ_{*co} ranged about 0.01 and was associated with the maximum value of e for large values of R_p).

The *effect of bed slope* can be readily incorporated in the context of the present dimensional treatment. In fact, for the typical case of small bed slopes, we may linearize the dependence of the relationship (179) on $\tan \theta$, to find:

$$\tau_{*c} = \tau_{*co}(R_p) \left(1 + c \tan \theta\right), \quad (183)$$

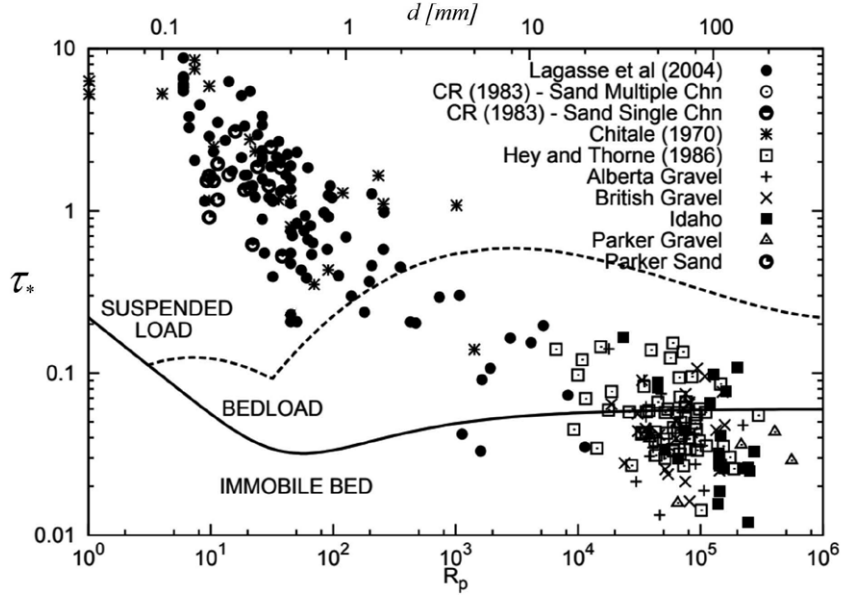


Figure 24. Threshold conditions for the initiation of motion are plotted in plane (R_p, τ_*) . Two curves are shown: the Brownlie (1981) approximation of the original Shields (1936) empirical criterion (τ_{*c0} solid line) and the curve representing Van Rijn (1984a) criterion for incipient transport in suspension (τ_{*s} dashed line). The points refer to data sets for a variety of rivers under bankfull conditions.

with c a constant and the obvious constraint that τ_{*c} must tend to τ_{*c0} as the slope vanishes. The constant c can be determined experimentally. However, a simple estimate of c is obtained by extending the validity of (183) up to values of θ comparable with the sediment angle of repose ϕ . Imposing the further constraint that τ_{*c} must vanish as $\theta \rightarrow \phi$, one finds:

$$\tau_{*c} = \tau_{*c0}(R_p) \left(1 - \frac{\tan \theta}{\tan \phi} \right). \quad (184)$$

An expression similar to (184) was first derived by Lysne (1969) who also tested it by performing a series of experiments on the effect of bed slope on the incipient motion of sand in a close channel. Results are quite well fitted by (184) with ϕ ranging about 47° . A similar value of ϕ was found by Luque and Van Beek (1976), who fitted a similar relationship to their experimental observations for the incipient motion of sand, gravel and magnetite in open channel flow on sloping beds. This suggests that a simple dimensional approach is significant in spite of the complexity of the process. The above discussion is sufficient for our present purposes. The reader interested in achieving a wider knowledge of the rich literature developed on the subject in the last few decades is referred to Garcia (2008).

In order to interpret the available experimental observations, attempts have been made to perform elementary analysis of the equilibrium of an isolated particle, resting on a granular bed. At incipient motion the sum of the destabilizing moments of drag and lift forces acting on the grain with respect to the points of contact of the grain with neighboring particles must balance the stabilizing moment of submerged particle weight. These attempts have qualitative significance. Several Authors have tried to go beyond qualitative reasoning. However, various difficulties arise. In particular, the statement of equilibrium should hold instantaneously but no rigorous knowledge exists of the instantaneous flow field acting on a sphere lying on a granular bed. Moreover, even neglecting the effect of turbulent fluctuations, the presence of the rough wall makes the hydrodynamic forces acting on the particle hardly predictable with accuracy. In spite of these difficulties, Coleman (1967), Ikeda (1982a) and Wiberg and Smith (1987) (among others) were

able to show that, with the help of reasonable empirical guesses for the values of the drag and lift coefficients, along with approximate assumptions on the velocity distribution of the fluid phase and the direction of particle drag and lift, the predicted criterion exhibits the general form of the Shields criterion. This will be discussed in Section 3.3.4.

3.3.2 Bedload transport capacity of homogeneous sediments in uniform open channel flow

Classical experimental observations

As mentioned above, provided the Shields stress acting on the bed exceeds the critical value τ_{*c} , grains are entrained by the stream and bedload transport occurs within a layer adjacent to the bed where particles slide, roll or saltate on the bottom.

In the classical experimental investigations of the mechanics of bedload transport appeared in the early literature, attempts were made to relate the average properties of particle motion to the mean flow properties. A great deal of our knowledge on the subject comes from the investigations of Francis (1973) and Abbott and Francis (1977). These works, along with a number of previous and later studies, employed photographic techniques to observe the motion of isolated particles saltating over a fixed bed. Investigations by Ikeda (1971), Luque and Van Beek (1976) and Niño and Garcia (1994) (among others) extended these observations to the more realistic case of bedload particles saltating over movable beds, restricting their attention to the case of *uniform sediments*. A number of important results emerged.

- Bagnold (1973) clarified the *distinction between bedload and suspended load*, emphasizing the role of turbulence as the supporting agent of suspended particles (“*the excess weight of the solid is supported wholly by a random succession of upward impulses imparted by eddy currents of fluid turbulence moving upwards relative to the bed.*”). Bedload transport was then defined as unsuspended in that “*no upward impulses are imparted to the solid other than those attributable to successive contacts between the solid and the bed*”. Vague as these statements may appear, they contain a fundamental idea, later confirmed by field and laboratory observations: bedload transport, as opposed to transport in suspension, is not associated with the occurrence of positive (i.e., upward directed) turbulent velocity fluctuations in the near wall region. Hence, it is not surprising that, as shown by some of Francis (1973) observations, saltation may occur also under laminar flow conditions.
- Abbott and Francis (1977) formulated a more precise definition of *saltation* as a *mode of transport where grains do never experience an upward acceleration* (except, of course for the very initial instant of particle motion).
- Few experimental observations analyzed the simultaneous occurrence of the rolling-sliding and saltation modes as a function of the so called *stage parameter* T , a measure of the intensity of transport defined as the ratio τ_*/τ_{*c} . In Abbott and Francis (1977) it clearly emerged that the rolling-sliding mode prevailed (roughly 60% of total time spent in transport) at threshold, then decreased rapidly (20% at $T = 1.4$) and practically disappeared as T reached a value of about 3. Qualitatively similar field observations have been reported by Drake et al. (1988). Thus *the rolling-sliding mode appears to be a relatively minor feature of bedload transport*.
- Both saltation lengths and saltation heights exhibit a monotonically increasing dependence on stage parameter in different sets of data, with the exception of those of Luque and Van Beek (1976) whose saltation lengths did not exhibit any Shields dependence and ranged about $16d$.
- The *average intensity of the particle velocity* $\langle v_P \rangle$ measured by various Authors was invariably found to depend on Shields stress in the form:

$$\langle v_P \rangle = \mathcal{A} \left(\sqrt{\tau_*} - \sqrt{\tau_{*c1}} \right), \quad (185)$$

where \mathcal{A} is a parameter and τ_{*c1} is a sort of *dynamic critical Shields stress* somewhat smaller than τ_{*c} . Hence, it is more difficult to mobilize a particle than to keep it in motion once it has been mobilized. The velocity is thus discontinuous at the threshold of sediment transport, even though determining this nonzero finite value remains an experimental challenge (Lajeunesse *et al.*, 2010).

- In interpreting the saltation mechanism, one may be tempted to take the view that particle rebound arises from an elastic collision between the hopping grain and the hit particle lying on the bed. Indeed, such a view is able to explain the process of aeolian saltation (Bagnold, 1941; Owen, 1964; Anderson and Haff, 1988). However Bagnold (1956) (pg. 244) first pointed out that the above viewpoint is not appropriate to interpret subaqueous saltation: “*owing to viscous effects in liquids the grain velocity on return to the bed is insufficient to cause any observable rebound or any disturbance of the bed grains*”. Bagnold again captures a basic physical idea: the interaction between a particle and the bed is a hydrodynamic process, affected by the dynamics of the fluid layer squeezed between the moving and the stationary grains. The details of this process have hardly been investigated. Bagnold intuition was confirmed by later observations. In particular Abbott and Francis (1977) state: “*there was not the slight evidence of a particle bouncing backwards after a collision*” while, often, the impacting grain “*rolls over the bed particle and is momentarily stopped by the next bed particle before being lifted away again by the flow*” and “*there are fewer impacts in which the grain glances off the bed into a low trajectory*”.

The average bedload transport rate per unit width

Using the notations of Figure 25, the *instantaneous volumetric bedload transport rate per unit width* can be given the following general form:

$$\int_{y-b_1/2}^{y+b_1/2} dy \int_0^{h_b} v_P(\mathbf{x}, t) dz. \quad (186)$$

In (186), \mathbf{x} is a point vector lying within the given cross-section, $v_P(\mathbf{x}, t)$ is a function which vanishes whenever \mathbf{x} is located outside the volume \mathcal{V}_s instantaneously occupied by sediment particles in motion, otherwise it coincides with the longitudinal component of the instantaneous particle velocity at locations \mathbf{x} contained within \mathcal{V}_s . Moreover, h_b is the thickness of the layer containing sediment particles in motion and b_1 is the dimensional unit width.

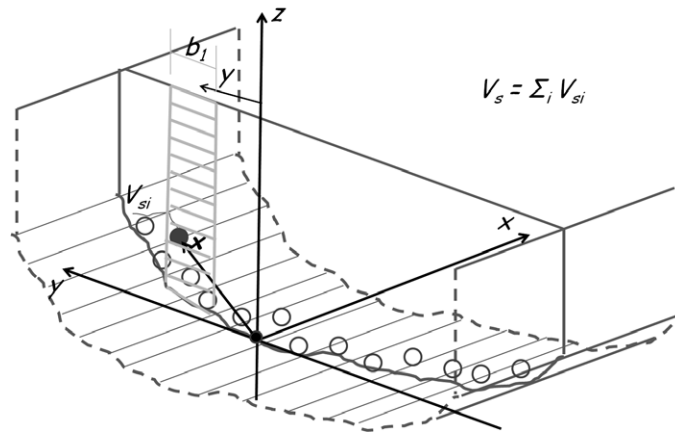


Figure 25. Sketch of particles in motion as bedload and notations.

Note that (186) essentially defines the instantaneous sediment flux per unit width in terms of a weighted average of the longitudinal components of the velocities of the particles crossing

the unit width of the stream at time t , with weights given by the areas of the instantaneous intersections of the particles with the stream cross-section. Both velocities and areas fluctuate in time due to particle motion. It is then convenient to define an average depth integrated volumetric sediment flux per unit width Q_s^b (or *average bedload transport rate per unit width*) by performing an ensemble average or an equivalent temporal average of (186). One finds:

$$Q_s^b = \lim_{\Delta t \rightarrow \infty} \left(\frac{N_P(\Delta t) \mathcal{V}_P}{\Delta t} \right), \quad (187)$$

where $N_P(\Delta t)$ is the number of grains (not necessarily an integer number) which have crossed the unit width of the stream in the time interval Δt . Note that, in the classical approach, the relative effect of fluctuations of $N_P(\Delta t)$ on Q_s^b is assumed to decrease as Δt increases, hence a fairly stationary limit is expected.

Let us now derive a general relationship for Q_s^b by purely dimensional arguments. On physical ground, it is reasonable to assume that, for a uniform sediment and a weak bottom slope, the intensity of bedload transport should depend on the excess bottom stress, particle size, submerged specific weight of solid particles and fluid properties. We then assume the following functional dependence:

$$Q_s^b = f[(\tau_0 - \tau_c), d, \varrho, \nu, g(\varrho_s - \varrho)]. \quad (188)$$

Application of the Buckingham theorem then allows to transform the latter equation into the following dimensionless form:

$$\tilde{Q}_s^b = \frac{Q_s^b}{\sqrt{(s-1)gd^3}} = \Phi^b(\tau_* - \tau_{*c}, R_p), \quad (189)$$

where we have employed the classical scaling for Q_s^b originally introduced by Einstein (1950).

Several data for Q_s^b , referring to plane bed conditions, are available in the literature (e.g. Gilbert, 1914a; Meyer-Peter and Müller, 1948; Guy *et al.*, 1966; Williams, 1970; Ashida and Michiue, 1972; Luque and Van Beek, 1976; Mantz, 1980, among others). Experimental results invariably suggest that Φ^b is a *monotonically and rapidly increasing* function of the excess Shields stress. This sensitive dependence of Φ^b on $(\tau_* - \tau_{*c})$ makes predictions of the average sediment transport rate subject to significant uncertainty.

A large number of empirical relationships of the general form (189) has been proposed in the literature (Garcia, 2008). An early assessment of their success as bedload predictors was the subject of the PhD Dissertation of Brownlie (1981). The early relationship of Meyer-Peter and Müller (1948), which has enjoyed a great popularity in both basic and applied research, deserves to be particularly mentioned. It reads:

$$\Phi^b = 8(\tau_* - 0.047)^{3/2}. \quad (190)$$

The tendency of this relationship to overpredict bedload rates has been recently corrected modifying both the factor 8 and the critical Shields stress, that respectively take the value 3.97 and the value 0.0495 in the formulation of Wong and Parker (2006), and the values 5 and 0.05 according to the proposal of Hunziker and Jäggi (2002). The Figure 26 shows a comparison with the original datasets of Meyer-Peter and Müller (1948). This plot also clarifies the relatively low degree of accuracy that empirical transport formulas are able to achieve.

This poor performance of empirical bedload predictions is strictly related to the fluctuations that, for a given flow condition, bedload measurements exhibit not only in the field (Recking *et al.*, 2012) but also in flume tests (Ancey, 2020b). In particular, the shorter is the sampling period, the higher are these fluctuations. In addition, because of their high variance, the time needed to obtain the mean sediment transport rate up to a prescribed accuracy (e.g 5%) may be very long even under controlled laboratory conditions (Ancey, 2020b). As a consequence, while most bedload transport formulas predict reasonably time integrated flume measurements, they exhibit

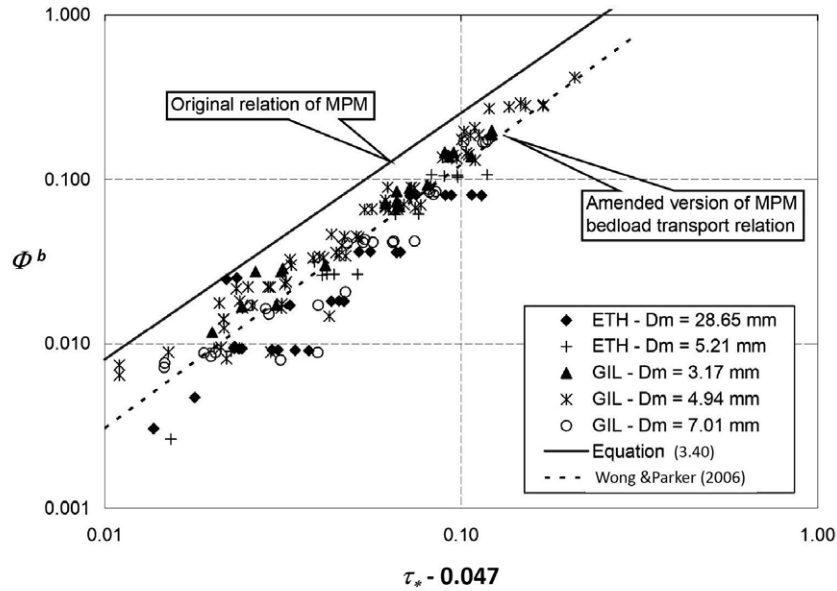


Figure 26. Comparison of original empirical relation for the dimensionless bedload transport capacity per unit width of a stream as proposed by Meyer-Peter and Müller (1948) (solid line) and the version proposed by Wong and Parker (2006) (dashed line). Data reported in this plot belong to the original dataset of Meyer-Peter and Müller (1948) (courtesy of Miguel Wong).

severe limitations when applied to field conditions, especially at low Shields stresses (Recking et al., 2012).

Bedload fluctuations are not only associated with processes typical of natural sediments (e.g. grain sorting, bed armouring, bed form migration, irregular bed geometry, variations in sediment supply), but they are also intrinsic to the complex dynamics of sediment particles transported by a turbulent stream. As briefly discussed below, at low transport rates this dynamics is essentially a noise-driven process which implies that Q_s^b depends not only on the mean flow properties (i.e. flow depth and mean velocity) but also on a diffusion term arising from the ensemble average of the fluctuating bedload rates (Furbish et al., 2017; Ancy, 2020b).

Bedload transport modeling: a still open issue

Modeling bedload transport even for a uniform flow under equilibrium conditions, i.e. such that the transport process is statistically stationary both in space and in time, is a formidable problem, which awaits to be fully understood. Indeed, even under these conditions, bedload transport exhibits considerable spatial and temporal fluctuations. Before modern observations clarified the role played by coherent wall structures suggesting the need for a new generation of theoretical models, a number of attempts appeared in the literature, where the process of bedload transport was described in some average fashion. We will not engage ourselves in the effort to provide a review of these attempts. But it may be instructive for the reader to get acquainted with the basic ideas underlying most of them, along with some thoughts about developments which appear to be necessary and feasible.

Let us return to our definition (187) of the average volumetric transport rate per unit width. If each particle moved with the *average longitudinal component of particle velocity* $\langle v_P \rangle$, then $N_P(\Delta t)\mathcal{V}_P$ would be exactly equal to $(C_a \langle v_P \rangle \Delta t)$, where C_a is the *average areal concentration of bedload particles* (a quantity having dimension of a length and often denoted as *particle activity*), namely the average volume of sediment particles transported as bedload per unit horizontal area.

Fluctuations of the average speed of different particles lead to fluctuations of $N_P(\Delta t)$. However, we have already pointed out that, as Δt increases in the classical approach, the effect of such fluctuations on the average transport rate is assumed to vanish. Hence, in the formal limit $\Delta t \rightarrow \infty$, the following relationship is found:

$$Q_s^b = C_a \langle v_P \rangle. \quad (191)$$

As mentioned above, equilibrium is assumed to imply that the process is statistically stationary both in space and in time hence, under equilibrium conditions, both C_a and $\langle v_P \rangle$ are constant. However, note that the latter definition can be readily extended to the more general case of non uniform flows, with the only constraint that the time scale of variations of the average flow field must be much larger than the *sufficiently large* value of Δt for which fluctuations of $N_P(\Delta t)$ become insignificant.

The equation (191) clarifies that any theoretical attempt to derive a relationship for Q_s^b requires a framework able to evaluate the quantities C_a and $\langle v_P \rangle$. And, indeed, most investigations have pursued this goal.

The efforts to estimate the average speed of saltating particles have been fairly successful. The earliest attempts (Bagnold, 1973; Ashida and Michiue, 1972; Engelund and Fredsøe, 1976; Bridge and Dominic, 1984) were based on a strongly idealized model. Particles would keep saltating indefinitely and their average motion would satisfy a steady dynamic balance between an average drag force acting on the particle and an average frictional force, somehow interpreting the effect of the intermittent interactions of particles with the bed. Modern experimental observations suggest that the latter scheme cannot be expected to fully represent the actual saltating process, which is inherently unsteady and intermittent. Moreover, the steady assumption rules out all the effects associated with spatial and temporal variations of the ambient flow field, notably added mass, shear, particle rotation and horizontal buoyancy. This notwithstanding, in spite of its clear oversimplification, this model problem leads to sensible results of the general form (185), i.e. in reasonable qualitative agreement with observations.

A second class of models (e.g. Van Rijn, 1984a; Wiberg and Smith, 1985; Sekine and Kikkawa, 1992; Niño and Garcia, 1994, among others) aimed at deriving a relationship for the average speed $\langle v_P \rangle$ of saltating particles by means of numerical simulations of the saltation process. This approach poses a hydrodynamical problem of formidable difficulty. In fact, the ambient fluid is subject to a turbulent shear flow, which is *disturbed* by the presence of bedload particles. Evaluating the hydrodynamic force acting on particles in relative motion at moderate Reynolds numbers and in the presence of other particles would require a full DNS solution in the near wall region. Moreover, particles are subject to a process of rebound which is controlled by a complex hydrodynamic interaction with a granular bed whose geometrical arrangement can only be described in statistical terms, a process that is, at present, outside the reach of any rigorous approach.

The analysis of the second problem, namely estimating the average areal concentration C_a of particles engaged in bedload transport, has been widely influenced by a fundamental assumption due to Bagnold (1973). The idea is extremely simple. At the top of the bedload layer, of thickness h_b , the average shear stress is equal to $\tau_0(1 - h_b/D_0)$ with τ_0 average bottom stress and D_0 uniform flow depth (see Figure 27). In the absence of any sediment transport, the amount $\tau_0(h_b/D_0)$, typically much smaller than τ_0 , balances the effect of gravity acting on the fluid layer of thickness h_b adjacent to the bottom. The argument put forward by Bagnold (1973) suggests that, in the presence of sediment transport, the entire stress $\tau_0(1 - h_b/D_0)$ available at the top of the saltation layer (except for a residual portion equal to the critical value for particle entrainment) must be “consumed” by the additional resistive stress associated with contacts of bedload particles with the granular bed. In other words, enough particles must be set in motion such that the residual average *fluid stress* acting on the granular bed does not exceed the critical stress τ_c . A simple dynamic equilibrium condition then allows to derive a *linear relationship between the areal concentration and the excess Shields stress* ($\tau_* - \tau_{*c}$).

The debate on the validity of Bagnold hypothesis has been intense through the years. In particular, the detailed experimental work of Luque and Van Beek (1976) on a stream flowing under pressure in a fairly narrow rectangular duct has shown that this assumption is not satisfied close to critical conditions and becomes less invalid as the stage parameter increases. More recently,

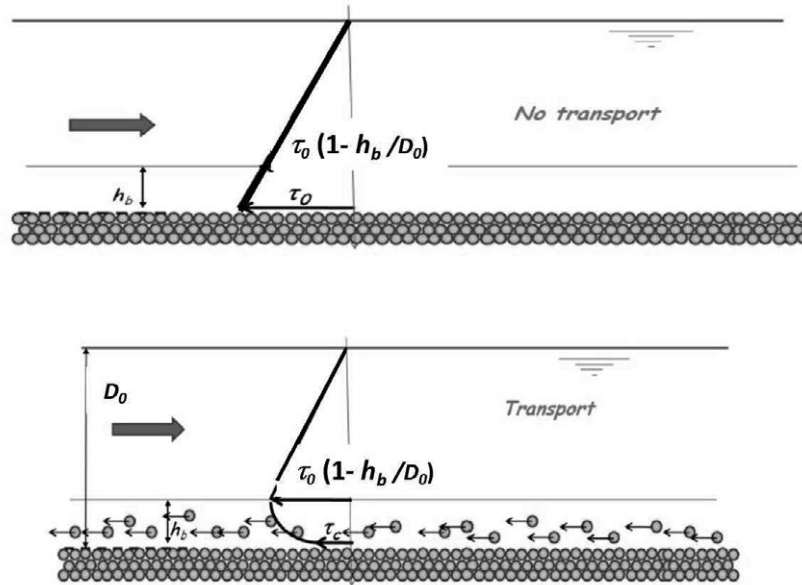


Figure 27. Sketch illustrating Bagnold hypothesis.

Seminara *et al.* (2002) have pointed out a conceptual failure of Bagnold hypothesis, which emerges when one attempts to generalize it to the important case of sloping beds. Essentially, analyzing Bagnold assumption more deeply, its inadequacy emerges clearly. In fact, the rationale behind it is essentially a *static* notion of equilibrium of the bed interface, whereby exposed particles should be subject to a mean stress smaller than the critical stress for particle motion. However, the experimental observations of particle dynamics suggest that, when bedload transport is present, the average equilibrium of the particle interface is, indeed, of *dynamic* nature: it arises from a balance between particles entrained by turbulent sweeps and particles distrained as these turbulent events decay. Hence, interpreting the process in terms of average quantities, one is led to infer that, contrary to Bagnold hypothesis, in order for particle entrainment to occur, the residual stress acting at the bed interface must indeed exceed the critical stress.

The failure of Bagnold hypothesis leaves us with our second fundamental problem, namely that of predicting the areal concentration of particles, unresolved. This difficulty equally limits the significance of numerical simulations of the saltation process, which are also able to evaluate the average longitudinal component of particle velocity through suitable ensemble averages of the longitudinal speed experienced by a large number of saltating particles throughout their jumping motion but *are unable to predict the average number of saltating particles per unit area*.

Another key question concerns the inability of saltation models to deal with irregular particle trajectories and velocities (Furbish *et al.*, 2017). Since the seminal work of Einstein (Einstein, 1926, 1937) it has been recognised that noise associated with bedload transport rate fluctuations is an intrinsic feature of bedload transport (Ancy, 2020a). The macroscopic treatment of bedload transport should thus reflect random particle motion at the grain scale, thus calling for a statistical approach even under equilibrium conditions. Various attempts have been pursued in this sense, e.g. exploiting the framework of discrete and continuous Markovian processes (Ancy *et al.*, 2008; Bohorquez and Ancy, 2015) and statistical theories of gas dynamics under rarefied transport conditions (Furbish *et al.*, 2012, 2017). We refer the interested reader to the review by Ancy (2020a) for a thorough description of these approaches. Here, we simply recall that, independently of the stochastic approach used to deal with particle positions and motions, the effect of fluctuations

of particle velocity and concentration implies that the mean bedload transport rate Q_s^b is, not only a local function of the mean particle concentration and mean particle velocity, as stated by equation (191), but includes a further contribution arising from averaging a product of fluctuating quantities, hence

$$Q_s^b = C_a \langle v_P \rangle + \langle c'_a v'_P \rangle. \quad (192)$$

The ensemble average of the product of the fluctuations of particle areal concentration c'_a and velocity v'_P may be expressed in a Fickian form (Furbish et al., 2017)

$$\langle c'_a v'_P \rangle = -\frac{\partial}{\partial x} \left(\mathfrak{D}_P C_a \right), \quad (193)$$

which involves a diffusive term reflecting a non-local behaviour quantified by the particle diffusivity \mathfrak{D}_P , and highly correlated with the average particle velocity. This purely kinematic definition of particle diffusivity does however provide no insight on the mechanisms of particle diffusion. Rather, a Lagrangian description focusing on the temporal statistics of particle displacements has to be used to provide information on particle spreading. As pointed out by Furbish et al. (2017), the challenge involves a number of further steps, i) clarifying how near-bed flow conditions and coupled fluid-granular behavior determine particle motions, ii) examining the consequences of transport under rarefied (i.e. low transport and, hence, low Shields stress) conditions involving patchy, intermittent particle motions, and iii) evaluating how particle rest times, not considered so far, affect particle diffusion. A further challenge consists of characterizing variations in particle spreading associated with the individual realizations about the expected ensemble behavior.

Concluding, even though the efforts made in the last few decades are certainly promising, no decisive breakthrough in the computation of bedload transport rates has so far been accomplished, nor is expected in the medium term (Ancy, 2020a). Saltation models have contributed significantly to progress in understanding of bedload transport. However, they have not yet been able to improve our predictive capabilities, mainly due to their inability to predict the areal concentration of saltating particles (Seminara *et al.*, 2002), as well as, to deal with irregular particle trajectories and velocities (Furbish et al., 2017).

This is a real challenge as it calls for a temporally and spatially detailed description of how the near-bed coupled fluid-grain and grain-grain interactions determine particle motion, its patchy character and its intermittency associated with particle rest times. As mentioned before, some progress in this direction has been made in the last decade with the help of recently developed computational tools.

3.3.3 The recent contribution of computational fluid dynamics (CFD) to modeling sediment transport in open channels.

Computational approaches.

Ideally, modelling sediment transport in open channels would require:

- (i) Solving numerically the Navier–Stokes equations in the time-dependent domain instantaneously occupied by the fluid phase, with the constraint that the no-slip condition should be satisfied at the instantaneous solid boundaries of the moving particles.
- (ii) Resolving the lubrication effects associated with particles closely approaching each other and evaluating the collision force generated when particles overcome the lubrication barrier and get in contact.

No contribution has yet been able to implement this whole strategy.

Great progress has been achieved on stage (i) with the help of CFD. Here, the issue is that, if the computational mesh were continuously adapted to the temporal variations of the fluid domain associated with grain motion, then the computational cost would become rapidly prohibitive as the

flow Reynolds number and the number of particles increase. To overcome the latter shortcoming that severely limited applications of the above technique to systems of large numbers of grains in motion, a major step forward was the recognition that the flow equations can be solved on a fixed grid provided the effect of solid particles in motion is accounted for through the addition of appropriate source terms to the Navier–Stokes equations. In particular, a major breakthrough was the contribution of Peskin (2002), who proposed the so called *immersed boundary method* (IBM), to calculate the blood flow driven in the human heart by the wall motion. Essentially, in the original method, the source term consisted of a distribution of forces expressed in terms of Dirac deltas, with intensities depending on the wall deformation and its elastic properties. Moreover, the wall was allowed to move with the local flow velocity.

IBM was later extended and modified in a number of contributions. Notable the work of Fadlun *et al.* (2000), where the force distribution was obtained by a formulation originally proposed in Goldstein *et al.* (1993), namely allowing for a feed-back mechanism to oppose deviations of the local velocity from the desired value. This approach is subject to time step restrictions needed to resolve the transient feedback process.

The later developments of Uhlmann (2005) have been particularly successful in overcoming the latter restrictions. The idea was again to employ a Cartesian, fixed uniform grid and replace each fluid-solid interface by a number of so called ‘Lagrangian force points’, which are evenly distributed and fixed relative to a reference frame attached to the particle. This is similar to Peskin’s approach, but two novel features were introduced. Firstly, unlike in the latter technique where the force points were advected with the local fluid velocity, Uhlmann’s Lagrangian force points followed the rigid-body motion of the particles. Moreover, a discrete volume and an associated volume force were defined at each force point, unlike the original IB method where a singular force was defined at each Lagrangian point. The method proved computationally very efficient: indeed, Uhlmann (2005) showed that the computational effort ‘needed for treating the pure fluid part of the code asymptotically outweighs the remaining contributions.’ The latter method was then employed in a number of applications of direct relevance to sediment transport modelling.

Before proceeding to discuss such applications, let us mention that an approach alternative to IBM was developed by Zhang and Prosperetti (2003, 2005). Essentially, it employs an appropriate analytic solution for the near particle flow which, as stated by the Authors, allows ‘to transfer the no-slip condition from the particle surface to the adjacent grid nodes.’ This is an alternative way to avoid the remeshing problems associated with particle motion and be able to employ fast solvers.

An advantage of IBM is to allow the direct computation of long-range interactions between the particles, but short-range lubricating interactions and particle collisions, i.e. stage (ii) of the general strategy, still require modeling. The most popular approach to model the collision of particles, described as *discrete-element model* (DEM), is based on a linear mass–spring–damper system (Kidanemariam and Uhlmann, 2014a, 2017). Briefly:

- particles ‘are in contact’ when the smallest distance between their surfaces Δ , is smaller than a force range Δ_c .
- the contact force is the sum of three contributions, namely elastic and damping normal components plus a tangential frictional component.
- the elastic part of the normal force component is proportional to the penetration length $\delta_c = \Delta - \Delta_c$, with assigned stiffness constant.
- the normal damping force is proportional to the normal component of the difference between the velocities of the two particles at the contact point with assigned proportionality coefficient.
- the tangential frictional force is proportional to the tangential relative velocity at the contact point, again with assigned proportionality coefficient.

An extensive validation of the above collision model is reported in Kidanemariam and Uhlmann (2014b). Note, that the four parameters involved in this model as well as the force range Δ_c must be prescribed for each simulation.

Applications to sediment transport processes.

In a series of papers (Kidānemariam and Uhlmann, 2014a,b, 2017; Scherer *et al.*, 2020; Kidāmenarian *et al.*, 2022), the Karlsruhe group has applied its computational model to analyze the mechanism of sediment transport in steady uniform turbulent open channel flows over cohesionless beds for low Shields stresses and relatively small Reynolds numbers. Later, the Genoa group led by Blondeaux (Mazzuoli *et al.*, 2016, 2019, 2020) used the same model to investigate sediment transport in oscillatory boundary layer flows over an erodible bed, a problem of relevance to patterns originated by sea wave propagation in the coastal zone. Details of these works are outside the scope of the present monograph and will be found in the literature cited above. However, some of the results reported in those papers are worth mentioning in the present context as they clarify some of the issues raised on the limits of the average treatment of sediment transport on which the formulation of morphodynamics relies.

The first issue is simply ascertaining to what extent we may rely on classical algebraic closures to evaluate the bedload flux under macroscopically steady equilibrium conditions, say a statistically unidirectional turbulent flow in an open channel with a cohesionless granular ‘plane’ bed.

The second, related, issue is the use of a ‘quasi-equilibrium’ formulation of sediment transport under spatially (and temporally) varying flow conditions. As we know, adopting this approach, the sediment flux is evaluated in terms of the local and instantaneous value of the relevant dimensionless parameters (notably the Shields stress). It has been argued that the sediment transport does not adapt instantaneously to a change in the flow conditions due to particle inertia (Nakagawa and Tsujimoto, 1980; Parker, 1975; Charru, 2006, among others) and adaptation is expressed in terms of a characteristic *saturation length*. While the effect of the latter is likely negligible when spatial-temporal variations are associated with large scale patterns of the kind treated in the present monograph, it has been argued that it plays a crucial stabilizing role in the process of small scale bed instability leading to the formation of bedforms like ripples and dunes (see Nakagawa and Tsujimoto, 1980; Charru *et al.*, 2013, for a review of several recent efforts of the French School). This is a picture of the process alternative to those originally proposed by Engelund and Fredsøe (1982) (where the stabilization mechanism was attributed to the effect of bed slope on bedload transport) and, more recently, by Colombini (2004), who argued that the perturbations of the fluid stress driving bedload transport should be evaluated at the top of the bed load layer as the phase-lag of bedload varies significantly in a neighborhood of the bed.

In the series of papers mentioned above, the Karlsruhe group investigated a statistically unidirectional turbulent flow in an open channel over a bed consisting of a large number of freely moving spherical solid particles. The initial configuration of the sediment bed was generated allowing particles to settle from random initial positions under the effects of gravity and particle collisions but no hydrodynamic forces. Next, the actual simulation started with the pseudo-randomly packed particles initially at rest.

In Kidānemariam and Uhlmann (2014a) one simulation was performed under turbulent flow conditions, with the following values of the relevant parameters: bulk Reynolds number 6022, relative density 2.5, relative roughness (diameter of spherical particles/flow depth) 25.05, Shields stress 0.17, domain size in the longitudinal (lateral, vertical) direction equal to 307.2 (38.4, 76.8) particle diameters, uniform step size equal to one tenth of particle diameter, number of particles 263 412. Various interesting results emerged from the simulation. A streamwise sequence of alternating ridges and troughs formed shortly after startup and migrated downstream. Occasionally, perturbations merged and, as a result, their wavelengths increased, and their migration speeds decreased. Eventually, the pattern stabilized, with two distinct bedforms with different amplitudes. The volumetric particle flow rate (per unit spanwise length) was evaluated and found to be very close to the value given by the empirical law of Wong and Parker (2006).

Later, Kidānemariam and Uhlmann (2017) performed similar simulations varying systematically the length of the computational domain to investigate its influence on pattern formation. In the case of a very long streamwise box (length 48 times the flow depth, roughly 11 ripple units with initial wavelength of 100–110 particle diameters) the pattern exhibited an initial exponential growth, followed by a nonlinear regime strongly dependent on the domain length. The volumetric sediment flux and the mean interface shear stress increased with increasing ripple amplitude, but

their relationship was again found to be well fitted by the formula of Wong and Parker (2006).

In their latest contribution Kidamenarian *et al.* (2022) performed one further set of simulations which did provide insight on some open issues. In this simulation, the computational box length was limited, such to force the ripple pattern to keep a steady configuration (constant shape, amplitude and migration speed) with a mean wavelength ranging from 100 to 180 grain diameters. The simulation could then be sufficiently long as to allow for phase averaging and analysis of the *spatio-temporal correlation* between hydrodynamics and sediment transport. The main result of this analysis was to show that the shear stress at the bed interface lags ahead of bed elevation, i.e., it peaks upstream of the ripple crests with an average phase shift in the range of 16 to 19 grain diameters, thus supporting the view of Charru *et al.* (2013) on fluid inertia being the mechanism responsible for ripple instability. Moreover, the depth integrated volumetric sediment flux, was found to be nearly in phase with bed elevation, hence it lagged behind the shear stress with a similar average phase shift. This suggests that, while the space- and time-averaged particle flux rate is well predicted by the algebraic expression of Wong and Parker (2006), the spatial dependence of the local sediment flux on the local shear stress is not well captured by an algebraic closure (Figure 28).

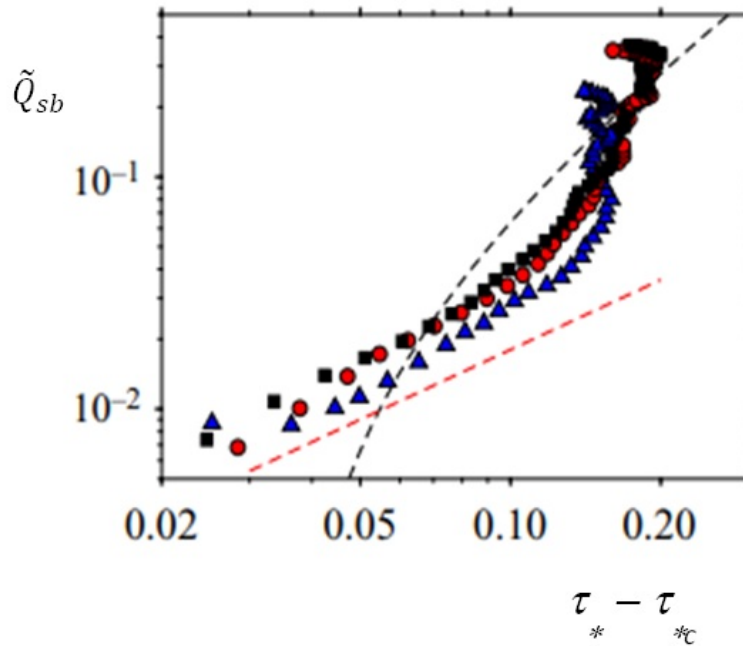


Figure 28. The local dimensionless volumetric bedload flux per unit width (Einstein's scale) calculated by Kidamenarian *et al.* (2022) on the stoss side of ripples is plotted versus the local excess Shields stress. Different colors correspond to different simulations. The black dashed line is Wong and Parker (2006) relationship, the red dashed line is a reference linear scaling.

It may be of interest in this context to also quote some recent results of Mazzuoli *et al.* (2020) who employed the same model to perform direct numerical simulations of sediment transport in a turbulent oscillatory boundary layer modeling the flow of small amplitude sea waves on shallow water. Figure 29 shows the values of the dimensionless bedload flux per unit width (scaled by the product between particle settling speed w_s and particle diameter d) as a function of the modulus of the Shields stress at various instants throughout the wave period. Different colors refer to distinct runs, characterized by different values of the Reynolds Number R_d (based on the amplitude of the oscillating speed and the thickness of the boundary layer). Arrows indicate the orbital direction. The blue dashed-dotted line is the steady relationship by Wong and Parker (2006). The figure

shows that, except for very low values of the Shields stress, the computed bedload flux agrees quite well with the predictions of a fairly established steady formula applied to the instantaneous flow conditions.

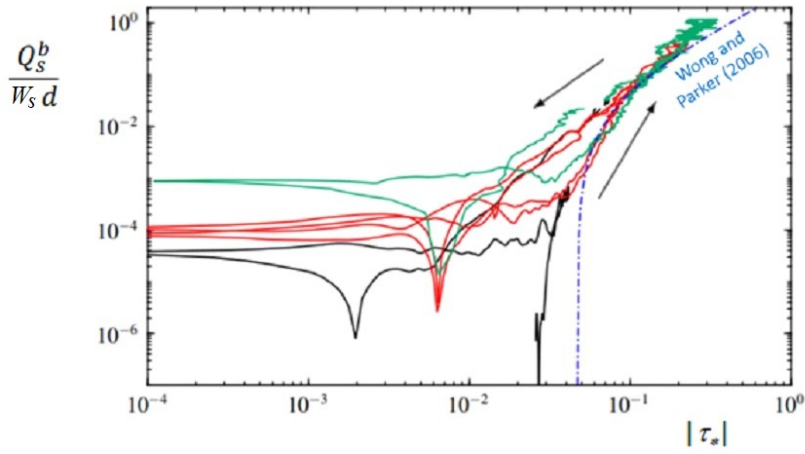


Figure 29. The dimensionless sediment flux per unit width driven by the flow in an oscillatory boundary layer on a cohesionless bottom is plotted as a function of the absolute value of the Shields stress for three runs (identified by different colors) characterized by different values of the Reynolds number. The blue dashed-dotted line represents the steady formula of Wong and Parker (2006) associated with instantaneous values of the modulus of the Shields stress (reproduced from Mazzuoli *et al.*, 2020, under the Creative Commons Attribution licence).

The above results provide a fairly optimistic picture, encouraging the highly specialized computational groups active in this research area to persevere in their efforts, which will eventually help substantiating and improving our present capability to predict the intensity and direction of sediment transport of homogeneous sediments under both steady and unsteady conditions. Computational approaches would also be helpful to substantiate the available models of *bedload transport in the mixed bedrock-alluvial case* (see Section 7.7), that need experimental and theoretical substantiation.

In the following, we will assume that the spatial scale of the inertially driven lag between bedload transport and bottom stress is much smaller than the scale of the sedimentary patterns of interest for the present and of the next monographs. This will allow us to adopt simplest semiempirical closures between depth integrated bedload flux per unit width and local excess mean bottom stress.

3.4. Threshold conditions for particle entrainment in suspension

Let us proceed to investigate the incipient transport of sediments under conditions such that the turbulent intensity is large enough and/or particles are small enough for sediments to be entrained in the bulk of the flow. In this mode of transport, the *transport in suspension*, two main mechanisms operate: particle *entrainment* and particle *deposition*. The deposition of a sphere in an unbounded fluid was analyzed in Section 3.1.4. The mechanism of particle entrainment in suspension, namely the strict correlation between particle pick-up and occurrence of flow ejections in the wall region, has been investigated through physical and numerical experiments and is outlined below.

3.4.1 The entrainment mechanism

The picture emerging unambiguously from both physical and numerical experiments, is as follows.

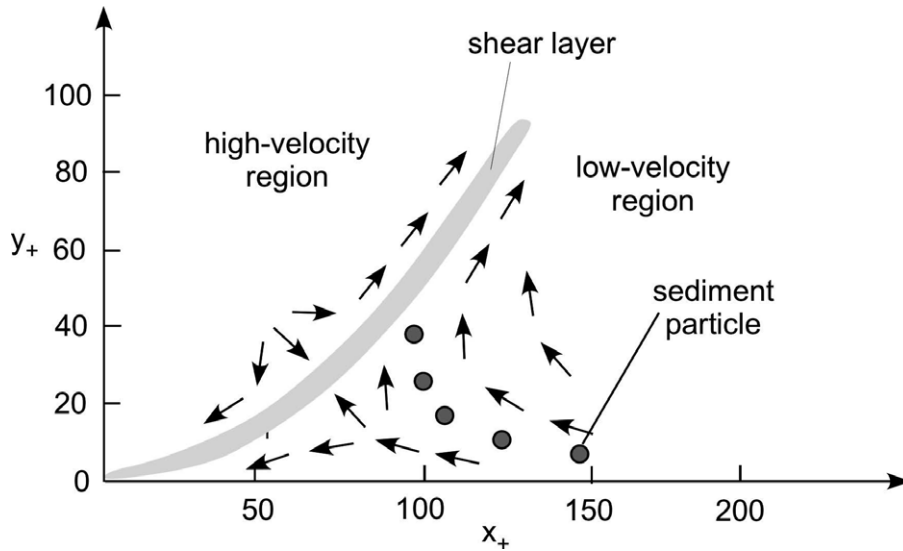


Figure 30. Sketch of the motion of fluid particles (arrows) and sediment particles (circles) relative to the shear layer originated by the ejection event (according to Urushihara *et al.*, 1993). The longitudinal x^+ and vertical y^+ coordinates are scaled as $x^+ = u_\tau x/\nu$, $y^+ = u_\tau y/\nu$.

Particles picked up from low-speed streaks are lifted away from the wall through a mechanism which has been clarified by several investigators starting from the detailed measurements of Urushihara *et al.* (1993). The Figure 30 shows a sketch of the relative velocity field, consisting of a shear layer extending a vertical distance of about 100 wall units, with a mean inclination angle of 14° , convection velocity ranging about $10 u_\tau$, life span of about $60 - 80 (\nu/u_\tau^2)$ and frequency of occurrence roughly equal to $0.003 u_\tau^2/\nu$. The relative velocity field exhibits the presence of a saddle point. In the upstream high-velocity region the relative motion is directed towards the shear layer, while downstream to the structure, in the low-velocity region, the relative velocity is negative, i.e. directed again towards the shear layer. Sediment particles (circles in Figure 30) are initially ejected from a region located about 100 - 200 wall units downstream from the structure. Then their relative motion direct them towards the shear layer where they get trapped and are then advected by the flow structure. Stretching of the latter towards the outer regions of the wall layer lets sediment particles lose correlation, lag behind the flow structure and eventually settle back to the bed (Figure 31a).

Flow ejection events are not always effective in entraining sediment particles in suspension. In some cases lifted particles lose correlation with the fluid motion and fall back to the bed well before the flow structure loses coherence (Figure 31b), a phenomenon pointed out by Well and Stock (1983) who called it *crossing trajectory effect*. The ability of ejections to suspend particles depends on both the intensity of these flow events, which are stochastic in nature, and on particle characteristics. The ratio between the number of ejected particles able to reach the bulk flow and the total number of ejected particles is found to increase with the Shields stress.

3.4.2 Incipient particle entrainment

The notion of threshold conditions for particle entrainment into suspension can perhaps be traced back to Bagnold (1966). He suggested that these conditions are reached when the destabilizing actions on particles associated with turbulence are balanced by the stabilizing effect of gravity. Bagnold (1966) took the intensity of vertical turbulent fluctuations of flow velocity $\langle |w'| \rangle$ as a measure of the former, while the particle settling speed was used to measure the tendency of particles to deposit. Further assuming, somewhat crudely, that $\langle |w'| \rangle \simeq u_\tau$, Bagnold (1966) ended

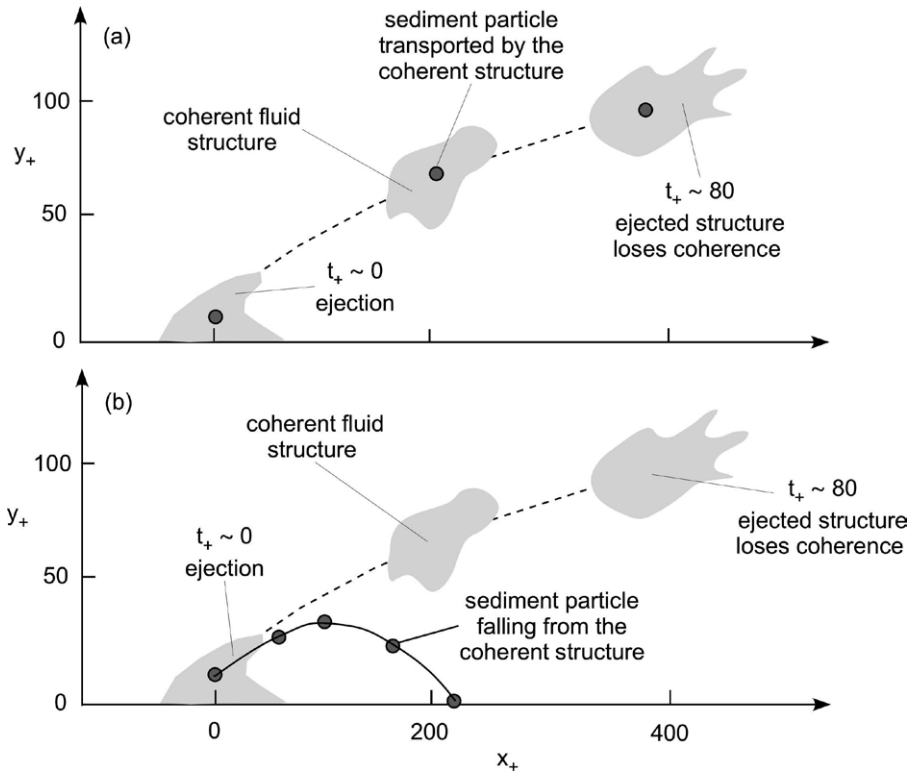


Figure 31. Sketch of the possible mechanisms of sediment entrainment by turbulent flow ejections according to Niño (1995). Sediment particles progressively lose correlation, lag behind the flow structure and eventually settle back to the bed. In some cases lifted particles lose correlation with the fluid motion and fall back to the bed well before the flow structure loses coherence (*crossing trajectory effect*) (redrawn from Figure 8.19 of Niño, 1995).

up suggesting the following threshold criterion:

$$\frac{u_\tau}{w_s} = 1. \quad (194)$$

Below, the quantity u_τ/w_s will be referred to as *Bagnold parameter*. Note that, making use of the following relationship:

$$\frac{u_\tau}{w_s} = \frac{\sqrt{\tau_*}}{\tilde{w}_s}, \quad (195)$$

and recalling that $\tilde{w}_s (= w_s / [(s-1)gd]^{1/2})$ is a known function of the particle Reynolds number R_p , the criterion (194) is readily transformed into a relationship between a threshold value of τ_* for entrainment into suspension (denoted as τ_{*s}) and the particle Reynolds number R_p .

Full theoretical understanding of the entrainment process will have to wait for a significant improvement of our ability to model the response of a single particle lying on a granular bed to the hydrodynamic actions induced by an ejection event. Fortunately, for the purposes of morphodynamics, empirically based criteria are often sufficient. It is somewhat surprising, in this respect, that few systematic experimental investigations have been performed. An obvious limitation of (194), emerged from these investigations, is that it does not involve some measure of the size of particles relative to the thickness of the viscous sublayer. Observations reveal that entrainment is made more difficult when particles are fully immersed into the viscous sublayer. The obvious parameter to account for this effect is the friction Reynolds number R_τ adopted by

Shields (1936); hence the threshold criterion may be given the general form:

$$\frac{u_\tau}{w_s} = f(R_\tau), \quad (196)$$

which is still equivalent to a relationship between τ_{*s} and the particle Reynolds number R_p .

Threshold relationships of the type (196), based on experimental observations, have been proposed by various Authors, notably Van Rijn (1984a) and Niño and Garcia (1996) (but see also Niño *et al.*, 2003). These two experimental works differed in some respect. In the former, the bed was cohesionless and consisted of uniform particles of the same size as those transported in suspension. In the latter, the bed was fixed and either smooth or artificially roughened by glueing sand particles of a given size (0.53 mm) to the originally smooth surface; particles were fed externally to the flow far upstream from the observation window and the establishment of equilibrium conditions was ascertained before measurements were performed.

The threshold criterion finally proposed by Niño *et al.* (2003) predicts values of u_τ/w_s slightly higher than those predicted by Van Rijn (1984a) for values of R_p in the range 10-25. For values of R_p smaller than 10, Van Rijn (1984a) criterion appears to underestimate sharply the threshold values of the Bagnold parameter observed by Niño and Garcia (1996). The two criteria read:

$$\frac{u_\tau}{w_s} = \begin{cases} 4 R_p^{-2/3} & (1 \leq R_p \leq 31.62) \\ 0.4 & (R_p > 31.62) \end{cases} \quad \text{Van Rijn (1984a),} \quad (197)$$

$$\frac{u_\tau}{w_s} = \begin{cases} 21.2 R_p^{-1.2} & (1 \leq R_p \leq 27.3) \\ 0.4 & (R_p > 27.3) \end{cases} \quad \text{Niño *et al.* (2003).} \quad (198)$$

The criterion (197), transformed into a relationship between τ_{*s} and R_p has been plotted in Figure 24. Note that the sharp change of the exponent from $-2/3$ to 0 occurring in equation (197) at $R_p = 31.62$ corresponds to a value of $R_\tau = (R_p \sqrt{\tau_*})$ of about 10. Hence, recalling that the conventional 'thickness' of the viscous sublayer is roughly equal to $11.6 \nu/u_\tau$, the above limit clearly corresponds to particle sizes comparable with the thickness of the viscous sublayer. In other words, as pointed out by Niño *et al.* (2003), grains protruding over the viscous sublayer, are more easily entrained than particles fully immersed into the viscous sublayer. As a consequence, the Shields stress tends to increase rapidly as R_p decreases.

3.5. Modeling the dynamics of suspensions

The subject of transport of suspensions is part of a wider and quite complex area of research that combines turbulence and multiphase flows, “*two of the most challenging topics in fluid mechanics*”, as pointed out by Balachandar and Eaton (2010) in a thorough review to which the interested reader is referred. Given the complexity of the subject, a variety of conceptual frameworks appropriate to different contexts have been proposed. Let us outline them briefly.

3.5.1 Modeling techniques

Modeling techniques may be distinguished on the basis of which description (Eulerian/Lagrangian) is used, the type of coupling between the motion of solid and fluid phases, and the computational methodology. Note that, for the time being, we use the word *concentration* as an intuitive local measure of the ratio between volume of the solid phase and volume of the mixture. This notion will be formally introduced later on, as an example of the averaging operation to be suitably defined.

Eulerian versus Lagrangian approaches

Eulerian approaches rely on the continuum approximation and define mean quantities for the mixture as Eulerian continuous functions of \mathbf{x} and t , governed by a set of conveniently derived differential equations expressing the basic conservation principles of sediment mixtures.

Lagrangian approaches solve the equations of motion of each particle subject to the hydrodynamic actions driven by the ambient fluid and, possibly, by the feedback of particle motion on the fluid itself.

Coupling

As for the effect of the motion of the fluid phase on sediment dynamics and the feedback of sediment motion on the fluid phase, known as *coupling problem*, models may involve various *degrees of coupling* described below.

One way coupling. In this case, the concentration of the solid phase is sufficiently small for the effect of the turbulent carrier flow on the dynamics of the dispersed phase to be dominant. No feedback is accounted for. Moreover, the motion of the solid phase may be taken as indistinguishable from that of the fluid phase (sediments treated as *passive tracers*) or it may differ slightly from that of the fluid due to various causes (e.g. particle settling and inertia).

Two-way coupling. For larger concentrations the effect of the dispersed phase on the motion of the carrier fluid may no longer be ignored. As discussed by Balachandar and Eaton (2010), coupling leads, on one hand, to the so called *turbulence modulation*. Essentially, the presence of particles enhances dissipation in the fluid phase, transfers kinetic energy to the fluid and generates 'turbulence' in the form of wakes and vortex shedding. On the other hand, turbulence affects the forces exerted by the fluid phase on sediment particles.

Four-way coupling. As the concentration increases further, the role of particle interactions (hydrodynamic or collisional) may no longer be neglected and requires ad-hoc modeling techniques.

When the sediment concentration approaches values comparable with the packing concentration of the granular medium, the role of the solid phase in the dynamics of the mixture becomes dominant and the concept of coupling loses significance as interparticle collisions prevail.

Computational approaches

Extensive investigations performed by the multiphase flow community (see the reviews of Elghobashi, 1991, 1994; Balachandar, 2009; Balachandar and Eaton, 2010) suggest that two main parameters control the range of applicability of different computational approaches, namely the particle Stokes number (equation 163) and the concentration of the solid phase.

The Figure 32 points out several important facts. Firstly, the transition from the dilute to the dense suspension regime is set at values of the concentration of the solid phase around 10^{-3} . Secondly, dilute suspensions require different modeling tools, depending on the particle Stokes number. Balachandar and Eaton (2010) list the following approaches.

Dusty gas approach (Carrier, 1958; Marble, 1970). It applies to the case of *very small particle Stokes numbers*. Here, particles are modeled as passive tracers: their effect is then only to change the density of the fluid depending on the local concentration. Hence, besides the equations for the fluid phase only the mass conservation equation for the solid phase, i.e. an equation for concentration, needs to be solved.

Equilibrium Eulerian approach (Ferry and Balachandar, 2001; Ferry *et al.*, 2003). It applies to the case of *small particle Stokes numbers*. This model differs from the dusty gas approach as the particle velocity is allowed to differ slightly from that of the fluid phase to account for settling and inertia. This is the approach underlying the models of transport in suspension commonly used in the morphodynamic literature and will be discussed extensively in the next Section.

Eulerian approach (Crowe *et al.*, 2012; Zhong *et al.*, 2010). It is also known as *two-fluid approach* and applies to the case of *fairly small particle Stokes numbers*. Both the fluid and the solid phase are treated as continua, for which governing conservation equations are derived through appropriate averaging procedures. Averaging leads to the generation of phase-interaction terms which require closure.

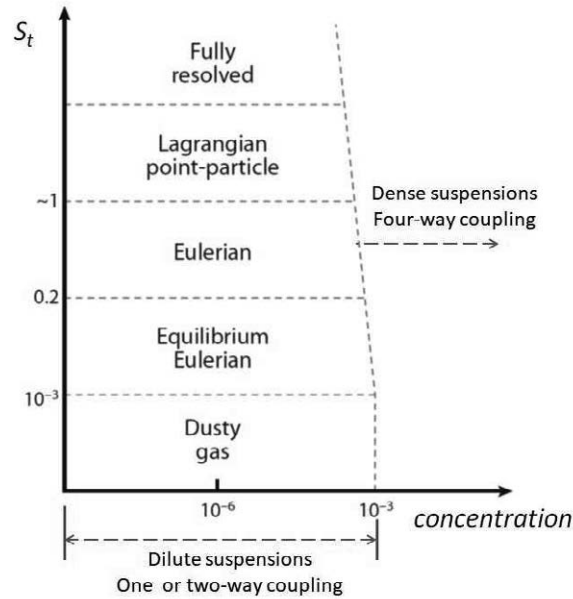


Figure 32. Range of applicability of different computational approaches to the dynamics of suspensions (according to Balachandar and Eaton, 2010) as a function of the solid concentration and the Stokes number defined by equation (163).

Lagrangian point particle approach. The main feature of these approaches is that the solid phase is no longer treated as a continuum, rather the trajectory of each point particle is tracked solving its equation of motion subject to the actions of the fluid phase, treated as a continuum. These actions are calculated solving the continuity and momentum equations in an Eulerian framework. One way coupling was initially adopted (Elghobashi, 1991). Later two way coupling (Elghobashi and Truesdell, 1993; Ferrante and Elghobashi, 2003) was developed, adding the reaction of the moving particles on the fluid phase to the Navier Stokes equations. Semiempirical attempts to extend the above approach to account for particle-particle collisions (four way coupling) have also appeared in the literature (e.g. Yamamoto *et al.*, 2001).

Fully resolved approach (Uhlmann, 2005; Picano *et al.*, 2005). When particle diameter is no longer smaller than the smallest eddies of the flow field (the Kolmogorov eddies), the only feasible approach is a full DNS, where all the scales of the turbulent flow of the fluid phase, including those generated by the motion of the solid phase, are fully resolved. As already discussed in Section 3.3.2, this is a computationally heavy approach which may hardly be applicable to practical contexts but plays an important scientific role to improve our understanding of the basic processes of morphodynamics.

In conclusion, the available modeling techniques range from relatively simple approaches that are readily applicable to practical problems although under fairly restricted conditions (very dilute suspensions of very small particles), to techniques (full numerical solution) that are generally valid but can hardly be implemented in practice. In the geophysical and hydraulic engineering literature of relevance to morphodynamics it is common to employ the Eulerian approach, which appears to be most suitable to applications. In order to engage ourselves in the effort to discuss the Eulerian approach in sufficient detail, it is necessary to derive the governing equations of sediment mixtures.

3.5.2 The Eulerian approach: governing equations of sediment mixtures

Deriving governing equations of sediment mixtures treated as continua is a long standing issue

that has attracted the attention of the Mechanics community since the early works of Fick (1855) and Stefan (1871). The approaches proposed so far belong to two major classes: *mixture theories* and *ensemble averaging approaches*. It falls outside the scopes of the present Monograph to provide deep reviews of these theories. Here, we simply outline the main ideas underlying each class of them.

Mixture theories are based on the assumption that the mixture may be viewed as a superposition of distinct continua, each following its own motion but simultaneously present at any time t and each location \mathbf{x} . Hence, material points belonging to distinct phases are not distinguishable, and different continua interpenetrate each other. Though the foundation of mixture theory may be traced back to the early works cited above, only in the second half of the last century those ideas led to the formulation of actual continuum theories (Truesdell, 1957; Bowen, 1971; Passman *et al.*, 1984). In the context of mixture theories, the governing equations are essentially postulated.

In *ensemble averaging approaches*, the motion of sediment mixtures is treated as a stochastic process. The flow properties are defined in statistical terms and *ensemble averages*, i.e. averages based on a large number of realizations of the process, are used to describe the average flow. This approach has indeed been widely employed in the literature (see, among others, Saffman, 1971; Lundgren, 1972; Drew, 1983; Joseph and Lundgren, 1990) and is quite elegant but, as pointed out by Batchelor (1988), it “*achieves rigor at the cost of introducing the intractable problem of closure of averages of a complicated kind*”. An alternative, physics-based, approach (Batchelor, 1970) is feasible provided one can recognize the existence of three distinct length scales in the dynamics of the mixture under investigation (Figure 33):

- a microscale s of the order of the average interparticle distance;
- an intermediate scale ℓ , large with respect to s , such that the average properties of the mixture do not vary significantly on this scale;
- a macroscale L , large with respect to ℓ , which measures the typical distance on which significant variations of the average properties are experienced.

Hence:

$$s \ll \ell \ll L. \quad (199)$$

The existence of an intermediate scale ℓ , on which the dynamics of the mixture (i.e., the stochastic process) may be assumed statistically stationary, suggests the opportunity to replace ensemble averaging with *spatial averaging*, thus postulating the validity of the so called ergodic hypothesis, widely employed in all theories concerning statistically homogeneous media (Hashin, 1964).

Let us consider a fixed volume \mathcal{V} of linear scale ℓ , contained within the region instantaneously occupied by the sediment mixture in a neighborhood of the point \mathbf{x} . Furthermore, let \mathcal{V}_k be the portion of \mathcal{V} occupied by the phase k (with $k = s$ for the solid phase and $k = f$ for the fluid phase, see Figure 34). The boundary of \mathcal{V}_f consists of the sum of the fluid portion S_f of the boundary of \mathcal{V} and of the boundary S_i of the portions of the solid particles contained in \mathcal{V} . Similarly, the boundary of \mathcal{V}_s consists of the sum of S_i and of the solid portion S_s of the boundary of \mathcal{V} .

With the above notations we may then define the volumetric concentration c of the solid phase in the form:

$$c = \frac{\mathcal{V}_s}{\mathcal{V}}. \quad (200)$$

Of course the concentration of the fluid phase is simply $(1 - c)$. Note that c is in general a function of position \mathbf{x} and time t .

Following Prosperetti and Jones (1984) the instantaneous and local value of the volume average of any scalar, vectorial or tensorial quantity f_k referring to phase k , denoted by an overbar, may be defined in the form:

$$\bar{f}_k = \frac{1}{\mathcal{V}_k} \int_{\mathcal{V}_k} f_k d\mathcal{V}. \quad (201)$$

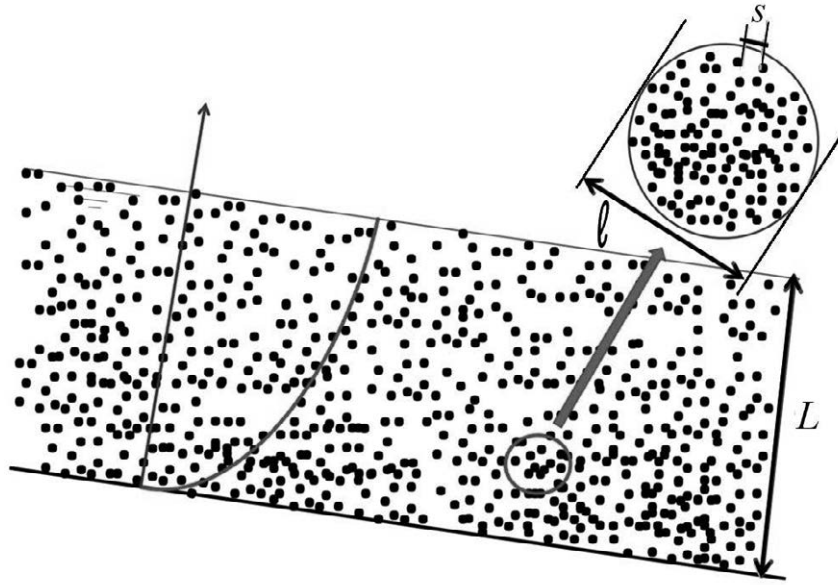


Figure 33. Sketch depicting the three distinct spatial scales s , l and L that can be used to characterize the dynamics of statistically homogeneous sediment mixtures.

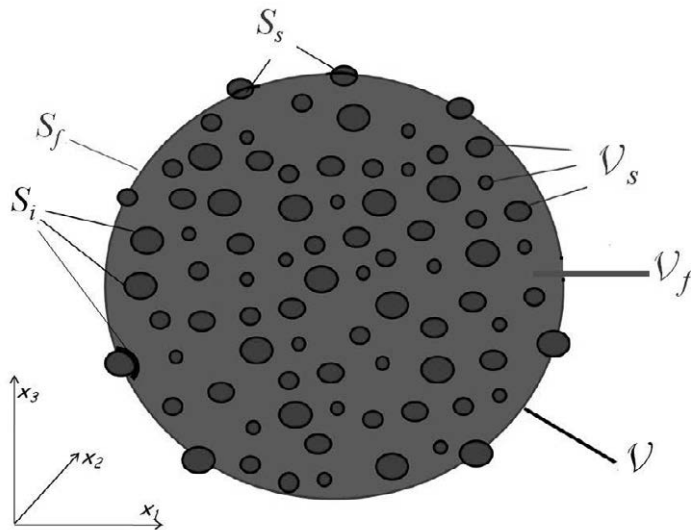


Figure 34. The averaging volume: notations.

In particular, we will denote by \bar{v} , \bar{v}_s and \bar{q}_s the instantaneous volume averaged values of the fluid phase speed, of the solid phase speed and of the instantaneous volume flux of the solid phase, respectively. Note that the accuracy in the definition of any averaged quantity depends on the level of fluctuation of that quantity, which varies as the size of the averaging volume varies. This may pose a severe constraint for dilute suspensions.

With the help of the above definitions, one may derive a general spatially averaged form of the conservation equation of any quantity transported by a fluid in motion (see, e.g. Prosperetti and Jones, 1984).

For the fluid phase, the continuity equation reads:

$$\varrho \left[\frac{\partial(1-c)}{\partial t} + \nabla \cdot \left((1-c) \bar{\mathbf{v}} \right) \right] = 0. \quad (202)$$

Similarly, the continuity equation for the solid phase reads:

$$\varrho_s \left(\frac{\partial c}{\partial t} + \nabla \cdot \bar{\mathbf{q}}_s \right) = 0, \quad (203)$$

where $\bar{\mathbf{q}}_s = c \bar{\mathbf{v}}_s$ denotes the *instantaneous spatially averaged sediment flux*.

Note that, in spite of the incompressible character of both the fluid and solid phases, their spatially averaged behavior in a sediment mixture is *compressible* due to the spatial and temporal variations of the concentration c .

The *equation of momentum conservation for the fluid phase* takes the following form:

$$\begin{aligned} \varrho \left\{ \frac{\partial}{\partial t} \left[(1-c) \bar{\mathbf{v}} \right] + \nabla \cdot \left[(1-c) \bar{\mathbf{v}} \bar{\mathbf{v}} \right] \right\} = -\varrho g (1-c) \hat{\mathbf{x}}_3 \\ + \nabla \cdot \left[(1-c) \mathbf{T}^{tot} \right] - \mathbf{i}. \end{aligned} \quad (204)$$

Here, \mathbf{i} is the *interactive specific force for the fluid phase*, i.e. the force per unit volume of the mixture arising from particle drag \mathbf{F}_D and buoyancy, that reads:

$$\mathbf{i} = \bar{\mathbf{F}}_D \frac{\mathcal{V}_s}{\mathcal{V}} + \varrho \frac{\mathcal{V}_s}{\mathcal{V}} g \hat{\mathbf{x}}_3 = c (\bar{\mathbf{F}}_D + \varrho g \hat{\mathbf{x}}_3), \quad (205)$$

where $\bar{\mathbf{F}}_D$ is the phase averaged particle drag and $\hat{\mathbf{x}}_3$ is the upward directed unit vector of the vertical axis.

Moreover, \mathbf{T}^{tot} is the *total stress tensor of the fluid phase*, which reads:

$$\mathbf{T}^{tot} = \bar{\mathbf{T}} + \mathbf{T}^t. \quad (206)$$

Here $\bar{\mathbf{T}}$ is the spatially averaged value of the viscous stress tensor and \mathbf{T}^t is the following Reynolds stress tensor:

$$\mathbf{T}^t = -\varrho \overline{\mathbf{v}' \mathbf{v}'}, \quad (207)$$

with \mathbf{v}' instantaneous fluctuation of the local fluid velocity with respect to its spatially averaged value $\bar{\mathbf{v}}$. Note that the dissipation of fluid momentum associated with flow perturbations induced by particle collisions is incorporated in the Reynolds stress tensor \mathbf{T}^t .

Employing the continuity equation (202) and the explicit form of the interactive force (205), the momentum equation for the fluid phase (204) is readily found to reduce to the simpler form:

$$\varrho (1-c) \frac{d\bar{\mathbf{v}}}{dt} = -\varrho g \hat{\mathbf{x}}_3 - c \bar{\mathbf{F}}_D + \nabla \cdot \left[(1-c) \mathbf{T}^{tot} \right]. \quad (208)$$

In conclusion, the average dynamics of the fluid phase is governed, in general, by a Cauchy equation which poses a closure problem for the total stress tensor of the fluid phase. A similar equation is derived for the solid phase. We do not report it here as the only case treated in this Monograph is that of dilute mixtures of small particles discussed in the next Section.

3.5.3 Governing equations of the dynamics of suspensions of uniform sediments in the dilute approximation

Let us examine the form taken by the conservation equations for the fluid and solid phases in the *dilute limit* ($c \ll 1$).

Momentum equations in the dilute approximation

We have seen (Section 3.1.2) that for *particles moving in a regime of small relative Reynolds number in a dilute turbulent suspension*, the dominant hydrodynamic force acting on particles is the Stokes drag. Hence, the Maxey-Riley-Gatignol equation of motion reduces to a balance between submerged weight and Stokes drag, which leads to the relationship (164). Spatial average of the latter equation gives:

$$\bar{\mathbf{v}}_s = \bar{\mathbf{v}} - w_s \hat{\mathbf{x}}_3. \quad (209)$$

As stated above, such approximation is strictly valid for particles not coarser than coarse silt. However, in the engineering literature, often and somewhat arbitrarily, it is employed for suspensions of larger particles in investigations focusing on the large scale features of the transport process. For particles coarser than coarse silt in water, the settling speed w_s is evaluated by the general expression (171) rather than by its low Reynolds number version (162). In conclusion, the algebraic equation (209) will be employed as the *phase averaged approximation of the full momentum equation for the solid phase appropriate to dilute turbulent suspensions of small particles*.

In order to examine the simplified (dilute) form of equation (204) for the fluid phase, let us first point out that, under the conditions discussed above, the interactive force per unit volume of the mixture arises from Stokes drag and Archimede buoyancy. Hence we can set $\bar{\mathbf{F}}_D = \bar{\mathbf{F}}_{S_t}$ in equation (205), where $\bar{\mathbf{F}}_{S_t}$ is the phase averaged Stokes drag, which reads:

$$\bar{\mathbf{F}}_{S_t} = 3\pi d\mu(\bar{\mathbf{v}}_s - \bar{\mathbf{v}}). \quad (210)$$

We next note that (205) suggests that the interactive force is $\mathcal{O}(c)$. It is also convenient to employ the constitutive law of viscous Newtonian fluids and write:

$$\bar{\mathbf{T}} = -\bar{p}\mathbf{I} + 2\mu\bar{\mathbf{D}}, \quad (211)$$

with \bar{p} spatially averaged fluid pressure, \mathbf{I} unit tensor and $\bar{\mathbf{D}}$ spatially averaged strain rate tensor of the fluid phase.

Taking advantage of the small value of c , we then neglect $\mathcal{O}(c)$ terms and, with the help of (211), the leading order approximation of the phase averaged form of the momentum equation (204) for the fluid phase takes the form:

$$\varrho \left(-g \hat{\mathbf{x}}_3 - \frac{d\bar{\mathbf{v}}}{dt} \right) = \nabla \bar{p} - \mu \nabla^2 \bar{\mathbf{v}} + \nabla \cdot \mathbf{T}^t. \quad (212)$$

Hence, at leading order, the momentum equation for the fluid phase is not affected by the presence of the solid phase. A closure problem, however, arises for the *turbulent stress tensor* \mathbf{T}^t which accounts for the inertial effect of spatial fluctuations of the fluid velocity inside the averaging volume \mathcal{V} .

Mass conservation equations in the dilute approximation

Neglecting $\mathcal{O}(c)$ terms, one readily finds that, at the leading order of approximation the mass conservation equation for the fluid phase reduces to the classical continuity equation of incompressible fluids, constraining the fluid speed to be divergence free (i.e. solenoidal)

$$\nabla \cdot \bar{\mathbf{v}} = 0, \quad (213)$$

while the mass conservation equation for the solid phase takes the form:

$$\frac{\partial c}{\partial t} + \nabla \cdot \bar{\mathbf{q}}_s = 0. \quad (214)$$

Using the relationship (209), the continuity equation of the solid phase (214) appropriate to the case of dilute suspensions is found to read:

$$\frac{\partial c}{\partial t} + \nabla \cdot (c \bar{\mathbf{v}}) - w_s \frac{\partial c}{\partial x_3} = 0. \quad (215)$$

Mass conservation at the boundaries impose that the free surface ($x_3 = H$) is impermeable to solid particles while a normal component of the relative sediment flux through the bed interface ($x_3 = \eta$) may arise as a result of an entrainment of sediments from the erodible bed or deposition on it. The instantaneous forms of these constraints read:

- *at the free surface* ($x_3 = H$):

$$\left[c \bar{\mathbf{v}}_s \cdot \hat{\mathbf{n}}_H - V_H c \right]_H = \left[(c \bar{\mathbf{v}} - w_s c \hat{\mathbf{x}}_3) \cdot \hat{\mathbf{n}}_H - V_H c \right]_H = 0, \quad (216)$$

where V_H is the velocity of the free surface (see equation (16));

- *at the bed interface* ($x_3 = \eta$):

$$\left[c \bar{\mathbf{v}}_s \cdot \hat{\mathbf{n}}_\eta \right]_\eta = \left[(c \bar{\mathbf{v}} - w_s c \hat{\mathbf{x}}_3) \cdot \hat{\mathbf{n}}_\eta \right]_\eta = \mathcal{D} - \mathcal{E}. \quad (217)$$

Here, \mathcal{D} is the intensity of the deposition flux, \mathcal{E} is the intensity of the entrainment flux, both positive quantities, hence $\mathcal{D} - \mathcal{E}$ is the net deposition at the bed interface (recall eq. (3.20) in Blondeaux *et al.*, 2018). This quantity needs to be defined as a function of the local and instantaneous velocity and concentration fields.

The above mathematical formulation of the dynamics of turbulent sediment mixtures is based on *averaged* quantities which filter out the effect of spatial fluctuations occurring at scales of the order of the mesoscale ℓ . The generation of microscopic stress tensors is a result of the averaging procedure and of the nonlinearity of the basic equations. Part of the total stress tensor \mathbf{T}^{tot} of the fluid phase, namely its viscous part $\bar{\mathbf{T}}$, can be expressed explicitly in terms of the unknown averaged quantities. However, just like in the context of LES techniques, a closure problem for the *turbulent* part \mathbf{T}^t still remains to be solved. Once the latter problem has been given some semiempirical solution, one ends up with a still formidable problem consisting of solving the equations (212), (213) and (215) with appropriate initial and boundary conditions. The outcome of such huge numerical effort would be the spatial-temporal distributions of the phase averaged quantities $\bar{\mathbf{v}}$, \bar{p} and c which still display spatial and temporal fluctuations associated with the large scale features of the turbulent transport process.

Alternatively one may attempt to average out also these effects by performing a second averaging process which generate a *macroscopic* Reynolds stress tensor for the fluid phase, as well as turbulent mass fluxes. This approach, vastly exploited in the engineering literature, is outlined below.

Reynolds averaged formulation of the spatially averaged conservation equations of sediment mixtures in the dilute approximation

Let us then decompose the *microscopically averaged* properties of the two phases into mean components and fluctuations where the words *mean* and *fluctuation* now refer to the *large scale features of the turbulent flow field*:

$$\left(\bar{\mathbf{v}}, \bar{p}, \bar{\mathbf{v}}_s, c \right) = \left(\mathbf{u}, \langle \bar{p} \rangle, \mathbf{u}_s, \langle c \rangle \right) + \left(\mathbf{u}', p', \mathbf{u}'_s, c' \right). \quad (218)$$

Here, the symbol $\langle \rangle$ denotes the *macroscopic average*, $\mathbf{u} = \langle \bar{\mathbf{v}} \rangle$ and $\mathbf{u}_s = \langle \bar{\mathbf{v}}_s \rangle$. Note that the microscopic average concentration c does not require an overbar recalling its definition (200).

Applying the decompositions (218) to the dilute form of the momentum equation for the solid phase (209), one readily finds:

$$\mathbf{u}_s = \mathbf{u} - w_s \hat{\mathbf{x}}_3. \quad (219)$$

Thus, the *macroscopically averaged* forms of the equations of continuity of the fluid phase and of the solid phase, equations (213) and (215), take the form:

$$\nabla \cdot \mathbf{u} = 0, \quad (220)$$

$$\frac{\partial \langle c \rangle}{\partial t} + \nabla \cdot (\langle c \rangle \mathbf{u}) + \nabla \cdot \langle \mathbf{u}' c' \rangle - w_s \frac{\partial \langle c \rangle}{\partial x_3} = 0. \quad (221)$$

The reader will note that the further *macroscopic* averaging process generates a turbulent contribution to the mass flux $\langle \mathbf{u}' c' \rangle$ which will be seen to affect crucially the dynamics of turbulent suspensions.

Similarly, applying the decompositions (218), the momentum equation of the fluid phase (212) becomes:

$$\rho \left(-g \hat{\mathbf{x}}_3 - \frac{d\mathbf{u}}{dt} \right) = \nabla \langle \bar{p} \rangle - \mu \nabla^2 \mathbf{u} - \nabla \cdot (\langle \mathbf{T}^t \rangle + \mathbf{T}^{tM}), \quad (222)$$

where we have defined a *macroscopic* Reynolds stress tensor \mathbf{T}^{tM} of the classical form:

$$\mathbf{T}^{tM} = -\rho \langle \mathbf{u}' \mathbf{u}' \rangle. \quad (223)$$

Here, as anticipated above, the *macroscopic* averaging process has generated a further contribution to the effective stress of the mixture in the form of a classical Reynolds stress tensor. Hence, two *macroscopic* closure problems are left open, namely providing a structure to the turbulent fluxes of mass, $\langle c' \mathbf{u}' \rangle$, and momentum, $\rho \langle \mathbf{u}' \mathbf{u}' \rangle$.

The Reynolds averaged forms of the mass conservation constraints at the free surface and at the bed interface are readily obtained:

- at the free surface ($x_3 = H$):

$$\left[\langle c' \mathbf{u}' \rangle - w_s \langle c \rangle \hat{\mathbf{x}}_3 \right]_H \cdot \hat{\mathbf{n}}_H = 0. \quad (224)$$

Note that here we have used the Reynolds averaged form of the kinematic boundary condition at the free surface (15), that gives: $\mathbf{u}|_H \cdot \hat{\mathbf{n}}_H = V_H$;

- at the bed interface ($x_3 = \eta$):

$$\left[\langle c' \mathbf{u}' \rangle - w_s \langle c \rangle \hat{\mathbf{x}}_3 \right]_\eta \cdot \hat{\mathbf{n}}_\eta = \mathcal{E} - \mathcal{D}, \quad (225)$$

having set $\mathbf{u}|_\eta = 0$.

In the next Section, we will discuss the classical solution for the simplest, yet fundamental, problem of *transport in suspension* by uniform free surface flows.

3.5.4 Equilibrium transport of dilute turbulent suspensions of small particles in open channel flows: the equilibrium Eulerian approach

Let us investigate the transport of dilute suspensions by *uniform turbulent free surface flows* under *equilibrium* conditions. Such conditions are rarely exactly met but are often closely approached in geophysical flows.

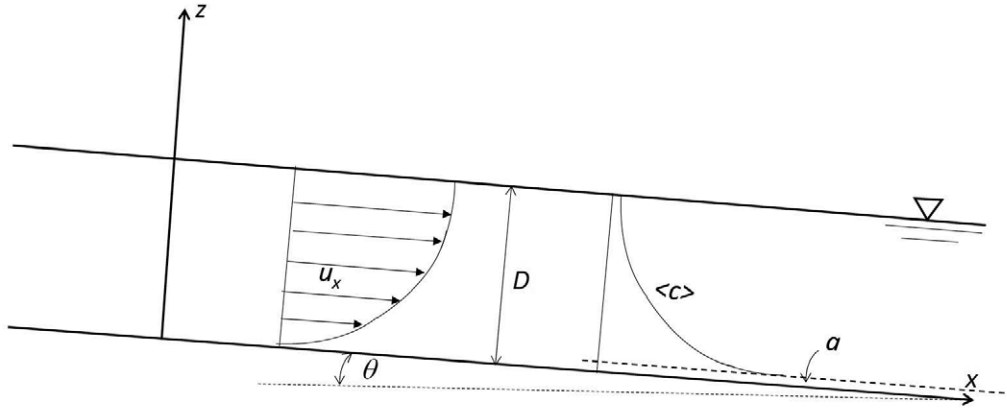


Figure 35. Plane steady and uniform free surface turbulent flow carrying sediment in suspension: sketch and notations.

Rouse solution

We refer the flow to a cartesian reference frame (x, y, z) chosen as in Figure 35 which illustrates the relevant notations. In particular, we denote by u_x the *macroscopic average* of the longitudinal velocity component. The flow is assumed to be steady, plane ($u_y = 0$), unidirectional ($u_z = 0$), and uniform in the mean. Hence temporal derivatives as well as lateral and longitudinal derivatives of mean and fluctuating quantities vanish identically.

Moreover, we assume that transport in suspension is *in equilibrium*. Physically, this condition implies that the sediment flux is constant both in space and in time, such that sediment is supplied upstream at the exact rate needed to meet the transport capacity of the stream averaged both in time and space. As a result, the *microscopically averaged* concentration of suspended particles c fluctuates around a *mean* distribution $\langle c \rangle$ which is also *steady and uniform*. Hence, we may write:

$$c(x, y, z, t) = \langle c \rangle(z) + c'(x, y, z, t). \quad (226)$$

Taking into account the steady, plane and unidirectional character of the flow, continuity of the fluid phase (equation 220) leads to the simple statement:

$$\frac{\partial u_x}{\partial x} = 0 \quad \Rightarrow \quad u_x = u_x(z). \quad (227)$$

Continuity of the solid phase (equation (221)) is readily shown to lead to a balance between the z -component of the upward sediment flux driven by turbulence and the z -component of the downward settling flux. Below we approximate the z -direction with the vertical direction. Hence, integrating along z ,

$$w_s \langle c \rangle - \langle u'_z c' \rangle = 0, \quad (228)$$

where the constant of integration has been set equal to zero in order to satisfy the boundary condition at the free surface (224), whereby the net flux of the solid phase normal to the free surface must vanish.

The momentum of the fluid phase (equation (222)) is similarly shown to reduce to the following simple governing equation:

$$\frac{d}{dz} \left(\langle T'_{zx} \rangle + T'_{zx} \right) + \rho g \sin \theta = 0. \quad (229)$$

Hence, in the infinitely dilute limit, not surprisingly, the stress of the mixture is purely turbulent and, in the context of our derivation where averaging proceeds in two steps, T_{zx} is expressed as a sum of microscopic ($\langle T_{zx}^t \rangle$) and macroscopic (T_{zx}^{tM}) contributions. Closure of (229) may then be achieved following the classical approaches employed in the case of turbulent uniform flows of homogeneous fluids. The output of the analysis for the mean flow is then the classical logarithmic distribution (Section 2.2.9). In other words, in the infinitely dilute limit, the flow field is not affected by the presence of suspended sediments.

The distribution of the mean concentration $\langle c \rangle(z)$ can be obtained from equation (228) once an appropriate closure is adopted for the turbulent diffusive flux $\langle u'_z c' \rangle$. The classical approach employs a *Fickian closure* which, in its simplest version, consists of assuming the turbulent flux proportional to the gradient of the mean concentration through some *turbulent diffusion coefficient* (or *turbulent diffusivity*) \mathfrak{D}_T , a scalar quantity which varies in space. Assuming the validity of the so called *Reynolds analogy*, it is often further assumed that the turbulent diffusivity coincides with the kinematic eddy viscosity. With the simplest choice of a classical parabolic distribution for \mathfrak{D}_T (see equation (90) with no wake correction, i.e. $w_f = 0$), in the uniform case we may write:

$$\langle u'_z c' \rangle = -\mathfrak{D}_T \frac{d\langle c \rangle}{dz} = -k u_\tau z (1-z) \frac{d\langle c \rangle}{dz}. \quad (230)$$

The equation (228) is thus immediately solved to give:

$$\frac{\langle c \rangle}{c_a} = \left(\frac{\zeta_a}{1-\zeta_a} \frac{1-\zeta}{\zeta} \right)^{\mathcal{Z}}, \quad (231)$$

where c_a is the mean concentration at some reference level a , ζ is a dimensionless coordinate and \mathcal{Z} is a dimensionless parameter, known as *Rouse parameter*, with:

$$\zeta = \frac{z}{D}, \quad \zeta_a = \frac{a}{D}, \quad \mathcal{Z} = \frac{w_s}{k u_\tau}. \quad (232)$$

The solution (231) was first derived by Rouse (1937). Note, that it is expressed in terms of the reference concentration c_a . This quantity will have to be specified on the basis of observations, as a sound, theoretically based, model for particle entrainment-deposition at the bed is not yet available. Indeed, the boundary condition at the bed interface (225) is of no help, as the assumed state of equilibrium implies that no net entrainment is allowed at the bed interface, hence $\mathcal{E} - \mathcal{D}$ vanishes and the boundary condition is automatically satisfied by (228).

The concentration distribution (231) has some interesting features (Figure 35). In fact, as $\mathcal{Z} \rightarrow 0$ the mean concentration $\langle c \rangle$ tends to become uniformly distributed and equal to c_a . This is the limiting case when suspended sediments are so fine that they are unable to settle. They form the so called *wash load*. The opposite limit of large \mathcal{Z} is also very interesting. Indeed, as \mathcal{Z} increases, the layer adjacent to the bed where the mean concentration is not negligible gets thinner. Hence, not surprisingly, *as \mathcal{Z} tends to the threshold value for particle entrainment in suspension, the behavior of suspended load tends to somehow resemble that of bedload*. This may be better appreciated by a simple example. For particles of size 1 mm ($R_p = 127$) the threshold value of \mathcal{Z} predicted by the criterion (198) is 5.55 and, for this value of \mathcal{Z} , the distribution (231) (with a assumed to be much smaller than the flow depth), predicts that at a distance $z = 2a$ the mean concentration $\langle c \rangle$ ranges about 0.02 c_a .

Reference concentration and reference level

The engineering literature abounds with relationships proposed to evaluate the reference concentration c_a . As it is reasonable to expect on purely dimensional ground, these relationships can be cast in the general form:

$$c_a = c_a \left(\tau_*, R_p, \frac{d}{D} \right), \quad (233)$$

having assumed that the stream bed keeps plane. Note that this assumption has been made throughout this Chapter as it allows one to discuss the basic mechanisms of sediment transport in the simplest context. In fact, when the bed is covered with small scale bedforms, like ripples and dunes, the mechanics of suspensions is also affected by flow separation. Below we will review a few relationships for the flat bed case, while the dune case will be assessed in Section 4.5.1.

Various empirical relations have been proposed for the functional dependence described by equation (233). The only criterion available to assess the significance of these relationships is their predictive capability. A useful exercise in this respect was performed by Garcia and Parker (1991), who evaluated the performance of seven relationships. Here, we report the widely employed predictor of Van Rijn (1984b), which reads:

$$c_a = 0.015 \frac{d}{a} (T - 1)^{1.5} R_p^{-0.2}, \quad (234)$$

$$a = \begin{cases} e_s & (e_s \leq 0.01 D) \\ 0.01 D & (e_s > 0.01 D), \end{cases} \quad (235)$$

where e_s is the absolute roughness estimated to be equal to d_{90} (the size such that 90% percent of the sediment sample is finer) and T is a *stage parameter* that Van Rijn (1984b) defines in the form:

$$T = \frac{\tau_* - \tau_{*c}}{\tau_{*c}}. \quad (236)$$

Note that equation (234) exhibits a non realistic behavior as the stage parameter T tends to infinity, since also c_a tends to infinity. However, the latter feature is of little relevance, as this relationship only applies to the case of fairly dilute suspensions, associated with fairly low values of the stage parameter.

Volumetric discharge of suspended sediments per unit width

Knowing the distribution of the average concentration we can now proceed to evaluate the mean volumetric discharge of suspended sediments per unit channel width, Q_s^s , defined as

$$\begin{aligned} Q_s^s &= \int_a^D \langle c \bar{v}_x \rangle dz = \int_a^D \left(u_x(z) \langle c \rangle(z) + \langle u'_x c' \rangle \right) dz \\ &= D \int_{\zeta_a}^1 u_x(\zeta) \langle c \rangle(\zeta) d\zeta, \end{aligned} \quad (237)$$

with the longitudinal component of the average turbulent diffusive flux $\langle u'_x c' \rangle$ ($= -\mathfrak{D}_T \partial \langle c \rangle / \partial x$) vanishing for uniform flow conditions. Assuming rough bed flow conditions (Section 2.2.9) and employing the logarithmic velocity distribution for u_x (equation 67) and the Rouse distribution (231) for $\langle c \rangle$, one readily derives the following relationship for Q_s^s :

$$Q_s^s = c_a \frac{u_\tau D}{k} \left[\ln \left(\frac{30 D}{e_s} \right) I_1 + I_2 \right], \quad (238)$$

where I_1 and I_2 read:

$$I_1 = \int_{\zeta_a}^1 \left[\frac{(1 - \zeta)/\zeta}{(1 - \zeta_a)/\zeta_a} \right]^Z d\zeta, \quad (239)$$

$$I_2 = \int_{\zeta_a}^1 \ln \zeta \left[\frac{(1 - \zeta)/\zeta}{(1 - \zeta_a)/\zeta_a} \right]^Z d\zeta. \quad (240)$$

The quantities I_1 and I_2 (multiplied by the factor $0.216/\zeta_a$) were first evaluated by Einstein (1950) and are plotted as functions of the parameters ζ_a and \mathcal{Z} in several textbooks (see for instance Graf, 1971).

It may be convenient to express Q_s^s in terms of the *flow discharge per unit width* UD as follows:

$$Q_s^s = U D \Phi^s, \quad (241)$$

where $\Phi^s = I c_a$ and I is given by the following relationship:

$$I = \frac{\sqrt{C_f}}{k} \left[\ln \left(\frac{30 D}{e_s} \right) I_1 + I_2 \right]. \quad (242)$$

The parameter I is plotted in Figure 36a as a function of the dimensionless parameters a/D and \mathcal{Z} , employing the relationship (235) to estimate ζ_a (Van Rijn, 1984b).

Validation of Rouse distribution

The Rouse formulation has been tested by several experimental investigations. Figure 36b shows a comparison, with the data taken from a variety of sources and based on measurements performed in natural streams, as well as in canals and in laboratory flumes. The grain size ranges from coarse silt to medium sand. A few comments are needed in order to fully appreciate what such comparison suggests.

Firstly, the relative concentration $\langle c \rangle / c_a$ rather than its absolute value is plotted. Hence, the satisfactory agreement undoubtedly exhibited by Figure (36) only tells us that the *shape* of the concentration profile is rather well predicted by the diffusive theory, at least within the range of Rouse numbers, particle sizes and concentrations characteristic of the experimental data employed. Moreover, the maximum volumetric concentration employed in the experimental observations ranges roughly between $5 \cdot 10^{-4}$ and $6.4 \cdot 10^{-3}$, hence the *dilute* approximation is fairly well satisfied. Finally, particles are small enough to keep the *Reynolds number* of the relative particle motion fairly *low*. However comparison becomes less satisfactory when particle concentration and/or particle size increase. As noted by Einstein and Chien (1955) and Coleman (1969) the vertical distribution of the mean concentration in a layer adjacent to the bed decreases less sharply than predicted by the Rouse distribution.

Even though more systematic simulations will be needed, some information can also be gathered from the numerical experiments carried out by Schmeeckle (2014). Tests concerning suspension conditions suggest that turbulence tends to be damped by vertical drag acting on suspended grains, leading to an increase of the rate of shear. Consequently, the vertical sediment diffusivity \mathcal{D}_T (Figure 37), modelled through Reynolds analogy using a Fickian approach is smaller than is commonly assumed in suspended sediment models.

The effects of density stratification on diffusivity can be parameterized by the gradient Richardson number, R_i , defined as

$$R_i = -g \left(\frac{\rho_s}{\rho} - 1 \right) \frac{d\langle c \rangle / dz}{d^2 u_x / dz^2}. \quad (243)$$

For example the correction of the parabolic distribution according to Gelfenbaum and Smith (1986), based on measurements of stably stratified wind profile (Figure 37), reads

$$\frac{\mathcal{D}_T}{u_\tau D} = \frac{k\zeta(1-\zeta)}{1 + [13.5 R_i / (1 + 1.35 R_i)]}. \quad (244)$$

Finally, simulations suggest that a nonlinear relation is likely to hold between the bed reference concentration c_a (e.g. Van Rijn, 1984b; Garcia and Parker, 1991) and the excess shear stress (i.e. the stage parameter T). Clearly, further progress in computational techniques and more simulations are needed before reliable practical formulas can be developed. Indeed, entrainment into suspension, and therefore c_a , are found to be strictly linked to near-bed turbulence structures which, in turn, are significantly different for plane and bedform covered beds.

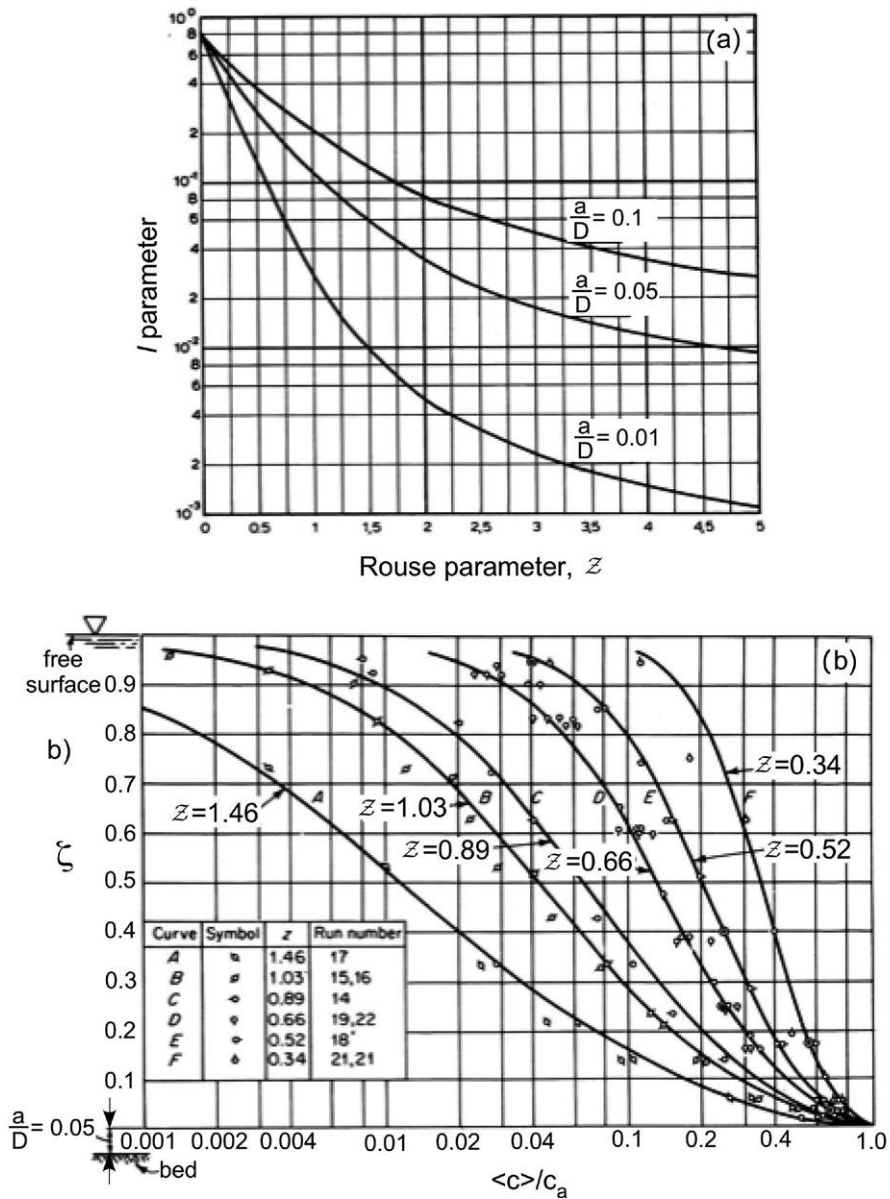


Figure 36. (a) The parameter I of equation (242) is plotted as a function of the Rouse number Z . (b) Comparison between the relation (231), describing the distribution of relative concentration $(c)/c_a$ computed by Rouse (1937), and experimental data of various Authors (modified from Vanoni, 1975).

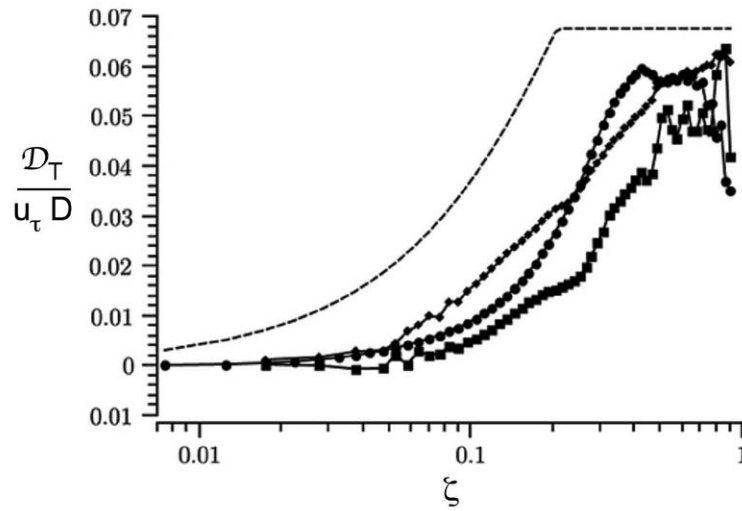


Figure 37. The normalized turbulent diffusivity, $\mathcal{D}_T/u_\tau D$ is plotted versus the dimensionless vertical coordinate $\zeta = z/D$. The dashed line corresponds to the distribution (92). Symbols refer to the numerical experiments carried out by Schmeeckle (2014) for $u_x = 1 \text{ m/s}$: diamonds are the momentum diffusivities corrected for density stratification effects according to the relation (244) of Gelfenbaum and Smith (1986); circles denote the normalized momentum diffusivity, $-\langle u'_x u'_z \rangle / (u_\tau D d\langle c \rangle / dz)$; squares denote the normalized sediment particle diffusivity, $\langle c \rangle u_z / (u_\tau D d\langle c \rangle / dz)$, where u_z is the vertical fluid velocity at the particle centers, averaged over a horizontal plane (modified from Schmeeckle, 2014).

4. Sediment transport in natural channels

In this Chapter, we investigate the additional complexities arising when the formulation of the problem of morphodynamics is extended to natural channels. Let us recall that, physically, the problem consists of determining the dynamics of the bed (and/or bank) interface between the flowing water and sediment mixture and the adjacent erodible medium. In the Introductory Monograph of the present series (Blondeaux *et al.*, 2018) the fundamental ingredient needed to formulate this problem, namely the evolution equation of the bed interface, known as *Exner equation*, has been derived. In the next Section we briefly recall this equation, which states that the temporal derivative of bed elevation is determined by the divergence of the sediment flux. In the previous Chapter, we have discussed the fundamental tools needed to evaluate the flux of homogeneous sediments in uniform steady flow in open channels with a plane sediment bed and under equilibrium conditions (sediment supply equal to transport capacity). In the rest of this Chapter we deal with the various features that complicate the evaluation of the sediment transport capacity in natural channels.

4.1. The evolution equation of the bed interface

The dimensional depth integrated form of the mass conservation equation for the solid phase can be demonstrated to give the following evolution equation of the bed interface (see equation (3.18) of Blondeaux *et al.*, 2018):

$$\frac{\partial(DC)}{\partial t} + c_M \frac{\partial \eta}{\partial t} + \frac{\partial Q_{sx}}{\partial x} + \frac{\partial Q_{sy}}{\partial y} = 0, \quad (245)$$

where t denotes time, x , y are the longitudinal and lateral Cartesian horizontal coordinates, η is the local bed elevation with respect to a reference horizontal plane and D is the local flow depth. Moreover, C is the *depth averaged concentration* of the flowing mixture, c_M is the packing concentration of the erodible bed, and \mathbf{Q}_s is the *depth integrated total sediment flux per unit width*. The depth-averaged concentration C and the j - component of the depth-integrated sediment flux per unit width Q_{sj} are defined as follows:

$$DC = \int_{\eta}^H \langle c \rangle dz, \quad Q_{sj} = \int_{\eta}^H \langle q_{sj} \rangle dz \quad (j = x, y), \quad (246)$$

where $\langle c \rangle$ is the Reynolds averaged local sediment concentration (see Section 3.5.4) and $\langle q_{sx} \rangle$, $\langle q_{sy} \rangle$ are the longitudinal and lateral components of the local Reynolds averaged total sediment flux, respectively. The equation (245) has a general form which is valid whatever type of sediment motion prevails in the flowing mixture. In general, we may write:

$$Q_{sj} = Q_{sj}^b + Q_{sj}^s \quad (j = x, y), \quad (247)$$

where Q_{sj}^b and Q_{sj}^s are the bedload and suspended load components of Q_{sj} , respectively. In order to complete the formulation we then need closure relationships for Q_{sj}^b and Q_{sj}^s as functions of the tangential stress at the bottom and of the local bed topography.

The one-dimensional version of equation (245) is easily obtained by averaging it in the transverse direction (recall Figure 20 for notations), applying the Leibnitz rule and introducing the following averaged quantities:

$$\int_{-B_{bR}}^{B_{bL}} \eta \, dy = 2B_b \bar{\eta}, \quad \int_{-B_R}^{B_L} CD \, dy = C \Omega, \quad \int_{-B_{bR}}^{B_{bL}} Q_{sx} \, dy = 2B_b Q_s \quad (248)$$

One eventually finds:

$$\frac{\partial(C \Omega)}{\partial t} + c_M \frac{\partial(2B_b \bar{\eta})}{\partial t} + \frac{\partial(2B_b Q_s)}{\partial x} = 0 \quad (249)$$

Indeed, all the terms involving quantities evaluated at the lateral boundaries, arising from the application of the Leibnitz rule, are identically zero, since the flow depth vanishes at $y = -B_{bR}$ and $y = B_{bL}$ and $\eta|_{B_{bL}} = \eta|_{-B_{bR}}$.

Considering a constant channel width and further assuming that the variations of the amount of sediments stored in the water column are small relative to the amount of sediments exchanged with the bed through the erodible interface (i.e. neglecting the first term in (249)), the one-dimensional version of the bed evolution equation takes the form derived by Exner (1925):

$$c_M \frac{\partial \bar{\eta}}{\partial t} + \frac{\partial Q_s}{\partial x} = 0 \quad (250)$$

In the previous Chapter we have outlined the mechanisms of transport of homogeneous sediments in the context of the simplest hydrodynamic conditions, namely a plane, steady and uniform (i.e. longitudinally homogeneous) turbulent free surface flow. However, sediment transport in natural channels has a number of features which complicate the latter picture. In particular:

- *Flows are non uniform*, they are spatially varying (in both lateral and longitudinal directions), and may be *unsteady*.
- *The local bed slope differs from the average bed slope* of the channel reach under consideration. This implies that secondary flows are generated and local particle trajectories are not aligned with the channel axis. This effect plays an important role in pattern formation and must be appropriately taken into account.
- *The bed may be covered by small scale bedforms* (ripples, dunes, antidunes). Their effect on the hydrodynamics of larger scale morphodynamic processes is often taken into account treating them as a macro-roughness affecting essentially the friction coefficient of the stream. Sediment transport is also significantly modified by the presence of small scale bedforms and this effect must also be accounted for in the modeling.
- *Natural river banks are typically not plane*. They are commonly characterized by the presence of small-scale features consisting of undulations due to a number of factors, such as erosion and slumping of bank material, as well as the presence of vegetation (roots, grass, etc.). Similarly to bedforms, bank undulations may be treated as macro-roughness leading to form drag which also affects the friction coefficient of the stream.
- *Natural sediments are heterogeneous*, hence the motion of grains of each size is affected by the presence of different sizes.
- *The channel boundary may be cohesive and only partially covered by alluvial sediments*. Under these conditions *sediment supply may be lower than the actual transport capacity* of the stream.
- *The concentration of sediment mixtures may not be small enough to treat them as dilute suspensions*.

In the next sections, we outline briefly the tools developed to deal with flow non-uniformity, sloping topography, small scale bedforms and small scale bank-forms, sediment heterogeneity. Cohesive effects and highly concentrated suspensions lead to a number of specific phenomena that deserve to be dealt with in special Monographs. The role of an insufficient sediment supply will be discussed in Chapter 6 in relation to the problem of bar formation.

4.2. Bedload transport of homogeneous sediments in non-uniform flows

4.2.1 Spatial non uniformities

Spatial variations of natural flows are driven by a variety of causes, e.g. the shape of the channel bottom deviates from a sloping plane both longitudinally and laterally, the free surface may differ from the constant slope plane surface characteristic of a uniform flow as a result of backwater effects. Fortunately, *the spatial scale of flow variations is usually much larger than the scale of turbulent events which control bedload transport*, such that we may reasonably assume, for our purposes, that the *transport capacity of the stream adapts to the local flow conditions*.

For sufficiently wide channels, lateral non uniformities may be treated adopting the approach discussed in Section 2.3.3. We recall that the basic idea is to treat the flow field as a sequence of locally uniform flows, each referring to a vertical strip of infinitesimal thickness dy , with properties that vary slowly in the lateral direction, as illustrated in Figure 15. Following this approach we may also associate a *local* value of the Shields stress $\tau_*(y)$ and depth averaged bedload flux per unit width $Q_s^b(y)$ to each strip, such that:

$$\tau_*(y) = \frac{Q^2(y)}{(s-1)\chi^2(y)D^2(y)d(y)g}, \quad Q_s^b(y) = Q_s^b[\tau_*(y)], \quad (251)$$

having denoted by $Q = DU$, χ , D and d the local values of the fluid discharge per unit width, the local flow conductance, the local flow depth and the local average grain size, respectively.

With the help of (251) one can calculate the *total bed load discharge* Q_s^b transported in the *cross-section* as follows:

$$Q_s^b = \int_{-B_{bL}}^{B_{bR}} Q_s^b[\tau_*(y)] dy. \quad (252)$$

The reader should note that, due to the nonlinear dependence of Q_s^b on $\tau_*(y)$, if the channel cross-section displays strong variations of bed elevation, the value of Q_s^b obtained with the help of (252) may differ significantly from the estimate obtained using the commonly employed approximation:

$$Q_s^b = 2B_b Q_s^b(\bar{\tau}_*), \quad (253)$$

having denoted by $\bar{\tau}_*$ the laterally averaged value of the Shields stress.

The exercise presented in Figure 38 illustrates the latter statement quantitatively.

4.2.2 Temporal non uniformities

Similar ideas apply when the flow under consideration is unsteady, as the temporal scale of flow variations in fluvial-tidal settings is much larger than the temporal scale of the events that control sediment transport.

4.3. Non uniform dilute suspensions of homogeneous sediments

4.3.1 The 3D Reynolds averaged advection-diffusion equation

We now extend the knowledge on the transport of suspended load established in Chapter 3 for the fundamental case of uniform conditions to flows that, as typical of natural settings, vary slowly both in space and in time. This approach also applies to investigations concerning large

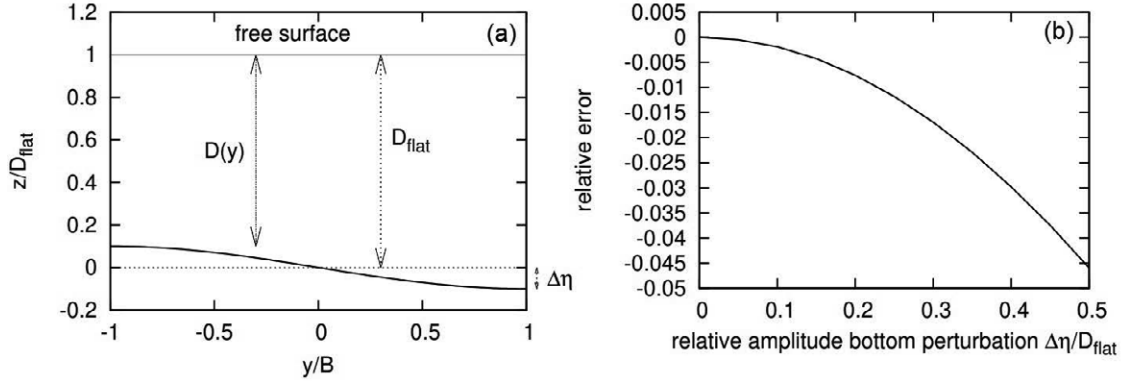


Figure 38. Panel (a) shows a sketch of the investigated cross section, characterised by a gradually varying perturbation of the bottom of maximum amplitude $\Delta\eta$. The corresponding lateral depth distribution has the form $D(y) = D_{flat} + \Delta\eta \sin(\pi y/(2B))$. Panel (b) shows how the relative error of the total bedload discharge estimate obtained using the laterally averaged value of the Shields stress (equation 253) instead of the integral (252) increases as the maximum amplitude of the bottom perturbation increases. The exercise has been performed assuming a sequence of locally uniform flows in the lateral direction with $S = 0.01\%$, $B_{bL} = B_{bR} = B$, $d = 0.5 \text{ mm}$ and $D_{flat} = 2 \text{ m}$.

scale bedforms (e.g. bars), while it progressively becomes less appropriate as the temporal/spatial scale of bedforms dynamics decreases (e.g. ripples).

Let us then recall the advection-diffusion equation governing the dynamics of dilute suspensions of small solid equally sized particles that was derived in Section 3.5.3 for the *macroscopically averaged* form of the equation of continuity of the solid phase. It reads:

$$\frac{\partial \langle c \rangle}{\partial t} + \nabla \cdot (\langle c \rangle \mathbf{u}) + \nabla \cdot (\langle \mathbf{u}' c' \rangle) - w_s \frac{\partial \langle c \rangle}{\partial z} = 0, \quad (254)$$

where the symbol $\langle \rangle$ denotes the *macroscopic average*.

As already pointed out, the rational framework underlying (254) is based on two main assumptions, namely that the suspension must be sufficiently *dilute* to make hydrodynamic interactions between solid particles weak and particle collisions highly unlikely, while solid particles must be *small enough* to induce negligible disturbances of the turbulence field down to its smallest scales. Though these assumptions are quite strict and apply rigorously to a relatively small subset of the actual suspensions observed in fluvial and tidal streams, however the above scheme is widely employed for its simplicity. In fact, the implication of the above assumptions can be summarized by stating that the motion of the solid phase is coupled to the motion of the fluid phase while, on the contrary, the fluid motion is not affected by the presence of the solid phase. Technically, this scheme is a particular case of the approach known as *one way coupling* (Section 3.5.1). It implies that *the sediment particles are advected by the fluid except for their tendency to settle as a result of their submerged weight*.

Mass conservation at the free surface $z = H$ imposes that this surface is impermeable to solid particles. The Reynolds averaged form of this constraint was introduced in the previous Chapter (equation 224) and reads:

$$\left[\langle c' \mathbf{u}' \rangle - w_s \langle c \rangle \hat{\mathbf{z}} \right]_H \cdot \hat{\mathbf{n}}_H = 0, \quad (255)$$

At the bed interface, under non equilibrium conditions, the boundary condition (225) states that the flux entrained by the stream does not coincide with the deposited flux, i.e. a net positive (negative) exchanged flux $\mathcal{E} - \mathcal{D}$ must be allowed at the reference elevation $z = \eta + a$. We now assume that this net flux is proportional to the defect (excess) concentration at the bed, relative

to the local and instantaneous value of the equilibrium concentration $c_a[\tau_*(\mathbf{x}, t)]$. More precisely, we set:

$$\mathcal{D} - \mathcal{E} = w_s \left[c_a - \langle c \rangle_{\eta+a} \right] \hat{\mathbf{z}} \cdot \hat{\mathbf{n}}_\eta \quad (256)$$

such that the boundary condition (225) takes the form:

$$\left[\langle c' \mathbf{u}' \rangle - w_s \langle c \rangle \hat{\mathbf{z}} \right]_{\eta+a} \cdot \hat{\mathbf{n}}_\eta = w_s \left[c_a - \langle c \rangle_{\eta+a} \right] \hat{\mathbf{z}} \cdot \hat{\mathbf{n}}_\eta \quad (257)$$

This relationship makes it clear that the form (256) assumed for the net exchanged flux, in particular the choice of w_s as proportionality factor, ensures that the boundary condition (257) applied to uniform streams in equilibrium reduces to the classical equality of entrainment and deposition. This is readily proved. Assume equilibrium conditions, such that the bed is flat and $\hat{\mathbf{z}} = -\hat{\mathbf{n}}_\eta$. The relationship (257) then becomes:

$$\left[\langle c' u'_z \rangle \right]_{\eta+a} = w_s c_a \quad (258)$$

i.e. the entrained flux equals the depositing flux. Since the *entrained flux* under equilibrium conditions is equal to $w_s c_a$, then the assumption (256) can be readily interpreted stating that the net exchanged flux is equal to the difference between the entrained flux, estimated by the equilibrium relationship in terms of the local and instantaneous conditions, and the depositing flux.

The differential system (254, 255, 257) will require some *closure* for the turbulent diffusive flux $\langle \mathbf{u}' c' \rangle$. Following the classical approach introduced in Section 3.5 we employ a gradient-diffusion assumption which is likely to hold for turbulent flows not far from uniformity. In the present general case it reads:

$$\langle u'_j c' \rangle = -\mathcal{D}_j \frac{\partial \langle c \rangle}{\partial x_j}, \quad (259)$$

where \mathcal{D}_j ($j = x, y, z$) is the j -th-component of the *turbulent diffusivity* vector, which is usually estimated using the Reynolds analogy, i.e. assuming that the turbulent diffusivity is equal to the eddy viscosity.

Once equation (254) has been solved with the appropriate boundary conditions, the components of the depth averaged sediment flux per unit width (Q_{sx}^s and Q_{sy}^s) are readily calculated from the following integrals:

$$(Q_{sx}^s, Q_{sy}^s) = \int_{\eta+a}^H (u, v) \langle c \rangle dz. \quad (260)$$

Note that, in principle, also the horizontal turbulent diffusive fluxes contribute to the depth-averaged fluxes. However, as discussed in the next Section, in most situations of interest for fluvial morphodynamics these contributions are much smaller than advective fluxes and, hence, are usually neglected.

4.3.2 Depth averaged model of transport in suspension

Most application problems of morphodynamics focus on predicting the short- or long-term evolution of relatively large river or estuarine reaches for which full-scale three-dimensional modeling is computationally inconvenient or even prohibitive. Moreover, in many cases (e.g. tidal flows, flood waves, large scale sedimentary patterns) the flow characteristics vary gradually both in space and time. Under these conditions, a depth-averaged model is most often adequate to investigate the hydrodynamics. Similarly, morphodynamic investigations would greatly benefit from the availability of an appropriate depth-averaged model to evaluate the flux of sediment transported in suspension.

Below, we follow the approach of Bolla Pittaluga and Seminara (2003) who were able to derive a sequence of higher order corrections for the local and instantaneous equilibrium solution for the

depth-averaged concentration. These corrections are found to be expressed in terms of the spatial and temporal derivatives of the depth-averaged equilibrium concentration. Below, we outline the analysis of Bolla Pittaluga and Seminara (2003) later extended by Federici and Seminara (2006).

Governing equations

Let us start from the advection-diffusion equation (254), rewritten in the explicit form:

$$\begin{aligned} \frac{\partial \langle c \rangle}{\partial t} + u \frac{\partial \langle c \rangle}{\partial x} + v \frac{\partial \langle c \rangle}{\partial y} + (w - w_s) \frac{\partial \langle c \rangle}{\partial z} = \\ \frac{\partial}{\partial x} \left(\mathfrak{D}_x \frac{\partial \langle c \rangle}{\partial x} \right) + \frac{\partial}{\partial y} \left(\mathfrak{D}_y \frac{\partial \langle c \rangle}{\partial y} \right) + \frac{\partial}{\partial z} \left(\mathfrak{D}_z \frac{\partial \langle c \rangle}{\partial z} \right). \end{aligned} \quad (261)$$

Next we make the relevant physical quantities dimensionless as follows:

$$(\tilde{x}, \tilde{y}, \tilde{z}) = \left(\frac{x}{L}, \frac{y}{2B}, \frac{z}{D_0} \right), \quad \tilde{t} = \omega t, \quad (262a)$$

$$(\tilde{u}, \tilde{v}, \tilde{w}) = \left(\frac{u}{U_0}, \frac{v}{V_0}, \frac{w}{W_0} \right), \quad \tilde{\mathfrak{D}}_j = \frac{\mathfrak{D}_j}{u_{\tau_0} D_0}. \quad (262b)$$

Here, ω is the inverse of the characteristic temporal scale of the flow, L is a longitudinal scale depending on the investigated problem and $2B$ is a lateral scale (e.g. the channel width). Moreover, D_0 and U_0 are the flow depth and the cross-sectional speed of some reference uniform flow. They are employed as spatial scale for the vertical coordinate and for the longitudinal velocity, respectively. Balancing the three terms of the Reynolds averaged continuity equation of the fluid phase (equation 71a), it follows that $V_0 = 2B U_0 / L$ and $W_0 = D_0 U_0 / L$ are the associated scales for the lateral and vertical components of the flow velocity. Finally u_{τ_0} is the friction velocity associated with the reference uniform flow.

Using the above dimensionless variables the equation (261) takes the form:

$$\begin{aligned} \delta_1 \frac{\partial \langle c \rangle}{\partial \tilde{t}} + \delta_2 \left[\tilde{u} \frac{\partial \langle c \rangle}{\partial \tilde{x}} + \tilde{v} \frac{\partial \langle c \rangle}{\partial \tilde{y}} + \tilde{w} \frac{\partial \langle c \rangle}{\partial \tilde{z}} \right] - \frac{\partial \langle c \rangle}{\partial \tilde{z}} = \\ \frac{1}{k \mathcal{Z}_0} \left[\frac{\partial}{\partial \tilde{z}} \left(\tilde{\mathfrak{D}}_z \frac{\partial \langle c \rangle}{\partial \tilde{z}} \right) + \delta_3 \frac{\partial}{\partial \tilde{x}} \left(\tilde{\mathfrak{D}}_x \frac{\partial \langle c \rangle}{\partial \tilde{x}} \right) + \delta_4 \frac{\partial}{\partial \tilde{y}} \left(\tilde{\mathfrak{D}}_y \frac{\partial \langle c \rangle}{\partial \tilde{y}} \right) \right], \end{aligned} \quad (263)$$

where the following dimensionless parameters arise:

$$\delta_1 = \frac{\omega D_0}{w_s}, \quad \delta_2 = \frac{U_0 D_0}{w_s L}, \quad \delta_3 = \left(\frac{D_0}{L} \right)^2, \quad \delta_4 = \left(\frac{D_0}{2B} \right)^2, \quad \mathcal{Z}_0 = \frac{w_s}{k u_{\tau_0}}. \quad (264)$$

In (263, 264) k is the von Karman constant and \mathcal{Z}_0 is the reference *Rouse number*. Note that the parameters δ_j ($j = 1, 4$) are typically small for slowly varying flows like tidal flows (Lanzoni and Seminara, 2002), flood waves (Bolla Pittaluga and Seminara, 2003) or large scale fluvial and estuarine sedimentary patterns (Federici and Seminara, 2006). In particular, δ_3 and δ_4 are usually much smaller than δ_1 and δ_2 and, therefore, the last two terms in the right hand side of (263) are usually neglected.

Let us next define a transformed vertical coordinate ζ as follows:

$$\zeta = \frac{z - \eta}{h - \eta} = \frac{z - \eta}{D} = \frac{\tilde{z} - \tilde{\eta}}{\tilde{D}}, \quad (265)$$

with $\tilde{\eta} = \eta / D_0$ and $\tilde{D} = D / D_0$. The reader must note that the transformed variable ζ falls in the range $[0, 1]$. Moreover, the governing equations must also be transformed. Indeed, as ζ depends on

\tilde{x} , \tilde{y} and \tilde{t} , the following coordinate transformations follow:

$$\frac{\partial}{\partial \tilde{z}} \rightarrow \frac{1}{\tilde{D}} \frac{\partial}{\partial \tilde{\zeta}}, \quad (266a)$$

$$\frac{\partial}{\partial \tilde{x}} \rightarrow \frac{\partial}{\partial \tilde{x}} + \frac{\partial \zeta}{\partial \tilde{x}} \frac{\partial}{\partial \tilde{\zeta}} = \frac{\partial}{\partial \tilde{x}} - \frac{1}{\tilde{D}} \left(\frac{\partial \tilde{\eta}}{\partial \tilde{x}} + \zeta \frac{\partial \tilde{D}}{\partial \tilde{x}} \right) \frac{\partial}{\partial \tilde{\zeta}}, \quad (266b)$$

$$\frac{\partial}{\partial \tilde{y}} \rightarrow \frac{\partial}{\partial \tilde{y}} + \frac{\partial \zeta}{\partial \tilde{y}} \frac{\partial}{\partial \tilde{\zeta}} = \frac{\partial}{\partial \tilde{y}} - \frac{1}{\tilde{D}} \left(\frac{\partial \tilde{\eta}}{\partial \tilde{y}} + \zeta \frac{\partial \tilde{D}}{\partial \tilde{y}} \right) \frac{\partial}{\partial \tilde{\zeta}}, \quad (266c)$$

$$\frac{\partial}{\partial \tilde{t}} \rightarrow \frac{\partial}{\partial \tilde{t}} + \frac{\partial \zeta}{\partial \tilde{t}} \frac{\partial}{\partial \tilde{\zeta}} = \frac{\partial}{\partial \tilde{t}} - \frac{1}{\tilde{D}} \left(\frac{\partial \tilde{\eta}}{\partial \tilde{t}} + \zeta \frac{\partial \tilde{D}}{\partial \tilde{t}} \right) \frac{\partial}{\partial \tilde{\zeta}}. \quad (266d)$$

Setting

$$\delta_2 = \delta, \quad \delta_1 = \gamma \delta, \quad \gamma = \frac{U_0}{\omega L} \sim \mathcal{O}(1), \quad (267)$$

employing the transformations (266) and neglecting the terms proportional to δ_3 and δ_4 , the advection-diffusion equation (263) becomes:

$$\begin{aligned} \frac{1}{k \mathcal{Z}_0} \frac{1}{\tilde{D}} \left[\frac{\partial}{\partial \tilde{\zeta}} \left(\tilde{\mathfrak{D}}_z \frac{\partial \langle c \rangle}{\partial \tilde{\zeta}} \right) \right] + \frac{\partial \langle c \rangle}{\partial \tilde{\zeta}} = \delta \left\{ \gamma \tilde{D} \frac{\partial \langle c \rangle}{\partial \tilde{t}} + \tilde{D} \tilde{u} \frac{\partial \langle c \rangle}{\partial \tilde{x}} + \tilde{D} \tilde{v} \frac{\partial \langle c \rangle}{\partial \tilde{y}} + \tilde{w} \frac{\partial \langle c \rangle}{\partial \tilde{\zeta}} \right. \\ \left. - \left[\gamma \left(\frac{\partial \tilde{\eta}}{\partial \tilde{t}} + \zeta \frac{\partial \tilde{D}}{\partial \tilde{t}} \right) + \tilde{u} \left(\frac{\partial \tilde{\eta}}{\partial \tilde{x}} + \zeta \frac{\partial \tilde{D}}{\partial \tilde{x}} \right) + \tilde{v} \left(\frac{\partial \tilde{\eta}}{\partial \tilde{y}} + \zeta \frac{\partial \tilde{D}}{\partial \tilde{y}} \right) \right] \frac{\partial \langle c \rangle}{\partial \tilde{\zeta}} \right\}. \end{aligned} \quad (268)$$

Boundary conditions

The boundary conditions to be associated with the equation (268) are obtained from (255) and (257), recalling also the no slip condition at the bed and the fixed nature of the bed interface in the present context, whereby $[\tilde{u}, \tilde{v}, \tilde{w}]_{\eta+a} = 0$. Again, one has to make the above relationships dimensionless with the help of (262b) and then perform the coordinate transformations (266). Use must also be made of the definitions of the unit vectors normal to the free surface and to the bed interface already introduced and employed in Chapter 2 (see equations (128a, b) and (13)). Finally, the mathematical definition of the normal velocity of the free surface V_H must be recalled (equation (16)).

Retaining only terms up to $\mathcal{O}(\delta)$, some algebraic work eventually leads to the following dimensionless form of the boundary conditions:

$$\frac{1}{k \mathcal{Z}_0} \left[\frac{\tilde{\mathcal{D}}_\zeta}{\tilde{D}} \frac{\partial \langle c \rangle}{\partial \tilde{\zeta}} \right]_1 + \langle c \rangle \Big|_1 = \delta \left[\left(\tilde{w} - \tilde{u} \frac{\partial \tilde{H}}{\partial \tilde{x}} - \tilde{v} \frac{\partial \tilde{H}}{\partial \tilde{y}} - \gamma \frac{\partial \tilde{H}}{\partial \tilde{t}} \right) \langle c \rangle \right]_1 \quad (269a)$$

$$\frac{1}{k \mathcal{Z}_0} \left[\frac{\tilde{\mathcal{D}}_\zeta}{\tilde{D}} \frac{\partial \langle c \rangle}{\partial \tilde{\zeta}} \right]_{\zeta_a} + c_a = 0 \quad (269b)$$

Here, ζ_a is the conventional dimensionless value of the reference elevation where the bed boundary condition is imposed under uniform conditions. As discussed in Section 3.5.4, several empirical expressions for c_a and ζ_a are available in the literature. They usually assume a dependence of c_a on the local and instantaneous value of the Shields parameter τ^* , and on the particle Reynolds number R_p .

Closure

A closure relation for the eddy diffusivity \mathfrak{D}_z is required. In the present context, the flow field is treated as a quasi-steady sequence of locally and instantaneously equilibrium states, hence we

write:

$$\tilde{\mathfrak{D}}_z = \tilde{D} \frac{u_\tau}{u_{\tau 0}} \mathcal{N}(\zeta), \quad (270)$$

with u_τ local and instantaneous value of the friction velocity and $\mathcal{N}(\zeta)$ vertical distribution of the eddy diffusivity at equilibrium. Using the classical parabolic distribution for $\mathcal{N}(\zeta)$ we may write:

$$\mathcal{N}(\zeta) = k \zeta (1 - \zeta). \quad (271)$$

Reduction of the mathematical problem

The last step is to remove the vertical velocity from the mathematical formulation. This is readily achieved recalling the continuity equation for the fluid phase, that in dimensionless form reads:

$$\frac{\partial \tilde{u}}{\partial \tilde{x}} + \frac{\partial \tilde{v}}{\partial \tilde{y}} + \frac{\partial \tilde{w}}{\partial \tilde{z}} = 0. \quad (272)$$

Employing the transformations (266) and performing integration in ζ we obtain:

$$\begin{aligned} \tilde{w} = & \left(\frac{\partial \tilde{\eta}}{\partial \tilde{x}} + \zeta \frac{\partial \tilde{D}}{\partial \tilde{x}} \right) \tilde{u} - \frac{\partial \tilde{D}}{\partial \tilde{x}} \int_{\zeta_a}^{\zeta} \tilde{u}(\xi) d\xi - \tilde{D} \int_{\zeta_a}^{\zeta} \frac{\partial \tilde{u}}{\partial \tilde{x}} d\xi \\ & + \left(\frac{\partial \tilde{\eta}}{\partial \tilde{y}} + \zeta \frac{\partial \tilde{D}}{\partial \tilde{y}} \right) \tilde{v} - \frac{\partial \tilde{D}}{\partial \tilde{y}} \int_{\zeta_a}^{\zeta} \tilde{v}(\xi) d\xi - \tilde{D} \int_{\zeta_a}^{\zeta} \frac{\partial \tilde{v}}{\partial \tilde{y}} d\xi. \end{aligned} \quad (273)$$

Assuming a self similar structure of the velocity field appropriate to slowly varying flows, we can write

$$(\tilde{u}, \tilde{v}) = (\tilde{U}, \tilde{V}) \mathcal{F}_0(\zeta). \quad (274)$$

Here, $\tilde{U}(\tilde{x}, \tilde{y}, \tilde{t})$ and $\tilde{V}(\tilde{x}, \tilde{y}, \tilde{t})$ are the dimensionless depth averaged longitudinal and lateral velocity components, with the obvious implication that, in the reference state, $\tilde{U} = 1$ and $\tilde{V} = 0$. Moreover, the function \mathcal{F}_0 is the one defined in (97) and is obviously characterized by the condition $\int_{\zeta_0}^1 \mathcal{F}_0 d\zeta = 1$. Below, we set $\int_{\zeta_a}^1 \mathcal{F}_0 d\zeta \simeq \int_{\zeta_0}^1 \mathcal{F}_0 d\zeta = 1$.

With the aid of (274) the vertical component of the velocity (273) takes the form:

$$\tilde{w} = \left(\frac{\partial \tilde{\eta}}{\partial \tilde{x}} + \zeta \frac{\partial \tilde{D}}{\partial \tilde{x}} \right) \tilde{u} + \left(\frac{\partial \tilde{\eta}}{\partial \tilde{y}} + \zeta \frac{\partial \tilde{D}}{\partial \tilde{y}} \right) \tilde{v} - \left[\frac{\partial(\tilde{D}\tilde{U})}{\partial \tilde{x}} + \frac{\partial(\tilde{D}\tilde{V})}{\partial \tilde{y}} \right] \mathcal{I}_{\mathcal{F}_0}(\zeta), \quad (275)$$

where

$$\mathcal{I}_{\mathcal{F}_0}(\zeta) = \int_{\zeta_a}^{\zeta} \mathcal{F}_0(\xi) d\xi. \quad (276)$$

Next, recall the shallow water formulation of the mass balance equation for the fluid phase (131) and make it dimensionless to find:

$$\gamma \frac{\partial \tilde{D}}{\partial \tilde{t}} + \frac{\partial(\tilde{D}\tilde{U})}{\partial \tilde{x}} + \frac{\partial(\tilde{D}\tilde{V})}{\partial \tilde{y}} = 0. \quad (277)$$

Substituting from (275), (277) and (270) into (268) and (269), we obtain the following final form

of the differential problem:

$$\frac{1}{k \mathcal{Z}} \frac{\partial}{\partial \zeta} \left[\mathcal{N}(\zeta) \frac{\partial \langle c \rangle}{\partial \zeta} \right] + \frac{\partial \langle c \rangle}{\partial \zeta} = \delta \tilde{D} \left[\gamma \frac{\partial \langle c \rangle}{\partial \tilde{t}} + \tilde{u} \frac{\partial \langle c \rangle}{\partial \tilde{x}} + \tilde{v} \frac{\partial \langle c \rangle}{\partial \tilde{y}} \right] + \delta \gamma \left[\frac{\partial \tilde{D}}{\partial \tilde{t}} \mathcal{I}_{F_0}(\zeta) - \left(\frac{\partial \tilde{\eta}}{\partial \tilde{t}} + \zeta \frac{\partial \tilde{D}}{\partial \tilde{t}} \right) \right] \frac{\partial \langle c \rangle}{\partial \zeta}, \quad (278a)$$

$$\frac{1}{k \mathcal{Z}} \left[\mathcal{N}(\zeta) \frac{\partial \langle c \rangle}{\partial \zeta} \right]_1 + \langle c \rangle \Big|_1 = -\delta \gamma \langle c \rangle \Big|_1 \frac{\partial \tilde{\eta}}{\partial \tilde{t}} \quad (278b)$$

$$\frac{1}{k \mathcal{Z}} \left[\mathcal{N}(\zeta) \frac{\partial \langle c \rangle}{\partial \zeta} \right]_{\zeta_a} + c_a = 0 \quad (278c)$$

where $\mathcal{Z} = w_s/k u_\tau$ is the local and instantaneous value of the Rouse number.

Perturbation solution for the slowly varying case ($\delta \ll 1$)

A formal perturbation solution of the differential equation (278a), associated with the boundary conditions (278b, 278c), can be obtained by expanding the concentration $\langle c \rangle$ in powers of the small parameter δ in the form:

$$\langle c \rangle = \langle c_0 \rangle(\zeta; \tilde{x}, \tilde{y}, \tilde{t}) + \delta \langle c_1 \rangle(\zeta; \tilde{x}, \tilde{y}, \tilde{t}) + \mathcal{O}(\delta^2). \quad (279)$$

By substituting from the latter expansion into the differential problem (278a, 278b, 278c) and equating likewise powers of δ we find a sequence of differential problems at the various orders of approximation.

- $\mathcal{O}(\delta^0)$: Leading order

$$\frac{1}{k \mathcal{Z}} \left[\frac{\partial}{\partial \zeta} \left(\mathcal{N}(\zeta) \frac{\partial \langle c_0 \rangle}{\partial \zeta} \right) \right] + \frac{\partial \langle c_0 \rangle}{\partial \zeta} = 0, \quad (280a)$$

$$\frac{1}{k \mathcal{Z}} \left[\mathcal{N}(\zeta) \frac{\partial \langle c_0 \rangle}{\partial \zeta} \right]_1 + \langle c_0 \rangle \Big|_1 = 0, \quad (280b)$$

$$\frac{1}{k \mathcal{Z}} \left[\mathcal{N}(\zeta) \frac{\partial \langle c_0 \rangle}{\partial \zeta} \right]_{\zeta_a} = -c_a \quad (280c)$$

This leads to the classical Rouse solution (231) associated with the local and instantaneous conditions, that can be cast in the form:

$$\langle c_0 \rangle = C_0(\tilde{x}, \tilde{y}, \tilde{t}) \phi_0(\zeta, \tau_*, R_p). \quad (281)$$

Here, C_0 is the lowest order approximation for the depth averaged concentration, such that:

$$C_0(\tilde{x}, \tilde{y}, \tilde{t}) = c_a(\tau_*, R_p) I_0(\tau_*, R_p), \quad (282)$$

while

$$\phi_0(\zeta, \tau_*, R_p) = \frac{1}{I_0(\tau_*, R_p)} \left(\frac{1 - \zeta}{1 - \zeta_a} \frac{\zeta_a}{\zeta} \right)^{\mathcal{Z}}. \quad (283)$$

with

$$I_0(\tau_*, R_p) = \frac{1}{1 - \zeta_a} \int_{\zeta_a}^1 \left(\frac{1 - \zeta}{1 - \zeta_a} \frac{\zeta_a}{\zeta} \right)^{\mathcal{Z}} d\zeta. \quad (284)$$

- $\mathcal{O}(\delta)$: First order

At the first order of approximation we find:

$$\begin{aligned} \frac{1}{k\mathcal{Z}} \left[\frac{\partial}{\partial \zeta} \left(\mathcal{N}(\zeta) \frac{\partial \langle c_1 \rangle}{\partial \zeta} \right) \right] + \frac{\partial \langle c_1 \rangle}{\partial \zeta} &= \gamma \tilde{D} \frac{\partial \langle c_0 \rangle}{\partial \tilde{t}} + \tilde{D} \mathcal{F}_0(\zeta) \left[\tilde{U} \frac{\partial \langle c_0 \rangle}{\partial \tilde{x}} + \tilde{V} \frac{\partial \langle c_0 \rangle}{\partial \tilde{y}} \right] \\ &+ \left[\frac{\partial \tilde{D}}{\partial \tilde{t}} \mathcal{I}_{F_0}(\zeta) - \left(\frac{\partial \tilde{\eta}}{\partial \tilde{t}} + \zeta \frac{\partial \tilde{D}}{\partial \tilde{t}} \right) \right] \gamma \frac{\partial \langle c_0 \rangle}{\partial \zeta}, \end{aligned} \quad (285)$$

$$\frac{1}{k\mathcal{Z}} \left[\mathcal{N}(\zeta) \frac{\partial \langle c_1 \rangle}{\partial \zeta} \right]_1 + \langle c_1 \rangle \Big|_1 = -\gamma \langle c_0 \rangle \Big|_1 \frac{\partial \tilde{\eta}}{\partial \tilde{t}}, \quad (286)$$

$$\frac{\partial \langle c_1 \rangle}{\partial \zeta} \Big|_{\zeta_a} = 0 \quad (287)$$

The expression of ϕ_0 indicates that it generally depends on \tilde{x} , \tilde{y} and \tilde{t} through the variations of ζ_a associated with τ_* . However, this dependence is very weak and, as a first approximation, can be neglected. We then set:

$$\left(\frac{\partial \langle c_0 \rangle}{\partial \tilde{t}}, \frac{\partial \langle c_0 \rangle}{\partial \tilde{x}}, \frac{\partial \langle c_0 \rangle}{\partial \tilde{y}} \right) = \phi_0(\zeta) \left(\frac{\partial C_0}{\partial \tilde{t}}, \frac{\partial C_0}{\partial \tilde{x}}, \frac{\partial C_0}{\partial \tilde{y}} \right), \quad \frac{\partial \langle c_0 \rangle}{\partial \zeta} = C_0 \frac{d\phi_0}{d\zeta}. \quad (288)$$

Recalling the structure of the forcing terms in the right hand side of (285) and the expressions (288), the solution for $\langle c_1 \rangle$ can then be written in the form

$$\langle c_1 \rangle = c_{11} \gamma \tilde{D} \frac{\partial C_0}{\partial \tilde{t}} + \tilde{D} \left(c_{12} \tilde{U} \frac{\partial C_0}{\partial \tilde{x}} + c_{13} \tilde{V} \frac{\partial C_0}{\partial \tilde{y}} \right) - \gamma C_0 \left[c_{14} \frac{\partial \tilde{\eta}}{\partial \tilde{t}} + (c_{15} - c_{16}) \frac{\partial \tilde{D}}{\partial \tilde{t}} \right], \quad (289)$$

where the functions c_{1j} ($j = 1, 6$) are solutions of the boundary value problems:

$$\mathcal{L} c_{1j} = a_j(\zeta), \quad (290a)$$

$$\mathcal{B} c_{1j} \Big|_1 = b_j \quad (290b)$$

$$\frac{dc_{1j}}{d\zeta} \Big|_{\zeta_a} = 0 \quad (290c)$$

with the following definitions of the operators \mathcal{L} and \mathcal{B} :

$$\mathcal{L} \equiv \frac{1}{k\mathcal{Z}} \left[\frac{d}{d\zeta} \left(\mathcal{N}(\zeta) \frac{d}{d\zeta} \right) \right] + \frac{d}{d\zeta}, \quad (291a)$$

$$\mathcal{B} \equiv \frac{\mathcal{N}(\zeta)}{k\mathcal{Z}} \frac{d}{d\zeta} + 1, \quad (291b)$$

and

$$a_1 = \phi_0, \quad a_2 = a_3 = \phi_0 \mathcal{F}_0, \quad a_4 = \frac{d\phi_0}{d\zeta}, \quad a_5 = \mathcal{I}_{F_0} \frac{d\phi_0}{d\zeta}, \quad a_6 = \zeta \frac{d\phi_0}{d\zeta}, \quad (292a)$$

$$b_1 = b_2 = b_3 = b_5 = b_6 = 0, \quad b_4 = \phi_0 \Big|_1. \quad (292b)$$

The boundary value problems (290) can be solved numerically using a shooting technique (Press *et al.*, 2007).

4.3.3 Analytical relationship for the depth integrated suspended sediment flux per unit width appropriate to slowly varying flows

Based on the above analysis, we can expand the *depth integrated suspended sediment flux per unit width*, denoted by \mathbf{Q}_s^s , in powers of the small parameter δ in the form:

$$\mathbf{Q}_s^s = \mathbf{Q}_{s0}^s + \delta \mathbf{Q}_{s1}^s + \mathcal{O}(\delta^2). \quad (293)$$

Let us make \mathbf{Q}_s^s dimensionless as follows:

$$\tilde{\mathbf{Q}}_s^s = \frac{\mathbf{Q}_s^s}{U_0 D_0}. \quad (294)$$

With the aid of (274) we can write:

$$\tilde{\mathbf{Q}}_s^s = (\tilde{U}, \tilde{V}) \tilde{D} \Phi^s(\tilde{x}, \tilde{y}, \tilde{t}), \quad (295)$$

where

$$\Phi^s(\tilde{x}, \tilde{y}, \tilde{t}) = \int_{\zeta_a}^1 \left[\langle c_0 \rangle + \delta \langle c_1 \rangle + \mathcal{O}(\delta^2) \right] \mathcal{F}_0(\zeta) d\zeta = \Phi_0^s + \delta \Phi_1^s + \mathcal{O}(\delta^2). \quad (296)$$

By substituting from (281) and (289) into (296) we end up with the relationships for $\tilde{\mathbf{Q}}_{s0}^s$ and $\tilde{\mathbf{Q}}_{s1}^s$ presented below.

- $\mathcal{O}(\delta^0)$: Sediment flux at leading order

$$\tilde{\mathbf{Q}}_{s0}^s = (\tilde{U}, \tilde{V}) \tilde{D} \Phi_0^s, \quad (297)$$

where:

$$\Phi_0^s = \int_{\zeta_a}^1 \phi_0 \mathcal{F}_0(\zeta) d\zeta. \quad (298)$$

The reader must recognize that the above solution is Rouse solution for the depth integrated sediment flux per unit width, evaluated locally and instantaneously (see equation (241) in Chapter 3).

- $\mathcal{O}(\delta)$: Sediment flux at first order

At first order Rouse solution is corrected by an $\mathcal{O}(\delta)$ contribution accounting for the effects of the slow spatial and temporal variations of the flow and concentration fields. We find:

$$\tilde{\mathbf{Q}}_{s1}^s = (\tilde{U}, \tilde{V}) \tilde{D} \Phi_1^s, \quad (299)$$

where

$$\begin{aligned} \Phi_1^s = & \tilde{D} \left(\gamma \frac{\partial C_0}{\partial \tilde{t}} I_{11} + \tilde{U} \frac{\partial C_0}{\partial \tilde{x}} I_{12} + \tilde{V} \frac{\partial C_0}{\partial \tilde{y}} I_{13} \right) \\ & - \gamma C_0 \left(\frac{\partial \tilde{\eta}}{\partial \tilde{t}} I_{14} + \frac{\partial \tilde{D}}{\partial \tilde{t}} (I_{15} - I_{16}) \right), \end{aligned} \quad (300)$$

and we have used the notation:

$$I_{1j} = \int_{\zeta_a}^1 c_{1j} \mathcal{F}_0(\zeta) d\zeta. \quad (301)$$

The coefficients ψ_0 and I_{1j} ($j = 1, 6$) are functions of ζ_a and \mathcal{Z} . They have to be determined numerically. An analytical interpolation of the numerical computations is reported in Bolla Pittaluga and Seminara (2003) and Federici and Seminara (2006).

The relationships (297, 298, 299, 300) thus provide a simple tool to be incorporated into morphodynamic computations of the suspended flux of homogeneous sediments in slowly varying flows. In summary, the three-dimensional equation (268) for the macroscopically averaged concentration $\langle c \rangle(\mathbf{x}, t)$, subject to the boundary conditions (269), is solved asymptotically in terms of the depth-averaged concentration $C(x, y, t)$ assuming that the vertical concentration profiles vary slowly in space and/or time. The first order solution can then be used to compute the correction (299) to the depth-integrated sediment flux provided by the Rouse solution (241).

It is appropriate at this stage to point out that the above described approach modifies and corrects a previous approach of Galappatti (1983) (see also Galappatti and Vreugdenhil, 1985) that has become very popular and is widely employed, especially in the Dutch literature. These Authors introduced small parameters analogous to those employed by Bolla Pittaluga and Seminara (2003) and set a perturbation expansion of concentration in terms of these small parameters. Correspondingly, the governing equations were also expanded but, in contrast to the classical approach of perturbation methods (Nayfeh, 2011), the boundary conditions were not expanded. Rather, Galappatti arbitrarily stipulated that the depth-averaged concentration was wholly determined by the lower order approximation of the solution, such that higher order terms were forced to possess vanishing depth averages. With the latter assumptions Galappatti derived solutions at all orders of approximation, each expressed in terms of the depth averaged concentration. Finally, the whole solution, truncated at some order of approximation, was forced to satisfy the boundary condition at the bed and this led to a relationship treated by Galappatti as a differential equation for the as-yet unknown depth-averaged concentration. The limits of this asymptotic approach have been discussed by Wang (1992) and Bolla Pittaluga and Seminara (2003).

More recently, Toffolon and Vignoli (2007) have explored in detail the limits of the depth-averaged approach comparing the outputs of the latter with results of fully 3D numerical solutions of the governing equations. This comparison indicates that applications of the depth-averaged approach should be restricted to flows characterized by *sufficiently* slow spatial-temporal variations as the straightforward expansion of Bolla Pittaluga and Seminara (2003) rapidly diverges when the value of the perturbation parameter δ increases. The detailed comparison between the fully 3D (Tubino *et al.*, 1999) and the 2D depth averaged approach (Federici and Seminara, 2006) applied to the problem of sand bar instability suggests that sand bars are sufficiently *long* to justify the use of the simpler approach described in the present Section.

Finally, it is worthwhile to note that many widely employed commercial numerical models (e.g. Delft3D (Lesser *et al.*, 2004), Telemac (Villaret *et al.*, 2013), Basement (Vetsch *et al.*, 2018), among many others), include a sediment transport module in which suspended load is evaluated by solving a two-dimensional advection-diffusion equation obtained by integrating (254) over the depth. The reader can easily demonstrate that, applying the boundary conditions (269), this equation reads:

$$\frac{\partial DC}{\partial t} + \frac{\partial D \left(U C - k_x \frac{\partial C}{\partial x} \right)}{\partial x} + \frac{\partial D \left(V C - k_y \frac{\partial C}{\partial y} \right)}{\partial y} = \mathcal{E} - \mathcal{D} \quad (302)$$

where the longitudinal and transverse mixing coefficients k_x and k_y are defined as:

$$k_x \frac{\partial C}{\partial x} = - \left(C - \langle c \rangle \right) \left(U - u \right) + \int_{\eta+a}^H \mathfrak{D}_x \frac{\partial \langle c \rangle}{\partial x} dz \quad (303a)$$

$$k_y \frac{\partial C}{\partial y} = - \left(C - \langle c \rangle \right) \left(V - v \right) + \int_{\eta+a}^H \mathfrak{D}_y \frac{\partial \langle c \rangle}{\partial y} dz \quad (303b)$$

In order to close the problem, suitable relations are needed to express the unknown mixing coefficients and the net sediment entrainment flux at the bed as functions of depth-averaged quantities. The coefficients k_x and k_y may be evaluated assuming the Reynolds analogy and taking

advantage of the knowledge gathered from mixing processes in rivers (see, e.g. Fisher *et al.*, 1979, Chapter 5). Much more complicated is the estimate of \mathcal{E} , since it would in principle require to solve the original advection-diffusion equation (254). In practice, empirical relations are used, with the obvious limitations related to the specific conditions for which they have been developed. For example, in the case of sufficiently fine sediments the exchange rate between the bed and the bulk of the flow can be expressed in the form (Wang, 1989; Hibma *et al.*, 2003):

$$\mathcal{E} - \mathcal{D} = a_{\mathcal{E}} w_s (C_0 - C), \quad (304)$$

where the proportionality coefficient $a_{\mathcal{E}}$ is in general function of bed shear stress and sediment characteristics. This coefficient essentially accounts for the distance needed for concentration to adapt to changing hydraulic conditions, the so called *adaptation length* (see e.g. Armanini and Di Silvio, 1980). Although several empirical and semi-empirical methods have been proposed to predict this length (see, e.g. Wu and Wang, 2008), significant differences exist among the various formulas. In our opinion, this makes the use of the rational perturbation framework described above preferable.

4.4. Bedload transport of homogeneous sediments on sloping beds

Extending our admittedly limited knowledge on the transport capacity of uniform streams flowing on a plane bed to the even more complex case of streams flowing on sloping beds is clearly a formidable problem which cannot be given a rigorous solution. This notwithstanding, some guidance for the interpretation of experimental observations is achieved through dimensional reasoning and model problems. The early literature focused on the case of weakly sloping beds. More recently, attempts have been made to extend the analysis to *finite slopes*, with the implicit assumption, however, that the bed inclination does never exceed the angle of repose of the sediment.

4.4.1 Threshold conditions for the inception of sediment motion on sloping beds

The general treatment presented below follows closely the work of Seminara *et al.* (2002).

Geometry of the bed surface: local slope

There are only two externally imposed directions in the problem: the vertical direction, described by the *vertical coordinate* z with unit vector \hat{z} , and the tangential direction to the bed aligned with the bottom shear stress $\hat{\tau}$. We then choose the right handed cartesian reference frame (x, y, z) centered at the point P of the bed surface, such that (see Figure 39): x (unit vector \hat{x}) is the horizontal axis through P lying in the vertical plane $(\hat{\tau}, \hat{z})$ and defines the local *longitudinal coordinate*, aligned with the *locally* prevailing motion of the stream; y (unit vector \hat{y}) is the horizontal axis through P orthogonal to the vertical plane $(\hat{\tau}, \hat{z})$ and defines the *local lateral coordinate*. The reader should note that the x -axis may be at an arbitrary angle with the channel axis, which does not enter the present analysis. Let us write the equation of the bed interface in the form:

$$\mathcal{F}_{\eta} = z - \eta(x, y, t) = 0. \quad (305)$$

The unit vector \hat{n} of the axis orthogonal to the bed at P then reads:

$$\hat{n} = \frac{\nabla \mathcal{F}_{\eta}}{|\nabla \mathcal{F}_{\eta}|}. \quad (306)$$

The coordinate plane (x, z) intersects the bed surface along a line the slope of which, S_x , will be called *the longitudinal slope*. Similarly, the coordinate plane (y, z) intersects the bed surface along a line whose slope S_y will be called *the lateral slope*. Note that the above lines through P are not orthogonal to each other in general. We may write:

$$S_x = \tan \alpha_x = -\frac{\partial \eta}{\partial x} \quad S_y = \tan \alpha_y = -\frac{\partial \eta}{\partial y}, \quad (307)$$

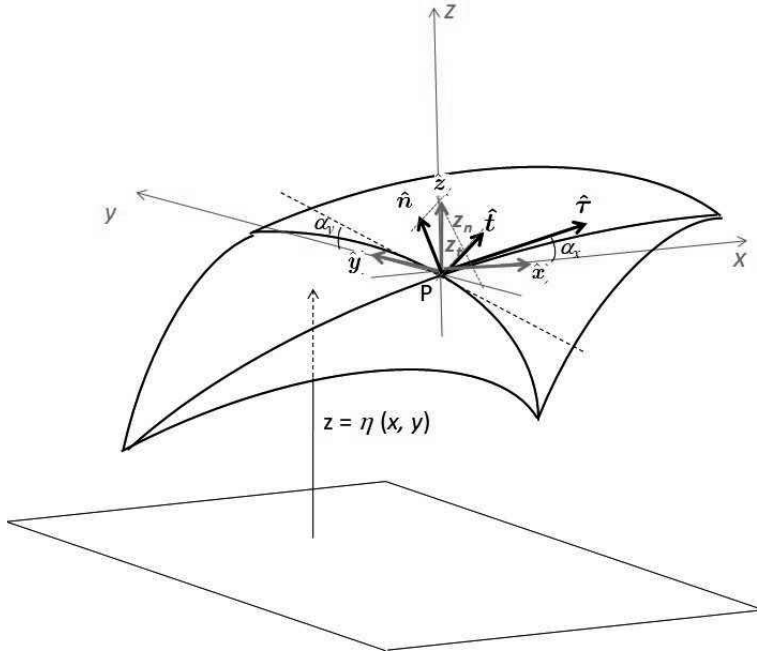


Figure 39. Sketch of a sloping bed and notations.

or, in vectorial form:

$$\mathbf{S} = -\nabla_h \eta. \quad (308)$$

where ∇_h denotes the two dimensional gradient operator $(\partial/\partial x, \partial/\partial y)$.

In order to formulate the threshold conditions for particle entrainment, it is useful to decompose the unit vector \hat{z} into its normal and tangential components, \mathbf{z}_n and \mathbf{z}_t respectively (see sketch in Figure 39). We find:

$$\mathbf{z}_n = (\hat{z} \cdot \hat{\mathbf{n}}) \hat{\mathbf{n}}, \quad \mathbf{z}_t = \hat{z} - \mathbf{z}_n. \quad (309)$$

Hence, the following relationships hold:

$$\hat{\mathbf{n}} = \frac{\left(-\frac{\partial \eta}{\partial x}, -\frac{\partial \eta}{\partial y}, 1\right)}{\sqrt{1 + \left(\frac{\partial \eta}{\partial x}\right)^2 + \left(\frac{\partial \eta}{\partial y}\right)^2}} = \frac{(\tan \alpha_x, \tan \alpha_y, 1)}{\sqrt{1 + \tan^2 \alpha_x + \tan^2 \alpha_y}}, \quad \hat{z} = (0, 0, 1), \quad (310a)$$

$$\mathbf{z}_n = \frac{(\tan \alpha_x, \tan \alpha_y, 1)}{1 + \tan^2 \alpha_x + \tan^2 \alpha_y}, \quad \mathbf{z}_t = \frac{[-\tan \alpha_x, -\tan \alpha_y, (\tan^2 \alpha_x + \tan^2 \alpha_y)]}{1 + \tan^2 \alpha_x + \tan^2 \alpha_y}. \quad (310b)$$

The reader must note that the quantities \mathbf{z}_n and \mathbf{z}_t are not unit vectors. They will be used to project the submerged weight force along the directions locally normal and tangent to the bed. Moreover, our choice of the reference frame implies that:

$$\hat{\boldsymbol{\tau}} = [\cos \alpha_x, 0, -\sin \alpha_x]. \quad (311)$$

The inception of motion on sloping beds: dimensional arguments

On purely dimensional ground, a general expression for the threshold value of the Shields stress for particle entrainment as bedload in terms of the longitudinal and lateral slopes may be written

in the form:

$$\tau_{*c} = \tau_{*c0} f_c(S_x, S_y; R_p, \phi). \quad (312)$$

Here, τ_{*c0} is the critical Shields stress for vanishing bed slope discussed in Chapter 3, R_p is the particle Reynolds number, ϕ is the angle of repose of the sediment composing the bed and f_c is a real function to be determined. Moreover, (312) must satisfy the constraint: $f_c \rightarrow 1$ as $\mathbf{S} \rightarrow 0$.

For weakly sloping beds ($S_x \ll 1$, $S_y \ll 1$), the latter relationship may be linearized in the form:

$$\tau_{*c} = \tau_{*c0} (1 + t_{cx} S_x + t_{cy} S_y), \quad (313)$$

with t_{cx} and t_{cy} two suitably chosen constants. Below we provide a theoretical estimate for the function f_c appearing in the equation (312). In particular, we show that:

- for weakly sloping beds, the critical value of the Shields stress is not affected by the lateral slope, i.e. $t_{cy} = 0$ in (313);
- on the contrary, a positive longitudinal slope reduces τ_{*c} and the constant t_{cx} in (313) takes the value obtained in Chapter 3 (equation (184)).

Theoretical estimates on a model problem

The treatment presented below extends ideas developed for the plane bed case by, among others, Coleman (1967), Ikeda (1982a) and Wiberg and Smith (1987). The rationale behind the use of idealized models of the actual phenomenon is that, provided they are able to capture the dominant mechanisms operating in the process, the information they provide is at least qualitatively significant and may guide the interpretation of experimental observations.

We consider the average static equilibrium of a spherical sediment particle lying on the cohesionless sloping bed of a channel and subject to the hydrodynamic actions of a turbulent free surface stream flowing in the channel. The forces which are assumed to interpret, in an average sense, the interactions of the particle with the flowing fluid and the adjacent sediment particles are the submerged gravity \mathbf{F}_G , directed vertically, the fluid drag \mathbf{F}_D and lift \mathbf{F}_L , directed tangentially and normally to the bed. In addition, the net resultant \mathbf{F}_N of the component of the submerged gravity normal to the bed and of the lift force gives rise to a static friction force \mathbf{F}_μ acting tangentially to the bed. Using the notations of Figure 40, the average equilibrium of the particle is governed by the following relationship:

$$\mu_s |\mathbf{F}_N| = |\mathbf{F}_t|, \quad (314)$$

where,

$$\mathbf{F}_N = |\mathbf{F}_G| \mathbf{z}_n - \mathbf{F}_L, \quad \mathbf{F}_t = -|\mathbf{F}_G| \mathbf{z}_t + \mathbf{F}_D, \quad (315)$$

and μ_s is the *static friction coefficient* (taken equal to $\tan \phi$).

Let us attempt an estimate of the above forces. The *particle submerged weight* \mathbf{F}_G may be written in the form:

$$\mathbf{F}_G = -\frac{\pi}{6} (\varrho_s - \varrho) g d^3 \hat{\mathbf{z}}. \quad (316)$$

The *average hydrodynamic drag force* acting on the particle may be estimated in terms of some *average drag coefficient* c_D as follows:

$$\mathbf{F}_D = \frac{1}{2} \varrho c_D \frac{\pi d^2}{4} |\mathbf{u}_{z_P}|^2 \hat{\boldsymbol{\tau}}. \quad (317)$$

Note that \mathbf{F}_D is aligned with the bottom stress and the mean flow velocity \mathbf{u}_{z_P} is evaluated at some conventional distance from the bed z_P , chosen such to interpret in an average sense the drag force on the particle which is in general a fluctuating function of time and space. Hence, in the absence of detailed knowledge of the latter function, the selection of characteristic values for c_D and z_P is empirical.

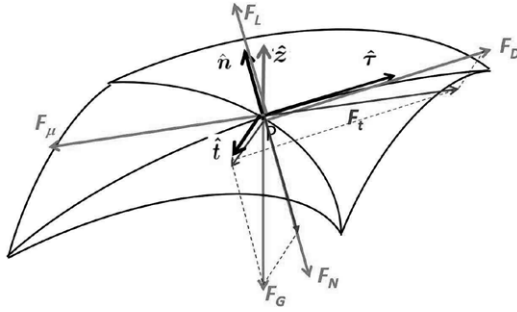


Figure 40. Sketch of forces acting on a sediment particle lying on a sloping bed.

Similarly, the *average hydrodynamic lift force* acting on the particle and aligned with the direction normal to the bed may be estimated in terms of some *average lift coefficient* c_L as follows (see, e.g. Auton, 1987):

$$\mathbf{F}_L = \frac{4}{3} \varrho c_L \frac{\pi d^3}{8} |\mathbf{u} \times \boldsymbol{\omega}|_{z_P} \hat{\mathbf{n}}, \quad (318)$$

where $\boldsymbol{\omega}$ is the average fluid vorticity and $|\mathbf{u} \times \boldsymbol{\omega}|_{z_P} = [u du/dz]_{z_P}$.

Using the relationships (316), (317), and (318), the equilibrium relationship (314) becomes:

$$\begin{aligned} \mu_s \left| \frac{\pi}{6} (\varrho_s - \varrho) g d^3 z_n - \frac{4}{3} \varrho c_L \frac{\pi d^3}{8} \left(u \frac{du}{dz} \right)_{z_P} \hat{\mathbf{n}} \right| = \\ \left| -\frac{\pi}{6} (\varrho_s - \varrho) g d^3 z_t + \frac{1}{2} \varrho c_D \frac{\pi d^2}{4} u_{z_P}^2 \hat{\mathbf{t}} \right|. \end{aligned} \quad (319)$$

where u_{z_P} denotes the modulus of \mathbf{u}_{z_P} . Employing (310a), (310b), and (311), it is easily demonstrated that in the case of a horizontal bed ($\alpha_x = \alpha_y = 0$) this equation simplifies to:

$$\mu_s \left[\frac{\pi}{6} (\varrho_s - \varrho) g d^3 - \frac{4}{3} \varrho c_L \frac{\pi d^3}{8} \left(u \frac{du}{dz} \right)_{z_P} \right] = \frac{1}{2} \varrho c_D \frac{\pi d^2}{4} u_{z_P}^2, \quad (320)$$

thus yielding the critical conditions for the incipient particle entrainment. Recalling the expression of the Shields stress:

$$\tau_* = \frac{\varrho u_\tau^2}{(\varrho_s - \varrho) g d}, \quad (321)$$

and noting that $u(z) = u_\tau f(z)$, with u_τ the friction velocity at the bed and f the logarithmic law of the wall (67), we eventually obtain the critical Shields stress for incipient sediment motion on a horizontal bed:

$$\tau_{*c0} = \frac{4 \mu_s}{3 c_D f^2|_{z_P}} \frac{1}{1 + \Delta}, \quad (322)$$

where the parameter

$$\Delta = \frac{4}{3} \mu_s \frac{c_L}{c_D} d \left(\frac{1}{f} \frac{df}{dz} \right)_{z_P} \quad (323)$$

accounts for the effects of lift.

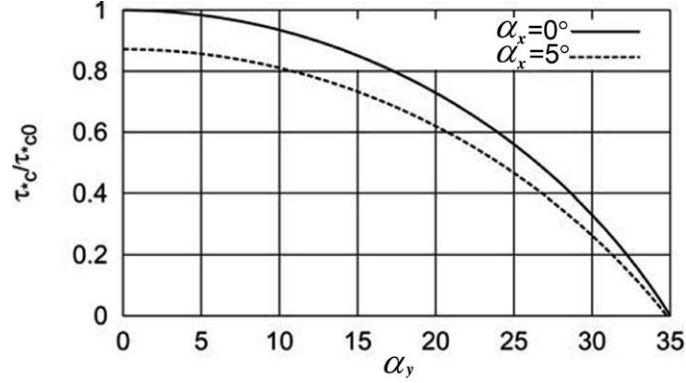


Figure 41. Plot of the ratio τ_{*c}/τ_{*c0} as a function of the lateral slopes for two values of the stream-wise angles α_x . The following values of the parameters have been employed in the calculations: $\phi = \arctan \mu_s = 35^\circ$, $f = 6.8$ (corresponding to $z_P = 0.5d$, hydraulically rough wall conditions, and a wall roughness $e_s = d$), $c_L/c_D = 0.85$ (reproduced from Seminara *et al.*, 2002).

Taking into account equation (322) and with the help of (310a), (310b), and (311) we finally obtain:

$$(1 - \Delta) \left(\frac{\tau_{*c}}{\tau_{*c0}} \right)^2 + 2 \left(\frac{\Delta}{\sqrt{1 + \tan^2 \alpha_x + \tan^2 \alpha_y}} + \frac{\sin \alpha_x}{\mu_s} \right) \frac{\tau_{*c}}{\tau_{*c0}} + \frac{1 + \Delta}{\mu_s^2} \frac{\tan^2 \alpha_x + \tan^2 \alpha_y - \mu_s^2}{1 + \tan^2 \alpha_x + \tan^2 \alpha_y} = 0. \quad (324)$$

From (324), with an appropriate estimate for the parameters Δ and ϕ , one readily determines the quantity τ_{*c}/τ_{*c0} as a function of the longitudinal and lateral slopes, i.e. the sought function f_c appearing in equation (312). An example of this dependence is shown in the Figure (41).

The case of weakly sloping beds

The case of weakly sloping beds is of special interest, as it applies to most natural sedimentary patterns. Let us first check that, as $\alpha_x \rightarrow 0$ and $\alpha_y \rightarrow 0$ the limit condition $\tau_{*c} \rightarrow \tau_{*c0}$ is recovered. In fact, in this limit, the relationship (324) becomes:

$$\left(\frac{\tau_{*c}}{\tau_{*c0}} - 1 \right) \left[\frac{\tau_{*c}}{\tau_{*c0}} (1 - \Delta) + (1 + \Delta) \right] = 0, \quad (325)$$

which is immediately seen to satisfy the above constraint.

Next, let us examine the case of α_x and α_y both being small enough to allow for the linearization of (324). Noting that α_y appears in (324) only through quadratic terms, we set:

$$\frac{\tau_{*c}}{\tau_{*c0}} = f_c = 1 + \epsilon f_{c1}(\mu_s, \Delta), \quad (326)$$

with $\epsilon = \sin \alpha_x \ll 1$. Substituting from (326) into (324) and equating likewise powers of ϵ , at the leading order of approximation ($\mathcal{O}(\epsilon^0)$) the relationship is identically satisfied. At first order ($\mathcal{O}(\epsilon)$) one finds:

$$2(1 - \Delta)f_{c1} + 2\Delta f_{c1} + \frac{2}{\mu_s} = 0, \quad (327)$$

whence:

$$f_{c1} = -\frac{1}{\mu_s} \quad \Rightarrow \quad \frac{\tau_{*c}}{\tau_{*c0}} = 1 - \frac{\sin \alpha_x}{\mu_s}. \quad (328)$$

The latter result confirms that, as anticipated above, *for weakly sloping beds, the critical value of the Shields stress is not affected by the lateral slope*. On the contrary, *a positive longitudinal slope reduces τ_{*c}* . The latter tends to vanish as the local longitudinal bed inclination tends to the angle of repose of the sediment (though, for finite values of α_x , linearization is no longer strictly valid).

An expression similar to (328) was first derived by Lysne (1969) who tested it by performing a series of experiments on the effect of bedslope on the incipient motion of sand in a close channel. Lysne results are found to fit quite well (328) with ϕ ranging about 47° . A similar value of ϕ was found by Luque and Van Beek (1976), who fitted a similar relationship to their experimental observations for the incipient motion of sand, gravel and magnetite in open channel flow on sloping beds. This is quite encouraging, suggesting that, in spite of their approximate character, averaged approaches may provide a reasonable guidance to the interpretation of these complex processes.

4.4.2 Bedload transport on sloping beds: dimensional arguments

We now extend to the general case of sloping beds, the classical bedload relationship valid under uniform equilibrium conditions. On purely dimensional ground, we write:

$$\mathbf{Q}_s^b = \mathbf{Q}_s^b(\boldsymbol{\tau}, \nabla_h \eta, \varrho_s - \varrho, g, d, \mu_s), \quad (329)$$

where $\boldsymbol{\tau}$ is the local value of the tangential stress at the bottom and \mathbf{Q}_s^b is the dimensional form of the bedload flux per unit width, a vector which also lies on the plane tangent to the bed interface. The latter assumption, essentially extends the classical treatment of bedload transport under uniform flow conditions in two ways: we are assuming that bedload transport is controlled by the *local* value of the bottom stress; moreover, we are postulating that a *local slope affects the direction and intensity of bedload transport*, making the latter deviate from the direction of the tangential stress at the bottom.

Having formulated the above ansatz, application of Buckingham theorem immediately leads to the following dimensionless form of the generalized bedload transport relationship:

$$\mathbf{Q}_s^b = \sqrt{(s-1)gd^3} \tilde{\mathbf{Q}}_s^b(\tau_* \hat{\boldsymbol{\tau}}, \nabla_h \eta, R_p), \quad (330)$$

having denoted by $\tilde{\mathbf{Q}}_s^b$ the dimensionless bedload flux per unit width, and by τ_* the local and instantaneous value of the Shields stress.

Next, we stipulate that, as $\nabla_h \eta$ tends to vanish, the latter relationship must reduce to the classical relationship valid under uniform flow conditions, namely:

$$\tilde{\mathbf{Q}}_s^b = \Phi^b(\tau_*; \tau_{*c0}, R_p) \hat{\boldsymbol{\tau}}, \quad (331)$$

where Φ^b is the equilibrium bedload function discussed in Section 3.3.2, evaluated for the instantaneous value of the Shields stress τ_* , and τ_{*c0} is the instantaneous value of the critical Shields stress for horizontal beds.

The general relationship for the bedload flux per unit width on sloping beds may then be written in the form:

$$\tilde{\mathbf{Q}}_s^b = \Phi^b(\tau_*; \tau_{*c}, R_p) [\hat{\boldsymbol{\tau}} + \mathbf{f}_G(\nabla_h \eta, \tau_*, R_p)], \quad (332)$$

with \mathbf{f}_G an unknown dimensionless vectorial function which vanishes as $\nabla_h \eta \rightarrow 0$, while the local value of the critical Shields stress τ_{*c} reduces to τ_{*c0} as $\nabla_h \eta \rightarrow 0$.

The particular case of weakly sloping beds is again of special interest. Assuming that $|\nabla_h \eta| \rightarrow 0$ we may linearize (332) to find:

$$\tilde{\mathbf{Q}}_s^b = \Phi^b(\tau_*; \tau_{*c0}, R_p) [\hat{\boldsymbol{\tau}} + \mathcal{G}(\tau_*, R_p) \cdot \nabla_h \eta], \quad (333)$$

where \mathcal{G} is a (2×2) tensor which needs to be determined either experimentally or theoretically. Recalling (311), the longitudinal and lateral components of (333) become:

$$\tilde{Q}_{sx}^b = \Phi^b(\tau_*, \tau_{*c0}, R_p) \left[1 + \mathcal{G}_{xx} \frac{\partial \eta}{\partial x} + \mathcal{G}_{xy} \frac{\partial \eta}{\partial y} \right], \quad (334a)$$

$$\tilde{Q}_{sy}^b = \Phi^b(\tau_*, \tau_{*c0}, R_p) \left[\mathcal{G}_{yx} \frac{\partial \eta}{\partial x} + \mathcal{G}_{yy} \frac{\partial \eta}{\partial y} \right]. \quad (334b)$$

In the next Sections we discuss some of the available attempts to estimate the components of the \mathcal{G} -tensor.

4.4.3 Bedload transport on sloping beds: Theoretical and experimental estimates

Theoretical estimates

We consider the average dynamic equilibrium of a spherical sediment particle saltating close to a sloping bed. We do not constrain the slope to be weak and denote by \mathbf{v}_P the *average* saltation velocity of the particle. The average dynamic equilibrium of the particle is governed by a relationship identical to (314): however, here \mathbf{F}_μ is a *frictional force* which is assumed to interpret, in an *average* sense, the contact forces experienced by the saltating particle. Similarly, \mathbf{F}_D is the average hydrodynamic drag force experienced by the particle throughout its saltating motion, which may still be estimated in terms of some *average drag coefficient* c_D as follows:

$$\mathbf{F}_D = \frac{1}{2} \varrho c_D \frac{\pi d^2}{4} (\mathbf{u}|_{z_P} - \mathbf{v}_P) \left| (\mathbf{u}|_{z_P} - \mathbf{v}_P) \right|, \quad (335)$$

having imposed that \mathbf{F}_D must be aligned with the relative flow velocity evaluated at some distance from the bed, z_P . This distance is chosen such to interpret in an average sense the drag experienced by the saltating particle throughout its trajectory. The reader is already aware of the severe approximation implied by the above assumption as the drag force is a fluctuating function of time and space. Note that \mathbf{F}_D lies on the tangent plane. The tangential component of the resultant active force \mathbf{F}_t arises from the vectorial composition of \mathbf{F}_D and the tangential component of the submerged particle weight, hence it is defined by a relationship identical to that in (315b), with \mathbf{F}_D given by (335).

The *average frictional force* \mathbf{F}_μ is now aligned with the particle velocity \mathbf{v}_P , hence it lies on the tangent plane. We will express it in terms of a *dynamic friction coefficient* μ_d as follows:

$$\mathbf{F}_\mu = -\mu_d \left| \mathbf{F}_N \right| \hat{\mathbf{v}}_P, \quad (336)$$

where $\hat{\mathbf{v}}_P$ is the unit vector in the direction of particle velocity. Neglecting as a first approximation the *average hydrodynamic lift force*, the *average normal reaction* \mathbf{F}_N (equation 315) reduces to the *static* approximation:

$$\mathbf{F}_N = \frac{\pi}{6} (\varrho_s - \varrho) g d^3 \mathbf{z}_n. \quad (337)$$

The dynamic equilibrium of the particle saltating along the tangent plane is then governed by the following relationship:

$$\begin{aligned} -\mu_d \frac{\pi}{6} (\varrho_s - \varrho) g d^3 \left| \mathbf{z}_n \right| \hat{\mathbf{v}}_P - \frac{\pi}{6} (\varrho_s - \varrho) g d^3 \mathbf{z}_t + \\ \frac{1}{2} \varrho c_D \frac{\pi d^2}{4} (\mathbf{u}|_{z_P} - \mathbf{v}_P) \left| \mathbf{u}|_{z_P} - \mathbf{v}_P \right| = 0. \end{aligned} \quad (338)$$

The latter vectorial relationship can be further reduced recalling the definitions (310a), (310b), (311) and noting that

$$\mathbf{u}|_{z_P} = u|_{z_P} \hat{\boldsymbol{\tau}}, \quad \hat{\boldsymbol{\tau}} = [\cos \alpha_x, 0, -\sin \alpha_y], \quad (339a)$$

$$\mathbf{v}_P = v_P \hat{\mathbf{v}}_P, \quad \hat{\mathbf{v}}_P = [\cos \psi \hat{\boldsymbol{\tau}} + \sin \psi (\hat{\mathbf{n}} \times \hat{\boldsymbol{\tau}})], \quad (339b)$$

where ψ is the angle that \mathbf{v}_P forms with the bottom shear stress vector $\boldsymbol{\tau}$ (Figure 42). Moreover, since both these vectors lie on the tangent plane, we have decomposed the vector \mathbf{v}_P into a component aligned with $\boldsymbol{\tau}$ and a second component still lying on the tangent plane but orthogonal to the first (i.e, aligned with $\hat{\mathbf{n}} \times \hat{\boldsymbol{\tau}}$).

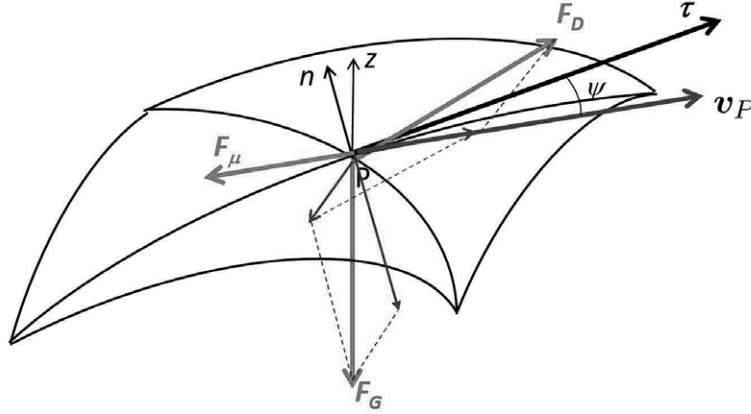


Figure 42. Sketch showing the particle velocity in the tangent plane and notations.

With simple algebraic manipulations we can reduce the relationship for $\hat{\mathbf{v}}_P$ to the form:

$$\hat{\mathbf{v}}_P = (\hat{v}_{Px}, \hat{v}_{Py}, \hat{v}_{Pz}), \quad (340)$$

where:

$$\hat{v}_{Px} = \cos \psi \cos \alpha_x - \frac{\sin \psi \sin \alpha_x \tan \alpha_y}{\sqrt{1 + \tan^2 \alpha_x + \tan^2 \alpha_y}}, \quad (341a)$$

$$\hat{v}_{Py} = \frac{\frac{\sin \psi}{\cos \alpha_x}}{\sqrt{1 + \tan^2 \alpha_x + \tan^2 \alpha_y}}, \quad (341b)$$

$$\hat{v}_{Pz} = -\cos \psi \sin \alpha_x - \frac{\sin \psi \cos \alpha_x \tan \alpha_y}{\sqrt{1 + \tan^2 \alpha_x + \tan^2 \alpha_y}}. \quad (341c)$$

With the help of (339) and (341), Parker *et al.* (2003) were able to derive a vectorial relationship for bedload transport on finite slopes. This is a complex derivation and the interested reader is referred to the latter paper. Here, we limit ourselves to considering the important case of weakly sloping beds that is of great relevance to the whole field of morphodynamics.

The weakly sloping bed case

In the weakly sloping bed case, we can derive the sought relationship for the angle ψ which describes the direction of sediment motion by linearizing the general equilibrium relationship (338). Let us then make the following approximations:

$$\cos \psi \simeq \cos \alpha_x \simeq \cos \alpha_y \simeq 1, \quad (342a)$$

$$\sin \psi \simeq \tan \psi \ll 1, \quad \sin \alpha_x \simeq \tan \alpha_x \ll 1, \quad \sin \alpha_y \simeq \tan \alpha_y \ll 1. \quad (342b)$$

Hence:

$$\mathbf{u}|_{z_P} \simeq u_{z_P}[1, 0, -\sin \alpha_x], \quad \mathbf{v}_P \simeq v_P[1, \sin \psi, -\sin \alpha_x], \quad (343a)$$

$$|\mathbf{z}_n| \simeq 1, \quad \mathbf{z}_t \simeq [-\tan \alpha_x, -\tan \alpha_y, 0]. \quad (343b)$$

The x -component of (338), at the leading order of approximation, then reads:

$$\mu_d \frac{\pi}{6} (\varrho_s - \varrho) g d^3 = \frac{1}{2} \varrho c_D \frac{\pi d^2}{4} (u|_{z_P} - v_P)^2. \quad (344)$$

If we define the *dynamic critical Shields stress* τ_{*cd} as follows:

$$\tau_{*cd} = \frac{4}{3} \frac{\mu_d}{c_D f^2|_{z_P}}, \quad (345)$$

we end up with the following relationship

$$u_{z_P} - v_P = f|_{z_P} \sqrt{\tau_{*cd}} \sqrt{(s-1)gd}, \quad (346)$$

which can be reduced to the form observed experimentally for uniform flows by Luque and Van Beek (1976) (see equation(185))

$$\frac{v_P}{\sqrt{(s-1)gd}} = f|_{z_P} (\sqrt{\tau_*} - \sqrt{\tau_{*cd}}). \quad (347)$$

Note that from equation (347), the experimental relation of Luque and Van Beek (1976) is recovered choosing $f|_{z_P} = 11.5$ and $\sqrt{\tau_{*cd}} = 0.7 \sqrt{\tau_{*co}}$.

Using the last few relationships, we then derive the leading order approximation of the y -component of (338), which reads:

$$\sin \psi = \frac{\frac{\pi}{6} (\varrho_s - \varrho) g d^3}{\frac{1}{2} \varrho c_D \frac{\pi d^2}{4} (u|_{z_P} - v_P) u|_{z_P}} \tan \alpha_y, \quad (348)$$

or, with some manipulations and the help of (345):

$$\sin \psi = \frac{1}{\mu_d} \sqrt{\frac{\tau_{*cd}}{\tau_*}} \tan \alpha_y. \quad (349)$$

This relationship is an important result: *it predicts the direction of bedload transport in the tangent plane of weakly sloping beds*. More precisely, it provides the angle that the direction of bedload transport forms with the local direction of the tangential stress at the bottom in terms of the lateral bed slope. Similar relationships for the angle ψ have been proposed in the literature. In particular, Engelund (1974) presented a simple derivation in the context of a pioneering investigation of the morphodynamics of river bends. Engelund's result was further developed by Hasegawa (1981), Ikeda (1982a), Engelund and Fredsøe (1982), Parker (1984) and Struiksmas *et al.* (1985).

Comparing (349) with (334b) we are now able to obtain the sought estimate of components of the \mathcal{G} -tensor:

$$\mathcal{G}_{yx} = 0, \quad \mathcal{G}_{yy} = -\frac{1}{\mu_d} \sqrt{\frac{\tau_{*cd}}{\tau_*}} = -\frac{r}{\sqrt{\tau_*}}. \quad (350)$$

The $\mathcal{O}(1)$ parameter r appearing in (350) can be readily estimated. Let us employ the following characteristic values for the parameters appearing in the relationship (345): $\mu_d \simeq \tan 30^\circ$, $c_D \simeq 0.4$,

$f|_{z_P} \simeq 2.5 \ln(z_P/e_s) + 8.5 = 6.7$, having assumed that the average distance of saltating particles from the bed ranges about $z_P = 1.5d$ and $e_s = 3d$. Using the latter values, (345) provides an estimate for the dynamic Shields stress τ_{*cd} ranging about 0.04, and the parameter r takes a value about 0.35. Below, we test this result against experimental observations. Note that (349) suggests that, in a linear context, the longitudinal slope does not affect the *direction* of bedload transport. However, even in a linear context, the longitudinal slope does affect the *intensity* of bedload transport. This is immediately appreciated, noting that, in the static limit ($v_P = 0$) the equilibrium relationship (338) reduces to the second of (328). We may then estimate the two remaining components of the \mathcal{G} -tensor appearing in the relationship (334a) as follows:

$$\mathcal{G}_{xx} = \left[-\frac{1}{\Phi^b} \frac{d\Phi^b}{d\tau_{*c}} \right]_{\tau_{*co}} \frac{d\tau_{*c}}{dS_x} = \frac{\tau_{*co}}{\mu_s} \left[\frac{1}{\Phi^b} \frac{d\Phi^b}{d\tau_{*c}} \right]_{\tau_{*co}}, \quad \mathcal{G}_{xy} = 0. \quad (351)$$

The relationships (351) and (350) complete our analysis, which can be summarized by stating that *the intensity of bedload transport on weakly sloping beds is affected by variations of the longitudinal slope and is insensitive to variations of the lateral slope. On the contrary, the direction of bedload transport is insensitive to variations of the longitudinal slope but is significantly affected by variations of the lateral slope.* The latter dependence involves the inverse square root of the local Shields stress, a feature which will be seen to have significant morphological implications.

A more ambitious attempt to predict the average direction of particle motion on a sloping bed was performed by Sekine and Parker (1992), based on the fairly detailed saltation model of Sekine and Kikkawa (1992). The significance of the latter contribution arises from its ability to clarify the physical mechanism whereby a lateral slope may drive a deviation of the average trajectories of saltating particles from the direction of the mean bottom stress. Indeed, one may argue that, in order to feel the downslope effect of gravity, a bed load particle should be in continuous contact with the bed. This condition is fulfilled by rolling or sliding particles but is not satisfied by saltating particles. On the contrary, Sekine and Parker (1992) argue that, though the placement of grains on the bed does not intrinsically bias rebound in either the positive or negative lateral direction, however the geometry of collision implies that particle rebound on a laterally sloping bed pumps lateral momentum on the bouncing particle. Less convincing is the assumption made in their saltation model that a particle would continuously saltate unless it enters a depression and cannot escape by rebound. In fact, as discussed in Chapter 3, modern observations suggest that saltation is sustained by wall events, hence its lifetime is controlled by the lifetime of sweeps. This notwithstanding the exercise of averaging several hundred individual realizations of the simulated saltation process is useful in order to evaluate the effect of lateral slope on the direction of particle motion. Indeed, the above Authors were able to derive a relationship of the type (334b) with

$$\mathcal{G}_{yx} = 0, \quad \mathcal{G}_{yy} = -f_{yy}(R_p) \left[\frac{\tau_{*c}}{\tau_*} \right]^{1/4}. \quad (352)$$

Note that, the dependence of the function f_{yy} on the particle Reynolds number was found to be weak, i.e. the function is nearly flat and takes values around 0.75. This work provides a further confirmation of the soundness of the structure (334b) of the linear bedload relationship, though the component \mathcal{G}_{yy} exhibits a somewhat weaker dependence on the Shields stress than predicted by (350).

Test of linear relationships against experimental data

Several experimental contributions have been reported in the literature. They are typically conducted measuring the intensity and direction of bedload transport in turbulent streams flowing in straight channels with laterally tilted cohesionless bed in the absence of bedforms. Experiments of this type were conducted in water by Hirano (1973), Hasegawa (1981), Ikeda (1982a) and, in air, by Yamasaka and Ikeda (1988). Results of these investigations have been summarized and compared with various theoretical estimates by Sekine and Parker (1992). Here it suffices to point out that the experimental data exhibit a considerable scatter and an equally acceptable agreement

is achieved using either the Sekine and Parker relationship (352) or the relationship (350) with $r \simeq 0.35$.

However, note that the above estimates (both theoretical and experimental) apply to bedload transport on *plane* (yet laterally tilted) beds. Talmon *et al.* (1995) reported observations performed on a turbulent water stream flowing over a cohesionless sandy bed where dunes had developed. Results of this investigation do confirm the suitability of (350), though with a somewhat larger value of r ($\simeq 0.56$). The effects of bedforms and sediment transport mode also emerge from the experiments carried out by Baar *et al.* (2018) in a rotating annular flume with counterrotating floor. However, the complexity of the experimental flow field, which includes secondary flows of uncertain interpretation, and the difficulties to collect local rather than global measurements prevented any definitive conclusion.

Finally, recent detailed measurements of particle motion over a laterally inclined fixed bed have been performed by Francalanci and Solari (2007) (see also Francalanci and Solari, 2008). The ultimate aim of these works was to test the validity of the nonlinear analysis of bedload transport on sloping beds proposed by Seminara *et al.* (2002) and Parker *et al.* (2003). This is briefly discussed in the Appendix to this Chapter.

4.5. Flow resistance in natural channels

4.5.1 Small scale fluvial bedforms

It has been known for longer than a century (Gilbert, 1914b) that a sequence of distinct small scale bedforms form in open channel streams flowing over erodible cohesionless beds as the flow and sediment discharges (hence the Shields stress) increase. The characteristics of these bedforms have been summarized in the first Monograph of the present series (Blondeaux *et al.*, 2018) and their description will not be repeated here. We simply reproduce in Figure 43 the sketch presented by Simons and Richardson (1966) to depict the shape of small scale bedforms they observed in classical laboratory experiments on uniform open channel flow with cohesionless beds.

Let us assume we generate a sequence of uniform flows in an open channel with cohesionless bed consisting of fine sand by progressively increasing the channel slope. As the Shields stress exceeds its critical value for incipient sediment motion, the following sequence of bottom patterns is typically observed.

- *Ripples*. Small triangular-shaped forms with typical wave-lengths of few tens of centimeters and heights of few centimeters.
- *Dunes*. Bed features longer and larger than ripples, associated with surface waves out of phase with the bed waves. Their amplitude and wavelength typically scale with the flow depth. Similarly to ripples, dunes are also approximately triangular, with fairly gentle upstream slopes on which ripples can form at low stages. Downstream slopes are often approximately equal to the angle of repose of the bed material, although gentler fronts are also observed. Dunes migrate slowly downstream.
- *Plane bed and stationary waves*. Somewhat abruptly, the dunes disappear, and are replaced by a bed devoid of significant irregularities (*plane bed*) or by trains of virtually stationary waves (sometimes called *nonbreaking antidunes*).
- *Antidunes*. At higher stage, upstream-migrating trains of fairly sinusoidal bottom waves (antidunes) develop. They are associated and strongly interact with surface waves in phase with them. Moreover, the amplitude of the surface waves is larger than the amplitude of antidunes. At even higher Froude numbers, the surface waves typically grow to the extent of becoming unstable and break in the upstream direction. Antidunes are then subject to cyclic processes of obliteration, re-initiation and growth.
- *Steps and pools*. At steep slopes and large values of water and sediment discharges, the channel displays a series of pools, where the flow is subcritical, connected by steps (*steep chutes*),

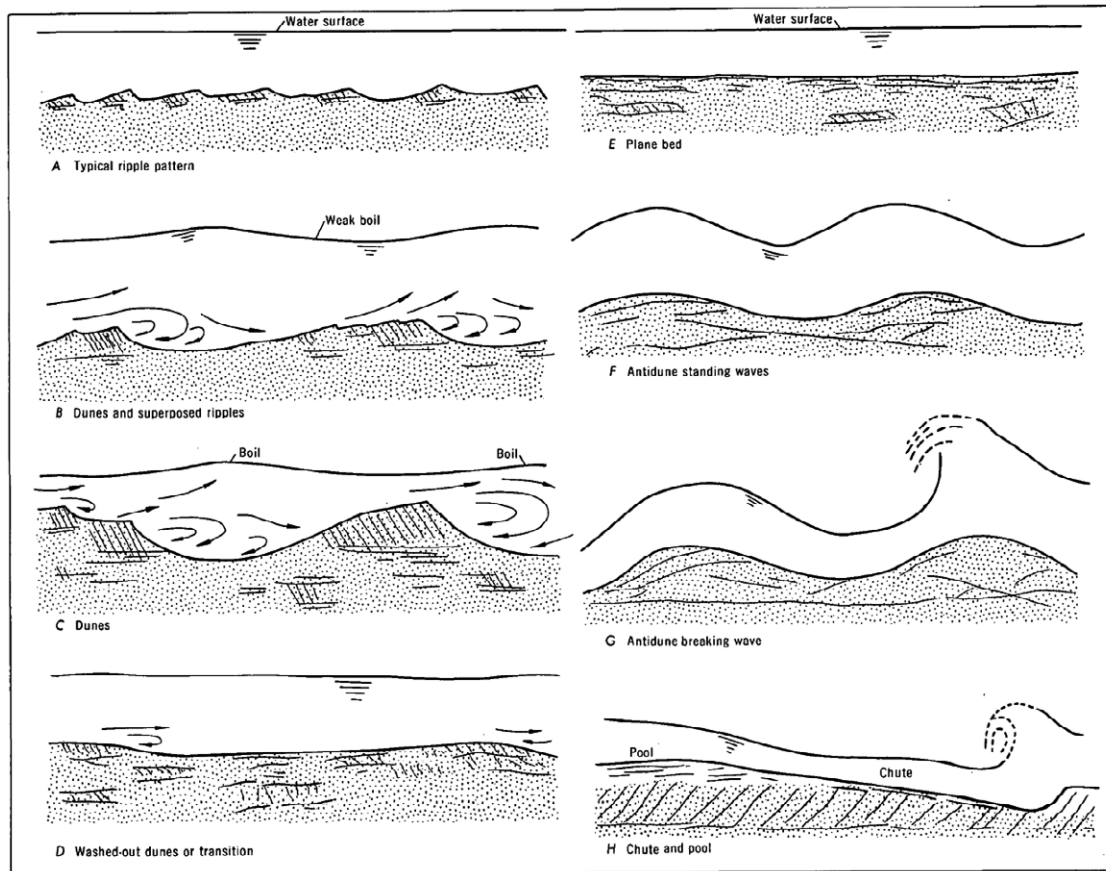


Figure 43. Sketch showing the sequence of small scale patterns observed in open channel flow over a cohesionless bottom by Simons and Richardson (1966).

where the flow is supercritical. Hydraulic jumps form where the chute merges into the pool. The step and pool train may slowly migrate upstream.

The formation of bed-forms poses a number of conceptual and practical problems that have been investigated by the scientific community for many decades and are not fully settled yet. Essentially, one would like to be able to understand why and when bedforms appear, what are their characteristic features (wavelengths, amplitudes, migration speeds) and what effects they induce on flow resistance and sediment transport. These goals are complex enough to deserve to be treated in a specific Monograph. Below, we restrict ourselves to provide a brief overview of the least amount of knowledge needed in order to proceed with the present exposition of principles of river meandering.

4.5.2 Bedform regime

A sound approach to formulating appropriate criteria for bed forms would be to identify and investigate the physical mechanisms underlying their formation. Indeed, it has been firmly established that bedforms originate from instabilities of the bed interface. This is a fundamental topic that has received attention from the scientific community since the late 1960's. Parallel to the theoretical investigations, a number of experimental investigations have been performed, in particular the extensive and accurate work of Guy *et al.* (1966) among many others. Based on these investigations, several empirically-based bedform regime criteria have been proposed.

A comprehensive review of the literature is presented in Chapter 2 of Garcia (2008). None of

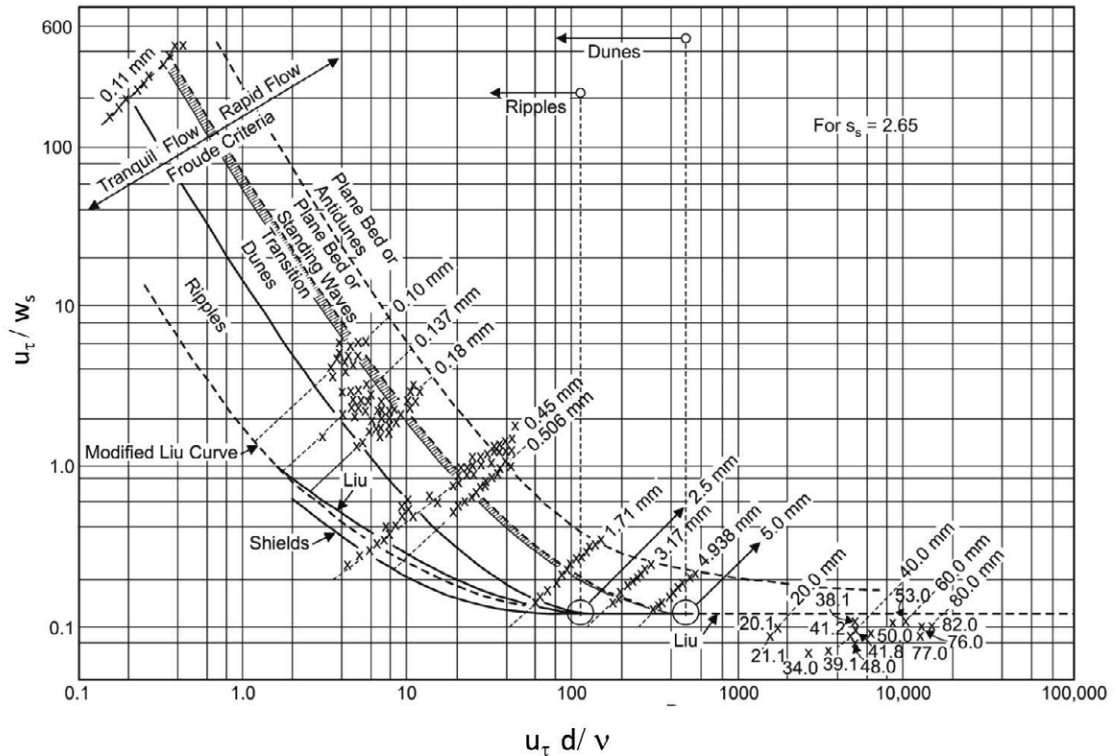


Figure 44. The bedform regime criterion proposed by Liu (1957) and later developed by Simons and Richardson (1961).

those criteria is fully satisfactory. Here, we limit ourselves to the illustration of few of them. Note that, on physical ground, one expects that the bedform regime depends on dimensionless parameters characterizing the *nature of sediments* (the *relative submerged density* ($s - 1$), the particle Reynolds number R_p and, possibly, the geometric standard deviation of the grain size distribution σ_g), the *intensity of sediment transport* (e.g. the Shields stress of the uniform flow τ_{*u}) and the *hydrodynamics* (the channel slope S or the relative roughness d_{50}/D_u , with d_{50} average grain size, or the Froude number F_{ru}). Most of the proposed criteria ignore the role of σ_g , assume $(s - 1) = 1.65$ and employ only two dimensionless parameters, that may be expressed in terms of R_p and τ_{*u} .

Figure 44 shows the bedform regime criterion originally proposed by Liu (1957) and later developed by Simons and Richardson (1961). The reader will readily demonstrate that the two parameters employed in this plot can both be expressed in terms of R_p and τ_{*u} . This plot suggests that neither ripples nor dunes form in the case of coarse material. However, dunes have been observed to form under subcritical flow conditions also in rivers with bed composed of coarse sand and fine gravel ($d_{50} = 1.8 - 9.1$ mm), e.g. the North Fork Toutle River at Kid Valley, Washington (Dinehart, 1989).

The above plot predicts that antidunes form only under supercritical conditions. This prediction is not correct, as shown by Figure 45 where Engelund and Hansen criterion (Engelund and Hansen, 1966) is reported. The diagram clearly demonstrates that antidunes do actually form within an extensive range of subcritical flow conditions. Nevertheless, a limit of this plot is that it does not include the role of the particle Reynolds number R_p . This parameter is instead accounted for in the last criterion we wish to mention, due to Van Rijn (1984c) (see also Van Rijn, 1993). This is

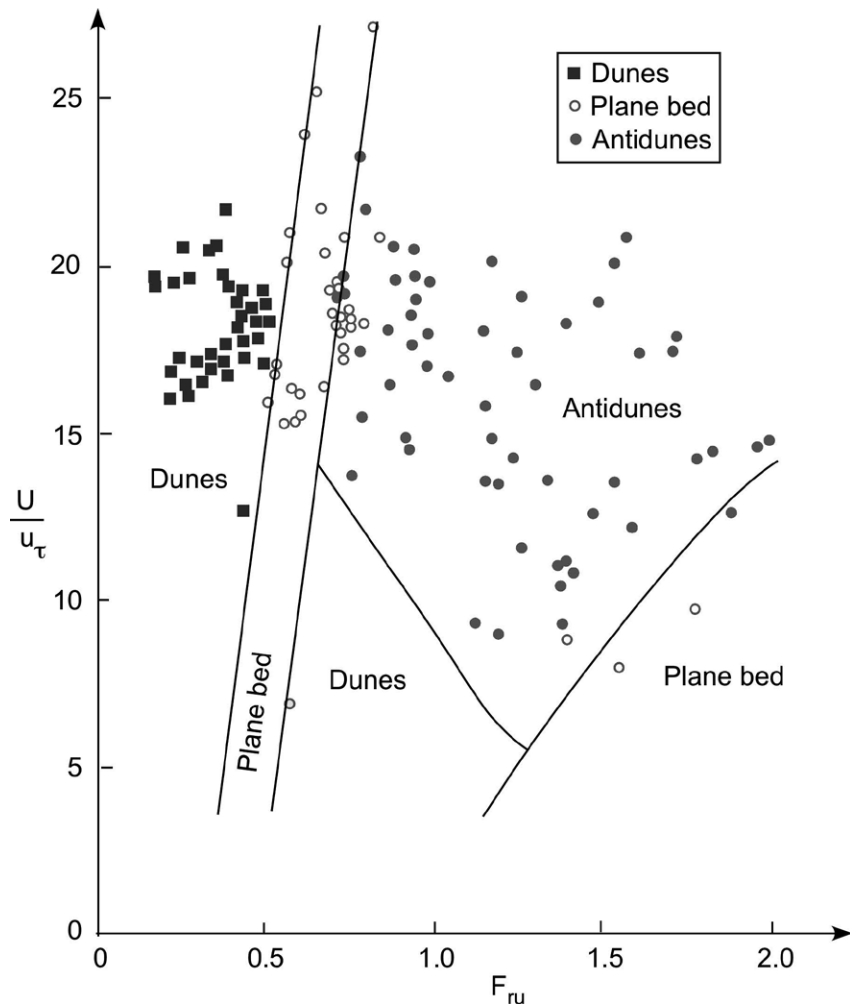


Figure 45. The bedform regime criterion proposed by Engelund and Hansen (1966).

probably the most comprehensive known classification scheme, that has the merit to be based on both laboratory and field data. It employs the so called *transport-stage parameter* T , defined in the form:

$$T = \frac{\tau_*' - \tau_{*c}}{\tau_{*c}}, \quad (353)$$

and the so called *Bonnefille dimensionless particle diameter* $D^* \equiv R_p^{2/3}$ (Bonnefille, 1963). In (353) τ_*' is the Shields stress associated with the grain roughness and τ_{*c} is the *critical Shields stress* obtained from the Shields diagram.

The bedform regime criterion by van Rijn, shown in Figure 46, suggests that ripples exist in the region defined by the conditions $D^* < 10$ and $T < 3$. Dunes are observed for values of $D^* > 10$ with $T < 3$ and for values of T in the interval $3 < T < 15$. They are washed out for values of T in the range $15 < T < 25$. However, also this criterion is not fully satisfactory. Indeed, as pointed out by Van Rijn himself (Van Rijn, 1996), in large rivers like the Mississippi, large dunes may be observed for values of T as large as 50 (see also Julien and Klaassen, 1995; Garcia, 2008).

4.5.3 Bedform characteristics at equilibrium

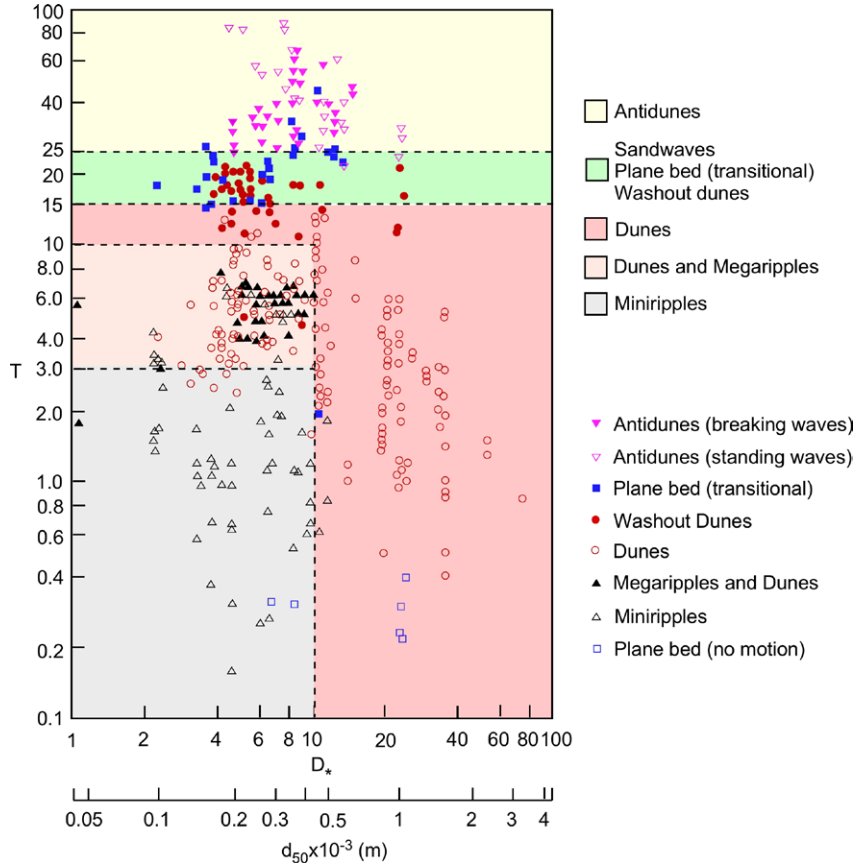


Figure 46. The bedform regime criterion proposed by Van Rijn (1984c).

Again, a comprehensive review of the literature concerning the prediction of bedform characteristics is found in Chapter 2 of Garcia (2008). Here, we restrict ourselves to results of few contributions concerning dunes, as these bedforms are quite common and significantly affect flow and sediment transport in open cohesionless channels. The available knowledge on the subject is still incomplete, even though, in the last two decades, significant advances in field, laboratory, and numerical investigations have contributed to unravel the principal features of mean and turbulent flow over alluvial sand dunes (Best, 2005). The data collected in extensive series of laboratory observations have in particular led to predictive relationships widely exploited in the morphodynamics literature, although they are not wholly satisfactory when applied to field conditions, especially to large rivers.

Predictors for the *dune height* A_d and the *dune wavelength* L_d were proposed by Van Rijn (1984c), based on data obtained from 84 flume experiments carried out by Guy *et al.* (1966) and various other Authors, as well as on field data collected in a few rivers (including the Mississippi, the Paraná, the Jissel and the Waal). Van Rijn (1984c) predictor for A_d reads:

$$A_d = 0.11 D \left(\frac{d_{50}}{D} \right)^{0.3} (1 - e^{-0.5T}) (25 - T), \quad (354)$$

with D and T average flow depth and transport stage parameter, respectively. According to Van Rijn (1984c), the *dune length*, scaled by the average flow depth, L_d/D , is constant and equal to 7.3, a value not far from the value 2π earlier suggested by Yalin (1964).

These relationships fit satisfactorily the experimental observations (Figure 47) but, as pointed

out by Julien and Klaassen (1995) and Van Rijn himself (Van Rijn, 1996), they tend to underestimate the dune height and the dune steepness observed in the field. The complexity of bottom patterns observed in large rivers, where large dunes typically coexist with smaller dunes, and their different response to variations of the flow discharge were discussed by Amsler and García (1997), while Carling et al. (2007) investigated the dynamics of large isolated sand dunes forming under supply-limited conditions. The role of viscous effects in smooth-transitional flows occurring in large rivers, ignored by Van Rijn (1984c), was extensively investigated by Amsler and Schreider (1999). These observations raise the need of further field investigations to improve our predictive capability.

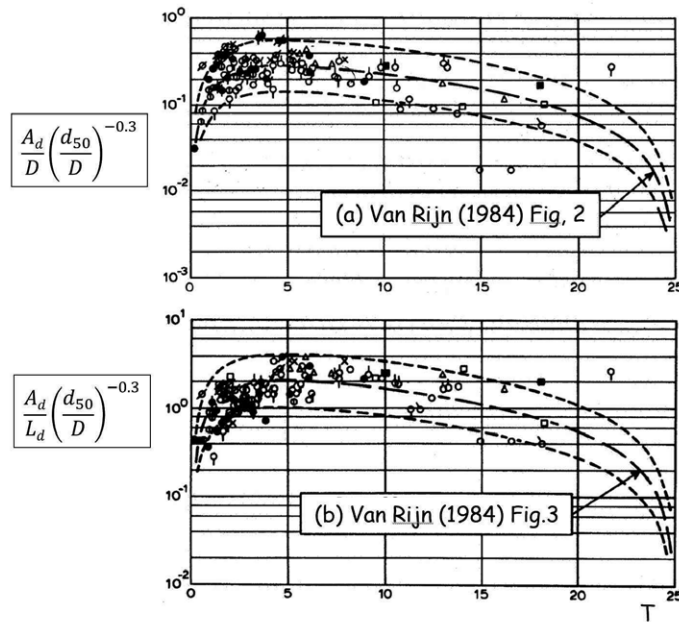


Figure 47. Comparison between Van Rijn predictors for (a) dune height and (b) dune steepness (Van Rijn, 1984c) and laboratory-field data of various Authors (modified from Van Rijn, 1984c, Figures 2 and 3).

Some attention has also been devoted to modeling the equilibrium shape of self-formed finite amplitude dunes, most notably by Fredsøe (1982) and Tjerry and Fredsøe (2005). These works exploit the linear relationship between local dune elevation and local sediment transport rate, which applies to migrating 2D bedforms of permanent form. With the help of some closure for the local bedload transport rate as a function of local Shields stress and local bed slope, these Authors derive a first order differential equation for the local dune elevation depending on the distribution of the Shields stress over the dune profile. This equation is then coupled to a hydrodynamic model able to predict the latter distribution. Results are of scientific interest as they suggest that various mechanisms, including the role of streamline curvature, control dune shape.

4.5.4 Bedforms and flow resistance

The effect of small scale bedforms on flow resistance is clearly illustrated in Figure 48. This figure requires some explanation to clarify the meaning of the average bottom shear stress $\bar{\tau}_0$ exerted on a bedform and its decomposition into grain roughness and form roughness components ($\bar{\tau}_{0g}$ and $\bar{\tau}_{0f}$, respectively). Let F_{Dd} denote the intensity of the drag force that the bottom exerts on the fluid over one bedform wavelength. We may then define the *average bottom shear stress* $\bar{\tau}_0$

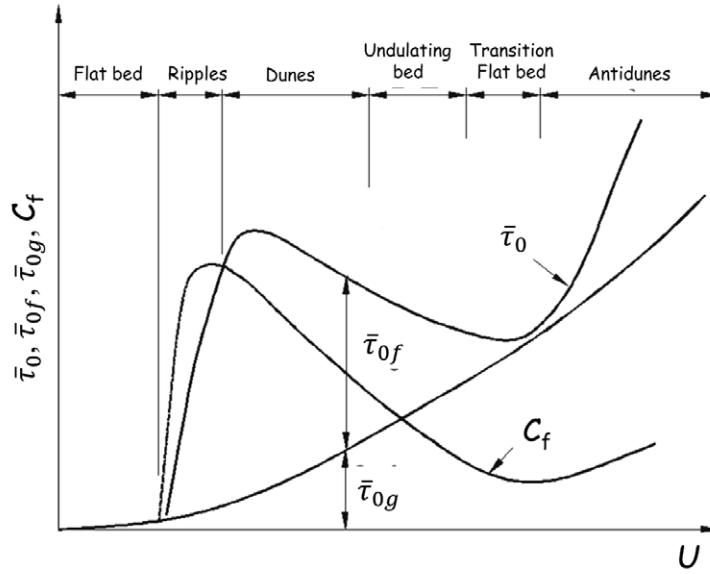


Figure 48. Dependence of the average bottom shear stress $\bar{\tau}_0$, of its grain and form components $\bar{\tau}_{0g}$ and $\bar{\tau}_{0f}$, and of the friction coefficient C_f on the average speed U according to Raudkivi (1990).

in the form:

$$\bar{\tau}_0 = \frac{F_{Dd}}{b_d L_d}, \quad (355)$$

where b_d is the dune width. The drag force F_{Dd} arises from two distinct contributions, the former associated with the effect of shear stresses, the latter arising from the normal stresses (pressures) acting on the bottom profile. This is clear if we decompose the stress vector \mathbf{t} acting on the bottom into its normal $(\mathbf{t} \cdot \hat{\mathbf{n}}) \hat{\mathbf{n}}$ and tangential $(\mathbf{t} \cdot \hat{\mathbf{\tau}}) \hat{\mathbf{\tau}}$ components. Here we have denoted by $\hat{\mathbf{n}}$ and $\hat{\mathbf{\tau}}$ the unit vectors in the directions normal and tangential to the bottom, respectively.

The drag force F_{Dd} is obtained projecting the stress vector in the longitudinal direction and integrating over one dune wavelength, to find:

$$F_{Dd} = \int \mathbf{t} \cdot \hat{\mathbf{x}} dx = \int [(\mathbf{t} \cdot \hat{\mathbf{n}}) \hat{\mathbf{n}} \cdot \hat{\mathbf{x}}] dx + \int [(\mathbf{t} \cdot \hat{\mathbf{\tau}}) \hat{\mathbf{\tau}} \cdot \hat{\mathbf{x}}] dx = F_{Df} + F_{Dg}. \quad (356)$$

Here F_{Df} and F_{Dg} denote the *form* and *grain roughness* components of the drag force. Hence, the grain ($\bar{\tau}_{0g}$) and form ($\bar{\tau}_{0f}$) components of the bottom shear stress read:

$$\bar{\tau}_{0g} = \frac{F_{Dg}}{b_d L_d}, \quad \bar{\tau}_{0f} = \frac{F_{Df}}{b_d L_d}. \quad (357)$$

The Figure 48 shows that the presence of bedforms significantly affects flow resistance. The form contribution increases as the flow speed increases, reaches a peak, decreases as the dune amplitude is reduced, and vanishes as the dunes are washed out. A smaller contribution arises in the upper regime due to antidune formation.

The reader should note that grain and form contributions to the bottom shear stress play different roles. The grain component is associated with turbulence and controls sediment transport, which is unaffected by the form component of the bottom stress. On the contrary, the form contribution to the bottom shear stress contributes significantly to flow resistance. This was first

recognized by Einstein (1950) who proposed a method to perform a partition of the average shear stress into grain and form components. An alternative proposal for a similar partition is due to Nelson and Smith (1989), building on previous work of Smith and McLean (1977).

Here, we refer to a physically based partition, originally suggested by Engelund (Fredsoe and Deigaard, 1992, p. 280), whereby the form contribution to the bottom shear stress can be estimated using the well known expression for the head loss due to a sudden flow expansion, a feature occurring at dune crests. This idea was pursued by Fredsoe (1982) who derived an expression for $\bar{\tau}_{*f}$, namely the Shields stress associated with $\bar{\tau}_{0f}$:

$$\bar{\tau}_{*f} = \frac{\bar{\tau}_{0f}}{(\rho_s - \rho)gd} = \frac{1}{2} \frac{U_u^2}{(s-1)gd} \frac{A_d}{D_u} \frac{A_d}{L_d}, \quad (358)$$

having denoted by D_u and U_u the average depth and speed of the flow, respectively.

The equation (358) is readily derived. Using the notations of Figure 49 the Borda-Carnot formula for the head loss associated with the abrupt expansion downstream to the dune crest, reads:

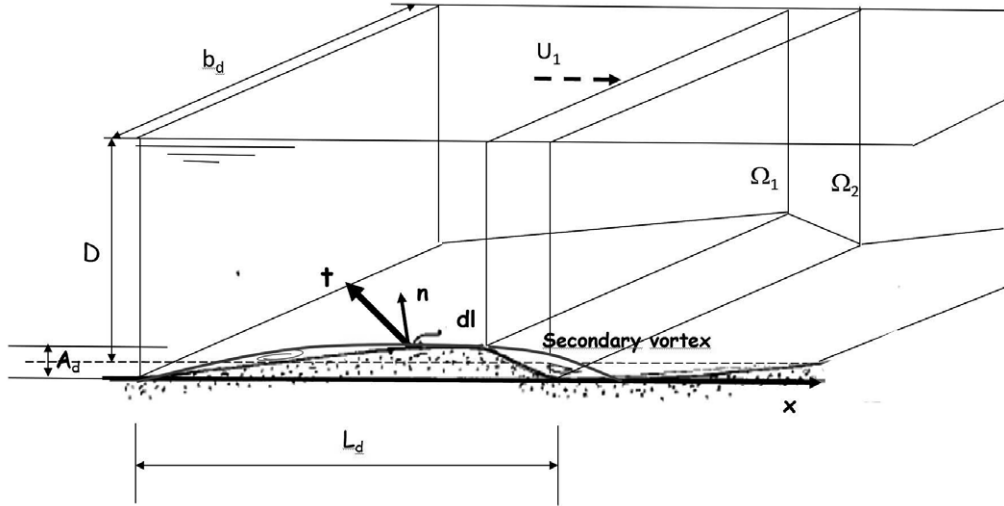


Figure 49. Sketch of a dune and notations.

$$\Delta\mathcal{H} = \frac{U_1^2}{2g} \left(1 - \frac{\Omega_1}{\Omega_2}\right)^2, \quad (359)$$

with \mathcal{H} total head, Ω_1 and Ω_2 the cross-sectional areas at the dune top and at the dune toe, respectively, and U_1 and U_2 the corresponding velocities. Employing the reasonable assumption $A_d/D_u \ll 1$, one immediately finds:

$$1 - \frac{\Omega_1}{\Omega_2} = 1 - \frac{b_d(D_u - \frac{A_d}{2})}{b_d(D_u + \frac{A_d}{2})} = \frac{A_d}{D_u} + \mathcal{O}\left(\frac{A_d}{D_u}\right)^2, \quad (360)$$

and

$$U_1 = \frac{Q}{b_d(D_u - \frac{A_d}{2})} = \frac{Q}{b_d D_u} \left[1 + \mathcal{O}\left(\frac{A_d}{D_u}\right)\right] = U_u \left[1 + \mathcal{O}\left(\frac{A_d}{D_u}\right)\right]. \quad (361)$$

Hence, denoting by J the energy slope:

$$\bar{\tau}_{0f} = \varrho g D_u J = \varrho g D_u \frac{\Delta \mathcal{H}}{L_d} = \frac{1}{2} \varrho U_u^2 \frac{A_d^2}{L_d D_u}, \quad (362)$$

we obtain the relationship (358) for the form Shields stress.

The *grain roughness* contribution to the bottom shear stress may be written in terms of a friction coefficient C_{fg} as:

$$\bar{\tau}_{*g} = \frac{\bar{\tau}_{0g}}{(\varrho_s - \varrho) g d} = \frac{C_{fg} U_u^2}{(s - 1) g d}. \quad (363)$$

Finally, the relationship between total and grain Shields stresses reads:

$$\bar{\tau}_* = \bar{\tau}_{*g} \left[1 + \frac{1}{2} C_{fg}^{-1} \frac{A_d^2}{L_d D_u} \right]. \quad (364)$$

This relationship was tested by Fredsøe (1982) using the set of laboratory data of Guy *et al.* (1966). In order to make it a tool of practical relevance, one would need to have reliable predictors for dune amplitude and dune wavelength.

Alternatively, one may rely on empirical relationships proposed by various Authors. Most of them refer to sand bed rivers. In particular Engelund and Hansen (1967) proposed a relationship between $\bar{\tau}_{*g}$ and $\bar{\tau}_*$ based on the laboratory data of Guy *et al.* (1966), which is plotted in Figure 50. The branches of this relation can be approximated as follows:

$$\bar{\tau}_{*g} = 0.06 + 0.4 \bar{\tau}_*^2, \quad 0.55 < \bar{\tau}_{*g} \quad (\text{lower regime}), \quad (365a)$$

$$\bar{\tau}_{*g} = \bar{\tau}_*, \quad 0.55 < \bar{\tau}_{*g} < 1 \quad (\text{upper-transitional}), \quad (365b)$$

$$\bar{\tau}_{*g} = \frac{\bar{\tau}_*}{(0.702 + 0.298 \bar{\tau}_*^{1.8})^{1/1.8}}, \quad \bar{\tau}_{*g} > 1 \quad (\text{upper-antidune}). \quad (365c)$$

The relation (365a) originally proposed by Engelund and Hansen (1967) to describe the lower branch was later modified by Engelund and Fredsøe (1982) who, on the basis of supplementary experiments, suggested to use the slightly different formula $\bar{\tau}_{*g} = 0.06 + 0.3 \bar{\tau}_*^{3/2}$. Note that the lower branch curve (*lower bed regime*) does not merge smoothly into the upper branch (*upper bed regime*) corresponding to plane bed, standing waves and anti-dunes. The range of plane bed and standing waves is characterized by the absence of expansion losses, hence in this regime $\bar{\tau}_* = \bar{\tau}_{*g}$. On the contrary, some expansion losses occur in the antidune regime, whose representative curve may be approximated by the relation (365c) suggested by Brownlie (1983).

The use of relationships like (365a) to construct stage-discharge curves spanning the lower regime for given channel slope S , channel width $2B$ and grain size d_{50} is straightforward. Essentially, one starts evaluating the flow characteristics assuming the absence of expansion losses. Hence, let D_{ug} denote the uniform flow depth that would occur under these conditions. For any given D_{ug} , we can estimate the associated friction coefficient C_{fg} using the logarithmic law in Keulegan form:

$$C_{fg} = \frac{1}{k} \ln \left(\frac{11 D_{ug}}{e_s} \right), \quad (366)$$

where e_s is the absolute roughness estimated by Engelund and Hansen (1967) as $2.5 d_{50}$. Chézy law then allows to calculate the average cross-sectional speed U_u . Next, we evaluate the frictional component of the average bottom stress $\bar{\tau}_{0g}$ ($= \varrho g D_{ug} S$) and its Shields associate $\bar{\tau}_{*g}$. The Engelund and Hansen relationship between $\bar{\tau}_{*g}$ e $\bar{\tau}_*$ (365a) is finally employed to evaluate the total Shields stress $\bar{\tau}_*$. The total dimensional stress $\bar{\tau}_0 = (\varrho_s - \varrho) g d_{50} \bar{\tau}_*$ and the total flow depth $D_u = \bar{\tau}_0 / (\varrho g S)$ follow. Finally, the sought value of the flow discharge \mathcal{Q} ($\equiv U_u D_u 2B$) associated with the flow depth D_u is readily calculated. A similar procedure can be used from the relation (365c) to compute the stage-discharge curves in the upper antidune regime.

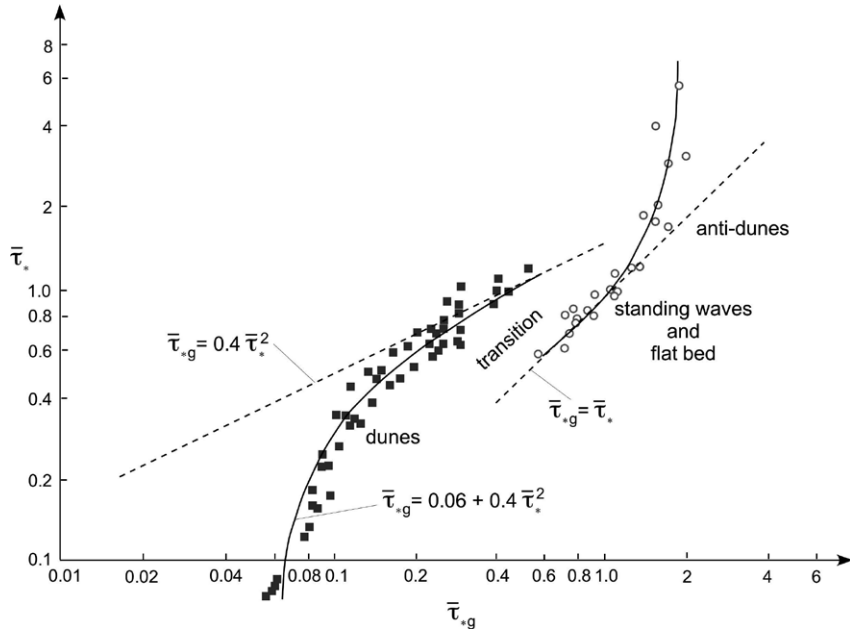


Figure 50. The relationship between $\bar{\tau}_{*g}$ e $\bar{\tau}_*$ proposed by Engelund and Hansen. Data points refer to laboratory observations of Guy *et al.* (1966) (modified from Engelund and Hansen, 1967).

The relationship of Engelund and Hansen (1967) performs well for laboratory flumes and small and medium scale sand bed streams. When applied to large rivers at high flows, the above approach tends to overpredict the grain contribution to flow resistance (Posada-García, 1995). This may be related to the fact that the transition from dunes to flat bed in large rivers occurs for values of the bed shear stresses higher than those observed in laboratory flumes.

A modified version of (365a) was proposed by Wright (2003) (but see also Wright and Parker, 2004a,b). It reads:

$$\bar{\tau}_{*g} = 0.05 + 0.7 (\bar{\tau}_* F_r^{0.7})^{0.8}. \quad (367)$$

As shown in Figure 51, this relationship performs satisfactorily for the sand rivers it was derived from, including small scale (Niobrara and Middle Loup), medium scale (Rio Grande) and large scale (Red, Mississippi and Atchafalaya) streams.

4.5.5 Bedforms and sediment transport

A number of empirical or semi-empirical predictors for the total sediment flux (bed load plus suspended load) have been proposed in the literature. A systematic comparison among the performances of various predictors applied to field conditions has been performed by Brownlie (1981). The survey concludes that the most successful predictor is the simplest formula proposed by Engelund and Hansen (1967):

$$\tilde{Q}_s = \frac{Q_s}{\sqrt{(s-1)gd^3}} = \frac{0.05}{C_f} \bar{\tau}_*^{5/2}. \quad (368)$$

Although the above relationship was essentially based on a fairly restricted set of laboratory data (Guy *et al.*, 1966), however the intensity of sediment transport predicted by (368) proves quite accurate even when applied to field conditions and fairly large values of the average total Shields stress.

4.5.6 Small scale fluvial bank-forms

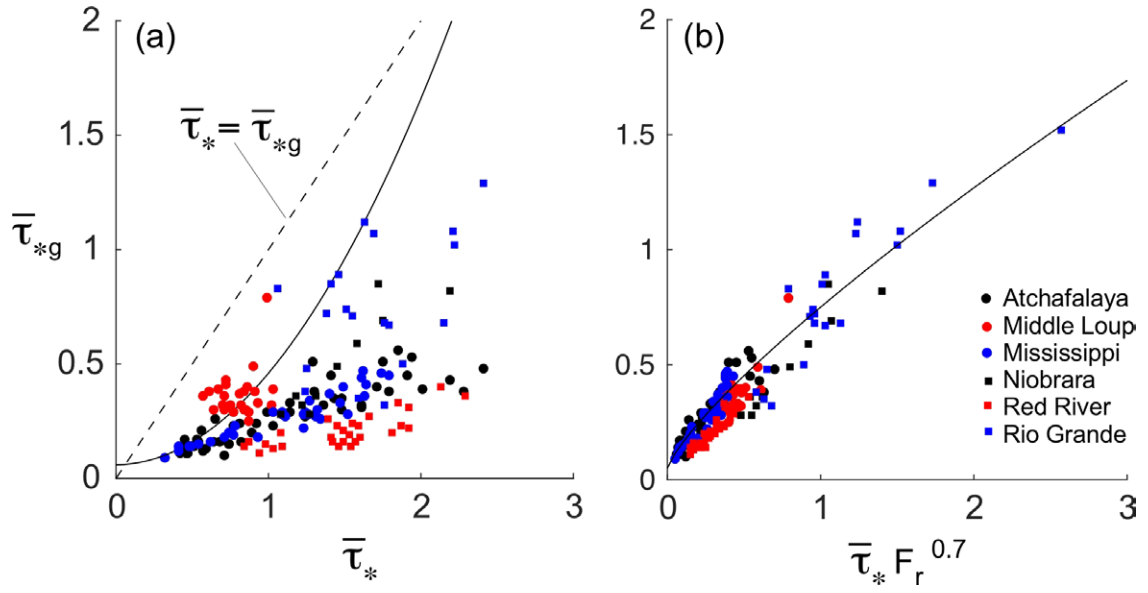


Figure 51. Comparison between the performances of (a) Engelund and Hansen resistance relationship and (b) relationship (367) applied to small, medium and large scale sand rivers (data courtesy of Wright, 2003).

While the role of small scale bedforms in open channel streams flowing over erodible cohesionless beds has been known since the early work of Gilbert (1914a), very little attention has been devoted to the effect of the small-scale features that commonly form on the banks of natural channels. They typically consist of undulations due to a number of factors, such as erosion and slumping of bank material as well as the presence of vegetation (roots, grass, etc.). As pointed out by Kean and Smith (2006a), “the size and spacing of adjacent features can vary considerably, usually more than the geometry of a set of dunes . . . bank features tend to be shorter, steeper, and more symmetric than dunes” resulting “in greater form drag relative to the dune situation”. Kean and Smith (2006a) characterized several streamwise bank surface profiles observed in the field and found that: i) the undulations develop a fairly two-dimensional shape in the longitudinal direction; ii) the shape of each undulation was well described by a Gaussian distribution (Figure 52). Kean (2003) (but see also Kean and Smith, 2006a) developed a model aimed at calculating the flow field and the associated boundary shear stress field over boundaries consisting of regular sequences of Gaussian shaped undulations mimicking those observed in natural river banks. In a companion paper, the same Authors (Kean and Smith, 2006b) extended the previous model, such to determine the form drag on irregular sequences of different-sized bank features. We refer the reader to the latter papers for details. It suffices here to outline briefly the main features of their modeling framework.

Following the approach of Smith and McLean (1977), the total shear stress on the average boundary, τ_T , was partitioned into an average component associated with skin friction acting on the actual surface, τ_{sf} , and an average component associated with form drag generated by the boundary irregularities, τ_D , noting that the former is typically an order of magnitude smaller than the latter. The form component τ_D was then expressed as follows:

$$\tau_D = \frac{F_{Db}}{L_p D_b} = \frac{1}{2} \rho c_{Db} \frac{a_p}{L_p} u_{ref}^2. \quad (369)$$

where F_{Db} is the form drag acting on an individual element of the bank undulation, c_{Db} is the associated drag coefficient, D_b is the flow depth at the bank, a_p and L_p are the amplitude and the wavelength of bank undulations, respectively (Figure 53), and u_{ref} is an appropriately determined reference velocity. The hydrodynamic model of Kean (2003) provided an approach to calculate

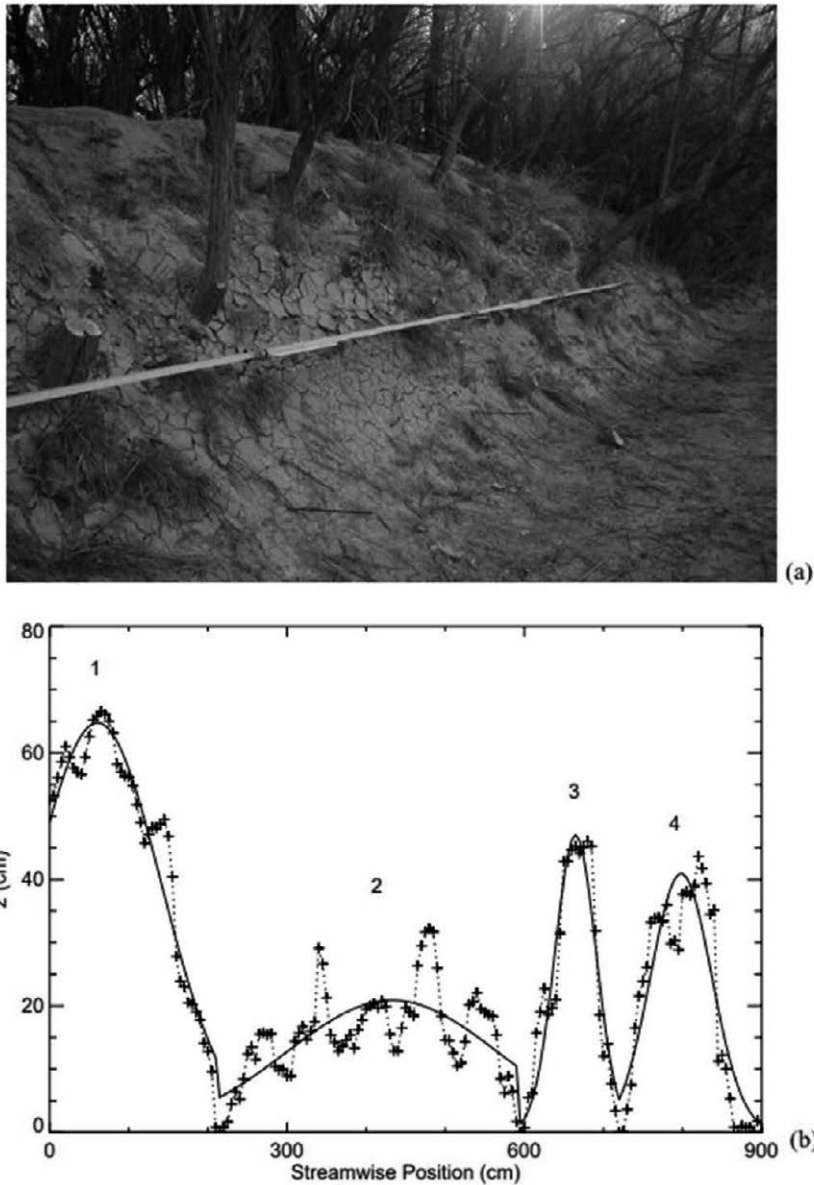


Figure 52. Small-scale bank roughness. (a) Picture of the bank of the inset channel of the Rio Puerco near Belen, New Mexico. (b) Measurements and Gaussian fit of bank undulations near the top of the bank. Note that the amplitude of the elements increases from bottom to top of the bank (reproduced from Figure 2.10 of Kean, 2003).

the two unknowns in (369), namely c_{Db} and u_{ref} . An estimate for c_{Db} was obtained from the experiments of Hopson (1999) on single (or sequences of) gaussian bank undulations. In order to evaluate u_{ref} , the solution for the velocity field was sought within each of the three adjacent flow regions which can be identified close to the banks, namely an internal boundary layer, a wake, and an outer boundary layer (Figure 53). Solutions were then patched at the boundaries between adjacent regions. Results show that the presence of topographic undulations and the inclusion of form drag are crucial ingredients in order to determine the spatial distribution of the flow and the boundary shear stress on the banks.

This is clarified in Figure 54 which shows a typical example of velocity (Figure 54a) and shear

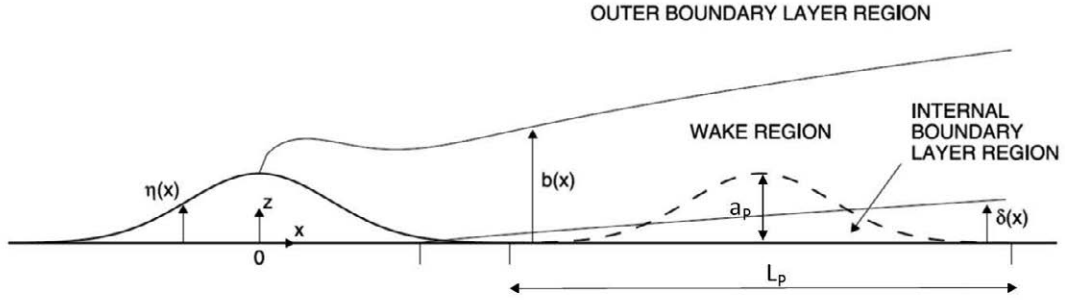


Figure 53. Plan view geometry of a regular sequence of bank undulations with indications of the distinct flow regions adopted in the model of Kean (2003) (internal boundary layer, wake, and outer flow region) (modified from Figure 2.2 of Kean, 2003).

stress (Figure 54b) distributions in the cross-section obtained applying the above model, jointly with the flow model of Kean and Smith (2004). Note that the stress profiles are scaled by the average stress τ_m of flow in an equivalent wide channel with flow depth equal to the actual depth D_m observed in the center of the channel (i.e. $\tau_m = \rho g D_m S$). The dashed lines represent the boundary shear stress distributions obtained assuming that the absolute roughness at the banks e_s^{bank} equals its value at the bed e_s^{bed} . Finally, the dotted lines represent the stress profiles obtained approximating the flow field as a lateral sequence of uniform flows with the local value D of the flow depth ($\tau = \rho g D S$). This Figure provides some measure of the reduction of near-bank velocity and the variations experienced by boundary shear stress due to the drag on bank protrusions. It also suggests that, as pointed out by Kean and Smith (2006a), in narrow channels the influence of the bank extends to the center of the channel.

In the companion paper, Kean and Smith (2006b), with the help of simulations performed on irregular sequences of bank roughness elements, show that “*the drag on an individual element is primarily controlled by the size and shape of the feature immediately upstream and that the spatial average of the boundary shear stress over a large set of randomly ordered elements is relatively insensitive to the sequence of the elements*” Moreover, they develop a method to transform the topography of irregular surfaces into a hydrodynamically equivalently rough surface consisting of regularly spaced, identical roughness elements. This allows the application of Kean and Smith (2006a) approach to natural contexts. In particular, the work of Darby *et al.* (2010) showed that, in the Lower Mekong river characterized by fine-grained cohesive banks, the boundary shear stress was mainly associated with form drag, ranging between 61% and 85% of the total shear stress.

4.6. Summary of the mathematical formulation for homogeneous sediments

Let us finally summarize the mathematical ingredients needed to formulate the problem of open channel morphodynamics.

3D Formulation

The governing equations of the hydrodynamics are the Reynolds equations and associated boundary conditions in the form presented in Section 2.3.2. The bed evolution equation in the form (245) is the fourth governing equation needed.

Reynolds equations need closures. For the scopes of large scale morphodynamics, it is usually sufficient to rely on a *slowly-varying assumption*. In other words, one may use the Boussinesq closure for Reynolds stresses (see equation (44) with a quasi-uniform relationship for the eddy viscosity expressed in terms of the local value of the friction velocity and flow depth. With the notations of equation (102), in dimensional form one may write:

$$\nu_T = u_\tau(x, y) D(x, y) \mathcal{N}(\zeta), \quad (370)$$

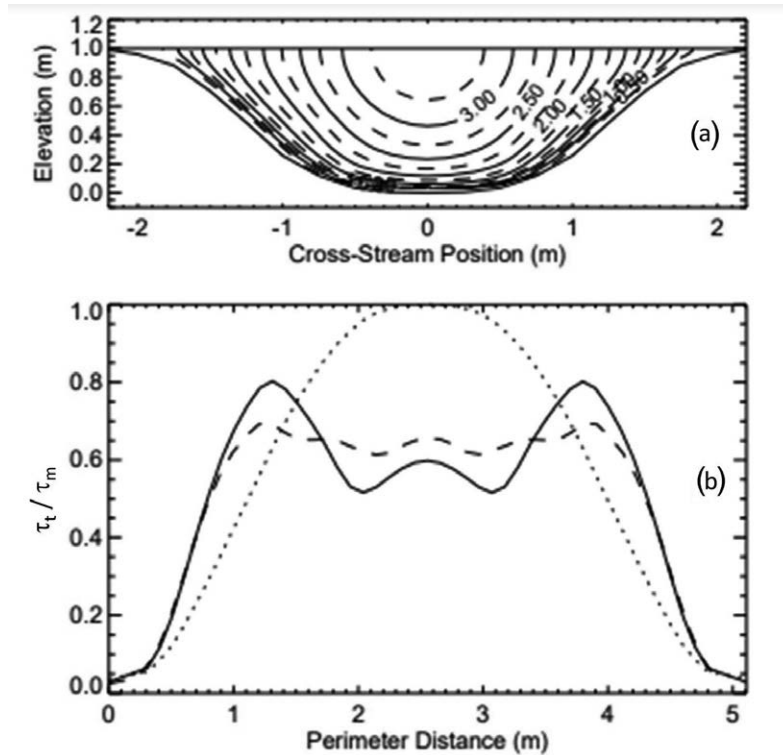


Figure 54. Reach-averaged (a) velocity (in m/s) and (b) boundary shear stress distributions obtained by Kean and Smith (2006a) applying their model to Lost Creek near Anaconda, Montana (continuous line). The stress profiles are scaled by $\tau_m = \rho g D_m S$, with D_m flow depth in the center of the channel. Dashed lines: boundary shear stress distributions for $e_s^{bank} = e_s^{bed}$. Dotted lines: stress profiles obtained using the approximation $\tau = \rho g D S$, with D the local flow depth (courtesy of Jason Kean).

Needless to say, more accurate closures may be employed if needed.

Exner equation (245) also need closure relationships for $Q_{s_j}^b$ and $Q_{s_j}^s$ as functions of the tangential stress at the bottom and of the local bed topography. They have been presented in Section 4.4 for their bedload component (equations (330), (334a) (334b), (350) and (351)). If suspended load is accounted for, then the 3D advection-diffusion equation for the Reynolds averaged concentration (254) must be solved with the closure (259) for the turbulent diffusion terms and the use of Reynolds analogy to estimate the turbulent diffusivity in terms of the eddy viscosity. Once the concentration equation has been solved, the components of the depth averaged sediment flux per unit width (Q_{sx}^s and Q_{sy}^s) are calculated from relations (260).

2D Formulation

The governing equations are now the shallow water equations and associated boundary conditions in the form presented in Section 2.4 along with the bed evolution equation in the form (245).

The only closure needed for the shallow water equations concerns the friction coefficient. Again, for the scopes of large scale morphodynamics, it is usually sufficient to rely on a *slowly-varying assumption*. In other words, one may use the expression for the friction coefficient appropriate to uniform flow expressed in terms of the local values of the roughness coefficient, flow depth and possibly Shields stress provided small scale bedforms are present on the bed.

As for the bedload component of the sediment flux per unit width, the closures for Exner equation do not differ from those for the 3D case summarized above. The components of the depth-integrated suspended sediment flux per unit width (Q_{sx}^s and Q_{sy}^s) can be calculated employing the

analytical approach appropriate to slowly varying flows described in Section 4.3.3.

Decoupling

The morphodynamic time scale for the evolution of morphological patterns under steady hydrodynamic conditions and constant sediment supply is typically much larger than the flow time scale. For example, the time required for the bar pattern to travel a given distance (say a bar wavelength) is much larger than the time needed for a fluid particle to travel the same distance. This physical fact justifies neglecting the temporal derivatives in the hydrodynamic equations. This simplified assumption, whereby one essentially assumes that the flow field adapts instantaneously (if viewed on the morphodynamic time scale) to temporal variations of the bed interface, is commonly described as *decoupling assumption*.

4.7. Extensions to heterogeneous sediments

In this section, we outline some additional features that complicate the picture of sediment transport further. They involve a number of partially settled issues, concerning the effects of sediment heterogeneity. The dynamics of sediment mixtures and sorting patterns may well deserve further specific attention in future Monographs of the present series. Below, we do not attempt to provide a comprehensive review of the state of the art on those issues. We simply seek to stimulate the interest of the readers providing them with brief introductions to the complexities of mechanisms that control such additional effects and to the novel modeling ingredients needed to investigate the formation of the so called *sorting patterns*.

The subject of bedload transport of heterogeneous sediments has been extensively reviewed in the recent past (e.g. Parker, 1992; Powell, 1998; Parker, 2008). We will largely refer to the latter works. Prerequisite to follow the present section is an elementary knowledge of the basic definitions of the geometrical characteristics of sediment mixtures (see, e.g. Chapter 1 of Blondeaux *et al.*, 2018).

4.7.1 Threshold for particle entrainment of heterogeneous sediments: Hiding

The dynamics of heterogeneous mixtures is dominated by the phenomenon of *hiding* whereby finer grains, protruding in the turbulent boundary layer less than larger grains, *feel* fluid drag less intensely than larger grains (Figure 55). This simple effect was recognized by Einstein (1950) and Egiazaroff (1965) and tends to counteract the opposite effect whereby reduced gravity makes the lighter finer grains more easily mobilized than the heavier coarser grains.

In order to appreciate the implications of hiding, let us first analyze how entrainment would operate in the absence of any effects of hiding. Let τ_{*cd} and τ_{*cg} be the critical values of the dimensionless Shields stress for the grains of size d and d_g , respectively, with d_g the geometric grain size of the mixture. They are defined in the form

$$\tau_{*cd} = \frac{\tau_{cd}}{(\varrho_s - \varrho) g d}, \quad \tau_{*cg} = \frac{\tau_{cg}}{(\varrho_s - \varrho) g d_g}, \quad (371)$$

with τ_{cd} and τ_{cg} dimensional values of the respective critical stresses. With *no-hiding*, one should set

$$\tau_{*cd} = \tau_{*cg}, \quad (372)$$

and, recalling the definitions (371),

$$\frac{\tau_{cd}}{\tau_{cg}} = \frac{d}{d_g}. \quad (373)$$

Hence, *in the absence of hiding, the dimensional values of the critical stresses for particle entrainment would be simply proportional to grain size*: finer grains would be more mobile than larger grains in proportion to the corresponding sizes. However, this is not what is observed in nature: sizes larger than the average are *slightly less mobile* while sizes smaller than the average are *slightly more mobile*.

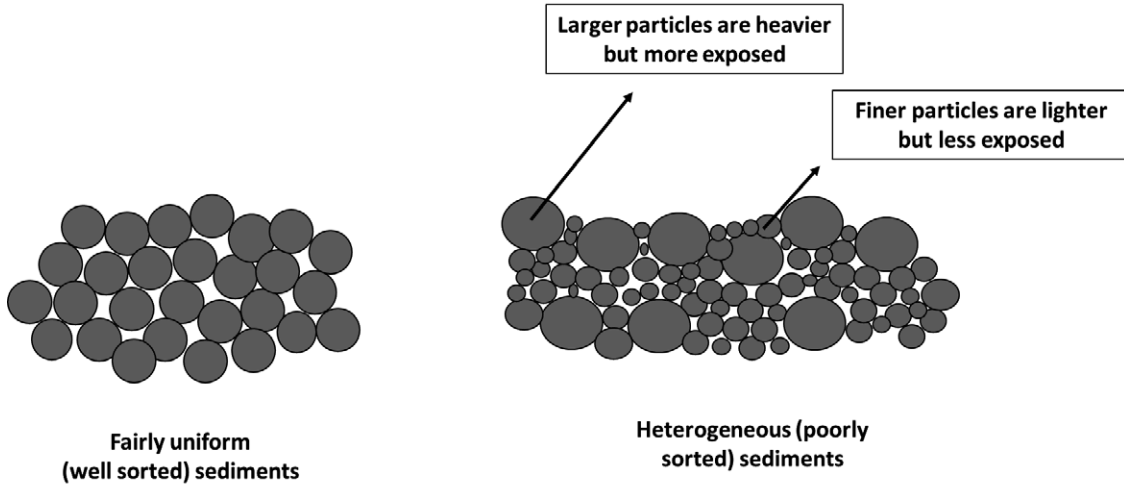


Figure 55. Sketch illustrating the mechanism, called *hiding*, whereby larger particles in a mixture are more prone to be mobilized than finer grains which *hide* between coarser grains

In order to account for hiding, Egiazaroff (1965) suggested to correct the dimensionless value of the critical Shields stress through a *hiding function* $\mathcal{H}(d)$, depending on grain size, defined in the form

$$\mathcal{H}(d) = \frac{\tau_{*cd}}{\tau_{*cg}}. \quad (374)$$

Two important limits deserve special attention.

- *No-hiding* corresponds to the hiding function \mathcal{H} being constant and equal to 1: in this case the differential mobility of large versus fine grains is maximum.
- *Perfect hiding* would be achieved if the *dimensional* values of the critical stresses were *size-independent* ($\tau_{cd} = \tau_{cg}$): in this case the hiding function \mathcal{H} would simply reduce to (d_g/d) . This condition was described as *equal mobility* by Parker and co-workers in a series of papers (Parker and Klingeman, 1982; Parker *et al.*, 1982a,b) which have strongly influenced the subject, determining a debate which is still not wholly settled (Parker and Toro-Escobar, 2002). We will discuss the dynamic implications of the notion of equal mobility in Section 4.7.2.

A number of expressions for \mathcal{H} have been proposed in the literature. In particular, the relationship suggested by Egiazaroff (1965), with some corrections introduced by Ashida and Michiue (1972), reads

$$\mathcal{H} = \left[1 + 0.782 \log \left(\frac{d}{d_g} \right) \right]^{-2} \quad \left(\frac{d}{d_g} \geq 0.4 \right) \quad (375)$$

$$\mathcal{H} = 0.843 \frac{d_g}{d} \quad \left(\frac{d}{d_g} < 0.4 \right). \quad (376)$$

An alternative form was proposed by Parker (1990),

$$\mathcal{H} = \left(\frac{d_g}{d} \right)^b \quad (b = 0.9), \quad (377)$$

where the degree of departure of the value of the exponent b from one measures the degree of unequal mobility of different grains in the mixture. To make the latter statement more quantitative,

we note that, using (377) with $\tau_{*cg} = 0.03$ and considering a sediment mixture with $d_g = 80$ mm, the ratio between the physical stresses required to mobilize two grains with sizes $d = 120$ mm and $d = 40$ mm is equal to 1.12. The same grains, each lying on a uniform cohesionless bed, would have mobilities differing by a factor 3. Note that Parker relationship (377) predicts differential mobilities significantly smaller than those predicted using the relations of Egiazaroff and Ashida-Michiue.

The figure 56 shows experimental observations and relationships proposed for the structure of the hiding function (Powell, 1998). The upper plot shows the hiding function of Egiazaroff and the data on which it was based. Figure 56b shows a larger set of data, collected by Ferguson *et al.* (1989), compared with results of theoretical analysis of Komar and Li (1986) and Wiberg and Smith (1987), as well as with the hiding function of Parker (1990) (equation 377) with $b = 0.88$ chosen by least squares regression for $d/d_g < 2$.

What can we conclude from Figure 56? Firstly, it appears that sizes larger (smaller) than the average are less (more) mobile than the average size, but this effect is indeed much weaker than it would be in the absence of hiding (see the equal mobility line). Secondly, although significant scatter is present, observations suggest that, in the range $d/d_g < 2$, hiding is *quasi perfect*, i.e. such that equal mobility is nearly achieved. On the contrary, in the range of high values of d/d_g , the trend tends to that of *no-hiding* (identified by the horizontal line), as noted much earlier by Ramette and Heuzel (1962). This was further substantiated by Wilcock (1993), who investigated the effect of the degree of mixture bimodality on differential entrainment and concluded that “*the critical shear stress of individual fractions τ_{cd} in unimodal and weakly bimodal sediments shows little variation with grain size and depends only on the mean grain size of the mixture. For strongly bimodal sediments, τ_{cd} increases with grain size*”.

Below, we analyze the transport of heterogeneous sediment mixtures. This process is also affected by hiding, which will then be further discussed.

4.7.2 Evaluation of grain size specific bed load transport capacity

Let us consider the uniform flow in a straight rectangular channel of width $2B$, subject to the supply of a constant discharge of heterogeneous sediments $Q_0^b = 2B Q_0^b$, where Q_0^b is the sediment supply per unit width and the subscript 0 stands for *reference uniform state*. Under equilibrium conditions sediment grain supply equals transport capacity. Let the sediment mixture be characterized by an assigned grain size distribution of density $f_0(d)$. The heterogeneous character of the sediments suggests that Q_0^b can be expressed as the integral of the transport capacity per unit width Q_{0d}^b of grains in the size range $d, d + dd$, of the form

$$Q_0^b = \int_0^\infty Q_{0d}^b dd. \quad (378)$$

We then need to evaluate the grain size specific transport capacity Q_{0d}^b . This quantity depends on the availability of sediments in the range $(d, d + dd)$ in the surface layer of the bed. It is then natural to assume that Q_{0d}^b is proportional to the probability density of sediments available for entrainment in the surface layer. Hence, we write

$$Q_{0d}^b = f_0(d) \sqrt{(s-1)gd^3} \Phi_{0d}. \quad (379)$$

where Φ_{0d} is the dimensionless form of the bedload transport capacity of homogeneous sediments in a uniform stream, subject to the Shields stress τ_{*d} associated with grains of size d . Following Parker and Klingeman (1982) we express Φ_{0d} as follows:

$$\Phi_{0d} = \tau_{*d}^{3/2} G(\tau_{*d}). \quad (380)$$

This definition is quite instructive. If G were constant the transport capacity would be size-independent as d is present in the scalings of both Φ_{0d} and $\tau_{*d}^{3/2}$ in identical form. In this case, the difference between transport capacities of different sizes would arise only from the

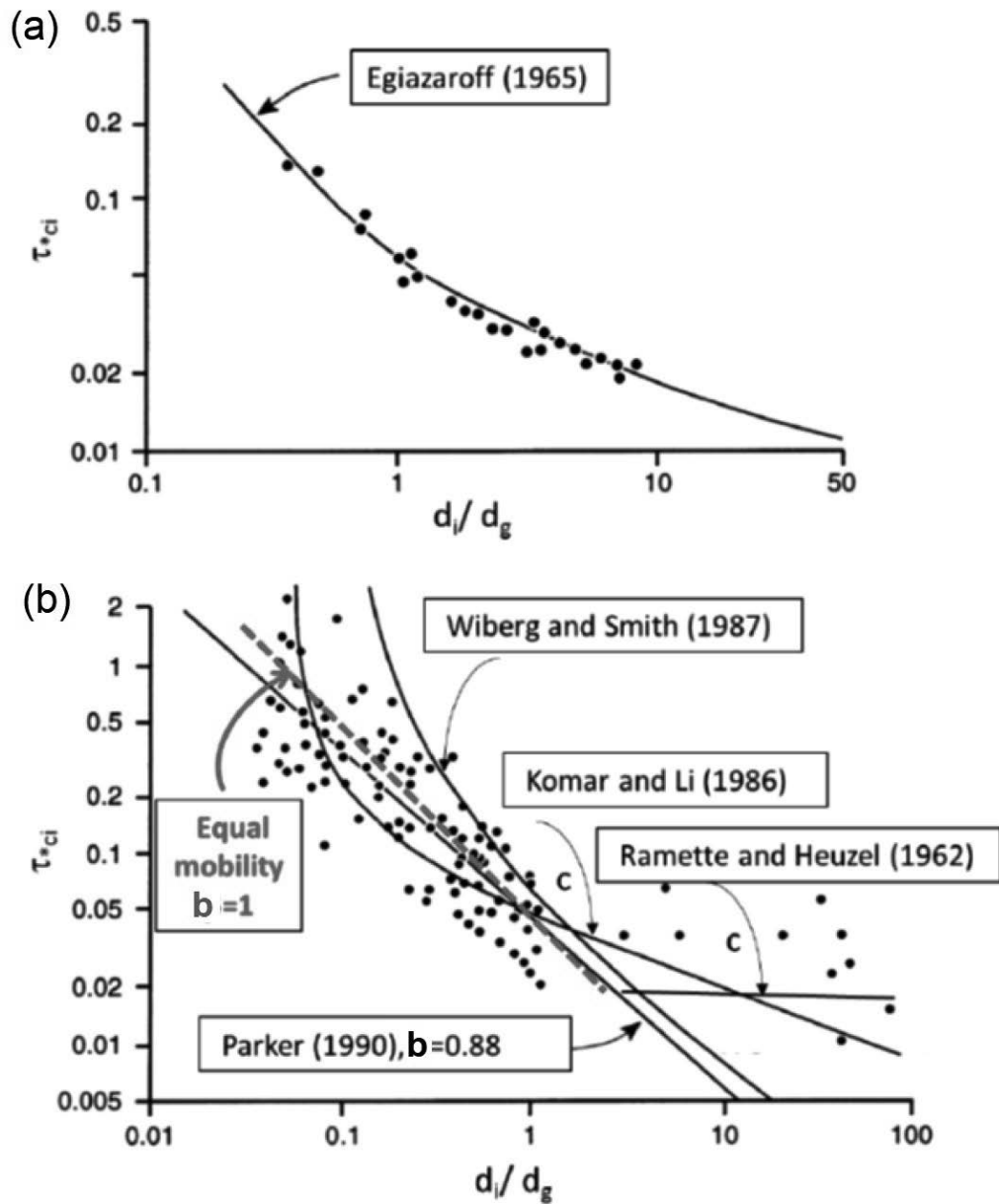


Figure 56. (a) The hiding function of Egiazaroff (equation 376) is plotted along with the data on which its derivation was based. (b) Data collected by Ferguson *et al.* (1989) are compared with results of theoretical analysis of Komar and Li (1986) and Wiberg and Smith (1987). The hiding function of Parker (equation 377) with $b = 0.88$ chosen by least squares regression for $d/d_g < 2$, as well as the equal mobility form of the function (dotted red line, $b = 1$) are also shown. The horizontal line illustrates the tendency of τ_{*cd} to attain constant values for large d/d_g as suggested earlier by Ramette and Heuzel (1962) (modified from Powell, 1998).

different availabilities of each size, as measured by the function $f_0(d)$ (equation 379). However, for nonhomogeneous sediments, G is not constant, it is rather an increasing function of τ_{*d} . Hence (380) predicts values of Φ_{0d} for finer grains quite larger than for coarser grains. This effect would

prevail over the effect of the reduced representation of finer grains in the surface layer. As a result, contrary to observations, (379) and (380) would lead to transport capacities of the fine fraction much larger than that of the coarse fraction.

The generalization of (380) to mixtures then requires a correction for hiding. *Dynamically*, this implies that the dimensionless Shields stress, which controls the transport rate of each size, must be corrected through the introduction of a hiding function. Following Parker and Klingeman (1982), we write:

$$Q_{0d}^b = \sqrt{(s-1)g d_g^3} f_0(d) \tau_{*g}^{3/2} G \left[\tau_{*g} \mathcal{H} \left(\frac{d}{d_g} \right) \right], \quad (381)$$

where τ_{*g} is the Shields stress associated with the geometric mean size of the surface layer d_g .

Various suggestions are available in the literature to quantify the function G (e.g. Ashida and Michiue, 1972; Parker, 1990; Powell *et al.*, 2001; Wilcock and Crowe, 2003). Below, we provide two examples and refer the reader to the extensive treatment of Parker (2008) for a more comprehensive overview of the available approaches.

Parker (1990) based his analysis on field observations performed on a small gravel bed river, Oak Creek, Oregon, USA (Milhous, 1973). Moreover, his approach ignored the sand component of the mixture. Hence, the probability density f_0 was renormalized removing the sand component and, similarly, the quantities d_g and τ_{*g} were based on the renormalized distribution. The outcome of the analysis was the following relationship for G ,

$$G(\xi) \equiv \begin{cases} 11.93 (1 - 0.853/\xi)^{4.5} & \xi > 1.59 \\ 0.00218 \exp [14.2(\xi - 1) - 9.28(\xi - 1)^2] & 1 < \xi < 1.59 \\ 0.00218 \xi^{14.2} & \xi < 1, \end{cases} \quad (382)$$

where ξ reads:

$$\xi = \omega \frac{\tau_{*g}}{\tau_{*r}} \left(\frac{d}{d_g} \right)^{-b}. \quad (383)$$

Here, τ_{*r} is a reference stress which replaces the usual notion of critical stress, b is a hiding parameter and ω is a straining coefficient. They read:

$$\tau_{*r} = 0.0386, \quad b = 0.0905, \quad \omega = 1 + \frac{\sigma_s}{\sigma_0} [\omega_0 - 1], \quad (384)$$

where σ_s is the standard deviation of the grain size distribution of the surface layer and ω_0, σ_0 are parameters plotted in Parker (1990) as functions of τ_{*g}/τ_{*r} .

The approach of Wilcock and Crowe (2003) differs from the approach of Parker (1990) in that the sand fraction is not excluded when computing the function G , which now reads:

$$G(\xi) \equiv \begin{cases} 0.002 \xi^{7.5} & \xi < 1.35 \\ 14 (1 - 0.894/\xi^{0.5})^{4.5} & \xi > 1.35 \end{cases} \quad (385)$$

Here, ξ is defined by (383) with $\omega = 1$. Moreover, τ_{*r} is replaced by τ_{*rg} where

$$\tau_{*rg} = 0.021 + 0.015 \exp(-20 F_{ss}), \quad b = \frac{0.67}{1 + \exp(1.5 - d/d_g)}. \quad (386)$$

In (386) we have denoted by F_{ss} the cumulative sand fraction in the surface layer, a fraction which rarely exceeds 30%.

The reader should note that the mean reference stress for the surface material τ_{*rg} , as predicted by (386), increases as the sand fraction decreases (Figure 57b). This is an important effect pointed out by Wilcock and Crowe (2003). *Increasing the sand content in the surface layer of a gravel-bed river enhances the mobility of the surface gravel.* Also, unlike in Parker (1990), the hiding exponent

is now a function of grain size. It corrects the reference stress of grain sizes smaller than the average differently from grain sizes larger than the average:

$$\frac{\tau_r}{\tau_{rg}} = \left(\frac{d}{d_g} \right)^{0.67} \left[1 + \exp \left(1.5 - d/d_g \right) \right]^{-1} \quad (387)$$

The Figure 57a shows how the latter relationship fits the experimental observations on which it was based (Wilcock and Crowe, 2003).

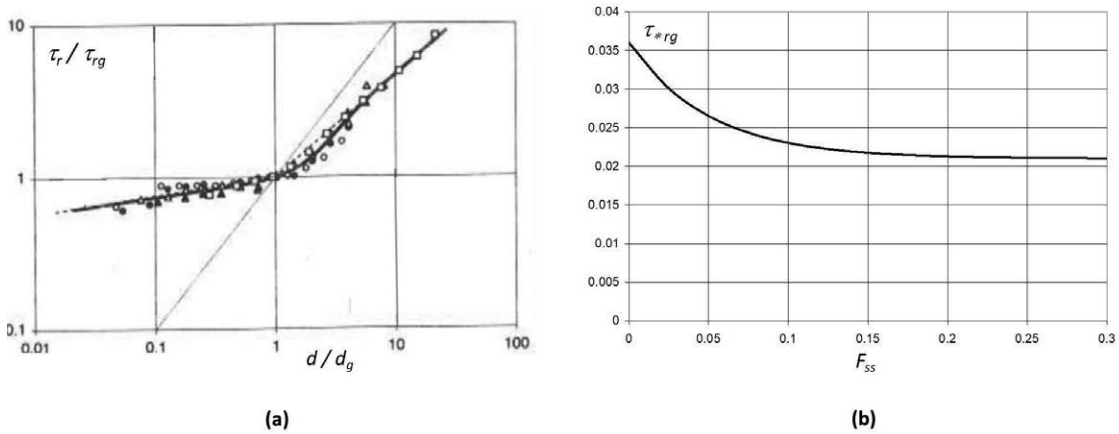


Figure 57. (a) Comparison between predictions of the reference stress of size d based on equation (387) and experimental observations (Wilcock and Crowe, 2003); (b) Dependence of the mean dimensionless reference stress for the surface material τ_{*rg} on the sand fraction, according to (386) (modified from Wilcock and Crowe, 2003).

4.7.3 Grain size specific formulation of Exner equation: Hirano's approach

The heterogeneous character of sediments also calls for the need to adapt the classical Exner equation, i.e. the differential formulation of mass conservation for the transport of sediments, such that the balance is satisfied for each grain size. The processes of particle mixing, through deposition, burial and re-entrainment, have attracted the attention of scientists for a long time (see the review of Hassan and Church, 1994). The first sound attempt at formulating a grain size specific form of the mass conservation equation is due to Hirano (1971). The latter approach has then dominated the subject for roughly three decades, although various improvements were proposed (e.g. Armanini and Di Silvio, 1988; Armanini, 1995). Parker *et al.* (2000) have introduced a novel approach able to account for the effects of vertical mixing and of the random nature of the geometry of the bed interface in the presence of large scale bedforms. Below, we outline the derivation of the model by Hirano (1971), the merits and limits of which have been fully ascertained. The probabilistic formulation of Parker *et al.* (2000), whose potential has not been fully exploited yet, will be briefly outlined in the next section.

The formulation of Hirano (1971) (see the extensive presentations in Parker, 1992, 2008) adopts a two layer structure to model the dynamics of a river bed: a surface exchange layer of thickness L_a , called *active layer*, and a *substrate* (Figure 58a). The probability density functions of a given grain size d within these two layers are denoted by f_a and f_s , respectively.

The active layer is taken to be vertically well mixed so that the probability density function f_a of the material within it has no vertical structure. On the contrary, the substrate has no direct interaction with bedload transport but can exchange material with the active layer if the bed undergoes aggradation-degradation and/or the bed pattern is affected by vertical mixing, through deposition, burial and re-entrainment, as typically occurs in the presence of large amplitude bedforms.

Thus, the grain-size distribution density f is in general discontinuous. In the active layer it may depend on the longitudinal and lateral cartesian coordinates, x and y , as well as on time t , i.e. $f_a = f_a(d; x, y, t)$, whereas in the substrate it can also vary with the vertical coordinate z , namely $f_s = f_s(d; x, y, z, t)$, the dependence on time being related to aggradation/degradation processes or bed reworking by large amplitude bedforms. Aggradation/degradation can be incorporated easily into the model. Conversely, as discussed below, the presence of large amplitude bedforms requires some more elaborate analysis able to describe vertical mixing, like the probabilistic framework proposed by Parker *et al.* (2000) that will be briefly outlined in the next Section.

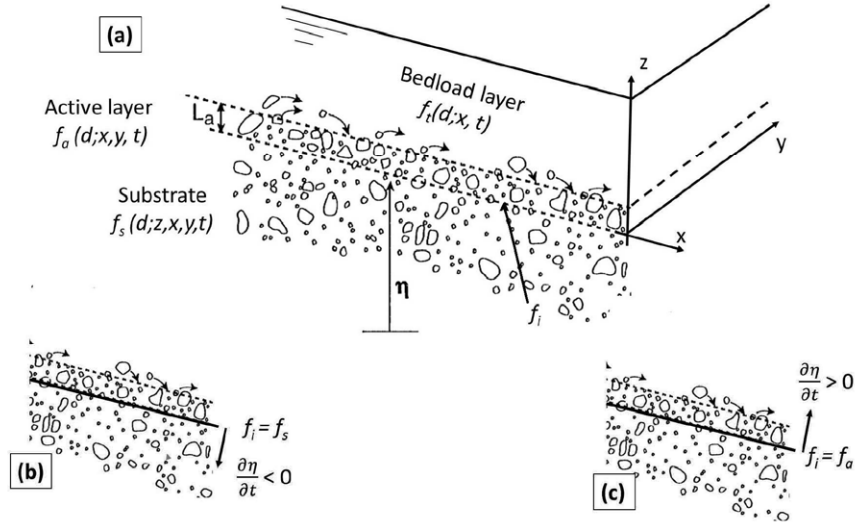


Figure 58. (a) Sketch of the two-layer structure in the model of Hirano (1971), with illustration of the flux exchanged through the interface between the active layer and the substrate in the case of (b) bed degradation and (c) bed aggradation (according to from Toro-Escobar *et al.*, 1996).

Within Hirano framework, the size specific form of the statement of mass conservation for the active layer can be written in the form:

$$(1 - p) \left[f_i \frac{\partial \eta}{\partial t} + L_a \frac{\partial f_a}{\partial t} \right] + \frac{\partial (f_a Q_{xd}^b)}{\partial x} + \frac{\partial (f_a Q_{yd}^b)}{\partial y} = 0. \quad (388)$$

Here, the thickness of the active layer L_a is assumed to be constant. Moreover, Q_{xd}^b and Q_{yd}^b are the longitudinal and lateral components of the size specific bedload transport vector per unit width, Q_d^b , p is the porosity of the granular mixture in the substrate, assumed to be constant, and f_i is the grain-size distribution density at the interface between the active layer and the substrate. Assigning the value of this function is not obvious due to the assumed discontinuous character of the grain-size density distribution. If the bed is degrading ($\partial \eta / \partial t < 0$), the common choice is to assume f_i equal to the value of f_s in the substrate just below the active layer (Figure 58b). In the aggrading case ($\partial \eta / \partial t > 0$), a variety of suggestions have been made, ranging from the original assumption (Hirano, 1971) that $f_i = f_a$, to the more recent suggestion, supported by laboratory experiments (Toro-Escobar *et al.*, 1996), that f_i may be expressed as a weighted average of the grain size density distributions of the active layer (f_a) and of the bedload (f_b) (Figure 58c).

The reader should note that, in the case of heterogeneous sediment, besides the four unknown functions (depth averaged velocities, free surface elevation and bed elevation) characteristic of the homogeneous case, one further unknown function is involved, namely the grain-size probability

density function $f_a(d; x, y, t)$, that must satisfy the obvious constraint:

$$\int_0^{\infty} f_a(d; x, y, t) dd = 1. \quad (389)$$

This is conceptually a major novel feature of the sorting problem. Indeed, the constraint (389) transforms the mathematical nature of the problem from differential into *integro-differential*.

The classical form of Exner equation for homogeneous sediments is immediately recovered integrating (388) over all grain sizes and using the constraint (389) and the similar constraint valid for the interfacial grain-size probability density function f_i .

The statement (388) differs from the classical Exner equation in various respects:

- variations of bed elevation now contribute to the grain specific sediment balance in proportion to the size probability density function f_i ;
- the divergence of the sediment flux per unit width is replaced by the divergence of the size specific sediment flux per unit width;
- an additional contribution to the size specific sediment balance arises from the volume of sediments of size d contained within the active layer per unit area: this undergoes temporal variations due to variations of the grain-size probability density function f_a .

The size specific form of Exner equation (388) requires closure relationships for Q_{xd}^b and Q_{yd}^b . Following Parker and Andrews (1985) appropriate closures may be obtained modifying the relationships (334a), (334b), (350), (351), valid for the case of homogeneous sediments and weakly sloping bed topography. Accounting also for the possible deviation of the bottom stress vector from the direction of the longitudinal axis induced by streamline curvatures, χ (see equation (181) of the companion Monograph Seminara *et al.*, 2023), we then write:

$$Q_{xd}^b = Q_{0d}^b \left[1 - \frac{\sqrt{\tau_{*cg}} \mathcal{H}(d/d_g)}{\mu_d} \frac{\partial \eta}{\partial x} \right], \quad (390a)$$

$$Q_{yd}^b = Q_{0d}^b \left[\sin \chi - \frac{r}{\sqrt{\tau_{*g}}} \sqrt{\frac{d}{d_g}} \mathcal{H}(d/d_g) \frac{\partial \eta}{\partial y} \right]. \quad (390b)$$

A few notes:

- the quantity Q_{0d}^b is the grain size specific transport rate at uniform conditions (equation 381) evaluated for the local and instantaneous values of the geometrical mean of the Shields stress τ_{*g} and for the sediment size d ;
- the effect of the lateral slope acts through the effective Shields stress associated with grain size d , accounting for hiding. More precisely, in order to derive (390b) we start from the relationship (349) and note that:

$$\sqrt{\frac{\tau_{*cd}}{\tau_{*d}}} = \sqrt{\frac{\tau_{*cg}}{\tau_{*d}} \mathcal{H}(d/d_g)} = \sqrt{\frac{\tau_{*cg}}{\tau_{*g}} \frac{d}{d_g} \mathcal{H}(d/d_g)}. \quad (391)$$

The relationship (390b) follows noting that the constant r is equal to $\sqrt{\tau_{*cg}}/\mu_d$.

4.7.4 Grain size specific formulation of Exner equation: The missing role of vertical sorting

The active layer introduced by (Hirano, 1971) has no vertical structure. As a result, the active layer approach is not suited to investigate sorting processes involving both the vertical and the

horizontal directions. This is typically the case of rivers with the bed covered with bedforms like dunes and bars.

The process of vertical sorting is the outcome of various distinct phenomena. Firstly, the bedload of mixtures gives rise to differential sediment transport leading to surficial sorting. Secondly, the spatial fluctuations of local bed slope associated with the presence of bedforms drives gravitational sorting whereby coarse material tends to accumulate in the troughs. Thirdly, bedform migration transforms the superficial sorting pattern into distinct stratigraphic patterns. Figure 59a shows a typical dune-covered bottom pattern measured in the experiments of Leclair (1999). Figure 59b visualizes the stratigraphic record resulting from the passage of dunes, obtained slicing the deposit. The picture shows a distinct pattern of cross-bedding associated with dune migration and confirms the tendency for the coarsest sediment to concentrate in the troughs of the dunes. Moreover, significant fluctuations of bedform amplitude are evident from the three lines demarcating the passage of dune troughs. Parker *et al.* (2000) point out that “*the line of deepest trough shown in Figure 59b could be thought of as an instantaneous realization of the bottom of the active layer for a dune covered bottom*”.

The probabilistic nature of fluctuations of bed elevation about a mean value driven by bedform migration emerges clearly from Figure 59c where the fraction of the bed record with elevation higher than the level y is plotted versus y itself.

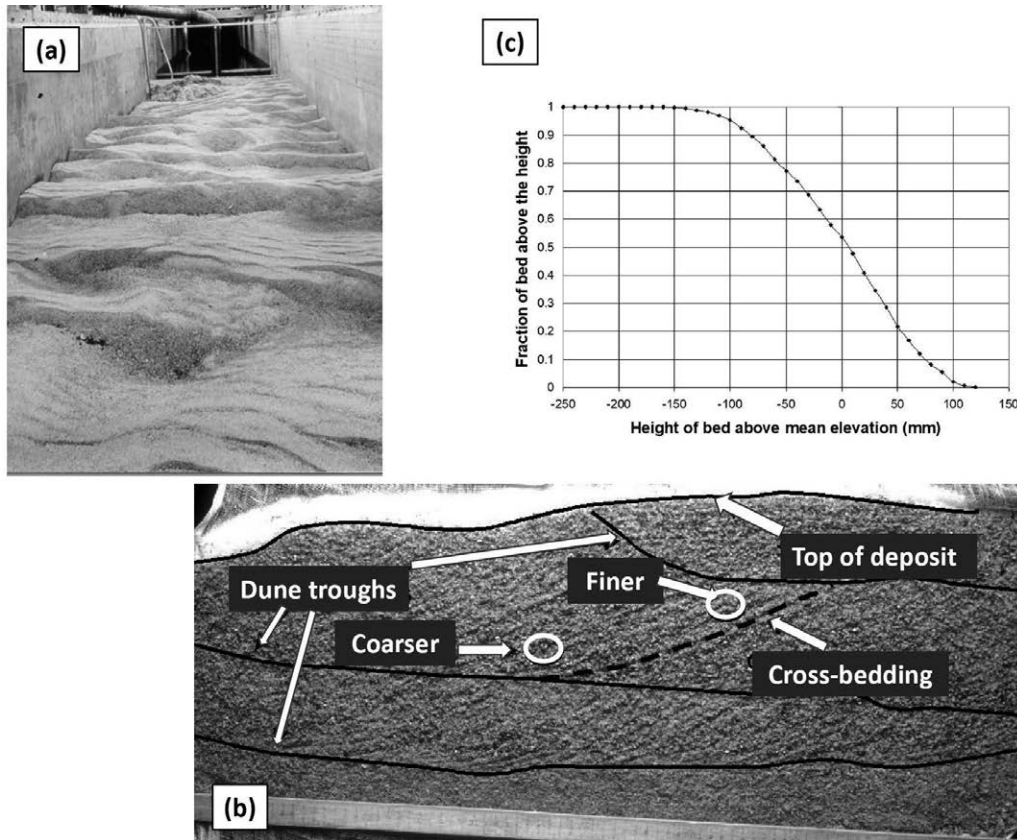


Figure 59. Bed features observed at the end of a dune-covered experiment (Run 33) carried out by Leclair (1999) using graded sediments. (a) Photograph of the flume bed covered by dunes and (b) picture of a typical peel of stratigraphy. (c) The fraction of bed with elevation higher than some level y , measured relative to mean bed level, is plotted versus y itself. Courtesy of Suzanne Leclair and Gary Parker.

Note that similar experiments had been conducted by Ribberink (1987). He was probably the

first to recognize clearly the role of vertical sorting and the need for a multi-layer reformulation of mass conservation of bed sediment in order to predict the vertical distribution of grain size. An idea also pursued by Armanini and Di Silvio (1988) and Armanini (1995). A more recent attempt to provide a conceptual framework equipped to incorporate information about the stochastic nature of bed elevation is found in the work of Parker *et al.* (2000). The probabilistic approach proposed there does not lead to a local statement of sediment continuity. Rather, it seeks a spatially averaged formulation, with averaging performed over a channel length “large compared to those associated with the fluctuations but small compared to those of variation of the mean bed”. Hence, this approach can hardly be employed to investigate vertical sorting at the scale of the single bedform. Given the complexity of the problem an intense research on vertical sorting is being pursued and a specific Monograph will likely be needed in the near future to provide an adequate assessment of the problem. For the time being we refer the reader to the paper of Parker *et al.* (2000) and to the subsequent developments pursued by Blom and coworkers (e.g. Blom *et al.*, 2008).

4.8. Appendix: Bedload transport of homogeneous sediments on finite slopes

In this Appendix, the theoretical framework developed in Section 4.4.3 will be used to outline an extension of the analysis of bedload transport on weakly sloping beds to the case of finite slopes.

Particle velocity on finite slopes

Recalling that:

$$\mathbf{u}|_{z_P} = u_\tau f|_{z_P} \hat{\boldsymbol{\tau}}, \quad \frac{4}{3} \frac{\mu_d}{c_D} = \tau_{*cd} f^2|_{z_P}, \quad \tau_* = \frac{u_\tau^2}{(s-1)gd}, \quad (392)$$

the equation (338), governing the dynamic equilibrium of a spherical particle saltating along the tangent plane, can be easily rewritten as:

$$\left(\sqrt{\tau_*} \hat{\boldsymbol{\tau}} - \frac{\tilde{v}_P}{f|_{z_P}} \hat{\mathbf{v}}_P \right) \left| \sqrt{\tau_*} \hat{\boldsymbol{\tau}} - \frac{\tilde{v}_P}{f|_{z_P}} \hat{\mathbf{v}}_P \right| = \tau_{*cd} \left(|z_n| \hat{\mathbf{v}}_P + \frac{z_t}{\mu_d} \right), \quad (393)$$

with $\tilde{v}_P = v_P / [(s-1)gd]^{0.5}$. Projecting this equation in the directions of $\hat{\boldsymbol{\tau}}$ and $(\hat{\mathbf{n}} \times \hat{\boldsymbol{\tau}})$, with the help of some algebraic manipulations, one finally derives two scalar relationships for the modulus (v_P) and direction (ψ) of particle velocity, $\mathbf{v}_P = v_P [\cos \psi \hat{\boldsymbol{\tau}} + \sin \psi (\hat{\mathbf{n}} \times \hat{\boldsymbol{\tau}})]$, which may be cast in the following form:

$$\tilde{v}_P = f|_{z_P} \sqrt{\tau_*} \mathcal{A}(\psi; \alpha_x, \alpha_y), \quad (394)$$

where the function \mathcal{A} reads:

$$\mathcal{A} = \frac{\cos \alpha_x \tan \alpha_y - \mu_d \sin \psi}{\cos \psi \cos \alpha_x \tan \alpha_y - \sin \psi \sin \alpha_x \sqrt{1 + \tan^2 \alpha_x + \tan^2 \alpha_y}}. \quad (395)$$

The angle ψ is given in implicit form, in terms of the local value of the Shields stress τ_* and of the angles α_x and α_y through the relationship:

$$\frac{\tau_*}{\tau_{*cd}} = \frac{\cos \alpha_x \tan \alpha_y - \mu_d \sin \psi}{\mu_d \mathcal{A} \sin \psi \sqrt{(1 - 2\mathcal{A} \cos \psi + \mathcal{A}^2)(1 + \tan^2 \alpha_x + \tan^2 \alpha_y)}}. \quad (396)$$

The reader will readily verify that relations (394), (395) and (396) reduce to (346) and (349) in the weakly sloping limit. In Figure 60 we plot the angle ψ as a function of the Shields stress τ_* for given values of the lateral bed inclination and vanishing longitudinal bed inclination.

Two comments are in order. Firstly, it is not surprising that the effect of the lateral slope on the direction of particle motion decreases as the Shields stress increases: this finding bears some relevance for the process of lateral sorting in meander bends. Secondly, less obvious is the observation that nonlinear effects are significant only for quite large values of the lateral bed inclination.

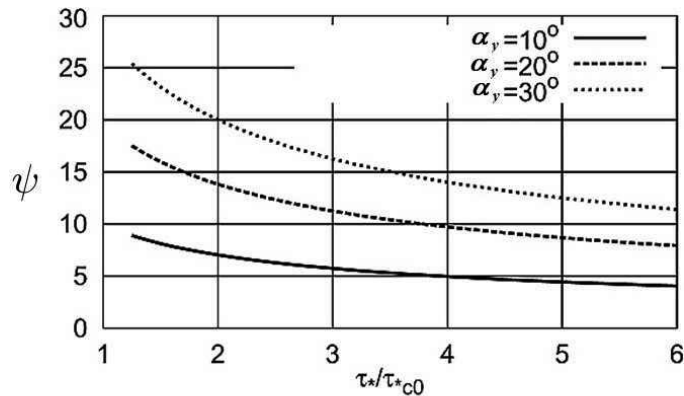


Figure 60. The average direction of bedload motion on a sloping bed, defined by the angle ψ , is plotted versus Shields stress τ_* , scaled by the critical Shields stress for incipient motion on a horizontal bed τ_{*co} , for different values of the lateral bed inclination α_y and vanishing longitudinal bed inclination α_x . The computations have been carried out by setting $\sqrt{\tau_{*cd}} = 0.7\sqrt{\tau_{*co}}$ and $f_{zP} = 11.5$. Modified from Seminara *et al.* (2002).

The general form of the average bedload flux per unit width

Having determined the average particle speed v_P , we may now write a *general relationship for the average bedload flux per unit width* Q_s^b in terms of the *average areal concentration of saltating particles* (volume of sediment particles in motion per unit area) C_a :

$$Q_s^b = C_a v_P \left[\cos \psi \hat{\tau} + \sin \psi (\hat{n} \times \hat{\tau}) \right]. \quad (397)$$

As already discussed in Section 3.3.2, predicting the areal concentration C_a is still a fairly open issue. The only simple tool proposed in the literature is based on the *Bagnold hypothesis* discussed in Section 3.3.2. Let us recall that essentially Bagnold notes that *the intensity of the clear water bed shear stress τ is reduced in the saltation layer by the transfer of momentum from the liquid to the solid phase*. As the number of particles mobilized by the stream increases, the residual shear stress at the bed interface decreases. This observation motivated the Bagnold assumption: *a sufficient number of particles must be entrained by the stream, such that the residual fluid shear stress at the bed drops to the critical value for particle motion*. However, as already pointed out in Section 3.3.2, this assumption is somewhat contradictory. Indeed, it stipulates that the rate of particle entrainment is determined by a constraint whereby *the bed interface should be in static equilibrium*. On the contrary, we know that *dynamic equilibrium* of the granular bed is maintained by a balance between entrainment and deposition of grains and *entrainment is only possible provided the mean residual fluid shear stress at the bed exceeds the critical value*.

Seminara *et al.* (2002) have proved that the above intuitive arguments do have a physical basis, as Bagnold constraint is found to fail when applied to sloping beds with lateral bed inclination exceeding some limiting value well below the angle of repose. The mathematical demonstration of this failure is rather long and we refer the interested reader to the above paper. The failure of the Bagnold criterion to predict an areal concentration of equilibrium bed load transport even on relatively mild transverse slopes clearly demonstrates that the criterion cannot be correct, even in the case of a nearly horizontal bed. This is why Seminara *et al.* (2002) concluded that *Bagnold hypothesis should be abandoned in favor of an alternative entrainment formulation*. Such a formulation, which was proposed by Parker *et al.* (2003) and further implemented by Francalanci and Solari (2008), is not described here. The interested reader is referred to the latter papers.

A much simpler approach, which allows one to get advantage of the present general formulation valid for arbitrarily sloping beds without embarking in the complex issue of guessing the structure

of the entrainment and deposition functions, was presented by Seminara *et al.* (2001b) and is outlined below. Specifically, this approach is based on the general form of the bedload relationship (397), which can be written in the dimensionless form:

$$\tilde{Q}_s^b = C_a \frac{\tilde{v}_P}{d} \left[\cos \psi \hat{\tau} + \sin \psi (\hat{\mathbf{n}} \times \hat{\tau}) \right], \quad (398)$$

or, recalling the equation (394):

$$\tilde{Q}_s^b = \frac{C_a}{d} f|_{z_P} \sqrt{\tau_*} \mathcal{A}(\psi; \alpha_x, \alpha_y) \left[\cos \psi \hat{\tau} + \sin \psi (\hat{\mathbf{n}} \times \hat{\tau}) \right]. \quad (399)$$

The major issue of predicting the structure of the areal concentration is then solved on the basis of the following arguments.

The excess residual stress acting on the bed interface seems to be the most reasonable candidate to measure the residual turbulent activity present close to the interface, hence the ability of the stream to produce the turbulent events (sweeps and inward interactions) which are the major hydrodynamic agents of bedload transport. It is then instructive to reinterpret detailed experimental results on bedload transport under uniform controlled conditions (e.g. Luque and Van Beek, 1976) in the light of the above viewpoint. For a uniform stream flowing on a planar bed the modulus of the residual stress τ_r , acting at the bed interface is readily calculated in the form:

$$\tau_r = \tau - \mu_d (\varrho_s - \varrho) g C_a, \quad (400)$$

or, with the help of simple manipulations,

$$\tau_{*r} = \tau_* - \mu_d \frac{C_a}{d} \quad (401)$$

in dimensionless form.

On physical ground, it is reasonable to expect that C_a is a nonnegative, monotonically increasing function of $(\tau_{*r} - \tau_{*c})$, with τ_{*c} critical value of the Shields stress evaluated with the local values of the longitudinal and lateral slopes. According to this hypothesis, in the presence of any bedload transport, the residual fluid Shields stress at the bed τ_{*r} must exceed the threshold value τ_{*c} . Equilibrium conditions are not reached when the fluid shear stress at the bed reaches the threshold value, but rather when the entrainment rate of bed particles into the bed load layer equals the deposition rate of bed load particles onto the bed. This condition implies a *dynamic equilibrium rather than a static equilibrium* at which no bed particles can be entrained at all.

As a first approximation, the structure of the function C_a can be assumed to coincide with that obtained by Luque and Van Beek (1976) for the plane case. In other words, the sloping character of the bed would affect the hydrodynamics and the direction of sediment particles, but it would leave the dependence of particle areal concentration on the local excess of the residual Shields stress unaltered. Conversely, the critical Shields stress is assumed to depend on the local values of the longitudinal and lateral slopes. This scheme is readily implemented using the expressions for \tilde{Q}_s^b and v_P obtained by Luque and Van Beek (1976) in the case of plane bed ($\tilde{Q}_s^b = \Phi^b$). One thus finds the following relationship for C_a :

$$C_a = 0.93 d \frac{(\tau_* - \tau_{*c})^{3/2}}{\sqrt{\tau_*} - 0.7 \sqrt{\tau_{*c}}}. \quad (402)$$

Note that the areal concentration tends to vanish as $\tau_* \rightarrow \tau_{*c}$ and becomes proportional to τ_* as $\tau_* \rightarrow \infty$. Recall, however, that the experimental results of Luque and Van Beek (1976) apply to the case of fairly low Shields stresses only. Below, we discuss the more recent experimental observations of Francalanci and Solari (2007) which substantiate the simplified approach described above.

The output of the above analysis is a simple calculation method for a bed with finite slope in an arbitrary direction. Feeding (402) into (399) and recalling the expression (395) for \mathcal{A} , one ends up with a relationship which gives the bedload flux per unit width for given external Shields stress, longitudinal and lateral slopes, once the angle ψ is evaluated from the implicit relationship (396). The recent work of Francalanci and Solari (2008) simplifies further the above procedure as it provides an explicit analytical approximation for ψ , of the general form:

$$\psi = \psi_1(\theta, \varphi) \left[\frac{\tau_*}{\tau_{*c0}} \right]^{\psi_2(\theta, \varphi)}, \quad (403)$$

where ψ_1 and ψ_2 are functions estimated from laboratory experiments while the critical Shields stress for incipient sediment entrainment τ_{*c0} may be determined through the relation (182).

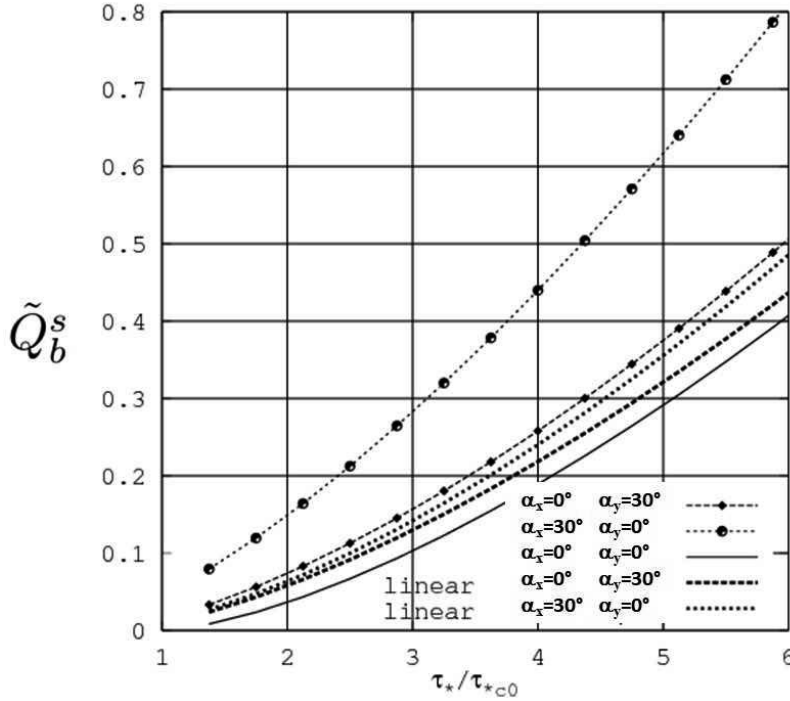


Figure 61. The dependence of \tilde{Q}_b^s on the parameter τ_*/τ_{*c0} as predicted by the nonlinear theory of Seminara *et al.* (2000) is compared with the linear predictions for various combinations of streamwise and lateral slopes. The computations have been carried out by setting $d=1\text{ mm}$, $\phi=40^\circ$, $c_D=0.32$, $c_L/c_D=0.85$, $\mu_d=0.8$. Modified from Seminara *et al.* (2000).

Before we discuss the experimental verification of the latter approach, it is instructive to ascertain the importance of nonlinear effects by performing a comparison between results of the present fully nonlinear formulation for bed load transport on finite slope and their linear approximation for small slopes. This comparison is shown in Figure 61 where \tilde{Q}_b^s is plotted against the ratio τ_*/τ_{*c0} for various values of α_x and α_y . The linear and nonlinear formulations obviously yield the same result for the case $\alpha_x = \alpha_y = 0^\circ$. On the other hand, the linearized formulation invariably tends to under-predict the transport rate on non negligible bed slopes: moderately when $\alpha_x = 0^\circ$ and $\alpha_y = 30^\circ$; strongly when $\alpha_x = 30^\circ$ and $\alpha_y = 0^\circ$.

Test of the nonlinear theory against experimental data

We now show to what extent the above approach has found a consistent substantiation based on laboratory observations. We refer to the recent detailed work of Francalanci (2005) (but see also

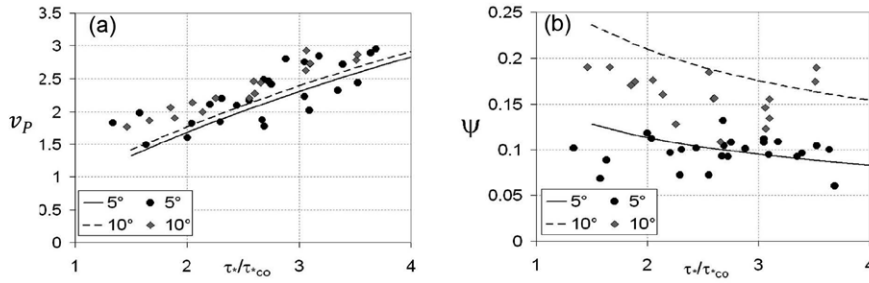


Figure 62. Comparison between the experimental values (Francalanci, 2005) of the particle speed v_P (a) and the deviation angle ψ (b) of particle trajectories (symbols) and the theoretical results of Seminara *et al.* (2002) (solid and dashed lines): α_x fixed (5°) and α_y variable (5° , 10°) (reproduced from Figure 2.18 of Francalanci, 2005).

Francalanci and Solari, 2007), who carried out a series of accurate tests in a laboratory tilting flume with the sediment bed composed of steel particles shaped as fairly flat disks. Techniques based on volumetric sampling, laser Doppler anemometry, image acquisition and processing were used to track bedload particles saltating over the bed. The collected data were plotted in terms of the average properties of the collective motion of sediment particles, for various hydraulic conditions and different longitudinal and lateral bed slopes. Finally, a comparison was performed with theoretical results.

The Figure 62 shows a comparison between the experimental values of the particle speed v_P and the deviation angle ψ of particle trajectories and the predictions of Seminara *et al.* (2002) for a few values of the longitudinal and lateral slopes. Although scattering of experimental data is large, observations confirm that the deviation angle tends to increase with the lateral slope and to decrease as the longitudinal slope and/or the Shields stress increase. Also, the weak predicted effect of longitudinal and lateral slope on the intensity of particle velocity is qualitatively confirmed.

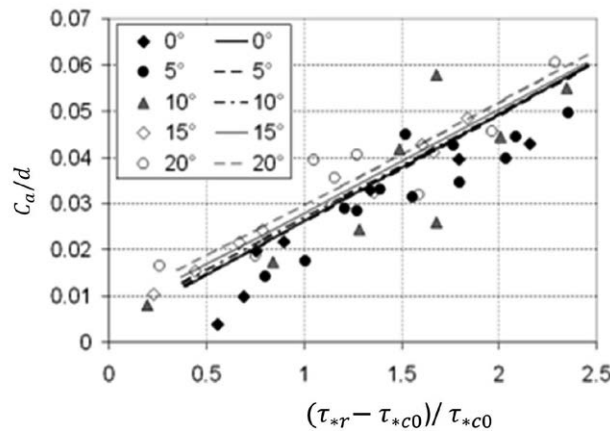


Figure 63. Comparison between the experimental values of the average areal concentration of sediment particles (symbols) and those predicted by the relationship for C_a employed by Seminara *et al.* (2001b) (solid and dashed lines). α_x fixed (5°) and various α_y (0° , 5° , 10° , 15° , 20°) (modified from Figure 2.21 of Francalanci, 2005).

In the Figure 63 the average areal concentration of sediment particles C_a obtained experimentally is compared with the relationship proposed by Seminara *et al.* (2001b). Note that, in the abscissa, the excess *residual* Shields stress $\tau_{*r} - \tau_{*c}$ rather than the excess *outer* Shields stress $\tau_* - \tau_{*c}$ is plotted. Moreover, the critical Shields stress τ_{*c} is corrected for the effects of longitudinal and lateral slopes. Observations confirm a fairly linear dependence of C_a on the excess residual stress and its negligible dependence on the lateral slope. On the contrary C_a appears to depend on the longitudinal slope more strongly than the theory predicts.

Finally, Francalanci and Solari (2007) also show that predictions for \tilde{Q}_b^s , v_P and ψ obtained from the linear formulation compare less satisfactorily with observed values than results obtained from the nonlinear theory. In particular, the particle speed is invariably under-predicted whilst the deviation angle is consistently over-predicted.

5. The basic state: Straight channels at equilibrium

Conceptually, rivers may be modeled as systems in a state of *quasi-equilibrium*, i.e. such that flow perturbations relative to some *equilibrium state* let the system evolve on spatial-temporal scales much larger than the hydrodynamic scale. As a preliminary step to our future efforts to understand the formation and evolution of fluvial patterns, in the present Chapter we attempt to provide a rational answer to the question: does a straight equilibrium configuration of an erodible channel actually exist?

5.1. The basic *equilibrium* profile of straight channels

5.1.1 The notion of morphodynamic equilibrium

Field evidence suggests that, on relatively small time scales (of the order of few years or decades) and in the absence of major anthropogenic effects, the average bed profile of rivers may be *in quasi equilibrium*. Loosely speaking, this implies that the laterally averaged elevation of the active bed $\bar{\eta}$, which is in general a function of the longitudinal coordinate x and time t , does not experience significant temporal variations except for fluctuations associated with a variety of natural factors.

The terminal reach of the Magra river (Italy), which will be used as a test case in this Chapter, provides a useful example of a river in quasi-equilibrium. The Magra River is located in the Northern part of Tuscany, a region of central Italy (Figure 64a). Details of the general characteristics of the Magra catchment can be found in Surian and Rinaldi (2003). It suffices here to mention that the catchment has an area of 1700 km^2 and consists of two distinct basins, the Vara River (length of about 65 km , area of 600 km^2) on the west side and the upper-middle Magra on the eastern side (length of about 54 km). The two basins merge into the lower Magra (length of about 16 km) which forms a microtidal estuary ending into the Ligurian sea, characterized by very small tidal oscillations (amplitude around 15 cm). The climate of the area is temperate, with mean and maximum annual precipitations around 1700 mm and 3000 mm , respectively. The mean of the maximum annual daily discharges recorded at the Calamazza station is $683 \text{ m}^3 \text{ s}^{-1}$. The monitoring station is located on the Magra, upstream of the Vara-Magra confluence, and refers to a draining area of 932 km^2 . The channel morphology varies from wandering in the upper basin to sinuous along the terminal reach (Figure 64b). Below we focus on the latter region, denoted by A in Figure 64a, where detailed and systematic surveys have been performed. It displays significant width variations and has a sandy bottom characterized by a mixture of fine and coarse sand (Figure 64b).

The morphology of the Magra river has undergone significant changes in the first half of the 20th century as a result of several anthropogenic factors, namely the construction of protection works, including a sequence of spur dykes in the lower reach, as well as few small dams and the massive exploitation of river sediments through extensive mining. As a result, the channel has narrowed and the braided pattern has slowly evolved into a transitional pattern, whilst strong bottom degradation occurred. The coastline underwent a significant regression, which stopped only around 1950 when it had attained a configuration quite close to the present one.

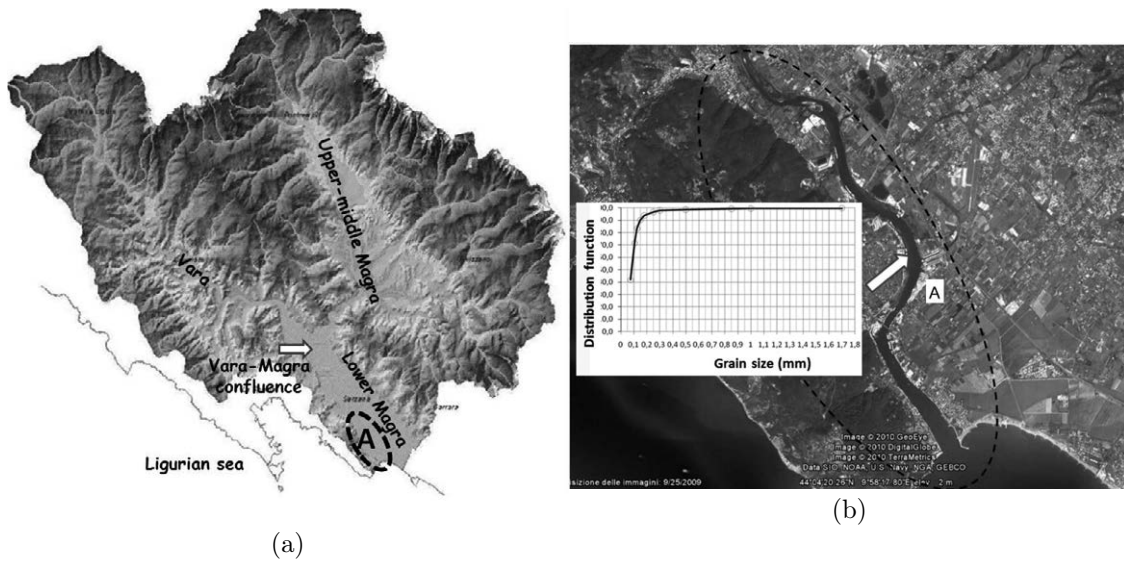


Figure 64. (a) The Magra river basin and the location of the investigated reach (dashed ellipse). (b) The terminal reach of the Magra river and the grain size distribution function.

This notwithstanding, the bed profile of the terminal reach of the river has recently been quite stable, as shown in Figure 65, where surveys performed in 2003, 2008 and 2010 are compared. It is important to note that, during this period, the Magra River experienced various flood events. Most notably, two large floods occurred in January 2009 and December 2009. They were characterized by peak discharges in the lower Magra of about $3550 \text{ m}^3 \text{ s}^{-1}$ and $4050 \text{ m}^3 \text{ s}^{-1}$ (Seminara *et al.*, 2011), corresponding roughly to 25 and 30 years recurrence interval, respectively. An even larger flood was experienced in October 2011, with an estimated peak of $4200 \text{ m}^3 \text{ s}^{-1}$ at the Calamazza station (recurrence interval ~ 100 years) and $5000 \text{ m}^3 \text{ s}^{-1}$ in the terminal reach (recurrence interval ~ 60 years, Seminara *et al.*, 2012).

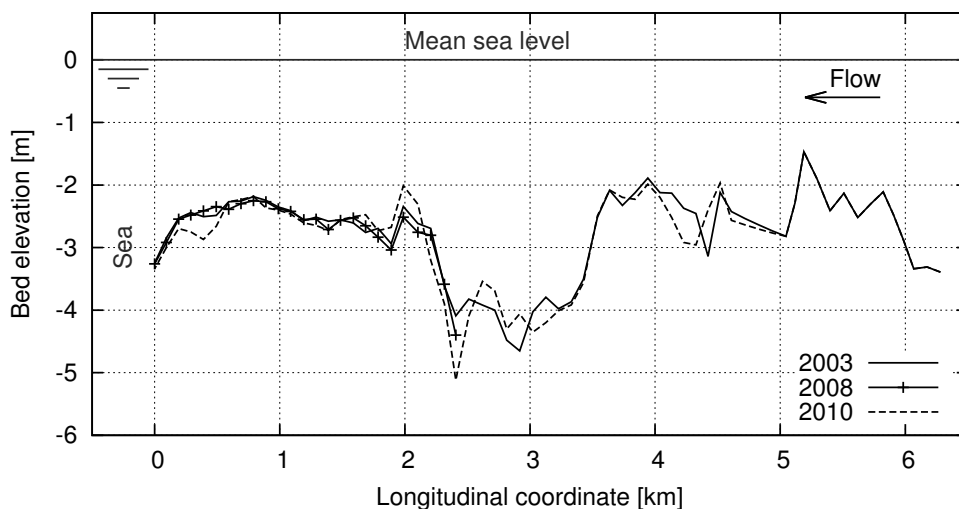


Figure 65. Bed profiles of the terminal reach of the Magra River (Italy) according to topographical surveys performed in 2003, 2008 and 2010 (reproduced from Bolla Pittaluga *et al.*, 2014a).

Note that the notion of *morphodynamic equilibrium* employed above relies on two related qualifications: the observed *equilibrium is only approximate* (quasi-equilibrium) and refers to the *cross-sectionally averaged bed elevation* rather than to its local value. Indeed, in the real world, rivers display spatial variations and temporal fluctuations of the flow properties acting on a variety of scales. The smallest scales are associated with the formation of free and forced bedforms: *free bedforms* arise from instabilities of the bed interface and are typically migrating features (see Chapter 6); *forced bedforms* are generated by end conditions or by deviations of channel geometry from the straight cylindrical configuration and are typically steady features. Larger scales are associated with variations of the driving forces, namely water discharge and sediment flux, forced by a variety of possible events: floods, natural seasonal oscillations, slow processes of degradation-aggradation induced by variations of sediment supply or abrupt variations of channel geometry (e.g. meander cutoffs), as discussed in later Chapters of this Monograph. At even larger time scales, the occurrence of geologic phenomena may strongly perturb the state of the river, leading to drastically different configurations.

In spite of such a wide spectrum of perturbations, the paradigm of morphodynamic equilibrium, defined in some appropriate *average* sense, proves quite instructive. In the classical geomorphological literature, equilibrium is traditionally associated with the notion of *formative discharge* of a river: a notion, which essentially assumes that the unsteady forcing on the river is morphologically equivalent to some effective steady forcing. More precisely, Copeland *et al.* (2000) define the formative discharge as a theoretical discharge that, maintained indefinitely, would produce the same channel geometry as the natural long-term hydrograph. This representative channel-forming discharge has been used mainly in *hydraulic geometry* theories to define the main morphological characteristics of alluvial rivers (Leopold and Maddock, 1953).

Various methods have been proposed in order to identify the channel-forming discharge including *bankfull* discharge, specified *recurrence interval* discharge, and *effective* discharge. Each of them can be calculated using a procedure based on field indicators. The *bankfull discharge* is defined as the flow discharge which fills the channel to the tops of the banks. The top of the bank is determined through several field indicators which, however, are not necessarily of general applicability nor they are free from subjectivity (Williams, 1978). A specific *recurrence interval discharge* has been associated with the bankfull stage, typically corresponding to a recurrence interval of the annual flood of approximately 1 to 2.5 years with the 1.5-year recurrence flood considered as a reasonable value (Leopold, 1994). However, this criterion is not verified in many rivers (Williams, 1978) implying that the specified recurrence discharge generates poor estimates of the formative discharge. The *effective discharge* is defined as the increment of discharge that transports the largest proportion of the annual sediment load over a period of many years (Andrews, 1980). It incorporates the idea introduced by Wolman and Miller (1960) according to which the channel-forming discharge, a function of both the magnitude of sediment-transporting events and their frequency of occurrence, may be identified as the value of the discharge which maximizes the product of the flow frequency and the sediment transport rate. A large amount of flow and sediment data is required to estimate this discharge, which makes it difficult to exploit this notion in many cases. This notwithstanding, it turns out that a fully mechanistic approach does support this definition, which turns out to be more easily implemented by means of numerical simulations (Bolla Pittaluga *et al.*, 2014a; Lanzoni *et al.*, 2015).

It is perhaps fair to state that the availability of field data and the characteristics of the site strongly influence the selection of the appropriate method and often limit the reliability of the final estimate of the formative discharge.

Below, we attempt to found the notion of morphodynamic equilibrium (and related formative discharge) on a mechanistic basis, making use of the available knowledge on morphodynamic modeling. In order to achieve this goal, we start treating the simplest configuration: a cylindrical cohesionless channel with constant slope subject to steady forcing, namely constant flow and sediment supply. Under these fairly ideal, yet conceptually important conditions, it will appear that a rigorous equilibrium state can be defined. This equilibrium configuration will play the role of the *basic morphodynamic state of the channel* for the variety of investigations required to explain the formation of fluvial patterns discussed in the present Monograph.

5.1.2 Mathematical formulation of 1D morphodynamic equilibrium

Strictly speaking, an erodible stream is in morphodynamic equilibrium provided its boundary does not undergo any temporal change. Hence, its bed should neither aggrade nor degrade ($\partial\eta/\partial t \equiv 0$) and its banks should neither retreat nor advance. Below, we restrict our attention on the former constraint and treat river banks as fixed at this stage. The conditions required for erodible banks not to retreat nor to advance determine the *equilibrium width* of erodible channels and will be discussed in Section 5.1.4.

Strict equilibrium naturally requires also steady hydrodynamic conditions. The 1D governing equations of morphodynamics, namely the de Saint Venant equation (150) derived in Section 2.5 and the 1D Exner equation (250) derived in Section 4.1, then reduce to the following form:

$$Q = \text{constant}, \quad (404)$$

$$Q_s = \text{constant}, \quad (405)$$

$$\frac{Q^2}{\Omega} \frac{d}{dx} \left(\frac{\beta_{cor}}{\Omega} \right) + g \frac{d\bar{H}}{dx} + \bar{C}_f \frac{U|U|}{R_h} = 0. \quad (406)$$

This system must be solved with the help of some closure algebraic relationship for the cross-sectionally averaged sediment flux $Q_s(x)$ which can be cast in the following general form:

$$Q_s = Q_s[\bar{\tau}_*(x); R_p], \quad (407)$$

with R_p particle Reynolds number and $\bar{\tau}_*(x)$ laterally averaged Shields stress:

$$\bar{\tau}_* = \bar{C}_f \frac{U^2}{(s-1)gd}. \quad (408)$$

Here, as usual, d is the sediment size assumed uniform at this stage. Note that the problem of morphodynamics is coupled to the hydrodynamic problem through the equation (408). Also note that the constraint (405) and the constitutive relationship (407) for given uniform grain size distribution imply that, at morphodynamic equilibrium, the following condition must also be satisfied:

$$\bar{\tau}_* = \text{constant}. \quad (409)$$

Finally, a boundary condition for one of the unknown functions $\bar{H}(x)$ or $\bar{\eta}(x)$ is required and may indifferently be assigned either upstream or downstream.

The equation (405) immediately suggests that there are two simplest conditions which would ensure the requirement of bed equilibrium. A first (trivial) condition is that *the sediment discharge vanishes everywhere throughout the reach investigated*. In other words, the average bed shear stress should nowhere exceed the threshold value for sediment entrainment as bedload or suspended load. In nature, this condition is indeed met, but only at very low stage. A second, less trivial, condition would be that *the total sediment discharge does not vanish but keeps spatially constant* throughout the investigated reach. This is a *dynamic condition* which can be readily analyzed under steady forcing. Below, we discuss systematically the consequences of the latter constraint and show that a distinct equilibrium state is associated with any given set of forcing conditions, namely given values of flow and sediment discharges.

5.1.3 The case of cylindrical channels

If the geometry of the channel is perfectly cylindrical the constraint (409), along with flow continuity equation (404), implies that the cross-sectional area and, consequently, the average flow depth ($D = \bar{H} - \bar{\eta}$) and the average fluid speed must also be constant throughout the reach. Recalling the momentum equation (406) we are then led to the conclusion that the slope of the free surface ($-d\bar{H}/dx$), which is equal to the channel slope S , must keep constant. In other words, *the flow must be strictly uniform* and the stream adjusts its slope and its flow depth to the driving inputs Q and Q_s .

This can be better understood referring to a straight wide rectangular channel with constant width. Then the bottom width ($2B_b$) is constant and equal to the width of the free surface ($2B$). Moreover, the Shields stress τ_* is uniformly distributed in the lateral direction (except within the boundary layers at the bank), such that, as a first approximation, one may set $\bar{\tau}_* \simeq \tau_*$. The constraints (404) and (405) then lead to the stricter requirements that the flow discharge per unit width Q and the depth integrated sediment flux per unit width Q_s should also be constant. Using Chézy law with Strickler closure for the conductance to express the constraint (404) and a general relationship for the transport capacity needed to express the constraint (405), we write:

$$Q = k_s \sqrt{S_e} \mathcal{D}_e^{5/3}, \quad Q_s = \sqrt{(s-1)gd^3} n (\tau_{*e} - \tau_{*c})^m, \quad (410)$$

with k_s Strickler parameter, \mathcal{D}_e equilibrium flow depth, S_e equilibrium slope, τ_{*e} equilibrium Shields stress, n empirical constant and m empirical exponent larger than one. Simple algebraic manipulations with the help of (408) then give:

$$S_e = \tilde{Q}^{-6/7} \tau_{*e}^{10/7}, \quad \frac{\mathcal{D}_e}{(s-1)d} = \tilde{Q}^{6/7} \tau_{*e}^{-3/7}, \quad (411)$$

where \tilde{Q} is the dimensionless flow discharge per unit width, which reads:

$$\tilde{Q} = \frac{Q}{k_s [(s-1)d]^{5/3}}. \quad (412)$$

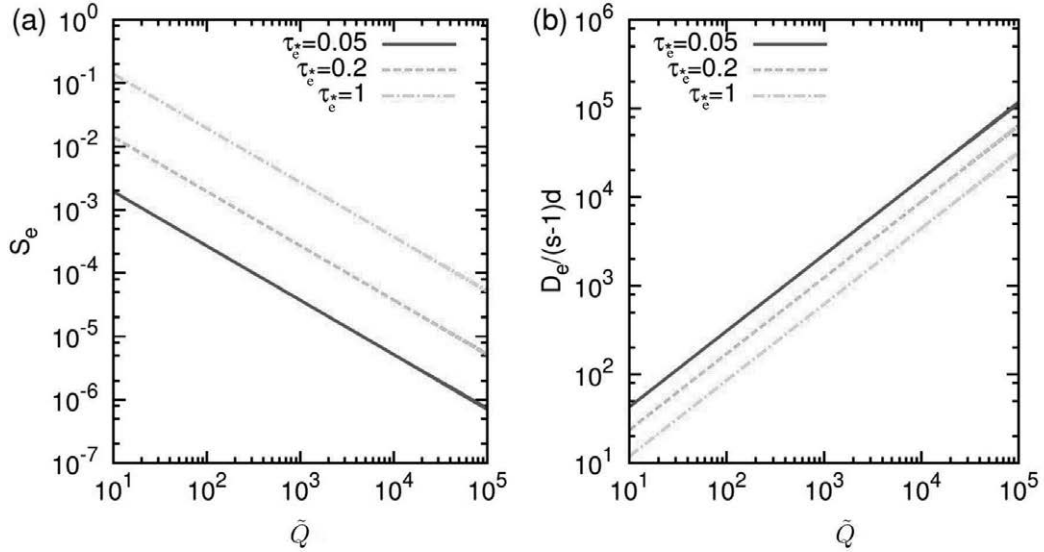


Figure 66. Equilibrium values of (a) the slope S_e and (b) the dimensionless flow depth $\mathcal{D}_e/(s-1)d$ are plotted in terms of the dimensionless flow discharge per unit width, \tilde{Q} , for different values of the Shields stress at equilibrium, τ_{*e} . We have chosen $m = 3/2$ corresponding to a Meyer Peter-Müller type of transport formula.

Hence, as shown in Figure 66, for given fluid discharge and average grain size, an increased sediment supply (associated with an increased Shields stress) tends to steepen the channel. On the contrary, for given sediment supply and average grain size, an increased fluid discharge tends to flatten the channel. Moreover, as the grain diameter increases for given flow discharge, the dimensionless quantity \tilde{Q} decreases and, consequently, the equilibrium slope increases.

Of course, we may establish equilibrium relationships similar to those reported in (411) for any pair of variables chosen among $\mathcal{D}_e, S_e, Q, Q_s$ as functions of the remaining two. In particular, the reader will readily show that:

$$\frac{Q_s}{\sqrt{(s-1)gd^3}} = n [\tilde{Q}^{3/5} S_e^{7/10} - \tau_{*c}]^m, \quad \frac{\mathcal{D}_e}{(s-1)d} = \left(\frac{\tilde{Q}}{\sqrt{S_e}} \right)^{3/5}. \quad (413)$$

The latter relationships may be of help to estimate the *formative sediment discharge* in equilibrium with some observed slope. The above simple results have a number of implications.

A simple application: Change of equilibrium slope arising from a step change in sediment size

As distinct equilibria are associated with any given set of forcing conditions, namely a given grain size distribution, a given channel geometry and specific values of the flow and sediment discharges *per unit width*, a step change in sediment size leads to a corresponding change of the equilibrium slope.

Let us illustrate this point considering a river characterized by a step change in the average grain size from d_0 upstream to d downstream (e.g. due to a gravel-sand transition). Assume the upstream reach is in a state of morphological equilibrium for prescribed values of the flow discharge per unit width Q_0 and of the depth integrated sediment flux per unit width Q_{s0} . Following Meyer-Peter and Müller (1948), the Strickler coefficient k_s may be taken as inversely proportional to the 1/6 power of the average grain size and the exponent of the transport formula m equal to 3/2.

Employing the equilibrium relationships (411) for the flow depth and setting $Q = Q_0$, one immediately obtains:

$$\frac{\mathcal{D}_e}{\mathcal{D}_{e0}} = \left(\frac{d}{d_0} \right)^{-2/7} \left(\frac{\tau_{*e}}{\tau_{*e0}} \right)^{-3/7}, \quad \frac{S_e}{S_{e0}} = \left(\frac{d}{d_0} \right)^{9/7} \left(\frac{\tau_{*e}}{\tau_{*e0}} \right)^{10/7}. \quad (414)$$

On the other hand, recalling (408), one readily finds that:

$$\frac{\tau_{*e}}{\tau_{*e0}} = \left(\frac{d_0}{d} \right)^{2/3} \left(\frac{\mathcal{D}_{e0}}{\mathcal{D}_e} \right)^{7/3}. \quad (415)$$

Next, setting $Q_s = Q_{s0}$, with the help of (410) one finds:

$$\frac{\tau_{*e}}{\tau_{*e0}} = \frac{d_0}{d} \left(1 - \frac{\tau_{*c}}{\tau_{*e0}} \right) + \frac{\tau_{*c}}{\tau_{*e0}}. \quad (416)$$

From (415) and (416) we then derive a relationship between the upstream and downstream flow depths as a function of d_0/d and τ_{*c}/τ_{*e0} :

$$\frac{\mathcal{D}_e}{\mathcal{D}_{e0}} = \left(\frac{d}{d_0} \right)^{-2/7} \left[\frac{d_0}{d} \left(1 - \frac{\tau_{*c}}{\tau_{*e0}} \right) + \frac{\tau_{*c}}{\tau_{*e0}} \right]^{-3/7}. \quad (417)$$

Finally, substituting from (416) into the expression for S_e/S_{e0} in (414) we find the following relationship between the upstream and downstream slopes:

$$\frac{S_e}{S_{e0}} = \left(\frac{d}{d_0} \right)^{9/7} \left[\frac{d_0}{d} \left(1 - \frac{\tau_{*c}}{\tau_{*e0}} \right) + \frac{\tau_{*c}}{\tau_{*e0}} \right]^{10/7}. \quad (418)$$

The latter two relationships are plotted in Figure 67.

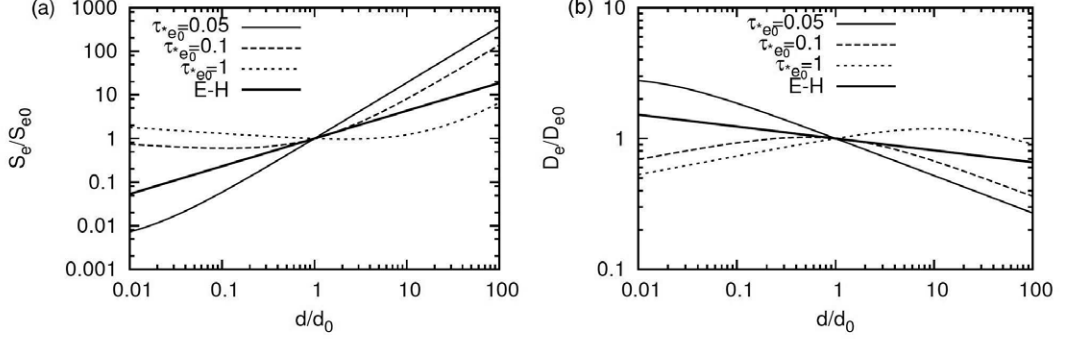


Figure 67. Ratios between upstream and downstream equilibrium values of (a) the slope S_e and (b) the flow depth D_e in response to a step change of the average grain size d . The black line is obtained employing the Engelund and Hansen predictor for the total load. The other lines refer to the case of dominant bed load and are obtained using Wong and Parker (2006) predictor.

Two simple limits of (417) and (418) are instructive. In the weak sediment transport limit ($\tau_{*c}/\tau_{*e0} \rightarrow 1$), one readily finds that $D_e/D_{e0} \rightarrow (d/d_0)^{-2/7}$ and $S_e/S_{e0} \rightarrow (d/d_0)^{9/7}$. Hence: the bed slope decreases and the flow depth increases if sediment size decreases and vice versa.

The opposite trend is obtained in the limit of intense sediment transport ($\tau_{*c}/\tau_{*e0} \rightarrow 0$) as $D_e/D_{e0} \rightarrow (d/d_0)^{1/7}$ and $S_e/S_{e0} \rightarrow (d/d_0)^{-1/7}$. However, in this limit, sediment transport is not restricted to bedload: transport in suspension is likely to occur. The simplest way to account for this effect is to use a transport relationship able to account for the total load. Indeed, if Engelund and Hansen formula is employed and the Strickler coefficient k_s is still taken to be inversely proportional to the 1/6 power of the average grain size, the reader will readily prove that the equilibrium relationships (417) and (418) become:

$$\frac{D_e}{D_{e0}} = \left(\frac{d}{d_0}\right)^{-1/11}, \quad \frac{S_e}{S_{e0}} = \left(\frac{d}{d_0}\right)^{7/11}. \quad (419)$$

They show that the bed slope decreases and the flow depth increases (albeit quite weakly) if the sediment size decreases and vice versa, a result which applies to any value of the Shields stress and is also plotted in Figure 67. This result is indeed consistent with field observations of sand bed rivers at bankfull stage. As it will be seen in Section 5.2.4 (see equation (463)), for given bankfull discharge, the bankfull depth and the average slope turn out to be proportional to powers of the median grain size with exponents -0.155 and 0.691 , respectively. This dependence is similar to that expressed by (419), with quantitative differences likely due to the fact that the exponent of the resistance relationship observed in the field for sand bed rivers at bankfull stage turns out to be 0.463 , much larger than the value $1/6$ adopted to derive (419).

The picture emerging from the above analysis, is based on the assumption of cylindrical channels. Of course, real rivers are hardly cylindrical. The next step is then to ascertain whether the notion of morphodynamic equilibrium can be extended to non cylindrical channels.

5.1.4 The case of non cylindrical channels: rectangular channels with variable width

The non cylindrical character of natural channels is felt by the bed profile at equilibrium, as the stream responds to variations of the cross-sectional area by modifying the flow depth such to keep the total sediment discharge constant. We illustrate this mechanism by analyzing firstly a simple configuration consisting of a rectangular channel with variable width, where variations of cross-sections arise only from channel narrowing or channel widening. This case has the advantage to be amenable to fully analytical treatment. In the next Section, resorting to numerical tools, we show that similar ideas apply to the irregular channel geometries observed in nature.

Let us consider a wide rectangular channel with variable width. The bottom width $2B_b$ then coincides with the width of the free surface $2B$ and we may simply write:

$$\mathcal{D}(x) = \bar{H} - \bar{\eta}, \quad \Omega = 2B(x)\mathcal{D}(x). \quad (420)$$

It is also convenient to define an *average configuration* characterized by an average channel width $2B_0$, such that, for given flow and sediment discharges, we may define an equilibrium slope S_{e0} and a uniform flow depth \mathcal{D}_{e0} .

The mechanism of morphodynamic equilibrium is immediately illustrated by imposing the constraint (405) that the solid discharge keeps constant along the channel. Adopting the general transport formula (410) with m constant, this constraint becomes:

$$\left(\frac{\tau_* - \tau_{*c}}{\tau_{*e0} - \tau_{*c}} \right)^m = \frac{B_0 n_0}{B n}, \quad (421)$$

having denoted by n_0 the coefficient of the transport relationship evaluated at equilibrium. Below, we will adopt a Meyer Peter–Müller type of transport formula (with $m = 3/2$ and $n = n_0$) at low Shields stress and Engelund and Hansen relationship (with $m = 5/2$, $n = 0.05/\bar{C}_f$, $n_0 = 0.05/\bar{C}_{f0}$ and $\tau_{*c} = 0$) at high Shields stress.

Note that the weak transport limit is subject to the constraint that transport occurs throughout the whole channel, which is ensured for narrowing channels, where Shields stress increases. On the contrary, for widening channels the Shields stress decreases hence τ_{*e0} must be sufficiently larger than τ_{*c} in order to satisfy the above constraint.

- Flow depth

Simple manipulations with the help of (408) lead to the following relationship:

$$\frac{\mathcal{D}}{\mathcal{D}_{e0}} = \left(\frac{B}{B_0} \right)^{(1/m-2)3/7} \left(\frac{n}{n_0} \right)^{3/(7m)} f^{-3/7}, \quad (422)$$

having denoted by f the following function:

$$f = 1 + \frac{\tau_{*c}}{\tau_{*e0}} \left[\left(\frac{B n}{B_0 n_0} \right)^{1/m} - 1 \right], \quad (423)$$

that is plotted in Figure 68a. The reader will readily show that, for large Shields stress (EH predictor), with \bar{C}_f expressed through the Gauckler-Strichler relation, $f = 1$ and $\mathcal{D}/\mathcal{D}_{e0} = (B/B_0)^{-8/11}$. Moreover, as $\tau_{*c}/\tau_{*e0} \rightarrow 1$ (MPM predictor), $f \rightarrow (B/B_0)^{2/3}$ and $\mathcal{D}/\mathcal{D}_{e0} \rightarrow (B/B_0)^{-6/7}$.

Differentiating (422) one finds:

$$\frac{d\mathcal{D}}{dx} = -\frac{\varphi_f}{\psi_f} \frac{\mathcal{D}}{B} \frac{dB}{dx}, \quad (424)$$

having set:

$$\varphi_f = \frac{3}{7} \left[2 - \frac{1}{m} \frac{1 - \tau_{*c}/\tau_{*e0}}{f} \right], \quad \psi_f = 1 - \frac{3}{7m} \frac{\mathcal{D}}{n} \frac{dn}{d\mathcal{D}} \left[\frac{1 - \tau_{*c}/\tau_{*e0}}{f} \right]. \quad (425)$$

One readily shows that, for low Shields stress (MPM predictor) φ_f is invariably positive (Figure 68b) and $\psi_f = 1$; for large Shields stress (EH predictor) φ_f is still invariably positive ($=24/35$) and $\psi_f = 33/35$. We may thus conclude that *the sign of $d\mathcal{D}/dx$ is opposite to that of dB/dx* , a result independent of whether the channel is steep or mild.

Hence, the equilibrium depth increases if the channel narrows and vice versa it decreases if the channel widens (Figure 69a).

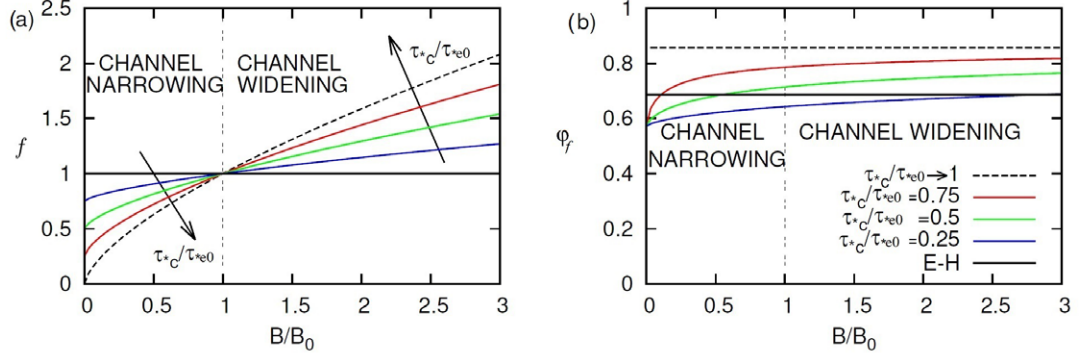


Figure 68. The functions f (equation (423)) and φ_f (equation (425)) are plotted in terms of the width ratio B/B_0 for different values of the ratio τ_{*c}/τ_{*e0} . We have adopted Meyer Peter–Müller type transport formula at low Shields stress ($\tau_{*c}/\tau_{*e0} = 0.25, 0.5, 0.75, \rightarrow 1$) and Engelund and Hansen relationship at high Shields stress ($\tau_{*c}/\tau_{*e0} = 0$).

- *Froude number*

The relationship (422) has some further interesting implications. Denoting by F_r the Froude number, one finds that:

$$\frac{F_r^2}{F_{r0}^2} = \left(\frac{B}{B_0}\right)^{4/7-9/(7m)} \left(\frac{n}{n_0}\right)^{-9/(7m)} f^{9/7}. \quad (426)$$

At low Shields stress (MPM predictor) the equation for the Froude number (426) becomes:

$$\frac{F_r^2}{F_{r0}^2} = \left(\frac{B}{B_0}\right)^{-2/7} \left\{ 1 + \frac{\tau_{*c}}{\tau_{*e0}} \left[\left(\frac{B}{B_0}\right)^{2/3} - 1 \right] \right\}^{9/7}. \quad (427)$$

In particular, in the limit $\tau_{*c}/\tau_{*e0} \rightarrow 1$, (427) becomes:

$$\frac{F_r^2}{F_{r0}^2} = \left(\frac{B}{B_0}\right)^{4/7}. \quad (428)$$

From (428) it follows that a subcritical flow ($F_{r0} < 1$) in a mobile bed channel at equilibrium keeps subcritical ($F_r < 1$) at a channel narrowing, whereas a supercritical flow ($F_{r0} > 1$) keeps supercritical ($F_r > 1$) at a channel widening (Figures 69b and 70). Note that this result applies to channel narrowing-widening sufficiently gradual that flow separation does not occur and one dimensional modeling is appropriate.

At large Shields stress (EH predictor) the equation for the Froude number (426) becomes:

$$\frac{F_r^2}{F_{r0}^2} = \left(\frac{B}{B_0}\right)^{2/35} \left(\frac{D}{D_{e0}}\right)^{-6/35} = \left(\frac{B}{B_0}\right)^{2/11}. \quad (429)$$

The trend predicted by (429) is qualitatively similar to that obtained in the low Shields limit (Figure 70) but with the iso-F curves reversed as small values of B/B_0 are approached. Note, that the above predictions differ significantly from those that one would find in the fixed bed case. This comparison is left to the reader as exercise.

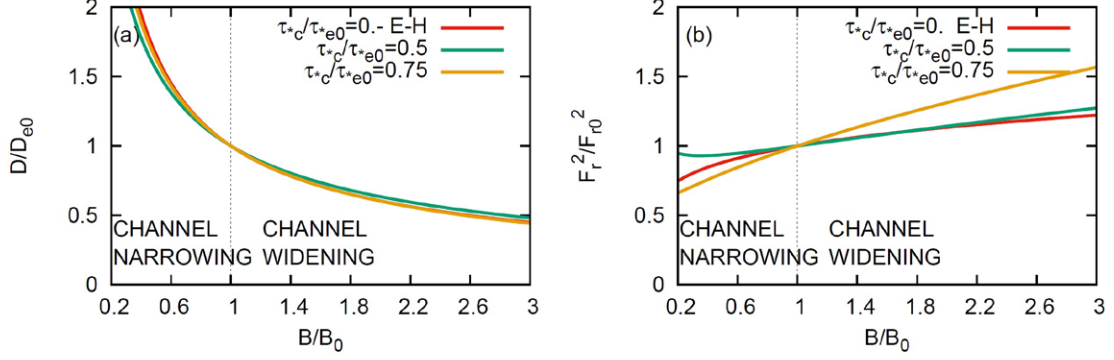


Figure 69. Equilibrium values of ratios of (a) flow depth D/D_{e0} and (b) Froude numbers F_r/F_{r0} as a function of the width ratio B/B_0 for different values of the ratio τ_{*c}/τ_{*e0} . We have adopted Meyer Peter–Müller type transport formula at low Shields stress ($\tau_{*c}/\tau_{*e0} = 0.5, 0.75$) and Engelund and Hansen relationship at high Shields stress ($\tau_{*c}/\tau_{*e0} = 0$).

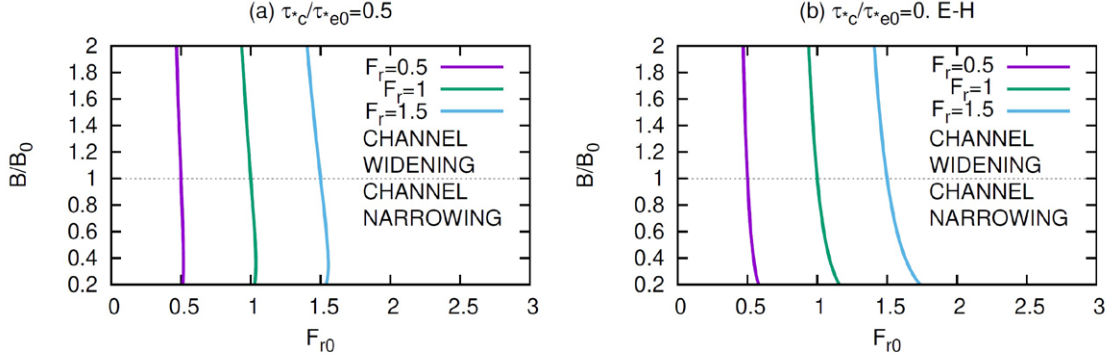


Figure 70. The solid lines describe in the $(F_{r0}, B/B_0)$ plane the iso- F_r curves for mobile bed streams flowing in narrowing or widening channels in equilibrium conditions. (a) $\tau_{*c}/\tau_{*e0} = 0.5$ (MPM predictor); (b) $\tau_{*c}/\tau_{*e0} = 0$ (EH predictor).

- *Free surface profile.*

Let us next examine the effects of channel narrowing–widening on the free surface profiles at equilibrium. We then need to solve the momentum equation. Let us denote by $\bar{H}_1(x)$ the component of free surface elevation driven by width variations and write:

$$\bar{H} = \bar{H}_0 - S_{e0} x + \bar{H}_1(x), \quad (430)$$

where \bar{H}_0 is the average free surface elevation at the cross-section $x = 0$. With the help of (430), the momentum equation (406) becomes an ordinary differential equation for the unknown function $\bar{H}_1(x)$, which reads:

$$\frac{d\bar{H}_1}{dx} = S_{e0} \left(1 - \bar{C}_f \frac{Q^2}{\Omega^2 g D S_0} \right) + \frac{Q^2}{g \Omega^2} \frac{1}{B} \frac{dB}{dx} \left(1 - \frac{\varphi_f}{\psi_f} \right), \quad (431)$$

having assumed the cross-section sufficiently large to allow approximating the hydraulic radius by the flow depth and taking the correction coefficient for fluid momentum β_{cor} equal to one.

Simple algebraic manipulations allow reduction of (431) to the following form:

$$\frac{d\bar{H}_1}{dx} = S_{e0} \left[1 - \left(\frac{F_r}{F_{r0}} \right)^2 \left(\frac{\mathcal{D}_0}{\mathcal{D}} \right)^{1/3} \right] + F_r^2 \frac{\mathcal{D}}{B} \frac{dB}{dx} \left(1 - \frac{\varphi_f}{\psi_f} \right). \quad (432)$$

With the help of (426) and (422) and replacing the undisturbed slope S_{e0} by the quantity $F_{r0}^2 \bar{C}_{f0}$, this equation is readily integrated in the form:

$$\bar{H}_1(x) = F_{r0}^2 \mathcal{D}_{e0} \left[\frac{L_r \bar{C}_{f0}}{\mathcal{D}_{e0}} \mathcal{I}_1^{H_1} + \mathcal{I}_2^{H_1} \right]. \quad (433)$$

Here, $\mathcal{I}_1^{H_1}$ and $\mathcal{I}_2^{H_1}$ are the following dimensionless quantities:

$$\mathcal{I}_1^{H_1}(\tilde{x}) = \int_0^{\tilde{x}} \left[1 - \tilde{B}^{6/7-10/(7m)} \left(\frac{n}{n_0} \right)^{-10/(7m)} f^{10/7} \right] d\tilde{x}', \quad (434a)$$

$$\mathcal{I}_2^{H_1}(\tilde{x}) = \int_0^{\tilde{x}} \tilde{B}^{-9/7-6/(7m)} f^{6/7} \left(\frac{n}{n_0} \right)^{-6/(7m)} \frac{d\tilde{B}}{d\tilde{x}} \left(1 - \frac{\varphi_f}{\psi_f} \right) d\tilde{x}', \quad (434b)$$

where $\tilde{x} = x/L_r$ and $\tilde{B} = B/B_0$, with L_r the length of the reach and B_0 the undisturbed half channel width, respectively.

The solution (433) deserves some comments. Not surprisingly, the perturbation of the free surface is a fraction of the undisturbed flow depth which scales with the square of the Froude number F_{r0}^2 . Hence, *the effect of width variations on the free surface decreases rapidly as the flow regime varies from supercritical to subcritical.*

The first term of (432) is driven by the perturbation of frictional terms induced by variations of flow speed and flow depth in the widening and narrowing reaches. The importance of this effect depends mainly on the length of the channel reach where width variations occur.

The role of sediment transport is readily illustrated. In the case of dominant bedload (MPM predictor) and in the limit of *weak sediment transport* ($\tau_{*c}/\tau_{*e0} \rightarrow 1$), one readily shows that:

$$\left[1 - \tilde{B}^{6/7-10/(7m)} \left(\frac{n}{n_0} \right)^{-10/(7m)} f^{10/7} \right] \rightarrow 1 - \tilde{B}^{6/7}.$$

Hence, in the weak sediment transport limit, the contribution of the integral $\mathcal{I}_1^{H_1}$ is negative where the channel is wider than the undisturbed channel ($\tilde{B} > 1$) and vice versa. A similar trend is obtained for large Shields stress as, using EH predictor, one finds:

$$\left[1 - \tilde{B}^{6/7-10/(7m)} \left(\frac{n}{n_0} \right)^{-10/(7m)} f^{10/7} \right] = 1 - \tilde{B}^{14/33}.$$

The second term of the solution (433) has the sign of $dB/d\tilde{x}$. Indeed, simple analysis of the relations (425) readily shows that $0 < \varphi_f/\psi_f < 1$ for any value of τ_{*e0} . Moreover, the quantity $\tilde{B}^{-9/7-6/(7m)} f^{6/7} (n/n_0)^{-6/(7m)}$ keeps invariably positive. Hence, at equilibrium, the effect of the second term is to let the free surface elevation rise when channels widen and vice versa.

In conclusion, the two contributions to the solution (433) have opposite effects on the perturbation of the free surface. The two examples discussed below will show that the role of the second term usually prevails.

- *Bed profile*

Let us finally determine the response of the bed elevation η to channel widening or narrowing. It is again convenient to introduce a perturbation $\bar{\eta}_1$ of the uniform bed profile by defining:

$$\bar{\eta} = \bar{\eta}_0 - S_{e0} x + \bar{\eta}_1(x), \quad (435)$$

where $\bar{\eta}_0 = \bar{H}_0 - \mathcal{D}_{e0}$. With the latter definition and recalling the solution (422) one finds:

$$\bar{\eta}_1(x) = \bar{H}_1(x) + \mathcal{D}_{e0} - \mathcal{D}(x) = \bar{H}_1(x) + \mathcal{D}_{e0} \left[1 - \tilde{B}^{(1/m-2)3/7} \left(\frac{n}{n_0} \right)^{3/(7m)} f^{-3/7} \right]. \quad (436)$$

This solution is readily interpreted. The reader will show that the role of the second term on the right hand side is to produce, as expected, bed aggradation in widening channels at equilibrium and, vice versa, degradation in narrowing channels. The role of $\bar{H}_1(x)$ has already been discussed and is proportional to the square of the Froude number (equation (433)). For low Froude numbers, in widening channels the bed elevation increases faster than the free surface elevation such to allow for the predicted reduction of flow depth. Just the opposite occurs for narrowing channels at equilibrium, where bed elevation decreases faster than free surface elevation, eventually leading to an increased flow depth. At high Froude numbers the role of $\bar{H}_1(x)$ tends to prevail on that of the term $\mathcal{D}_{e0} - \mathcal{D}(x)$ which is independent of the Froude number. As a result, the perturbation of bed elevation tends to follow closely the perturbation of free surface elevation.

In order to make our arguments quantitative, below we consider two instructive examples.

Example 1: Sinusoidal channel.

Let us consider the rectangular channels depicted in Figure 71, which undergo either a widening (Figure 71a) or a narrowing (Figure 71b), such that, in both cases, the channel eventually recovers its original width $2B_0$. More precisely, let us assume that $\tilde{B} = 1 + 0.5\delta [1 - \cos(2\pi\tilde{x})]$ with $\tilde{x} \in [0, 1]$ and δ a parameter measuring the degree of narrowing/widening. The Figure 71 shows that, for the case considered,

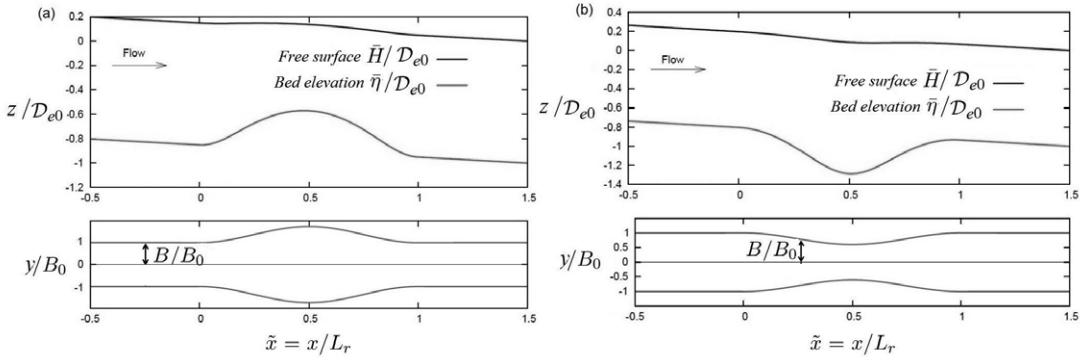


Figure 71. Sketch of two examples of channel undergoing (a) widening and (b) narrowing in reversed sequences. Input data: $S_{e0} = 10^{-3}$; $d = 0.01$ m; a) $\delta = 1.5$; $F_{r0} = 0.46$; $\tau_{*e0} = 0.308$; b) $\delta = -0.78$; $F_{r0} = 0.44$; $\tau_{*e0} = 0.227$ (modified from Bolla Pittaluga et al., 2014a).

widening channels ($\delta > 0$) at equilibrium experience rising of the free surface and, vice versa, in narrowing channels ($\delta < 0$) the free surface lowers. Is this invariably true? In order to answer this question, in Figure 72 we have reported the two integrals (434a) and (434b) computed for $\tilde{x} = 0.5$ and plotted as functions of the parameters τ_* and δ . It appears that, as expected, the integral $\mathcal{I}_2^{H_1} \Big|_{0.5}$ has the sign of δ . On the

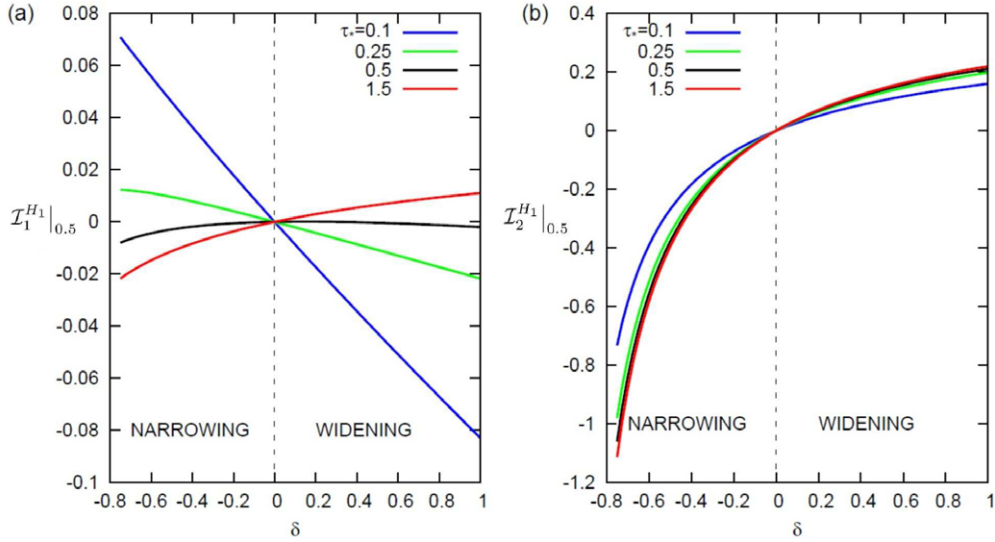


Figure 72. The integrals $\mathcal{I}_1^{H_1}|_{0.5}$ and $\mathcal{I}_2^{H_1}|_{0.5}$ as functions of the Shields parameter τ_* and the amplitude of width variations δ .

contrary, the integral $\mathcal{I}_1^{H_1}|_{0.5}$ may have the same sign or the opposite sign, depending on the intensity of sediment transport. However, the Figure 72 suggests that $\mathcal{I}_1^{H_1}|_{0.5}$ is at least an order of magnitude smaller than $\mathcal{I}_2^{H_1}|_{0.5}$. If the factor $L_r \bar{C}_{f0}/\mathcal{D}_{e0}$ is $\mathcal{O}(1)$, then the modulus of the first term in (433) is smaller than the second, i.e. widening channels at equilibrium experience rising of the free surface and vice versa. Note that this result suggests that *local widening of alluvial channels is not an appropriate solution to reduce the risk of flooding*.

A second interesting feature of this solution is that, for symmetric width perturbations, the net effect of the second term of (433) vanishes ($\mathcal{I}_2^{H_1}|_1 = 0$) whilst the net effect of the first term does not vanish and ($\mathcal{I}_1^{H_1}|_1 = 2\mathcal{I}_1^{H_1}|_{0.5}$). Hence, except for the case of intense sediment transport, in channels wider than the undisturbed reach, the first term of (433) is negative and leads to net lowering of the free surface downstream or net rising upstream. Conversely, net rising downstream or net lowering upstream will result in channels undergoing narrowing. In each case, whether the net effect is felt upstream or downstream depends on the boundary condition.

Example 2: Diverging river mouth.

Next, let us consider a second instructive example, namely a divergent river mouth. The channel width $2B$ is assumed to vary exponentially in the landward direction according to the following relationship:

$$B = B_0 + (B_{mouth} - B_0) \exp\left(-\frac{x}{L_B}\right), \quad (437)$$

where x is the longitudinal coordinate with origin at the estuary mouth directed landward, L_B is the channel convergence length, B_{mouth} is half width at the mouth and B_0 is the half width asymptotically reached upstream by the river (Figure 73b). Furthermore we assume that the sea level H_{mouth} , the flow discharge Q and the average channel slope S_{e0} are known. In Figure 73 we show the equilibrium configuration of the bed and the corresponding free surface elevation for a specific case.

Results show that, in order to accommodate both flow and sediment discharge prescribed upstream, the equilibrium flow depth must decrease as the width increases, leading to a negative bed slope close to the estuary mouth. Such a tendency of the bed profile is typically observed in many micro-tidal estuaries, where the role of tide is negligible (e.g. in the estuary of the Magra river shown in Figure 65). In other words, this mechanism is exclusively associated with river widening close to the estuary mouth. For the general estuarine case the reader is referred to Bolla Pittaluga et al. (2014b).

5.1.5 The case of non cylindrical channels: natural rivers

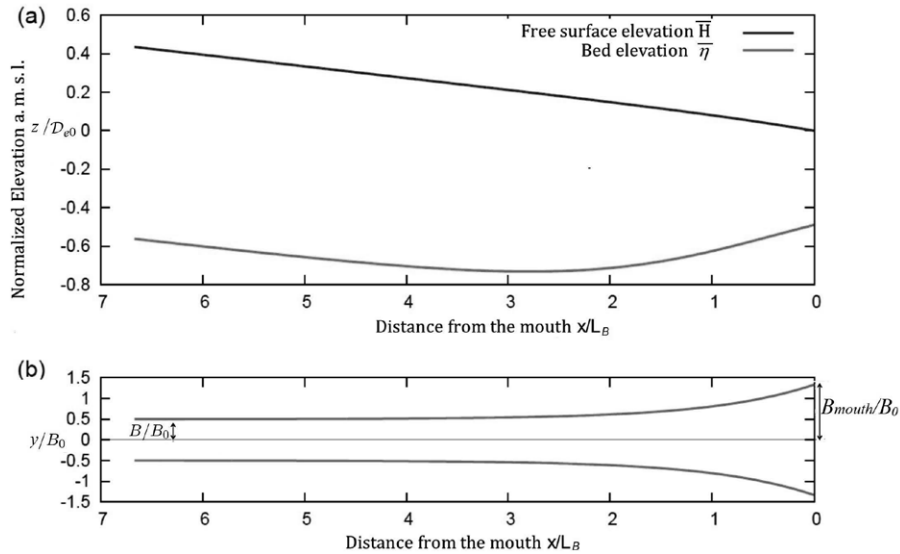


Figure 73. (a) The equilibrium configuration of the bed and the corresponding free surface elevation associated with a convergent microtidal estuary with shape described by the relationship (437). (b) Planform configuration. Data: $B_{mouth}/B_0 = 8/3$; $L_B = 1500$ m; $H_{mouth} = 0$ m; $S_{e0} = 10^{-4}$; $F_{r0} = 0.13$; $\tau_{*e0} = 0.15$; $d = 1$ mm (modified from Bolla Pittaluga et al., 2014a).

The analysis presented in the previous Section has shown that, given the spatial distribution of channel width and the grain size distribution of a rectangular channel, an equilibrium bed profile can be associated with any assigned values of the flow and sediment discharges along with some boundary condition. However, the analysis does not help identifying the *formative* values (if any) of flow and sediment discharges.

To make some progress in this direction it is convenient to ascertain whether our *steady equilibrium* paradigm does indeed help us interpreting field observations. With this goal in mind, we then analyze the terminal reach of the Magra River where the latter ideas have been tested (Seminara et al., 2011). Following the approach extensively discussed by Bolla Pittaluga et al. (2014a), we now show that the observed bed profiles are fairly closely fit by the equilibrium profile associated with some steady discharge. Note, that a similar exercise, which led to similar conclusions, was performed by Lanzoni et al. (2015) on a long reach of the Po river.

The equation (406) was solved numerically for different values of the flow discharge \mathcal{Q} , starting from the downstream end where the free surface elevation was set equal to the mean sea level. In other words, tidal oscillations were neglected given the fluvially dominated character of the river mouth. Simulations were performed assuming the shape of the cross-sections obtained in the 2003 survey and following the approach of Engelund described in Section 2.3.5 to calculate the flow properties in each cross-section.

The sediment transport capacity associated with each flow discharge was evaluated using equation (410) with the observed value of the average bed slope in the upstream river reach. The transport capacity was evaluated using Engelund and Hansen (1967) predictor. The average value of the Strickler coefficient was set equal to 30 $m^{1/3}s^{-1}$. Results of the calculation are reported in Figure 74. They suggest that the bed profile observed in 2003 fits well the equilibrium profile associated with a discharge close to 500 m^3s^{-1} , except for an intermediate reach (about 2.5-3.5 km from the mouth) where the river exhibits a strong constriction. Here the 2003 profile is closer to the equilibrium profile corresponding to a discharge of 1000 m^3s^{-1} . As the assigned discharge increases, the corresponding equilibrium profile deepens.

The value 500 m^3s^{-1} is close to the mean annual discharge of the Magra River in the reach investigated here (347 m^3s^{-1}), a value significantly lower than the mean annual flood discharge

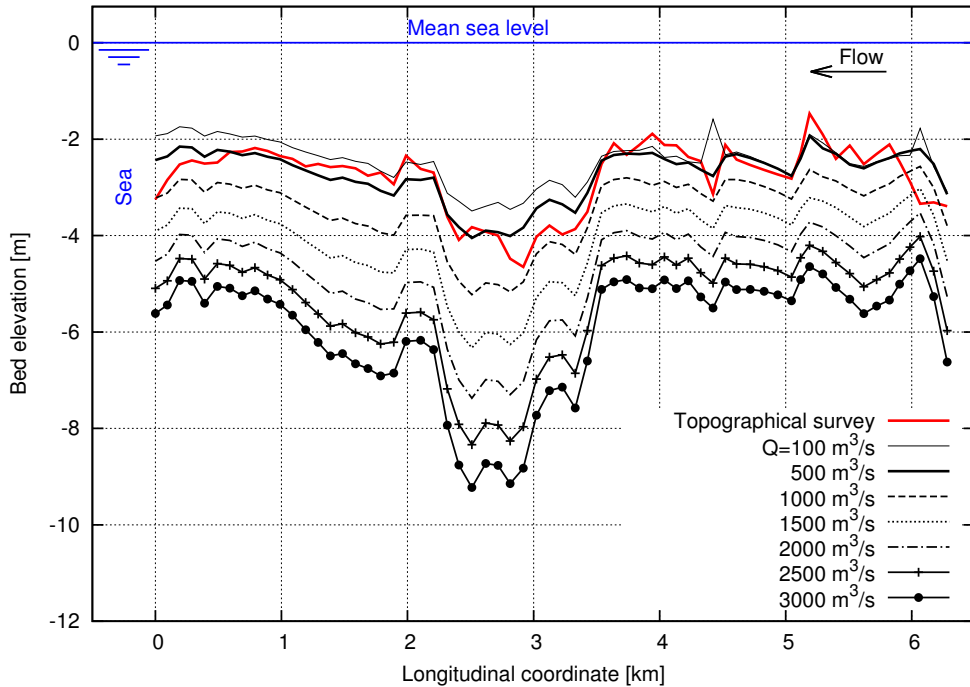


Figure 74. The equilibrium profiles of the terminal reach of the Magra River (Italy) associated with various values of the flow discharge are compared with the observed profile, based on the detailed survey performed in 2003 (from Bolla Pittaluga et al., 2014a).

($1702 \text{ m}^3 \text{ s}^{-1}$). However, note that the relative high value of the mean annual flood discharge might be due to the rather short time period (8 years) on which the above statistics is based, noting that in this short period three very intense flood events have been experienced by the river.

Similarly, in the case of a lowland reach of the Po River, Lanzoni *et al.* (2015) found that the discharge ($2300 \text{ m}^3 \text{ s}^{-1}$) ensuring the best fit between computed and observed bed profiles is close to the mean annual discharge ($1500 \text{ m}^3 \text{ s}^{-1}$) at Pontelagoscuro gauge station. The latter quantity, on the other hand, is close to the discharge for which the unvegetated (and hence highly mobile) point bars forming in the active river section begin to be submerged.

These results suggest that, in spite of the strong fluctuations of flow and sediment discharges undergone by a river, the bed profile tends to settle around an equilibrium state which is associated with steady forcing values of flow and sediment discharge falling in the lower range of values experienced by the river. It remains to be clarified how this equilibrium state survives the strong fluctuations of bed elevation driven by the likely propagation of sediment waves during flood events. This goal cannot clearly be pursued in the context of a steady treatment of the problem. Much can be learnt on this problem from unsteady numerical simulations of the evolution of the bed profile in river reaches subject to observed sequences of hydrographs. This goal has been pursued by Bolla Pittaluga et al. (2014a) to whom the reader is referred for details. The latter Authors concluded with the following picture of river equilibrium: “*we interpret the dynamic state of the system as a strict equilibrium state subject to fluctuations: essentially, we may always interpret a hydrograph as the sum of some steady constant discharge plus fluctuations driven by variations of external forcing (at any temporal scale). The issue is then to decide what is the appropriate value of the steady component of the forcing such that fluctuations of the forcing produce fluctuations of the bed profile which have zero mean when averaged over a sufficiently long period. This is the concept of effective forcing which can be also expressed as follows: the river morphology chooses the (effectively) steady forcing which is able to maintain its associated equilibrium by smoothing out the perturbations*

intermittently induced by flood events. In other words, the sediment transport associated with low-stage flows must be statistically able to suppress the deviations from the equilibrium profile driven by the propagation of flood waves."

5.1.6 Additional effects

The picture emerged from the above analysis is appropriate to river reaches sufficiently short to justify the assumptions of constant discharge and uniform grain size. A number of additional effects (sediment abrasion, effect of tributaries, grain sorting, subsidence) must be accounted for when extending the analysis to river reaches of length scale comparable to the size of the basin. At that scale, the analysis must be simplified such to allow to detect the average trend of the bed profile, smoothed out from the perturbations of the bed elevation driven by local width variations like those analyzed above. Such an extension is outside the scopes of the present Monograph. The interested reader is referred to Sinha and Parker (1996).

5.2. The basic *equilibrium* cross-section of straight channels

5.2.1 The early field observations

The shape of the cross-section of river channels adjusts, through the processes of erosion and deposition, to the need to accommodate the fluid discharge and the sediment load supplied from the drainage basin, subject to the additional constraints posed by the boundary composition and the valley slope.

Since the discharge increases downstream with the drainage area, the average channel size, grossly described in terms of some characteristic width $2B$ and depth \mathcal{D} of its cross-section, should vary accordingly. A pioneering contribution aimed at quantifying the latter dependence is due to Leopold and Maddock (1953). Averaging values for a number of selected river reaches in the United States, Leopold and Maddock (1953) established empirical relationships between the mean annual discharge Q_{ma} and geometrical properties of the channel cross-section (top bank width $2B$, cross-sectionally averaged depth \mathcal{D}) or flow properties (cross-sectionally averaged speed at mean annual discharge U). These relationships are known in the literature as *regime equations* and read:

$$2B = a_{LM} (Q_{ma})^b, \quad \mathcal{D} = c_{LM} (Q_{ma})^f, \quad U = k_{LM} (Q_{ma})^m \quad (438a,b,c)$$

with a_{LM} , c_{LM} and k_{LM} dimensional constants and

$$b = 0.5, \quad f = 0.4, \quad m = 0.1. \quad (439)$$

Parker (1979) suggested that the scale factors a_{LM} , c_{LM} and k_{LM} vary at different sites but the exponents, b , f , and m , exhibit a remarkable degree of consistency, i.e. they appear to be fairly independent of location and only weakly dependent on channel type. This was indeed confirmed by Griffiths (1981) and Hey and Thorne (1986) who investigated six large, coarse gravel-bed rivers in New Zealand and a few stable gravel-bed river reaches in the United Kingdom, respectively. The values of b , f and m found in the former work were 0.48, 0.43 and 0.11 respectively. The latter Authors report slightly different values, namely $b = 0.52$ and $f = 0.39$.

Other researchers have pointed out that, although discharge has a dominant control on channel size, additional factors such as the dominant form of sediment transport (bed load vs. suspended load), bank composition and vegetation also play some role. Notable is the early work of Schumm (1960), who showed that the shape of stable cross-sections, identified by the ratio between the channel width and the maximum flow depth, can be expressed as a function of the mean percentage of silt and clay along the entire perimeter (banks and bed), the latter quantity accounting for the boundary resistance to erosion. Empirical evidence, obtained for channels containing only small amounts of gravel, shows that the width to depth ratio can change over two orders of magnitude, ranging from over 100 when silt-clay is less than 1% to less than 10 when silt-clay is more than

20%, see Figure 75. In other words, channels containing little silt-clay are relatively wide and shallow; whereas those composed of predominantly silt-clay are relatively narrow and deep. Note that small percentages of silt-clay indicate bedload dominated channels while high values are representative of suspended-load channels.

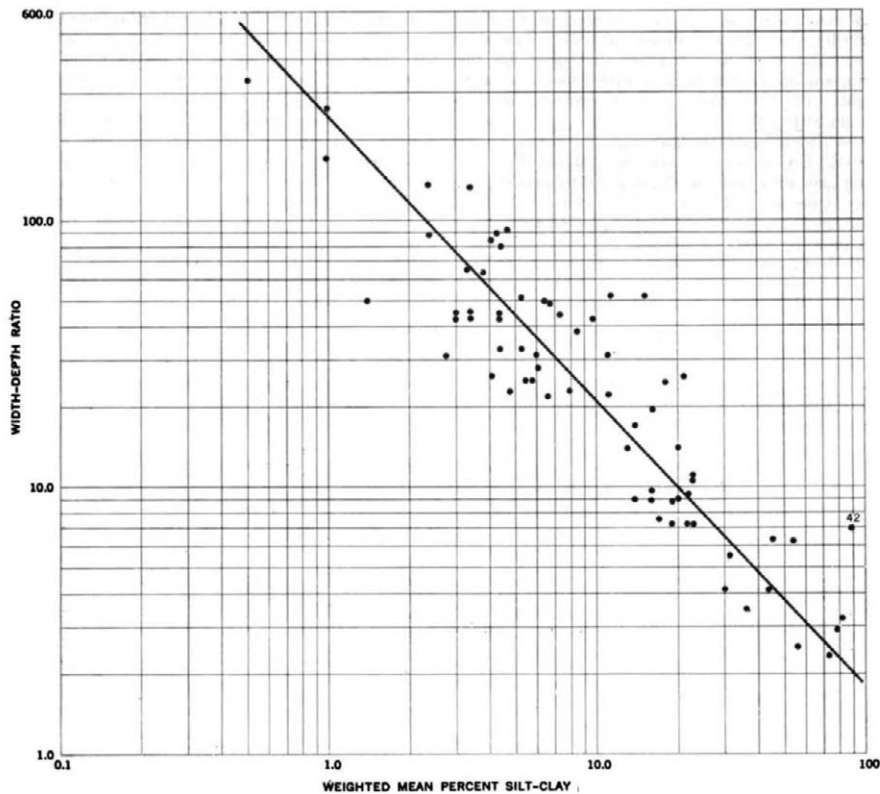


Figure 75. The width to depth ratio as a function of weighted percentage of silt and clay (modified from Schumm, 1960).

Vegetation is generally expected to increase bank resistance which leads to channel narrowing. Hey and Thorne (1986) found that channels with grassed banks are up to 1.8 times wider than those that are tree-lined. However, data analysis showed that the inclusion of vegetation did not affect the value of the exponent b of Leopold and Maddock (1953) relationship.

The actual physical interpretation of the empirical correlations (438), which turn out to apply to so many river reaches around the world, has been the subject of a large number of investigations. Below, we provide an overview of the main mechanistic approaches, which succeeded in determining the shape of the cross-section of straight cylindrical channels with erodible banks at equilibrium. We start from the simplest case, that of channels which convey an assigned fluid discharge without transporting any sediment.

5.2.2 The equilibrium shape of channels unable to transport sediments

This problem was first investigated by Glover and Florey (1951) using the so called tractive force approach: essentially, one imposes that, in a stable geometry of the cross-section, all the sediment particles along the channel boundary must be at threshold conditions for the onset of particle motion. The shape of the cross-section is then obtained coupling a hydrodynamic model for the distribution of water shear stresses along the wetted perimeter with the condition that the boundary shear stress must be critical.

The mathematical treatment of this problem considers a symmetrical cross-section (see sketch in Figure 76). The channel is taken to be erodible, cylindrical and characterized by constant longitudinal bed slope S . The flow field is steady and uniform. Bed and banks are assumed to be composed of loose gravel of similar size and cannot be suspended. The system is referred to a curvilinear coordinate system (s, p, ζ) where s is the longitudinal coordinate, p the curvilinear coordinate defined along the wetted perimeter, and ζ is the coordinate normal to the boundary. We denote by $2B$ the width of the free surface, \mathcal{P}_w the wetted perimeter, D the local flow depth and Ω the liquid cross-sectional area.

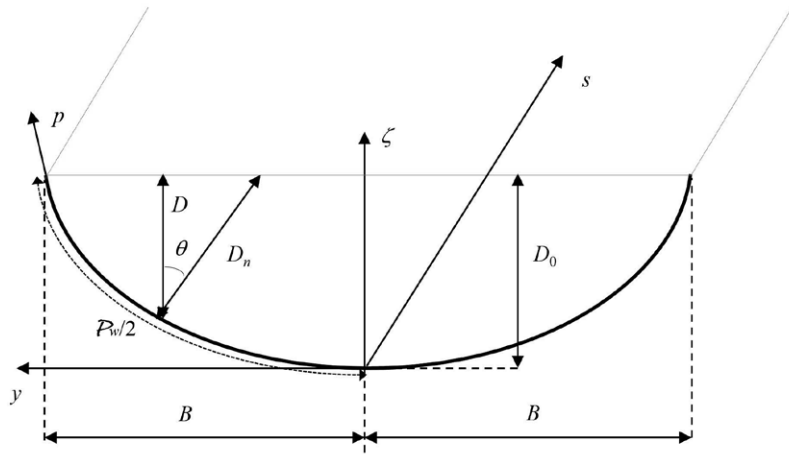


Figure 76. Sketch and notations of a cross-section that keeps in equilibrium being unable to transport sediments.

With these notations, the longitudinal component of the Reynolds equations can be written as:

$$\frac{\partial(T_{\zeta s}^t h_p)}{\partial s} + \frac{\partial T_{ps}^t}{\partial p} + \varrho g S h_p = 0, \quad (440)$$

where \mathbf{T}^t is the Reynolds stress tensor and h_p is the metric coefficient of the lateral curvilinear coordinate. Note that in equation (440) the effect of the weak convective motions due to secondary flows associated with turbulence anisotropy is neglected. As a matter of fact, in straight channels, such secondary velocities are very weak, typically 1 to 2% of the main longitudinal velocity.

The metric coefficient arises from the local inclination and curvature of the wetted perimeter and has the following expression:

$$h_p = 1 + \zeta \frac{\frac{d^2 D}{dp^2}}{\left[1 - \left(\frac{dD}{dp}\right)^2\right]^{1/2}}. \quad (441)$$

By integrating equation (440) from the bed to the free surface, and taking into account the dynamic boundary condition imposing that the stress tensor vanishes at the free surface, we obtain:

$$\tau = \varrho g S \frac{d\Omega}{dp} + \frac{d}{dp} \left(\int_0^{D_n} T_{ps}^t d\zeta \right), \quad (442)$$

where $d\Omega$ is the liquid area between the normals to the bed at p and $(p + dp)$, such that:

$$\frac{d\Omega}{dp} = D_n = \frac{D}{\cos \theta}. \quad (443)$$

Glover and Florey (1951), quite arbitrarily, introduced the following approximation in the previous expression:

$$D_n \cong D \cos \theta. \quad (444)$$

Equation (442), with equation (444) and neglecting the effect of redistribution of Reynolds shear stress T_{ps}^t , then gives:

$$\tau = \rho g S D \cos \theta. \quad (445)$$

The shape of the channel cross-section was finally found by imposing that the boundary shear stress (445) must be equal to its critical value for the onset of sediment motion along the entire wetted boundary.

In order to formulate the problem in a dimensionless form, we now introduce the following scaled variables:

$$\tilde{D} = D/D_0, \quad \tilde{y} = y/B, \quad (446)$$

with $D_0 = D(0)$ the flow depth at the channel centerline, and y the horizontal lateral coordinate (see the sketch in Figure 76). The following governing equation is found:

$$\frac{d\tilde{D}}{d\tilde{y}} = \mu_s \beta \left[1 - \left(\frac{1-r}{1+r} \right) \tilde{y}^2 - \left(\frac{2r}{1+r} \right) \tilde{y} \right]^{1/2}, \quad (447)$$

with $r = \mu_s c_L/c_D$ and β the aspect ratio defined as B over D_0 . The equation (447) is to be solved with the following boundary conditions at the channel centre, $\tilde{y} = 0$, and at the bank, $\tilde{y} = 1$:

$$\tilde{D}|_0 = 1, \quad \tilde{D}|_1 = 0. \quad (448)$$

Eventually, the following cosine shape of the cross-section is obtained:

$$\tilde{D} = \frac{1}{1-r} \left\{ \cos \left[\mu_s \beta \tilde{y} \left(\frac{1+r}{1-r} \right)^{1/2} \right] - r \right\}, \quad (449)$$

with

$$\beta = \frac{\arccos(r)}{\mu_s} \left(\frac{1-r}{1+r} \right)^{1/2}. \quad (450)$$

Setting $c_L/c_D = 0.85$, the cross-section profile can be integrated to yield the following relationships for water surface width ($2B$), cross-sectional area (Ω) and wetted perimeter (\mathcal{P}_w):

$$\frac{2B}{D_0} = 3.14 \phi^{-1.038}, \quad \frac{\Omega}{B D_0} = 0.66 \phi^{0.021}, \quad \frac{\mathcal{P}_w}{D_0} = 3.59 \phi^{-0.950}, \quad (451)$$

where $\phi = \arctan \mu_s$ is the angle of repose of the granular material lying on the wetted perimeter. Note that equation (451) predicts quite 'narrow' channels: for example, in the case of $\phi = 40^\circ$, the ratio $2B/D_0$ is only about 4.5.

Using Strickler formula to evaluate the flow resistance, the flow discharge pertaining to the equilibrium cross-section is found to read:

$$Q = 1.437 k_s \sqrt{S} \phi^{-1.06} D_0^{8/3}, \quad (452)$$

where the flow depth at the channel centerline has been specified through the relation:

$$\tau|_0 = g D_0 (\varrho_s - \varrho) \tau_{*c0}. \quad (453)$$

The original formulation of Glover and Florey (1951) was revised and improved by Tubino and Colombini (1992) who removed the approximation (444) and retained the effect of lateral

variation of the Reynolds shear stress T_{ps}^t . A simplest analytical solution of this more complex problem was found in terms of friction velocity. Essentially, Tubino and Colombini (1992) used a perturbation approach getting advantage of the slowly varying character of the cross-section in the lateral direction, measured by the small parameter $\epsilon = D_0/(\mathcal{P}_w/2)$. Using the simplest closure provided by the *slip-velocity* method of Engelund (1964), the analysis led to the evaluation of a correction of the shear stress distribution at the boundary. From a physical point of view, this correction is driven by the local slope and curvature of the perimeter and it represents a redistribution of the longitudinal momentum from the central region of the cross-section, where the velocity is higher, to the side wall regions, where velocity is smaller due to the retarding effect of the banks. This redistribution reduces the bed shear stress at the channel axis and increases it near the banks (see Figure 77).

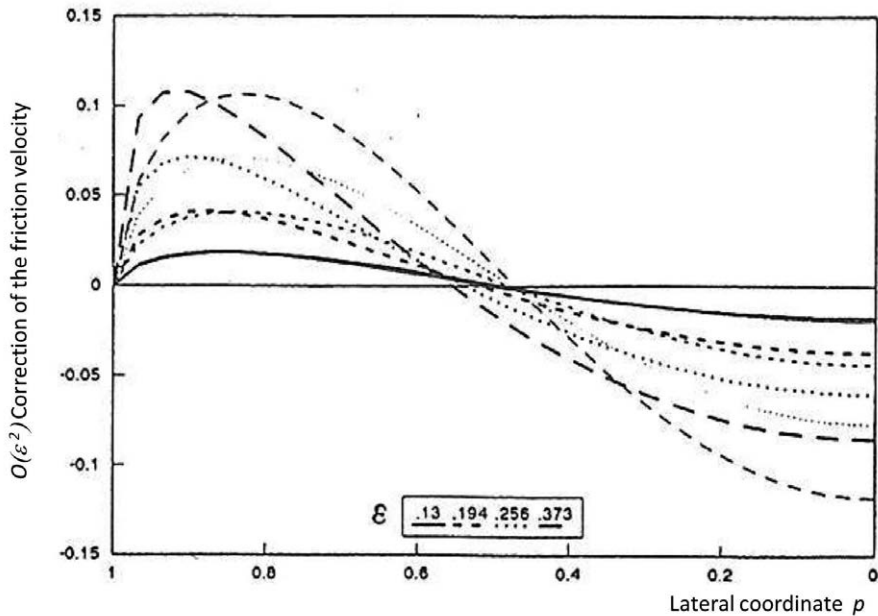


Figure 77. Comparison between the perturbation solution (thin curves) and the full numerical solution (thick curves) for the lateral distribution of the $\mathcal{O}(\epsilon^2)$ correction of the friction velocity for different values of the perturbation parameter $\epsilon = D_0/(\mathcal{P}_w/2)$ (reproduced from Tubino and Colombini, 1992).

Tubino and Colombini (1992) explored also the effect of different turbulence closures on the hydrodynamic solution. Finally, Tubino (1992) applied the latter hydrodynamic model to determine the shape of the cross-section at equilibrium. Results show that momentum redistribution leads to wider cross-sections with typical aspect ratios B/D_0 ranging about 3.6. Similar results were also obtained by Diplas and Vigilar (1992) and Dey (2001). The difference between the *cosine* cross-section obtained by Glover and Florey (1951) and the *threshold* channel of Tubino and Colombini (1992) is sketched in Figure 78.

5.2.3 The equilibrium shape of channels able to transport sediments: solution of the stable channel paradox for gravel rivers

Parker (1978a) was the first scientist to clarify an important apparent paradox arising when one attempts to apply the ideas underlying the tractive force approach to an active gravel river. Parker (1978a) examined the following fundamental problem. Consider the simplest channel cross-section, consisting of a flat central region bounded by two lateral banks. As long as bed load is present in the central region, the bottom stress must exceed the threshold of motion there. Adopting the simplest approach of Glover and Florey (1951), the distribution of bottom stress in the central

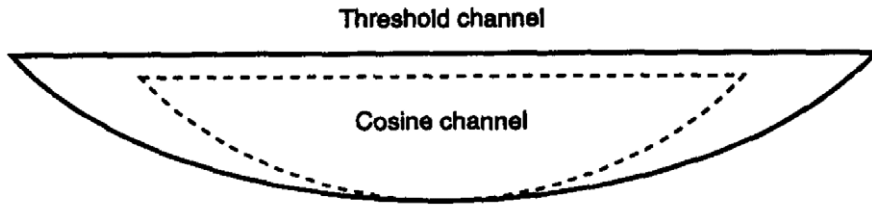


Figure 78. Comparison between the cosine cross-section derived by Glover and Florey (1951) and the threshold cross-section of Tubino and Colombini (1992) (according to ASCE Task Committee, 1998).

region would then be flat (recall equation (445) and set $\theta = 0$). But, in this case, a portion of the bank adjacent to its toe should also experience a bottom stress exceeding the critical value, hence some grains on the banks should also be in motion. This would cause bank erosion and thus a widening of the cross-section until the stress in the central region would decrease enough to reach its critical value for sediment transport. This apparent contradiction was called *stable-channel paradox* by Parker (1978a).

Parker (1978a) solved this paradox for the case of gravel bed rivers (no suspension) revisiting the approach of Glover and Florey (1951) such to take into account the turbulence driven lateral transfer of longitudinal momentum in the cross-section. The theory was formulated for a river reach satisfying the following criteria: i) the channel is straight and laterally symmetrical; ii) the perimeter, both bed and banks, is entirely composed of loose coarse gravel; iii) most grain sizes are mobile at bankfull discharge; and iv) the channel is self-formed and has a stable width. Parker (1978a) was able to show that the lateral momentum transfer leads to a redistribution of the bed shear stress which decreases from the central region towards the banks. In order to achieve equilibrium, the channel widens until the bed shear stress reaches its critical value for sediment motion at the bank toe. In other words, the shape of an equilibrium cross-section capable of transporting sediment is composed of two regions: a central flat region where sediment is transported and the bed shear stress is larger than its critical value and a bank region, where sediment is not transported and the bed shear stress is critical (Figure 79). Parker (1978a) also found that, in the central region, the Shields stress exceeds its critical value by about 14 – 16%.

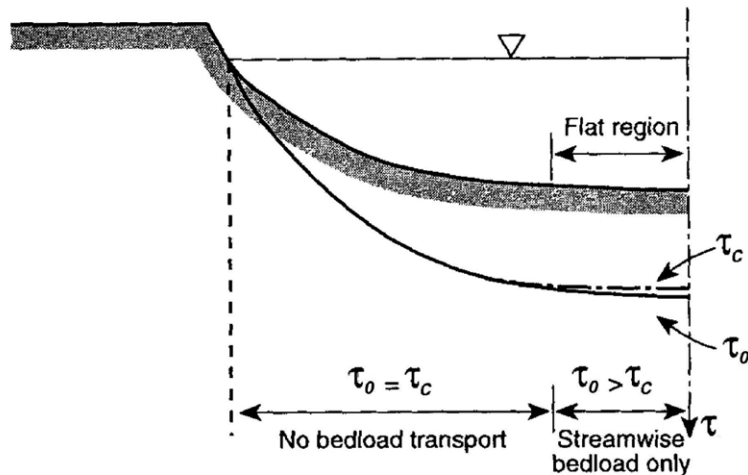


Figure 79. Sketch of an equilibrium cross-section with bedload transport in a straight gravel channel.

The analysis of Parker (1978a) was revisited by Tubino and Colombini (1992) through a rational

perturbation approach that essentially confirmed the previous findings. Later, Kovacs and Parker (1994) developed a mathematical model to simulate the widening process of a straight, initially trapezoidal, channel subject to bank erosion. They found that the evolution leads to an equilibrium cross-section such that the bed shear stress along the banks just equals the threshold for sediment transport, hence sediments are transported in the central region only, in accordance with the previous finding of Parker (1978a). However, the latter analysis made use of a relationship for bedload transport on a laterally sloping bed with finite slope, based on a generalization of the so called Bagnold hypothesis, that was later shown to be incorrect (Seminara *et al.*, 2002). Tubino (1992), by imposing $\tau_* = 1.15 \tau_{*c0}$ and considering the cross-section wide enough to approximate the hydraulic radius with the local flow depth, derived the following *first rational regime equation*:

$$\frac{D_0}{d_{50}} = 1.15 (s - 1) \tau_{*c0} S^{-1} \cong 0.057 S^{-1}, \quad (454)$$

having assumed that $\tau_{*c0} \cong 0.03$ as appropriate to gravel bed rivers. Note that the equation (454) is practically identical to the first regime equation proposed by Parker (1978a).

A *second rational regime equation* can be obtained for a given equilibrium cross-section, composed of a central flat region of width $2B$ and depth D_0 connected to stable banks. Integrating the logarithmic velocity distribution in the direction normal to the bed and using the friction velocity obtained by Tubino and Colombini (1992), the flow discharge pertaining to the equilibrium cross-section was found to read:

$$Q = 0.036 \sqrt{(s - 1) g d_{50}^3} S^{-1.22} 2B \left(1 - 2.23 \frac{D_0}{2B} \right). \quad (455)$$

A direct comparison between the equations (454)-(455) and the regime equations 438a,b is not straightforward, as the latter implicitly contain a dependence on the bed slope. However, relations (454-455) are not in contradiction with the regime equations. Assuming the flow depth proportional to $Q^{0.4}$ (equation 438b), equation (454) predicts that the bed slope is proportional to $Q^{-0.4}$. Substituting this finding into (455) and considering a *wide* cross-section, it turns out that $B \propto Q^{0.51}$, i.e. we recover equation (438a).

A *third rational regime equation* is obtained integrating the bed load discharge per unit width associated with the local value of the bed shear stress in the lateral direction. One finds:

$$Q_s = 0.46 10^{-5} \sqrt{(s - 1) g d_{50}^3} S^{-0.278} 2B \left(1 - 4.52 \frac{D_0}{2B} \right). \quad (456)$$

Parker (1979) notes that, according to this equation and for a given flow discharge, a 30% increase in bedload leads to a 25% reduction of the flow depth in the central region, a 40% increase in width and a 32% increase in slope.

Equations (454)-(456) have been tested with laboratory and field data regarding straight reaches of gravel rivers. This comparison supports the validity of the proposed approach.

More recently, Parker *et al.* (2007) revisited the *rational regime equations*, seeking *quasi-universal* forms for the geometrical properties of channel cross-section at bankfull stage. In particular, using their notations, the bankfull depth D_{bf} , the total bankfull width B_{bf} and the downstream channel slope S_{bf} are expressed as functions of the bankfull channel discharge Q_{bf} and of the median diameter of the bed surface d_{50} . Using a dataset of alluvial single-thread gravel-bed reaches of rivers in Canada, USA and Great Britain, they were able to obtain dimensionless relations which show a remarkable degree of universality despite the wide range of variation of river geometries investigated. The approach they employed relied on dimensional analysis and interpolation of the observed data. It is noteworthy that the relationships they derived apply to reaches of single-thread gravel bed rivers, with stable width, surface median grain size greater than 25 mm, definable channels and flood plains, regardless of the type of banks and channel planform.

The *quasi-universal* relations read as follows:

$$\tilde{B} = 4.63 \tilde{Q}^{0.0667}, \quad \tilde{D} = 0.382 \tilde{Q}^{-0.0004}, \quad S_{bf} = 0.101 \tilde{Q}^{-0.344}, \quad (457)$$

with

$$\tilde{B} = \frac{g^{1/5} B_{bf}}{Q_{bf}^{2/5}}, \quad \tilde{D} = \frac{g^{1/5} D_{bf}}{Q_{bf}^{2/5}}, \quad \tilde{Q} = \frac{Q_{bf}}{\sqrt{g d_{50}^5}}. \quad (458)$$

The reader interested in plots showing how accurately the above relationships fit the available data is referred to Parker *et al.* (2007). The same equations take the following dimensional form:

$$B_{bf} = 4.63 \frac{Q_{bf}^{0.4}}{g^{1/5}} \left(\frac{Q_{bf}}{\sqrt{g d_{50}^5}} \right)^{0.0667}, \quad (459a)$$

$$D_{bf} = 0.382 \frac{Q_{bf}^{0.4}}{g^{1/5}}, \quad (459b)$$

$$S_{bf} = 0.101 \left(\frac{Q_{bf}}{\sqrt{g d_{50}^5}} \right)^{-0.344}. \quad (459c)$$

Equations (459a,b) predict that a doubling of bankfull discharge results in an increase in bankfull depth by a factor of 1.32 and in bankfull width by 1.38. Note that the bankfull width is proportional to the 0.467 power of the discharge (close to the exponent 0.5 of equation (438a)) and to the -0.167 power of the sediment diameter; moreover, the exponent in equation (459b) is the same as in (438b).

Furthermore, Parker *et al.* (2007) performed a back-calculation to identify parameters (exponents and coefficients) of three physical relationships taken to be the governing laws of bankfull morphodynamics of gravel-bed rivers: a generalized Manning-Strickler resistance relation; a relation for the channel-forming Shields number (in accordance with the results obtained by Parker (1978a)); a relation for *gravel yield* at bankfull flow. These relationships read as follows:

$$\frac{U_{bf}}{u_{\tau bf}} = a_U \left(\frac{D_{bf}}{d_{50}} \right)^{n_r}, \quad \bar{\tau}_{*bf} = a_\tau \tau_{*c0}, \quad \tilde{Q}_s^b = a_Q (\tilde{Q})^{n_y}. \quad (460a,b,c)$$

Application of the equation (460a) may lead to some inaccuracies associated with the following facts: the skin friction due to grain roughness is usually associated with sizes coarser than d_{50} such as d_{90} or d_{84} ; at bankfull flow, form drag (due to a number of factors such as the presence of bars, planform shape, bank undulations and bank vegetation) may play a non-negligible role. Note that, in equation (460b), a_τ can be interpreted as a surrogate for bank strength. Moreover, the equation (460c) empirically stipulates that river catchments organize themselves at bankfull flow such that the gravel discharge \tilde{Q}_s^b scales as proportional to some power of the water discharge.

Substituting from (457) into (460) and using water continuity as well as the bed load transport relationship proposed by Parker (1978a), the following physically based relationships are finally obtained:

$$\frac{U_{bf}}{u_{\tau bf}} = 3.71 \left(\frac{D_{bf}}{d_{50}} \right)^{0.263}, \quad (461a)$$

$$\bar{\tau}_{*bf} = 0.0233 \tilde{Q}^{0.0561}, \quad (461b)$$

$$\tilde{Q}_s^b = 0.0033 \tilde{Q}^{0.551}. \quad (461c)$$

A few notes are in order:

- The exponent in the right hand side of equation (461a) is larger than the classical value of the Manning-Strickler exponent ($1/6 \simeq 0.165$);
- The very low exponent in the right hand side of equation (461b) reveals that the bankfull Shields number exhibits an almost negligible dependence on \tilde{Q} , also recalling that in gravel bed rivers τ_{*bf} attains an average value of about 0.05;

- The exponent in the *gravel yield* equation (461c) indicates that the gravel transport rate at bankfull flow increases roughly with the square root of the bankfull discharge. Moreover, since the latter typically increases nearly linearly with the contributing drainage area, this relation predicts that the volume concentration of transported gravel declines downstream. The reason for this is likely related to the decrease in bed slope with increasing flow discharge (see equation (459c)), as well as with the obvious fact that the hillslopes adjacent to the river course become progressively less steep and thus deliver less sediment for the same unit rainfall.

5.2.4 The equilibrium shape of channels able to transport sediments: sand rivers

In a companion paper, Parker (1978b) extended the previous analysis for the gravel case (Parker, 1978a) to the case where suspension is the dominant component of sediment transport. This extension was performed keeping the *cohesionless* assumption for the channel boundary, including both the bed and the banks. With this, admittedly severe and somewhat unrealistic constraint, Parker (1978b) was able to show that a mechanism leading to cross-section equilibrium can still be envisaged. Two components of the lateral sediment flux, acting in the opposite directions, are now present: a gravity driven bed load flux directed from the banks to the central region and a diffusive flux of suspended sediment from the central region, where concentration is maximum, to the banks where concentration is minimum and sand is deposited. Imposing that these fluxes balance everywhere in the cross-section, Parker (1978b) was able to determine its shape. This analysis, later corrected by Ikeda and Izumi (1991), represented the first attempt to provide a mechanistic interpretation of the equilibrium cross-section of sand bed rivers. However, other features of natural rivers ignored in the latter works, such as cohesion and form drag of river banks, play a major role.

More recently, Wilkerson and Parker (2011) turned to field observations and extended the work of Parker *et al.* (2007) to the case of single-thread sand bed rivers. The analysis was based on the interpolation of a world-wide dataset including rivers with characteristic median surface diameter between 0.062 mm and 0.50 mm.

The following relationships were derived by data interpolation:

$$\tilde{B} = 0.00398 \tilde{Q}^{0.269} R_p^{0.494}, \quad \tilde{D} = 22.9 \tilde{Q}^{-0.124} R_p^{-0.31}, \quad S_{bf} = 19.1 \tilde{Q}^{-0.394} R_p^{-0.196}, \quad (462)$$

where dimensionless quantities are defined as in equation (458). Note that, in contrast with correlations (457) for the gravel case, the particle Reynolds number R_p is explicitly included as independent variable in (462). This is not surprising as such variable is needed to account for the presence of both fine ($d_{50} \leq 0.062$ mm) and coarse (0.062 mm $\leq d_{50} \leq 0.50$ mm) suspended-load. The reader interested in plots showing how accurately the above relationships fit the available data is referred to Wilkerson and Parker (2011).

Equations (462), in dimensional form, read:

$$B_{bf} = 0.0398 \left(\frac{\sqrt{s-1}}{\nu} \right)^{0.494} g^{-0.0875} Q_{bf}^{0.669} d_{50}^{0.0685}, \quad (463a)$$

$$D_{bf} = 22.9 \left(\frac{\sqrt{s-1}}{\nu} \right)^{-0.310} g^{-0.293} Q_{bf}^{0.276} d_{50}^{-0.155}, \quad (463b)$$

$$S_{bf} = 19.1 \left(\frac{\sqrt{s-1}}{\nu} \right)^{-0.196} g^{0.099} Q_{bf}^{-0.394} d_{50}^{0.691}, \quad (463c)$$

with s relative particle density. Comparing equations (463) with their gravel counterparts (459), it appears that the channel width B_{bf} increases with flow discharge Q_{bf} faster (exponent 0.669) than for gravel-bed rivers (exponent 0.467), and even faster than predicted by the regime equations (438) (exponent 0.4). On the contrary, the flow depth D_{bf} increases at a lower rate (exponent 0.276) than in the gravel case (exponent 0.4). Finally, the slope S_{bf} of sand- and gravel-bed rivers decreases with flow discharge at similar rates.

Furthermore, following the approach of Parker *et al.* (2007), Wilkerson and Parker (2011) performed a back-calculation to identify parameters of three physical relationships taken to be the governing laws of bankfull morphodynamics of sand-bed rivers, namely:

$$\frac{U_{bf}}{u_{\tau bf}} = b_U \left(\frac{D_{bf}}{d_{50}} \right)^{n_s}, \quad \bar{\tau}_{*bf} = b_\tau \tilde{Q}^{m_\tau}, \quad \tilde{Q}_s = b_Q \tilde{Q}^{m_y}. \quad (464a,b,c)$$

As noted by the authors, equation (464a) is a bulk resistance relationship and neglects the presence of bed form thus leading to some inaccuracies. Equation (464b) is again based on the assumption that river basins are self-organized such that the bankfull Shields stress can be expressed as a function of the channel-forming bankfull discharge. Equation (464c) has the same structure as its counterpart (equation (460c)) for gravel-bed rivers, but involves the total sediment transport outflowing from the river basin at bankfull conditions.

Substituting from equations (464) into equations (463) and using Engelund-Hansen formula to evaluate the total sediment transport, one ends up with the following expressions:

$$\frac{U_{bf}}{u_{\tau bf}} = 0.144 R_p^{0.197} \left(\frac{D_{bf}}{d_{50}} \right)^{0.413}, \quad (465a)$$

$$\bar{\tau}_{*bf} = 265 R_p^{-0.506} \tilde{Q}^{-0.118}, \quad (465b)$$

$$\tilde{Q}_s = 80.5 R_p^{-0.633} \tilde{Q}^{0.602}. \quad (465c)$$

Various observations arise from a glance at (465). Equation (465a) suggests that, as pointed out by Wilkerson and Parker (2011), when dealing with sand-bed rivers no physical basis exists for using an exponent of 1/6 in the resistance relationship: the exponent for D_{bf} is 2.5 times larger than the classical exponent of the Manning-Strickler relationship. The reason for this large difference is likely connected with the presence of bed forms at bankfull flow. Equation (465b) points out the tendency of the bankfull Shields number to decrease with particle Reynolds number, i.e. with grain size. Equation (465c) suggests that the sediment load increases with bankfull discharge but sand concentration decreases. This trend is similar to that found for gravel-bed rivers (see equation (461c)).

These findings are the result of incorporating the observed hydraulic geometry relationships into the proposed physical framework. They provide a dimensionally homogeneous tool to predict the bankfull discharge as a function of bankfull width, bankfull depth, bed slope, and bed-material median grain size in the case of sand bed rivers.

More recently, Francalanci *et al.* (2020) pointed out the importance of explicitly accounting for channel bank influence on the flow to better clarify the basic mechanisms whereby a river selects its width. Focusing their attention on lowland rivers with cohesive banks, they formulated a theoretical model that evaluates the equilibrium width of river cross sections modelling the interaction between the core flow in the central part of the channel section and the boundary layers that form near to the cohesive banks. The model computes equilibrium configuration of the cross-section such that the shear stresses on the banks equal a critical threshold value, $\tau_{c,bank}$. These stresses are computed by partitioning the total shear stress into an effective grain roughness component and a form component (Kean and Smith, 2006a), as described in the Section 4.5.6. The model is applied to a large data set, concerning the features of both sand and gravel bed rivers at bankfull conditions, and it is used to determine the relations expressing the channel width and the bankfull flow depth as function of the bankfull discharge, which appear to provide a unitary description of bankfull hydraulic geometry.

In particular, the model was first used in conjunction with power law regressions of the available river data to express the average height of the bank undulations and the critical shear stress at the bank as a function of the bankfull discharge through the relations:

$$\frac{a_{reg}}{d_{50}} = 0.0768 \tilde{Q}^{0.3967}, \quad (466a)$$

$$\tau_{*c,bank} = 0.0003679 \tilde{Q}^{0.2878}, \quad (466b)$$

where a_{reg} is the amplitude of an equivalent regular sequence of bumps surrogating the actual distribution of bank undulations, d_{50} is the mean grain size of the channel bed, and $\tau_{*c,bank}$ is the Shields stress associated with the the threshold for bank erosion ($= \tau_{c,bank}/[(\rho_s - \rho) g d_{50}]$).

Next, using a_{reg} and $\tau_{c,bank}$ as relevant parameters, and through power law regressions of the available data set, Francalanci et al. (2020) were eventually able to derive, and subsequently validate, the following power law relations, appropriate for both gravel- and sand-bed rivers

$$\frac{B_{bf}}{a_{reg}} = 10.294 \left(\tilde{Q} \tau_{*c,bank}^{0.20} \right)^{0.4429}, \quad (467a)$$

$$\frac{D_{bf}}{a_{reg}} = 0.7658 \left(\tilde{Q} \tau_{*c,bank}^{0.15} \right)^{0.3456}. \quad (467b)$$

These relations (467) can be used to predict the water depth and the equilibrium cross-section width on the basis of the dimensionless bankfull discharge, \tilde{Q} , and the parameters a_{reg} and $\tau_{*c,banks}$. These two latter quantities, in turn, can be either known directly from field measurements, or determined through equations (466), requiring, besides \tilde{Q} , knowledge of the median sediment grain size d_{50} of the channel bed.

The bankfull equilibrium relations (467) are plotted in Figure 80 together with the quasi-universal relations (457) and (462) derived by (Parker *et al.*, 2007) and (Wilkerson and Parker, 2011), respectively. Despite some scatter, the collapse of gravel- and sand-bed data around the universal relations (467) is remarkable and indirectly confirms the importance of bank undulations in controlling, through skin friction, grain-by-grain bank erosion and, ultimately, the equilibrium bankfull geometry of both sand-bed and gravel-bed rivers with cohesive banks.

The importance of the role exerted by the critical shear stress of the material composing the banks has also been confirmed by the analysis carried out by Dunne and Jerolmack (2020) combining a global dataset of river data with a specific field study. The analysis supports the idea that the cross-section of alluvial rivers adjusts its geometry to the threshold fluid stress for particle entrainment of the most resistant material lining the channel. Hence, in accordance with the finding of Francalanci et al. (2020), a threshold-limiting channel model is a suitable tool to describe the average hydraulic state of alluvial river cross-sections across a wide range of conditions.

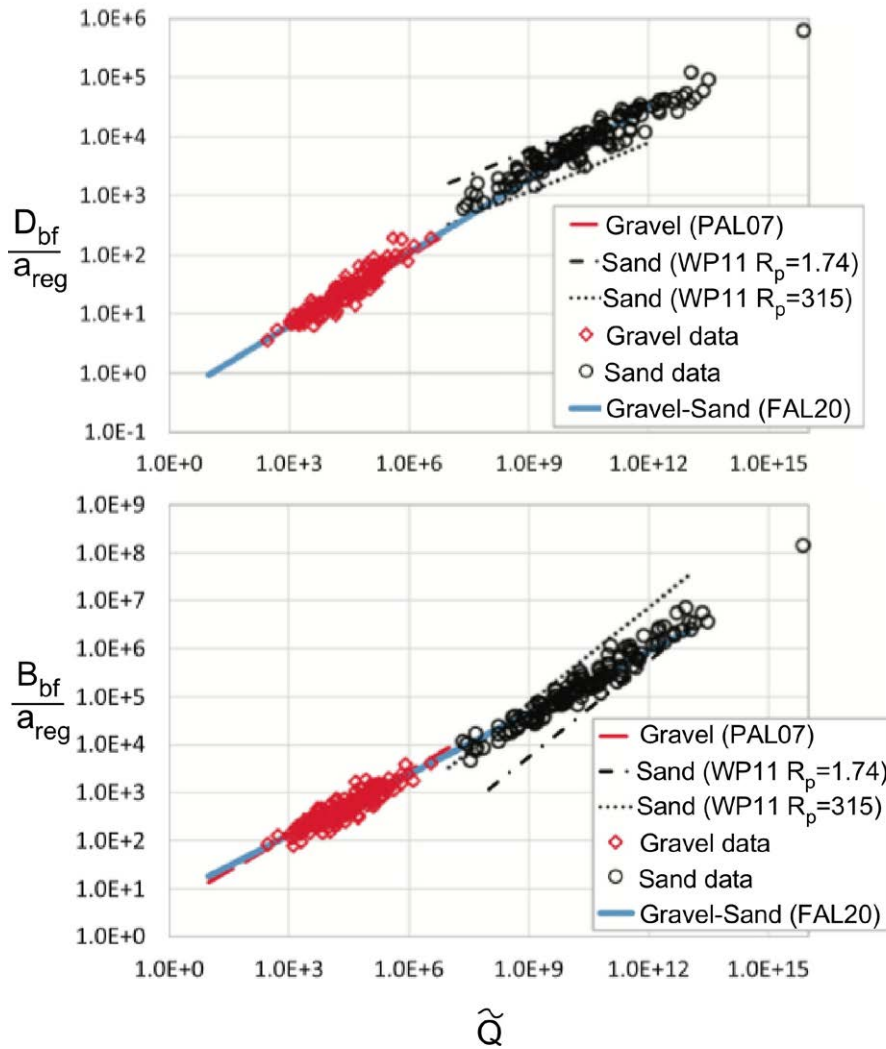


Figure 80. Comparison of the universal relations derived by Francalanci et al. (2020) for both gravel-bed and sand-bed rivers with cohesive banks (FAL20, equations (467)) with the quasi-universal relations derived empirically through linear regression and back data analysis by (Parker *et al.*, 2007) for gravel-bed rivers (PAL07, equations (457)) and by Wilkerson and Parker (2011) for sand-bed rivers (WP11, (462)), for two different values of particle Reynolds number, R_p .

6. Free and forced bars in straight channels

The present Chapter is devoted to a survey of the large body of research developed to understand theoretically and experimentally the physical mechanisms underlying the formation and development of bars. As briefly outlined in Chapter 1, they consist of rhythmic sequences of regions of scour (*pools*) and deposit (*riffles*), i.e. bed interfacial waves, with wavelengths scaling with channel width and amplitudes scaling with flow depth. We also pointed out that bars may develop spontaneously at the bed interface as a result of a bottom instability. In this case they are called *free bars* and are typically migrating features. Alternatively, they may arise in response to some steady, local or distributed, forcing: in this case they are called *forced bars* and are typically non-migrating features.

This distinction was first introduced by Seminara and Tubino (1989) and immediately lends itself to an obvious question: may free bars coexist with forced bars? The first answer to this fundamental question was provided by an outstanding Japanese geomorphologist (Kinoshita, 1961), who published an extensive set of field observations, performed on the Ishikari River few years after the publication of Leopold and Wolman (1957). Unfortunately, the works of Kinoshita were published in Japanese and thus remained largely unknown to the western scientific community. However, thirty years later, G. Parker kindly provided a translation of one of Kinoshita's paper (Kinoshita and Miwa, 1974), where a major observation was reported: free bars may migrate through meandering rivers, thus coexisting with the forced (point) bars driven by curvature, as long as the river sinuosity does not exceed some threshold value. In the companion Monograph we will formulate a rational theory of fluvial meandering and provide a mechanistic interpretation of the fundamental observation of Kinoshita and Miwa (1974). However, in the present chapter we will see that the issue of the coexistence of free and forced bars is a fundamental one and is encountered also in the case of straight channels.

Below, we start with a brief phenomenological introduction on the characteristics of bars observed in laboratory experiments (Section 6.1) that raise a number of questions requiring theoretical understanding. We then formulate the mathematical problem of bar morphodynamics in dimensionless form (Section 6.2). Next, we present the theories that explain the formation of free (Section 6.3) and forced (Section 6.4) bars, their development in the weakly nonlinear regime where they attain finite but *moderately large* amplitudes (Section 6.5), and their fully nonlinear evolution (Section 6.6). We conclude with a discussion of the additional complexities usually observed in the field. This will allow us to outline the role of some further effects on bar development, including unsteadiness of the basic flow, insufficient sediment supply, sorting, and the coexistence of bars with smaller scale bedforms (Section 6.7).

The whole theoretical treatment relies heavily on the classical methods of stability theory. For the benefit of the reader unfamiliar with the subject we have added a Mathematical Appendix (Chapter 9) where we provide an introduction to some mathematical tools employed in the present Monograph, and in particular we summarize the main ideas of stability theory. Note that by no means this Mathematical Appendix pretends to provide a comprehensive survey of the subject. It is limited to a presentation of the least set of introductory concepts and routine techniques needed to understand the formation and development of bars investigated in this Chapter.

6.1. Free and forced bars in the laboratory

Laboratory observations have played a major role to guide theoretical interpretations of bar formation and bar development, as they allow one to isolate single processes reducing the complexity of the natural phenomenon. In particular, sediment may be modeled at first as uniform, the laboratory channel is straight and rectangular, the flow is steady. Field observations have recently become more feasible thanks to the development of modern measuring techniques, like in situ flow and bathymetric surveys, remote sensing-satellite imagery and ground penetrating radar. Field studies do not suffer from the intrinsic limits of laboratory experiments, though it is less easy to extract from the collected data general indications about the underlying physical mechanisms. In the present Section, we restrict ourselves to laboratory observations, that provide an appropriate introduction to the theoretical analysis developed later on. We will go back to field observations in Section 6.7 where we will also discuss recent attempts to assess the applicability of theoretical models to the real world.

After a number of previous non systematic attempts by various Authors, a detailed and comprehensive set of laboratory observations of free bars was reported by Fujita and Muramoto (1985) (but see also the previous work of Fujita and Muramoto, 1982). This is a cornerstone paper for the development of bar morphodynamics. For two reasons. Firstly, the large size of the facilities employed reduced the scale effects that unavoidably affect experiments of this kind. Three flumes of the Ujigawa Hydraulic Laboratory of the Disaster Prevention Research Institute of Kyoto University were used, the largest of them was 7.5 m wide, 1.5 m deep and 243 m long. Secondly, the goal of the investigation was not purely descriptive but aimed at understanding the mechanisms of bar formation and bar development. Indeed, various important observations emerged from the experiments, as shown in Figure 81, illustrating the temporal development of bars in the initial reach of the experimental flume. Short diagonal forms appear in the very initial stage, they then develop into well defined forms exhibiting diagonal fronts with clearly recognizable wavelength. Note that bars develop both in time and in space and reach eventually an equilibrium state, characterized by an equilibrium height and an equilibrium wavelength, both exhibiting small fluctuations (Figure 82). It is also noteworthy that the initial bar wavelength is significantly smaller than its equilibrium value. We will show that nonlinearity is responsible for this effect. Linear theories of bar formation do predict values of the bar wavelength much smaller than those predicted by fully nonlinear theories.

A second significant set of laboratory observations was published by Lanzoni (2000a) (but see also Lanzoni, 1995). Also these experiments employed a quite large flume (a rectangular channel 55 m long, 1.5 m wide, 1 m deep) and were performed under well controlled steady flow conditions. Novel features of Lanzoni (2000a) experiments were:

- differently from Fujita and Muramoto (1985), where the Froude number was relatively large (roughly falling in the range 0.8 – 1.2), the flow conditions in Lanzoni (2000a) fell in the low Froude number range;
- the initial bed configuration was covered by ripples and/or dunes;
- besides the free bar tests, the formation of forced bars was also investigated: forcing consisted of a localized reduction of channel width obtained by inserting a plate orthogonal to the left wall near the flume inlet.

The free bar tests of Lanzoni (2000a) essentially confirmed the observations of Fujita and Muramoto (1985). On the other hand, Figure 83 shows the results of three forced bar tests. Note that the plotted values were calculated averaging over 19, 29, and 26 independent soundings, respectively. Moreover, data were filtered by using a four points moving average procedure, in order to smooth out the effect of small scale bedforms.

The pattern observed in the forced experiments is of great interest and calls for some theoretical explanation. In two runs (P1204 and P2804) the bar perturbation driven by the initial forcing exhibited a strong downstream damping. On the contrary, in one run (P1202) the pattern was not damped. Thus various issues arise. In particular, what controls the degree of spatial damping

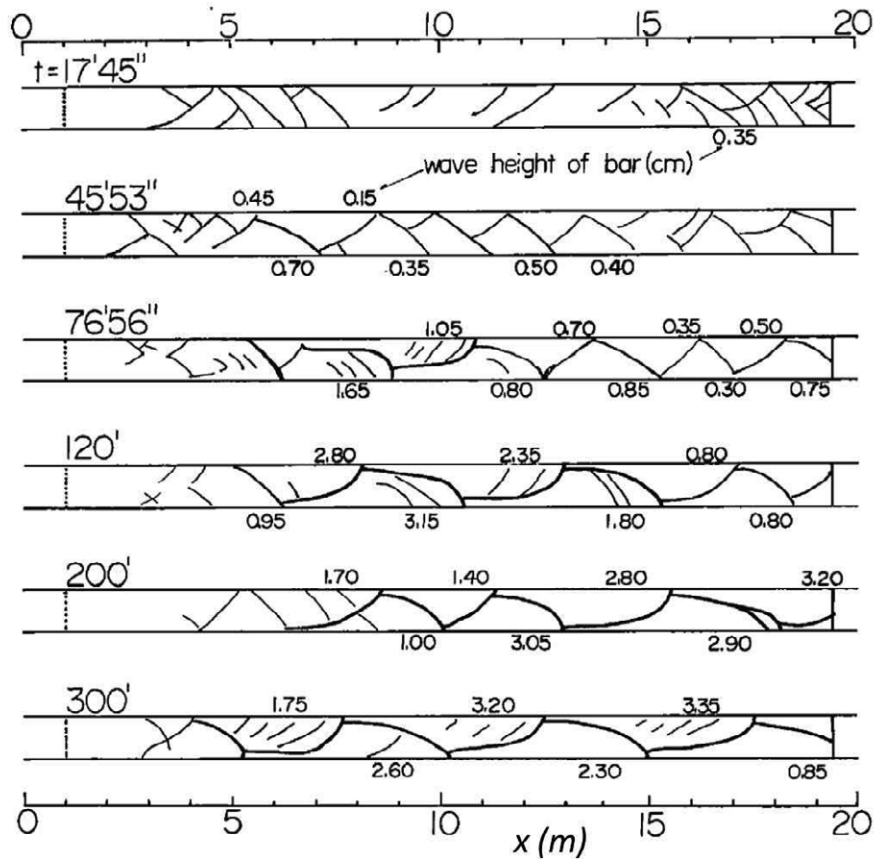


Figure 81. Sketch of the spatially and temporally developing bars observed in run H2 of Fujita and Muramoto (1985) (modified from the latter paper)

(or amplification) undergone by the forced bar sequence? In the case of bar amplification, is an equilibrium amplitude reached asymptotically in space? Is the forcing effect of the obstruction felt only downstream or may there be an upstream influence? All these questions will be answered in this Chapter.

A second important observation of Lanzoni (2000a) concerns the possible coexistence of forced and free bars: in each of the forced runs an extremely irregular sequence of free bars was detected toward the downstream end of the flume and their amplitude was apparently reduced by their coexistence with forced bars. Again, this observation raises an important theoretical question: under what conditions free and forced bars may coexist?

Note, that similar flume observations of forced bars had been previously made in experiments of Struiksma and Crosato (1989) (Figure 84). The investigated flow regime fell again in the low Froude number range, sediment was fine sand and small scale bedforms were present. Stationary forced bars (wavelength about 6.6 m), mildly damped in the longitudinal direction, were found to coexist with shorter free bars (wavelength about 3.9 m) migrating downstream at the speed of 10 cm/h.

More recently, Crosato *et al.* (2012) repeated the latter experiment in the context of a numerical and laboratory investigation aimed at ascertaining the existence of free non-migrating bars. The distinct feature of this experiment consisted of its long duration as runs lasted several weeks. The outcome of the investigation was twofold.

In the *forced* experiment a transverse plate was located at the entrance section. Migrating

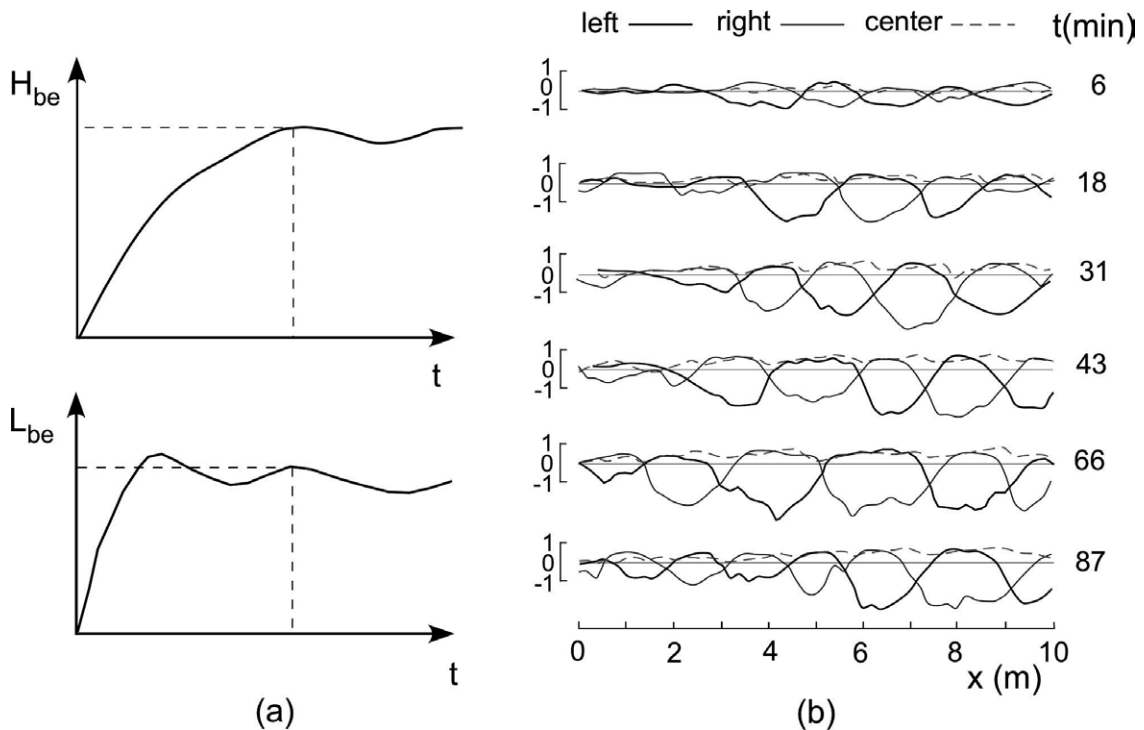


Figure 82. (a) Sketch of the temporal increase of the bar height H_b and the bar wavelength L_b in the experiments of Fujita and Muramoto (1985). H_{be} and L_{be} denote their equilibrium values; (b) Spatial and temporal evolution of the bed elevation at the side walls and at the channel centerline in run C-2 (redrawn from Fujita and Muramoto, 1985).

bars were found to coexist with the stationary spatially damped bars forced by the initial channel obstruction, although the former migrating features were present only in the second half of the flume. Migrating bars appeared to be suppressed in the region where steady bars had a comparable or larger amplitude. The Authors also reported some cyclic fluctuation of the amplitude of migrating bars that sometimes vanished to reform later.

In the *free* experiment, carried out without the transverse plate at the flume entrance, the picture reported was surprisingly similar to that of the *forced* experiment. Both migrating and stationary bars formed. Initially, migrating bars were present along almost the entire flume length but four weeks later, they were observed only in the second half of the flume. This change of morphodynamic behaviour occurred simultaneously with the emergence of a steady bar in the upstream part of the flume. Finally, the migrating bars had again a cyclic behavior, forming, reducing in size, and reforming roughly every two weeks.

All these observations, and in particular the presence of a stationary bar in the *free* experiment call for a clear theoretical explanation, noting that the latter feature did not emerge in the numerical experiments performed by Crosato *et al.* (2012).

6.2. Bars: The simplest theoretical framework.

The simplest framework adequate to explain the formation and development of free bars in open erodible channels consists of analyzing how the initially uniform flow and bed topography in a sufficiently wide rectangular channel responds to perturbations, ignoring the role of the side wall boundary layers that play a fairly passive role in the process. The latter assumption allows one to simplify the structure of the *basic state*, that may be assumed to consist of an effectively *plane* uniform open channel flow in equilibrium with its erodible bed (see Chapter 2). Consequently,

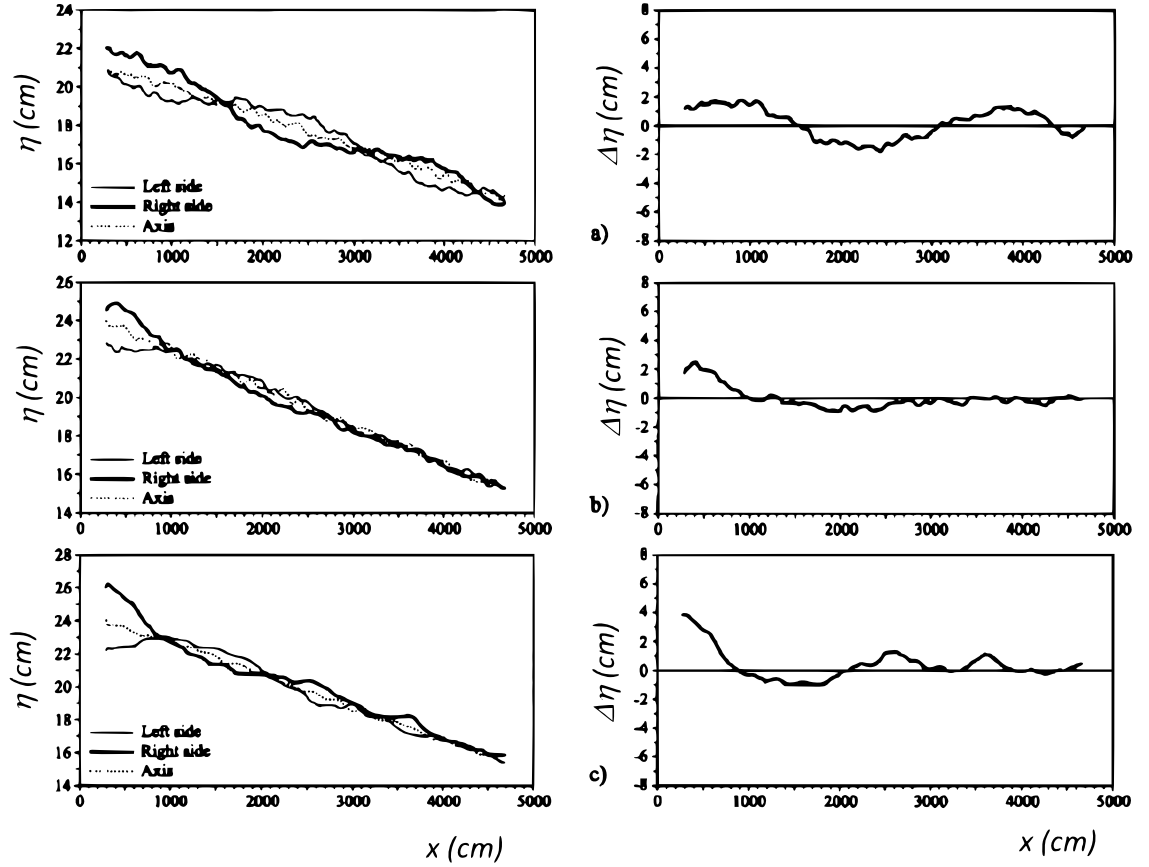


Figure 83. Longitudinal distribution of the bed elevation at the side walls and at the channel centerline in runs a) P2102, b) P1204 and c) P2804 of Lanzoni (2000a) (left plots) and difference between right and left side bed elevation ($\Delta\eta$) in the same runs (right plots) (modified from Lanzoni, 2000a).

the basic state is independent of the longitudinal coordinate (*uniform*), of the lateral coordinate (*plane*) and of time (*steady*). Albeit these assumptions are inessential, they greatly simplify the analysis.

Hydrodynamics

Let us then consider a wide rectangular channel with width $2B$, slope S , erodible bottom and inerodible side-walls. We refer the flow to a cartesian reference system (x, y, z) with x longitudinal and y lateral coordinate lying on the undisturbed plane bed (Figure 85). Moreover, let t denote the time variable. We adopt the notation of Section 2.3.3 for the case of infinitely wide channels. Hence, we denote by D_u and U_u the flow depth and the vertically averaged flow speed, respectively, and by C_{fu} , F_{ru} and $u_{\tau u}$ the corresponding values of the friction coefficient, the Froude number and the friction velocity, respectively. We also recall that the above quantities satisfy the following relationships:

$$u_{\tau u}^2 = C_{fu} U_u^2 = g S D_u, \quad F_{ru}^2 = \frac{U_u^2}{g D_u}. \quad (468a,b)$$

We then formulate the problem of morphodynamics in dimensionless form. Since field observations suggest that the bar wavelength scales with channel width (Figure 3), it is convenient to

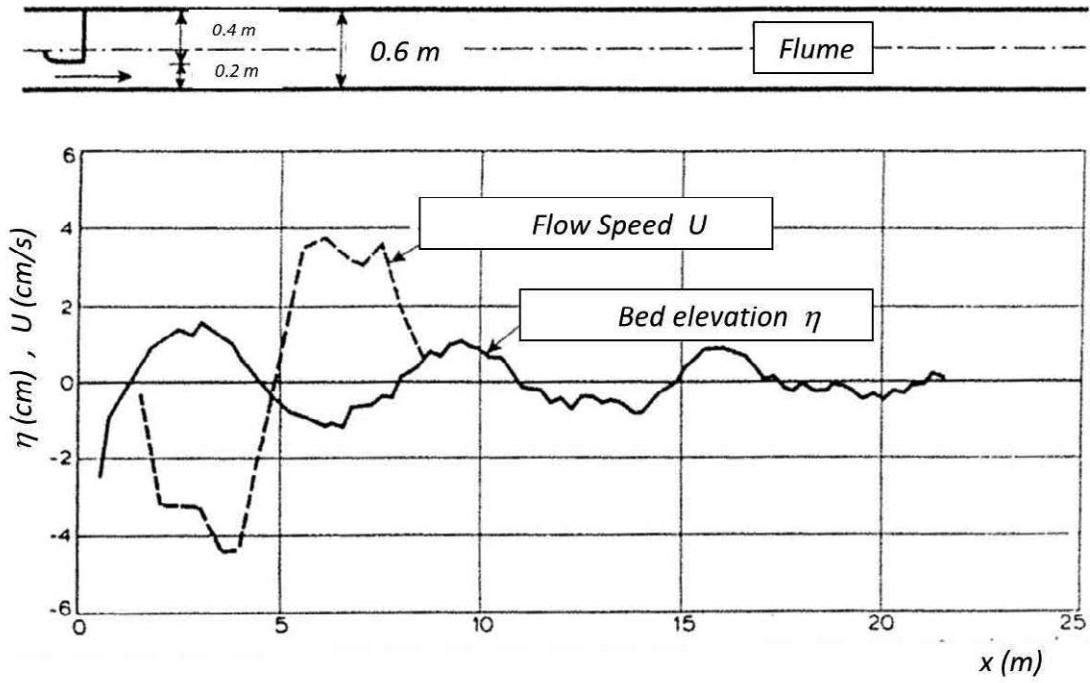


Figure 84. Longitudinal distribution of the bed elevation close to a side wall and of the flow speed in the *forced bar* experiment of Struiksma and Crosato (1989) (modified from Struiksma and Crosato, 1989).

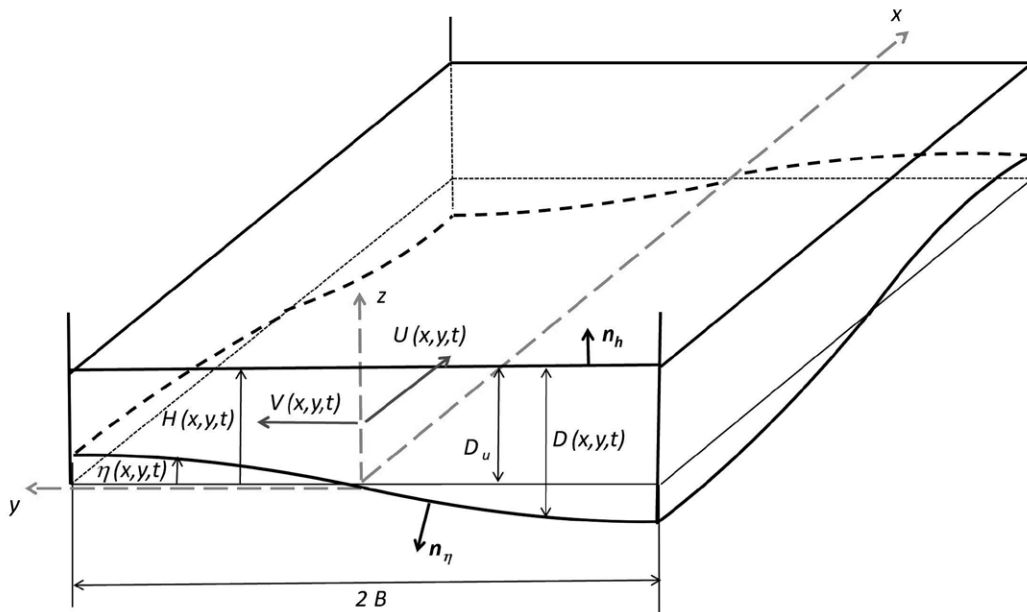


Figure 85. Flow over a free bar in a straight channel: sketch and notations

set:

$$(\tilde{x}, \tilde{y}) = \frac{(x, y)}{B}, \quad \tilde{t} = \frac{t}{B/U_u}, \quad (\tilde{U}, \tilde{V}) = \frac{(U, V)}{U_u}, \quad \tilde{D} = \frac{D}{D_u}, \quad \tilde{H} = \frac{H}{F_{ru}^2 D_u}, \quad (469)$$

where a tilde denotes a dimensionless quantity. Note that time has been scaled by the *hydrodynamic temporal scale* B/U_u , namely the time required by the base flow to travel a distance equal to the spatial scale B . However, other temporal scales may play an important role. A *flood time scale* may be externally imposed if the flow discharge supplied to the channel reach varies in time. Moreover, as illustrated below, a *morphological time scale* controls the response of the bed interface to spatial variations of sediment transport capacity. Flood and morphological time scales are often comparable and are much larger than the hydrodynamic time scale. This suggests that in most cases, though not always, the flow field may be assumed to adapt almost instantaneously to temporal variations of sediment supply and morphological changes.

Also, note that the scaling adopted for free surface elevation H allows us to remove F_{ru} from the formulation. This occurs because the size of perturbations of free surface elevation is $\mathcal{O}(F_{ru}^2)$. This means that they are negligible at low Froude numbers and may be significant in the transitional and high Froude number regimes.

With the help of the latter definitions, the shallow water equations take the following dimensionless form:

$$\frac{\partial \tilde{D}}{\partial \tilde{t}} + \frac{\partial(\tilde{D}\tilde{U})}{\partial \tilde{x}} + \frac{\partial(\tilde{D}\tilde{V})}{\partial \tilde{y}} = 0, \quad (470)$$

$$\frac{\partial \tilde{U}}{\partial \tilde{t}} + \tilde{U} \frac{\partial \tilde{U}}{\partial \tilde{x}} + \tilde{V} \frac{\partial \tilde{U}}{\partial \tilde{y}} + \frac{\partial \tilde{H}}{\partial \tilde{x}} + \beta C_f \frac{\tilde{U} \sqrt{\tilde{U}^2 + \tilde{V}^2}}{\tilde{D}} = 0, \quad (471)$$

$$\frac{\partial \tilde{V}}{\partial \tilde{t}} + \tilde{U} \frac{\partial \tilde{V}}{\partial \tilde{x}} + \tilde{V} \frac{\partial \tilde{V}}{\partial \tilde{y}} + \frac{\partial \tilde{H}}{\partial \tilde{y}} + \beta C_f \frac{\tilde{V} \sqrt{\tilde{U}^2 + \tilde{V}^2}}{\tilde{D}} = 0. \quad (472)$$

In this formulation, the two dimensionless parameters controlling the process under investigation emerge.

- The first is the local and instantaneous value of the friction coefficient, C_f . The reader should recall that in rough uniform turbulent flow this parameter depends on the relative bottom roughness.
- The second is the *aspect ratio* β defined as:

$$\beta = \frac{B}{D_u}. \quad (473)$$

Below we will show that β plays a major role in the instability process from which bars originate.

Also, note that employing the governing equations in dimensionless form has a second major advantage: it allows one to seek solutions based on rational perturbation procedures. This will be illustrated in the next Sections.

Evolution of the bed interface

In order to obtain a dimensionless form of the evolution equation of the bed interface, we start from the simplified form of the two-dimensional Exner equation (245) with negligible suspended load and define the dimensionless quantities:

$$\tilde{\eta} = \frac{\eta}{D_u}, \quad (\tilde{Q}_{sx}^b, \tilde{Q}_{sy}^b) = \frac{(Q_{sx}^b, Q_{sy}^b)}{\sqrt{(s-1)g d^3}}. \quad (474)$$

Here, η is the elevation of the bed surface relative to the unperturbed plane bed with constant slope S . Moreover, again, a tilde denotes dimensionless quantities and the Einstein scale has been

used for the bedload contribution \mathbf{Q}_s^b to the total sediment flux \mathbf{Q}_s . With the help of the above definitions and some algebraic manipulations we eventually find:

$$\frac{\partial \tilde{\eta}}{\partial \tilde{t}} + \epsilon_M \left(\frac{\partial \tilde{Q}_{sx}^b}{\partial \tilde{x}} + \frac{\partial \tilde{Q}_{sy}^b}{\partial \tilde{y}} \right) = 0. \quad (475)$$

The parameter ϵ_M represents the ratio between the chosen morphological and hydrodynamic time scales, namely:

$$\epsilon_M = \frac{\sqrt{(s-1)gd^3}}{c_M D_u U_u}. \quad (476)$$

It usually attains quite small values. For example, assuming $U_u \sim 1 \text{ m/s}$, $D_u \sim 1 \text{ m}$, $d \sim 1 \text{ mm}$, it follows that $\epsilon_M \sim \mathcal{O}(10^{-4})$ and this estimate decreases rapidly for finer sediments.

The equation (475) thus implies that the bed morphology undergoes very small ($\mathcal{O}(\epsilon_M)$) changes on the fast hydrodynamic time scale. In other words, morphological changes are slow processes described by the *slow variable* $\tilde{t}_M = \epsilon_M \tilde{t}$. Hence, (475) may be written in the alternative clearer dimensionless form:

$$\frac{\partial \tilde{\eta}}{\partial \tilde{t}_M} + \frac{\tilde{Q}_{sx}^b}{\partial \tilde{x}} + \frac{\tilde{Q}_{sy}^b}{\partial \tilde{y}} = 0. \quad (477)$$

In the general case, we must include also the contribution of the components of the sediment flux transported in suspension, for which the appropriate scale is $C_u D_u U_u$, where C_u is the depth averaged concentration of the basic uniform flow. Hence we write:

$$(\tilde{Q}_{sx}^s, \tilde{Q}_{sy}^s) = \frac{(Q_{sx}^s, Q_{sy}^s)}{C_u D_u U_u}. \quad (478)$$

Recalling equation (245), the complete dimensionless form of the evolution equation of the bed interface reads:

$$\frac{C_u}{c_M} \frac{\partial}{\partial \tilde{t}_M} \left(\tilde{D} \frac{C}{C_u} \right) + \frac{\partial \tilde{\eta}}{\partial \tilde{t}_M} + \frac{\partial \tilde{Q}_{sx}^b}{\partial \tilde{x}} + \frac{\partial \tilde{Q}_{sy}^b}{\partial \tilde{y}} + r_{sb} \left(\frac{\partial \tilde{Q}_{sx}^s}{\partial \tilde{x}} + \frac{\partial \tilde{Q}_{sy}^s}{\partial \tilde{y}} \right) = 0, \quad (479)$$

where r_{sb} is the following dimensionless parameter:

$$r_{sb} = \frac{1}{\epsilon_M} \frac{C_u}{c_M}. \quad (480)$$

Note that for dilute suspensions ($C_u \ll c_M$), the first term of (479) is typically negligible. Ignoring this term, the general dimensionless form of the evolution equation of the bed interface takes the final form:

$$\frac{\partial \tilde{\eta}}{\partial \tilde{t}_M} + \frac{\partial \tilde{Q}_{sx}^b}{\partial \tilde{x}} + \frac{\partial \tilde{Q}_{sy}^b}{\partial \tilde{y}} + r_{sb} \left(\frac{\partial \tilde{Q}_{sx}^s}{\partial \tilde{x}} + \frac{\partial \tilde{Q}_{sy}^s}{\partial \tilde{y}} \right) = 0. \quad (481)$$

The role of suspended load may be negligible with respect to, comparable with or dominant over that of bed load, depending on the values experienced by the dimensionless parameter r_{sb} .

Closures

In order to make any progress with (481), we need the closure relationships for the dimensionless quantities \tilde{Q}_s^b and \tilde{Q}_s^s presented in Chapter 3. Moreover, closure is needed for the friction coefficient C_f .

As far as \tilde{Q}_s^b is concerned, we may make use of the relationships (334a), (334b), (350), (351) appropriate to bedload transport on sloping beds. However, caution is needed as those relationships

were established assuming a cartesian coordinate system with x aligned with the tangential stress at the bottom. In order to apply them to a fluvial context where x is aligned with the longitudinal component of flow velocity, we must allow for the effects of rotation of the (x, y) coordinate axes by an angle equal to the angle χ that the bottom stress forms with the longitudinal axis. In the context of a linearized approximation (weakly sloping beds) adopted here, we readily find that:

$$\sin \chi = \frac{\tilde{V}}{\sqrt{\tilde{U}^2 + \tilde{V}^2}}. \quad (482)$$

With the help of this relationship, we end up with the following closures for \tilde{Q}_{sx}^b and \tilde{Q}_{sy}^b :

$$\tilde{Q}_{sx}^b = \Phi_0^b \left(1 - R_x \frac{\partial \tilde{\eta}}{\partial \tilde{x}} \right), \quad \tilde{Q}_{sy}^b = \Phi_0^b \left(\frac{\tilde{V}}{\sqrt{\tilde{U}^2 + \tilde{V}^2}} - R_y \frac{\partial \tilde{\eta}}{\partial \tilde{y}} \right), \quad (483a,b)$$

where

$$R_x = -\frac{1}{\Phi_0^b} \frac{\tau_{*c0}}{\beta \mu_s} \left[\frac{d\Phi^b}{d\tau_{*c}} \right]_{\tau_{*c0}}, \quad R_y = \frac{r}{\beta \sqrt{\tau_*}}, \quad (484a,b)$$

and $\Phi_0^b = \Phi^b|_{\tau_*, \tau_{*c0}}$. We stress that in (483) the coordinates \tilde{x} and \tilde{y} , as well as the bed elevation $\tilde{\eta}$ are dimensionless. This leads to the presence of the width to depth parameter β in the denominator of the expressions for R_x and R_y . The fact that β is most often large enough confirms the validity of the weakly sloping approximation, except close to possible fairly sharp fronts of the bed interface.

Closure for the dimensionless suspended flux per unit width \mathbf{Q}_s^s can be obtained using the full 3D formulation (261) for the advection-diffusion equation. Alternatively, under spatially and/or temporally slowly varying conditions in the sense discussed in Chapter 4, one may employ a simpler 2D (depth averaged) approach. Bars are sedimentary patterns, sufficiently long and slow to justify the use of such an approach. Using the notations of Section 4.3.2 and noting that the longitudinal scale appropriate to free bars is B , we set:

$$\delta = \frac{U_u}{w_s \beta}. \quad (485)$$

Recalling the dimensionless closure relationship (295), we may eventually write:

$$(\tilde{Q}_{sx}^s, \tilde{Q}_{sy}^s) = \tilde{D}(\tilde{U}, \tilde{V}) [\Phi_0^s + \delta \Phi_1^s + \mathcal{O}(\delta^2)], \quad (486)$$

where Φ_0^s and Φ_1^s are respectively given by the relationships (298) and (300), with the coefficient γ set equal to one.

Closure for the friction coefficient depends on whether the undisturbed bed may be treated as plane or covered by small scale bedforms, to be treated as macro-roughness elements as discussed in Section 4.5.

6.3. The formation of free bars: Linear stability analysis

6.3.1 Bar formation under bedload dominated conditions

Let us now investigate the formation of free bars theoretically, starting from the case when sediment is dominantly transported as bed load.

As pointed out in Section 6.1, free bars develop because a uniform turbulent open channel flow over an erodible cohesionless bed is most often unstable. Physically, instability arises because the bed topography is never perfectly plane (even in a laboratory experiment) and the associated flow

field is never perfectly uniform. In other words, the basic uniform state is invariably *perturbed* in the real world. Perturbations may be unable to grow, if their growth is inhibited by sufficiently strong damping mechanisms. On the contrary, instability arises if destabilizing mechanisms prevail on damping effects. The mathematical framework developed to ascertain under what conditions a *basic state* is unstable and to predict the new state arising from the instability process is known as *stability theory*, the elements of which are outlined in the Mathematical Appendix to the present Monograph (Chapter 9).

In order to ascertain instability, the first step is to restrict the class of perturbations assumed to act on the basic state considering *small* (strictly infinitesimal) perturbations. This simplifies the analysis considerably as the governing equations may be linearized. A number of linear stability theories dealing with free bar formation in straight erodible channels with inerodible banks have been proposed since the late 1960's (see, among others, Adachi, 1967; Hansen, 1967; Callander, 1969; Hayashi, 1971; Hayashi and Ozaki, 1980; Engelund and Skovgaard, 1973; Parker, 1976; Fredsøe, 1978). Most of them were ultimately motivated by the aim to understand the mechanism of river meandering and river braiding, with the implicit assumption that the formation of alternate bars would be the precursor of meander formation (*bar theory*) and the formation of multiple row bars would evolve into a braided pattern. In the companion Monograph we will discuss and pursue a different viewpoint that originated from the seminal work of Ikeda *et al.* (1981) and was later developed by Blondeaux and Seminara (1985). The idea was to relax the assumption of inerodible banks and associate the formation of meanders with a mechanism of planform instability driven by bank erosion (*bend instability theory*).

However, in this Chapter we ignore the implications for river meandering and restrict our attention to the process of bar formation in straight channels with erodible bed but inerodible banks. Let us then consider a *basic state*, consisting of a uniform turbulent open channel flow. Below, we will employ the dimensionless formulation *removing the tildes for the sake of simplicity*. With the notations of Section 6.2, the basic state in dimensionless form reads:

$$U = 1, \quad V = 0, \quad D = 1, \quad H = H_0(x) = H_{00} - \beta S x, \quad (487)$$

Here, H_{00} sets the (dimensionless) free surface elevation at some initial cross-section.

Next, we perturb the basic state by infinitesimal perturbations, expanding U , V , D and H as follows:

$$(U, V, D, H) = (1, 0, 1, H_0) + \epsilon(U_1, V_1, D_1, H_1) + \mathcal{O}(\epsilon^2), \quad (488)$$

with ϵ small (strictly infinitesimal) parameter measuring the amplitude of perturbations.

We then substitute from the expansions (488) into the governing equations (470, 471, 472, 477) and the closure relationships (483, 484). Since the flow field evolves on a hydrodynamic time scale which is much faster than the morphodynamic time scale, temporal derivative are neglected in equations (470)-(472). Next, we perform the linearization procedure, consisting of expanding each quantity in powers of the small parameter ϵ and retaining only terms $\mathcal{O}(\epsilon^0)$ and $\mathcal{O}(\epsilon)$. At $\mathcal{O}(\epsilon^0)$ one recovers the basic state, while the $\mathcal{O}(\epsilon)$ equations provide the sought differential system governing the evolution of small perturbations.

Linearization

We now provide some details of the linearization procedure.

In order to linearize the bottom stress, we need to expand the friction coefficient. Assuming that small scale bedforms are not present and the sediment size (i.e. the absolute bottom roughness) is uniform, the friction coefficient may vary spatially and temporally only because the flow depth varies. Let us then set $C_f = C_f(D)$ and expand:

$$C_f = C_{f0} + \epsilon \left. \frac{dC_f}{dD} \right|_1 D_1 + \mathcal{O}(\epsilon^2) = C_{f0} [1 + \epsilon c_{fD} D_1 + \mathcal{O}(\epsilon^2)] , \quad (489)$$

where $C_{f0} = C_{fu}$ and

$$c_{fD} = \left. \frac{1}{C_{f0}} \frac{dC_f}{dD} \right|_1. \quad (490)$$

Substituting from (488, 489) into the shallow water equations (470, 471, 472) and performing the linearization, we find the following results.

$\mathcal{O}(\epsilon^0)$

The only equation contributing to the leading order is the longitudinal momentum equation, which reduces to:

$$F_{ru}^2 = \frac{S}{C_{f0}}, \quad (491)$$

that is simply a dimensionless version of Chézy law.

$\mathcal{O}(\epsilon)$

$$\frac{\partial U_1}{\partial x} + \frac{\partial V_1}{\partial y} + \frac{\partial D_1}{\partial x} = 0, \quad (492)$$

$$\frac{\partial U_1}{\partial x} + \frac{\partial H_1}{\partial x} + \beta C_{f0} [2U_1 + (c_{fD} - 1)D_1] = 0, \quad (493)$$

$$\frac{\partial V_1}{\partial x} + \frac{\partial H_1}{\partial y} + \beta C_{f0} V_1 = 0. \quad (494)$$

In order to linearize the evolution equation of the bed interface, we expand the Shields stress as follows

$$\begin{aligned} \tau_* &= \frac{\rho C_{f0} U_u^2}{(\rho_s - \rho) g d} \frac{C_f}{C_{f0}} (U^2 + V^2) \\ &= \tau_{*u} [1 + \epsilon c_{fD} D_1 + \mathcal{O}(\epsilon^2)] [1 + \epsilon (2U_1) + \mathcal{O}(\epsilon^2)] \\ &= \tau_{*u} [1 + \epsilon (c_{fD} D_1 + 2U_1) + \mathcal{O}(\epsilon^2)]. \end{aligned} \quad (495)$$

Recalling that η is equal to $F_{ru}^2 H - D$, we then linearize (483) and (484) to find:

$$Q_{sx}^b = \Phi_u^b \left\{ 1 + \epsilon \left[\Phi_T^b (c_{fD} D_1 + 2U_1) - R_{xu} \left(F_{ru}^2 \frac{\partial H_1}{\partial x} - \frac{\partial D_1}{\partial x} \right) \right] + \mathcal{O}(\epsilon^2) \right\}, \quad (496a)$$

$$Q_{sy}^b = \epsilon \Phi_u^b \left[V_1 - R_{yu} \left(F_{ru}^2 \frac{\partial H_1}{\partial y} - \frac{\partial D_1}{\partial y} \right) \right] + \mathcal{O}(\epsilon^2), \quad (496b)$$

where we have used the following notations:

$$\Phi_u^b = \Phi_0^b|_{\tau_{*u}}, \quad \Phi_T^b = \frac{\tau_{*u}}{\Phi_u^b} \frac{d\Phi_0^b}{d\tau_*}|_{\tau_{*u}}, \quad (497a)$$

$$R_{yu} = R_y|_{\tau_{*u}}, \quad R_{xu} = R_x|_{\tau_{*u}}. \quad (497b)$$

With the help of (496a, 496b) we can next linearize the bed evolution equation to find:

$$\begin{aligned} \left(F_{ru}^2 \frac{\partial H_1}{\partial t} - \frac{\partial D_1}{\partial t} \right) + \epsilon_M \Phi_u^b \left[\Phi_T^b \left(c_{fD} \frac{\partial D_1}{\partial x} + 2 \frac{\partial U_1}{\partial x} \right) - R_{xu} \left(F_{ru}^2 \frac{\partial^2 H_1}{\partial x^2} - \frac{\partial^2 D_1}{\partial x^2} \right) \right] \\ + \epsilon_M \Phi_u^b \left[\frac{\partial V_1}{\partial y} - R_{yu} \left(F_{ru}^2 \frac{\partial^2 H_1}{\partial y^2} - \frac{\partial^2 D_1}{\partial y^2} \right) \right] = 0. \end{aligned} \quad (498)$$

The boundary conditions associated with the linearized governing equations (492), (493), (494) and (498) impose that the lateral components of the flow velocity and sediment flux vanish at the banks, hence, recalling (496b):

$$V_1 \Big|_{y=\pm 1} = 0, \quad \left[F_{ru}^2 \frac{\partial H_1}{\partial y} - \frac{\partial D_1}{\partial y} \right]_{y=\pm 1} = 0, \quad (499)$$

Normal modes

We then perform a normal mode analysis of perturbations. As clarified in Chapter 9, the steady character of the basic state implies that the linear system admits of solutions that are exponential in time. Moreover, the spatial uniformity of the basic state allows us to represent the perturbations as Fourier integrals in the longitudinal coordinate (that is unbounded) and Fourier series in the lateral coordinate (that is defined in the finite interval $[-1, 1]$). Taking advantage of the linearity of the problem, we can investigate each component of the perturbation separately. Thus we set:

$$(U_1, D_1, H_1, V_1) = [(u_m, d_m, h_m) \mathcal{S}_m(y); v_m \mathcal{C}_m(y)] \exp i(\lambda x - \omega t) + c.c., \quad (500)$$

where *c.c.* stands for the *complex conjugate* of a complex number and we have used the following notations:

$$\mathcal{S}_m(y) = \sin\left(\frac{\pi}{2}my\right), \quad \mathcal{C}_m(y) = \cos\left(\frac{\pi}{2}my\right) \quad (\text{odd } m), \quad (501a)$$

$$\mathcal{S}_m(y) = \cos\left(\frac{\pi}{2}my\right), \quad \mathcal{C}_m(y) = \sin\left(\frac{\pi}{2}my\right) \quad (\text{even } m). \quad (501b)$$

Moreover, λ is the (real) *bar wavenumber* and $\omega (= \omega_r + i\omega_i)$ is a *complex growth rate*. Note that lateral Fourier modes have been chosen in (500) such to satisfy the boundary conditions (499) at the banks.

Let us further clarify the structure of the perturbation. Consider the perturbation of flow depth and assume its amplitude d_m is a real quantity. We may then write the perturbation in the clearer real form:

$$D_1 = 2d_m \sin\left(\frac{\pi}{2}my\right) \exp(\omega_i t) \cos(\lambda x - \omega_r t). \quad (502)$$

Hence, each *mode*, identified by an integer value of m , is essentially a *wave* characterized by a dimensionless *longitudinal wavenumber* λ and a dimensionless *angular frequency* ω_r , such that:

$$\lambda = \frac{2\pi B}{L}, \quad \omega_r = \frac{2\pi B/U_u}{T}, \quad (503)$$

with L wavelength and T wave period. The wave amplifies (or decays) depending on the dimensionless *growth rate* ω_i being positive or negative. The wave migrates with dimensionless *wavespeed* $c = \omega_r/\lambda$: migration is downstream if $\omega_r > 0$ and upstream if $\omega_r < 0$. The aim of the stability analysis is precisely to determine the growth rate (and speed) of perturbations as functions of the bar wavenumber and of the physical parameters that characterize the hydrodynamics and sediment transport.

Also note that other properties of the perturbation (velocity, free surface elevation) are waves that exhibit a phase lag with respect to the perturbation of the flow depth. Mathematically, this is equivalent to stating that the amplitudes of the velocity (or free surface) perturbation are not real quantities in general. Indeed, examine the perturbation of free surface elevation with h_m assumed to be complex, i.e. of the form $|h_m| \exp(-i\phi)$. Then, ϕ is precisely the phase lag of free surface elevation relative to flow depth, as illustrated by the following relationship:

$$H_1 = 2|h_m| \sin\left(\frac{\pi}{2}my\right) \exp(\omega_i t) \cos(\lambda x - \omega_r t - \phi). \quad (504)$$

The Figure 86 shows the shape of different bar modes. The mode $m = 1$ is called *alternate bar*, modes with $m > 1$ are referred to as *multiple row bars*. In particular the case $m = 2$ is associated with *central bars*. Alternate bars lead the thread of high velocity to follow a meandering path and this is the reason why alternate bars have been considered as precursors of river meanders. Central bars are often precursors of island formation as a result of vegetation growth whereby bar migration is stopped. Multiple row bars are considered as precursors of river braiding. The reader will then immediately appreciate why the analysis of bar formation has played an important role in the development of fluvial morphodynamics.

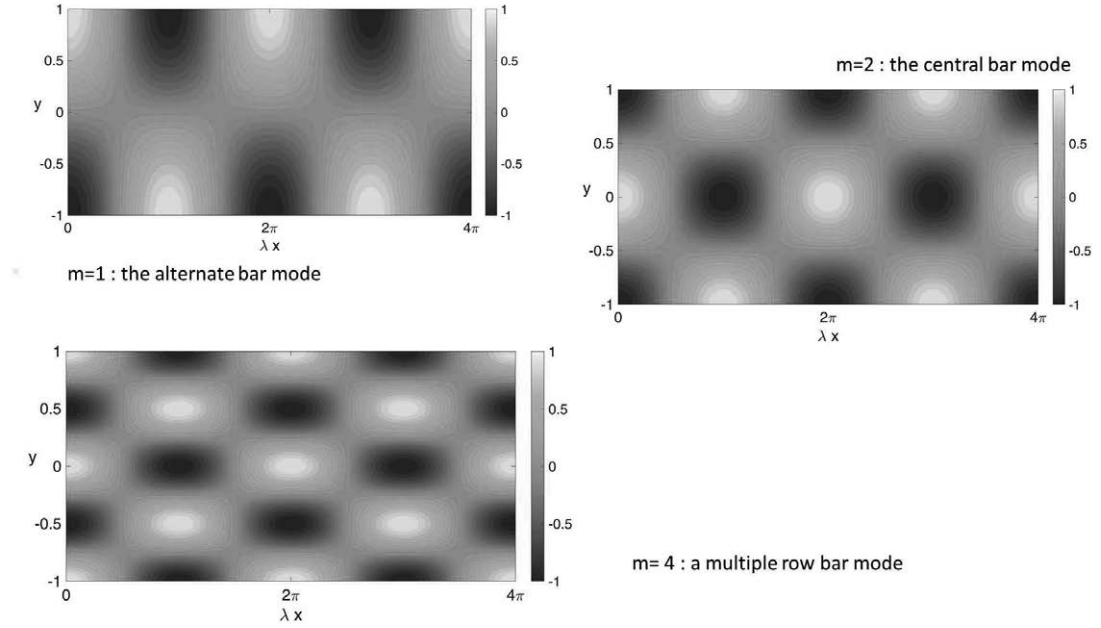


Figure 86. Sketch displaying the bed topography of different linear bar modes. Bed elevation is scaled by the bar amplitude. Note the alternate sequence of pools (blue regions) and deposits (yellow regions) that leads the thread of high velocity to follow a meandering ($m = 1$) or braiding ($m > 1$) pattern.

Normal mode analysis

On substituting from (500) into the linearized form of the governing differential equations (492, 493, 494, 498), one readily finds the following linear algebraic homogeneous system for the perturbation amplitudes u_m , v_m , d_m and h_m :

$$a_{1j} u_m + a_{2j} v_m + a_{3j} h_m + a_{4j} d_m = 0 \quad (j = 1, 4), \quad (505)$$

where:

$$a_{11} = i\lambda, \quad a_{21} = -M, \quad a_{31} = 0, \quad a_{41} = i\lambda, \quad (506a)$$

$$a_{12} = i\lambda + 2\beta C_{f0}, \quad a_{22} = 0, \quad a_{32} = i\lambda, \quad a_{42} = \beta C_{f0} (c_{fD} - 1), \quad (506b)$$

$$a_{13} = 0, \quad a_{23} = i\lambda + \beta C_{f0}, \quad a_{33} = M, \quad a_{43} = 0, \quad (506c)$$

$$a_{14} = 2i\lambda \Phi_T^b, \quad (506d)$$

$$a_{24} = -M, \quad a_{34} = F_{ru}^2 \left(-\frac{i\omega}{\epsilon_M \Phi_u^b} + \lambda^2 R_{xu} + M^2 R_{yu} \right), \quad (506e)$$

$$a_{44} = \frac{i\omega}{\epsilon_M \Phi_u^b} - M^2 R_{yu} + i\lambda c_{fD} \Phi_T^b - \lambda^2 R_{xu}, \quad (506f)$$

while the parameter M is defined as follows:

$$M = \frac{\pi}{2} m. \quad (507)$$

The homogeneous character of the linear algebraic system (505) implies that a solvability condition must be satisfied. This consists of imposing that the determinant of the matrix associated

with the linear system must vanish. We find:

$$-\frac{i\omega}{\epsilon_M \Phi_u^b} = -\lambda^2 R_{xu} - M^2 R_{yu} + \lambda \frac{A_0 + A_1 \lambda + A_2 \lambda^2 + A_3 \lambda^3}{B_0 + B_1 \lambda + B_2 \lambda^2 + B_3 \lambda^3}, \quad (508)$$

where

$$A_0 = -i M^2 \beta C_{f0} (-3 + c_{fD} + 2 \Phi_T^b), \quad A_1 = -M^2 (1 - c_{fD} \Phi_T^b), \quad (509a)$$

$$A_2 = -i \beta C_{f0} \Phi_T^b (c_{fD} - 2), \quad A_3 = \Phi_T^b (c_{fD} - 2), \quad (509b)$$

$$B_0 = -2 M^2 \beta C_{f0}, \quad B_1 = i [-M^2 + F_{ru}^2 (\beta C_{f0})^2 (c_{fD} - 3)], \quad (509c)$$

$$B_2 = \beta C_{f0} [-1 + F_{ru}^2 (4 - c_{fD})], \quad B_3 = i (F_{ru}^2 - 1). \quad (509d)$$

The algebraic constraint (508) establishes a relationship between the complex growth rate $-i\omega$ and the relevant physical parameters, namely the dimensionless *bar wavenumber* λ , the *aspect ratio* β , the undisturbed *Shields stress* τ_{*u} and the *relative roughness* d_s defined as:

$$d_s = \frac{d}{D_u}. \quad (510)$$

Note that the latter parameter determines the undisturbed friction coefficient C_{f0} in the absence of small scale bedforms. The equation (508) is called *dispersion relationship*.

A few observations arise immediately from a glance at (508).

Long bars are invariably stable. Indeed,

$$\lim_{\lambda \rightarrow 0} Re[-i\omega] = -\epsilon_M \Phi_u^b M^2 R_{yu}, \quad (511)$$

i.e. the bar growth rate ω_i is invariably negative.

A similar behavior is found in the opposite limit of *short bars*:

$$\lim_{\lambda \rightarrow \infty} Re[-i\omega] = -\epsilon_M \Phi_u^b \lambda^2 R_{xu}. \quad (512)$$

The reader should note that, in both cases, the stabilizing mechanism is gravity, acting either in the lateral direction or in the longitudinal direction.

One further limit, the case of *very wide channels* ($\beta \rightarrow \infty$), deserves attention. This limit was investigated by Hall (2007) who showed that, as $\beta \rightarrow \infty$, the parameter β can be scaled out of the analysis and the bar characteristics scale with flow depth.

The above results differ from those derived by Blondeaux and Seminara (1985) only for the inclusion of the effect of spatial variations of the local longitudinal slope on the longitudinal component of the depth averaged sediment flux (term proportional to R_{xu} in the dispersion relationship).

One further point deserves attention. As first pointed out by Fredsøe (1978), m can be scaled out of the dispersion relationship (508) through the simple transformations:

$$\omega|_m = m \omega|_1, \quad \beta|_m = m \beta|_1, \quad \lambda|_m = m \lambda|_1. \quad (513)$$

Essentially, the complex growth rate for mode m at $(m\lambda, m\beta)$ is m times the growth rate of the first mode at (λ, β) . In particular, the marginal stability curve of mode m is obtained from the marginal stability curve of the first mode through the transformation (513) and the critical conditions for mode m can be written in the form:

$$\beta_{cm} = m \beta_{c1}, \quad \lambda_{cm} = m \lambda_{c1}. \quad (514)$$

It is customary to represent the dispersion relationship in a plane with the value of some control parameter (β in our case) in the ordinate and the value of the perturbation wavenumber (λ in our case) in the abscissa. For any given mode m and given values of τ_{*u} and d_s , any point in this plane is associated with a unique value of the bar growth rate $Im[\omega_m]$ and the bar wavespeed $Re[\omega_m]/\lambda$. One may then draw iso-growth lines and iso-speed lines for any mode (Figure 87). In particular, the zero-growth line (assuming it exists) is commonly called *marginal or neutral stability curve*. When the marginal stability curve exhibits a minimum, as in Figure 87, this minimum determines the so called *critical conditions for linear instability*, i.e. a *critical wavenumber* λ_{cm} and a *critical value of the control parameter* β_{cm} . Under these conditions the linear theory predicts that bars of mode m amplify as the aspect ratio exceeds its critical value β_{cm} and the fastest growing perturbation has wavenumber λ_{cm} and wavespeed $Re[\omega_{cm}]/\lambda_{cm}$.

The dependence of β_c from the parameters τ_{*u} and d_s is shown in Figure 88.

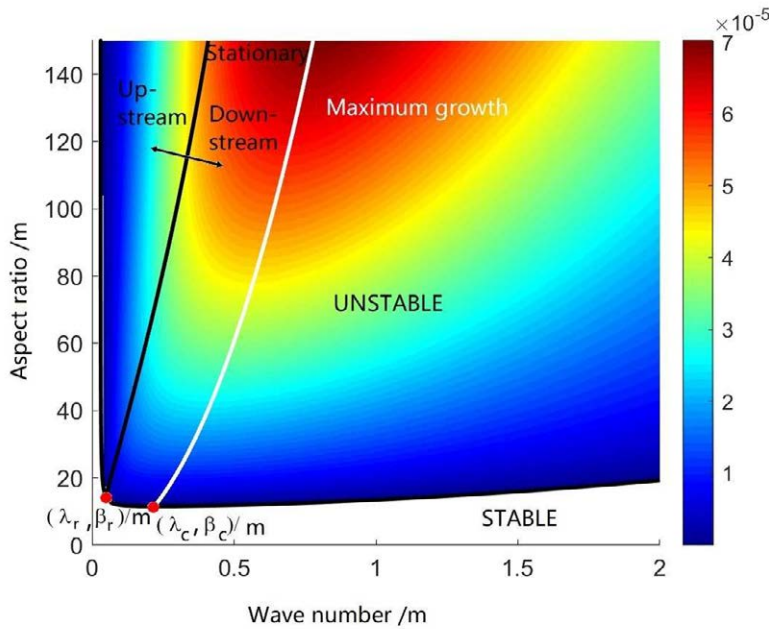


Figure 87. Formation of bars of mode m . The grey line separating the stable (white) and unstable (coloured) regions represents a typical neutral curve. The black line intersecting the neutral curve at $(\lambda_R, \beta_R)/m$ represents the zero bar speed line and separates the region of the stability plane where bars migrate downstream from the region where bars migrate upstream. On the white solid line bars are characterized by the maximum growth rate (adapted from Seminara, 2010).

Another important feature emerging from the plot shown in Figure 87 is the zero-speed line, that will be seen to play a special role in the bend theory of river meanders. Bars characterized by values of β and λ lying on the zero-speed line are *non-migrating*. They may be stable, marginally stable or unstable but, in the present linear context, they do not develop spontaneously because they are not the fastest growing perturbations, as clearly emerges if one compares the zero speed line and the maximum growth line in Figure 87. This notwithstanding, forcing mechanisms may excite the formation of non-migrating disturbances. Below we denote by β_R and λ_R the values of β and λ associated with the intersection of the zero-growth line with the zero-speed line. Also, note that the fastest growing bars migrate downstream, but upstream migrating bars are also allowed by the system. Again, upstream migrating bars do not develop spontaneously, at least at a linear level, as they are not the fastest migrating perturbations. But, in sufficiently wide channels ($\beta > \beta_R$), upstream bar migration may be forced by external mechanisms. This is an interesting feature with fundamental implications as migrating bars are also vectors of morphodynamic information.

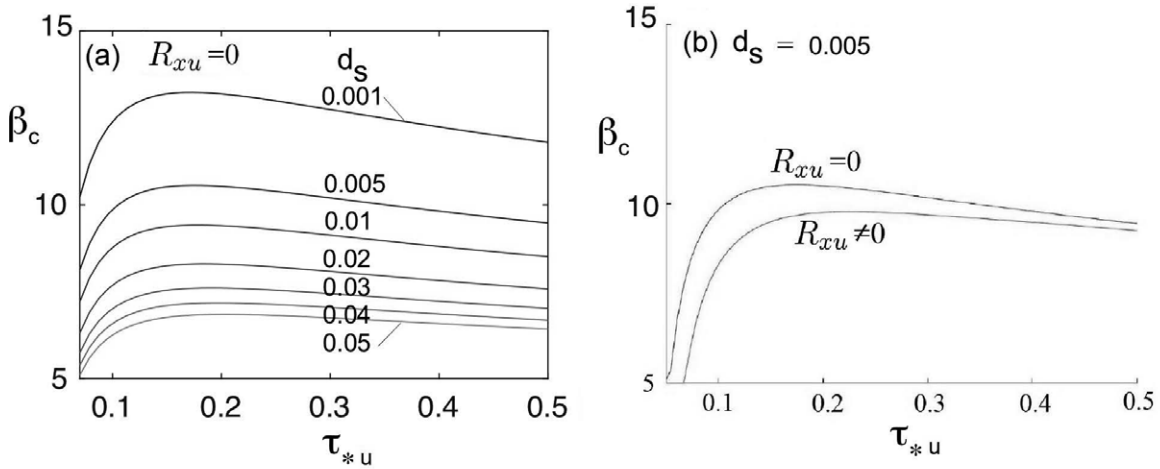


Figure 88. (a) The critical value of the aspect ratio β_c for alternate bar formation predicted by the theory of Blondeaux and Seminara (1985) ($R_{xu} = 0$) is plotted versus τ_{*u} for some values of d_s ; (b) Comparison with the case of a non-vanishing R_{xu} for $d_s = 0.005$ (in both cases the unperturbed bed is assumed to be plane).

In other words, we are implicitly stating that, under suitable conditions, river morphodynamics may display *upstream influence*. This issue will be discussed in the companion Monograph, in the context of the theory of river meandering.

The physical mechanism of bar instability

The physical mechanism controlling the onset of instability is related to the spatial distributions of the longitudinal and transverse components of bedload. Indeed, Exner equation predicts that a bedform amplifies provided the divergence of bedload transport is negative at the crest. The bed perturbation drives spatial variations of flow and sediment transport, which exhibit some lag with respect to the bottom profile. Perturbations will then be amplified provided the longitudinal transport decreases at the crests and/or the lateral transport is directed from the troughs towards the crests (Figure 89). To clarify this point, we follow Colombini *et al.* (1987) and write:

$$\eta_1 = F_{ru}^2 H_1 - D_1 = \eta_r \sin\left(\frac{\pi}{2} m y\right) \exp(\omega_i t) \cos(\lambda x - \omega_r t), \quad (515)$$

with η_r arbitrarily small amplitude of the initial bed perturbation. Any other property P of the linear perturbation can be written as proportional to $\cos(\lambda x - \omega_r t - \delta_P)$ where δ_P is the phase lag of the property P relative to bottom elevation. In particular, we may write

$$Q_{sx1}^b = Q_{sxr}^b \sin\left(\frac{\pi}{2} m y\right) \exp(\omega_i t) \cos(\lambda x - \omega_r t - \delta_{Q_{sx}}), \quad (516a)$$

$$Q_{sy1}^b = Q_{syr}^b \cos\left(\frac{\pi}{2} m y\right) \exp(\omega_i t) \cos(\lambda x - \omega_r t - \delta_{Q_{sy}}), \quad (516b)$$

where $\delta_{Q_{sx}}$ and $\delta_{Q_{sy}}$ are the phase lags of the longitudinal and lateral components of the perturbation of sediment flux. Substituting from (515), (516a) and (516b) into the Exner equation (475), one readily finds:

$$\frac{\omega_i}{\epsilon_M} = -\frac{\lambda Q_{sxr}^b}{\eta_r} \sin(\delta_{Q_{sx}}) + \frac{M Q_{syr}^b}{\eta_r} \cos(\delta_{Q_{sy}}), \quad (517)$$

where we have chosen the origin of the x -axis such that $\lambda x = \omega_r t$. Note that the peak of the longitudinal component of bottom stress is very close to the peak of the longitudinal component of bed load. The latter typically occurs upstream of the peak of bed elevation, i.e. $\delta_{Q_{sx}}$ falls

in the interval $(\pi, 2\pi)$, which implies a destabilizing contribution to bar growth. However, as λ increases, the peak of the longitudinal component of the bedload flux moves towards the bar crest and eventually overcomes the crest: at this stage, the longitudinal component of the bedload flux no longer plays a destabilizing role. On the other hand, the contribution of the lateral component of sediment transport to the bar growth rate consists of two terms. The former is proportional to the lateral component of the shear stress, which lags behind bed elevation, with δ_{τ_y} falling in the interval $(3\pi/2, 2\pi)$, hence this contribution is destabilizing. The second contribution of the lateral component of sediment transport is associated with the effect of gravity which is obviously stabilizing. As a result, the phase lag of the transverse sediment transport $\delta_{Q_{sy}}$ ranges between $\pi/2$ and π , thus implying a stabilizing contribution to ω_i . This effect is inversely proportional to the width ratio (recall equations 484 and 508), which explains the existence of the threshold value of β below which bars cannot form. The stabilizing effect is also proportional to M^2 . This inhibits the development of high-order modes and the balance of this effect with the destabilizing effects previously discussed determines the number of braids (m) selected by the instability process.

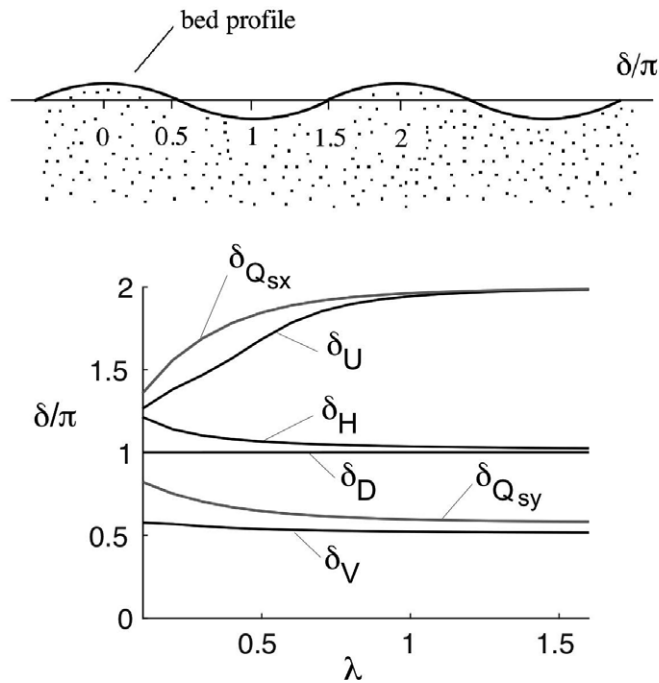


Figure 89. The phase lags of various flow and sediment properties with respect to bed profile are plotted versus bar wavenumber according to Lanzoni and Tubino (1999). The relevant parameters are: $\beta = 15$; $\tau_{*u} = 0.08$; mean dimensionless sediment size $d_s = 0.001$.

Alternate bars: theory and observations

Let us first check if the theory is successful in predicting the conditions for bar formation. The line $\beta = \beta_c$ in Figure 90 separates the region where alternate bars are not expected to form on the basis of the theory of Blondeaux and Seminara (1985) from the region where they are expected to form. Symbols correspond to data of a variety of Authors. The agreement is quite satisfactory with some scatter in the region close to τ_{*c} , owing to the uncertainties associated with the predictors of incipient particle motion and the rapid variability of β_c as τ_{*c} is approached. Also, note that the theory fails in a neighborhood of the critical condition as sediment transport may not occur in the whole region.

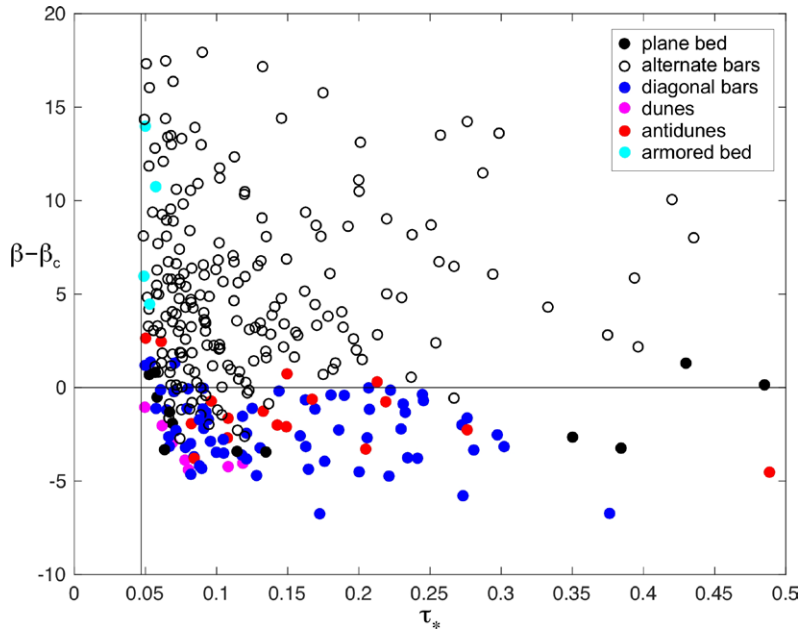


Figure 90. Comparison between the criterion for alternate-bar formation according to the theory of Blondeaux and Seminara (1985) and experimental observations of various authors documenting the formation (○) or the absence (●) of alternate bars.

Let us next compare our predicted critical wavelengths with experimental values. This comparison is shown in Figure 91. Note that the critical wavelength is typically larger than that

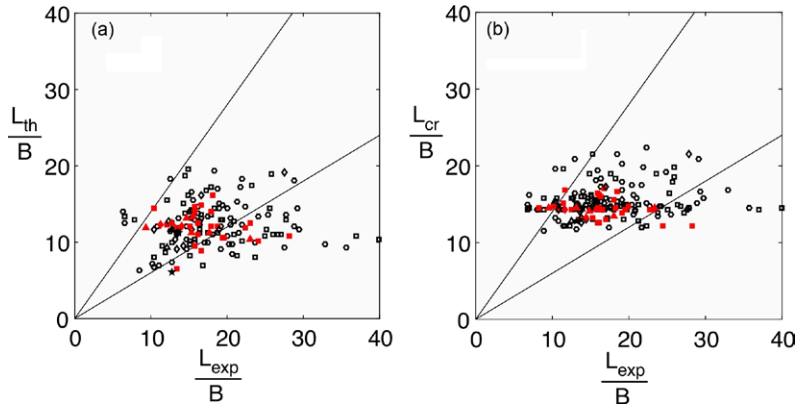


Figure 91. (a) The wavelength L_{th} of alternate bars (scaled by the half channel width B) associated with the maximum growth rate as predicted by the linear theory of Blondeaux and Seminara (1985) is compared with experimental data L_{exp} of various authors: ○ Jaeggi (1983) PVC; ● Jaeggi (1983) sand; Sukegawa (1971); Kinoshita (1961); ◇ Muramoto and Fujita (1978); Ashida and Shiomi (1966); △ Ikeda (1982b); Chang *et al.* (1971). (b) Similar comparison for the bar wavelength at critical conditions L_{cr} .

selected by maximum linear growth. Moreover, though the theory is qualitatively in agreement with observations, a significant scatter is present. This is partly unavoidable, due to the semiempirical nature of the closures employed. But the intrinsic limits of the model are not the whole story. We will show in Section 6.6 that the wavelength of alternate bars increases considerably during the growth process. In other words, when bars have achieved a finite amplitude, their wavelength has changed significantly with respect to the wavelength observed in the initial stage of the process.

Hence, a more appropriate comparison should be performed using theoretical predictions for bar wavelength in the finite amplitude regime.

6.3.2 Free bar formation: the effect of suspended load

The effect of suspended load on bar formation has been investigated by Fredsøe (1978), Olesen (1984), Talmon (1992), Tubino *et al.* (1999) and Federici and Seminara (2006). It is not easy to perform a comparison among results of different Authors, as their approaches employ different parameters which make a detailed comparison hard. Here, we will refer to the works of Federici and Seminara (2006) and Tubino *et al.* (1999), who adopted the approach presented in this Monograph. In particular, in Tubino *et al.* (1999) a fully 3D formulation was employed for both the hydrodynamics and the concentration field. The closures adopted in the model concerned: the vertical structures of eddy viscosity (Dean, 1974) and eddy diffusivity (McTigue, 1981); the friction coefficient (Engelund and Fredsøe, 1982) and the sediment entrainment in suspension (Van Rijn, 1984b; Garcia and Parker, 1991).

A normal mode analysis was then performed. The solution of the linearized governing equations (including the advection-diffusion equation for the concentration) was expanded in a form analogous to (500). Reduction of the linear algebraic system obtained through this approach leads to a dispersion relationship from which one can determine the marginal stability conditions.

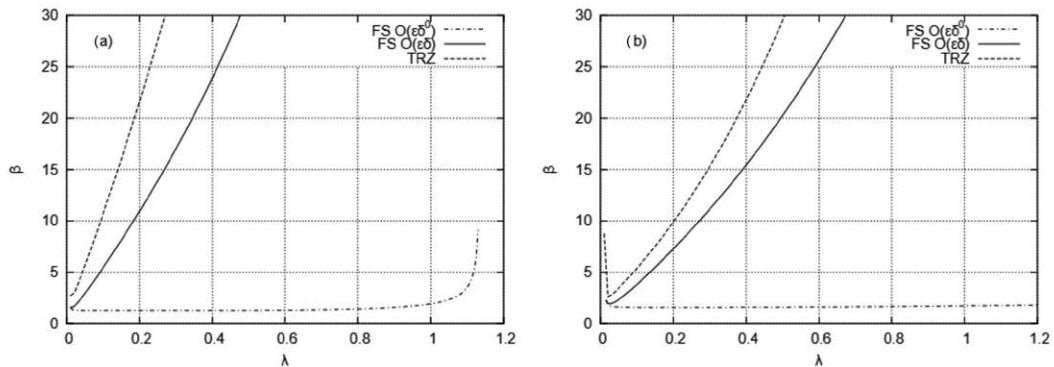


Figure 92. Typical neutral curves for alternate-bar formation with transport in suspension for a value of the undisturbed Shields parameter $\tau_{*u} = 1.5$ and $R_p = 4$. The undisturbed bed has been assumed to be either (a) plane, or (b) dune covered, with $d_s = 0.0001$. The plots compare the marginal stability curves obtained at the leading order of approximation $\mathcal{O}(\epsilon\delta^0)$ and at first-order $\mathcal{O}(\epsilon\delta)$ by the 2-D formulation of Federici and Seminara (2006) with those obtained by the fully 3-D approach of Tubino *et al.* (1999) (reproduced from Federici and Seminara, 2006).

The overall effect of suspended load turns out to be destabilizing. The critical value of the aspect ratio β_c decreases and tends to vanish as τ_{*u} increases, i.e. as the ratio of suspended load to bed load increases. This occurs in the case of both plane and dune covered beds. As pointed out by Tubino *et al.* (1999), the tendency of β_c to vanish is due to the decreasing role of the stabilizing effect of gravity as τ_{*u} increases (recall equations (483a,b) and the coefficients (484a,b) therein). Moreover, as the Shields stress increases, the aspect ratio β does no longer play the role of control parameter of bar instability as suspended load has a significant effect. It appears that, at large values of τ_{*u} , the width of the unstable region decreases and the unstable wavenumber range is gradually shifted towards smaller values of λ , that is to longer bars. Moreover, the bar growth rate is largely dominated by suspended load and bar perturbations in the range $\lambda = 0.3 - 0.6$, that would be unstable under bedload dominated conditions, are now strongly damped.

A further interesting feature of the results obtained by Tubino *et al.* (1999) deserves to be mentioned. Unlike in the case of dominant bed load, where β_{cm} satisfies the condition (514), in the presence of suspended load the critical conditions for different lateral modes tend to collapse within

a very narrow range of values of the aspect ratio. As a consequence, when the role of suspended load is dominant, the equilibrium topography is likely to result from the nonlinear competition among several unstable lateral modes, a scenario conforming to the flume observations of Lanzoni (1995).

The physical mechanism underlying the effect of suspended load on bar growth was clarified by Tubino *et al.* (1999). It turns out that, when suspended load is dominant, the stabilizing effect of the lateral transport plays a minor role and bar instability crucially depends on the phase lag of the longitudinal transport relative to the peak of bed elevation. For small wavelengths the longitudinal component of sediment flux lags behind bed elevation, and thus plays a destabilizing role. As the bar wavenumber increases the peak of longitudinal transport moves ahead of the bar crest and its role is no longer destabilizing. As the Shields parameter increases, the threshold wavenumber at which the contribution of suspended load to bar growth rate becomes negative shifts to smaller and smaller values.

The above picture has essentially been confirmed by Federici and Seminara (2006), who tested the suitability of the simpler depth averaged approach of Bolla Pittaluga and Seminara (2003) to investigate bar instability. Employing the latter, it turns out that a depth averaged approach to bar instability is adequate even in the presence of significant suspended load, leading to predictions in fairly satisfactory agreement with those of Tubino *et al.* (1999) (Figure 92). The approach fails when the size of sediments is so small that gravitational settling becomes comparable with advection. Under these conditions the slowly varying framework is no longer valid and the full 3D model of transport in suspension is required.

Recently, Bertagni and Camporeale (2018) extended the analysis of Federici and Seminara (2006) to the weakly nonlinear level using the Center Manifold Projection technique (Wiggins, 2003) to derive a Stuart-Landau equation (see Section 6.5.1) eventually yielding the bar amplitude. The results confirm that suspended load reduces both the critical aspect ratio for bar formation and the corresponding wavenumber, and therefore leads to finite amplitude longer bars under conditions for which the bedload is not even sufficient to trigger the instability.

Surprisingly, systematic laboratory observations of bars under conditions of substantial transport in suspension have not appeared in the literature and this has prevented to substantiate the theoretical findings presented above. This is an important topic for future research.

6.3.3 Convective versus absolute instability

The distinction between convective and absolute instabilities has to do with the way the system responds to the occurrence of an initially localized disturbance. It has been established that two fundamentally distinct mechanisms may operate and identify the nature of the instability. Instability is described as *locally convective* provided an initial small perturbation localized in space is swept away from the source and convected downstream leaving the flow domain unperturbed as time tends to infinity. By contrast, instability is described as *absolute* whenever the initial small localized perturbation spreads in any direction as time grows, affecting eventually the whole flow domain (Figure 93).

This distinction was originally proposed in the field of plasma physics (see Briggs, 1964; Bers, 1975, 1983) and has since then been applied and developed in hydrodynamic stability by several authors (see the review of Huerre and Monkewitz, 1990).

Temporal stability analyses of bar formation of the kind performed by most investigators, as analysed in Sections 6.3.1 and 6.3.2, consider small perturbations which amplify in time, starting from some initial spatially periodic configuration. This corresponds to assuming that the perturbation wavenumber λ is real while its frequency ω is complex (equation (500)). Temporal analyses allow us to distinguish between stable configurations (all wavenumbers decay in time) and unstable systems (some wavenumbers are amplified as in Figure 87). When the nature of the instability is convective a *spatial stability analysis* is applicable, considering perturbations which evolve in space, starting from a given temporal distribution at some *initial* location. This is equivalent to assuming that the perturbation wavenumber is complex and the perturbation frequency is real.

In order to ascertain the nature of the instability, the response of the system to impulsive forcing

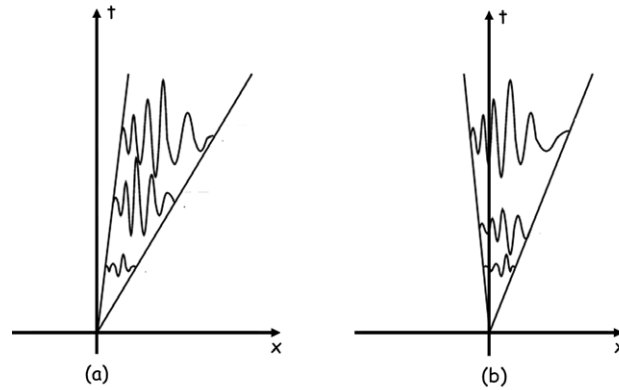


Figure 93. Sketch illustrating the response to a localized impulsive perturbation in (a) convectively unstable and (b) absolutely unstable flows.

must be investigated. This analysis, originally proposed by Briggs (1964), requires some tools that are outlined in the Mathematical Appendix (Chapter 9), to which the reader interested in the mathematical aspects of the problem is referred. Here, we limit ourselves to discuss the results of the application of the above analysis to the case of free bar instability, a problem investigated by Federici and Seminara (2003). The main outcome of the latter paper is to show that bar instability is invariably convective. In other words, the linear response of flow and bed topography to either randomly distributed or localized spatial initial perturbations gives rise to the unbounded growth of wave groups which migrate downstream leaving the flow domain unperturbed. This conclusion, reached by an analytical approach, is confirmed by the numerical solution of the initial value problem posed by the linearized hydrodynamic equations (492, 493, 494), the linearized Exner equation (498), the boundary conditions (499) and the following initial conditions:

$$\eta_1|_{t=0} = H_1|_{t=0} - D_1|_{t=0} = \eta_r(x, y), \quad U_1|_{t=0} = V_1|_{t=0} = H_1|_{t=0} = 0, \quad (518)$$

with η_r an arbitrarily small function that describes the shape of the initial perturbation of bed elevation. This numerical exercise is left to the reader. The above findings have been further substantiated at a nonlinear level by the numerical simulations on the fully nonlinear equations governing the morphodynamical problem performed by Federici and Seminara (2003). This will be discussed in Section 6.6.1.

6.3.4 A conceptual digression: is 2D morphodynamics a well-posed problem?

The mathematical framework employed in the present chapter has proven fairly successful in predicting river morphodynamics, suggesting that, in spite of the simplifications introduced and the (mild) use of empirical inputs, the main physics of the process is successfully captured. However, recently, Chavarrías *et al.* (2019), following previous contributions of Ribberink (1987) and Stecca *et al.* (2014), noted that a fundamental problem arises when the above framework is extended to the case of mixed size sediments. Under certain conditions the formulation of the mathematical problem of morphodynamics is no longer well-posed, i.e. it does not admit of a unique solution depending continuously on the data (Hadamard, 1923). The occurrence of these conditions is strongly suggestive of the failure of the physical model, which must lack some crucial ingredient needed to fully capture the essence of the real phenomenon. However, Chavarrías *et al.* (2019)'s results suggest that, in the case of uniform sediments, the problem is invariably well-posed.

6.4. Forced bars in straight channels

6.4.1 Excitation of non migrating spatial modes in straight rectangular channels

The analysis presented so far has concerned the *spontaneous* formation of free bars in straight channels, i.e. large scale perturbations that grow/decay in time and migrate in the longitudinal direction. On the contrary, at a given time, these perturbations do not display any spatial growth/decay. For these reasons, in the language of stability theory, they are also called *temporal modes*.

However, as discussed in Section 6.3.3, an open channel with erodible bottom and inerodible banks subject to a steady uniform turbulent stream admits of a second class of perturbations, that do not amplify in time but do amplify/decay in space. They are called *spatial modes* and can be represented in the same form as temporal modes (500), simply allowing λ to be complex rather than real and, viceversa, constraining ω to be real.

In the present Section, we are concerned with a particular class of spatial modes, those characterized by vanishing migration speed, i.e. such that $\omega = 0$. They play an important role in practical applications, as they are excited by the occurrence of some steady forcing perturbations at some initial cross-section.

In real form, linear non migrating spatial modes read:

$$(\mathcal{U}_1, D_1, H_1, \mathcal{V}_1) = 2 [(u_m, d_m, h_m) \mathcal{S}_m, v_m \mathcal{C}_m] \exp(-\lambda_i x) \cos(\lambda_r x). \quad (519)$$

Here, \mathcal{S}^m and \mathcal{C}^m are defined by (501). Moreover, λ_r is the *wavenumber* and $(-\lambda_i)$ is the *spatial growth rate*. Perturbations are thus stationary waves that may grow ($\lambda_i < 0$), decay ($\lambda_i > 0$, Figure 94) or keep their initial amplitude ($\lambda_i = 0$).

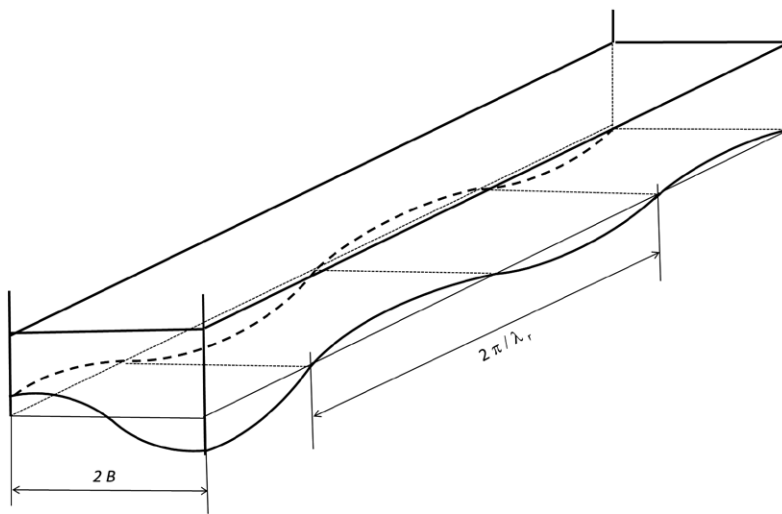


Figure 94. Sketch illustrating the shape of a decaying non-migrating spatial mode of the alternate bar type ($m=1$). The flow is from left to right.

We emphasize that, although these perturbations are allowed by the system (i.e., they satisfy the linearized governing equations), they are not *free* modes as they do not develop spontaneously (their temporal growth rate vanishes). However, provided some forcing effect is present, they do form. Forcing effects (Figure 95) may be the presence of a permanent obstacle in a straight channel (see the laboratory experiments of Struiksmas and Crosato, 1989; Lanzoni, 1995; Crosato *et al.*, 2012) or permanent bed perturbations maintained at some initial cross-section by some other mechanism, as in a straight reach following a curved reach (e.g. in the experiments of Struiksmas *et al.*, 1985; Zolezzi *et al.*, 2005).

Spatial non-migrating modes were first investigated by Olesen (1984) in the bed load dominated case. More recently, Zolezzi and Seminara (2001) have reexamined their role, showing that it also determines the direction along which the morphodynamic influence propagates and, consequently,

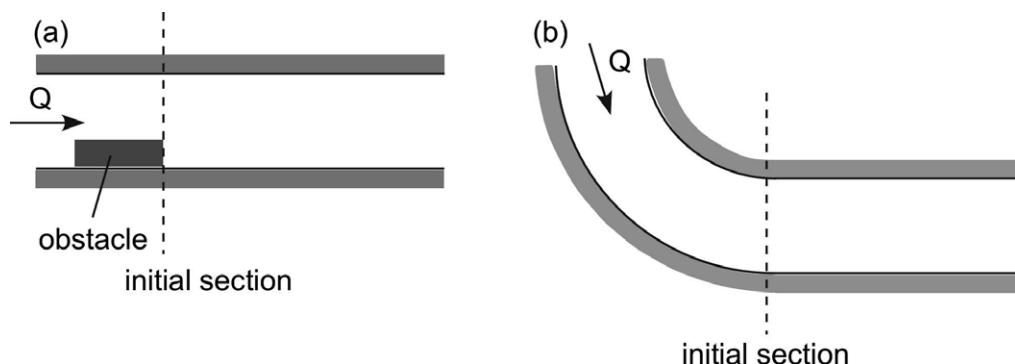


Figure 95. Sketch of (a) a channel with a permanent obstacle narrowing the cross-section and (b) a straight reach following a curved reach that imposes an external forcing on the the downstream channel bed.

controls the planform development of meandering rivers (Seminara *et al.*, 2001a). These aspects will be discussed in the companion Monograph.

In the case of bars forming in straight channels, Federici and Seminara (2006) analyzed the characteristics of spatial non-migrating modes for dominant bedload and then also in the presence of suspended load. The dispersion relationship obtained allowing λ to be complex and setting $\omega = 0$ in equation (508) was found to reduce to a fourth order algebraic equation for λ , if one ignores the small term associated with the longitudinal effect of gravity on sediment transport. This fourth order equation admits of four complex solutions λ_{jm} ($j=1-4$). For dominant bedload transport, a typical dependence of these four solutions on the aspect ratio β is plotted in Figure 96 for given values of the Shields stress τ_{*u} , particle Reynolds number R_p , relative roughness d_s and for the first spatial mode $m = 1$.

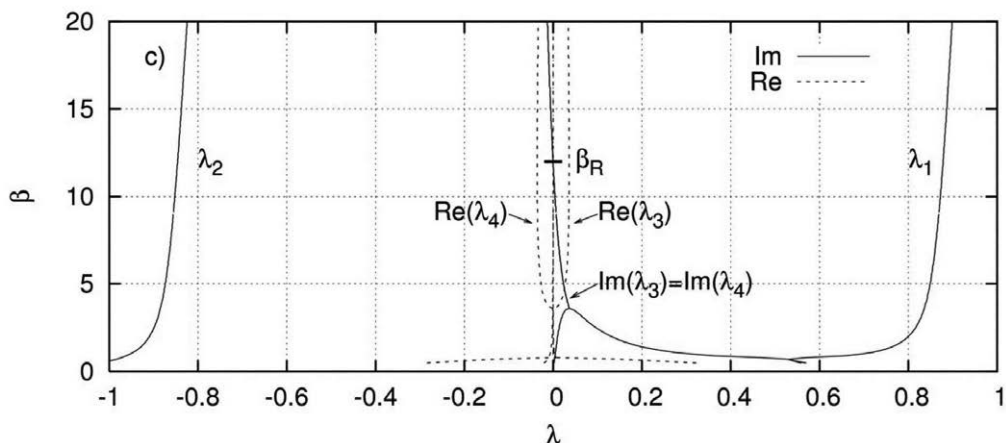


Figure 96. The four complex wavenumbers describing the first spatial mode ($m=1$) are plotted versus β for the case of dominant bed load ($d_s = 0.001$, $\tau_{*u} = 0.5$, $R_p = 40$) (reproduced from Federici and Seminara, 2006, Figure 5c).

It is important to observe that two solutions, λ_1 and λ_2 , play a minor role as they are purely imaginary and have values around 1, with opposite signs. Hence, they describe non oscillatory spatial perturbations which grow/decay fairly fast either downstream or upstream. Indeed, recalling that they are dimensionless quantities scaled by the channel half-width, it follows that these spatial modes vary on a spatial scale of the order of one channel width. The other two solutions λ_3 and λ_4 play a major role in bar morphodynamics. They are complex conjugate with real and imaginary parts having values around 0.1. Hence they describe spatially oscillatory perturbations which vary fairly slowly, i.e. their influence is felt over a considerable channel length. It is important to point

out the role played by the aspect ratio β : the sign of $Im(\lambda_3)$ ($= Im(\lambda_4)$) is positive or negative depending on β being smaller or larger than a threshold value, β_R . This mathematical feature has major physical consequences: for $\beta > \beta_R$ the influence of the perturbation is felt (amplifies) in the upstream direction. On the contrary, for $\beta < \beta_R$ the influence of the perturbation is felt downstream. The upstream influence was firstly pointed out by Zolezzi and Seminara (2001). At threshold the perturbations are purely oscillatory and, for the lowest mode, they describe a periodic sequence of non migrating and non amplifying alternate bars quite similar to the sequence of point bars observed in meandering channels. Indeed, we will see in the companion Monograph that these spatial non-migrating modes can be resonantly excited in meanders with a periodic distribution of channel curvature (Blondeaux and Seminara, 1985). For this reason, we will describe channels characterized by aspect ratios β such that $\beta < \beta_R$ as *sub-resonant* whereas channels with $\beta > \beta_R$ will be called as *super-resonant*.

The first experimental verification of the role of spatial modes was achieved by the curved flume experiments of Struiksma *et al.* (1985) that will also be discussed in the companion Monograph. For straight channels, the above picture has received some substantiation through the laboratory experiments of Lanzoni (2000a). Indeed, as discussed in Section 6.1, both spatially damped and spatially periodic bars were generated in those experiments introducing a lateral obstruction at the flume entrance. Moreover, the values of β_R calculated for runs P1204 and P2804, exhibiting spatially damped bars, fell slightly below resonant conditions ($\beta = 10$, $\beta_R = 10.5$), whilst run P2102, characterized by spatially periodic bars, had a value of β (10.3) well above the resonant value β_R (5.5). The *forced* experiment of Struiksma and Crosato (1989) did also substantiate

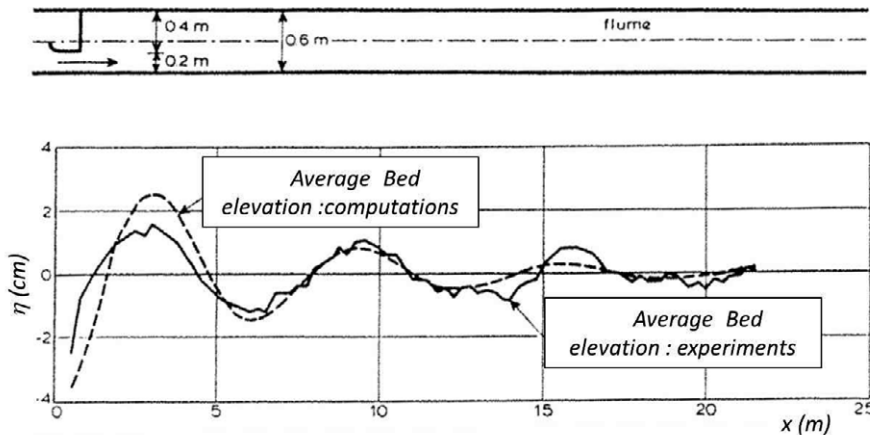


Figure 97. Comparison between experimental results for the spatial mode in the *forced* experiment of Struiksma and Crosato (1989) and the theoretical interpretation of the same Authors in terms of linear spatially damped modes (modified from Struiksma and Crosato, 1989, Figure 9).

theoretical predictions. The configuration was clearly sub-resonant and was successfully interpreted in terms of the linear spatially damped modes predicted by the theory of Struiksma *et al.* (1985) (Figure 97).

The effect of suspended load on spatial modes

The effect of suspended load on the characteristics of spatial modes was also analyzed by Federici and Seminara (2006) and can be envisaged from Figure 98 (where the plot *b*) is simply an enlargement of plot *a*). This effect can be summarized as follows.

Firstly, the value of β_R such that both ω and $Im(\lambda)$ vanish is significantly reduced. For the case depicted in Figure 98, depending on whether bed load or suspended load is dominant, β_R reduces from 12 to 3.5. Secondly, a further threshold value β_1 appears such that in the super

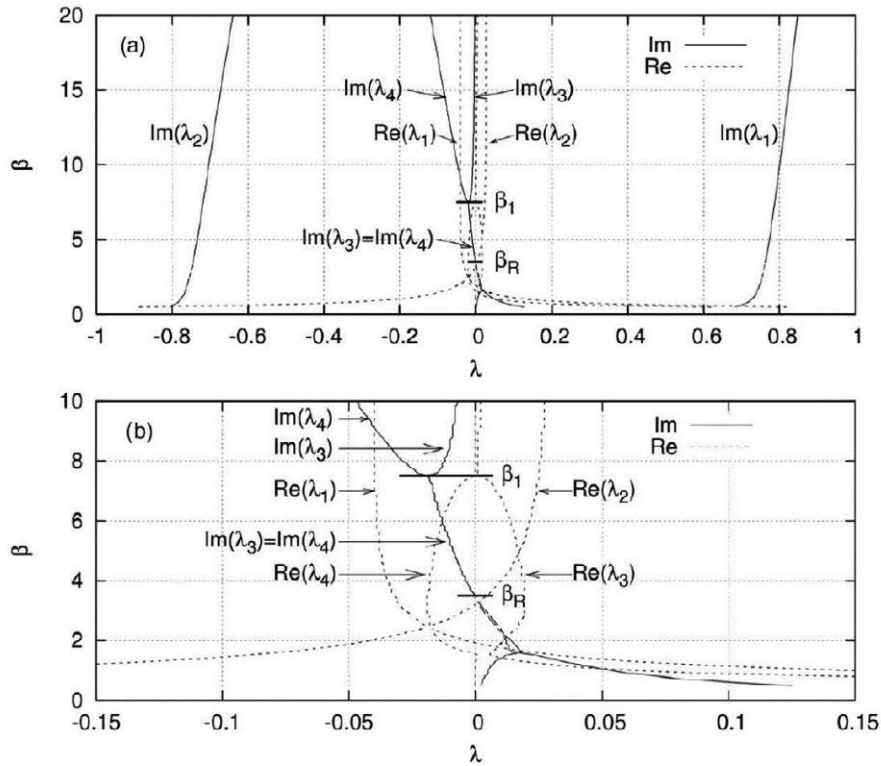


Figure 98. The four complex wavenumbers describing the first spatial mode ($m=1$) are plotted versus β for the case of sediment transport including suspended load. The plot (b) shows an enlargement of the region of (a) around β_R and β_1 ($d_s = 0.00001$, $\tau_{*u} = 1$, $R_p = 4$) (reproduced from Federici and Seminara, 2006, Figure 5).

resonant region corresponding to $\beta_R < \beta < \beta_1$, the picture found in the bed load dominated case is modified as follows. The two eigenvalues λ_1 and λ_2 which were purely imaginary and $\mathcal{O}(1)$ now become complex with small real part, while the remaining two are still complex conjugates and small. They again describe the morphodynamic influence discussed above (see Section 6.4.1). Thirdly, for $\beta > \beta_1$ the two complex conjugates solutions keep complex but lose their conjugate character. Furthermore their real parts are fairly small, such that the solutions become nearly purely imaginary in this regime, under suspended load dominated conditions. Physically, this implies that upstream influence displays itself through spatially damped oscillations which do not have the characteristics of a bar. The relevance of this last regime is however difficult to assess as it involves relatively large values of β such that higher order modes might prevail. Anyhow, to our knowledge, no experimental validation of the above findings has been obtained so far.

6.4.2 Bars forced by channel width variations

It is a common observation that rivers often display spatial oscillations of their widths. This is particularly true for actively migrating meandering rivers (Leopold and Wolman, 1960; Richards, 1976; Brice, 1984; Luchi *et al.*, 2010). Two examples are reported in Figure 99. The first (Figure 99a) suggests that channel width may be maximum close to bend apexes and minimum close to bend crossings. Conversely, the second example (Figure 99b) refers to a case in which the channel width peaks at inflection points. The above distinction is reproduced in existing geomorphic classifications of alluvial channel patterns. In particular, Brice (1984) defines as *sinuous point bar rivers* (wide-bend streams) fluvial patterns of the former type, with prominent point bars, typically scrolled and visible at normal stage. On the contrary, according to Brice (1984) classification, *sinuous canaliform rivers* (equi-width streams) have weakly variable width, not clearly correlated

with channel curvature, and narrow, crescent-shaped, point bars. These observations will need some clarification in the context of the theory of meandering channels presented in our companion Monograph. Width variations are also a distinctive feature of the individual channels of the

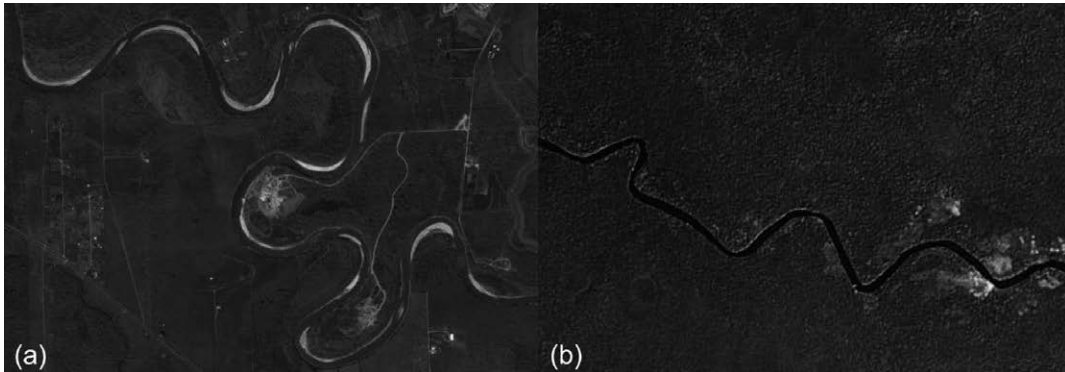


Figure 99. Typical behaviour of channel width in two meandering rivers. In (a) (Brazos River, Texas) the maximum widths are experienced at bend apices; in (b) (tributary of the Amazon River, Brazil) the minimum widths are found at bend apices and local widening is experienced in straight reaches (source Google Earth, courtesy of Rossella Luchi).

networks that shape braided rivers. Mosley (1976) suggested that a sequence of a channel narrowing with a deep central pool, followed by a wider reach with a central bar may be considered as the *unit pattern* of braided rivers. Repetto *et al.* (2002) state: “*width variations appear to be crucial in understanding the bifurcation mechanism that leads to production of new channels in braided rivers*”. Ashmore (1982, 1991) point out a further fundamental mechanism associated with width variations, namely the suppression of free migrating bars, a process similar to that observed by Kinoshita and Miwa (1974) in meandering rivers, where sufficiently high curvature is able to suppress free bar migration through meandering bends.

An even more important role, albeit much less investigated, is played by streamline divergence in the case of alluvial fans. Here, divergence is not only self-generated by the stream flowing on the bar topography, but is also forced by the natural tendency of the stream to expand over the fan (see the work of Tambroni *et al.*, 2019).

While braiding and fans fall outside the scope of the present Monograph, the observation that actively migrating meandering rivers often display spatial oscillations of their widths deserves some attention herein. The above observation has motivated a number of contributions dealing with straight rivers with variable width, starting from the work of Bittner (1994). Below, we refer closely to the comprehensive analysis of Repetto (2000) (but see also Repetto *et al.*, 2002). These Authors investigated, both theoretically and through laboratory experiments, the steady three-dimensional flow field and bottom topography in a straight channel with small amplitude sinusoidal width oscillations.

1D approach

The first consequence of the presence of spatial oscillations of channel width under steady equilibrium conditions is the development of spatial oscillations of the cross-sectionally averaged flow properties. This is readily shown employing a simplest 1D formulation. We then seek the morphodynamic equilibrium of an erodible stream undergoing spatial oscillations of channel width. Strictly speaking, an erodible stream is in morphodynamic equilibrium provided its boundary does not undergo any temporal changes. Hence, its bed should neither aggrade nor degrade ($\partial\eta/\partial t \equiv 0$) and its banks should neither retreat nor advance. Below, we restrict our attention on the former constraint and treat river banks as fixed at this stage. Also, for the sake of simplicity, we assume that the channel has a rectangular cross-section such that the free surface width coincides with the width of the bed. With the notations of Figure 100 and referring again to dimensional variables,

we then assume that:

$$B = B_0 + \delta B_1(x) = B_0 [1 + \delta (\exp i \lambda_b x + c.c.)], \quad (520)$$

with δ small parameter and λ_b (dimensional) wavenumber of the spatial oscillations of channel width.

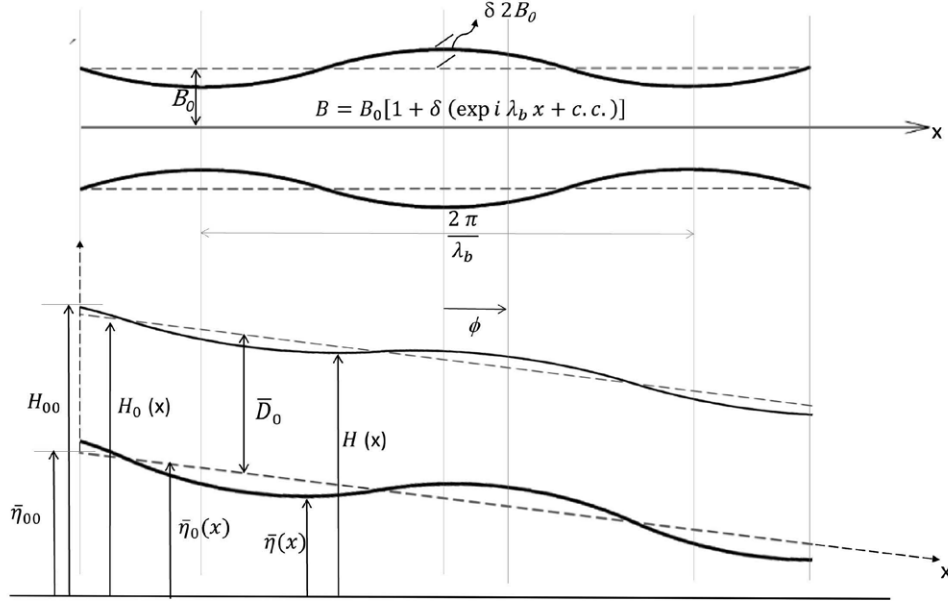


Figure 100. Sketch and notations for a channel with small amplitude sinusoidal width oscillations.

Strict equilibrium naturally requires also steady hydrodynamic conditions, that is the cross-sectional area Ω does not vary in time ($\partial\Omega/\partial t \equiv 0$). With the notations of Chapter 2, the 1D governing equations of morphodynamics then reduce to the form (404), (405) and (406).

Below, for the sake of simplicity the correction coefficient for stream momentum β_{cor} will be set equal to 1, and we will assume the cross-section wide enough to approximate the hydraulic radius with the flow depth. The latter system must be solved with the help of some closure relationship for the average sediment flux per unit width $Q_s(x, t)$ and for the average friction coefficient C_f . Let us assume:

$$Q_s = 2B \sqrt{(s-1)gd^3} n (\bar{\tau}_* - \tau_{*c})^m, \quad C_f^{-1/2} = \frac{k_s}{\sqrt{g}} D^{1/6}, \quad (521)$$

with n empirical constant, m empirical exponent larger than one, k_s average Strickler coefficient, D the cross-sectionally averaged flow depth and $\bar{\tau}_*$ laterally averaged Shields stress. The latter quantity, which couples morphodynamics to hydrodynamics (see Section 5.1.2), reads:

$$\bar{\tau}_* = \frac{Q^2 C_f}{\Omega^2 (s-1)gd}, \quad (522)$$

with the sediment size d assumed uniform.

Note that the equation (405) states that the condition insuring bed equilibrium is that *the total sediment discharge keeps spatially constant* throughout the reach investigated. This is a *dynamic equilibrium condition* which predicts a distinct equilibrium state associated with any given set of forcing conditions, namely given values of flow and sediment discharges.

For the present configuration the solution for the equilibrium state is readily obtained taking advantage of the assumption of small amplitude oscillations of channel width, that suggests to expand the solution in powers of the small parameter δ as follows:

$$(D, \mathcal{U}, \bar{\tau}_*, C_f) = (D_0, \mathcal{U}_0, \bar{\tau}_{*0}, C_{f0}) + \delta(D_1, \mathcal{U}_1, \bar{\tau}_{*1}, C_{f1}), \quad (523)$$

where

$$\left(\frac{D_1}{D_0}, \frac{\mathcal{U}_1}{\mathcal{U}_0}, \frac{\bar{\tau}_{*1}}{\bar{\tau}_{*0}}, \frac{C_{f1}}{C_{f0}} \right) = (d_1, u_1, t_{*1}, \xi_1) \exp(i \lambda_b x) + c.c. \quad (524)$$

Moreover, the laterally averaged free surface elevation \bar{H} is expanded in the form:

$$\bar{H} = H_0 + \delta H_1 = H_{00} - Sx + \delta D_0 (h_1 \exp(i \lambda_b x) + c.c.). \quad (525)$$

with S channel slope and H_{00} value of H_0 at some initial cross-section.

Substituting from (523, 524, 525) into the governing equations, one may readily derive their linearized form and, with the help of algebraic manipulations that are left to the reader, the solution is eventually found to read:

$$d_1 = \frac{3}{7m} \left(1 - \frac{\tau_{*c}}{\bar{\tau}_{*0}}\right) - \frac{6}{7}, \quad u_1 = -\frac{3}{7m} \left(1 - \frac{\tau_{*c}}{\bar{\tau}_{*0}}\right) - \frac{1}{7}, \quad (526a)$$

$$h_1 = F_0^2 (1 + d_1) - i \frac{S}{\lambda_b D_0} \left(2 + \frac{10}{3} d_1\right). \quad (526b)$$

with F_0 Froude number of the unperturbed uniform flow ($F_0^2 \equiv \mathcal{Q}^2 / (4g B_0^2 D_0^3)$).

Since $m > 1$, (526a) suggests that d_1 and u_1 are real negative quantities, hence the oscillations of average flow depth and average velocity are out of phase relative to oscillations of channel width. In other words, the flow depth and the flow speed peak at the narrowest cross-sections and are minimum at the widest cross-sections. On the contrary, h_1 is a complex quantity with positive real part: it describes a spatial oscillation which lags relative to channel width (see Figure 101). The reader will readily show that the phase lag ϕ reads:

$$\phi = \arctan \left(-\frac{S}{F_0^2 \lambda_b D_0} \frac{\frac{10}{7m} \left(1 - \frac{\tau_{*c}}{\bar{\tau}_{*0}}\right) - \frac{6}{7}}{\frac{3}{7m} \left(1 - \frac{\tau_{*c}}{\bar{\tau}_{*0}}\right) + \frac{1}{7}} \right). \quad (527)$$

Assuming a value 3/2 for the exponent m , (527) predicts values of ϕ ranging from negative to positive as $\bar{\tau}_{*0}$ exceeds a value equal to $10 \tau_{*c}$.

2D approach

The above 1D approach is able to capture the response of the cross-sectionally averaged flow and bed topography to width variations, but is obviously unable to reproduce the tendency to form forced bars. The work of Repetto *et al.* (2002) overcomes this limitation. The reader is referred to the latter paper for details of the analysis. Here, we outline the main features of the results.

One may at first expect that a 2D approach might be sufficient to reproduce bar formation. However, this expectation turns out to be wrong. Indeed, the linear analysis of Repetto (2000) shows that results of a 2D approach do not differ significantly from results of our previous simpler 1D model. Figure 102a shows that the perturbation of bed elevation relative to the mean uniform slope consists of a sequence of undulations out of phase with respect to width oscillations.

This behavior appears clearly in Figure 102b showing the corresponding perturbation of longitudinal and lateral depth averaged velocities relative to the uniform flow, as well as the perturbation of the bed elevation at the banks. In particular, the longitudinal perturbations of cross-sectionally averaged velocity and bed elevation exhibit a trend quite similar to that predicted

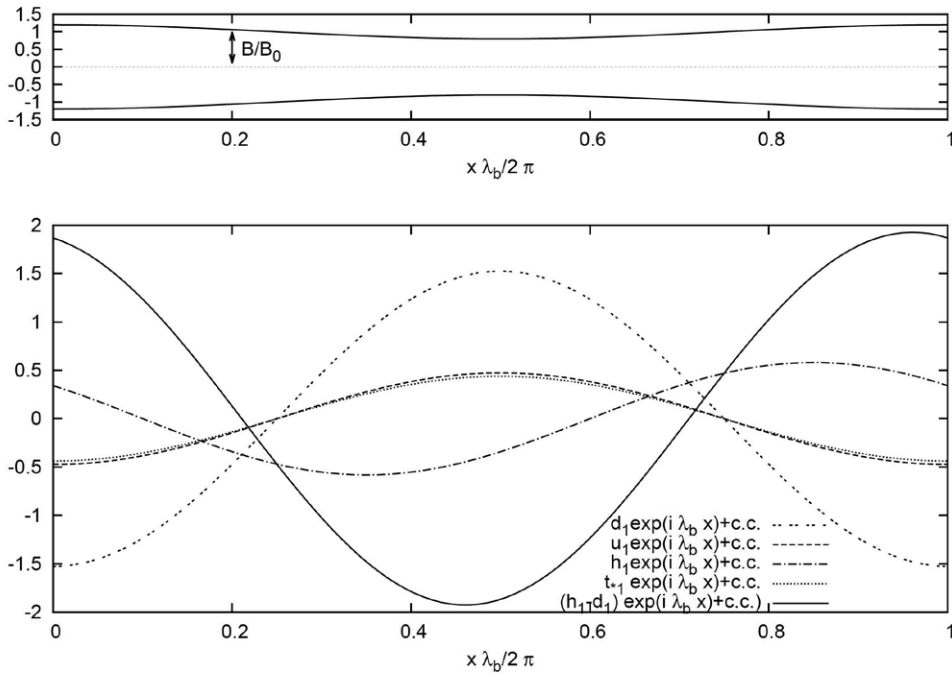


Figure 101. Longitudinal profiles of the perturbations of the cross-sectionally averaged flow depth and velocity, as well as of the laterally averaged bottom stress and free surface elevation obtained by the 1D model. Dimensionless parameters have been chosen in order to reproduce the same flow conditions employed in Figure 102: $m = 1.5$, $\tau_{*c} = 0.047$, $\bar{\tau}_{*0} = 0.07$, $F_0 = 0.85$, $S/(D_0 \lambda_b) = 0.43$.

by the 1D model, with maximum scour and maximum longitudinal speed occurring almost exactly at the narrowest cross-section. Also, note that the predicted lateral variations of the flow field are very weak as compared with longitudinal variations. However, there is a major novel feature of the 2D solution, that the 1D approach is unable to predict. The 2D solution displays the occurrence of a resonant response under suitable values of the relevant dimensionless parameters. Specifically, resonance occurs when the average aspect ratio of the channel β and the wavenumber of width oscillations λ_b are close to the values β_R and λ_R that characterize steady non migrating bars allowed by the channel for the given values of $\bar{\tau}_{*0}$ and $d_s = d/D$ defined in Section 6.3.1. Under these conditions the width forcing excites a steady free response of the channel. The possibility of resonance of free and forced bars was first discovered by Blondeaux and Seminara (1985) in the case of meandering channels where forcing is associated with curvature and may excite free bars of the alternate type. This will be extensively discussed in the companion Monograph. In the case of width oscillations, the forcing effect is symmetrical with respect to the channel axis, hence only symmetrical modes, such as central bars (or possibly higher-order even modes) may be excited.

An example of resonance is given in Figure 103. The amplitude of bed elevation at the centreline relative to its value at the bank, plotted versus λ_b , displays an infinite peak. Of course, close to resonance, the linear theory fails and nonlinearity must be accounted for. Needless to say, exact resonance hardly occurs in reality. However, the distinction between sub- and super-resonant conditions has fundamental implications that have been investigated in the meandering case by Zolezzi and Seminara (2001) (see the companion Monograph).

3D approach

The limit of the 2D model is its inability to represent secondary flows appropriately. Secondary flows are generated because the spatial oscillations of channel width force the streamlines to follow

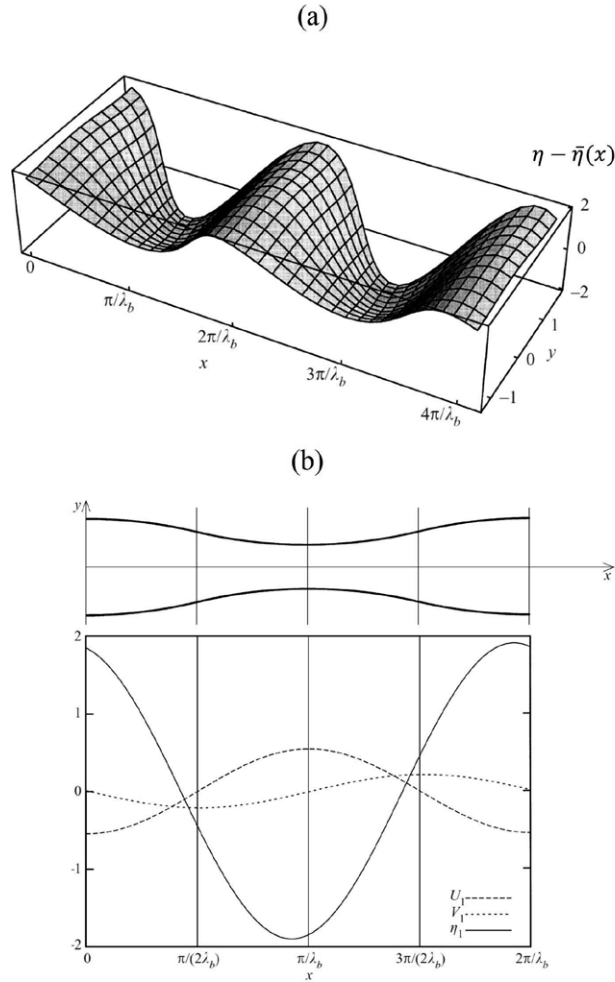


Figure 102. (a) Typical equilibrium bed configuration and (b) longitudinal profiles of the perturbations of the bed elevation (η_1) and of the depth-averaged velocity components (U_1, V_1) at the bank, obtained by the 2D model of Repetto (2000). The relevant dimensionless parameters are: wavenumber of the width oscillation $\lambda_b = 0.2/B_0$, average aspect ratio $\beta \equiv B_0/D_0=15$, average Shields stress $\bar{\tau}_{*0}=0.07$ and average relative channel roughness $d_s = d/D_0=0.05$ (modified from Figures 3.2 and 3.3 of Repetto, 2000).

curvilinear paths. As a result, one may think of a channel with oscillating width as a pair of back to back meandering channels, each generating a sequence of point bars and pools at the wide and narrow reaches respectively. It is then not surprising that the 3D model of Repetto *et al.* (2002) predicts the formation of a central bar in phase with channel width (Figure 104). Indeed, a central bar may be interpreted as a pair of point bars arising from streamline curvature. The analysis carried out by Repetto (2000) also shows that the amplitude of the central bar varies with λ_b and peaks for $\lambda_b \simeq 0.3/B_0$, a value which corresponds to a longitudinal wavelength of about 10 channel widths. Under these conditions, the amplitude of the bar is comparable with the amplitude of the mean oscillations. Higher-order lateral modes are also present but keep small for all values of λ_b . These findings have been substantiated through a set of experiments which led to results in reasonable agreement with the theory.

Finally, let us mention that the work of Repetto (2000) and Repetto *et al.* (2002) on the

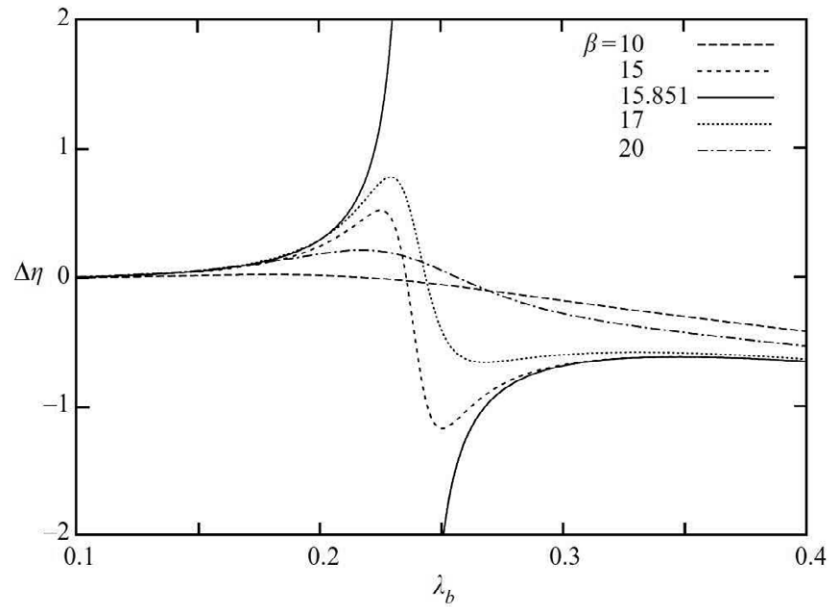


Figure 103. The amplitude of bed elevation $\Delta\eta$ (value at the centreline relative to its value at the bank in the widest cross-section) is plotted versus λ_b , for different values of the aspect ratio β . The values of the relevant parameters are: $\beta_R = 15.85$, $\bar{\tau}_{*0} = 0.07$, $d/D_0 = 0.05$ (reproduced from Figure 3.8 of Repetto, 2000).

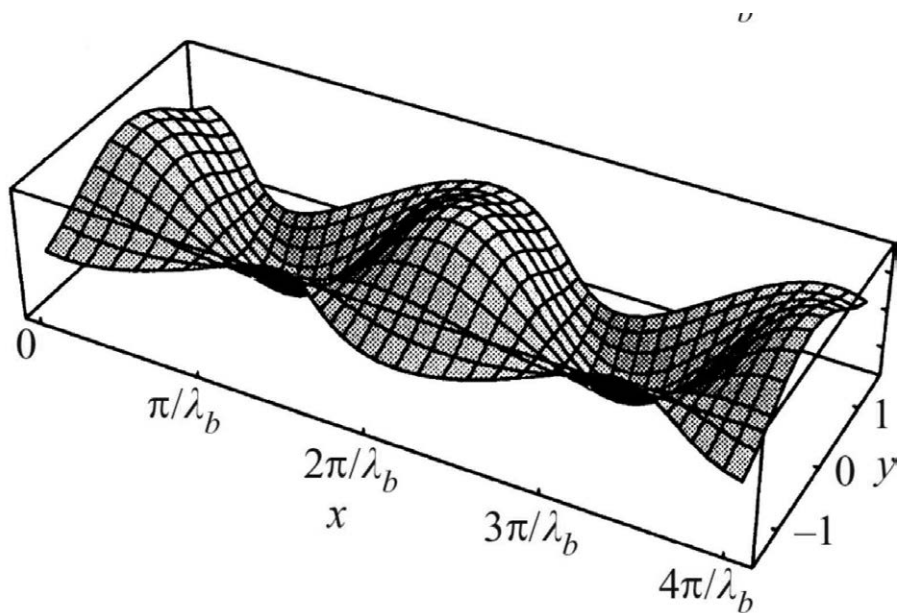


Figure 104. The bed topography predicted by the 3D model of Repetto (2000), displaying the formation of a central bar in phase with width oscillations. The relevant parameters are: $\lambda_b = 0.3/B_0$, $\beta = 15$, $\bar{\tau}_{*0} = 0.1$, $d/D_0 = 0.05$ (reproduced from Figure 3.6 of Repetto, 2000).

formation of forced bars in channels with oscillating width, was later revisited by Wu and Yeh (2005), who proposed a slightly modified version of the 2-D theoretical model. The reader is referred to the latter paper for details.

6.5. The development of free and forced bars of finite amplitude: weakly nonlinear theories

Linear instability theories are unable to predict the final fate of perturbations as linearization is a valid approximation only in the initial stage of the process, when the amplitudes of perturbations are small (strictly infinitesimal). As perturbations grow, the role of nonlinear interactions among the various components of the perturbation increases and this may prevent the indefinite growth of the linearly most unstable mode. To overcome the linear restriction, one may resort to numerical approaches that allow to follow the evolution of perturbations from the initial stage to their fully nonlinear state. This exercise has been performed for free bars by various Authors, as we will see in Section 6.6.

However, before discussing full numerical simulations, it proves instructive to gain some understanding of how perturbations evolve in what is called the *weakly nonlinear regime*, i.e. in a sufficiently small neighborhood of the critical conditions for linear instability. The analysis requires some technicalities that are presented in the Mathematical Appendix (Chapter 9) to which we refer the reader interested in the mathematical aspects of the problem. Below, we limit ourselves to outlining the main ideas of the analysis and discuss results obtained in the case of bars. It is convenient to distinguish the case of free bars from that of forced bars.

6.5.1 Weakly nonlinear free bars

Below we report results of two distinct approaches to the weakly nonlinear analysis. The former approach, originally postulated by Landau (1944) and later derived by Stuart (1958) for the hydrodynamic instability of parallel laminar flows, consists of predicting the nonlinear evolution of the most unstable wave predicted by the linear theory. For free bars this approach was followed by Colombini *et al.* (1987). The latter approach was proposed by Ginzburg and Landau (1950) and consists of analyzing the nonlinear evolution of the whole spectrum of unstable waves within a neighborhood of the critical conditions. For free bars this approach was applied by Schielen *et al.* (1993).

In both cases, we seek a finite-amplitude solution, assuming that the control parameter of free bar instability, namely the aspect ratio β falls within a neighborhood of the critical conditions for linear instability defined by the relationship:

$$\beta = \beta_c (1 + b \epsilon^2). \quad (528)$$

where $\epsilon \ll 1$ and b is a dummy parameter the sign of which determines whether we are considering super- or sub-critical conditions (Figure 105).

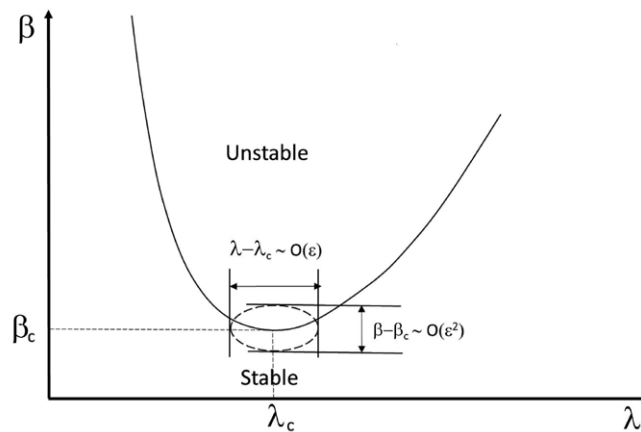


Figure 105. Sketch illustrating the region of the stability plane where the weakly nonlinear analysis of free bars is expected to hold.

The weakly nonlinear evolution of the single most unstable wave

The seminal work of Colombini *et al.* (1987) considers the bar formation as a process fully belonging to the realm of nonlinear Mechanics. To understand the general ideas behind the weakly nonlinear analysis, it is instructive to analyze the form taken by the linear solution within the neighborhood of the critical conditions defined by (528). Recalling the dispersion relationship (508) we may expand ω in powers of $(\beta - \beta_c)$ as follows:

$$\omega = \omega_c + \left. \frac{\partial \omega}{\partial \beta} \right|_{\lambda_c, \beta_c} (\beta - \beta_c) + H.O.T. = \omega_c + (\nu_\beta + i \mu_\beta) \beta_c b \epsilon^2 + H.O.T., \quad (529)$$

where ω_c is a real number as the growth rate vanishes at criticality.

Next, we substitute from (529) into the linear solution for the perturbation. For example, the perturbation of the longitudinal component of the flow velocity, reads:

$$U_1 = A_0 \sin(\pi y) \exp i(\lambda_c x - \omega_c t) \exp [\mu_\beta (\beta - \beta_c) + \dots] t + H.O.T., \quad (530)$$

where A_0 is an arbitrary infinitesimal constant and we have neglected the $\mathcal{O}(\epsilon^2)$ correction of the angular frequency ω_c associated with the coefficient ν_β . This relationship shows that the growth rate in the neighborhood of critical conditions is proportional to $(\beta - \beta_c)$, i.e. it is of $\mathcal{O}(\epsilon^2)$. We may then rearrange (530) in the compact form:

$$U_1 = \sin(\pi y) A(\tau) \exp i(\lambda_c x - \omega_c t), \quad (531)$$

where τ is the following *slow* variable:

$$\tau = \epsilon^2 t, \quad (532)$$

and the linear form of the *amplitude function* $A(\tau)$ reads:

$$A(\tau) = \exp [\mu_\beta b \beta_c] \tau. \quad (533)$$

The compact form of the linear solution (531) clarifies that the critical wave with wavenumber λ_c and frequency ω_c is modulated through an *amplitude function* A depending on the *slow* time variable $\epsilon^2 t$. Growth occurs on a time scale which is $\mathcal{O}(\epsilon^{-2})$ larger than the characteristic period of the critical wave $2\pi/\omega_c$.

The above analysis clarifies that, *the main scope of the weakly nonlinear approach is to derive a nonlinear evolution equation for the amplitude function* $A(\tau)$ and the derivation must be able to take into account the dependence of the process on both the fast scale (t) and the slow scale (τ). As discussed in the Mathematical Appendix reported in Chapter 9, the mathematical technique appropriate to this goal is the so called *method of multiple scales* (see Nayfeh, 2000). The outcome of the analysis is the so-called Landau-Stuart amplitude equation for $A(\tau)$, which reads:

$$\frac{dA}{d\tau} = b \beta_c [\mu_\beta + i \nu_\beta] A + [a_r + i a_i] A^2 \bar{A}. \quad (534)$$

where an overbar denotes complex conjugate. It is a nonlinear ordinary differential equation that describes the long-term behavior of the single most unstable wave. The reader will readily verify that, neglecting the nonlinear term, the solution of (534) reduces to the linear form (533). In the nonlinear case, the equation is readily solved in closed form, as discussed in the Mathematical Appendix, and leads to a rich picture, encompassing two fundamentally distinct cases.

The first case is described as *super-critical instability*. It occurs when the coefficient a_r is negative. Under this condition perturbations tend to an equilibrium solution, asymptotically reached as $\tau \rightarrow \infty$ (Figure 106a), such that:

$$|A_e|^2 = -\frac{b \beta_c \mu_\beta}{a_r}. \quad (535)$$

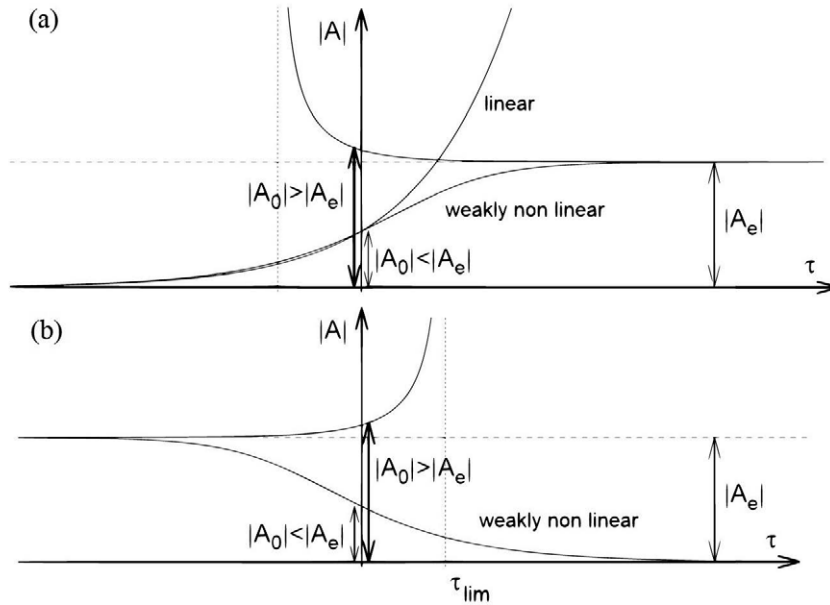


Figure 106. Sketch illustrating the solution of Landau-Stuart equation in the (a) super-critical and (b) sub-critical case.

Moreover, this equilibrium solution is stable. Hence, in the context of a Landau-Stuart approach, one is able to predict the final fate of bar perturbations undergoing a so called *super-critical bifurcation* in the unstable region of the linear theory.

Bar instability is an example of supercritical bifurcation as the coefficient a_r is found to be negative. With the help of (535) one can thus compute the height of alternate bars at equilibrium, defined as the difference between the maximum and minimum bed elevations within a bar unit (Ikeda, 1982b). This quantity, scaled by D_u , will be denoted by H_{BM} and, neglecting $\mathcal{O}(\epsilon^3)$ terms, reads:

$$H_{BM} = b_1 \left[\frac{(\beta - \beta_c)}{\beta_c} \right]^{1/2} + b_2 \left[\frac{(\beta - \beta_c)}{\beta_c} \right], \quad (536)$$

where $b_1(\tau_{*u}, d_s)$ and $b_2(\tau_{*u}, d_s)$ are functions of the components of flow field at $\mathcal{O}(\epsilon)$ and $\mathcal{O}(\epsilon^2)$. The coefficients b_1 and b_2 are plotted in Figure 107.

Figure 108a shows a comparison between the experimental values of H_{BM} and the theoretical predictions obtained using (536). Since $|A_e|$ takes values about (0.2 – 0.3) the range of values of ϵ included in Figure 108a is rather wide, showing that a satisfactory agreement is found even for values of ϵ of $\mathcal{O}(1)$. A satisfactory agreement is also found between the weakly nonlinear prediction of the maximum relative scour (η_M/H_{BM}) , around 0.57 (Figure 108b), and the value 0.5 reported by Ikeda (1982b). Note that the maximum scour η_M is defined as the difference between the elevation of the bed profile averaged over a bar unit and the minimum bed elevation observed in the same unit.

Finally, Figure 109 provides an overall prospective view of the bed topography predicted by Colombini *et al.* (1987) truncating their expansion at $\mathcal{O}(\epsilon)$: physical parameters were chosen such to reproduce the experimental run n.22 of Ikeda (1982b). Although this representation is obviously inaccurate due to the approximate nature of the weakly nonlinear expansion, some of the features of alternate bars observed in nature, in particular the formation of diagonal fronts and the increased steepness of the bed profile downstream of the fronts, do emerge. This is a sign of the tendency to flow separation that cannot be fully predicted in the present context due to the limitations of the shallow water representation of the flow field.

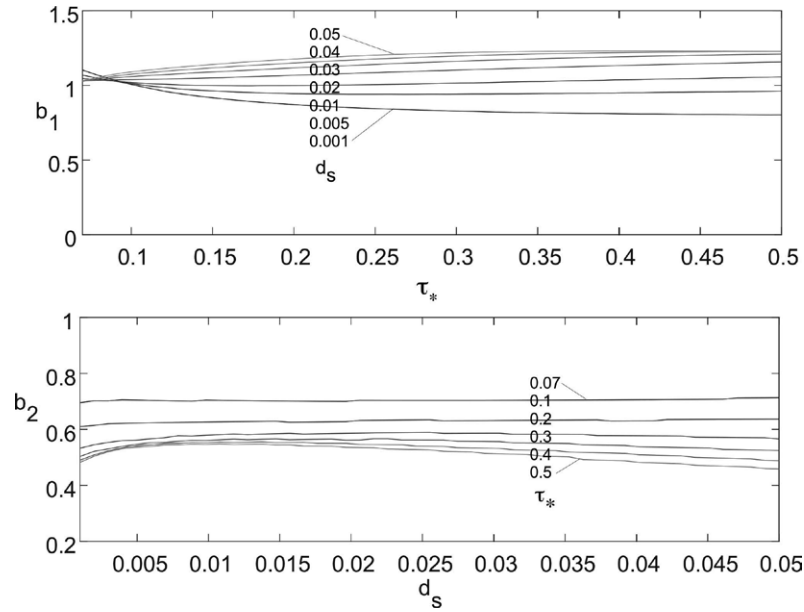


Figure 107. The coefficients b_1 and b_2 of the relationship (536) for the height of alternate bars at equilibrium are plotted as functions of the unperturbed Shields stress τ_{*u} and the relative roughness $d_s = d/D_u$ (modified from Colombini *et al.*, 1987).

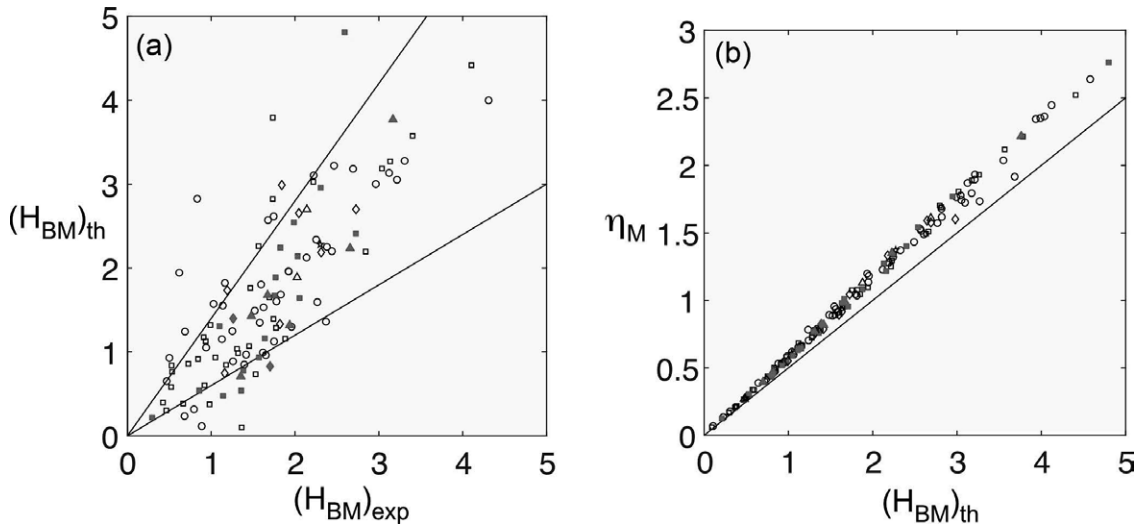


Figure 108. (a) The dimensionless values of the height of alternate bars at equilibrium predicted by the relationship (536) are compared with values observed by various Authors: \circ , Jaeggi (1983) PVC; \bullet , Jaeggi (1983) sand; \square , Sukegawa (1971); \blacksquare , Kinoshita (1961); \diamond , Muramoto and Fujita (1978); \blacklozenge , Ashida and Shiomi (1966); \triangle , Ikeda (1982b). Data falling between solid lines are such that $|(H_{BM})_{th} - (H_{BM})_{exp}| < 40\% (H_{BM})_{exp}$. (b) The dimensionless maximum scour η_M calculated for the values of (τ_{*u}, d_s) corresponding to the experiments listed above is plotted versus the dimensionless maximum bar height H_{BM} . The solid line represents the average dependence reported by Ikeda (1982b) (redrawn from Colombini *et al.*, 1987).

A second type of instability, described as *sub-critical instability*, occurs when the coefficient a_r of Landau-Stuart equation is positive (Figure 106b). Under these conditions an equilibrium amplitude of the perturbation is asymptotically reached as $\tau \rightarrow -\infty$ in the sub-critical regime ($\beta < \beta_c$) corresponding to negative values of the dummy parameter b . As illustrated in the

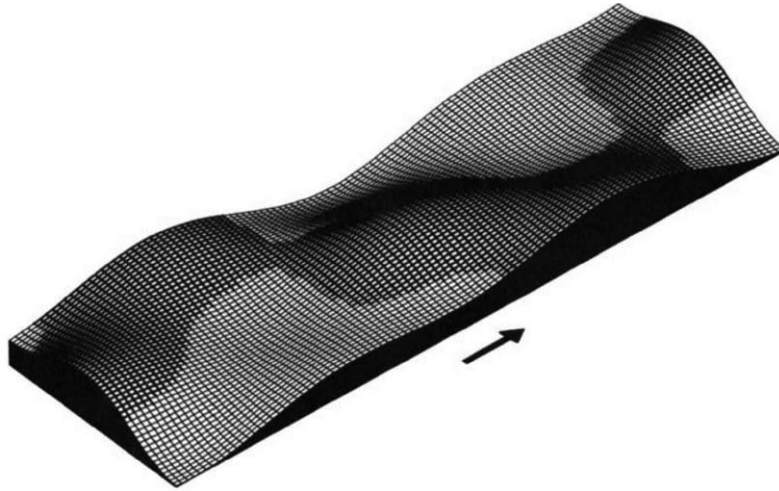


Figure 109. Prospective view of the bed topography predicted by Colombini *et al.* (1987) for the run n. 22 of Ikeda (1982b). The weakly nonlinear expansion was truncated at $\mathcal{O}(\epsilon)$ (reproduced from Colombini *et al.*, 1987).

Mathematical Appendix, this equilibrium solution sets a *threshold amplitude for the perturbation*, such that perturbations exceeding this threshold are able to destabilize the system that is stable to infinitesimal perturbations. On the contrary, *finite* amplitude perturbations that do not exceed the threshold decay. The notion of subcritical instability clarifies that, in some cases, the linear stability theory is unable to predict that the system is unstable, as instability depends on the 'size' of the perturbation acting on the system.

The weakly nonlinear evolution of the spectrum of unstable waves

The above analysis is quite successful but it is restricted to the evolution of the most unstable wave predicted by the linear theory. However, we know that a spectrum of waves is excited as the critical conditions for linear instability is exceeded. In order to take this feature into account, the Landau-Stuart approach must be appropriately corrected, following the analysis of Ginzburg and Landau (1950). This approach was applied to the bar case by Schielen (1995), but see also Schielen *et al.* (1993).

Again, it is firstly instructive to analyze the form taken by the linear solution within the neighborhood of the critical conditions defined by (528) allowing the wavenumber λ to vary within a *small* neighborhood of its critical value λ_c . Recalling the dispersion relationship we may then expand ω in powers of $(\beta - \beta_c)$ and $(\lambda - \lambda_c)$ as follows:

$$\omega = \omega_c + \nu_\lambda (\lambda - \lambda_c) + (\nu_\beta + i\mu_\beta)(\beta - \beta_c) + \frac{1}{2}(\nu_{\lambda^2} + i\mu_{\lambda^2})(\lambda - \lambda_c)^2 + H.O.T. \quad (537)$$

where:

$$\nu_\lambda = \left. \frac{\partial \omega}{\partial \lambda} \right|_{\lambda_c, \beta_c}, \quad \nu_\beta + i\mu_\beta = \left. \frac{\partial \omega}{\partial \beta} \right|_{\lambda_c, \beta_c}, \quad \nu_{\lambda^2} + i\mu_{\lambda^2} = \left. \frac{\partial^2 \omega}{\partial \lambda^2} \right|_{\lambda_c, \beta_c}. \quad (538)$$

The term proportional to $(\lambda - \lambda_c)$ in (537) is purely real as the growth rate has a maximum at criticality. Also, note that the coefficient ν_λ is the group velocity. This relationship shows that the growth rate in the neighborhood of critical conditions has now two contributions. Besides the term proportional to $(\beta - \beta_c)$, that is of $\mathcal{O}(\epsilon^2)$, a second contribution, proportional to $(\lambda - \lambda_c)^2$, appears. In order for the two contributions to have the same order, we then require that $(\lambda - \lambda_c) \sim \mathcal{O}(\epsilon)$ and set the following expansion:

$$\lambda = \lambda_c (1 + r_\lambda \epsilon), \quad (539)$$

with r_λ an $\mathcal{O}(1)$ parameter.

Substituting from (537) and (539) into the linear solution for the perturbation, we obtain:

$$U_1 = \sin(\pi y) A(\tau, \xi) \exp i(\lambda_c x - \omega_c t). \quad (540)$$

Hence, the amplitude function A is now dependent on the following two *slow* variables, τ and ξ :

$$\tau = \epsilon^2 t, \quad \xi = \epsilon(x - \nu_\lambda t). \quad (541)$$

The linear form of $A(\tau, \xi)$ reads:

$$A(\tau, \xi) = \exp \left[\left(\mu_\beta b \beta_c + \frac{1}{2} \mu_{\lambda^2} \lambda_c^2 r_\lambda^2 \right) \tau \right] \exp i(\lambda_c r_\lambda \xi). \quad (542)$$

The compact form of the linear solution (540) suggests that the critical wave with wavenumber λ_c and frequency ω_c is now modulated through an amplitude function A that describes both a *slow* temporal growth and a *slow* migration of the envelope of the wave packet. The slow migration is accounted for by the dependence of A on the slow, moving coordinate, ξ , which travels with the group velocity ν_λ .

The derivation of a nonlinear evolution equation for the amplitude function $A(\tau, \xi)$ is pursued by the *method of multiple scales* (see the Mathematical Appendix) and leads to a fundamental *nonlinear partial differential equation* known as the *Ginzburg-Landau equation* (Ginzburg and Landau, 1950):

$$\frac{\partial A}{\partial \tau} = b \beta_c [\mu_\beta + i \nu_\beta] A - \frac{1}{2} [\mu_{\lambda^2} + i \nu_{\lambda^2}] \frac{\partial^2 A}{\partial \xi^2} + [a_r + i a_i] A^2 \bar{A}. \quad (543)$$

Some discussion of the properties of Ginzburg-Landau equation is given in the Mathematical Appendix. Herewith, we limit ourselves to point out that it admits of periodic solutions of the form:

$$A(\xi, \tau) = \mathcal{A} \exp i(K \xi - \Omega \tau). \quad (544)$$

with \mathcal{A} , K and Ω real quantities. The amplitude \mathcal{A} takes the form:

$$\mathcal{A}^2 = |A_{e, Landau}|^2 - \frac{1}{2} \frac{\mu_{\lambda^2}}{a_r} K^2. \quad (545)$$

Hence, noting that the coefficient μ_{λ^2} is negative and recalling that we are considering supercritical bifurcations ($a_r < 0$), it follows that \mathcal{A} peaks and coincides with the equilibrium amplitude A_{e0} predicted by the Landau-Stuart equation (534) for $K = 0$. This solution, associated with the critical value of the perturbation wavenumber, is called *Stokes wave*. As $|K|$ increases in the interval $|K| < K_M$, with $K_M = (-2b\beta_c\mu_\beta/\mu_{\lambda^2})^{1/2}$, the perturbation amplitude decreases. For $|K| > K_M$ the Stokes wave does no longer exist. The condition $|K| = K_M$ defines a *nonlinear marginal stability curve* (dotted line in Figure 110). Moreover, periodic solutions may be unstable. More precisely within the region of the (λ, β) plane bounded by the nonlinear marginal stability curve, two subregions can be defined. In the inner region periodic solutions are stable, whilst they are unstable in the outer region (Figure 110).

Schielen (1995) also shows that the criterion that controls the shift from stable to unstable periodic solutions depends on the values of the friction coefficient C_{f0} and of the exponent b_s of the transport formula employed by these authors, which expresses the volumetric sediment discharge as proportional to the b_s power of the modulus of the local flow velocity. Figure 111 shows that instability is predicted only for values of $b_s > 3$, corresponding roughly to dune-covered beds. In other words, the periodic bar pattern predicted by the Landau-Stuart approach employed by Colombini *et al.* (1987) is stable if the unperturbed bed is plane, while when the bed is dune covered, more complicated bed profiles may be expected, depending on the value of C_{f0} .

Numerical simulations carried out by Schielen (1995) showed that in the unstable region of periodic solutions, various other types of solutions are possible. Besides the stable *periodic* Stokes

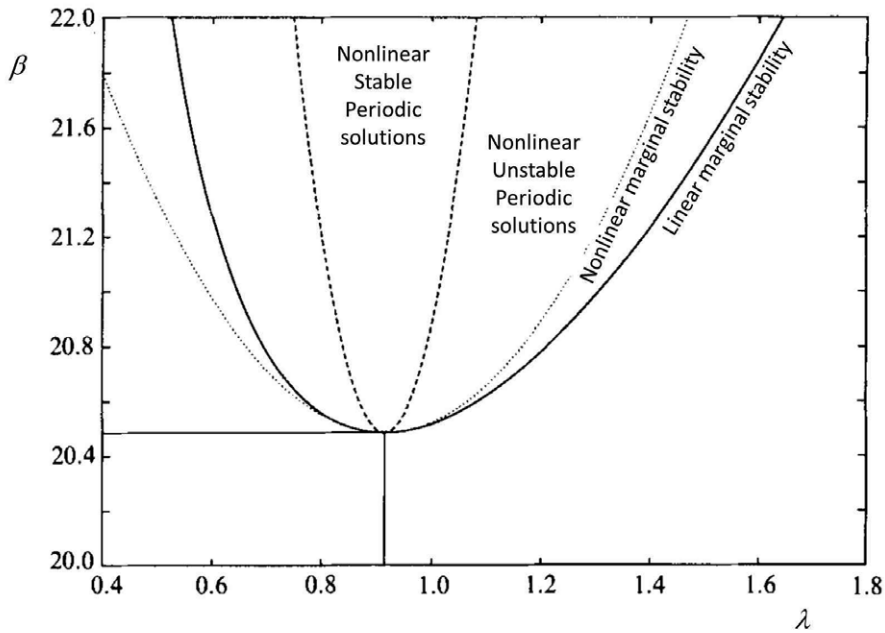


Figure 110. The stability plane (λ, β) arising from the analysis of the Ginzburg-Landau equation (543). Various regions may be identified. Within the region bounded by the solid line bars are linearly unstable; a second order (nonlinear) correction of the linear marginal stability curve is the dotted line, that identifies the region where nonlinear periodic bars exist. Finally, the dashed line separates an inner region where periodic solutions are stable, from an outer region where they are unstable (modified from Figure 2.5 of Schielen, 1995).

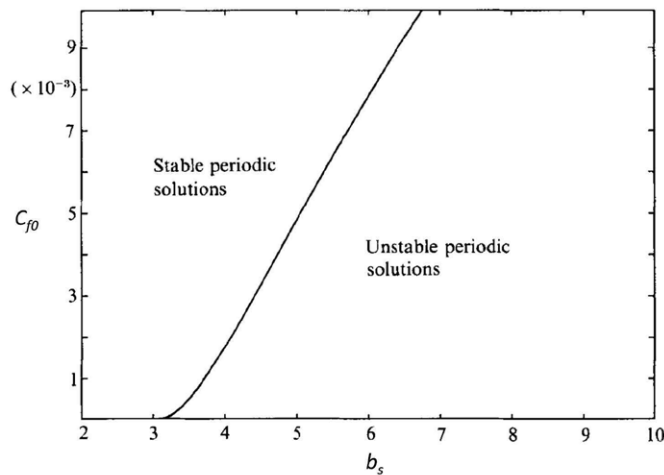


Figure 111. The marginal stability curve for periodic bar patterns in the $b_s - C_{f0}$ plane, separating the region where the standard Landau-Stuart approach applies from a region where different bed profiles may be expected (modified from Figure 2.6 of Schielen, 1995).

waves, *quasi-periodic* patterns were also found: they displayed a range of frequencies that are integer combinations of two fundamental frequencies which are mutually irrational (Figure 112).

Although *chaotic* solutions of the Ginzburg-Landau equation have been found in other contexts (Keefe, 1985; Doelman, 1991), no chaotic patterns emerged from the simulations of Schielen (1995). In summary, the analysis carried out by Schielen (1995) is surely of great conceptual relevance.

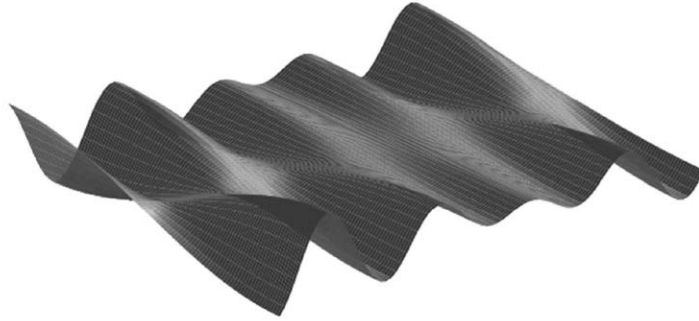


Figure 112. An example of quasi-periodic bars obtained as solutions of the Ginzburg-Landau equation by Schielen (1995). The values of the relevant parameters were chosen as follows: $b_s = 5$, $\epsilon = 0.2$, $C_{f0} = 0.001$ (reproduced from Figure 2.10 of Schielen, 1995).

The novel features brought up by the Ginzburg-Landau model applied to free bar instability would then deserve to be confirmed by laboratory or field observations.

6.5.2 Weakly nonlinear forced bars

We now consider the nonlinear evolution of non-migrating bars forced by some initial condition of the type discussed in Section 6.4.1. There, we pointed out that in the laboratory experiments of Lanzoni (1995), where both super-resonant and sub-resonant spatial bars were generated introducing an obstruction at the flume entrance, it clearly emerged that sub-resonant bars decayed, whilst super-resonant bars developed a finite amplitude.

In this Section, we show that this behavior is theoretically founded. This goal is achieved developing a weakly nonlinear expansion in a neighborhood of the resonant conditions, as shown by Seminara and Tubino (1992). This approach is similar to that employed in the previous Section for the case of free temporally growing migrating bars, but for two fundamental differences:

- the solution is centered around the critical conditions for spatial (rather than temporal) growth, namely $Re(\lambda) = \lambda_R$, $\beta = \beta_R$, $\omega = 0$, hence solutions are sought in the weakly nonlinear regime defined as follows:

$$Re(\lambda) = \lambda_R, \quad \beta = \beta_R (1 + b \epsilon^2), \quad (546)$$

with $\epsilon \ll 1$.

- the complex amplitude A is a function of the slow spatial (rather than temporal) coordinate $\xi = \epsilon^2 x$.

In other words, any property of the perturbation, say the longitudinal component of the flow velocity U_1 , at leading order reads:

$$U_1 = \epsilon u_1^R \sin(\pi y) A(\xi) \exp(i \lambda_R x), \quad (547)$$

where R denotes resonant conditions, and the scope of the weakly nonlinear analysis is to derive an evolution equation for the amplitude function $A(\xi)$.

Physically, this approach interprets the outcome of an experiment performed on a uniform straight channel flow with cohesionless bottom and aspect ratio β slightly perturbed with respect to the threshold value β_R for spatial growth of non-migrating mode-1 (i.e. alternate) bar perturbations.

A steady perturbation is imposed at the initial cross-section and is allowed to grow (or decay) spatially. The sought amplitude equation should enable us to ascertain under what conditions the mode-1 component of the initial perturbation grows and reaches asymptotically an equilibrium amplitude.

Given the analogy with the approach pursued by Colombini *et al.* (1987) in the case of free migrating bars (but see Seminara and Tubino (1992) for the details), it is not surprising that the outcome of the analysis is an amplitude equation of a form similar to (534):

$$[\alpha_r^R + i\alpha_i^R] \frac{dA}{d\xi} = b\beta_R [\mu_\beta^R + i\nu_\beta^R] A + [a_r^R + ia_i^R] A^2 \bar{A}. \quad (548)$$

where the complex coefficients of both the linear and nonlinear terms in the right hand side of (548) are identical with the corresponding terms of (534) evaluated at the *resonant* conditions (λ_R, β_R) .

Equation (548) is again a nonlinear ordinary differential equation of Landau-Stuart type. It is solved in the same closed form reported in the Mathematical Appendix, and allows for the two distinct cases of super-critical (here super-resonant) and sub-critical (here sub-resonant) bifurcations, depending on the sign of a_r^R . In Figure 113 we plot the real parts of the two coefficients that determine the character of the bifurcation. These plots show the supercritical character of the bifurcation within a wide range of values of the Shields parameter and of the relative grain roughness. Hence, under super-resonant conditions, an initial S_1 perturbation does develop asymptotically in space into an equilibrium periodic configuration consisting of steady alternate bars with equilibrium amplitude:

$$|A_e|^2 = -b\beta_R \frac{\mu_\beta^R}{a_r^R}. \quad (549)$$

In general, the initial perturbation will contain more than one lateral mode. If the width parameter falls close to the resonant value for the first lateral mode, then higher modes will be sub-resonant and will decay in space leaving only the alternate bar mode. We may conclude noting that the above analysis confirms qualitatively the observations of Lanzoni (1995); a quantitative verification has not been performed yet.

6.6. Fully nonlinear free and forced bars

The weakly nonlinear approach discussed in the previous Section is of great conceptual relevance, but it is still restricted to a small region of the parameter space close to the critical conditions for free or forced bar formation. The latter constraint may be relaxed resorting to full numerical solutions of the governing equations. Below, we will again treat free and forced bars separately.

6.6.1 Numerical simulations of finite amplitude free bars

Several Authors engaged in numerical simulations of the nonlinear development of free bars, mostly under steady conditions. Pioneering works are due to Nelson and Smith (1989) and Shimizu and Itakura (1989). In particular, Nelson and Smith (1989), using a finite difference method, were the first to point out that finite amplitude free bars, during their nonlinear development, lengthen and slow down, in agreement with the experimental observations of Fujita and Muramoto (1985), later confirmed by Lanzoni (1995) (see also Lanzoni, 2000a). Colombini and Tubino (1991), using a spectral method, focused on the importance of strongly nonlinear interactions among various harmonics during bar development.

More recently, Defina (2003) investigated the dependence of the bar response on the type of initial disturbance triggering bar formation. Numerical simulations were performed on a numerical flume with length 117.5 m and width 1.5 m, long enough to host several bar units and allow their development towards an equilibrium state. The most important result, emerged from these simulations, was described by the Author as follows: “*the initial disturbance is quickly eroded but lasts long enough to promote the formation of new bars close downstream ... the height of the first*

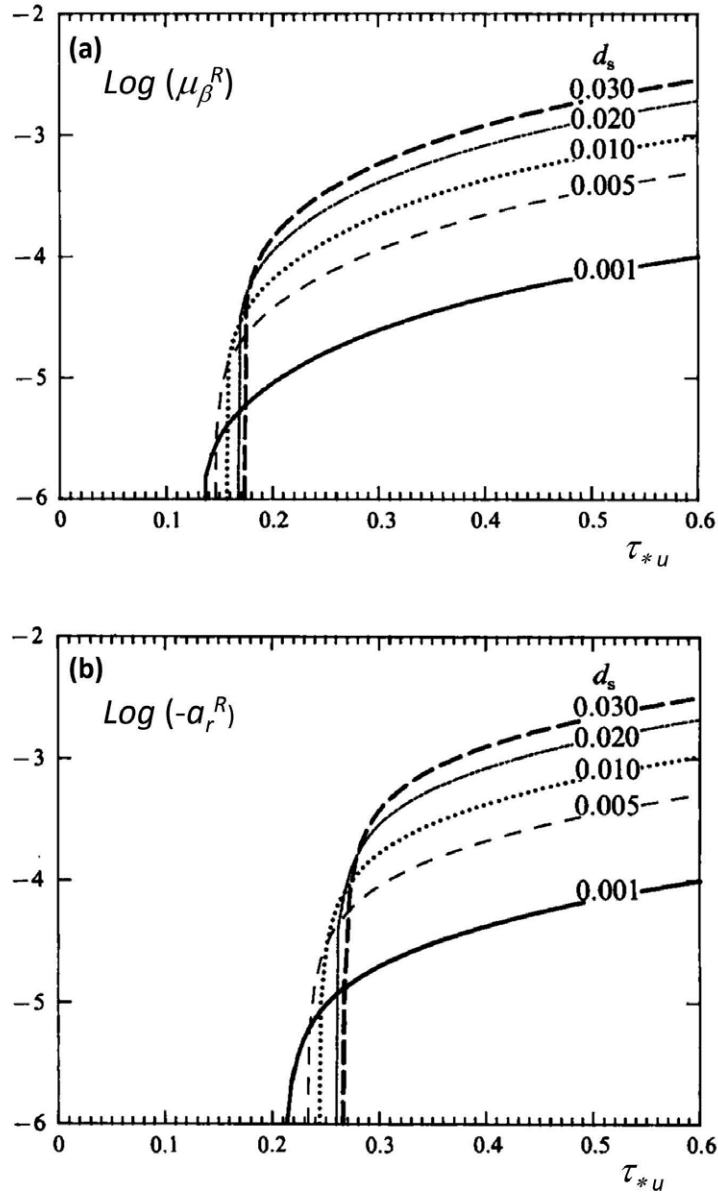


Figure 113. The real part of (a) the linear coefficient and (b) of the nonlinear coefficient of the Landau-Stuart amplitude equation (548) of spatial bars (modified from Seminara and Tubino, 1992).

bars generated by the initial bump, ... gently decay after a slow initial growth. This is a general behavior found in all the simulations". Although the Author did not interpret this finding in terms of the distinction between convective and absolute instabilities, he had demonstrated numerically the convective nature of free bar instability. Not being aware of the implications of the above distinction, the Author did not perform simulations with a persisting perturbation imposed at the initial cross-section. As a result, perturbations did not actually reach equilibrium conditions.

Let us be more precise. A set of simulations were performed assuming an initial perturbation

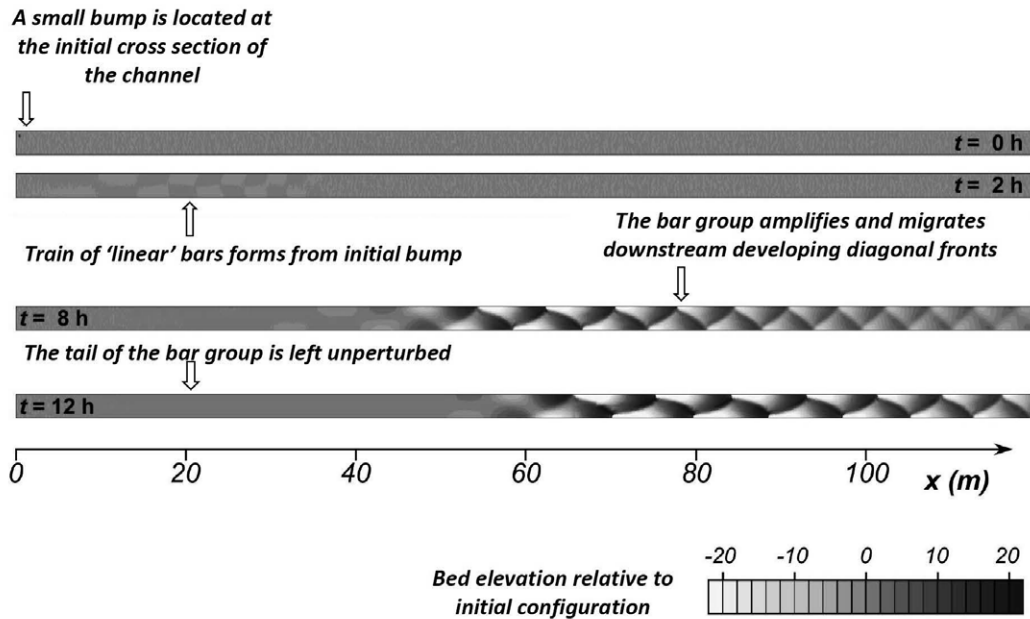


Figure 114. Results of simulation of the evolution of bed topography for the flume experiment P1505 of Lanzoni (2000a). Note that scales are distorted: the longitudinal scale is half the lateral scale (courtesy of Andrea Defina).

in the form of a small *bump*. According to the Author, these numerical experiments gave results comparing favourably with the experimental observations of Fujita and Muramoto (1985) and Lanzoni (2000a). Essentially, results showed that, following the generation of a *first bar*, a train of bars formed and propagated downstream in the form of a wave group leaving its tail unperturbed (Figure 114). As a result, no actual steady state was reached. Below, we discuss the work of Federici and Seminara (2003), appeared the same year as that of Defina (2003), where it was shown that, due to the convective nature of the free bar instability, a persisting perturbation must indeed exist at the initial cross-section of the channel in order for a steady state to be actually reached asymptotically in space and time. Hence, the agreement found by Defina (2003) was based on a comparison of the frontal region of a train of numerically generated bars migrating downstream with the characteristics of the steady state bars observed in the laboratory experiments. This notwithstanding, a number of important features of the actual phenomenon emerged from the simulations. In particular, the shape of bars was initially in reasonable agreement with the shape of linear bars. As the bars grew, nonlinear effects led fronts to become much steeper and rotate such to produce the characteristic diagonal patterns predicted by the weakly nonlinear theories (Figure 114). Simulations also confirmed the processes of bar lengthening and slowing down occurring when bars reach finite amplitudes.

The analysis performed by Federici and Seminara (2003) was aimed at clarifying the fundamental nature of free bar instability in both a linear and nonlinear context. The linear aspects of the problem have already been discussed in Section 6.3.3. Federici and Seminara (2003) substantiated the linear analysis by numerical experiments performed on the full nonlinear governing equations. More precisely, these Authors performed numerical simulations of bar evolution under two different initial conditions. In the first case, similarly to Defina (2003), a localized spatial perturbation of bed topography in the form of a bump with an emi-symmetric lateral profile and a sinusoidal longitudinal shape was forced at the beginning of the flume. In the second case, a randomly distributed perturbation of bed topography was assigned throughout the channel at the start of

the simulation. Both the initial conditions gave rise to the growth of wave groups which migrated downstream leaving the flow domain unperturbed, for every aspect ratio of the channel (Figure 115). The convective nature of free bar instability was thus confirmed at a nonlinear level.

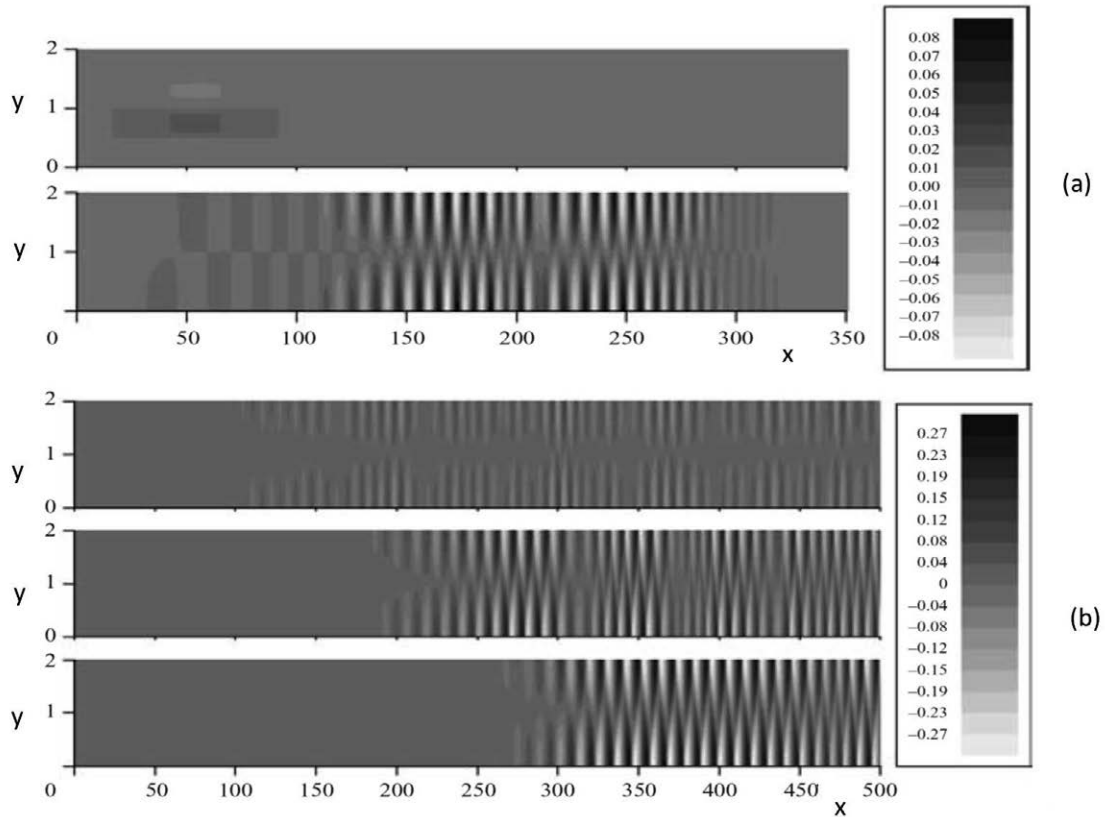


Figure 115. (a) Bed topography at the initial time and at $t_M = 500$ in a simulation where bars were triggered by an initial localized bump ($\beta = 15$, $\tau_{*u} = 0.09$, $d_s = 0.04$). The bump gives rise to wave groups that grow and migrate downstream. (b) Bed topography at $t_M = 500$, 1000 and 1500, in a simulation where bars are generated by an initial small randomly distributed perturbation ($\beta = 12$, $\tau_{*u} = 0.09$, $d_s = 0.04$). Time t_M is scaled by the morphodynamic time scale defined in Section 6.2. Longitudinal and lateral coordinates are scaled by half the channel width (modified from Federici and Seminara, 2003).

The main consequence of the latter finding is that the equilibrium pattern of bars actually observed in the laboratory may only arise from some persistent forcing, no matter how small. Thus, Federici and Seminara (2003) investigated the dependence of the nonlinear development of free bars on the type of persistent forcing present at the initial cross-section. Numerical simulations were also aimed at answering some questions that arise naturally, namely: Does the bar development lead to the establishment of an equilibrium amplitude as predicted by Colombini *et al.* (1987)? Is such an equilibrium amplitude dependent on the amplitude of the perturbation forced at the initial cross-section? How long must a flume be in order to allow for the spatial development of the initial perturbation to reach its equilibrium state? Does the selection of the bar mode depend on the spatial rather than temporal character of bar development?

In the first numerical experiment, denoted as '1Freq', forcing consisted of a small amplitude perturbation of bottom elevation at the initial cross-section of the flow domain. The perturbation had a lateral distribution corresponding to an alternate bar and oscillated with the frequency associated with the most unstable wavenumber of the linear theory. Figure 116a-c shows the outcome of simulations in the form of plots of bed topography at different dimensionless times. In this case, a wave group still forms and migrates downstream undergoing spatial and temporal

amplification, but, unlike in the previous simulations, the tail of the group does not leave the generation area. Moreover, nonlinear saturation of the perturbation leads to the establishment of an equilibrium amplitude. This is clearly shown by Figure 116d where the distribution of bottom elevation along the right bank is plotted for different times.

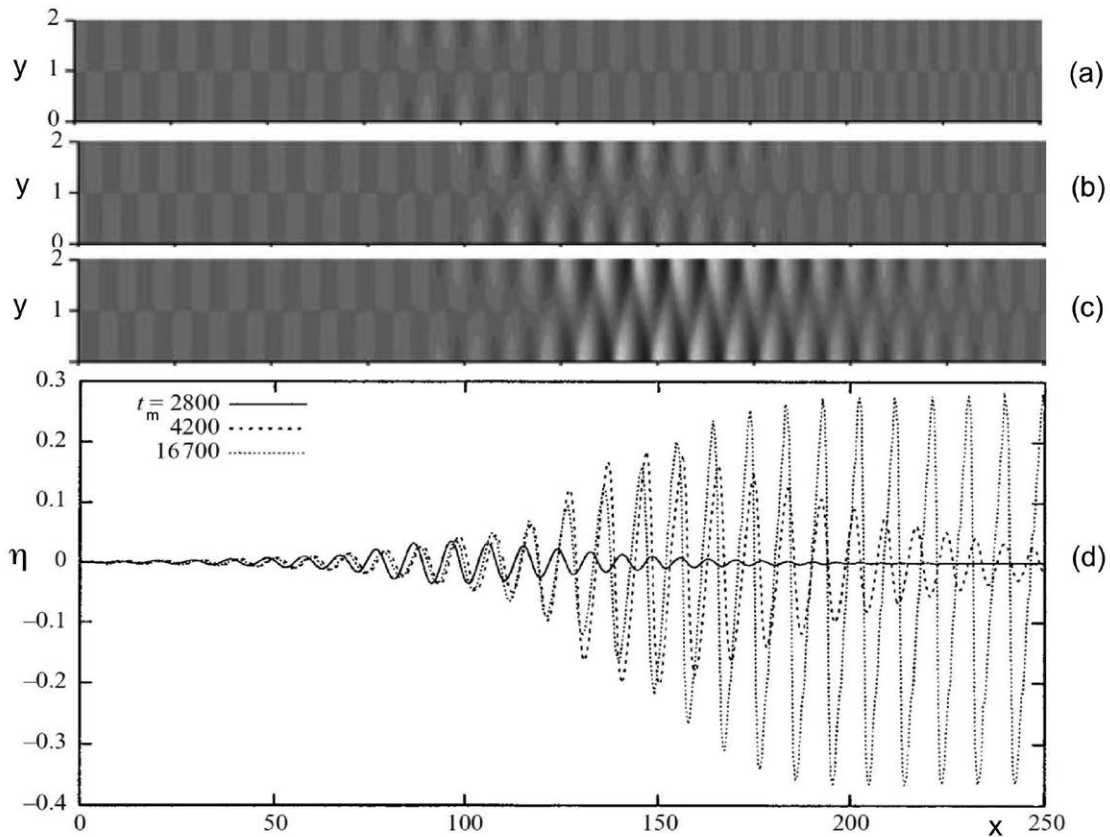


Figure 116. Bed topography generated numerically in run '1Freq' by forcing a single harmonic oscillation of bottom elevation at the initial cross-section. The monitored instants correspond to $t_M =$ (a) 2800, (b) 3700, (c) 4200. The plot in (d) shows the distribution of bed elevation along the right bank of the channel at different times ($\tau_{*u} = 0.057$, $d_s = 0.053$, $\beta = 8$ and $\beta_c = 5.6$). Time t_M is scaled by the morphodynamic time scale defined in Section 6.2. Longitudinal and lateral coordinates, as well as bed elevation are scaled by half the channel width (modified from Federici and Seminara, 2003).

Moreover, *the equilibrium amplitude does not depend on the chosen amplitude of the initial perturbation*. This is shown in Figure 117 where we plot the outcomes of two different simulations with identical initial conditions except for the amplitudes of the prescribed perturbations that differed by a factor two. It appears that the equilibrium amplitude is practically identical in the two simulations. On the contrary, the distance from the initial cross-section where equilibrium is reached increases with decreasing values of the initial amplitude.

In a second set of numerical experiments the initial perturbation was chosen such to model the random character of actual perturbations that are invariably present in the real world. The most appropriate procedure would have been to impose in the initial cross-section a random oscillation with the same lateral structure as in the '1Freq' experiment. However, this leads to numerical instabilities due to the presence of too large frequencies in a random forcing. To avoid this problem, Federici and Seminara (2003) chose an initial perturbation consisting of the superposition of 20 harmonics with equal amplitudes. Their frequencies were chosen as those prescribed by the dispersion relationship for 20 equally spaced unstable wavenumbers at a given value of the aspect

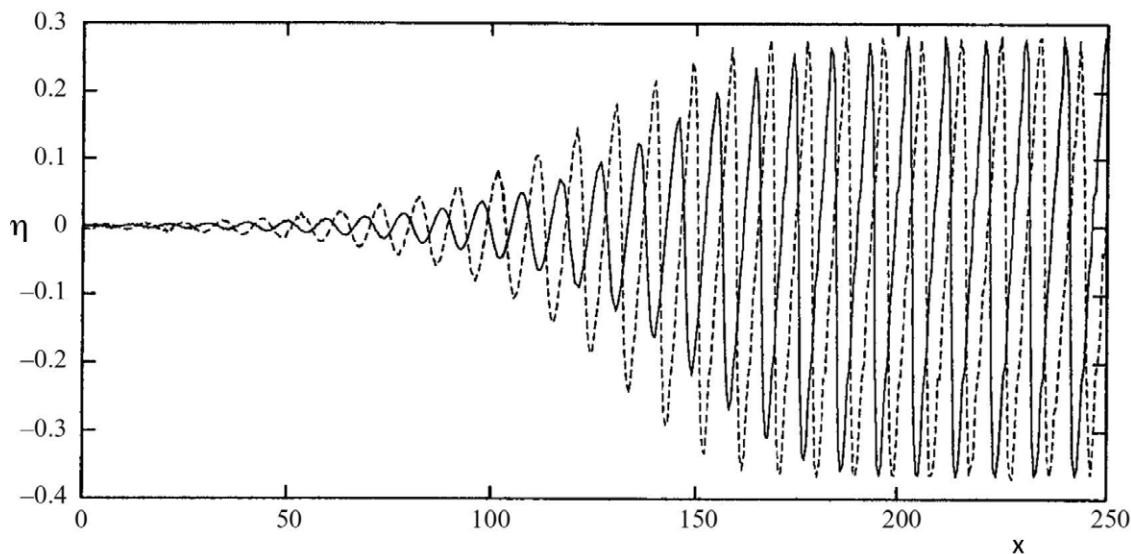


Figure 117. The distribution of bed elevation along the right bank of the channel in two numerical simulations with identical initial conditions except for the amplitudes a of the prescribed dimensionless perturbations that differed by a factor two. The system was forced with a single harmonic perturbation of the bottom elevation at the initial cross-section. Solid line, $a = 0.001$; dashed line, $a = 0.002$ ($\tau_{*u} = 0.057$, $d_s = 0.053$, $\beta = 8$ and $\beta_c = 5.6$). Time is scaled by the morphodynamic time scale. Longitudinal and lateral coordinates are scaled by half the channel width (modified from Federici and Seminara, 2003).

ratio β (Figure 118). In order to ascertain the possible dependence of the bar response on the harmonic content of the initial perturbation, simulations were then repeated halving the number of components of the forcing oscillation (run denoted '10Freq').

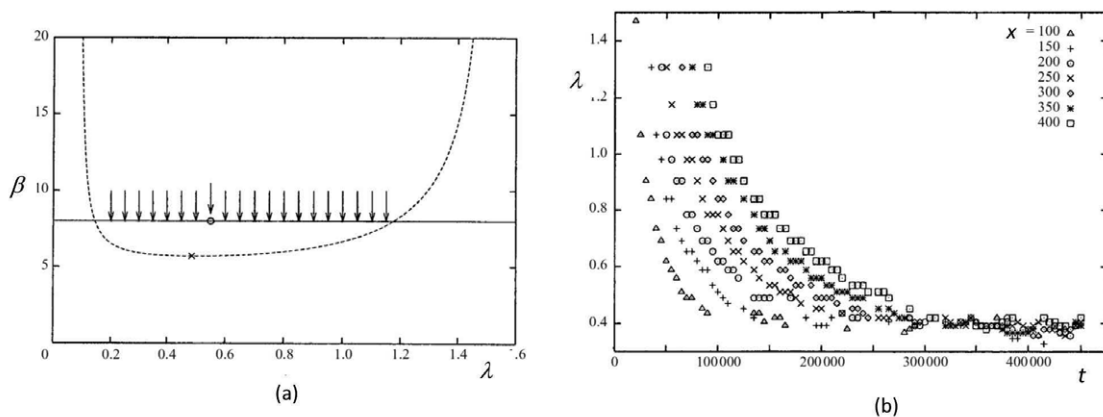


Figure 118. (a) The sketch shows 20 equally spaced unstable wavenumbers for a given value of the aspect ratio β , chosen employing the linear dispersion relationship and determining the harmonic content of the initial perturbation of run '20Freq' ($\tau_{*u} = 0.057$, $d_s = 0.053$, $\beta = 8$ and $\beta_c = 5.6$). The circle indicates the linearly most unstable wavenumber for the given aspect ratio β ; the cross indicates the critical wavenumber. (b) Temporal development of the bar wavenumber observed at different cross-sections (reproduced from Federici and Seminara, 2003).

Results show that the spatial-temporal amplification of the initial perturbation leads to the asymptotic emergence of a preferred mode. The *equilibrium* wavenumber turns out to be close to (but smaller than) the wavenumber characterized by the maximum linear growth rate for the

given value of the aspect ratio β . It is worth noting that *neither the equilibrium amplitude nor the equilibrium wavenumber and wavespeed asymptotically reached by the perturbation are affected significantly by the harmonic content of the initial perturbation*. Simulations also confirm that, during the evolution process, perturbations lengthen (Figure 118b) and slow down significantly.

More recently, Crosato *et al.* (2011) have published the results of a series of numerical simulations aimed at ascertaining whether stationary bars may also arise freely, i.e. in the absence of permanent forcing of the type previously investigated by Struiksma and Crosato (1989) and Lanzoni (2000a). Simulations were performed using a fully nonlinear, time-dependent, 2D morphological model. Their distinct feature was the *size* of the system considered in the simulation: a channel with length of 20 km and longitudinal bed slope 10^{-4} . Moreover, the duration of the process simulated was of the order of tens of years, such that some runs took more than 40 days to be completed even adopting a value of the so called *morphological factor* as large as 10. Essentially, the morphological factor employed in some numerical models of morphodynamic processes is the ratio between the time step of morphological updating of the bottom topography and the time step of hydrodynamic simulations (see Roelvink, 2006).

Two runs were performed with initial conditions at the entrance section consisting of a uniform flow perturbed by small amplitude random perturbations of the inflow discharge imposed at each node of the computational grid. In the first run the maximum amplitude of perturbations was equal to 1% of the discharge and the frequency was 1 min^{-1} ; in the second run these values were changed to 5% and 3.5 h^{-1} . The boundary condition at the downstream end consisted of imposing the uniform flow depth.

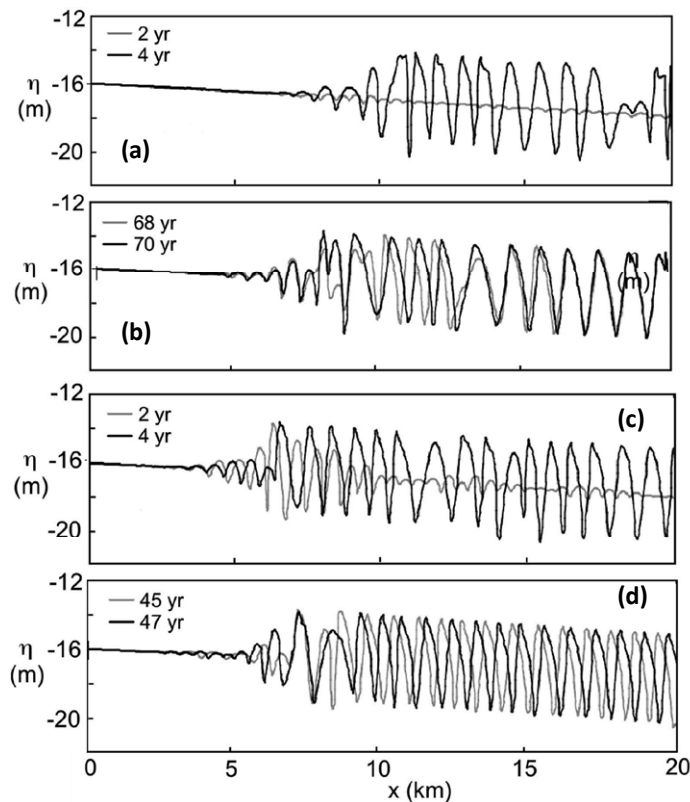


Figure 119. The plots show the longitudinal bed profile at 15 m from the left bank at various times from the start of the 'free' simulation (RUN 1) of Crosato *et al.* (2011). In the simulation the uniform inflow was perturbed imposing at each node of the inlet section random perturbations with maximum amplitude equal to (a,b) 5% and (c,d) 1% of the average discharge (data from Crosato *et al.*, 2011).

Results did not differ initially from those obtained in previous simulations, in that a train of migrating bars in the form of a wave group formed rapidly. Bars were fairly short but their wavelengths gradually increased and their migration speed decreased. However, after a long time (of the order of decades) part of the bars stopped migrating. Figure 119 shows that this feature appeared in the upstream reach in the 1% discharge perturbation experiment and in the downstream reach in the 5% discharge perturbation experiment. Simulations were stopped as soon as the first bars reduced significantly their migration speed, hence in the final configuration shown in Figure 119 part of the bar train was not stationary. The Authors conclude stating that "*Apparently, fast growing migrating bars represent a transient stage and are not representative for the final channel bed topography*". However this conclusion has no theoretical substantiation yet. Indeed, the theoretical foundations of bar theory are quite firm and the main body of knowledge established so far is substantiated by a number of laboratory observations, as discussed in this Chapter. Of course, new features of the process may always emerge but they will remain elusive until it will be demonstrated that they are amenable to a sound theoretical interpretation.

And, indeed, in a follow up paper, Crosato *et al.* (2012) repeated similar long term simulations with slightly changed simulation parameters (longitudinal bed slope 2×10^{-4} , random initial perturbation with amplitude equal to 0.5% of the discharge and frequency 2.3 day^{-1} , simulated time 7 years , morphological factor 25): results of these simulations did not confirm the formation of steady bars observed by Crosato *et al.* (2011). Moreover, a sharp decrease of bar amplitude was found to occur periodically, as shown in Figure 120. The latter finding is clearly reminiscent of the

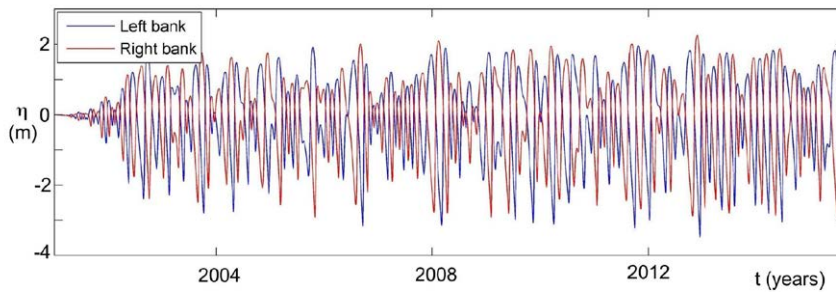


Figure 120. Temporal evolution of the longitudinal bed profile near the right and left bank at the cross-section located 15 km downstream from the inlet section in Run 2 of Crosato *et al.* (2012) (data from Crosato *et al.*, 2012).

results obtained by Schielen *et al.* (1993) on the instability of the periodic solutions of Ginzburg Landau equation discussed in Section 6.5.1. Nevertheless, just like for *free* stationary bars, no clear theoretical interpretation of the modulation of bar amplitude displayed by Figure 120 has been proposed so far.

6.6.2 Numerical simulations of finite amplitude forced bars

Less attention has been devoted in the literature to numerical simulations of finite amplitude forced bars. Two recent works on the subject are the already mentioned paper by Crosato *et al.* (2011) and the contribution by (Siviglia *et al.*, 2013). Besides the *free* numerical experiments discussed in Section 6.6.1, Crosato *et al.* (2011) performed also a *forced* experiment. A permanent finite perturbation (a groyne) similar to those employed by Struiksma and Crosato (1989) and Lanzoni (2000a) was imposed at the upstream boundary. Figure 121 shows that forcing gives rise to a wave group which reaches asymptotically a stationary periodic equilibrium pattern: this suggests that the flow conditions in this run were near-resonant, rather than sub-resonant as stated in the paper.

Considering a similar forced configuration (an asymmetric obstacle that locally reduces the cross-section width to its half value), Stecca (2012) (but see also Siviglia *et al.*, 2013) carried out experiments keeping τ_{*u} , d_s and, hence the resonant value β_R , fixed. Both sub-resonant ($\beta < \beta_R$)

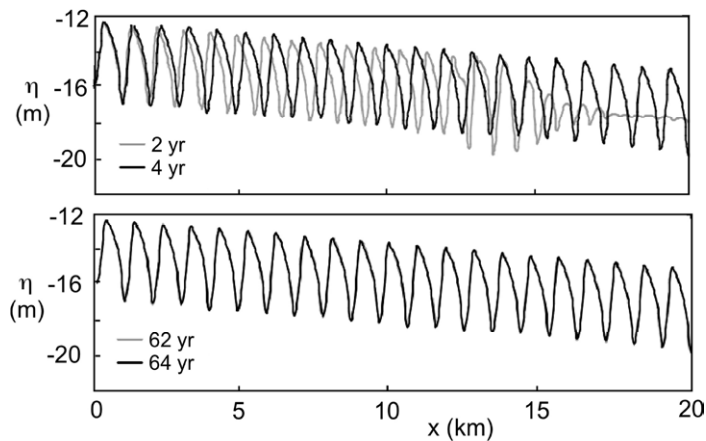


Figure 121. The plots show the longitudinal bed profile at 15 m from the left bank at various times from the start of the forced simulation (RUN 1) of Crosato *et al.* (2011) (data from Crosato *et al.*, 2011).

and super-resonant ($\beta > \beta_R$) conditions were analyzed. In the early stages of each simulation, the channel bed was typically subject to a relatively fast evolution, with migrating alternate bars forming downstream of the obstacle. As the simulations proceeded, new bars were generated either downstream (Figure 122a) or upstream (Figure 122b) of the obstacle, depending on the sub-resonant or super-resonant character of the simulation. These bars grew in amplitude at a relatively slow rate, progressively elongating and slowing down, eventually ceasing to migrate. The final wavelengths of these forced bars were invariably larger than those typical of free migrating bars (ranging about 7-8 channel widths). Specifically the wavelength of sub-resonant forced bars was about 16 channel widths, while under super-resonant conditions forced bars exhibited a slightly smaller wavelength, around 12 channel widths.

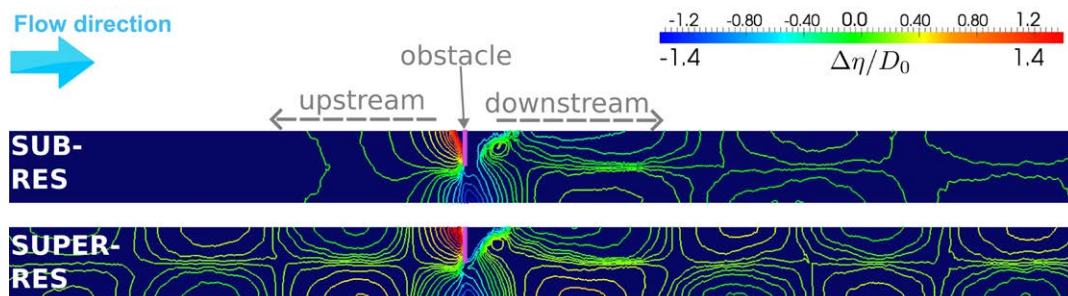


Figure 122. The plot shows variations of bed elevations scaled by the uniform flow depth, computed for a straight channel containing a local asymmetric obstacle that halves the cross-section width. Upper panel refers to sub-resonant conditions ($\beta = 10.42$), whereas lower panel corresponds to super-resonant conditions ($\beta = 16.72$). The relevant parameters had the following values: $\tau_{*u} = 0.1$, $d_s = 0.067$, $\beta_R = 13.28$, $\beta_c = 8.06$ (reproduced from Figure 7.10 of Stecca, 2012, under License Creative Commons Attribution Non-commercial No Derivatives).

6.6.3 Interaction between free and forced bars in straight cohesionless channels

The interaction between free and forced bars driven by width variations was investigated theoretically by Repetto (2000) (but see also Repetto and Tubino, 1999a,b) who developed a weakly non linear analytical approach, assuming a small amplitude periodic width oscillations. Denoting by δ a dimensionless measure of such amplitude, scaled by the averaged channel width, they found that the linear growth rate of free bars exhibits an $\mathcal{O}(\delta^2)$ correction due to width changes. This correction which was found to depend on the dimensionless wavenumber of width oscillations λ_b , was invariably negative and its intensity increased with the Shields parameter. Furthermore, width variations slowed down the propagation of free bars, except in the range of small λ_b values. The analysis allowed to determine a threshold value of δ above which bars are suppressed. The predicted value of the δ threshold is plotted in Figure 123 as a function of the width ratio β for different values of the unperturbed Shields stress τ_{*0} . However, the reader should note that, at threshold, the $\mathcal{O}(\delta^2)$ correction of the bar growth rate has the same magnitude and opposite sign of the unperturbed growth rate: under these conditions the assumed asymptotic character of the expansion does not strictly apply.

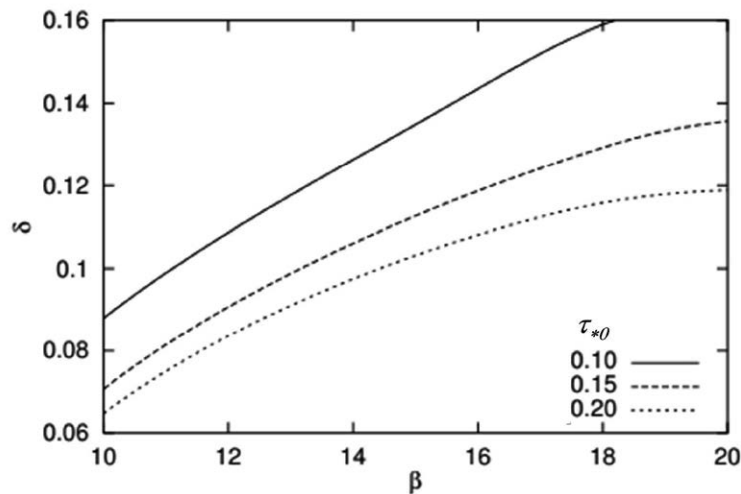


Figure 123. The threshold value of the dimensionless amplitude of width oscillations for free bar suppression predicted by Repetto (2000) is plotted versus the width ratio β for different values of the unperturbed Shields stress τ_{*0} . Grain size scaled by unperturbed flow depth $d_s = 0.05$; dimensionless wavenumber of width oscillations $\lambda_b = 0.3$ (reproduced from Figure 4.3 of Repetto, 2000).

Repetto (2000) (but see also Repetto *et al.*, 2002) performed also some laboratory experiments on a flume whose banks had a sinusoidal shape, thus allowing for periodic width oscillations. For small amplitudes of the latter ($\delta = 0.125$) and sufficiently large width to depth ratio, migrating alternate bars were observed to form in the flume, as expected based on theoretical predictions of Colombini *et al.* (1987). However, their development was strongly affected by bank oscillations, leading to highly unsteady, irregular bars. More precisely, central bars formed initially in the wider sections of the flume and, once they reached a sufficient amplitude, they migrated downstream. However, as the front of the bars approached the narrowest section of the flume, they slowed down significantly: typically, they were unable to migrate through the constraint, whilst a new bar formed in the upstream expansion. Eventually, the central bar decayed into a series of short migrating alternate bars, though regular bar trains migrating through the full channel length were never observed: on the contrary, bars with variable lengths and heights repeatedly formed and disappeared in a sequence of pulses. At $\delta = 0.25$ alternate bars were suppressed in favor of a steady forced bed configuration, consisting of a strong longitudinal deformation almost in phase with the bank profile along with a transverse deformation, in the form of a central bar located at the wide section. Repetto (2000) concludes that periodic width variations (of sufficient amplitude) may

trigger the transition from migrating alternate bars to steady central bars with the longitudinal wavenumber of the bank profile. Qualitatively similar conclusions had been previously reached by Bittner (1994), who performed analogous laboratory experiments.

The weakly non linear analysis of Repetto (2000) was later extended numerically to the fully nonlinear regime by Wu *et al.* (2011), who solved the full depth averaged shallow water equations and the two-dimensional Exner equation corrected for secondary flows induced by streamline curvature as in Wu and Yeh (2005). A finite element method, based on a characteristic dissipative Galerkin up-winding scheme, was used to discretize the resulting system of partial differential equations. A sinusoidal perturbation was imposed to the channel width, with dimensionless amplitude δ and wavelength λ_b , both scaled by half the channel width. The overall forcing effect was measured through a single factor,

$$F_b = \delta \exp \lambda_b. \quad (550)$$

Results of Wu *et al.* (2011) confirm that width variations invariably tend to damp both the height and wavelength of free bars, and this reduction effect increases with the intensity of the width variations imposed to the channel. Conversely, as the forcing progressively increases, bar celerity first undergoes a slight increase and subsequently experiences a damping for large values of F_b . The maximum increase in bar celerity exceeds the migration speed developed in the reference straight channel by less than 5%.

Note that, for the investigated ranges of values of δ (0.1-0.4) and λ_b (0.2-0.8) free bars were always observed to form, even when A_b exceeded the threshold value (0.2 for the considered morphodynamic parameters) below which the weakly nonlinear stability analysis would predict a full free bar suppression (Figure 123). This discrepancy still needs to be explained. Clearly, the small perturbation assumption adopted in the linear stability analysis does not account for self-interactions among the various modes.

However, free bar suppression was also observed in the laboratory experiments of both Bittner (1994) (“*as the channel width perturbation was increased, it was found that migrating bedforms were totally suppressed*”) and Repetto (2000). This sheds some uncertainty on the numerical results, leaving the issue of free bar suppression in the present context as yet unsettled.

6.7. Bars in the field: additional complexities of bar morphodynamics

6.7.1 The effect of flow unsteadiness

A feature of the natural phenomenon ignored in most laboratory experiments and theoretical investigations is the unsteady character of the flows responsible for pattern formation. Taking into account this effect turns out to be crucial if one wants to interpret field observations correctly. Indeed, during the propagation of a flood in a channelized river, the flow discharge increases, reaches a peak and then decays until a new event occurs. The flow depth has a similar trend and drives an opposite behavior of the width to depth ratio β , which decreases throughout the rising limb of the flood, reaches a minimum and then increases again.

In conclusion, if one simply interprets the response of free alternate bars to flood propagation based on results discussed for the steady case and assumes, for the time being, that β_c keeps constant through the flood, then the following scenario would arise. Bars form at some relatively low stage (sufficient to mobilize sediments), develop a finite amplitude that decreases throughout the rising limb of the flood (as $(\beta - \beta_c)$ decreases), may even vanish at some high stage (when $\beta \leq \beta_c$) to increase during the falling stage (when $(\beta - \beta_c)$ increases).

On the other hand, the critical value of the width to depth ratio β_c varies as a function of the Shield stress (that follows a trend similar to the flow discharge) and of the roughness parameter (that is proportional to the inverse of the flow depth), as shown in Figure 88. As a result, the picture would be slightly more complex than described above.

Is the expected picture correct? In other words, can we interpret the response of alternate bars as a *slowly varying* sequence of equilibrium states associated with the instantaneous discharge? Or, alternatively, can we define, for a given hydrograph, some *reference flow stage* to which we can

attach the concept of a *finite equilibrium amplitude* of bars established by Colombini *et al.* (1987)? And, in this case, can we establish some relationship between the actual amplitude attained by the bed configuration in response to a flood (or a sequence of floods) and the equilibrium amplitude associated with the reference state mentioned above? The works of Tubino and Seminara (1987) (hereafter TS) and Tubino (1991) attempt to provide an answer to the above questions based on an extension of the weakly nonlinear analysis of Colombini *et al.* (1987) as well as on laboratory experiments.

Theory

The starting point of the theoretical analysis of TS is the recognition of the existence of three time scales in the process under investigation:

- a *hydrodynamic time scale*, say B/U_0 , with U_0 reference speed associated with some chosen mean flow;
- a *morhodynamic time scale*, say $B/(U_0 \epsilon_M)$, with ϵ_M appropriately defined in the present context;
- a *flood time scale* T_F defined by a typical hydrograph. This scale is typically much larger than the hydrodynamic time scale, i.e. it is such that the dimensionless parameter $\sigma \equiv B/(U_0 T_F)$ is also small.

TS then introduces a *dimensionless parameter* ϵ_M/σ measuring the ratio between the flood time scale and the morhodynamic time scale, hence three conditions are conceivable:

- $\epsilon_M/\sigma \gg 1$: in this case, bars develop much more slowly than the basic flow, whose variations are thus unable to affect bar development;
- $\epsilon_M/\sigma \ll 1$: bars develop much faster than the basic flow, such to reach their steady equilibrium amplitudes corresponding to the instantaneous flow characteristics;
- $\epsilon_M/\sigma \sim \mathcal{O}(1)$: bars develop as fast as the basic flow, implying that flow changes do affect bar development.

We will see that typically the last condition is encountered in nature and calls for an appropriate analysis. TS first assume that the average reference state falls within a neighborhood of the critical conditions for alternate bar formation, such that one may write:

$$q = 1, \quad D = 1, \quad \beta_0 = \beta_c (1 + b \epsilon^2), \quad (551)$$

where q is the dimensionless flow discharge per unit width, scaled by $(D_0 U_0)$, D is the dimensionless flow depth scaled by D_0 , and β_0 is the width to depth ratio at the reference state B/D_0 .

Moreover, let us recall that the *slow* time variable describing bar growth is defined in the form of equation (532). TS assume that the basic unsteady state varies on a similar time scale (i.e. $\epsilon_M/\sigma \sim \mathcal{O}(1)$). Moreover, he restricts the analysis to the case of *weak* unsteadiness, such that the unsteady basic state can be expressed in the following form:

$$q = 1 + \epsilon^2 q_1(\tau), \quad D = 1 + \epsilon^2 D_1(\tau), \quad \beta = \beta_0 (1 - \epsilon^2 D_1(\tau)). \quad (552)$$

Note that this *weak unsteadiness* assumption should not be regarded as a too severe constraint, as gravel-bed rivers typically become active at high flows such that only a portion of the hydrograph is able to mobilize the bed. On the other hand, this is quite a convenient assumption as it allows to extend easily the weakly nonlinear theory of Colombini *et al.* (1987) to the unsteady case. And, indeed, following closely the approach of Colombini *et al.* (1987), TS obtained the following slightly modified version of the Landau-Stuart amplitude equation (534):

$$\frac{dA}{d\tau} = [b \beta_c (\mu_\beta + i \nu_\beta) + \alpha_0 q_1(\tau)] A + (a_r + i a_i) A^2 \bar{A}. \quad (553)$$

where the complex coefficients $(\mu_\beta + i\nu_\beta)$ and $(a_r + ia_i)$ are identical with those of the steady case and α_0 is a further complex parameter that accounts for the effect of the unsteadiness of the basic flow. All these coefficients are functions of the average values of the Shields parameter τ_{*0} and roughness parameter d_{s0} .

The equation (553) shows that unsteadiness is felt by the bar growth at a linear level, i.e. it affects the instantaneous bar growth rate and the phase of bar perturbations. For any given time dependence of the basic flow, described by the function $q_1(\tau)$, equation (553) can be readily solved in closed form and allows one to determine the unsteady response of bar amplitude to a single flood or a sequence of floods. TS applied the above formulation to some field data available at the time, namely observations carried out by Lewin (1976) on a reach of the Ystwyth River that had been artificially straightened. Unfortunately, Lewin did not measure the amplitude of bars, but the flood event could be qualitatively reconstructed (Figure 124a) and application of the theory led to results depicted in Figure 124b.

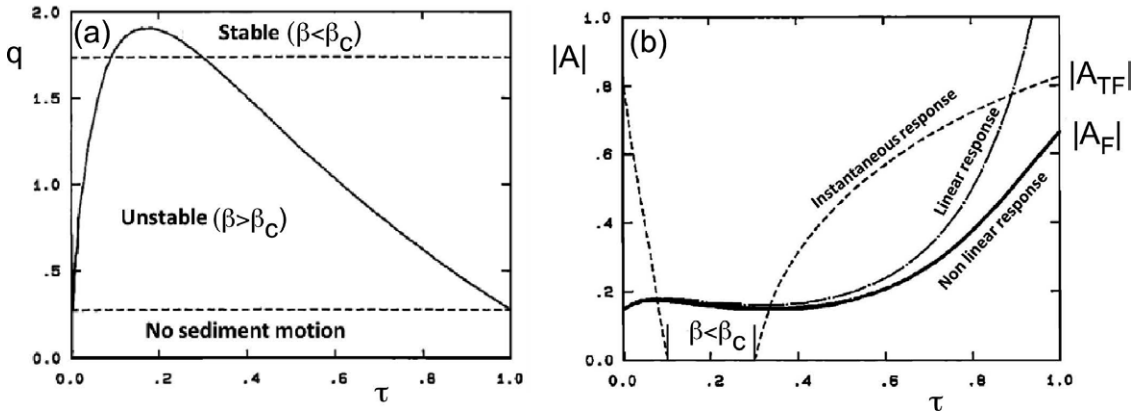


Figure 124. (a) The flood event propagated through an artificially straightened reach of the Ystwyth River, reconstructed by TS on the basis of Lewin (1976) observations. (b) Temporal evolution of the modulus of the bar amplitude predicted by TS theory for the reconstructed event: nonlinear unsteady solution (solid line); equilibrium solution corresponding to the instantaneous flow conditions (dashed line); linear unsteady solution (continuous-dot line) (modified from TS).

The picture arising from Figure 124 suggests that during the rising stage ($\tau \lesssim 0.1$) bars undergo a quasi-linear growth, followed by a weak decay at the peak stage ($0.1 \lesssim \tau \lesssim 0.3$) when the width to depth ratio falls below its critical value. The falling stage ($0.3 \lesssim \tau \lesssim 1$) is the actual formative part of the flood, where nonlinear bar growth is experienced.

In order to assess the role of the unsteadiness parameter ϵ_M/σ , TS then performed a set of simulations assuming the following hydrograph shape function:

$$q_1(\tau) = (1 + \hat{q}_1) \sin \left\{ \log \left[1 + \tau (\exp(\pi) - 1) \right] \right\} - 1. \quad (554)$$

The ratio between the actual bar amplitude reached at the end of the flood A_F and the equilibrium amplitude associated with the final state A_{TF} turns out to depend on the unsteadiness parameter ϵ_M/σ and on the initial value A_0 of the bar perturbation, for given values of \hat{q}_1 and of the additional parameter $-Re(\alpha_0)/(b\beta_c\mu_\beta)$. Results are plotted in Figure 125 that confirms that three possible conditions may occur. Indeed, the final bed configuration is the result of a strong interaction between bar development and unsteady flow provided ϵ_M/σ falls within a limited range of values close to 1, whereas $A_F \rightarrow A_0$ if $\epsilon_M/\sigma \gg 1$ and $A_F \rightarrow A_{TF}$ if $\epsilon_M/\sigma \ll 1$. Moreover, it is found that the final bar amplitude A_F increases as the initial value A_0 increases, such that the final amplitude reached by perturbations may tend to A_{TF} after a sequence of flood events.

Laboratory experiments

Tubino (1991) performed also two series of laboratory experiments to substantiate the above

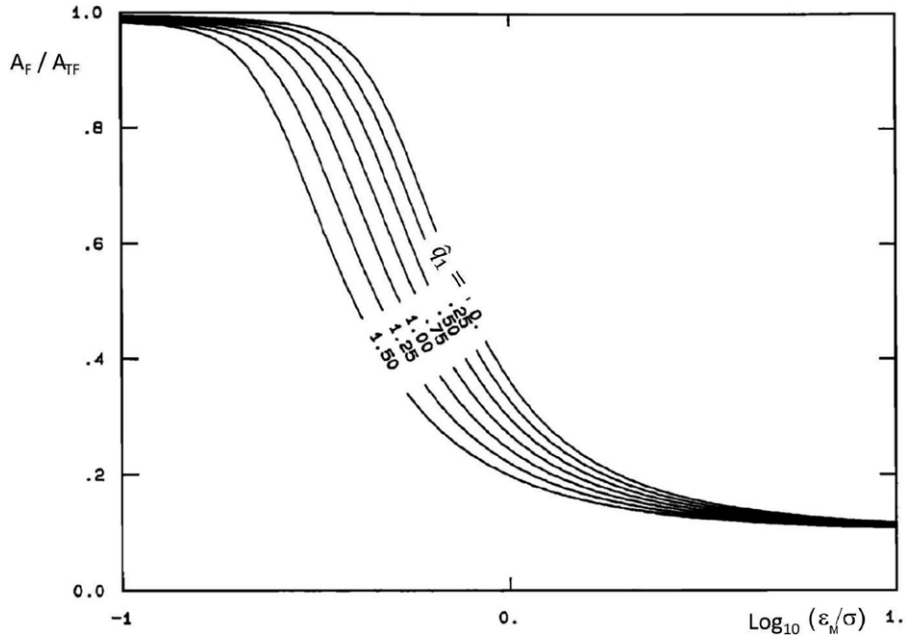


Figure 125. The bar amplitude reached at the end of the flood event A_F , scaled by the equilibrium amplitude associated with the final state A_{TF} , as predicted by the nonlinear solution of TS for the hydrograph (554), is plotted versus the unsteadiness parameter ϵ_M/σ for different values of \hat{q}_1 ($A_0 = 0.1$, $Re(\alpha_0)/(b\beta_c\mu_\beta) = -0.8$) (modified from TS).

picture. Each series was characterized by the same initial slope and the same (triangular) shape of the hydrograph, simulated using a step-like sequence of discharges. The duration T_F of various runs was different but the relative duration of single steps was identical in each run. Results of these experiments (Figure 126) show that:

- in each series the final bar height H_F exhibited a strong dependence on the duration of the flood T_F ;
- the dependence on the unsteadiness parameter ϵ_M/σ shown by the ratio between the bar height reached at the end of the flood event H_F and the equilibrium bar height associated with the final state H_{TF} follows the trend predicted theoretically. In particular, in the experiments the interaction between bar development and flow unsteadiness occurs mainly for values of ϵ_M/σ close to unity, as predicted theoretically;
- the quasi-linear initial growth, the bar damping at the flood peak and the formative role of the falling limb of the flood are all confirmed by the experiments;
- the Figure 126b suggests clearly that the bar height reached at the end of a sequence of flood events tends to an upper bound consisting of the final value H_{TF} of bar height corresponding to the instantaneous response.

Field observations

Besides the already mentioned field investigations performed by Lewin (1976), a further interesting field work was performed by Welford (1994) to test the theory by Tubino (1991). The study site was a channelized section of the Embarras River (Champaign, Illinois), with length 60 m, width 12 m, depth 1.5 m, bed material sorted to well-sorted, mean grain size of 0.53 mm. The hydrographic regime of the river consists of low quasi-steady flows interspersed by brief summer flood events,

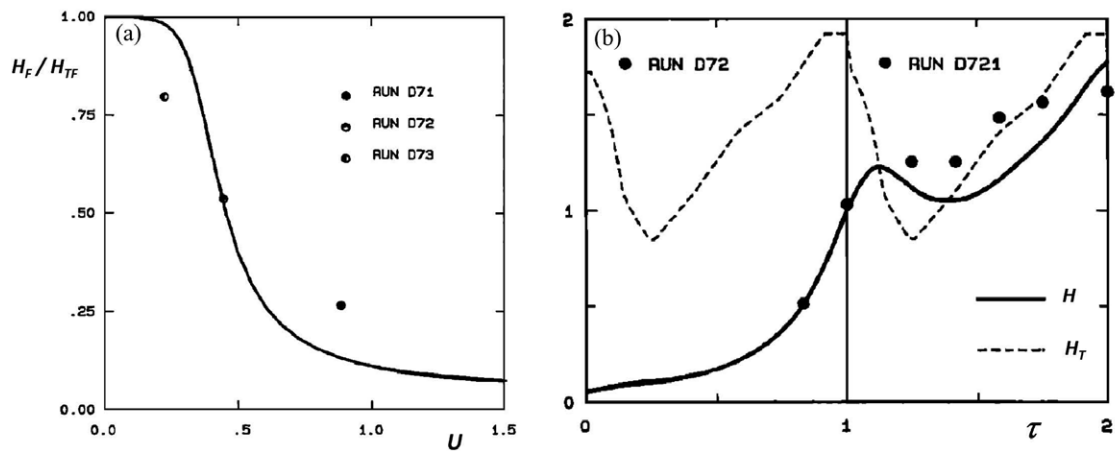


Figure 126. (a) The bar height H_F reached at the end of the flood event in the experiments of Tubino (1991) (black circles) is plotted versus the unsteadiness parameter ϵ_M/σ . The bar height H_F is scaled by the equilibrium bar height associated with the final state H_{TF} . The solid line represents theoretical results. (b) Temporal variation of the dimensionless bar height H (scaled by the reference flow depth D_0). The solid line corresponds to the weakly nonlinear theory of TS, the dashed line represents the theoretical equilibrium value H_T associated with the instantaneous conditions. Data (black circles) refer to the two runs D72 and D721 characterized by identical hydrographs but different initial conditions. The former run started from a plane-bed initial configuration, whereas in the run D721 the bed configuration obtained at the end of experiment D72 was used as initial configuration (modified from Tubino, 1991).

during which alternate bars develop rapidly. This turned out as a most appropriate site for the tests pursued by the Author. The general trend in bar height observed during flood evolution exhibited the main feature of the theoretical solution. In particular, bar damping occurred close to the peak of the hydrograph and was followed by bar growth in the decay stage of the flood. However, not surprisingly, in many cases the weakly nonlinear assumption was violated and a strong dependence of the final bar height on the value assumed for the initial amplitude emerged. Finally, Welford (1994) noted that pre-existing bars, with different sediment size distributions, may be present along the reach under investigation, and affect the bed response to new floods. This feature could not be accounted for by TS' theory which assumed uniform grain size and Welford (1994) concludes suggesting the need to extend the theoretical approach, such to account for the effects of strong nonlinearities and grain sorting.

More recently, a somewhat similar field investigation was pursued by Eekhout (2014) (but see also Eekhout *et al.*, 2013) on the Hooge Raam, a tributary of the river Meuse, a lowland Dutch sandy stream (median grain size of $218 \mu m$). A $600 m$ reach of this small river was straightened in 2009 in the context of a stream restoration project that included the construction of a sinuous channel pattern, just downstream of the straight reach. Figure 127 shows an important feature of this investigation. After 320 – 350 *days* from the start of the experiment dense vegetation appeared in the upstream reach, possibly due to nutrient supply from the neighboring agricultural lands. As a result, an irregular bed morphology, without a clear pattern of alternate bars, was observed upstream and a regular alternate bar pattern developed in the downstream reach. Digital Elevation Models (DEMs) of bed topography were constructed, based on 13 GPS-surveys characterized by an accuracy of 1 – 2 *cm*, conveniently filtered by subtracting the average bed elevation associated with the average longitudinal channel slope and further using a LOESS regression algorithm (Figure 128). The pattern emerged from this procedure was initially fairly regular, with individual bars clearly distinguishable. In total, six bars were identified, three on each side of the channel, having excluded the most downstream bar, that the Authors assume was possibly affected by the downstream boundary. Later, starting from the fifth survey, a sort of sinuous thalweg appeared and the bed pattern became more complex. The bar development was investigated analyzing the variations of bar wavelength, bar amplitude, and longitudinal bar position.

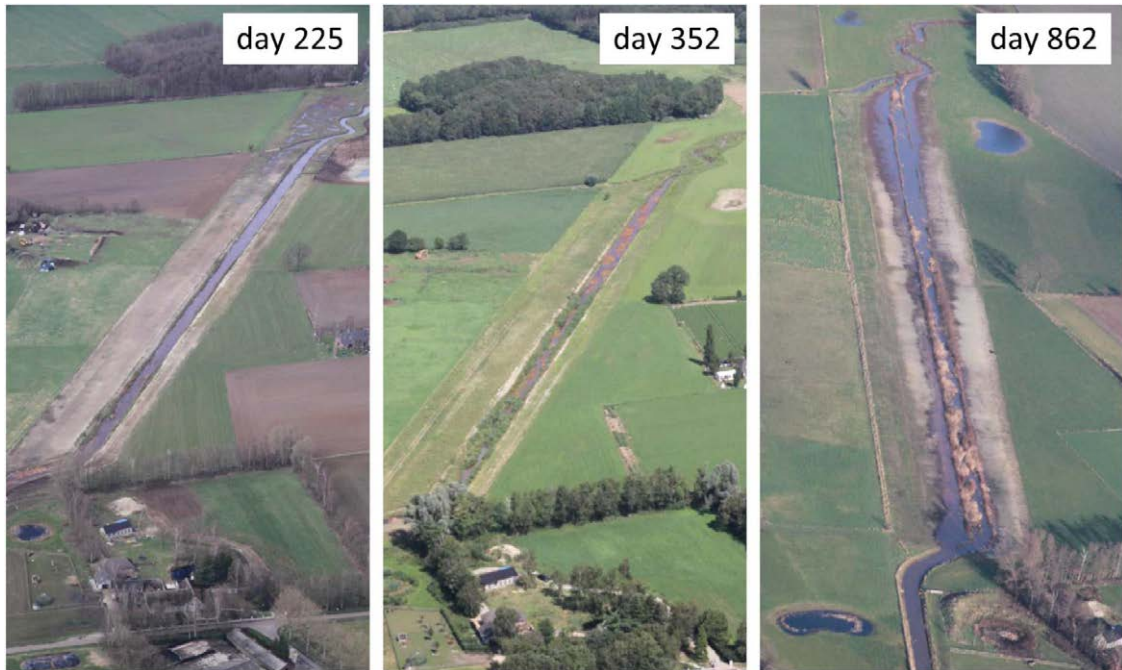


Figure 127. Three aerial photos of the river patterns taken on the Hooge Raam, at different times from the start of the field experiment (flow from bottom to top). Note, in the middle photo the irregular vegetated pattern in the upstream reach, as opposed to the regular alternate bar pattern in the downstream reach (reproduced from Figure 3.3 of Eekhout, 2014, courtesy of Joris Eekhout).

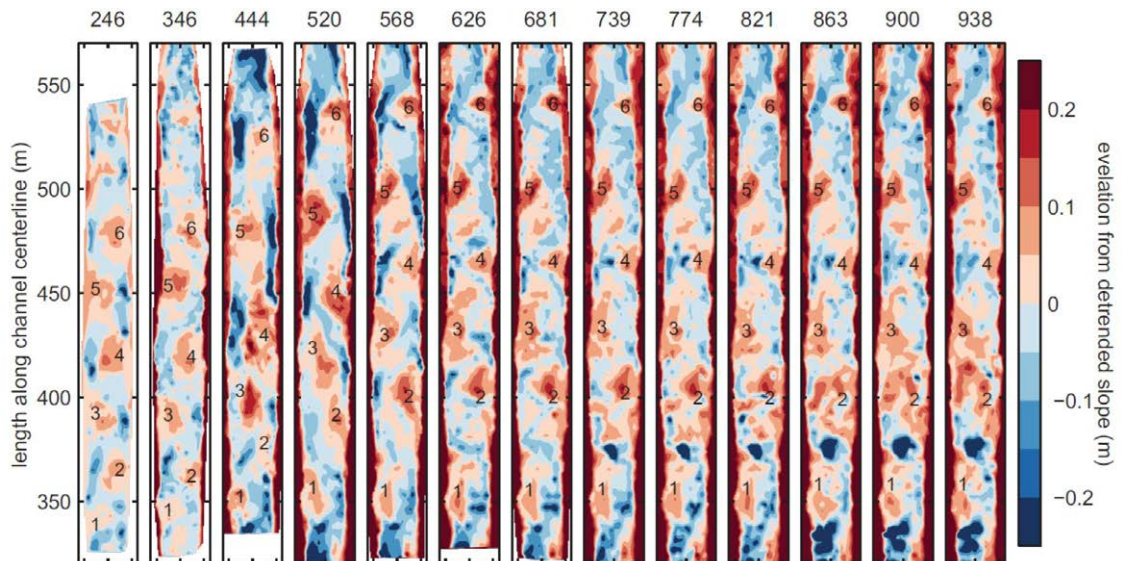


Figure 128. Bed topography from the 13 GPS-surveys of the Hooge Raam reach investigated by Eekhout (2014). The bars are numbered to locate them easily. Flow from bottom to top (reproduced from Figure 3.6 of Eekhout, 2014, courtesy of Joris Eekhout).

Figure 129 shows that the bars lengthen until the fifth survey and then reach an approximate equilibrium. The bar amplitude exhibits a similar trend, although much less regular. Note

that when (around half of the experiment) the regular pattern of alternate bars evolved into an irregular one, the bar amplitudes declined. Bar migration was observed to occur around the half of the experiment and then declined just like the bar lengthening. The Authors interpreted

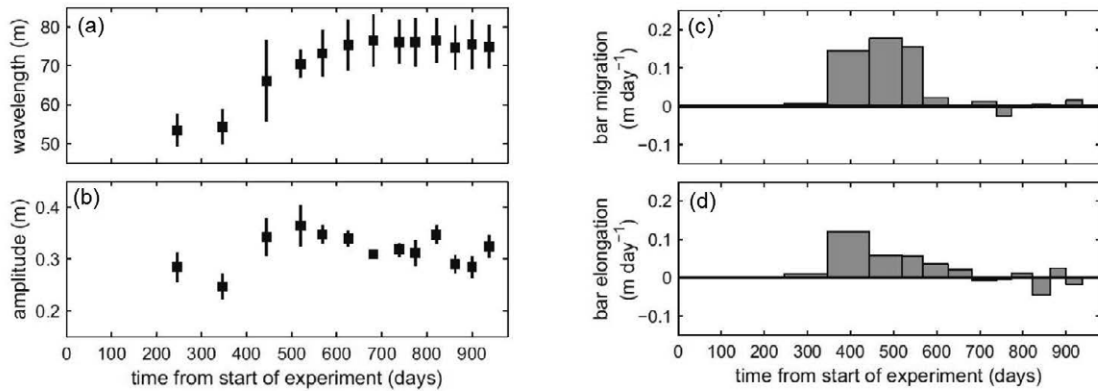


Figure 129. Temporal variations of (a) the bar wavelength, (b) the bar amplitude, (c) the bar migration rates and (d) the bar elongation, averaged over five bars (modified from Figure 3.7 of Eekhout, 2014, courtesy of Joris Eekhout).

these observations noting that, during the experiment, the bed slope decreased and reached half its initial value after 938 *days*. In response to the declined bed slope, the average flow velocity, the average Shields parameter and the average Froude number also declined, such that the flow conditions became increasingly unfavorable for alternate bar formation. Moreover, the declining observed values of the bar migration rates led the Authors to classify bars as nonmigrating.

Once again, the physical and theoretical basis justifying these conclusions remains unexplored. In particular, one would like to answer some reasonable questions. In particular: were the initial bars able to migrate through the meandering reach? Indeed, as pointed out at the beginning of this chapter, it has been known since the work of Kinoshita and Miwa (1974) that sufficient sinuosity makes free bars unable to migrate through a meandering channel. If this were the case in the experiments of Eekhout (2014), then the explanation of the observed behavior might point at the presence of a meandering reach downstream of the straight reach that would force bars to stop migrating. Further work will be needed to clarify these aspects.

6.7.2 Recent field observations of alternate bar migration

As mentioned in Section 6.1, field observations have recently become easier with the help of a variety of modern techniques. Many of the recent field studies focus on wandering (e.g. Church and Rice, 2009) or braiding rivers (e.g. Henshaw *et al.*, 2013). Few studies focus on the dynamics of alternate bars, in an attempt to verify the applicability of the outcomes of theoretical analysis and laboratory observations to the actual phenomenon observed in the field. The most comprehensive of these studies is perhaps the work of Adami (2016) (but see also Adami *et al.*, 2016), that focuses on the long-term dynamics of alternate bars in the Alpine Rhine River. This is the most classical example of channelized river where a long and regular sequence of alternate bars has formed and has been monitored for decades since the pioneering work of Jaeggi (1984). The hydrology of this river is dominated by snow-melt in spring-summer and larger floods in autumn, with artificial perturbations due to hydropower production. The sequence of hydrographs recorded in a period of around 30 years, starting from 1984 is reported in Figure 130.

Data for the wavelength, height and migration speed of alternate bars were calculated from images acquired by Landsat 4-5 TM (30 *m* resolution), Landsat 7 ETM+, and Landsat 8 OLI (15 *m* resolution of the panchromatic band) in the 58 dates displayed in Figure 130. Emerged gravel bars were clearly visible only for discharge values lower than a threshold $Q_F = 350 \text{ m}^3 \text{ s}^{-1}$, whilst

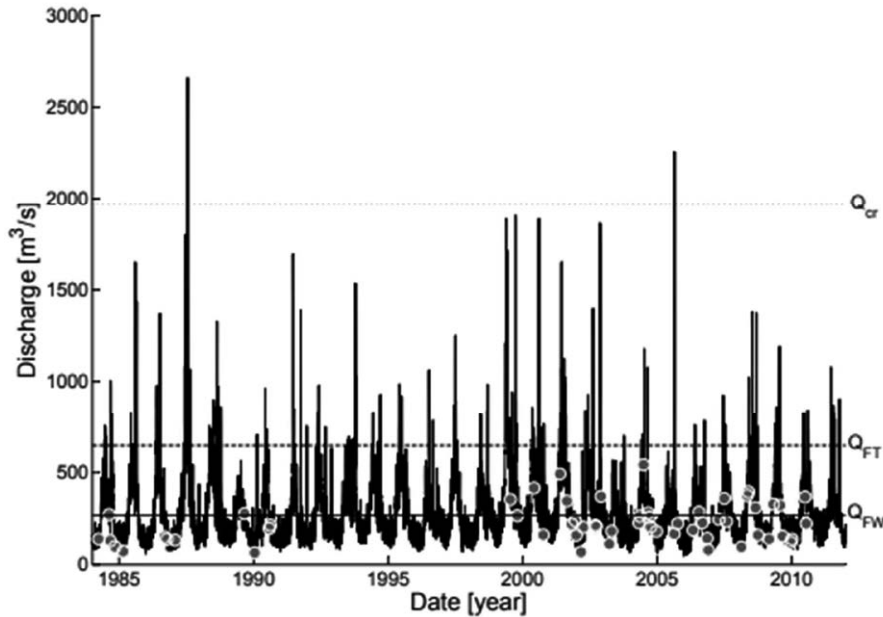


Figure 130. Sequence of hydrographs recorded in the Alpine Rhine River during the period 1984–2012. Grey circles correspond to dates when the analyzed Landsat images were acquired. Fully wet discharge $Q_{FW} \simeq 300 \text{ m}^3 \text{ s}^{-1}$ (solid line); discharge for full cross-sectional transport $Q_{FT} \simeq 650 \text{ m}^3 \text{ s}^{-1}$ (dashed line); critical discharge for alternate bar formation (Colombini *et al.*, 1987) $Q_{cr} \simeq 1900 \text{ m}^3 \text{ s}^{-1}$ (dotted line) (reproduced from Adami, 2016, under License Creative Commons Attribution Non-commercial No Derivatives).

the discharges covered by the complete data set fell in the range $64 - 540 \text{ m}^3 \text{ s}^{-1}$.

The Figure 131a shows the spatial distribution of the *cumulative migration* of single bars over the period 1999–2010. Downstream migration amounting to 9–10 river widths peaks in the downstream region; minima (smaller than one river width) occur in the upstream region near planform obstacles; only 3 bars out of 77 showed a slight upstream migration. At the scale of a single flood event, it turned out that bars migrated at most a few channel widths even during the largest floods. Moreover, bars never disappeared completely to reform later. Two different sets of bars were identified (Figure 131b): *stationary bars*, located in the upstream reach near bends and ramps, and *migrating bars*, located in the downstream reach, sufficiently far from bends and ramps. The Figure 131b also shows that bar migration occurred exclusively during larger floods. In the absence of significant events (e.g. in 2006–2007) hardly any migration occurred, even in the case of free bars. Steady bars (closed symbols) moved slightly upstream and downstream in a narrow range of about two river widths, and were not affected by floods. Analyzing the effect of different floods on bar migration in the whole observation period, Adami (2016) defined a *morphologically relevant threshold for the flow discharge* $Q_2 = 780 \text{ m}^3 \text{ s}^{-1}$, such that full transport occurred in the cross-sections whilst no significant bar migration was detected for less intense floods. As Q increased starting from Q_2 , migration increased, peaked at $Q = 1800 \text{ m}^3 \text{ s}^{-1}$ and then decreased until it vanished for the largest floods when bar formation was prevented.

The ensemble of *bar wavelengths* of each monitored bar unit is plotted in Figure 132, along with their *lengthening/shortening*, i.e. the (positive or negative) variations of bar lengths recorded in the period 1999 – 2010. The bar wavelengths fall in the range $750 - 1700 \text{ m}$, corresponding

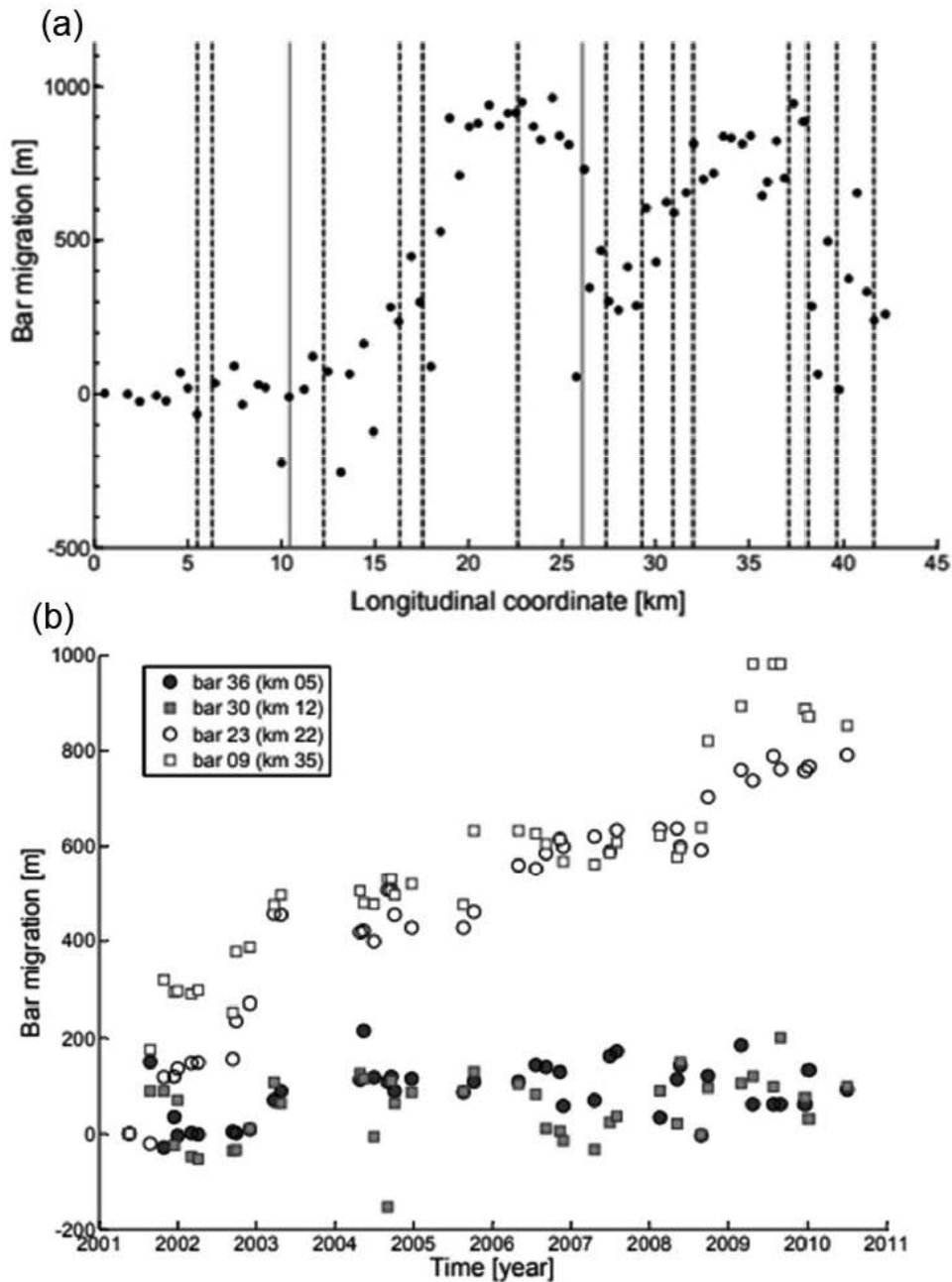


Figure 131. (a) Cumulative bar migration of single bars in the Alpine Rhine River during the period 1999-2010. (b) Temporal variation of the migration of four bars monitored in the period 1999-2010. Open symbols: migrating bars; closed symbols: steady bars. Vertical lines represent the sequence of hydrographs recorded in the same period, with the discharge Q scaled by Q_{FT} (reproduced from Adami, 2016, under License Creative Commons Attribution Non-commercial No Derivatives).

roughly to 7 – 17 average channel widths. The local elongation/shortening of bars is driven by ramps (solid vertical lines in Figure 132), single bends or sequences of bends (dashed vertical lines), that generate discontinuities in the process of bar formation. Comparison with the theory of Colombini *et al.* (1987) showed that almost every flood (with only two exceptions in 30 years)

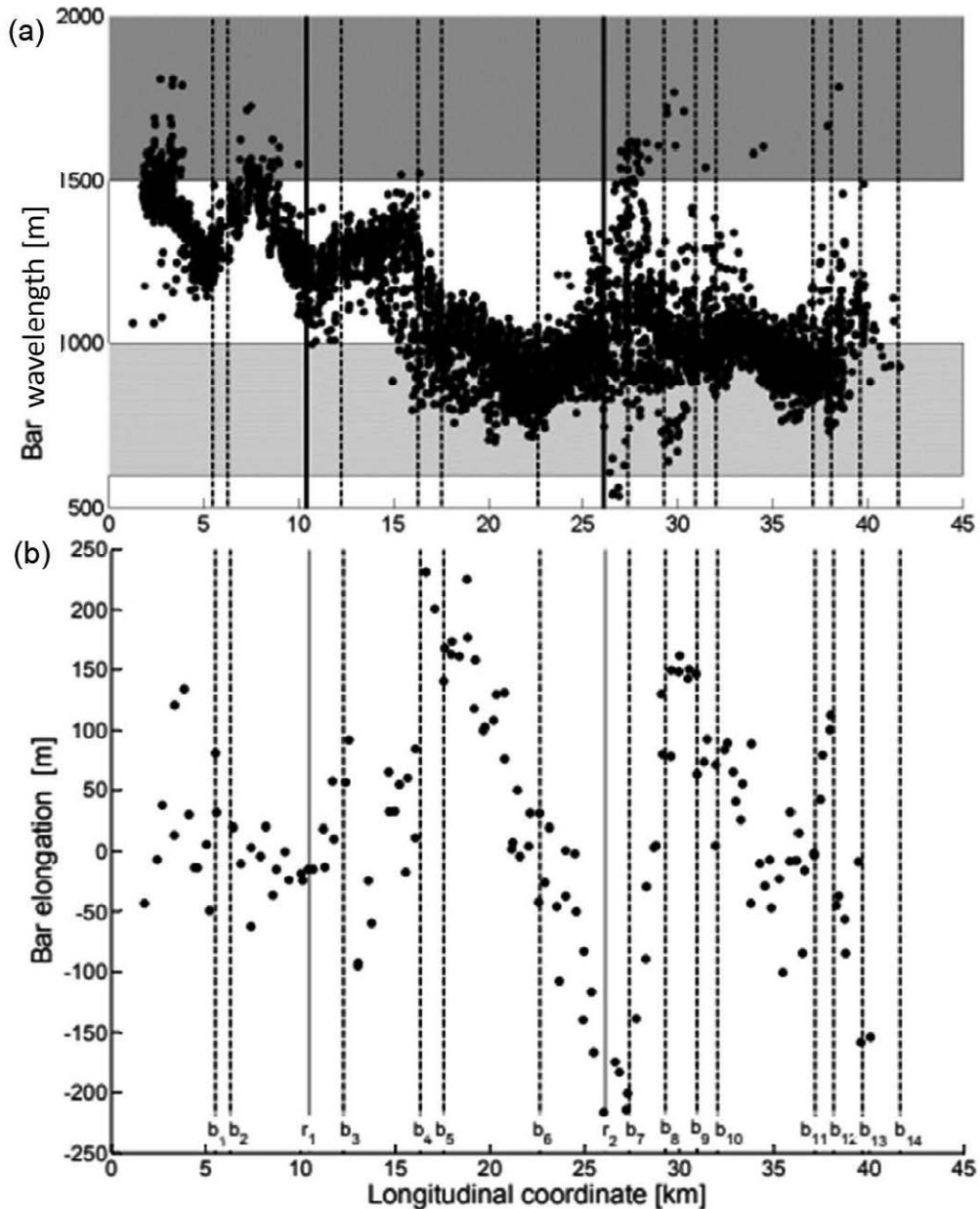


Figure 132. (a) Bar wavelength of each monitored bar unit, based on the complete Landsat imagery data set (1984 – 2013). Light grey area: theoretical wavelength range of free bars; dark grey area: theoretical range of forced bars. (b) Bar elongation in the period 1999 – 2010. Vertical dashed lines represent bends, solid vertical lines represent ramps (reproduced from Adami, 2016, under License Creative Commons Attribution Non-commercial No Derivatives).

had peak value falling within the regime where alternate bars should form and, most of the time when the discharge exceeded the Q_{FT} threshold, the channel was subject to free bar instability.

Also, linear theory predicted values of the most unstable *free* bar wavelengths around 750 m, a nearly constant value in the whole reach. Note that, unlike the bar height, the most unstable bar wavelength is very weakly dependent on the width to depth ratio, hence its critical value may be reasonably taken as representative of bar instability for the whole duration of the flood. The

predicted value of wavelengths of migrating alternate bars is slightly smaller than the measured values (750 – 1000 *m*). One may reasonably wonder why, as we have seen that nonlinear effects do lengthen bars significantly. The likely explanation is possibly related to the small duration of the floods. Indeed, Adami (2016) states that the value of the unsteadiness parameter ϵ_M/σ of Tubino (1991), computed for several floods examined in their study, is approximately as large as 20. This is a very large value that does not allow free bars to develop their nonlinear equilibrium states during a single flood.

On the other hand, Adami (2016) computed the wavelength of *forced* steady bars according to the theory of Zolezzi and Seminara (2001) and found that it falls in the range 2000 – 3200 *m*. This is almost twice as much as the observed wavelengths (1200 – 1500 *m*) of the bars they classified as non-migrating. This is a severe discrepancy that calls for theoretical understanding. Adami (2016) suggests the possibility that the interaction between free and forced bars might be responsible for the shortening of stationary bars.

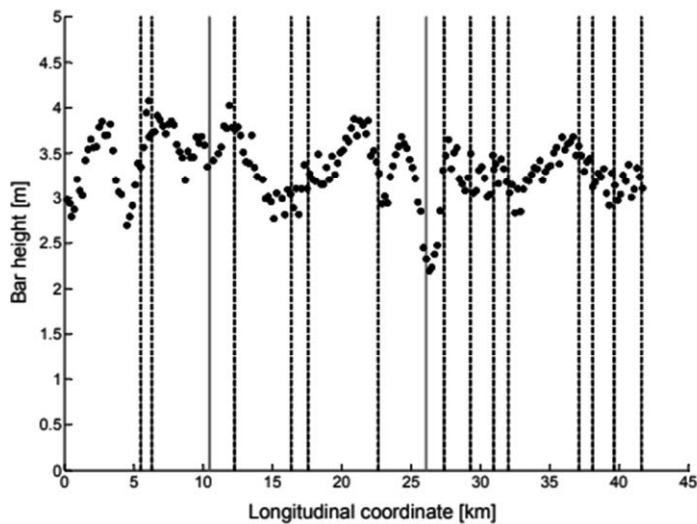


Figure 133. Longitudinal distribution of bar heights along the Alpine Rhine river centerline in the observations of Adami (2016). Vertical dashed lines represent bends; solid vertical lines represent ramps (reproduced from Adami, 2016, under License Creative Commons Attribution Non-commercial No Derivatives).

Finally, *bar height* fell in the range 2.5 – 4 *m*, amounting to about 1-1.5 times the reach averaged water depth (Figure 133), with fluctuations near bends and ramps where bar height was damped. Observed values were compared with the values of the equilibrium amplitude of free migrating bars predicted by Colombini *et al.* (1987) and Ikeda (1982b). This exercise, however, is not an easy one as in both formulations the bar height is a function of the width to depth ratio, which varies strongly during a flood. Hence, applying such theories leads to bar heights decreasing from an upper limit, associated with the flow discharge Q_2 , to zero as Q approaches Q_{cr} . Choosing a flow discharge to perform a comparison theory versus observations is then quite arbitrary as clarified by the theory of Tubino (1991). This notwithstanding, Adami (2016) evaluated the bar height for $Q = Q_2$ and found that the observed bar heights were on average smaller than the predicted values.

6.7.3 The role of sediment heterogeneity: sorting patterns

Sorting is a process whereby, starting from a spatially uniform grain size distribution, the

distinct motion of different grain sizes leads to clearly identifiable, *organized non uniformities* in the horizontal and/or in the vertical directions. The expression of such non-uniformities are typical *patterns*. As pointed out by Seminara (1995), some fluvial bedforms are genuinely *sorting patterns*, in that they exist only if the bed consists of heterogeneous sediments. They are generated by a *rearrangement of the grain size distribution of the surface layer*, hence the active layer approach of Hirano (1971) is an appropriate tool to model the process. Below, we outline two such horizontal patterns, namely bedload sheets and longitudinal streaks.

More challenging sorting phenomena are those which arise in free bedforms characterized by amplitudes much larger than grain size. In this case, besides the horizontal rearrangement of the grain size distribution, bedform migration leads to vertical mixing and consequent *vertical sorting*. The latter process cannot be modeled in the context of the classical active layer framework except for the very initial stage of bedform development, when the amplitude of perturbations is very small. Below, we provide a brief overview of the effects of sorting on the characteristics of free bars.

Sorting patterns originating from a rearrangement of the grain size distribution of the surface layer

Although, in this Monograph we focus on large scale bedforms, it is instructive to provide a brief overview of small scale sorting patterns.

Bedload sheets

Bedload sheets are the smallest dune-type transverse bedforms observed in gravel bed rivers (Whiting *et al.*, 1988) and consist of rhythmic sequences of coarse and fine material (Figure 134). Their amplitudes are very low (of the order of few grain sizes) and they are observed to migrate

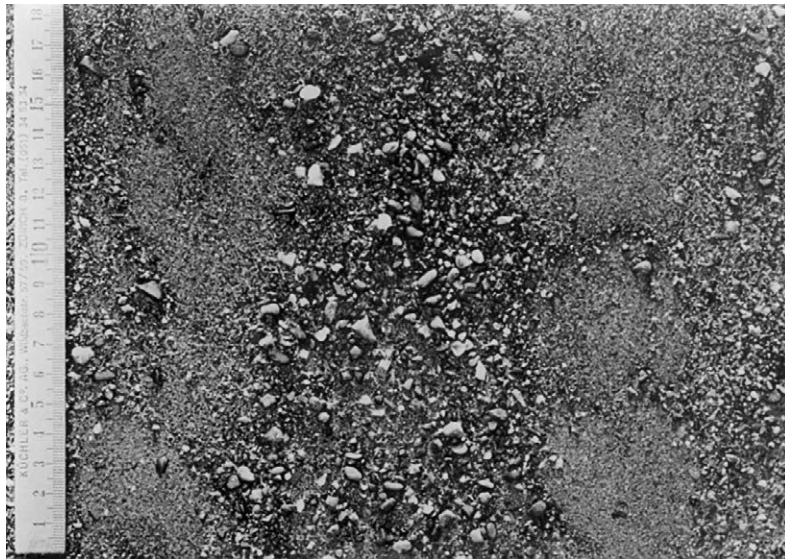


Figure 134. Bedload sheets observed in the laboratory. Courtesy of Peter Whiting.

downstream, i.e. they are sorting waves. Whiting *et al.* (1988) note that “*Bed load sheets form and migrate downstream as a consequence of the catch and mobilize process, in which large grains are caught in the wakes of other large grains, followed by infilling of their interstices by smaller particles, which can in turn smooth out hydraulic wakes causing large particles to be remobilized*”. A theoretical explanation of the mechanism of bedload sheet formation was provided by Seminara *et al.* (1996) who formulated the first stability theory of fluvial bedforms in heterogeneous sediments. They showed that bedload sheets are sorting waves, exhibiting distinct coarse fronts which arise

from a peculiar instability of the grain size distribution. Their growth is strictly due to grain sorting, which drives spatial variations of bottom roughness, which in turn modifies the fluid motion. This leads to perturbations of bedload transport which give rise to small perturbations of bed elevation with amplitude scaling with grain size.

Bedload sheets are dune-like but differ from dunes as sorting is the dominant effect controlling their growth, whilst sorting in dunes is a relatively small perturbation of a pattern which would exist anyway, independently of sorting. Note that a sort of sheets, i.e. secondary dunes of a few grain diameters in height and a few tens of grain diameters in length, have been reported to form in experiments with unimodal bed material (gravel with diameter ranging 6-64 mm with no sand) (Gomez *et al.*, 1989). Later observations of Nelson *et al.* (2009) in sand free experiments suggest that it is the heterogeneous character of the sediment (ratio of coarse to fine grain sizes) rather than the presence or absence of sand that drives the formation of bedload sheets. This finding is in agreement with the theory of Seminara *et al.* (1996).

Bedload sheets belong to a wider class of patterns that geomorphologists call *patches* (Dietrich *et al.*, 2005; Nelson *et al.*, 2009). A clear classification of these sorting features does not seem to exist. Nelson *et al.* (2009) distinguish between free and forced patches (with a further class of *fixed* patches in between). *Free patches* develop spontaneously in the absence of topographic forcing, i.e. they coincide with bedload sheets. *Forced patches* are driven by external forcing (e.g. curvature in meandering rivers or obstacles affecting the flow and sediment transport). Nelson *et al.* (2009) include among the forced patches also the sorting patterns developing when large amplitude bedforms migrate in the channel. Migrating bedforms are actually free patterns as they arise spontaneously. However, in this case, sorting is *forced* by the spatial variations of the bottom stress due to the spatially varying topography, as well as by the vertical mixing induced by bedform migration.

Below, we outline some observations on *free patches*. The first set of experiments (Dietrich *et al.*, 1989; Kirchner *et al.*, 1990) was conducted at the University of Tsukuba in Japan in 1987. The sediment supply to a small flume was progressively reduced, keeping the water discharge, the flume slope and the bulk (sediment feed) grain size distribution constant. The width-to-depth ratio was maintained small enough to suppress the development of any large scale bedform. The main observation consisted of the fact that the bed surface displayed the formation of patches, i.e. regions with some recognizable degree of coarseness, measured by their coarse mean grain size, varying for different patches. Four distinct patch types were observed. They were classified as

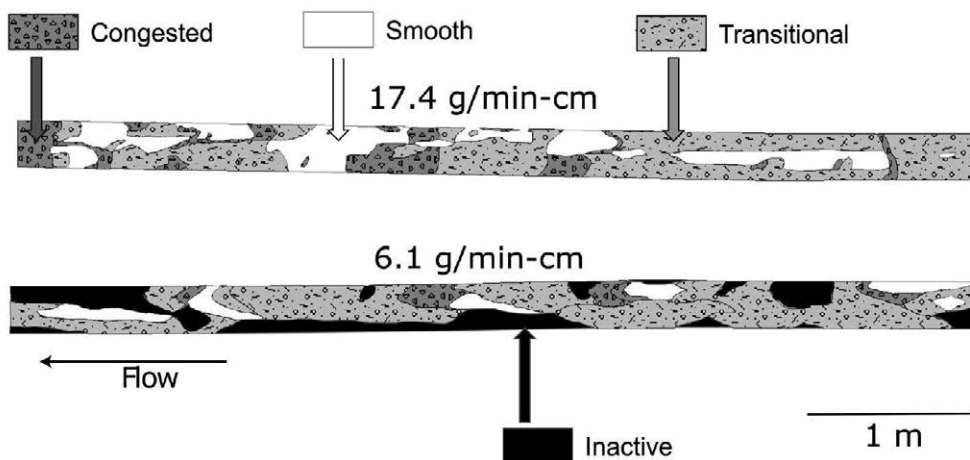


Figure 135. Sorting pattern map in the Tsukuba experiments of Dietrich *et al.* (1989) at the end of the runs characterized by sediment feeds (a) 17.4 g/min cm and (b) 6.1 g/min cm, respectively. Courtesy of Peter Nelson.

smooth, transitional, congested and inactive, corresponding to increasing values of their coarse mean grain size. The last type displayed no active bed load transport. Figure 135 provides a visual picture of patches under different sediment feed conditions. Moreover, as mentioned by Dietrich *et al.* (1989), “*inactive and congested zones expanded as the sediment supply was reduced. Active transport became confined to a corridor down the center of the channel, the width of which narrowed as sediment supply was reduced. At the lowest sediment transport rate the bed ultimately exhibited a virtually uniform pavement*”. Similar results were obtained in a second set of experiments (Nelson *et al.*, 2009), conducted at the University of California in 2005.

To our knowledge no theoretical interpretation of these experiments in the line of the work of Seminara *et al.* (1996) has been provided so far.

Longitudinal streaks

These patterns consist of rows of streaks aligned with the flow in a straight channel. They are not genuine sorting patterns as they form also if the sediment is homogeneous. In this case they are usually called *sand ridges* and their expression consists of lateral periodic oscillations of bed elevation. The process from which they originate is an instability mechanism which drives the

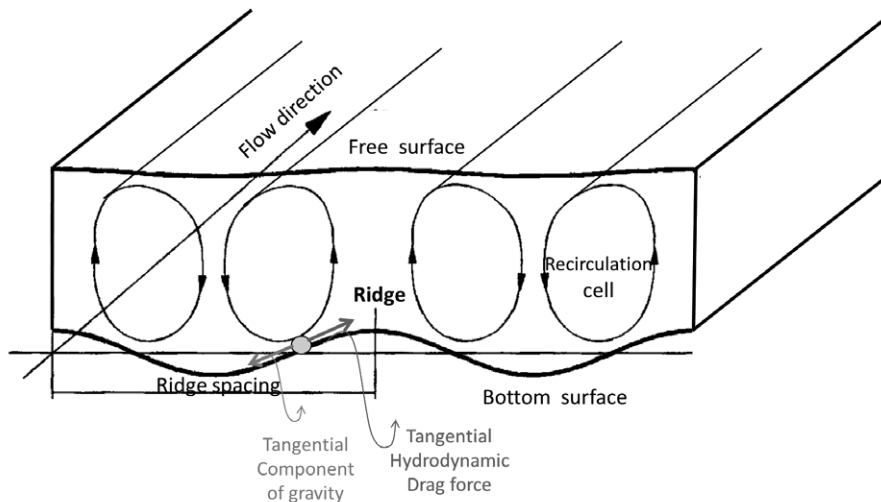


Figure 136. Sketch of sand ridges with lateral recirculation cells.

development of lateral recirculation cells. Note that instability is strictly linked to the anisotropy of turbulence, hence a second order closure model is required to provide a theoretical interpretation. The theory of Colombini (1993) successfully predicts the formation of longitudinal streaks. The secondary flow associated with recirculation cells tends to displace grains from the bottom troughs towards the bottom crests. Equilibrium is achieved when the tangential force associated with the secondary flow at the bed is balanced by the tangential lateral component of the grain weight (Figure 136). The amplitude of sand ridges is rarely larger than one or two grain diameters, and the transverse spacing is invariably of the order of the flow depth. Linear stability results suggest that sand ridge formation apparently requires rather high values of the Shields stress, i.e. rather strong sediment transport. However, sand ridges are commonly observed at Shields stresses as low as only slightly above the threshold of motion.

If sediments are heterogeneous a second independent (sorting) mechanism contributes to the destabilization of the bed. Finer (coarser) material accumulates on the crests (troughs) of the ridges and the resulting bedforms are then called *longitudinal streaks*. The theory of Colombini and Parker (1995) shows that allowing for even slight heterogeneity of bed sediment results in the formation of streaks at any Shields stress above the threshold of motion (Figure 137).

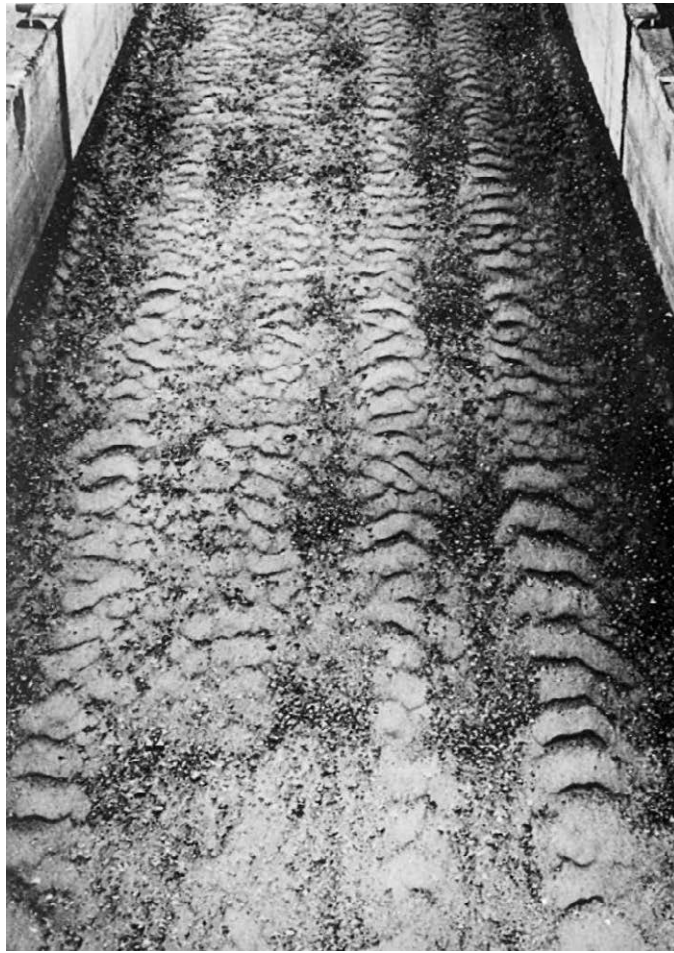


Figure 137. Longitudinal streaks with ripples superimposed on the fine streaks. Flow is from bottom to top (courtesy of Gary Parker).

Very recently, Scherer *et al.* (2022) have reconsidered the problem for the case of homogeneous sediments with the help of Karlsruhe's computational model that we have discussed in Section 3.3.3. Their results also reproduce the formation of secondary cells.

Sorting patterns originating from rearrangement of the grain size distribution in both horizontal and vertical directions: free bars

We briefly describe some observations of sorting patterns in large scale fluvial bedforms and outline first attempts at providing mechanistic interpretations of their formation.

The heterogeneous character of natural sediments generates mechanisms of *grain sorting* that may affect bar development. Early laboratory investigations, performed by Lisle *et al.* (1991), showed a sequence of events. Coarse particles accumulated at bar heads; flow and bedload transport were diverted across the flume towards a pool; sorting in the pool directed coarse particles onto the next bar head downstream. As a result of coarsening of bar heads, erosion at the heads was prevented and, consequently, downstream migration of bars was inhibited. The later extensive investigation of Lanzoni (2000b) confirmed that selective transport of individual size fractions leads to intense longitudinal sorting and coarsening of the bar crests. As a consequence, bar height turned out to be invariably damped with respect to the case of uniform sediment, while the trend exhibited by the bar wavelength was less clear (Figure 138). Note that the damping

effect associated with sediment heterogeneity was found to increase as the unperturbed Shields parameter τ_{*g0} decreased, leading to a maximum 50% reduction of bar height when τ_{*g0} fell in the range 0.05 – 0.06. As τ_{*g0} approached the value 0.1, damping disappeared.

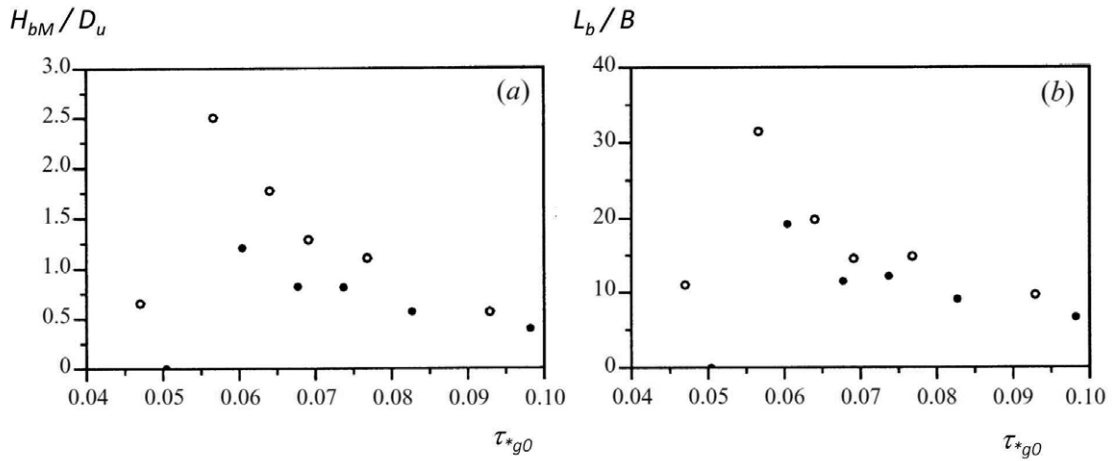


Figure 138. Experimental results of Lanzoni *et al.* (1994) for (a) maximum bar height H_{BM} (scaled by the unperturbed uniform flow depth D_u) and (b) bar wavelength L_b (scaled by channel half-width B). These results were obtained in experiments where uniform glass spheres with size 1.5 mm (open circles) and bimodal mixtures of glass spheres with sizes of 1 mm and 2 mm (full circles) were used. Data are plotted versus the unperturbed average Shields parameter (reproduced from Lanzoni and Tubino, 1999).

A few contributions (Seminara, 1995; Lanzoni and Tubino, 1999) have also attempted to analyze theoretically the effect of sorting on bar formation through appropriate modifications of the classical stability theories. The approach employed in these papers follows closely the lead of Seminara *et al.* (1996). It may be of interest for the reader to appreciate the novel features of the stability analysis brought up by the heterogeneous character of the sediments. We then outline briefly the work of Lanzoni and Tubino (1999).

The formulation of the problem differs from the classical free bar stability analysis for the distinct approach required to model sediment transport. Hence, we still consider the flow in a straight wide alluvial channel with non-erodible banks and model the flow as 2D. The motion of the sediment mixture is however modeled as discussed in Section 4.7. In particular, Lanzoni and Tubino (1999) use the active layer approach of Hirano, which had successfully been employed by Seminara *et al.* (1996) to explain the formation of gravel sheets. As already pointed out this model rules out the possibility to account for vertical sorting, implying that the validity of the analysis will be restricted to the incipient formation of free bars, when vertical mixing does not play a significant role yet.

We employ notations and methods discussed in Section 6.3 to investigate the linear response of a uniform turbulent open channel stream flowing over a cohesionless heterogeneous bottom to infinitesimal perturbations of bed topography and grain size distribution. In the present case, besides (U, V, D, H) , unknown functions of (x, y, t) , an additional unknown is the probability density function of grain size $f(\phi; x, y, t)$, with ϕ geologic scale for the grain size. Note that Lanzoni and Tubino (1999) follow the original Hirano approach and assume that $f_i = f_a = f$, i.e. they denote by $f(\phi; x, y, t)$ the probability density function of grain size in the active layer which they assume to coincide with its value at the interface between the active layer and the substrate.

Using the dimensionless formulation introduced in Section 6.3, our basic state reads:

$$U = 1, \quad V = 0, \quad D = 1, \quad H = H_0(x) = H_{00} - \beta S x, \quad f = f_0(\phi). \quad (555)$$

Here, $f_0(\phi)$ is the unperturbed probability density function of grain size.

Next, we perturb the basic state by infinitesimal perturbations, expanding U , V , D , H and f as follows:

$$(U, V, D, H, f) = (1, 0, 1, H_0, f_0) + \epsilon (U_1, V_1, D_1, H_1, f_1) + \mathcal{O}(\epsilon^2), \quad (556)$$

with ϵ a small (strictly infinitesimal) parameter measuring the amplitude of perturbations. A similar expansion is used to express the longitudinal and transverse components of bedload and bottom stress, like in the uniform sediment case.

Having perturbed the probability density function of grain size, it follows that the average grain size ϕ_g , the standard deviation σ of the distribution and the thickness of the active layer L_a (which is typically taken to be proportional to the size of the coarse fraction) are also perturbed as follows:

$$(\phi_g, \sigma, L_a) = (\phi_{g0}, \sigma_0, L_{a0}) + \epsilon (\phi_{g1}, \sigma_1, L_{a1}) + \mathcal{O}(\epsilon^2), \quad (557)$$

where:

$$\phi_g = \int_{-\infty}^{\infty} f \phi d\phi, \quad \sigma = \int_{-\infty}^{\infty} f (\phi - \phi_g)^2 d\phi. \quad (558)$$

On substituting from (556) and (557) into the flow and sediment transport equations and performing linearization, one obtains a linear partial differential system, amenable to a normal mode solution of the form:

$$(U_1, D_1, H_1, V_1, f_1) = \left[\left(\hat{U}_1(t), \hat{D}_1(t), \hat{H}_1(t), \hat{f}_1(\phi, t) \right) \mathcal{S}_1(y); \hat{V}_1(t) \mathcal{C}_1(y) \right] e^{i\lambda x} + c.c., \quad (559)$$

where \mathcal{S}_1 and \mathcal{C}_1 are defined as in (501) and, for the sake of simplicity, the analysis is restricted to the first lateral mode.

Employing (559), the linearized form of the flow equations leads to a linear algebraic relation involving the quantities $\hat{U}_1(t)$, $\hat{D}_1(t)$, $\hat{H}_1(t)$, $\hat{V}_1(t)$, $\hat{f}_1(\phi, t)$. It reads:

$$\sum_{j=1}^3 \left[a_{1j} \hat{U}_1(t) + a_{2j} \hat{V}_1(t) + a_{3j} \hat{H}_1(t) + a_{4j} \hat{D}_1(t) + a_{5j} (\hat{\phi}_{g1} - \hat{\sigma}_1) \right] = 0, \quad (560)$$

where a_{kj} ($k = 1, 2, 3, 4$, $j = 1, 2, 3$) are identical with the coefficients (506) for the case of homogeneous sediments and

$$a_{51} = 0, \quad a_{52} = -\beta C_{f0} d_\sigma c_{fD} \ln 2, \quad a_{53} = 0, \quad (561)$$

with $d_\sigma = d_g 2^\sigma$.

The reader should note that, in the context of the present theory, the heterogeneous character of sediments affects the flow field only through its effect on bottom roughness. On the contrary, the grain size specific form of the sediment continuity equation is drastically different from its homogeneous counterpart. Making use of (560) and expressing $\hat{U}_1(t)$, $\hat{V}_1(t)$, $\hat{D}_1(t)$, $\hat{H}_1(t)$ in the form

$$[\hat{U}_1, \hat{V}_1, \hat{D}_1, \hat{H}_1] = (b_{10}, b_{20}, b_{30}, b_{40}) \hat{\eta}_1 + (b_{11}, b_{21}, b_{31}, b_{41}) (\hat{\phi}_{g1} - \hat{\sigma}_1), \quad (562)$$

with b_{kj} ($k = 1, 2, 3, 4$, $j = 1, 2$) known coefficients, as reported by Lanzoni and Tubino (1999), the linearized form of the Exner sediment balance equation takes the form

$$f_0 \hat{\eta}_{1,t} + L_{a0} \hat{f}_{1,t} = \Gamma_f \hat{f}_1 + f_0 \left(\Gamma_\phi \hat{\phi}_{g1} + \Gamma_\sigma \hat{\sigma}_1 + \Gamma_\eta \hat{\eta}_1 \right), \quad (563)$$

where Γ_f , Γ_ϕ , Γ_σ and Γ_η are functions of the parameters of the problem and, except for Γ_f , they also depend on grain size ϕ (see Lanzoni and Tubino (1999), relations 3.20a-d). The ϕ -dependence of (563) can be removed imposing the integral condition (389) which, at $\mathcal{O}(\epsilon)$, reads:

$$\int_{-\infty}^{\infty} \hat{f}_1(\phi) d\phi = 0. \quad (564)$$

Requiring that (563) must satisfy (564), one ends up with the following integro-differential equation:

$$\hat{\eta}_{1,t} = \hat{\phi}_{g1} \int_{-\infty}^{\infty} f_0 \Gamma_{\phi} d\phi + \hat{\sigma}_1 \int_{-\infty}^{\infty} f_0 \Gamma_{\sigma} d\phi + \hat{\eta}_1 \int_{-\infty}^{\infty} f_0 \Gamma_{\eta} d\phi + \int_{-\infty}^{\infty} \Gamma_f \hat{f}_1 d\phi. \quad (565)$$

Note that the integro-differential nature of (565) is the price one has to pay to get rid of the ϕ -dependence in the sediment continuity equation.

We can finally substitute from (565) into (563) to find:

$$\begin{aligned} L_{a0} \hat{f}_{1,t} = & \left[\Gamma_f \hat{f}_1 - f_0 \int_{-\infty}^{\infty} \hat{f}_1 \Gamma_f d\phi \right] + f_0 \left[\Gamma_{\phi} - \int_{-\infty}^{\infty} f_0 \Gamma_{\phi} d\phi \right] \hat{\phi}_{g1} \\ & + f_0 \left[\Gamma_{\sigma} - \int_{-\infty}^{\infty} f_0 \Gamma_{\sigma} d\phi \right] \hat{\sigma}_1 + f_0 \left[\Gamma_{\eta} - \int_{-\infty}^{\infty} f_0 \Gamma_{\eta} d\phi \right] \hat{\eta}_1. \end{aligned} \quad (566)$$

This is also an integro-differential equation that, along with (565), represents the main novel feature of the stability analysis for heterogeneous sediments. These equations show that, on one hand, the heterogeneous character of sediments affects the evolution equation for bed topography (565), on the other hand flow and bed topography do affect the spatial distribution of grain size (equation 566).

The above two integro-differential equations essentially govern the growth of perturbations of bed elevation and grain size distribution and were solved by Lanzoni and Tubino (1999) following the analytical approach proposed by Seminara *et al.* (1996). The sediment mixture is represented by N discrete sizes, such that the probability density function f is expressed as a sum of N delta Dirac functions $\delta(\phi - \phi_i)$, each centred at ϕ_i . Hence, one writes:

$$\left[f_0(\phi, t), \hat{f}_1(\phi, t) \right] = \sum_{i=1}^N \left[f_0(t), \hat{f}_{1i}(t) \right] \delta(\phi - \phi_i). \quad (567)$$

With the help of (567), the equations (565),(566) can be transformed into N ordinary differential equations describing the temporal evolution of $(N-1)$ perturbations $f_{1i}(t)$ of the grain size distribution function and of the perturbation of bed elevation $\hat{\eta}_1(t)$. Details of the analysis are found in Lanzoni and Tubino (1999).

Eventually, one obtains a homogeneous differential system with constant (i.e. time independent) coefficients. This system is then readily transformed into an algebraic eigenvalue problems setting:

$$\left[\hat{\eta}_1(t), \hat{f}_{1i}(t) \right] = \sum_{k=1}^N \left[\hat{\eta}_{1k}, \hat{f}_{1ik} \right] \exp(-i\omega_k t). \quad (568)$$

Here, $\omega_k (k = 1, 2, \dots, N)$ is the complex frequency of the k -th mode, with $Im(\omega_k)$ growth rate and $Re(\omega_k)$ angular frequency.

Results for the case of a bimodal mixture suggested the following effects of sediment heterogeneity.

The critical value of the width parameter β for bar instability is only slightly affected, but a significant reduction of the growth rate of bar perturbations generally occurs. Damping is found to increase for small values of the unperturbed Shields stress τ_{*g0} and relative grain roughness d_{g0} (Figure 139). As d_{g0} increases, sorting may even play a slightly destabilizing role (Figure 139(b)). Figure 140 reports the theoretical predictions for the maximum growth rate and angular frequency corresponding to the experimental data of Lanzoni *et al.* (1994) (see Figure 138). Comparison between open and full circles allows one to estimate the effect of heterogeneity in those experiments. Theory is qualitatively in agreement with observations as the predicted damping effect (Figure 140a) is stronger at low values of τ_{*g0} and vanishes as τ_{*g0} reaches a value around 0.1. The latter finding is not surprising as, at large values of Shields stress, equal mobility is progressively

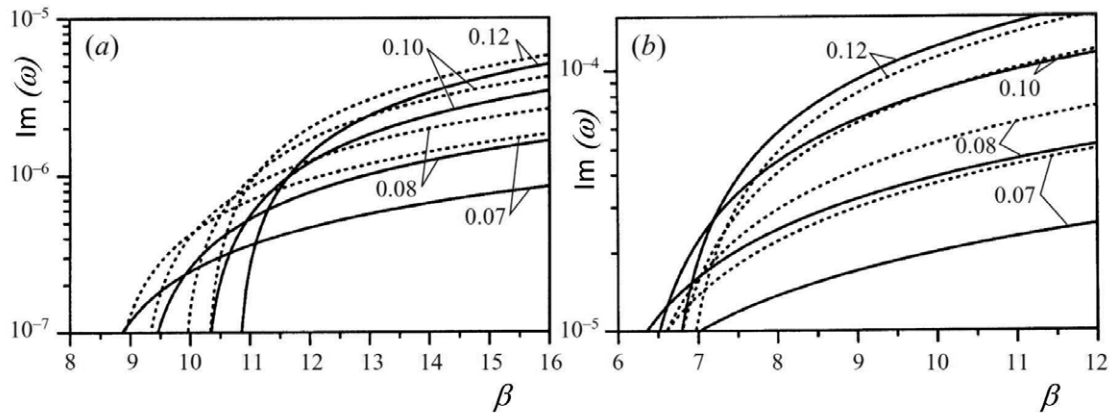


Figure 139. Theoretical predictions for the maximum bar growth rate are plotted versus the aspect ratio β for some values of the unperturbed Shields stress τ_{*g0} and relative grain roughness d_{g0} (solid lines). They are also compared with the corresponding theoretical curves for the uniform sediment case (dotted lines): (a) $d_{g0} = 0.001$; (b) $d_{g0} = 0.01$ (reproduced from Lanzoni and Tubino, 1999).

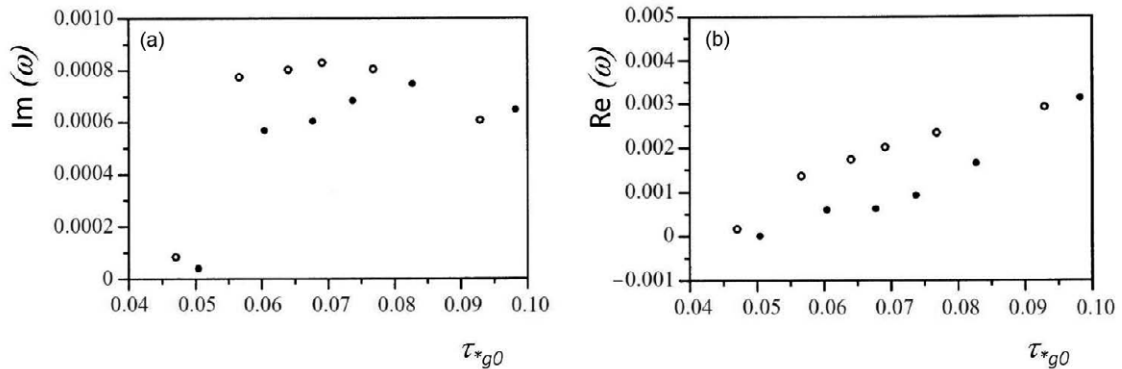


Figure 140. Theoretical predictions for (a) the maximum bar growth rate and (b) angular frequency corresponding to the experimental data of Lanzoni *et al.* (1994) (see Figure 138). Open (full) circles refer to uniform (bimodal) sediments. Calculations have been carried out setting $b = 0.2$ in relation (383) (reproduced from Lanzoni and Tubino, 1999).

attained, such that the transport function $G(\zeta)$ (equation 382) becomes independent of grain size. Theoretical predictions (Figure 140b) also reproduce the tendency of sediment heterogeneity to slow down bar migration as found by Lisle *et al.* (1991) in flume experiments with strongly graded sediments.

Theory also agreed with the observation that bar wavelengths are shortened with respect to the case of uniform sediments. The tendency of coarser particles to pile up at the bar crests was also confirmed. The above results appear to be fairly encouraging. However, they leave the effect of *vertical sorting* completely unexplored. This mechanism is strictly associated with bar migration, whereby transported sediments settle at the troughs, are buried by front migration and reemerge as the bar has migrated one wavelength. Some progress in this area of research has been recently made (e.g. Blom *et al.*, 2008; Stecca *et al.*, 2014, 2016; Cordier *et al.*, 2019), suggesting that an assessment of the whole subject will likely be needed in the near future.

6.7.4 The role of insufficient sediment supply

Sediment supply is one of the controlling factors of bar topography in alluvial channels. However,

the mechanisms whereby such control is expressed have not been investigated in depth.

Lisle (1982) performed some field observations on various creeks following a large flood occurred in 1964 in northern California. Channels had undergone significant widening and strong aggradation with fining of bed material. Moreover, as a result of the excessive sediment load, pools had diminished and bar relief had decreased. Lisle (1982) observed that, as a consequence of these changes, the morphodynamic effectiveness of moderate discharges in the following years increased. Later, Lisle *et al.* (1993) analyzed in a laboratory flume the response of a cohesionless channel with coarse sediment and quasi-stationary bars formed under equilibrium conditions, to reductions in sediment supply. The feed rate was first reduced to one third and then to one tenth of the initial value whilst the discharge was held constant. The main observation of the Authors was the coarsening of bed surface, along with a sharp channel incision (twice the mean water depth on average) followed by emergence of distal bars as terrace like features.

A somewhat similar experiment modeling a gravel bedded river was later performed by Venditti *et al.* (2012) to investigate the role of sediment supply in bar formation and stability. Two large flumes were employed in two linked experiments with distinct unimodal sediment mixtures.

In the smaller scale (Berkeley) experiment, alternate bars formed in the initial stage when the flow was steady and the sediment supply constant. Figure 141 shows the bed topography surveyed at different stages of the experiment. In the first phase (Figure 141b-f), with flow and sediment supply constant, bars migrated downstream, lengthened and slowed down, as expected. Also, the surfaces at the bar fronts were coarser than the pools. As the sediment supply was removed (Figure 141g-q), 22 h from the start of the experiment, the immediate response of the bed was the erosion of the bars, that migrated out of the flume and were not replaced by new bars in the upstream end of the flume, though new bars did form in the lower end. This result differs from the earlier observations in the experiment of Lisle *et al.* (1993) where bars did not disappear but rather emerged. Here, the bed, following the cut in sediment supply, appeared to lose any pattern, including a sharp reduction of surface grain-size heterogeneity, with slightly coarsened surface and slightly reduced slope.

In the larger scale (SAFL) experiment, forced (non migrating) bars were induced by an imposed upstream flow constriction and no free migrating bars formed. After sediment supply was terminated, bars were progressively eroded, the bed surface coarsened and the slope was significantly reduced. The alternate bar pattern reformed after the sediment supply was restored and sufficient deposition had occurred to regenerate the original channel slope.

This investigation was further developed in the work of Bankert and Nelson (2018) where migrating alternate bars were initially developed in a gravel-sand mixture under constant discharge and sediment supply, exhibiting the known sorting pattern, with coarse bar tops and fine pools. Supply was then increased in various stages. During the first of them, the bars remained stable while the pools aggraded; the second supply increase led to further pool aggradation and increased boundary shear stress over the bar tops. As a result, the bars recovered the capacity to migrate downstream and eventually stabilize. During aggradation, the subsurface maintained its original sediment sorting pattern, thus generating a heterogeneous stratigraphy. Next, the supply was reduced back to its initial rate, leading the bed to degrade through that stratigraphy. As a result, incision occurred through the pools and the bars eroded laterally until coarse sediment deposited during the previous bar-building phase was exposed. The conclusion was that a heterogeneous stratigraphy *can play an important role in determining whether bars persist or disappear after a sediment supply reduction.*

As a final note, let us point out that the above interesting investigations underline the link between sorting, sediment supply and bed topography, suggesting a relation between bar disappearance and suppression of sediment supply. The mechanics of such processes awaits to be fully explored theoretically.

6.7.5 Further effects that influence the development of alternate bars in the field

A further effect that may influence the properties of alternate bars observed in the field is the non-alluvial character of the channel that will be dealt with in the next chapter. The effect of

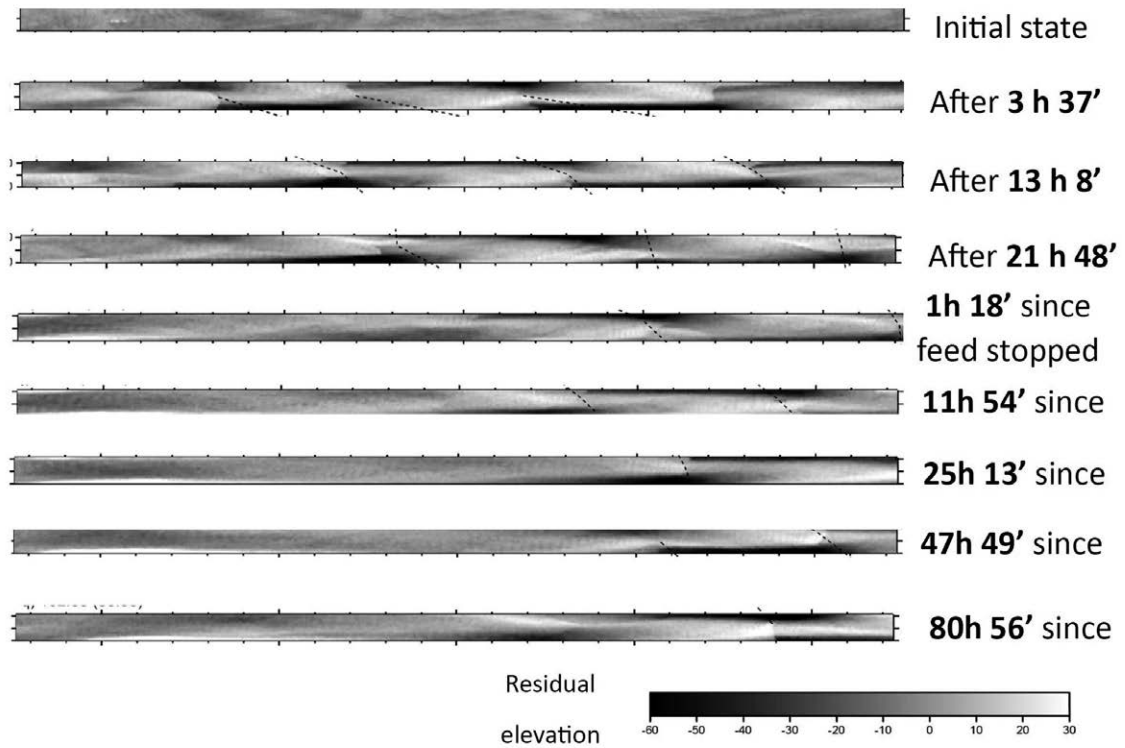


Figure 141. Sequence of bed topographies observed at different stages of Berkeley's experiment. The bed was initially flat. Alternate bars developed and slowed down when sediments were fed. As supply was removed, bars were eroded, disappeared from the upstream reach but reformed downstream (courtesy of Peter Nelson).

interactions with vegetation will be mentioned in the final Chapter 8 as part of the developments foreseen for the near future.

7. Introduction to the morphodynamics of mixed alluvial-bedrock straight channels

Although more refined classifications of channel type have been proposed in the geomorphologic literature (e.g. Howard, 1980, 1987; Howard *et al.*, 1994) the simplest classification, encompassing two major channel types, namely *alluvial* and *bedrock* channels is sufficient for our present introductory purposes. At one extreme, bedrock channels may be defined as channels lacking an alluvial bed, a condition occurring when their sediment transport capacity exceeds the sediment supply rate associated with all grain sizes. Alluvial channels are found at the other extreme, i.e. when the underlying bedrock is nowhere exposed (Figure 142). In practice, a continuum of

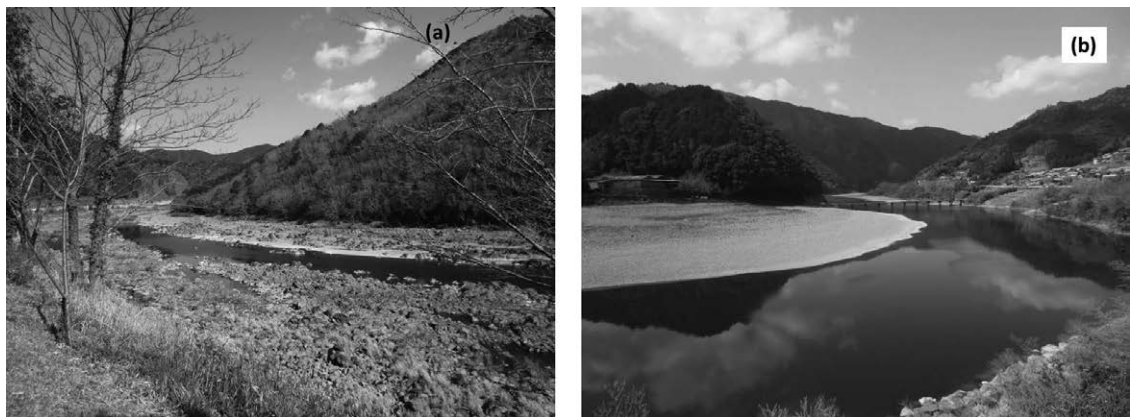


Figure 142. Pictures of two different reaches of the Shimanto River, Shihoku (Japan), taken in March 2013: (a) bedrock; (b) alluvial (courtesy of Gary Parker).

patterns is observed in nature, where actively incising channels often exhibit a mixed bedrock-alluvial character, with exposed bedrock surrounded by regions of coarse alluvium. Also, note that mixed bedrock-alluvial channel characteristics can also be found in sand-bed rivers. This is the case of the lowermost Mississippi River near its outlet (Figure 143), where recent observations have shown that “... *despite proximity to its outlet and marine- and deltaic-depositional settings ... the channel bed is incompletely covered with alluvial sediment ... Alluvial sediments are intermixed amongst channel-bottom substrate and sidewall substrate* ” (Nittrouer, 2010).

7.1. Detachment limited versus transport limited

The basic distinction between bedrock and alluvial channels has a major consequence in terms of the fundamental equation of conservation of sediment mass. In alluvial channels, the local net variation of bed elevation (absolute variation minus tectonic uplift) is determined by the divergence of the sediment transport capacity of the stream. This is the well known Exner equation that has been our major tool of investigation so far. Alluvial channels are thus described by

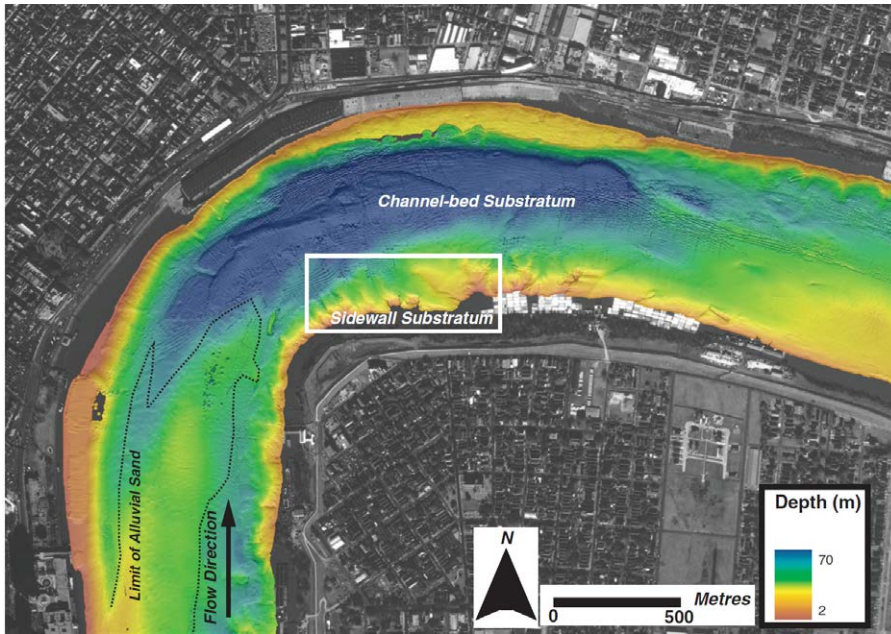


Figure 143. Bathymetry of the French Quarter bend of the Mississippi River in New Orleans. Note the mixed rock-alluvial character of the channel. Alluvial sediment is absent from the bottom of the outer region of the bend. The limit of alluvial sand is shown by a dashed line (reproduced from Figure 2.11 of Nittrouer, 2010).

geomorphologists as *transport limited* environments. In an important paper, Howard *et al.* (1994) introduced the notion of *detachment limited* systems, noting that in bedrock channels it is the *detachment capacity of the stream*, measured by the absolute *erosion rate* \mathcal{E} ($\equiv LT^{-1}$), that determines the local net variation of bed elevation. Under these conditions, sediment continuity takes the following simplest form:

$$\frac{\partial \eta}{\partial t} = \mathcal{U}_t - \mathcal{E}. \quad (569)$$

where \mathcal{U}_t ($\equiv LT^{-1}$) is the rate of tectonic uplift (the subscript is introduced to avoid confusion with the cross sectionally averaged stream velocity \mathcal{U}). As described in the next Section, \mathcal{E} is determined by a number of processes. Their understanding will require the development of physically based models, some of which will be discussed in Section 7.5.

7.2. Mechanisms of bedrock erosion

River incision into bedrock is driven by the mechanisms outlined below (see, e.g. Whipple *et al.* (2000) and the review of Whipple (2004)).

Abrasion

Although the term *abrasion* should be more appropriate to describe the wear induced by particles sliding with friction over the bedrock surface (Chatanantavet and Parker, 2009), in the bedrock literature the common usage of the word refers to the wear induced by the impact of both suspended and bedload particles on the boundary of bedrock channels. Abrasion dominated channels are typically characterized by bed and banks sculpted by small scale patterns called *flutes* and *potholes* (see next Section).

Plucking

Also known as *quarrying* and *jacking*, it consists of the destabilization of blocks of the channel boundary, which progressively detach from the adjacent blocks due to crack widening, crack propagation and chemical-physical weathering (Figure 144). Once detached, a block can be entrained by the stream under the action of lift and drag forces (Whipple *et al.*, 2000; Chatanantavet and Parker, 2009).



Figure 144. Bed structure in a plucking-dominated bedrock stream (Southern Indiana), courtesy of Pailin Chatanantavet.

Dissolution

This is a process which affects *soluble rocks* (including limestone, marble and evaporites) and *chemically reactive rocks* (including feldspars, olivine and sulfide minerals). Their degradation gives rise to products which are readily entrained by the flow. Dissolution may be enhanced by the growth of algae, moss and lichen (Richardson and Carling, 2005).

Physical weathering

Further mechanisms may operate in specific contexts. In particular, *physical weathering* may be induced by wetting and drying cycles, crystallization of salts and freeze-thaw cycles.

7.3. Morphology of bedrock channels

An extensive descriptive literature has been devoted to field observations of the morphological characteristics of bedrock channels. Various recent comprehensive assessments are available (e.g. Whipple, 2004; Richardson and Carling, 2005; Lamb *et al.*, 2015). The reader interested in a wide overview of the subject is then referred to the latter reviews and to the literature cited therein.

7.3.1 Large scale morphological features of bedrock channels

As pointed out by Whipple (2004), the average width B of bedrock channels displays a distinct correlation with some power of the upstream drainage area \mathcal{A} , considered as a proxy for water and sediment discharge. The observed exponent falls in the range 0.3 – 0.5. This dependence is also a well known feature of alluvial channels (Hack, 1957). The recent assessment of field data of Wohl and David (2008) suggests the validity of similar power law relationships for both alluvial and bedrock channels: namely, $B \sim \mathcal{A}^{0.3}$ and $B \sim Q^{0.5}$ for channel width, $\mathcal{D} \sim \mathcal{A}^{0.2}$ and $\mathcal{D} \sim Q^{0.3}$ for the flow depth, respectively. In other words, these Authors suggest that “*the erosional resistance of channel boundaries is not the primary control on scaling relations for channel geometry*”. Whether river width does also depend on the rock uplift rate is left as an unsettled issue, though Finnegan *et al.* (2005) developed a relation between width, discharge, slope, and roughness suitable to be applied to terrain with spatially nonuniform rock uplift rates with some apparent success.

The longitudinal bed profile of bedrock rivers is often characterized by discontinuities in either channel elevation or slope called *knickpoints*. They have been extensively discussed in the literature, although Crosby and Whipple (2006) point out that their origin and dynamics are not wholly clear yet. Essentially, knickpoints are thought to be the expression of the dynamic response of bedrock rivers to disequilibrium conditions associated with regional or local perturbations, e.g. a base-level fall, the channel encountering a resistant substrate, changes in tectonic uplift rates, climate-induced changes in river incision rate and glaciation. These responses lead to the development of landforms that can range from high gradient rapids to waterfalls. However, sequence of knickpoints, in the form of waterfalls formed in a fairly homogeneous rock formation (the Kohala Peninsula, Hawaii, USA), in the absence of any apparent external forcing was also observed (Scheingross *et al.*, 2019). Observations of this kind led Mike Lamb and Joel Scheingross to take a different viewpoint, developed in a series of papers culminating in an experimental paper (Scheingross *et al.*, 2019) and a recent review paper (Scheingross *et al.*, 2020). Essentially, these Authors argue that waterfalls may also form as a *free* instability process, whereby bottom perturbations are amplified by a feedback between water flow, sediment transport and bedrock incision, in the absence of any external forcing. In other words, waterfalls would result from the finite amplitude evolution of the so called *cyclic steps*, i.e the repeating sequence of undulating chutes and pools forming in incising steep river beds. Cyclic steps differ from waterfalls, because their step heights is small relative to their wavelengths, and they lack a free falling jet. A mechanistic interpretation of this process was proposed by Scheingross and Lamb (2017) and, due to its relevance for the general theme of the present Monograph, it will be briefly discussed in Section 7.6.3.

Between successive knickpoints the profile is typically *concave-up* and such to satisfy a distinct correlation of channel slope with some negative power θ of the upstream drainage area. This law is found to apply for $\mathcal{A} > \mathcal{A}_{cr}$, with \mathcal{A}_{cr} some critical value for \mathcal{A} of the order of 1 km^2 , below which channel slope is likely to be limited by the role of debris flows. Sklar and Dietrich (2008) note that the expected value of the exponent θ (*concavity index*) has been the subject of much debate. Simple scaling arguments proposed by Howard and Kerby (1983) and Rodriguez-Iturbe and Rinaldo (2010) predict $0.35 < \theta < 0.5$. However, according to Sklar and Dietrich (2008), over the length of a bedrock channel between the critical point and the alluvial transition, θ may reach values up to 1.2. Sklar and Dietrich (2008) point out further limits based on empirical analysis of the slope-area scaling. In particular, headwater channel slopes, dominated by debris flow scour (Stock and Dietrich, 2003), do not appear to exhibit a log-log linear relationship between slope and drainage area.

Some progress over the above empirical approach has been made with the help of the mechanistic approach of Sklar and Dietrich (2008) and will be outlined in Section 7.6.2.

7.3.2 Small scale morphological features of bedrock channels



Figure 145. The 40 metre, 3-tiered Kitekite falls (Auckland, New Zealand), along with the cascades above the falls and the natural pool at its base. (Credit: By MattWT - Own work, CC BY-SA 3.0, <https://commons.wikimedia.org/w/index.php?curid=4584188SA> 3.0).

Small scale bedrock patterns share some properties of alluvial bedforms. In particular, they may develop in the form of single isolated patterns or as trains of perturbations. However, they also exhibit distinct features. Indeed, they are purely erosional forms, unlike alluvial patterns which evolve in response to the balance between erosion and deposition of sediments transported by the stream. This raises an interesting question of whether and how purely erosional features may reach equilibrium conditions. Some trains of migrating concave features called *scallops* have indeed been observed to reach equilibrium, displaying a permanent shape while migrating (Curl, 1966; Blumberg and Curl, 1974). Other concave sub-spherical features called *potholes*, do not migrate and retain constant form as they grow (Springer and Wohl, 2002). A variety of classification criteria can be used for small scale bedrock patterns, as extensively discussed by Richardson and Carling (2005) (but see also Carling *et al.*, 2009). These Authors provide wide reference to previous works, starting from the early seminal contributions of Allen (1971a,b). For the present purposes, it is sufficient to identify a few typologies of small scale patterns which call for theoretical interpretation. A rich illustration of the variety of patterns observed in nature is also contained in Bourke and Viles (2007).

A first useful classification criterion consists of distinguishing between *abrasion driven patterns* and *dissolution driven forms*.

Abrasion driven patterns

A further morphological subdivision of this class of patterns was made by Richardson and Carling (2005), who distinguished between *concave* and *convex-undulating* forms. The common feature of *concave* forms is the presence of local concave depressions. They display variable degrees of



Figure 146. Bourke's Luck Potholes in quartz arenite, Blyde River, Mpumalanga, South Africa (reproduced from <https://pixabay.com/photos/bourke-luck-potholes-south-africa-163065>, pixabay licence).

elongation. The latter may range from weak (as in round-elliptical plan views typical of *potholes*, Figure 146), to strong (as in *furrows*). This latter group of features includes patterns suggestive of active suspended load abrasion denoted as *flutes*. Note that the spectrum of potholes and furrows observed in the field is very wide, encompassing a variety of orientations (from longitudinal to transverse). Also, note that field observations of Nittrouer (2010) have revealed that the channel-bottom substrate of the lowermost reach of the Mississippi River displays similar erosional features.

Convex-undulating forms comprise a smaller variety of typologies. Their common expression is the presence of bedrock undulations, either rounded or sharp-crested, called *hummocky forms*. Examples found in limestone environments are fairly regular sequences of bedforms resembling alluvial ripples or dunes depending on their scale. They are called *pseudo-ripples* (Figure 147a) and *pseudo-dunes* (Figure 147b), respectively.

Dissolution driven forms

These forms develop significantly in soluble rocks and particularly in limestone. The classification proposed by Richardson and Carling (2005) includes: *solution pits* and *scallops*.

Solution pits are small depressions, of millimeter-centimeter size, that may also act as initial perturbations to trigger further more intense erosion, eventually leading to the development of larger bedforms, such as potholes, flutes and scallops (Figure 148).

Scallops are sequences of depressions bounded by sharp transversely oriented crests (Figure 149). Following Allen (1971a) and Allen (1971b), Richardson and Carling (2005) argue that all scallops derive from the coalescence and mutual interaction of flutes and/or solution pits.

Note that the above classification is based on morphology. The mechanisms underlying the formation of the above patterns are unexplored, though some preliminary attempts (e.g. the

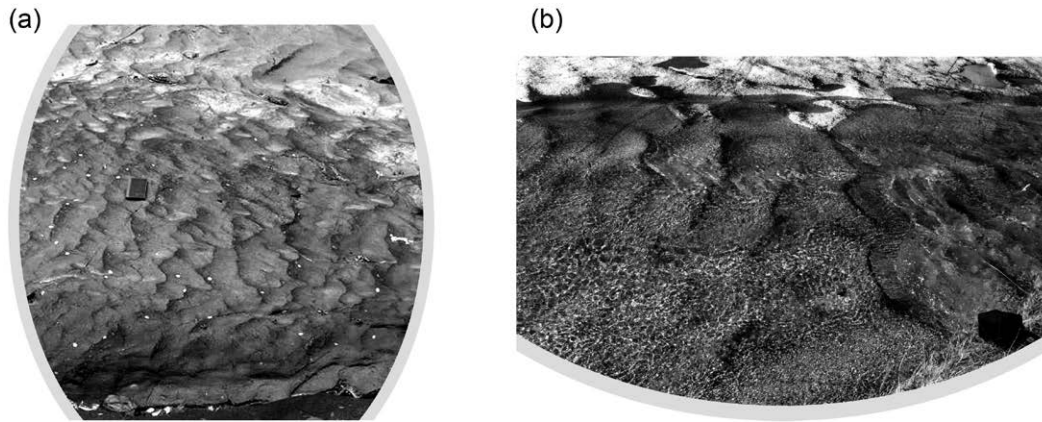


Figure 147. (a) Pseudo-ripples in Andesite observed at Than Rattana, Thailand. Scale: notebook 15 cm. (b) Pseudo-dunes in granite observed at Allt Ceitlein, UK. Scale: camera bag, 20 cm. In both cases flow is from left to right, courtesy of Keith Richardson and Paul Carling.

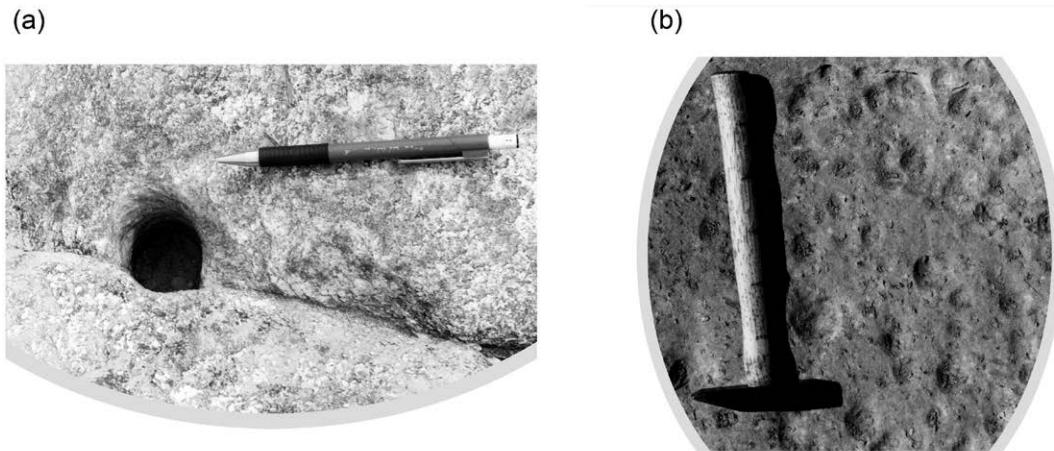


Figure 148. (a): Deep circular solution pit in granitic gneiss observed at Nam Mae Chaem (Ob Luang), Thailand. (b): Shallow circular solution pits in limestone observed in the River Dee, UK. Flow is from top to bottom. Scale: hammer (30 cm). Courtesy of Keith Richardson and Paul Carling.

analysis of the formation of longitudinal incisional grooves of Inoue and Nelson (2020)) have appeared in the recent literature. Theoretical understanding will likely allow revisiting the above descriptive classification.

7.4. Early morphological models of the reach-basin scale

In the early literature on the subject (see e.g. the review by Howard *et al.*, 1994) a number of semi-empirical relationships expressing \mathcal{E} in terms of global properties of the river basin were proposed. They can all be written in the form of power laws as follows:

$$\mathcal{E} = k_{\mathcal{E}} \mathcal{A}^m S^n. \quad (570)$$

Here, \mathcal{A} is the drainage area of the river basin at the given cross section, S is channel slope, m and n are positive exponents and $k_{\mathcal{E}}$ is an empirical constant. The particular case $m = n = 1$ has been

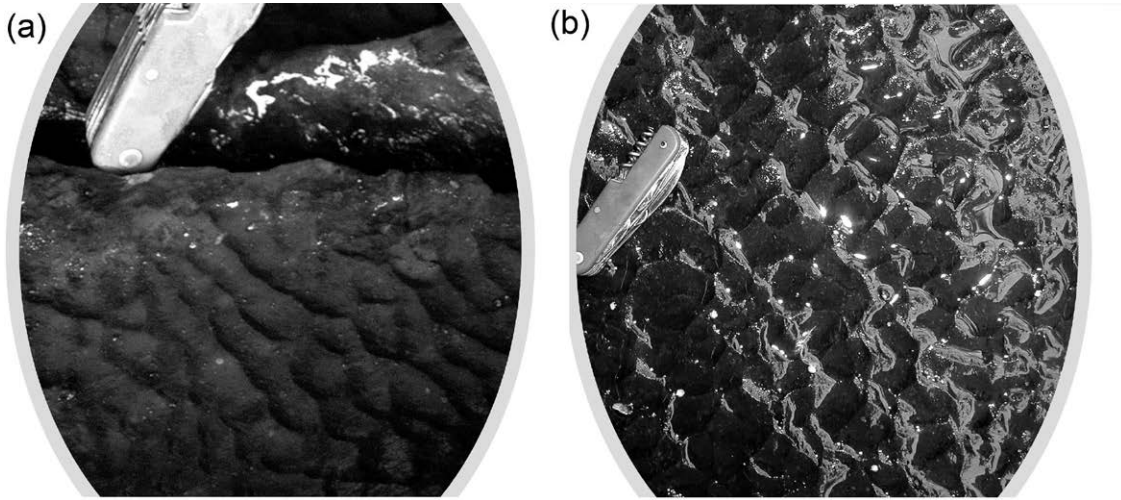


Figure 149. (a): Two-dimensional scallops in limestone. Flow from bottom left to top right. (b): Three-dimensional scallops in limestone. Flow from bottom to top. Both features have been observed at Sleightholme Beck, UK (courtesy of Keith Richardson and Paul Carling).

interpreted as the condition whereby erosion rate would be proportional to *unit stream power* \mathcal{P} , i.e. the stream power per unit bed area. According to Howard *et al.* (1994), this interpretation would rely on the assumption that the bankfull flow discharge at a given cross section Q would be proportional to the drainage area. Since $\mathcal{P} = \rho g (Q/B) S$, the actual assumption required to state that $\mathcal{E} \approx \mathcal{P}$ would be $(Q/B) \approx \mathcal{A}$. However, the latter relationship is not supported by the field observations of Wohl and David (2008), discussed in Section 7.3.1.

The empirical character of (570) is reflected in its dimensional nature. In particular, the factor $k_{\mathcal{E}}$ has different dimensions depending on the value chosen for the exponent m . This notwithstanding, the above formulation for the erosion rate has been widely employed to develop 1D simulation models of stream profile evolution. Instructive simulations were performed by Howard *et al.* (1994). They considered a channel characterized by drainage area and flow discharge increasing as the square of distance downstream. Moreover, the stream was assumed to be initially bedrock with a concave profile in equilibrium with a slow, constant rate of base level lowering. Simulations were able to predict stream profiles developed in response to a base level lowering scenario characterized by long periods of stability interrupted by brief episodes of uplift. It turns out that, as gradients decline due to bed erosion, a minimum gradient, just sufficient to transport sediment supplied from upstream, is reached. The stream cross section where this condition is met is then converted from rock to alluvial. This occurs first at the downstream end and then migrates upstream. Thus, the model is able to predict the occurrence of a transition from bedrock to alluvial bed and its dependence on the history of tectonic uplift.

The detachment limited model of Howard *et al.* (1994) was further explored by a number of Authors, notably Whipple and Tucker (1999) (but see also Whipple, 2004). These Authors exploited a property of the model already noted by Rosenbloom and Anderson (1994). Indeed, substituting from (570) into (569), one derives an evolution equation for the bed profile which has the form of a *nonlinear kinematic wave equation*:

$$\frac{\partial \eta}{\partial t} + c(S, x) \frac{\partial \eta}{\partial x} = \mathcal{U}_t(x, t), \quad (571)$$

where the *wavespeed* $c(S, x)$ reads:

$$c(S, x) = k_{\mathcal{E}} \mathcal{A}^m S^{n-1} \operatorname{sgn}\left(\frac{\partial \eta}{\partial x}\right). \quad (572)$$

Hence, $c(S, x)$ depends nonlinearly on the local bed slope $S \equiv |\partial\eta/\partial x|$ and on the longitudinal coordinate x through the drainage area \mathcal{A} . Also, note that, as $\partial\eta/\partial x$ is typically negative, (572) shows that perturbations migrate upstream. It is well known (Whitham, 1974) that a kinematic wave equation is readily transformed into a total derivative equation for an observer moving along a *characteristic line* C defined as follows:

$$C : \quad \frac{dx}{dt} = c(S, x). \quad (573)$$

Such an observer *sees* variations of bed elevation governed by (571), that, with the help of (573), takes the form:

$$\frac{d\eta}{dt} = \frac{\partial\eta}{\partial t} + \frac{dx}{dt} \frac{\partial\eta}{\partial x} = \mathcal{U}_t. \quad (574)$$

The model lends itself to exploring a number of issues that are discussed at length in the papers cited above. Here, we are only interested in some conceptually important outcomes that emerge immediately from the model.

Firstly, the environmental control on the morphodynamic evolution of a bedrock channel arises from two physical mechanisms, namely uplift (tectonic forcing) and bottom erosion (climatic-lithologic forcing). Whipple and Tucker (1999) derive a dimensionless parameter measuring the ratio between the intensities of the two effects.

Secondly, a steady configuration of the river profile is only possible provided the rate of tectonic uplift does not vanish. Indeed, for a temporally constant value of \mathcal{U}_t , setting $\partial\eta/\partial t = 0$ in equation (569) and recalling (570), one readily finds

$$S_e = -\frac{d\eta}{dx} = \left(\frac{\mathcal{U}_t}{k_\varepsilon}\right)^{1/n} \mathcal{A}^{m/n}, \quad (575)$$

having denoted by S_e the local slope at equilibrium. With some Hack's type relationship for the x -dependence of the drainage area (say $\mathcal{A} = k_a x^h$), the latter ordinary differential equation allows one to derive the bed elevation profile $\eta(x)$. For the simplest case of spatially constant rate of tectonic uplift, uniform lithology, precipitation, and erodibility ($k_\varepsilon = \text{const}$), $m = n = 1$ and $h = 1/2$, the bed profile solution is a parabola with upward concavity (Figure 150, $t = 0$).

Thirdly, the model allows one to evaluate the response of a bedrock channel to changes in tectonic and climatic conditions. Figure 150 shows the temporal evolution of a bedrock profile starting from the initial equilibrium profile associated with some spatially uniform rate of tectonic uplift. At $t = 0^+$, a sudden base level drop is imposed at $x = 0$. Thereafter \mathcal{U}_t is assumed to vanish everywhere. Under these conditions, equation (574) simply tells us that the sudden base level drop occurred at $x = 0$ migrates upstream in the form of a so called knickpoint to a distance depending on time according to the solution of the characteristic equation (573). This procedure is visualized in Figure 150, $t > 0$.

The main conclusion reached by Whipple and Tucker (1999) was that “*both the magnitude and timescale of the bedrock channel response to an imposed tectonic or climatic forcing are largely governed by a single dimensionless parameter, the uplift-erosion number, raised to a power determined by the slope exponent in the stream power erosion law*” (see equation 570).

A number of further investigations have explored the dependence of long-term bedrock incision on the magnitude and variability of flow events. The interested reader is referred to Lague *et al.* (2005) and references therein.

7.5. Mechanistic models of bedrock erosion

The approach discussed in the previous section, in the many versions appeared in the literature, has played a useful role in the development of the subject. However, it is intrinsically limited by the lack of a mechanistic basis for the empirical correlations which are meant to account for the effects of rock strength, channel slope, discharge, sediment supply and grain size. In the last two decades, physics based models of bedrock erosion have overcome some of the above limitations.

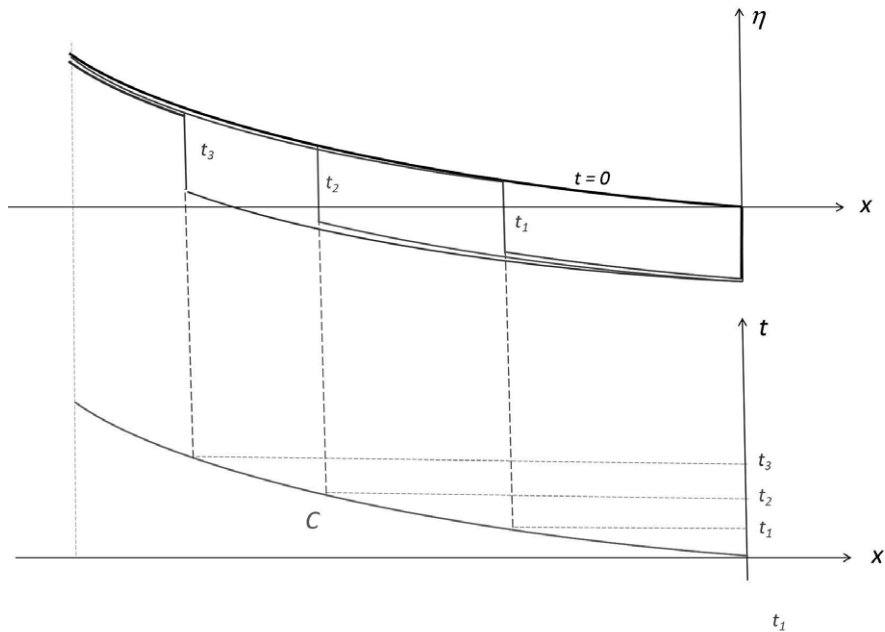


Figure 150. Temporal evolution of a bedrock profile. $t < 0$: initial equilibrium profile associated with some spatially uniform rate of tectonic uplift; $t=0$: sudden base level drop; t_i ($i=1,2,3$): profiles at various times showing the location reached by the migrating knickpoint.

These models have mainly concerned the abrasion mechanism. Below, we concentrate on the latter and ignore other mechanisms (but see Chatanantavet and Parker (2009) and Wilkinson *et al.* (2018) for an introduction to the mechanics of plucking).

7.5.1 The saltation-abrasion model

The development of the subject has been deeply influenced by a cornerstone paper, Sklar and Dietrich (2004), that marks the first successful attempt to formulate a physically based model of bedrock abrasion driven by saltating bed load. This work disclosed the dependence of the process on the fraction of the bed that is not armored by transient deposits of alluvium, which is in turn related to the ratio of coarse sediment supply to bed load transport capacity. Note that Sklar and Dietrich (2004) neglect any other erosion mechanism concentrating on the effect of bed load which they assume to be dominant. The later extension of the model to account for the effect of suspended load will be discussed in Section 7.5.3.

In a preliminary experimental investigation that employed a bedrock abrasion mill, Sklar and Dietrich (2001) measured bedrock wear resulting from the impact of saltating particles. These experiments supported the view of the process of bedrock incision proposed in the early work of Gilbert (1877). Incision would be controlled by two contrasting effects of sediment supply. Supply provides the abrasive tools needed for bedrock erosion (*tool effect*) but it may also lead to temporary deposits which prevent contacts of saltating particles with the bedrock substrate (*cover effect*). In other words, river incision requires that the sediment supply be lower than the transport capacity of the stream.

The model of Sklar and Dietrich (2004) assumes that a constant fluid discharge flows in a rectangular channel with a plane bed consisting of a bedrock surface, on which patches of alluvial deposits with uniform grain size are present. The bedrock erosion rate is expressed as follows:

$$\mathcal{E} = V_i I_r F_e, \quad (576)$$

where V_i is the average volume of rock detached per particle impact, I_r is the number of particle

impacts per unit area and unit time, and F_e is the fraction of the river bed where the bedrock substrate is exposed. Note that, in the context of Sklar and Dietrich (2004) model, \mathcal{E} , V_i and I_r are assumed to be uniformly distributed in the lateral direction. Alternatively, they may be assumed to provide an average measure of the integrated effect of bedrock erosion throughout the cross section.

The evaluation of V_i was based on early work of Bitter (1963) concerning the erosion of elastic brittle materials by repeated impacts. This process is called *deformation wear* and arises from the dynamics of the network of cracks generated by the tensile stresses excited by the deformation of the rock in a neighborhood of the impact point. As pointed out by Engle (1978), the volume eroded by a single impact, averaged over a large number of impacts, scales with the kinetic energy transferred to the rock surface through particle collisions. As the magnitude of the peak tensile stress generated by the particle impact depends on the component of the impact velocity orthogonal to the rock surface (Engle, 1978), the wear model of Bitter (1963) was cast in the form

$$V_i = \frac{1}{e_u} \left(\frac{1}{2} m_p w_p^2 - E_t \right), \quad (577)$$

where m_p is the particle mass, w_p is the component of the impact velocity orthogonal to the rock surface, E_t is the threshold energy required for detachment to occur and e_u is the energy required to erode a unit volume of rock. Note that the above model assumes that the particle mass keeps constant and ignores the contribution to erosion driven by the tangential component of particle velocity, significant for ductile materials (*cutting wear*).

The linear relationship (577) was essentially confirmed by the later experiments of Head and Harr (1970). However, no erosion threshold was detected, contrary to the observations of Bitter (1963), who had used ductile rather than brittle abrasive material. Similar conclusions were later reached by Sklar and Dietrich (2001), who found that measurable bedrock wear was induced even by fine sand. As a result, Sklar and Dietrich (2004) simply neglected E_t in (577). The parameter e_u is a measure of the material toughness, namely the rock resistance to abrasion by impacting particles. Following Engle (1978), Sklar and Dietrich (2004) expressed this quantity in terms of the capacity of the material to store energy elastically (β), measured by the area under the stress-strain curve at the yield stress. Hence, they set:

$$e_u = k_v \beta = k_v \frac{\sigma_T^2}{2Y}, \quad (578)$$

where σ_T is the rock tensile yield strength, Y is Young elastic modulus, and k_v is a dimensionless empirical coefficient depending on the material properties of the impacting particle.

The number of particles impacting the bedrock surface per unit time and per unit area (I_r) is readily calculated dividing the number of bedload particles per unit time and unit width, namely $Q_{sup}/(\pi d^3/6)$, by the average distance traveled by particles between impacts, i.e. the saltation length L_s . Note, that the number of particles participating in the bedload transport per unit time and unit width is determined by the sediment supply rate per unit width Q_{sup} , which does not coincide with the bedload transport capacity per unit width Q^b . Hence, Sklar and Dietrich (2004) write:

$$I_r = \frac{6 Q_{sup}}{\rho_s \pi d^3 L_s}. \quad (579)$$

Finally, based on their own flume observations (Sklar and Dietrich, 2002), they simply assume that the fraction of the exposed bedrock varies linearly with the defect of sediment supply rate Q_{sup} relative to the bedload transport capacity Q^b (both per unit width), i.e

$$F_e = 1 - \frac{Q_{sup}}{Q^b}. \quad (580)$$

With the help of (577), (578), (579), (580), the expression (576) leads to the following final relationship for \mathcal{E} :

$$\mathcal{E} = \frac{Q_{sup} w_p^2 Y}{L_s k_v \sigma_T^2} \left(1 - \frac{Q_{sup}}{Q^b} \right). \quad (581)$$

In order to complete the formulation, Sklar and Dietrich (2004) needed *closure* relationships for Q^b , L_s and w_p as functions of Shields stress and grain size. The bedload capacity was evaluated using the formula of Fernandez Luque and van Beek (1976)

$$Q^b = 5.75 \rho_s \sqrt{(s-1)gd^3} (\tau_* - \tau_{*c})^{3/2}, \quad (582)$$

The properties of saltation trajectories were obtained through appropriate relationships that best fit the trends of a large set of published data. The final form of the saltation-abrasion bedrock incision model of Sklar and Dietrich (2004) was then found to read:

$$\mathcal{E} = \frac{0.08(s-1)Yg}{k_v^2 \sigma_T} \frac{Q_{sup}}{(\tau_*/\tau_{*c} - 1)^{1/2}} \left(1 - \frac{Q_{sup}}{Q^b}\right) \left[1 - \left(\frac{u_\tau}{w_s}\right)^2\right]^{3/2}, \quad (583)$$

where w_s is the settling speed of sediment particles and u_τ is the friction velocity of the flow. Note that the term between square brackets accounts for the shift from bedload mode to suspended mode, which is taken to occur when $w_s = u_\tau$. In this model, above the latter threshold, the length of saltation hops rapidly diverges and erosion driven by the impact of saltating particles vanishes. In the real world, transport in suspension coexists with bedload motion, such that a fraction of the erosion rate is driven by saltating bed load particles even when suspended load is significant. This feature is accounted for in the extension of Sklar and Dietrich (2004) model discussed in Section 7.5.3.

A simpler form of (583) was obtained neglecting the suspension effect term, i.e. restricting the analysis to excess shear stresses well below the threshold of suspension (say, $0 < (\tau_*/\tau_{*c} - 1) < 10$) and to values of the sediment supply rate smaller than the bedload transport capacity. Under these conditions, substituting from the relationship (582) into (583) and rearranging, Sklar and Dietrich (2004) find:

$$\mathcal{E} = k_1 \frac{Q_{sup}}{(\tau_*/\tau_{*c} - 1)^{1/2}} - k_2 \frac{Q_{sup}^2}{d^{3/2} (\tau_*/\tau_{*c} - 1)^2}, \quad (584)$$

with

$$k_1 = \frac{0.08Y(s-1)g}{k_v \sigma_T}, \quad k_2 = \frac{0.014Y \sqrt{(s-1)g}}{k_v \sigma_T^2 \rho_s \tau_{*c}^{3/2}}. \quad (585)$$

The form (584) of the bedrock incision formula has the advantage to display distinctly the roles of the tool effect (first term) and of the cover effect (second term). The dimensionless factor k_v was estimated from the experimental measurements of bedrock wear of Sklar and Dietrich (2001). Its value, corrected for a typo in the original paper of Sklar and Dietrich (2004) (Peter Nelson, personal communication), reads: $k_v \simeq 10^6$.

Figure 151 shows the dependence of the erosion rate predicted by equation (583) on the rate of supply of sediment mass ($\rho_s Q_{sup}$). Also shown are the single factors contributing to \mathcal{E} . The main message delivered by Figure 151 is that, for increasing sediment supply, at low supply rates incision rate is dominated by the increase in the impact rate (I_r) which prevails on the decrease of the bed area exposed to particle impact (F_e). On the contrary, at high supply rates, the incision rate decreases as the reduction in the fraction of bed area exposed prevails over the increase in the impact rate. When the variation of the tool effect balances the variation of the cover effect, the incision rate attains a peak. Three limits for which the erosion rate vanishes deserve special interest: vanishing sediment supply rate, fully alluvial bed (sediment supply rate equal to bedload transport capacity) and transport stage approaching the threshold of transport in suspension. This is further clarified in Figure 152 where the dimensionless erosion rate $\tilde{\mathcal{E}} = \mathcal{E} \sigma_T^2 / [\rho_s Y (gd)^{3/2}]$ is plotted in the plane $(\tau_*/\tau_{*c}, Q_{sup}/Q^b)$. The erosion rates predicted by the saltation-abrasion model were compared with the laboratory measurements in rotational bedrock abrasion mills performed by Sklar and Dietrich (2004) with the primary goal of calibrating the free parameter k_v of the model. The erosion rates predicted by the saltation-abrasion model closely fit the observed

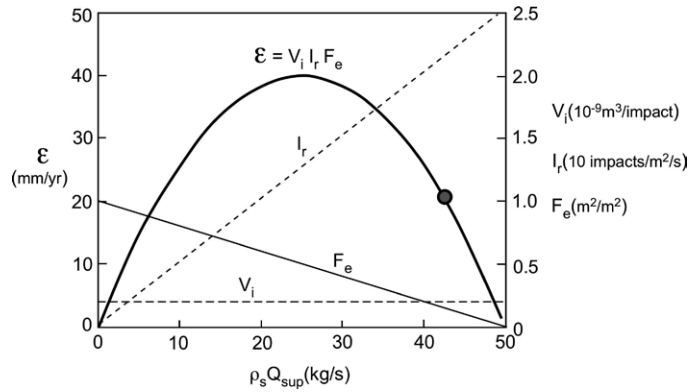


Figure 151. The erosion rate \mathcal{E} predicted by equation (583) is plotted as a function of the rate of supply of sediment mass $\rho_s Q_{sup}$. The single factors contributing to the erosion rate, namely the average volume of rock detached per particle impact (V_i), the number of particle impacts per unit area and unit time (I_r) and the fraction of the river bed where the bedrock substrate is exposed (F_e) are also plotted. Input parameters, shown in the legend, were chosen to model a gauged reach of the South Fork Eel River, Mendocino County, California. The open circle denotes the predicted instantaneous erosion rate at this reference site (modified from Sklar and Dietrich, 2004).

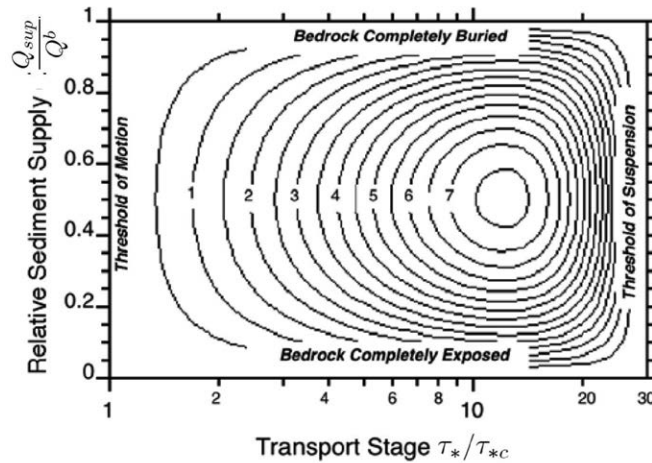


Figure 152. The dimensionless erosion rate $10^{-15} \tilde{\mathcal{E}}$ ($\tilde{\mathcal{E}} \equiv \mathcal{E} \sigma_T^2 / [\rho_s Y (gd)^{3/2}]$) is plotted in the plane $(\tau_* / \tau_{*c}, Q_{sup} / Q^b)$ (modified from Sklar and Dietrich, 2004).

trend as grain size decreases from near the threshold of motion ($d = 0.035 \text{ m}$) to the threshold of suspension ($d = 0.001 \text{ m}$). On the contrary, erosion rates for sand sizes could not be adequately predicted because the model does not account for the dynamics of suspended sediment transport.

7.5.2 Developments of Sklar-Dietrich model

Various Authors built up on the work of Sklar and Dietrich (2004) to propose modifications of that model.

Exponential decay of the cover effect

Turowski *et al.* (2007) derived a new functional form for the cover effect based on the following argument. The channel bed erosion rate may be reasonably taken to be proportional to the ratio $R_a = a_{exp} / a_{tot}$ of bed area exposed to particle impact a_{exp} to the total bed area a_{tot} . Denoting by q the ratio Q_{sup} / Q^b , Turowski *et al.* (2007) argue that an infinitesimal increment of relative

sediment supply dq will not give rise to an equal decrement of relative exposed bedrock area (as implied by the linear assumption of Sklar and Dietrich (2004)). Part of dq will affect portions of the channel bed that are already (statically) covered by sediment. In other words, Turowski *et al.* (2007) assume that the decrement of the relative exposed bedrock area $-dR_a$ is equal to a fraction dq of the relative portion R_a of bed area already exposed to the flow. This assumption leads to a simple ordinary differential equation for R_a , readily solved to give an exponential (rather than linear) decay of R_a with increasing q . Using the latter relationship one can then calculate the erosion rate as a function of sediment supply. Figure 153 shows the dependence of erosion rate

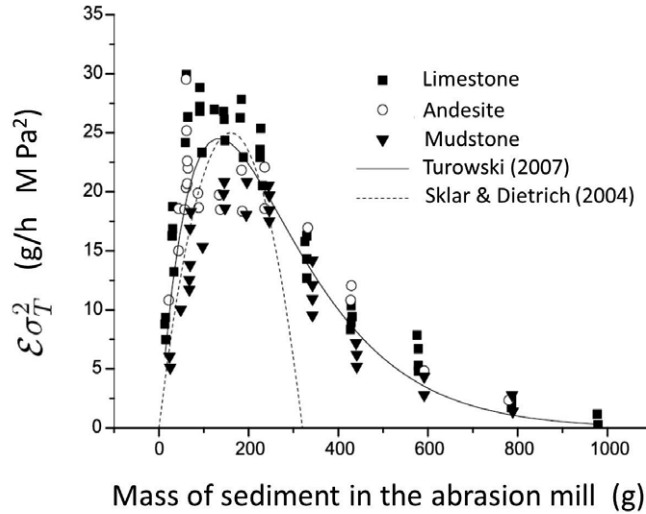


Figure 153. The dependence of bedrock erosion rate (multiplied by square of tensile strength) on the total mass of sediment in the abrasion mill experiments of Sklar and Dietrich (2001) is compared with theoretical predictions of Sklar and Dietrich (2004) (dashed line) and the best fit curve obtained through the corrected formulation of Turowski *et al.* (2007) (solid line) (modified from Turowski *et al.*, 2007).

on sediment load data obtained by Sklar and Dietrich (2001) in their abrasion mill experiments. Note that data refer to three rock types. In order to remove the dependence on the rock type, the Authors multiply the erosion rate \mathcal{E} (measured in g/h) by the squared tensile strength σ_T^2 (measured in MPa^2) (recall equation (581)). The quantity plotted in the abscissa is the total mass of sediment placed in the abrasion mill, which controls the sediment supply rate. In each experiment the grain size and the lithology of both bedrock and sediment were held constant. It clearly appears that the best fit obtained through the corrected formulation of Turowski *et al.* (2007) does improve the agreement of theory versus experiments as compared with the theoretical predictions provided by the original saltation-abrasion model of Sklar and Dietrich (2004).

Discrete element simulations

An interesting confirmation of the soundness of the saltation-abrasion model of Sklar and Dietrich (2004) and of the correction proposed by Turowski *et al.* (2007), has been recently provided by Aubert *et al.* (2016). The approach pursued by the latter Authors was based on the method of discrete-element simulations commonly employed for granular materials. Essentially, Aubert *et al.* (2016) simulate the dynamics of spherical pebbles entrained by a turbulent water flow over a fixed rough bedrock surface area of width B and length L . Roughness is modeled by *glueing* on a horizontal surface a number of spheres, of radius R equal to that of saltating pebbles, centred at some reference height. They are fixed, i.e. they are part of the bedrock and model natural patches of immobile pebbles.

The bedload is modeled by a set of N spheres of given density and radius R , taken as constant through all the simulation. An important parameter is the so called *dimensionless surface density*

σ , defined as the ratio between the N bedload spheres and the maximum number of spheres that can be accommodated on the bedrock surface area ($BL/(4R^2)$) assuming the spheres are arranged in a square grid). A uniform turbulent flow is assumed to act over the bedrock surface. Aubert *et al.* (2016) do not perform a two-way coupling, i.e. they do not account for variations of the turbulent flow resulting from the presence and motion of bedload particles. Rather, they rely on the recent 2D model of Duran *et al.* (2012) who, accounting for the reactions of solid particles on the water flow, found that the fluid velocity vanishes where the local solid fraction is high enough (say one or two grain diameters within the bedload layer), and tends towards a logarithmic profile in the clear water region. Hence, at each time step, Aubert *et al.* (2016) compute the average solid fraction in horizontal slices. Next, they assume that the velocity profile is logarithmic, i.e. not affected by the presence of solid particles, if the average solid fraction is less than 0.5 and vanish otherwise.

The motion of particles is tracked solving the equations of motion with semiempirical closures for the drag and torque coefficients. Particle-particle and particle-wall collisions are modeled introducing a restitution coefficient and modeling the tangential force generated at contact by a regularized form of Coulomb law of solid friction. The cover fraction evolves in time and is updated assuming that pebbles with velocity lower than 1/10 of the maximum velocity are immobile. Denoting by $n(t)$ the number of cells covered by immobile pebbles at time t , the time-averaged static cover fraction C is evaluated as $n(t)4R^2/(WL)$. Finally, all the energy lost during an impact with the bedrock is assumed to contribute to its abrasion.

With the help of the above procedure Aubert *et al.* (2016) are able to estimate the amount of energy that successive impacts of bedload particles transfer to the bedrock surface (a proxy for bedrock erosion), as a function of both the amount of sediment available, strictly related to the dimensionless surface density, and the Shields number. Results show that as the bedload flux

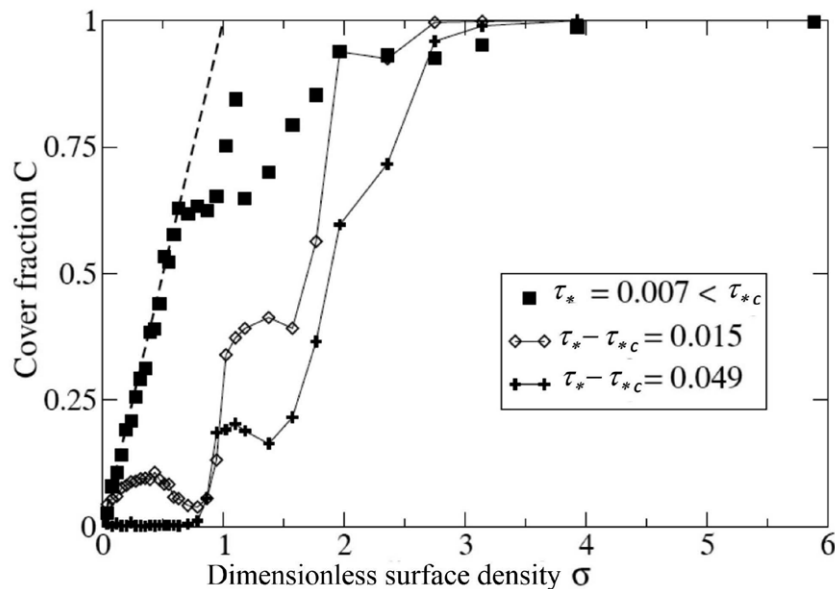


Figure 154. The static cover fraction C obtained by the numerical simulations of Aubert *et al.* (2016) is plotted as a function of the dimensionless surface density σ , measuring the intensity of sediment supply, for different values of the Shields number. The dashed line represents the function $C = \sigma$ (modified from Aubert *et al.*, 2016) (work distributed under the Creative Commons Attribution 3.0 License).

of sediments increases, the dimensionless surface density increases and saturates when exceeding some threshold value σ_0 which increases linearly with the Shields stress. The asymptotic value of the bedload flux of sediments (measuring the bedload transport capacity of the stream) increases with the Shields stress following a trend compatible with known bedload transport formulas. The

static cover fraction C , i.e. the alluviated fraction of the bedrock surface, is plotted as a function of the dimensionless surface density, for different values of the Shields number in Figure 154. Below the critical value of the Shields stress, C first increases linearly with the sediment supply but departs from the function $C = \sigma$ beyond $\sigma = 0.5$ (Figure 154). Indeed a fraction of the bedrock may be covered by two layers of immobile particles, while other areas may be bare. For values of the Shields stress larger than critical, the static cover fraction is very small for $\sigma < 1$ while for larger values of σ the fraction increases until it fills the entire bedrock surface for $\sigma > 3$.

Converting the energy transferred to the bedrock surface per unit time and unit area Φ_E into an average long-term bedrock incision rate, Aubert *et al.* (2016) make predictions consistent with the experimental observations of Sklar and Dietrich (2001). This is shown in Figure 155. Various

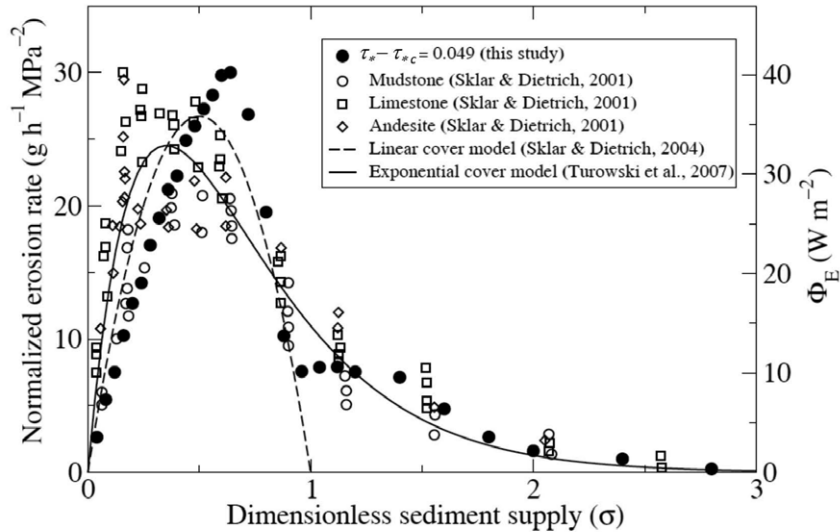


Figure 155. Numerical predictions of Aubert *et al.* (2016) for the energy flux Φ_E transferred to the bedrock surface (full circles) are compared with erosion rates measured experimentally by Sklar and Dietrich (2001) (empty symbols), and the best fits of Sklar and Dietrich (2004) (dashed line) and Turowski *et al.* (2007) (solid line). The peak of Φ_E has been forced to coincide with the maximum erosion rate observed experimentally (modified from Aubert *et al.*, 2016) (work distributed under the Creative Commons Attribution 3.0 License).

features emerge. Firstly, the *tool* and the *cover* effects are clearly confirmed. The cover term turns out to decay almost linearly at low sediment supply, while the trend is exponential at high sediment supply, thus supporting the corrections proposed by Turowski *et al.* (2007). The total energy transferred to the bedrock surface vanishes for $\sigma > 3$ as the bedrock surface is completely alluviated at that stage.

The only feature that does not confirm previous results is the growth of the incision rate with the Shields number for given sediment supply.

Effects of fluctuations of bedrock elevation

Various contributions have emphasized the need to overcome a limit of Sklar and Dietrich (2004) model, namely the assumption that abrasion occurs on an *approximately planar* river bed. Indeed, as pointed out by Huda and Small (2014), bed irregularities may affect abrasion by saltating sediment due to a variety of factors. Firstly, the horizontal component of particle velocity is an order of magnitude larger than its vertical component, hence a *horizontal impact* transfers a much larger kinetic energy to the bedrock surface. Secondly, the impact rate likely increases. Thirdly, the near bed flow characteristics may change significantly, leading to an increased form drag and a decrease of the boundary shear stress. Fourthly, the mechanics of sediment transport is likely affected.

Huda (2013) (but see also Huda and Small, 2014) examined some of these aspects and showed that, including schematically the effects of bedrock topography leads to significant changes in the relationship between erosion, transport stage and grain size. The analysis incorporates most of the assumptions made by Sklar and Dietrich (2004), in particular it is restricted to abrasion of rock by bed load and neglects all other incision mechanisms.

Model modifications include the following. Firstly, the bed profile consists of a regular sequence of triangular 2D bumps with steeper stoss side (Figure 156) and the scale of bumps is much larger than sediment size, such that saltating grains can be modeled as point particles. Secondly, particle

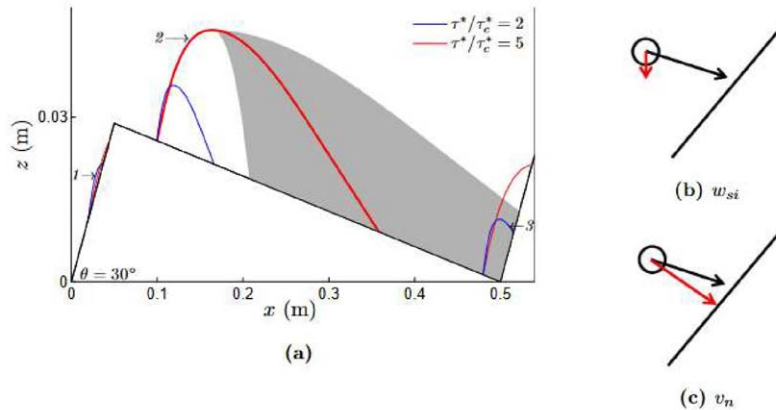


Figure 156. Sketch of the bed profile employed by Huda (2013) with the indication of sample trajectories calculated for particles of grain size of 7 mm with two different values of the Shields stress. The grey region indicates the area where trajectory 2 could fall depending on the turbulent intensity. Three types of impact emerge: (1) up-slope ascending; (2) down-slope; and (3) up-slope descending (reproduced from Figure 2.2 of Huda, 2013).

trajectories are computed assuming that the presence of bumps does not alter the solution of the equations of motion in the plane bed case. Thirdly, the calculated component of particle velocity in the direction normal to the local bed alignment is assumed to determine local erosion. The volume eroded per impact then changes significantly depending on whether impacts occurs up-slope during the descending part of the trajectory (blue region in Figure 157a), up-slope during the ascending part of the trajectory (red region in Figure 157a) or down-slope (black circles in Figure 157a). Finally, averaging over a large number of particles moving from random initial locations, using model parameters appropriate to the South Fork Eel River, California, Huda (2013) calculates the yearly averaged value of the bedrock incision rate.

Figure 157b shows the results obtained using two variants of the saltation-abrasion model: the *planar* model originally developed by Sklar and Dietrich (2004), based on a planar bed topography and the energy transferred by the vertical velocity component of particles impacting the bed; the *bump-normal* model, based on a bumped topography and the energy transfer associated with the normal component of velocity of impacting grains. Results show that the introduction of bed topography leads to erosion rates much higher (from 10 to 100 times) than for the case of planar bed. Moreover, erosion rate increases monotonically with transport stage, a trend opposite to that found in the planar case. A third feature emerging from numerical simulations concerns the dependence of erosion rate on grain size for given bed geometry, Shields stress and sediment supply. The erosion rate decreases monotonically with grain size, unlike in the planar case where maximum erosion occurs at some intermediate grain size.

While the work of Huda (2013) warns that an important role may be played by macro-roughness, however it ignores the strong interaction between the presence of macro-roughness and the turbulent flow field, as well as the fact that the process of bed alluviation is likely to be strongly affected by sharp fluctuations of bed elevation. A different (statistical) approach to account for the latter

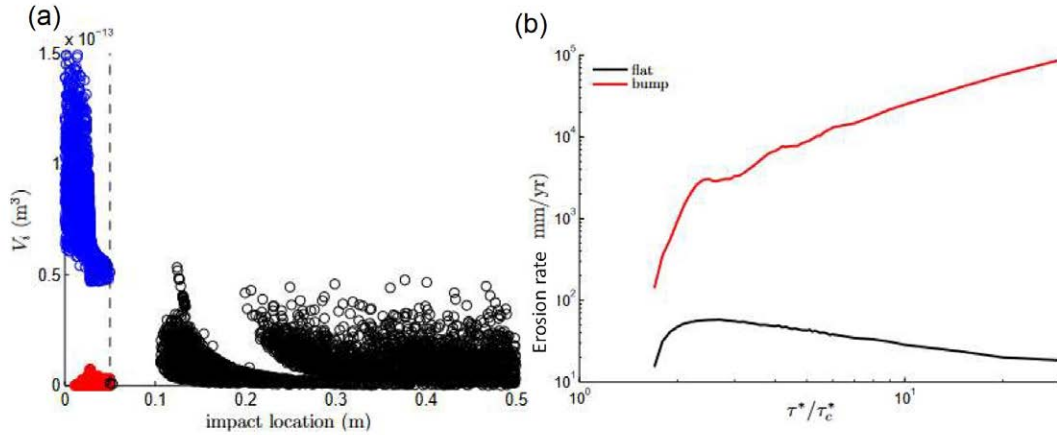


Figure 157. (a) Spatial distribution of volume eroded per impact. The dashed line shows the position of the bump crest. Blue and red points represent up-slope descending and up-slope ascending impacts, respectively, while black points represent down-slope impacts. (b) Erosion rate is plotted versus transport stage for the planar and bump-normal models for given grain size, bedform geometry and sediment supply (modified from Figures 3.1 and 3.4 of Huda, 2013).

effects was pursued by Zhang *et al.* (2015) in a paper aimed at removing another constraint of Sklar and Dietrich (2004) model, namely the assumption that local bed load transport coincides with sediment supply. We outline its main outcomes in Section 7.7.5.

Effects of wet-dry cycles on the rate of bedrock erosion

Inoue *et al.* (2017) performed laboratory experiments to ascertain the effect of wet-dry weathering cycles on the rate of erosion of bedrock river channels by saltating gravel. They found that the tensile strength of the bedrock decreases exponentially as a result of repeated wet-dry cycles according to the relationship:

$$\sigma_T = \sigma_{T0} \exp \left[-\frac{c_T N W_{a0}}{\sigma_{T0}} \right], \quad (586)$$

where σ_{T0} is the initial tensile strength, W_{a0} is the initial normalized rate of water absorption, N is the number of wet-dry cycles, and c_T is a constant.

Moreover, they confirmed that the dependence of erosion rate on tensile strength varies from σ_{T0}^{-2} for fresh bedrock to $\sigma_{T0}^{-1.5}$ for weathered bedrocks.

7.5.3 Extension of the saltation-abrasion model to total load

A limit of Sklar and Dietrich (2004) model was its restriction to conditions of dominant bedload. Indeed, as pointed out in Section 7.3, the role of suspended sediment may be as important as that of bedload or even dominant, in streams characterized by the presence of polished bedrock surfaces and erosional patterns like flutes, potholes, and undulating canyon walls. This led Lamb (2008) (but see also Lamb *et al.*, 2008) to extend the model of Sklar and Dietrich (2004) removing the constraint of dominant bedload.

The approach of Lamb (2008) followed closely that of Sklar and Dietrich (2004), hence a planar bed was considered and the bedrock erosion rate \mathcal{E} was expressed using the relationship (576). Some novelties were instead introduced in order to evaluate the rate of particle impacts per unit bed area I_r and the fraction of exposed bedrock on the river bed F_e .

The quantity I_r could not be estimated in terms of observed trajectories of suspended particles. It was then assumed to be on average proportional to the normal component of the average sediment settling flux, i.e. to the product of the near-bed sediment concentration, C_b , by the particle velocity normal to the bed, W_i . The number of particles impacting on the bed per unit area and unit time is then obtained dividing the product $C_b W_i$ by the particle volume. Hence, Lamb (2008) writes

$$I_r = \frac{A_1 C_b W_i}{\pi d^3}, \quad (587)$$

with the dimensionless coefficient A_1 accounting for the fact that not all the particles settling near the bed do impact the bed. Some of them are resuspended by near bed ejection events. Note that the settling velocity w_s of falling particles at impact depends on the fall distance and does not necessarily coincide with the terminal (constant) settling velocity as the falling distance may not be sufficient. Hence, Lamb (2008) first derived a relationship for the dependence of w_s on the falling distance. Next, he calculated an *effective falling distance* H_f performing an average over all the settling particles. This average accounted for two effects. On one hand, settling particles originated from a variable falling height z ; on the other hand, the proportion of sediments settling from the falling height z varied with z in proportion to the volumetric concentration $C(z)$.

Calculation of the average impact velocity was based on a major hypothesis: sediments were assumed to behave as passive tracers, i.e. such to follow the motion of the fluid phase. We know from Chapter 3 that this assumption is rational only for sufficiently small sediment size (small Stokes numbers) and fails for sediment of the size of gravel. This notwithstanding, Lamb (2008) summed up the component of the gravitational settling velocity with the vertical component of the turbulent velocity fluctuation w' , which was assumed to have a gaussian distribution. Integrating over all possible values of the turbulent fluctuation such that the total particle velocity was directed toward the wall, they were finally able to estimate the particle impact velocity. Note, that the importance of turbulent fluctuations is enhanced by the fact that the erosion rate depends on the cube of the individual particle velocities. For this reason, Lamb (2008) defined an *effective impact velocity* obtained by nonlinear averaging as follows:

$$W_{i,eff} = \left[\int_{-w_s}^{6\sigma_w} (w_s + w')^3 P dw' \right]^{1/3} \quad (588)$$

where P is the probability density function for particle velocity fluctuations, σ_w is the corresponding standard deviation and integration is extended to the range of non negligible positive values of particle velocity fluctuations.

Also note that, even for gravel particles, the gravitational settling velocity is unlikely to be much larger than turbulent velocity fluctuations.

The second novel feature of the analysis carried out by Lamb (2008) concerned the evaluation of the near bed sediment concentration C_b . Indeed, we know that, in alluvial rivers with unlimited sediment supply, the value of C_b under steady state conditions is set by the requirement that the settling sediment flux per unit area at the bed must be equal to the entrainment capacity of the stream from the same area. Under supply limited conditions, it is argued that the concentration of particles in suspension (hence C_b) is independent of the entrainment capacity and is rather determined by the sediment supplied to the flowing stream from the bed, banks, and the upstream reach. Hence, Lamb (2008) wrote:

$$Q_{sup} = Q_{sup}^b + Q_{sup}^s = C_b (U D \chi + V_p H_b) \quad (589)$$

Here, Q_{sup} , Q_{sup}^b and Q_{sup}^s are the volumetric flux of sediment supplied per unit width, its bedload component and its suspended component, respectively. Note that sediment is assumed to be homogeneous, i.e. the same size is transported as bedload and suspended load. U and D are depth averaged flow speed and flow depth, respectively. The coefficient χ accounts for the vertical distributions of the flow speed (assumed to be logarithmic) and of the suspended sediment concentration (assumed to follow the Rouse equilibrium profile, as shown in Figure 158). Moreover,

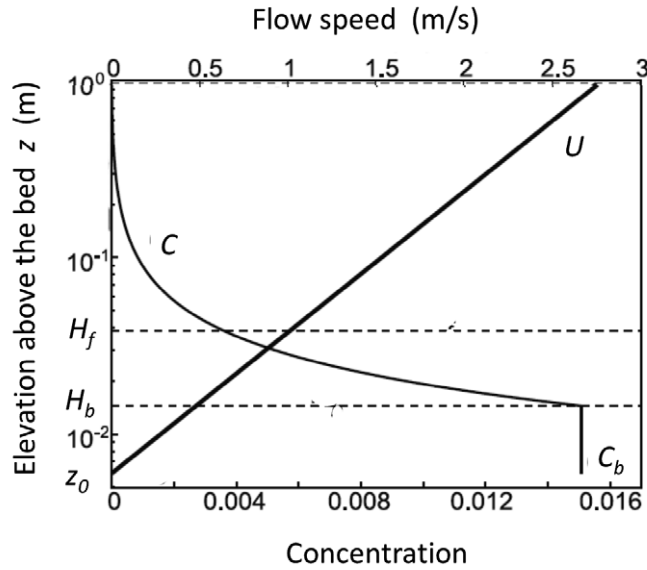


Figure 158. Sketch showing the vertical profiles of sediment concentration C and flow speed U calculated by Lamb (2008) for conditions typical of the Eel River and for a 1 mm sand. Also shown are the thickness of the bed load layer H_b and the effective particle fall height H_f as well as the near-bed sediment concentration C_b (modified from Figure 1, p. 249 of Lamb, 2008).

V_p and H_b are the average speed of saltating particles and the thickness of the bedload layer, respectively.

With the help of the above relationships Lamb (2008) expressed the bedrock erosion rate in the presence of suspended load as

$$\mathcal{E} = \frac{A_1 \rho_s Y}{k_v \sigma_T^2} \frac{Q_{sup} W_{i,eff}^3}{U D \chi + V_p H_b} \left(1 - \frac{Q_{sup}^b}{Q^b}\right), \quad (590)$$

where we recall that Q^b denotes the bedload transport capacity per unit width. Note that the supplied bedload flux per unit width can be readily obtained from equation (589), expressing C_b in terms of the total sediment flux supplied per unit width. Hence,

$$Q_{sup}^b = C_b V_p H_b = \frac{V_p H_b}{U D \chi + V_p H_b} Q_{sup}. \quad (591)$$

Using the above formulation and further empirical closures, Lamb (2008) was able to predict the dependence of the bedrock erosion rate on the controlling parameters. In particular, Figure 159 shows the predicted instantaneous erosion rate as a function of transport stage for 60 mm gravel and 1 mm sand. Note that predicted values (31 mm/yr and 10 mm/yr for the representative event of the South Fork Eel River, respectively) must be multiplied by an appropriate intermittency factor to account only for events that cause erosion. Using an intermittency factor of 0.06, appropriate to the Eel River, yields an average erosion rate of 1.9 mm/yr for 60 mm gravel and 0.6 mm/yr for 1 mm sand.

In the gravel case, erosion vanishes for transport stage in the range $\tau_*/\tau_{*c} < 1.5$ where the bed turns out to be alluviated. As the transport stage increases, the bed is exposed and erosion increases. A peak is reached at $\tau_*/\tau_{*c} \simeq 2.5$ and then erosion starts to decrease with transport stage. This trend persists for any transport stage in the constant slope case. On the contrary, in the constant depth case, erosion reaches a minimum at $\tau_*/\tau_{*c} \simeq 50$ and then increases indefinitely

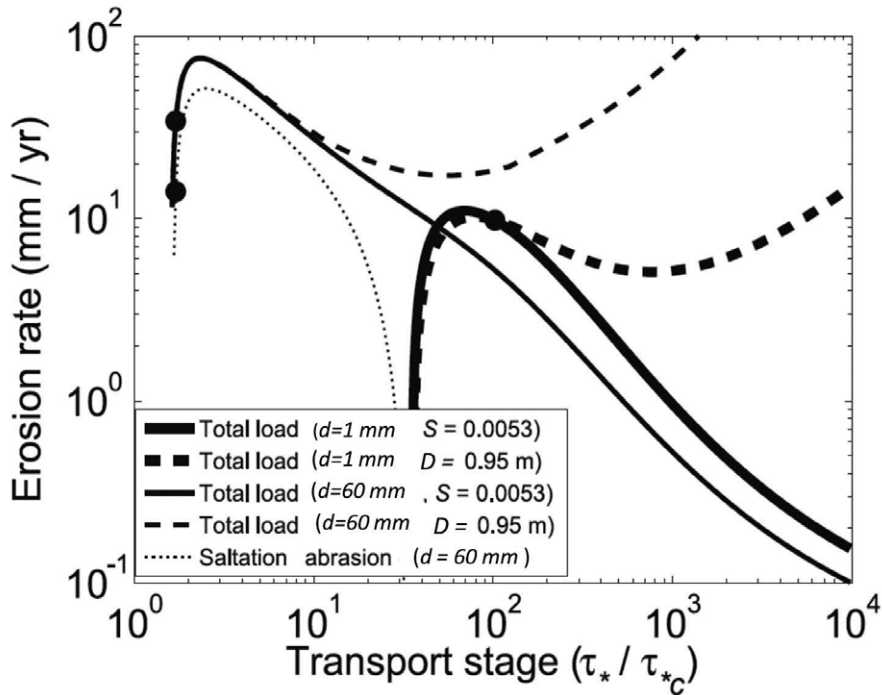


Figure 159. The erosion rate predicted by Lamb (2008) is plotted as a function of transport stage for 60 mm gravel and 1 mm sand. Solid lines correspond to the case of given channel slope ($S = 0.0053$) and flow depth varying with transport stage. Dashed lines correspond to the case of given flow depth ($D = 0.95$ m) and channel slope varying with transport stage. The rate of volumetric sediment supply is assigned at $8.9 \times 10^{-4} \text{ m}^2/\text{s}$. The dotted line shows results of the saltation-abrasion model only for 60 mm gravel. The black circles correspond to conditions for the field site of the Eel River (modified from Figure 4, p. 264 of Lamb, 2008).

with stage. In order to interpret these trends, one has to evaluate the dependence of the flow and sediment parameters controlling the erosion rate on Shields stress, for given sediment supply, grain size and channel slope (or channel depth). This exercise is left to the reader. Predictions for 1 mm sand are qualitatively similar.

It is of great interest to compare predictions from the saltation-abrasion model for the 60 mm gravel with those of the total load model (dotted line in Figure 159). The two trends are similar for small transport stage (with a slightly higher erosion peak for the total load case) but differ significantly for large transport stages, when the saltation-abrasion model forces the erosion rate to vanish. For 1 mm sand, the saltation-abrasion model invariably predicts vanishing erosion due to alluviation for almost all transport stages.

Figure 160 shows the erosion rate as a function of relative sediment supply for 60 mm gravel and 1 mm sand, and hydraulic conditions corresponding to transport stages 1.7 and 10^2 , respectively. With constant values of transport stage, flow depth, and channel slope, the saltation-abrasion model predicts a peak in erosion rate when the supplied sediment flux is one half the bed load transport capacity. Moreover, the erosion rate obviously vanishes as supply vanishes or supply equals bed load capacity, thus leading to alluviation. On the contrary, the total load model predicts that erosion is still possible for supply exceeding the bed load capacity, as the part of load transported in suspension prevents bed alluviation. This effect is obviously more pronounced for sand than for gravel.

A number of simplifying assumptions adopted in the model will require improvements. Lamb *et al.* (2008) discuss some of them. In particular, the assumption that particle impacts invariably cause erosion is unlikely to hold for fine particles whose motion approaching the wall may be damped by fluid viscosity. This is suggested by theoretical and experimental results (e.g. Joseph

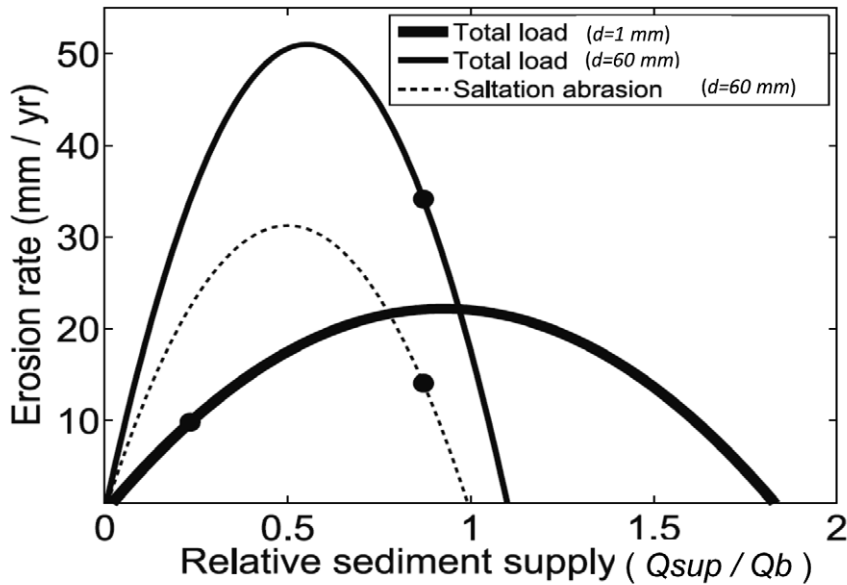


Figure 160. The erosion rate is plotted as a function of relative sediment supply for 60 mm gravel and 1 mm sand and hydraulic conditions corresponding to a transport stages equal to 1.7 and 10^2 , respectively. The dotted line shows results of the saltation-abrasion model only for 60 mm gravel. The black circles correspond to conditions for the field site of the Eel River (modified from Figure 6, p. 268 of Lamb, 2008).

and Hunt, 2004), which clearly show that the degree of damping is a function of the particle Stokes number S_t at impact conditions. Specifically, impacts of glass spheres were found to be partially damped for $S_t < 100$ and completely damped for $S_t < 30$. Improvements are also needed to model the near bed concentration established under mixed bedload-suspended load conditions, a subject very little explored in the literature.

The above limits do not undermine the merits of the total load erosion model which displays significant differences from the saltation-abrasion model for high transport stages and high relative sediment supply rates. As pointed out by Lamb *et al.* (2008), these differences may play a major role for gravels subject to very large stresses during intense floods and in mountain streams but may also be important for fine sediments, which can experience frequent high transport stages. Modeling results of Lamb (2008) were substantiated by the laboratory experiments of Scheingross (2016) (but see also Scheingross *et al.*, 2014) performed in abrasion mills identical to those used by Sklar and Dietrich (2001) in their study of erosion rates in the bedload regime. Observations allowed to identify a suspension erosion-regime with near bed particle impacts and active interchange between a highly concentrated bedload layer and an upper, less concentrated, suspended-load layer. A reduction of the erosion rates was observed moving from the bedload to the suspension regime. This was due to the experimental procedure whereby grain size was reduced, with sediment load and flow speed held constant. Figure 161a shows a comparison between the various models described so far. The saltation-abrasion model of Sklar and Dietrich (2004) predicts vanishing erosion for $d \lesssim 2$ mm corresponding to the onset of suspension. The total-load model of Lamb (2008) with no viscous damping of particle impacts overpredicts erosion rates in the suspension regime. Finally, the total-load abrasion model with impacts viscously damped for $S_t < 75$ leads to the best fit with the experimental observations of Scheingross (2016). However, note that the erosion rate in the suspension regime would be comparable or much larger than in the bedload-regime if sediment load were allowed to increase with the friction velocity holding grain size constant (Figure 161b).

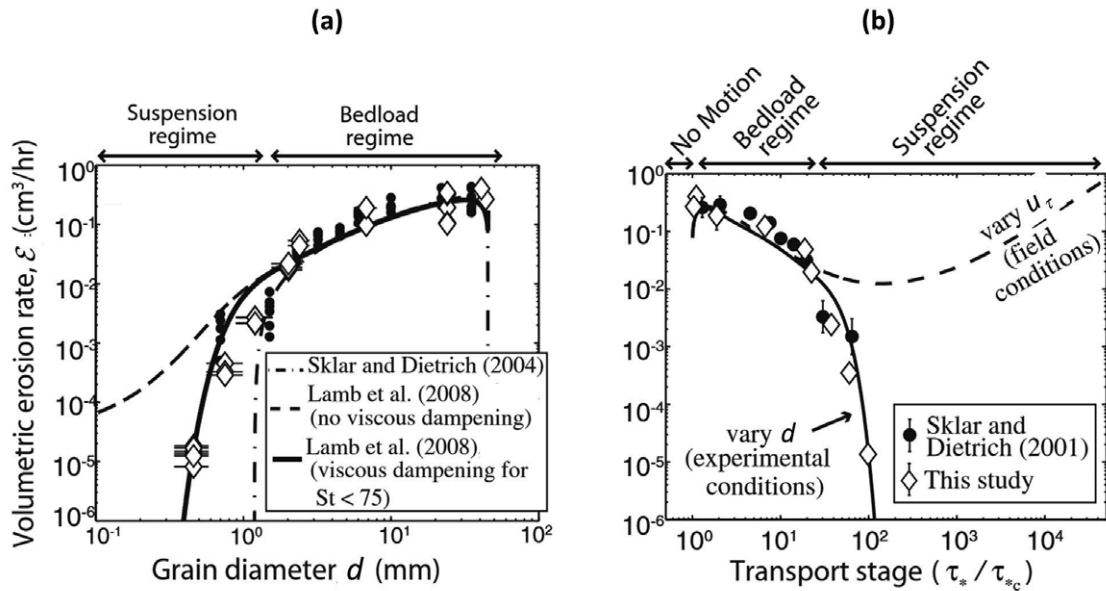


Figure 161. (a) Volumetric erosion rates observed in the foam experiments of Scheingross (2016) (\diamond) and in the limestone experiments of Sklar and Dietrich (2001) (\bullet) are compared with the saltation-abrasion model of Sklar and Dietrich (2004) (dashed dotted line), the total-load model of Lamb (2008) with no viscous damping of particle impacts (dashed line), and the total-load abrasion model with impacts viscously damped for $St < 75$, which leads to the best fit with the experimental observations (solid line). (b) Volumetric erosion rates are plotted as a function of the transport stage in the two cases of variable grain size (continuous line) and variable friction velocity (dashed line) (modified from Figures 3.3 and 3.4 of Scheingross, 2016).

7.6. Mechanics of bedrock channel incision

7.6.1 Insight on the bedrock incision process from laboratory observations

Various laboratory investigations of the bedrock incision processes have been performed. Leaving aside earlier studies, we start outlining the work of Finnegan (2007), but see also Finnegan *et al.* (2007), who explored how channel incision and morphology responded to variations of sediment supply. More precisely, in the transient evolution of the laboratory bedrock channel they investigated, channel slope, width, roughness, alluvial cover, and incision rate were left free to adjust.

The material used to model bedrock was a mixture of cement, fine sand ($< 600 \mu\text{m}$), fly ash, and a flow additive. The flume was equipped with a motor-driven auger sediment able to feed gravel at a fixed rate at the upstream end of the channel, an equipment to measure the bed load flux debouched at the downstream end of the flume and a laser scanning system for high resolution measurements of bed elevation. An initial trapezoidal channel was excavated throughout the flume (Figure 162a). Initial channel geometry, bed slope and sediment grain size were chosen such to give rise to mean Shields stresses allowing for the transport of a wide range of sediment supply rates without significant bed aggradation. Moreover, the grain size was large enough to drive rapid, measurable bed incision, while hindering suspension. Also, the channel aspect ratio was large enough to allow sediment transport in a significant portion of the cross section and produce partial bed cover.

The main observations at the end of the 60 hours experiment may be summarized as follows:

- a weakly meandering *slot incision* with width varying from 2 to 20 cm developed along the channel (Figure 162d-f);

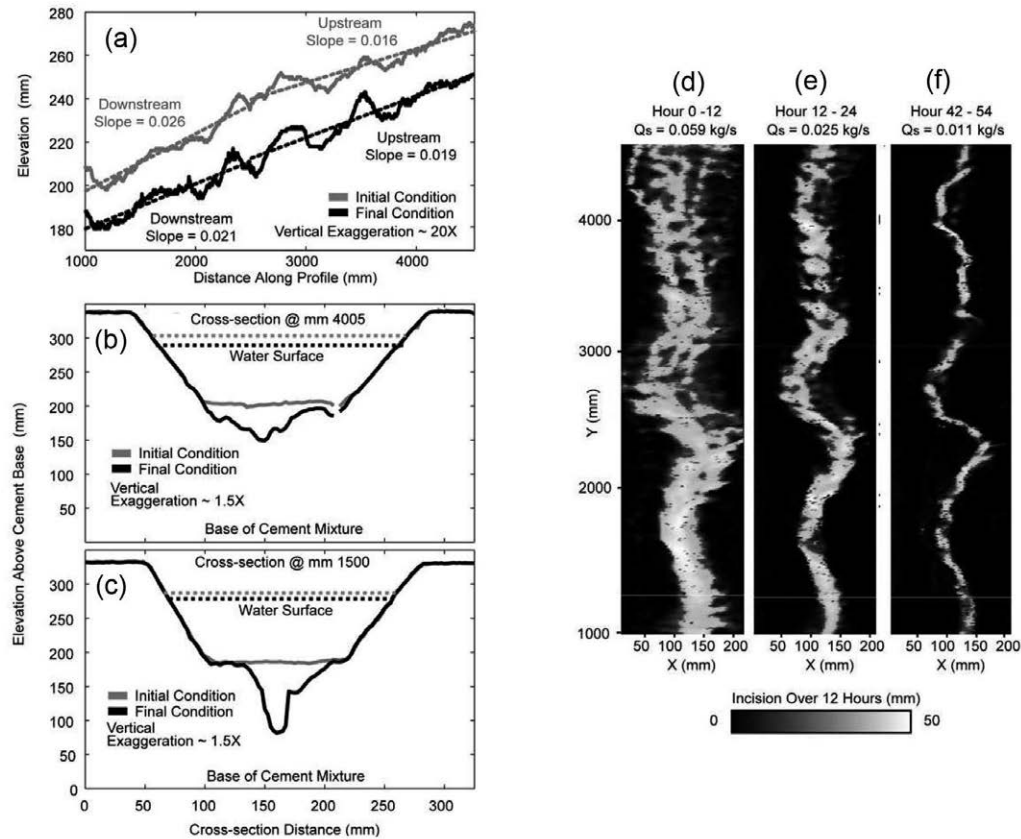


Figure 162. (a) Bed profiles at the initial and final stages of the laboratory experiment performed by Finnegan (2007)(Ch. 3). Dotted lines are linear fits to the upper and lower halves of the flume. (b,c) Shape of cross section and water surface elevation at two flume locations at the initial and final stages of the experiment. (d-f) Patterns and intensities of bedrock incision observed during three consecutive periods each lasting 12 h in which the sediment supply rate was set to (d) 0.059 kg/s, (e) 0.025 kg/s and (f) 0.011 kg/s. A distorted 5 : 1 scale has been used in the three plots (reproduced from Figure 4 and Figure 10 of Finnegan, 2007).

- an average bed degradation was experienced by the entire bed (Figure 162a);
- local incision reached peaks of 9 cm (Figure 162c);
- the walls of the initial trapezoidal channel were not eroded except in a few cross sections that experienced some lateral erosion at the bank toe.

A consistent response of channel incision to variations of sediment supply was observed. The Authors distinguished between slot-averaged incision (*SAI*), and bed-averaged incision (*BAI*). The former average is performed only over the bed area where the incising slot is active. Observations revealed that the *SAI* rate declined steadily when the sediment supply rate was kept constant, a condition which led to a progressively increasing alluviation of the bed area (Figure 163a-c). On the other hand, a reduction in the rate of sediment supply led to an increase of the *SAI* rate, associated with temporary removal of alluvial cover. Conversely, slot incision vanished when the rate of bed load supply increased and a thick alluvial layer filled the incised slot. Moreover, since incision was concentrated within the strip where active bedload transport occurred, the width of the incising slot varied correspondingly (Figure 163a,b).

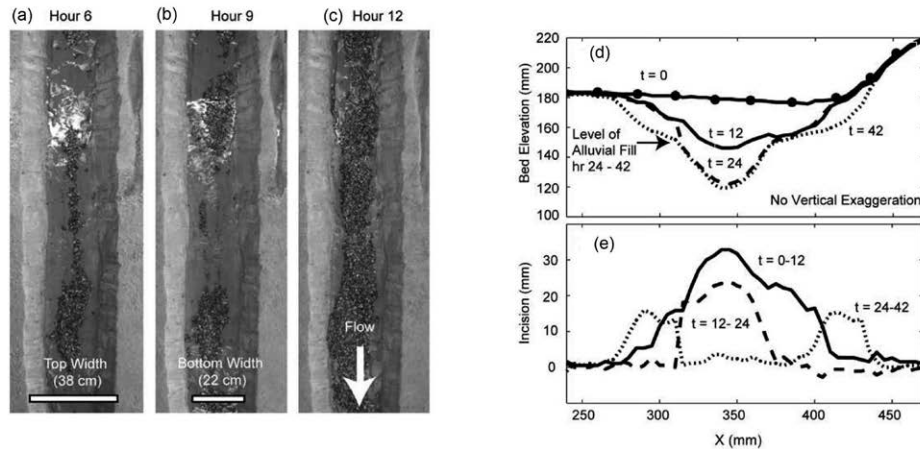


Figure 163. (a-c) Rapid variation of the extension of the alluvial cover observed in the upper ~ 2 m of the flume used by Finnegan (2007) to study bedrock channel incision for a constant bed load supply of 0.059 kg/s . (d) Changes undergone by the channel cross section as the sediment supply rate and the alluvial cover varied with time t (expressed in h). Arrows denote the approximate level of alluvial fill developed in the interval 24-42 h . (e) Vertical incision calculated as differences of the bed elevation shown in (d) (reproduced from Figure 7 and Figure 13 of Finnegan, 2007).

The above observations are summarized and detailed in Figure 163d,e showing the temporal sequence of bed elevations and the associated incisions experienced by a typical cross section. Note the initial incision driven by the first value of sediment supply rate ($t = 0-12 \text{ h}$), the subsequent narrowing and continued incision following the reduction in sediment supply rate ($t = 12-24 \text{ h}$) and the extensive alluvial cover developed as the sediment supply rate was returned to its initial value ($t = 24-42 \text{ h}$). In this last stage, vertical incision moved at the intersection of the alluvial deposit with the channel boundary, driving widening of the slot.

The final conclusion of Finnegan *et al.* (2007) was: “*Our experiments suggest that variation in sediment supply relative to transport capacity results in complex patterns of incision within a channel related to the changing width of bed load transport and due to formation of alluvial cover . . . natural stochasticity in both river stage and sediment delivery, although difficult to recreate in the laboratory, is likely to be essential to understanding the dynamics of natural channels . . . In our experiments, bed load supply varied at a much shorter timescale than the timescale of adjustment for the whole channel. Consequently, a channel with a single width never evolved. Rather, the channel was a composite of the initial channel and the slots formed under the various bed load supply rates* (Figure 164a).” Note that an implication of this work is that an alluvial cover shields the bedrock surface from the erosive effect of bedload particle impact. This issue was analyzed in detail by Turowski and Bloem (2015) through laboratory experiments where these Authors measured the decline of energy transferred through sediment covers of increasing thickness. It turned out that, although the cover thickness does heavily influence the energy transmission at a given point, “*when averaging over the whole bed, cover-free areas dominate total energy delivery, making partial energy transfer through the cover negligible when a small or intermediate fraction of the bed is covered by sediment*”, hence “*partial energy delivery to the bed through a sediment layer can be neglected for most modeling purposes*”.

Examples of bedrock channels exhibiting the presence of a sequence of wider channels reminiscent of geological periods when the channel was characterized by larger sediment supply rates are not uncommon in nature. A striking example, a reach of the Watkins Glen Canyon, New York, was pointed out by Finnegan (2007) and is shown in Figure 164b.

Experiments similar to those performed by Finnegan (2007) were reported by Johnson and Whipple (2007, 2010). They confirmed the feedbacks between erosion and sediment transport

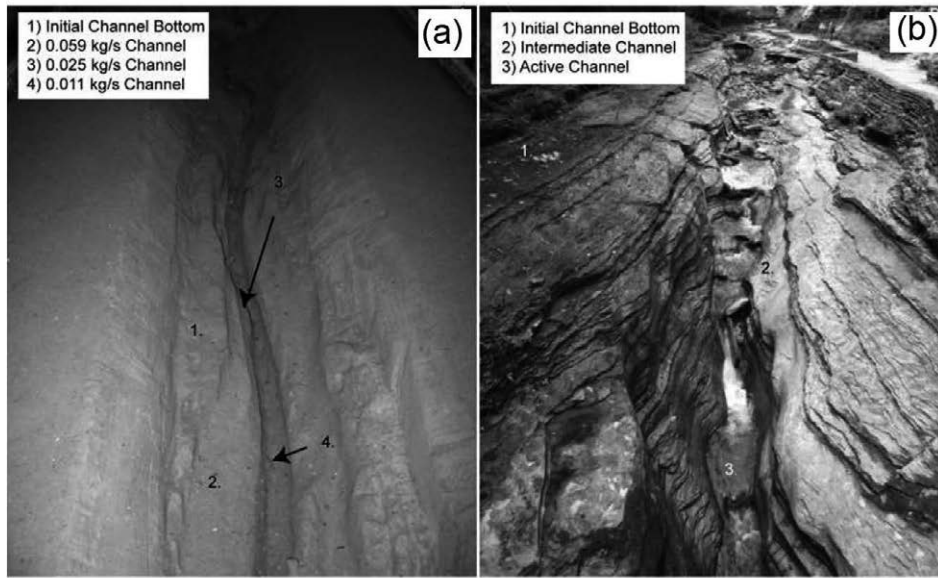


Figure 164. (a): Shape of the channel formed in the experiment of Finnegan (2007), after 60 *h* of incision at variable bed load supply rates. (b): Picture of Watkins Glen Canyon, New York. This is an example of a similar incision process observed in nature, exhibiting a reduction in channel width driven by the progressive incision. The latter occurred as sediment supply dropped throughout the late Pleistocene and early Holocene (reproduced from Figure 19 of Finnegan, 2007).

discussed above. In particular, a gently sinuous incised groove developed over most of the flume length and local erosion rate clearly depended on the local sediment flux, reflecting first tool and then cover effects. In addition, some specific observations emerged. In the highest slope experiment (10%) of Johnson and Whipple (2007), short scale oscillations of bed elevation formed and migrated downstream with migration rate somewhat larger than the vertical incision rates. Moreover, wall undulations and potholes developed, showing morphological similarities with those observed in many natural bedrock channels. Finally, the controversial prediction of the saltation-abrasion model that erosion rates would decrease at high shear stresses was not confirmed by the observations.

The experiments of Chatanantavet and Parker (2008) focused on understanding the dependence of bedrock channel alluviation on sediment supply and hydraulic conditions. Their investigation extended previous work of Demeter *et al.* (2005), which had focused on very low channel slope (≤ 0.007), very low width to depth ratios (≤ 3) chosen such to suppress alternate bar formation and fairly low bedrock roughness. The experiments of Chatanantavet and Parker (2008) started from an initial configuration characterized by the presence of some previous cover of alluvium, examined a range of slopes much larger than in previous experiments, and considered width-depth ratios between 11 and 31, much larger than in Demeter *et al.* (2005), thus allowing for bar formation. Moreover, simulated bedrock morphologies encompassed three types of roughness, namely longitudinal grooves, smooth random abrasion and rough random abrasion.

Results showed that a major control on the outcome of the experiments was the initial condition. This is clarified in Figure 165. The plot of Figure 165a shows results from three experiments which started from a bare bed. In the two runs characterized by relatively high slopes ($S = 0.02$ and $S = 0.0115$), as the sediment supply rate was increased, the bed always remained bare of sediment until the sediment supply rate reached some threshold value ($Q_{sup,0}$) at which runaway alluviation occurred suddenly. However, in the third run, characterized by lower slope ($S = 0.003$) alluviation increased gradually, i.e. the bed exposure gradually reduced to zero, as the sediment flux reached

a second threshold value $Q_{sup,al}$ different from $Q_{sup,0}$. Also, note that the decrease of the fraction of bed exposure with the ratio $Q_{sup}/Q_{sup,al}$ was found to be approximately linear as predicted by the model of Sklar and Dietrich (2004).

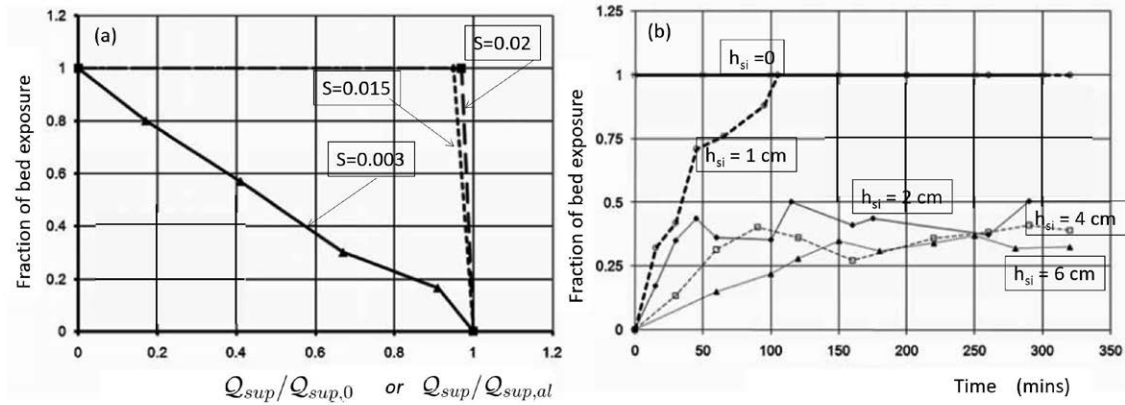


Figure 165. Results of the experiments carried out by Chatanantavet and Parker (2008). (a) Experiments starting from a bare bed. (b) Experiments starting from an initial condition of complete cover. Depending on whether the initial alluvium thickness h_{si} was below or above some critical value h_{sic} a complete wash off of the alluvial cover or a partial bed alluviation were observed, respectively (modified from Chatanantavet and Parker, 2008).

In the range of higher slopes, partial bed cover may be produced under below-capacity conditions provided the initial condition is one of complete cover. More precisely, two scenarios emerged. If the initial thickness of the alluvium h_{si} was below some critical value h_{sic} , then the alluvial cover was completely washed off as time progressed, i.e. the response of the channel replicated that found in runs where the initial condition was one of bare bed. This is shown in Figure 165b (runs with $h_{si} = 0$ and $h_{si} = 1$ cm). On the contrary, if h_{si} exceeded the critical value, the response of the channel at equilibrium displayed partial bed alluviation, i.e. cover fraction less than one (Figure 165b, runs with $h_{si} = 2, 4, 6$ cm). Moreover, the exposed fraction of bedrock area decreased as the sediment supply rate increased and reached unity for a value of the sediment supply rate $Q_{sup,al}$ significantly smaller than $Q_{sup,0}$.

Various other observations emerged from the work of Chatanantavet and Parker (2008). In particular, the exposed fraction of the bed turned out to depend strongly on the ratio $Q_{sup}/Q_{sup,al}$ as well as on the slope S , but did not show significant dependence on the Shields number. Moreover, the addition of *boulders*, in the high slope case prevented bed exposure in the range of low values of $Q_{sup}/Q_{sup,al}$.

Chatanantavet and Parker (2008) concluded that the linear formulation of Sklar and Dietrich (2004) for the relationship between the degree of bedrock exposure and the ratio of sediment supply rate to transport capacity is appropriate for low bed slopes (less than 0.005 in their experiments) or for very large bed roughness (say in the presence of boulders). The discontinuous model, whereby the bed configuration shifts abruptly from *bare* to *alluviated* as the sediment supply exceeds the transport capacity (Howard *et al.*, 1994) applies to sufficiently high slopes (larger than 0.015 in their experiments).

Hodge and Hoey (2012) revisited the work of Chatanantavet and Parker (2008) with the help of a cellular automaton model and concluded that the behavior displayed in Figure 165 is crucially dependent on the difference in grain dynamics on bedrock and alluvial surfaces.

Experimental observations aimed at investigating how the bed roughness affects the alluvial cover were performed by Inoue *et al.* (2014) on a 0.8 m wide and 300 m long artificial channel excavated near the left bank of a reach of the Ishikari River, Japan. Their main conclusion was that hydraulic roughness decreases as the alluvial cover increases. Moreover, the erosion rate of

cover-free sections was found to be proportional to the sediment supply rate and independent of the bed shear stress.

More recently, Mishra and Inoue (2020) have further investigated the same issue and found that the dependence of the alluvial cover on sediment supply rate is controlled by hydraulic roughness. More precisely, if the hydraulic roughness of the bedrock substrate is larger than the hydraulic roughness of the alluvial bed, then the alluvial cover increases proportionally to the sediment supply rate and reaches an equilibrium state. In the opposite case, i.e. bed smoother than transported sediment, no deposition occurs unless the rate of sediment supply exceeds the transport capacity, such that the whole bed is abruptly alluviated.

The experimental findings discussed in this section have generated various theoretical efforts to develop physically based models of the morphodynamics of bedrock and mixed bedrock-alluvial channels that will be discussed in the next sections.

7.6.2 1D incision models

Sklar and Dietrich (2008) investigated implications of the saltation-abrasion model at a landscape scale, and used their model to assess the relative merits and limits of various other models.

They first show how the saltation-abrasion model, which is based on the analysis of individual particle impacts, i.e. on processes involving small spatial and temporal scales, can be scaled up in time and space such to interpret the process of landscape adjustment to rock uplift. The scaling up procedure involves an estimate of various parameters, namely an intermittency parameter measuring the fraction of total time during which a conveniently defined *representative discharge* occurs, the fraction of the total runoff carried by high flows and the bedload fraction of the total load.

They next apply their model to the prediction of the channel slope at equilibrium S_e . Under equilibrium conditions, one can set $U_t = \mathcal{E}$ (recall equation (569)) and write the bedrock incision formula (583) in the form:

$$U_t = \frac{0.08 (s-1) Y g}{k_v^2 \sigma_T} \frac{Q_{sup}}{\sqrt{\frac{S_e R_h}{(s-1) d \tau_{*c}} - 1}} \left(1 - \frac{Q_{sup}}{Q^b}\right) \left[1 - \frac{g S_e R_h}{w_s^2}\right]^{3/2}, \quad (592)$$

with R_h hydraulic radius of the stream treated as uniform. This equation can be solved for the equilibrium slope S_e once the rock properties, sediment size, representative flow rate and sediment supply rate are given. Note, that R_h is also dependent on S_e through Chézy relationship. Parameters were tuned by the Authors such that the model would predict the assumed long-term incision rate at the South Fork Eel reference site. Their calculations showed that the channel slope at steady state attains typical values in the range 3×10^{-3} - 3×10^{-2} as the rate of tectonic uplift varies in a wide range (Figure 166).

Variations of the equilibrium slope are found to depend mainly on grain size, with the supply rate of coarse sediments playing the second most important role. Changes in rock uplift rate and rock strength do not affect the equilibrium slope significantly except for their possible indirect influence on the size distribution of sediments delivered to channel networks by hillslopes. Finally, comparison between the saltation-abrasion model and a range of other bedrock incision models, shows that each of them fails to capture at least one of the four effects of sediment emerged from the saltation-abrasion model (threshold of motion effect, cover effect, tool effect, suspension).

A notable observation concerns the actual existence of a steady-state profile. Indeed, the saltation-abrasion model of Sklar and Dietrich (2004) predicts that the rate of bedrock incision by bedload abrasion increases with excess shear stress up to a maximum, attained when the progressive elongation of saltation hop trajectories leads to a reduction of the particle impact frequency at a rate faster than the rate of increase of impact energy. Hence, for given discharge, sediment supply, grain size and rock strength, a slope producing the maximum possible incision rate exists. If the latter is smaller than the rate of rock uplift, then steady state cannot be achieved throughout the profile. The importance of this observation is related to the interpretation of field

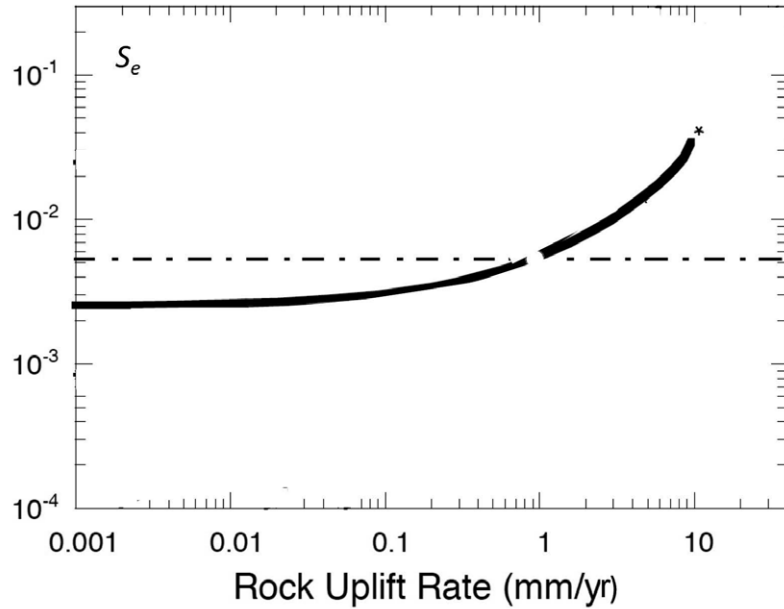


Figure 166. Channel slope at steady state according to the saltation-abrasion model of Sklar and Dietrich (2006) is plotted as a function of the rate of tectonic uplift. Representative parameters were chosen such that the model predicts the long-term incision rate estimated for the South Fork Eel reference site (modified from Sklar and Dietrich, 2006).

observations which suggest the frequent occurrence of knickpoints and fluvial hanging valleys at junctions when the small tributaries are characterized by lithology more resistant than that of the main channel (Crosby, 2006; Crosby *et al.*, 2007). Indeed, if the slope of the tributary exceeds the maximum, then a further increase in slope leads to lower values of the incision rate, hence a runaway increase in slope with the formation of a knickpoint can occur (Figure 167). As pointed out by Sklar and Dietrich (2008), for steady-state relative base level lowering the knickpoint can then grow infinitely large.

In the work of Sklar and Dietrich (2008) the saltation-abrasion model is used to further investigate the relative influence of discharge, grain size, sediment supply, rock uplift rate and rock strength on the *concavity* and *relief* of the bed profile. Scaling up of the model is achieved as in Sklar and Dietrich (2006), hence all transport of coarse sediment and bedrock incision is assumed to take place during a representative high-flow discharge with duration equal to some fraction $F_t = 0.0437$ of the total time. The long-term incision rate \mathcal{E}_t is then evaluated as $\mathcal{E}_i F_t$, with \mathcal{E}_i instantaneous incision rate calculated using Sklar and Dietrich (2004) formula. Assuming a steady state condition, it follows that the tectonic uplift rate (\mathcal{U}_t) must be equal to the long-term incision rate \mathcal{E}_t . This condition allows one to estimate the coarse sediment supply rate Q_{sup} . Indeed the rate of production of sediment volume (due to long-term incision) delivered to a given cross section can be expressed as $\mathcal{E}_t \mathcal{A}/F_t$. Hence,

$$Q_{sup} = \frac{\mathcal{E}_t \mathcal{A}}{F_t} F_b, \quad (593)$$

where F_b is the bedload fraction of the total sediment load. Channel width and flow discharge were assumed to be power functions of drainage area \mathcal{A} , which was expressed as a given power function of distance downstream of the channel head. Similar assumption was made for grain size. With the help of the above assumptions, Sklar and Dietrich (2008) can impose the steady state condition, namely rate of rock uplift balancing rate of bedrock incision, at any cross section along the river profile.



Figure 167. Google Earth image of a part of the Waipoua River catchment in the North Island of New Zealand, showing sub-catchments separated from the main stem by large steps in channel elevation.

They also introduce an intuitively appealing decomposition of the total shear stress τ_t into three components

$$\tau_t = \tau_c + \Delta\tau_{Q_{sup}} + \Delta\tau_{\mathcal{E}}, \quad (594)$$

with τ_c shear stress required to initiate grain motion, $\Delta\tau_{Q_{sup}}$ increment of shear stress required to transport the bedload at the supply rate and $\Delta\tau_{\mathcal{E}}$ further increment of shear stress required to erode bedrock at the rate of rock uplift. Analytical expressions for the first two components are readily obtained from the definition of critical Shields stress and from the bedload transport formula employed. The further contribution $\Delta\tau_{\mathcal{E}}$ can be determined from Sklar and Dietrich (2004) erosion formula.

The decomposition (594) is best illustrated in the plane defined by the relative sediment supply (Q_{sup}/Q^b) and the transport stage τ_*/τ_{*c} . Figure 168 shows this plane where contours of the dimensionless bedrock incision rate ($\hat{\mathcal{E}}$) are plotted according to Sklar and Dietrich (2004) saltation-abrasion model. The bed keeps fully alluviated for values of τ_{*t} less than $\tau_{*c} + \Delta\tau_{*Q_{sup}}$. As the latter threshold is overcome, i.e. some bed shear stress $\Delta\tau_{*\mathcal{E}}$ is available for erosion, then bedrock incision occurs. The heavy line shows a typical trajectory followed as τ_{*t} increases for a representative case. Increasing the shear stress, a fraction of the channel bed is exposed as the transport capacity exceeds supply (downward shift of the plotting position) and incision occurs.

An example of steady-state profile was calculated by Sklar and Dietrich (2008) using values for the relevant physical parameters appropriate to the South Fork Eel River, in Northern California (Figure 169). For simplicity, the rock uplift rate, the rock strength, the channel roughness and

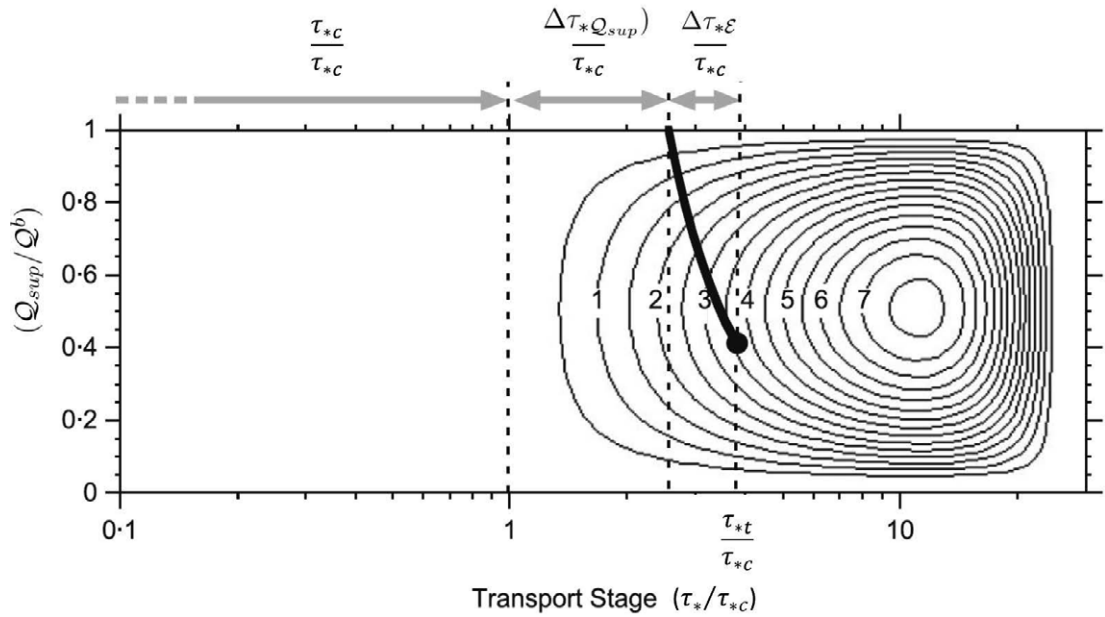


Figure 168. Illustration of the decomposition of the total dimensionless Shields stress τ_{*t} into its three contributions (τ_{*c} , $\Delta\tau_*Q_{sup}$, $\Delta\tau_*\mathcal{E}$) in the plane defined by the relative sediment supply Q_{sup}/Q^b and the transport stage τ_*/τ_{*c} . Contour lines denote the dimensionless bedrock incision rate $\tilde{\mathcal{E}}$. The heavy line shows the trajectory followed in this map as τ_{*t} increases for $Q_{sup} = 0.06 \text{ m}^3/\text{s}$, $d = 0.06 \text{ m}$, $B = 18 \text{ m}$, $\sigma_T = 7 \text{ MPa}$ (modified from Sklar and Dietrich, 2008).

runoff were assumed to be spatially uniform. Moreover, the fraction of total load transported as bedload was also taken to be constant along the channel. Figure 169 shows that the equilibrium profile predicted by the saltation-abrasion model has the expected features: it is concave-up and exhibits approximately log-log linear scaling between channel slope and drainage area, with $\theta = 0.41$.

An attempt to assess the adequacy of various incision models to describe the *temporal development of bedrock incision* for a single bedload transport event was pursued by Beer and Turowski (2015). These Authors performed very accurate field measurements of hydraulic and bedload transport properties on an artificial bedrock slab installed in a steep mountain stream. They used these data to evaluate the incision rate with the help of various theoretical or empirical models and then compared results of the calculations with observed values of the rate of incision, recorded with high accuracy. It turned out that, for the basin under investigation, the influence of bedload transport on erosion rate (the *tools effect*) dominated over other effects. This led the Authors to propose a simplest model for the temporal evolution of incision where the erosion rate was assumed to be proportional to bedload transport rate. The Authors conclude that “*this simple model performs similarly well or better than more complex models from the literature, including the mechanistically based saltation-abrasion model (Sklar and Dietrich (2004)), and several models from the stream-power incision model family*”. However, while this conclusion may apply to the field site analyzed in this paper, it may hardly be generalized as the importance of the *cover effect* has been confirmed by a number of field observations.

In particular, a thorough investigation of the role of sediment cover in bedrock channel incision was performed through field observations in the Henry Mountains, Utah (Johnson *et al.*, 2009). The chosen site is particularly suited for such an investigation as it contains several small channels that share tributary junctions and have incised into the same sedimentary bedrock unit (Navajo

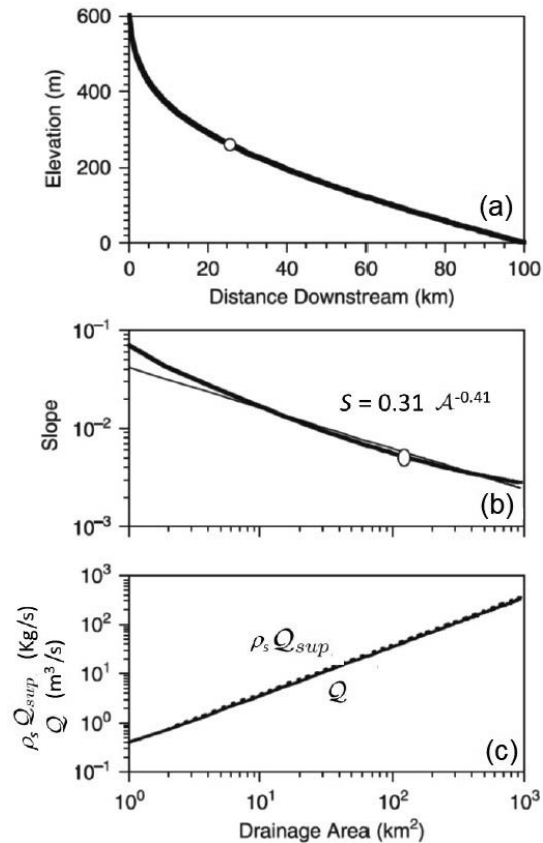


Figure 169. Steady-state profile predicted by Sklar and Dietrich (2008) for values of the relevant parameters fitting the South Fork Eel River reference site (indicated by an open circle). (a) Bed profile. (b) Reduction of channel slope as drainage area increases: model prediction (heavy line) and best-fit log-log linear regression (thin line). (c) Increase of flow discharge Q and rate of the supplied sediment mass $\rho_s Q_{sup}$ with drainage area (modified from Sklar and Dietrich, 2008).

Sandstone). Moreover, different tributaries contain differing amounts of coarse diorite clasts depending on the spatial distribution of sediment sources. As a result, the diorite-poor tributaries were found to have incised more deeply and achieved average slopes lower than found for tributaries containing abundant clasts, i.e. diorite-rich. Moreover, coarse sediment blanketing bedrock channel beds appeared to reduce the efficiency of incision, thus validating the role of the cover effect in the incision process. A further issue analyzed by Johnson *et al.* (2009) was to ascertain what mechanism sets the slope of bedrock channels. It appears that when abundant sediment is available, the channel slope needed to transport the sediment load can be larger than that needed to erode bedrock, hence it is the transport capacity to control bedrock channel slope.

7.6.3 Stability of the longitudinal bed profile and autogenic development of knickpoints

Having established the occurrence of an equilibrium longitudinal bed profile, it is natural to investigate whether such equilibrium state is stable. This is a fairly wide subject recently reviewed by Scheingross *et al.* (2020) and may be described as the shaping of erosional landscapes by what geomorphologists call *autogenic* mechanisms. In our language, they are essentially free unstable responses of erosional environments to the occurrence of spontaneous perturbations. Here, we briefly discuss one of the various processes reviewed by Scheingross *et al.* (2020), namely the autogenic development of knickpoints introduced in Section 7.3.1.

The hypothesis that bedrock waterfalls can develop as finite amplitude evolution of cyclic steps, i.e. of autogenic erosional patterns, was tested by Scheingross (2016) (but see also Scheingross *et al.*, 2019) with the help of laboratory experiments. They constructed a steep *bedrock channel* using foam, a uniform material able to resist erosion by water and devoid of any of the lithologic heterogeneities known to cause waterfall formation in nature. The scaling of erosion rate driven by bedload transport was chosen such to simulate incision of natural rivers with a temporal scale of approx 30 years per experiment hour. The experimental observations, described in Figure 170, displayed the following sequence of processes.

- An initial formation of a slot canyon by bed abrasion and channel incision.
- The development of a sequence of small amplitude perturbations (of the order of $10^{-1} m$) in the form of convex bedrock crests followed by concave depressions, which amplified and formed cyclic steps, similar to previously observed features (Taki and Parker, 2005). These steps migrated downstream due to erosion of the upstream side of the crests; the flow was supercritical in chutes and subcritical in pools with hydraulic jumps in between (Figure 170b).
- The development of some cyclic steps into waterfalls, roughly after after 2-3 hours of experiment. Deeper pools trapped sediment that prevented further base erosion, while the following chute continued to erode and steepened. Steepening eventually led to flow detachment with the formation of a fully ventilated jet and plunge pool. Note, that, unlike cyclic steps, waterfalls did not display any significant migration.
- Waterfall destruction, after about 20 min of experiment (roughly 100 years in natural rivers) as erosion at the waterfall brink led to flow reattachment to the river bed.
- Incipient formation of a new waterfall and plunge pool as, following waterfall destruction, the plunge-pool lip upstream of the waterfall steepened.

The conclusion of Scheingross *et al.* (2019) is that knickzones and waterfalls do not necessarily represent the response of landscapes to external forcing, as commonly assumed. Rather, the above results suggest that they may spontaneously develop in uniform lithologies undergoing no external perturbation. A satisfactory theoretical interpretation of the above observations will require the formulation of a stability theory of the type proposed by Parker and Izumi (2000) and Izumi *et al.* (2017).

7.6.4 The interplay of incision and alluviation in shaping the cross section of bedrock channels

Various 2D numerical models have been proposed to determine the evolution of the cross section of bedrock channels subject to erosive actions under uniform flow conditions.

In particular, the works of Stark (2006), Wobus *et al.* (2006, 2008) and Turowski *et al.* (2009) have some common features. They quantify the erosive action of the stream in terms of some power of the excess shear stress relative to an erosional threshold, following the early approach of Howard *et al.* (1994). Hence, they are unable to account for the dependence of the incision process on the characteristics of sediment transport. Secondly, they assume detachment limited conditions, hence they ignore the possible role of the interaction between bedload erosion and alluvial cover. Thirdly, they evaluate the distribution of bed shear stress adopting simplified approaches that are adequate for sufficiently wide and smooth cross sectional shapes. These models are ultimately aimed at predicting the characteristics of the cross section at equilibrium, i.e. under conditions such that the average incision rate is equal to the rate of tectonic uplift. Hence, they provide some insight on how discharge and slope variations, as well as tectonic effects, can influence width adjustment in bedrock channels.

A different viewpoint was pursued by Nelson and Seminara (2011), who modeled the evolution of the bedrock channel shape in response to the erosive action of saltating particles carried by bed load. The basic goal of this investigation is to show that it is the shape of the channel which ultimately controls the mechanics of bed erosion and determines the fraction F_e of bed area

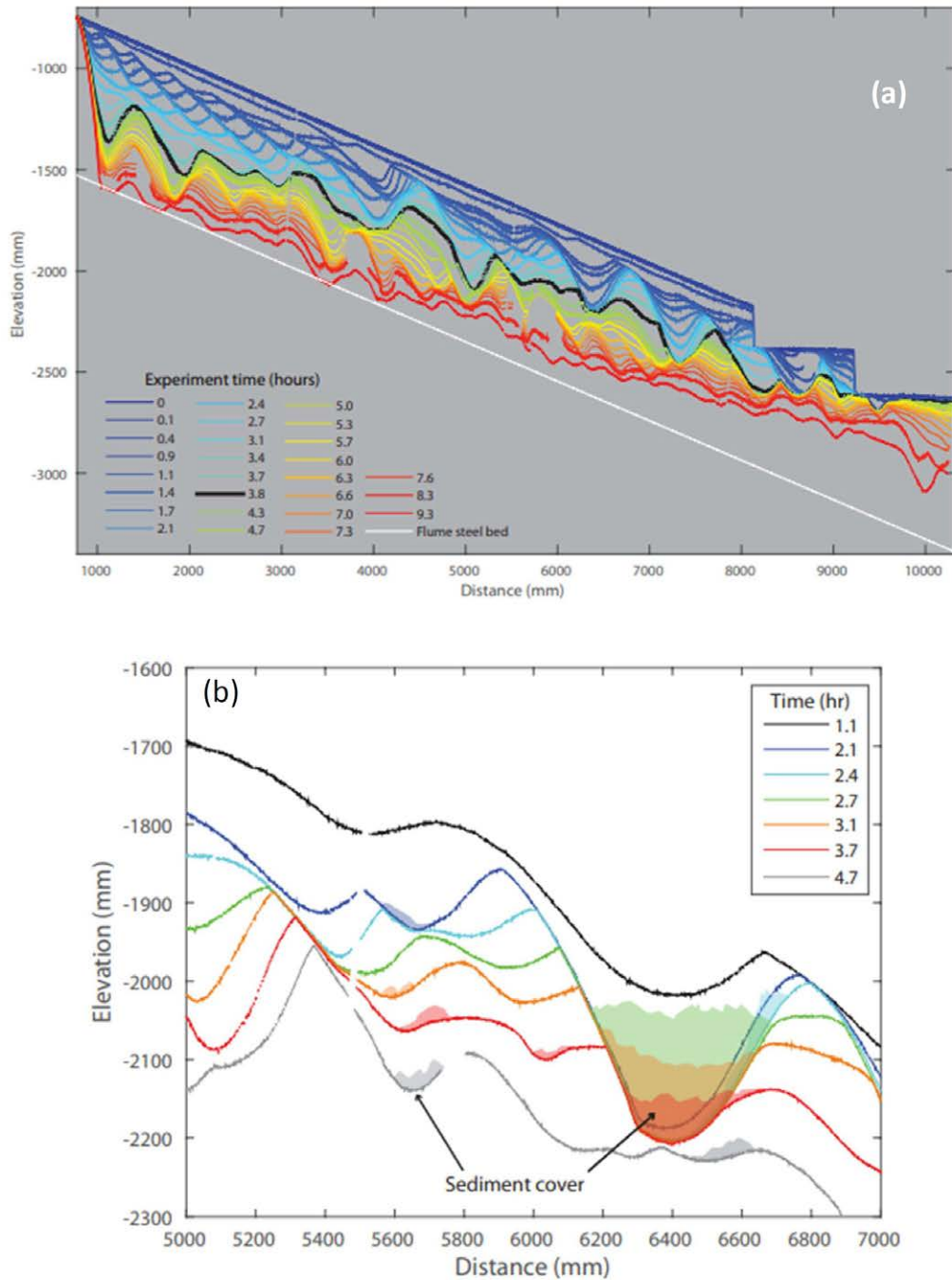


Figure 170. (a) Evolution of the profiles of the laboratory bedrock channel and of the water surface observed by Scheingross (2016) at different times. (b) Formation of cyclic steps and their development into waterfalls. Waterfall destruction and incipient waterfall rebuilding. Shaded areas mark extent of sediment cover (reproduced from Figures 6.3 and 6.10 of Scheingross, 2016).

exposed to the erosive action of saltating particles. This occurs because the lateral slope of the bed tends to concentrate the bedload flux towards the lowest parts of the cross section. The work

then clarifies the actual meaning of the F_e term in Sklar and Dietrich (2004) erosion law, which may be thought of as a parameter that incorporates the effects of channel shape on the pattern of bed load transport and local alluviation.

To illustrate this concept, we consider a straight uniform channel with the schematic cross section depicted in Figure 171, referred to cross-stream and vertical coordinates (y and z , respectively).

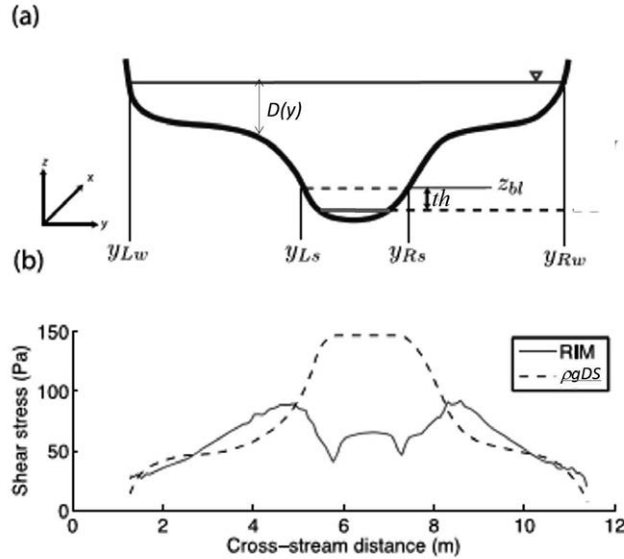


Figure 171. (a) Sketch of the configuration considered by Nelson and Seminara (2011). Bed load transport occurs between y_{Ls} and y_{Rs} , with a maximum elevation z_{bl} . Local alluviation is assumed to occur within the strip where $z_{bl} - z(y) > th$, with th empirical threshold value. In this example, the red solid horizontal line is the upper boundary of the alluviated region. (b) Distribution of boundary shear stress computed with the help of the ray-isovel model (RIM). The locally uniform bottom stress distribution $\rho g D(y) S$ is also shown for comparison (modified from Nelson and Seminara, 2011).

The fundamental assumption made by Nelson and Seminara (2011) is that, over the long-term, gravitational effects should force bed load to concentrate in the lowest portions of the channel. There, it would be transported at the *local* sediment transport capacity per unit width, $Q_b(y)$, which can be evaluated with the help of a bed load transport equation, e.g. relation (582) proposed by Fernandez Luque and van Beek (1976). With the latter assumption, it is then easy to calculate the width of the strip where bed load transport concentrates. Indeed, imposing that the total sediment flux in the cross section must be equal to the imposed sediment supply rate Q_{sup} , one finds:

$$Q_{sup} = \int_{y_{Ls}}^{y_{Rs}} Q_b(y) dy. \quad (595)$$

Here, y_{Ls} and y_{Rs} are the locations of the left and right edges of the bed load layer. These values can be iteratively determined by starting at the lowest point in the channel and moving outward along the boundary until equation (595) is satisfied. Once y_{Ls} and y_{Rs} have been determined, one can determine whether part of the channel will alluviate. Nelson and Seminara (2011) assume that alluviation occurs within the strip $z_{bl} - z(y) > th$, where z_{bl} is the bedrock elevation at y_{Ls} and y_{Rs} , $z(y)$ is the bedrock elevation at the coordinate y , and th is an alluviation threshold (see Figure 171a). Based on the observations of Finnegan *et al.* (2007) (Figure 10) and Johnson and Whipple (2010) (Figure 4), Nelson and Seminara (2011) tentatively assume that $th \sim 5d$.

Of course, in order to pursue the above procedure, one needs to know the distribution of shear stress along the cross sectional boundary. The flow model needed to achieve this goal

must be sufficiently refined to be able to describe both wide and narrow cross sections, possibly characterized by fairly sharp variations of boundary curvature. The choice made by Nelson and Seminara (2011) was to employ the ray-isovel model, described in Section 2.3.5. Figure 171b shows the computed boundary shear stress distribution. Also shown is the bottom shear stress $\tau_u(y)$ ($= \rho g D(y) S$) that would be experienced in a uniform flow with flow depth $D(y)$. Comparison shows that, in this example, $\tau_u(y)$ dramatically overpredicts the boundary shear stress in the deepest part of this relatively narrow channel.

Another novel feature of the approach of Nelson and Seminara (2011) concerns the way bedrock erosion is calculated. Bedrock erosion is again assumed to be entirely the consequence of abrasion by saltating bed load particles but the approach of Sklar and Dietrich (2004) is now adapted to be employed in the context of a local theory. As a consequence, only two of the three contributions to the erosion rate \mathcal{E} in Sklar and Dietrich (2004) model, namely the volume of bedrock eroded per particle impact (V_i) and the number of impacts per unit time (I_r), must be retained. Indeed, the model of Nelson and Seminara (2011) explicitly calculates where sediment transport occurs and, hence, the fraction of the bed area exposed in the whole cross section arises at each step from the approach outlined above. The local erosion rate $\mathcal{E}(y)$ is eventually evaluated as

$$\mathcal{E}(y) = \begin{cases} V_i(y) I_r(y) & 0 < z_{bl} - z(y) < th \\ 0 & \text{otherwise} \end{cases} \quad (596)$$

where I_r must be evaluated in terms of the local value of the bedload transport capacity per unit width $Q_b(y)$. The above formulation ensures that bedrock is eroded only at locations where bed load transport is occurring ($z_{bl} - z(y) \geq 0$) but not in topographically low areas that have been alluviated ($z_{bl} - z(y) > th$). To remain consistent with the assumptions implicit in the Sklar and Dietrich (2004) model, the erosion rate calculated in equation (596) is directed vertically. In other words, the lateral erosion driven by particle saltation over sloping surfaces is neglected.

The above model was tested applying it to the experimental setting of Finnegan *et al.* (2007). This is an ideal test case as, in that experiment, the sediment supplied to the experimental bedrock channel was varied and the channel was allowed to adapt its geometry to variations of the external forcing. Figure 172 compares the results of the numerical simulations of Nelson and Seminara (2011) with the experimental observations of Finnegan *et al.* (2007). It appears that the model, while overpredicting width and depth of erosion in some places, does capture the essential dynamics observed in the experiment. Indeed, it reproduces the formation of an erosional slot which becomes narrow when the sediment supply is reduced (in the time interval 12 – 24 h). Also, the low part of the channel alluviates when the sediment supply is subsequently increased (in the time interval 24 – 42 h), and erosion then concentrates on the higher, lateral portions of the cavity.

Finally, Nelson and Seminara (2011) reproduce and provide a theoretical interpretation of the so-called *tools* and *cover* effects that Sklar and Dietrich (2004) modeled through the F_e term included in their formulation. To achieve this goal Nelson and Seminara (2011) derive from their local theory a cross sectionally averaged formulation, defining a laterally averaged value of the erosion rate $\bar{\mathcal{E}}$ in the form:

$$\bar{\mathcal{E}} = \frac{1}{y_{Rw} - y_{Lw}} \int_{y_{Lw}}^{y_{Rw}} \mathcal{E}(y) dy, \quad (597)$$

where y_{Rw} and y_{Lw} are the lateral coordinates of the right and left edges of the water surface, respectively. They then calculate $\bar{\mathcal{E}}$ as a function of the sediment flux Q_{sup} supplied to a parabolic channel for given average boundary shear stress.

The resulting curve is plotted in Figure 173 and compared with the corresponding curve obtained using Sklar and Dietrich (2004) model. Both of them exhibit a rising (tools-dominated) limb followed by a falling (cover-dominated) limb. Note that in the theoretical model of Nelson and Seminara (2011) the falling limb initiates when the rate of sediment supply is such that alluviation starts. Moreover, as the quantities y_{Ls} , y_{Rs} , and z_{bl} are strongly dependent upon channel shape, the shape of the theoretical curve will be different for different channel shapes.

In conclusion, in zero-dimensional saltation-abrasion models (e.g. Sklar and Dietrich, 2004; Turowski *et al.*, 2007) the shape of the curve relating erosion rate to sediment supply (Figure 173)

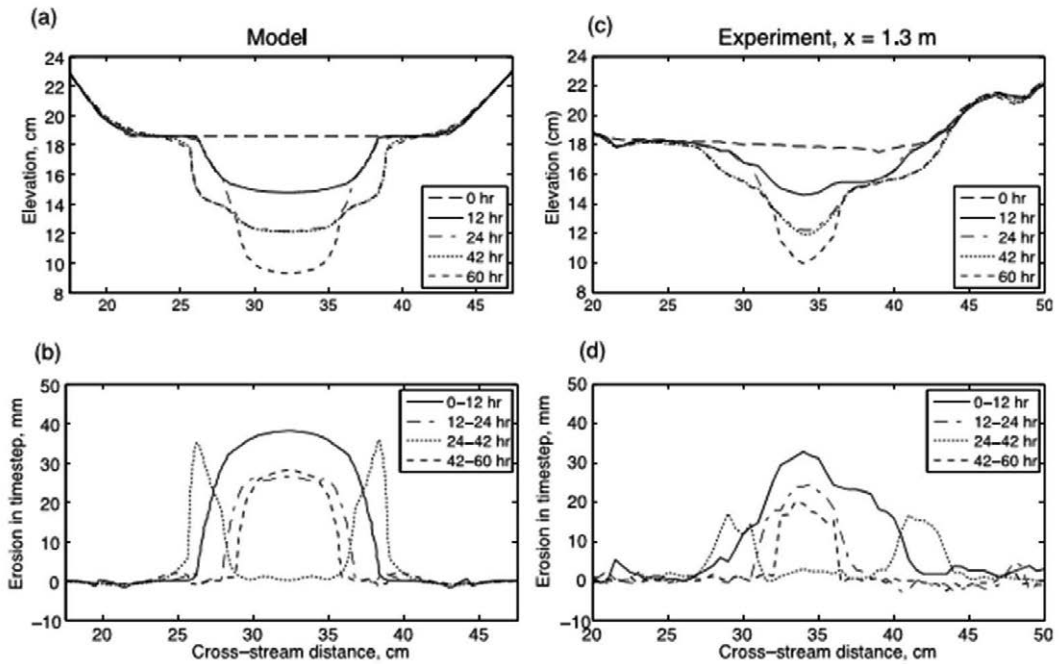


Figure 172. (a) The bed topography predicted by Nelson and Seminara (2011) for the experimental setting of Finnegan *et al.* (2007) is compared with (c) the experimental observations at the end of each period of constant sediment feed, i.e. $\rho_s Q_{sup} = 59$ g/s from 0 – 12 h; 25 g/s from 12 – 24 h; 59 g/s from 24 – 42 h; 11 g/s from 42 – 60 h. (b,d) Distribution of the erosion experienced by the bed during each feed period, obtained by differencing the bed profiles of Figures 172a and 172c (reproduced from Nelson and Seminara, 2011).

depends upon the choice of the function F_e , which is expressed in terms of the ratio between the rate of sediment supplied to the whole channel and its transport capacity. This function takes values increasing from 0 to 1 as the latter ratio increases from 0 to 1. In the local model of Nelson and Seminara (2011), essentially, the *local* value of F_e is always either 1 (in the region where bedload occurs and is assumed to be always transported at capacity) or 0 (in bare regions). It is the integrated effect of the local value of F_e over the cross section that leads to a relationship between the laterally averaged erosion rate and the sediment supplied to the whole channel similar to those of zero-dimensional models. In other words, it is ultimately the channel shape that controls where bed load occurs, alluviation is possibly produced, and erosion is active depending on the amount of sediments supplied to the channel.

7.7. Towards a theoretical framework for the morphodynamics of mixed bedrock-alluvial channels

7.7.1 Particle entrainment in mixed bedrock-alluvial channels

An important observation, common to the experiments of Finnegan *et al.* (2007) and Chatanantavet and Parker (2008), was that, even if the experiment started from a random distribution of gravel patches, a coherent pattern of bedload transport develops. The mechanism underlying the first set of observations was theoretically explained by Nelson and Seminara (2011) in terms of the gravitational effect of the lateral slope of the bed surface. On the other hand, the pattern observed by Chatanantavet and Parker (2008) consisted of a sequence of bars in the “*form of a longitudinal strip of alluvial cover that curved alternately from one side of the channel to the other*”. This strip was observed to propagate downstream and maintain a constant amount of bedrock exposure. For low sediment volumes dispersed patches and bars are typically one or two grains thick, but, as the sediment volume increases, their areal extent grows and their depth may reach thicknesses

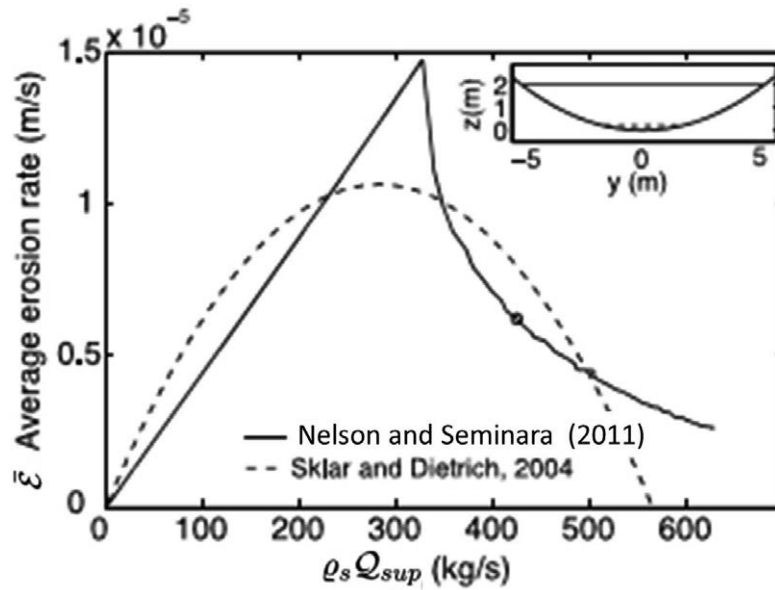


Figure 173. The width-averaged erosion rate predicted by Nelson and Seminara (2011) for the parabolic cross-section shown in the inset and constant average boundary shear stress ($\bar{\tau}_*/\tau_{*c} = 5$) is plotted versus the sediment supply rate $\rho_s Q_{sup}$. Also shown is the erosion rate computed with the help of Sklar and Dietrich (2004) model. The circled point corresponds to the water surface and alluviated layer shown in the inset figure. Parameters employed in the simulation are reported in the original paper (modified from Nelson and Seminara, 2011).

of the order of a meter. Hence, the motion of saltating particles may occur on a continuum of bed configurations associated with increasing rates of sediment supply. This finding calls for the need to analyze the mechanics of bedload transport under different conditions of bed alluviation, a subject that has been recently investigated by various Authors.

Indeed, the knowledge established in the field of sediment transport of alluvial rivers (see Chapters 3 and 4) suggests that particle entrainment is affected by the particle size, as well as by the flow velocity (hence surface roughness) and by the sheltering effect of adjacent grains.

Hodge *et al.* (2011) employ the model of Kirchner *et al.* (1990) to ascertain how differently the above factors operate in alluvial and bedrock areas of a mixed alluvial-bedrock channel. The model of Kirchner *et al.* (1990) elaborates on the approach of Wiberg and Smith (1987) (see Section 4.7.1), applying it to direct measurements of friction angles, grain projection and exposure, and small-scale topographic structure on a variety of water-worked, mixed-grain sediment surfaces. These applications show that the distribution of critical shear stress for idealized spherical grains on the measured bed topography is characterized by a probability distribution, rather than a single value. This is due to the friction angle, projection, and exposure of single grain sizes varying widely from point to point within a given bed surface. Hodge *et al.* (2011) model the bed surface of a mixed bedrock-alluvial channel as a granular material with grain size k . When a grain with size d is entrained from an alluvial portion of the bed surface both d and k are drawn from the same grain size distribution. When a grain is entrained from a bedrock portion of the surface, the size k determines the local roughness of the surface. Modeling based on this simple idea leads to values of the critical Shields stress for a particle lying within the bedrock area that are about an order of magnitude lower than for the same grain lying on the alluvial surface. This bears a direct relevance to the grain dynamics, as particles initially entrained from an alluvial region require a significantly lower shear stress when they are re-entrained from a bedrock region. Moreover, for the same shear stress, the excess shear stress ($\tau_* - \tau_{*c}$) for a grain transported on a bedrock surface is larger than for a grain in motion across an alluvial surface.

In a more recent paper Hodge *et al.* (2016) investigated the production and erosion of sediment

patches. The presence or absence of patches was shown to have a major effect on the flow hydraulics and particle entrainment. In particular, when sediment patches have formed in the flume, isolated grains are entrained at a comparable mean discharge to grains in the sediment patches. In other words, the critical shear stress in bedrock-alluvial channels appears to be a function of the extent of the sediment cover. As discharge is increased, patches are eroded at approximately linear rate. Erosion leads to patch reshaping, with patches becoming more flow oriented and sometimes more elongated.

Chatanantavet *et al.* (2013) (following previous works quoted therein) performed laboratory experiments on coarse grain saltation dynamics in supercritical flows in bedrock channels with smooth bed. Their main conclusions do not modify the general picture available from previous extensive investigations on this longstanding subject. However, the new saltation data were interpreted adopting a scaling different from the one traditionally employed. Indeed, Chatanantavet *et al.* (2013) note that a Froude (rather than Shields) based scaling is more successful to fit both the new data and data from previous investigations, encompassing a wide range of channel roughness and including alluvial transport. This is mainly due to the fact that the classical Shields scaling involves an estimate of the critical Shields stress τ_{*c} which is subject to large uncertainty.

A number of further models aimed at predicting the mechanics of the cover effect have appeared in the recent literature, including the probabilistic approach of Turowski and Hodge (2017), that describes the formation of sediment cover in terms of the probability of sediment being deposited on already alluviated areas of the bed.

7.7.2 Modeling bedload transport in mixed bedrock-alluvial channels

Let us now model the effects of sediment patches on bedload. To this aim we consider a mixed bedrock-alluvial channel and refer it to cartesian longitudinal and lateral coordinates, x and y , respectively. In non fully alluviated portions of the bed, we may assume the presence of a one-grain layer of sediments with a spatial-temporal dependent *areal concentration* $C_a(x, y, t)$, defined as the volume of the surface sediment layer per unit area of the bed. Hence, $[C_a] = L$ and its value may vary between zero and a maximum C_m corresponding to the bed being fully alluviated. Assuming that the sediment consists of spheres of uniform diameter d , a simple calculation shows that $C_m = \pi d/6$. It is then convenient to define a dimensionless areal concentration $\tilde{C}_a = C_a/C_m$ such that $0 < \tilde{C}_a < 1$, with $\tilde{C}_a = 0$ corresponding to a fully exposed bed and $\tilde{C}_a = 1$ to a fully alluviated bed.

We know that bed load particles are entrained in response to local turbulent fluctuations. It is then reasonable to formulate a simple but fundamental extension of the classical approach to bedload transport in alluvial environments to the present mixed bedrock-alluvial case. This extension is based on the following assumptions:

- the intensity of the local bed load transport rate is proportional to the areal concentration C_a of sediment available on the bed;
- for consistency with the alluvial case, the bedload flux per unit width for mixed bedrock-alluvial channels Q^{br} must satisfy the relationship

$$|Q^{br}| = \tilde{C}_a Q^b, \quad (598)$$

where Q^b is the bedload transport capacity per unit width for an alluvial channel under the same conditions;

- the direction of bed load flux deviates from the direction of the local average bottom stress vector $\boldsymbol{\tau}^b$ by an amount proportional to the bed slope vector $\nabla\eta$ according to the relationships (334a), (334b), (351), (350) established for the alluvial case. Note that in the present context, η is the sum of the elevation of the bedrock surface η_R and the thickness of the alluvial cover e .

The above assumptions deserve some comments. The first assumption may look similar to the basic relationship (191) adopted to express the bedload transport rate in alluvial channels. However, there is a fundamental difference which should be appreciated. In the fully alluviated case the areal concentration C_a is a temporally and spatially averaged quantity: averaging smooths out the small scale effects of turbulent fluctuations. As a result, C_a depends only on Shields and possibly particle Reynolds numbers. This implies that, in the fully alluviated case, C_a may be spatially and temporally dependent only *implicitly*, through the spatial-temporal dependence of the Shields stress. In the present mixed bedrock-alluvial case the spatial-temporal dependence of C_a is *explicit* as variations of C_a are also driven by spatial-temporal sediment redistribution on the bedrock surface leading to variations of sediment availability for transport.

The assumption leading to (598) is a first reasonable guess. However, as discussed in Section 7.7.1, the mechanics of bedload transport of isolated grains on bedrock may differ from that of grains saltating on alluviated portions of the bed surface. In the latter scheme, this effect is only felt through the factor Q^b , which is a function of \tilde{C}_a through the dependence of flow roughness on the amount of sediment locally available for transport under partially alluviated conditions. Indeed, Nelson and Seminara (2012) assume that the absolute roughness k_t , which controls the flow hydrodynamics and the transport capacity through the bottom shear stress, can be estimated accounting for contributions from both bedrock and sediment. More precisely, as a first approximation, they weigh the contribution of sediment roughness to total roughness by the local mean areal sediment concentration \tilde{C}_a according to the following relationship:

$$k_t = k_s [\tilde{C}_a + (1 - \tilde{C}_a) \tilde{k}_r] \quad (599)$$

Here, k_s is the absolute sediment roughness (e.g. $k_s = 2.5 d$ according to Engelund and Hansen (1967)), k_r is the absolute roughness of the rock surface, and $\tilde{k}_r = k_r/k_s$. This relationship predicts a linear variation of k_t in the range $[k_r, k_s]$ as \tilde{C}_a increases from zero to one. Progress in the understanding of bedload mechanics under mixed bedrock-alluvial conditions will likely allow to improve the above formulation in the near future. It is also worth pointing out that a similar roughness relationship was used by Luu *et al.* (2004) and, later, by Inoue *et al.* (2014).

7.7.3 Bed evolution equations for mixed bedrock-alluvial rivers

The distinct feature of bedrock channels is the coexistence of three different environments, namely fully exposed bedrock surface, partially covered bedrock surface and alluviated bed. As a result, the morphodynamic evolution of bedrock channels arises from two classes of processes characterized by significantly different time scales. A very long time scale is associated with tectonic uplift and bedrock incision while a fairly small timescale is associated with sediment redistribution and aggradation-degradation processes. As the two timescales differ by orders of magnitude, the mathematical description of the two classes of phenomena may be decoupled. Physically, this implies that the rate of sediment production driven by channel incision is so small that its contribution to sediment mass conservation may be neglected. Hence, the classical Exner equation for alluvial rivers must be replaced here by two distinct statements.

To describe the short time scale we need an appropriate statement of sediment conservation able to account for both sediment redistribution on a partially covered bedrock surface (a process characterized by no variation of bed elevation) and aggradation-degradation of the alluviated portions of the bed. Nelson and Seminara (2012) propose the following modified form of the 2D Exner equation:

$$\frac{\partial C_a}{\partial t} + (1 - p) \frac{\partial e}{\partial t} + \nabla \cdot \mathbf{Q}^{br} = 0, \quad (600)$$

where p denotes porosity of the alluvial cover. This framework is able to describe the evolution of both alluviated and non alluviated regions of the bed surface. Indeed:

- in alluviated regions $\tilde{C}_a = 1$, hence $\partial C_a / \partial t = 0$: the thickness of the alluvial cover e changes in response to the divergence of sediment transport and its changes have a direct feedback on the hydrodynamics;

- in non alluviated regions ($\tilde{C}_a < 1$), e does not change and the divergence of sediment transport leads to sediment redistribution over the bedrock surface, i.e. to spatial and temporal variations of C_a . These variations, in turn, have an indirect feedback on the hydrodynamics and local transport through modifications of the local roughness.

The long-term morphodynamic processes governing channel incision are governed by equation (569) with $\eta = \eta_R$. The elevation of the bedrock surface η_R will then evolve in response to tectonic uplift and bedrock incision.

A similar, though not identical, form of the Exner equation was used by Inoue *et al.* (2016) (following a previous formulation proposed for heterogeneous sediments by Luu *et al.* (2004)). Essentially, these Authors replace the volume of the surface sediment layer per unit area of the bed (i.e. the areal concentration C_a employed in Nelson and Seminara, 2012) by the volume of sediment transported in the bedload layer V_b , which is assumed to vary between zero and an upper *saturated* value V_{bc} . Correspondingly, the ratio V_b/V_{bc} replaces the dimensionless quantity \tilde{C}_a . The formulation is otherwise identical. There is, however, a subtle difference between the two formulations, as Nelson and Seminara (2012) postulate that the physical mechanism controlling the intensity of the local bed load transport rate is the actual availability of sediment on the bed.

7.7.4 Consistency of the theoretical framework: Free bars in mixed bedrock-alluvial channels

We now test the consistency of the framework proposed in the previous section, investigating the following issue: *is an initial, uniform distribution of sediment cover on a flat bed stable?* Answering this question will allow us to ascertain whether the adopted framework is able to predict the observed short-term tendency of sediment to concentrate into regions where distinct mixed bedrock-alluvial patterns form. Such a tendency leads to the development of a variety of patterns reported in the literature. They encompass small scale 3D isolated patterns migrating downstream like barchan dunes (e.g. Hersen, 2005), large scale free patterns of the alternate bar type where alluvial regions migrating downstream are separated by exposed portions of the bed surface (e.g. Chatanantavet and Parker, 2008), and large scale forced patterns of the point bar type, i.e. steady alluvial regions observed in inner bends of meandering rivers whose outer bed surface is exposed (e.g. Nittrouer *et al.*, 2011). In the present section we concentrate on the formation of perturbations of the alternate bar type. The case of point bars will be dealt with in the companion Monograph.

The formulation of a linear theory of alternate bar formation in mixed bedrock-alluvial channels proposed by Nelson and Seminara (2012) follows the lines of the corresponding formulation for alluvial rivers, with some notable differences. The major difference is that coupling between the hydrodynamics and the morphodynamics occurs through the dependence of bed roughness on bed areal concentration (recall equation (599)) while no perturbation of the thickness of the alluvial cover e is allowed ($\partial e/\partial t = 0$ in the Exner equation (600)). The latter assumption has a significant consequence: the stabilizing effect on the initial growth of bar perturbations associated with the laterally sloping character of the bed, a crucial mechanism for alluvial bars, is missing in the mixed bedrock-alluvial case. Of course, the assumption only applies at the initial stage of bar formation and must be relaxed as soon as sediment redistribution leads to the alluviation of part of the bed. In the absence of the gravitational mechanism the aspect ratio of the channel is no longer a control parameter for the selection of the bar wavelength. The only physical mechanism operating in the present case is the effect of the different values of roughness of the bare bedrock compared with that of sediments.

Nelson and Seminara (2012) consider a basic state consisting of a uniform flow with a uniform distribution of dimensionless areal sediment concentration $\tilde{C}_{a0} < 1$. Associated with this basic state are a basic Shields stress τ_{*0} and an associated sediment supply $\tilde{C}_{a0} Q_0^b$. A normal mode analysis of small amplitude perturbations of the basic state of the free bar type is then performed, focusing on the first lateral mode, corresponding to alternate bars in the alluvial analogy. As usual, the longitudinal structure of the perturbation is described by the function $\exp i(\lambda x - \omega t)$, representing a harmonic wave with dimensionless longitudinal wavenumber $\lambda = 2\pi/(L/B)$. Here, L is bar wavelength and B is channel half-width. This wave migrates in the downstream direction with dimensionless wavespeed ω_r/λ , and grows with dimensional growth rate $\omega_i T$, with $T(=$

$C_m B / \sqrt{(s-1)gd^3}$ relevant time scale. We do not reproduce the analysis here: the reader has developed sufficient expertise at this stage to attempt pursuing the analysis her/himself or, alternatively, may refer to Nelson and Seminara (2012). Here, it suffices to state that the above

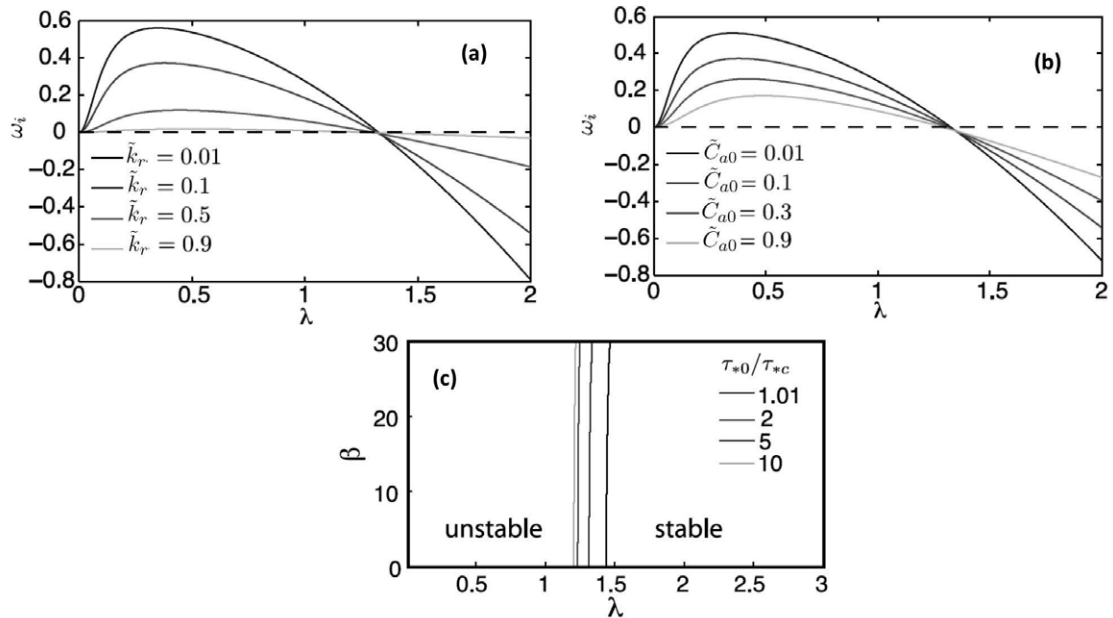


Figure 174. The dimensionless growth rate ω_i of mixed bedrock-alluvial bars is plotted as a function of the bar wavenumber λ for various values of relative bedrock roughnesses \tilde{k}_r and of unperturbed areal concentrations \tilde{C}_{a0} . (a): $\tilde{C}_{a0} = 0.3$, $\tilde{k}_r = 0.01, 0.1, 0.5, 0.9$; (b): $\tilde{k}_r = 0.1$; $\tilde{C}_{a0} = 0.01, 0.1, 0.3, 0.9$. (c) Marginal stability curves for $\tilde{k}_r = 0.1$, $\tilde{C}_{a0} = 0.3$. Perturbations grow for values of the wavenumber smaller than a threshold which is weakly dependent on stage. In all plots the values of the relevant physical parameters have been estimated from experiment 1-A2 of Chatanantavet and Parker (2008): $B = 0.45$ m, $D_0 = 0.338$ m, $d = 2$ mm, $s = 2.65$, $\tau_{*0} = 0.118$, $\tau_{*c} = 0.0549$ (modified from Nelson and Seminara, 2012).

analysis allows one to derive a dispersion relationship for the complex frequency ω as a function of the bar wavenumber λ . The function $\omega_i(\lambda)$ is plotted in Figure 174 by either keeping fixed \tilde{C}_{a0} and varying \tilde{k}_r (Figure 174a), or fixing \tilde{k}_r and varying \tilde{C}_{a0} (Figure 174b). In all cases, the growth rate is positive for values of λ smaller than about 1.4, indicating that the system is unstable to bar type perturbations with wavelengths longer than about 2 m. The maximum growth rate is found to be associated with values of λ in the range 0.35 - 0.49, corresponding to wavelengths L between 5.8 and 8.05 m. This estimate is in satisfactory agreement with the length (6.5 - 8 m) of the slightly sinuous longitudinal strip observed in the experiments of Chatanantavet and Parker (2008) (see their Figure 8). Moreover, the wave speed of the most unstable perturbations is found to be positive (between 0.014 m/s and 0.025 m/s) in agreement with observations.

Marginal stability curves ($\omega_i = 0$ in the plane (λ, β)) are nearly vertical lines (Figure 174c). This suggests that, in contrast with the case of alluvial alternate bars, the initial instability of areal sediment concentration in bedrock channels does not depend on the aspect ratio β . Moreover, instability is found to depend only weakly on stage, i.e. on the ratio τ_{*0}/τ_{*c} .

Finally, note that in the above analysis it has been assumed that the most unstable *bar* mode is the first (alternate bar) mode. This is an arbitrary assumption. Indeed, in the absence of the effects of alluviation, which are known to suppress the onset of higher order braiding modes for relatively narrow channels, we have no alternative stabilizing mechanism.

An instructive exercise to achieve a better understanding of the instability mechanism consists of investigating the limit of the dispersion relationship when the friction coefficient of the basic state tends to vanish, i.e. for $\beta C_{f0} \rightarrow 0$. Since the aspect ratio of bedrock channels is often

relatively small and a reasonable estimate for C_{f0} is smaller than 10^{-2} , the latter assumption appears to be reasonable. Neglecting terms $\mathcal{O}(\beta C_{f0}, \sqrt{C_{f0}})$ (or smaller) in the (dimensionless) dispersion relationship (S6) reported in the Appendix of Nelson and Seminara (2012), the reader will readily find the following simplified form:

$$\omega_i = -5 \frac{\tilde{C}_{a0} Q_0^b \beta C_{f0}^{3/2} (1 - \tilde{k}_r)}{\sqrt{(s-1) g d^3} [\tilde{k}_r + \tilde{C}_{a0} (1 - \tilde{k}_r)]} \left[1 - \left(\frac{3 \tau_{*0}}{\tau_{*0} - \tau_{*c}} \right) + \frac{12 \tau_{*0}}{\tau_{*0} - \tau_{*c}} \frac{\lambda^2}{\pi^2} \right] \quad (601)$$

Imposing the instability constrain $\omega_i > 0$ on (601) the reader will then find the following instability criterion:

$$\lambda < \frac{\pi}{\sqrt{6}} \sqrt{1 + \frac{1}{2} \frac{\tau_{*c}}{\tau_0}} \quad (602)$$

which predicts values for the critical wavenumber λ_c in the range $1.28 - 1.57$ as τ_{*0} varies in the interval $(\infty, \tau_{*c}]$. Note that this critical condition for instability is insensitive to variations of the relative bedrock roughness \tilde{k}_r even though the growth rate decreases as \tilde{k}_r increases and vanishes when the difference in roughness between bedrock and sediments vanishes ($\tilde{k}_r = 1$, see equation (601)).

The reader will also readily find that the shift from stable to unstable conditions occurs approximately when the lateral component of the perturbation velocity changes sign. This finding suggests that, not surprisingly, it is the sign of the lateral component of sediment transport that dominantly determines whether the local defect (excess) of concentration driven by the initial perturbation will be enhanced or damped. The weak dependence of the instability criterion on τ_{*0} also suggests that a minor role is played by perturbations of the longitudinal component of sediment transport associated with the initial perturbation of the areal concentration.

Note that the solution obtained in the limit $\beta C_{f0} \rightarrow 0$ is not uniform and fails for small values of the bar wavenumber λ , as comparison between (601) and Figure 174 immediately confirms.

Developments

Any development of the theory outlined above must abandon the linear approximation, allowing for perturbations to attain finite amplitude. The occurrence of a discontinuity, as soon as perturbations lead to alluviation of part of the bed surface, implies that a numerical approach is needed in the nonlinear regime. Inoue *et al.* (2016) have investigated numerically the development of alternate bars under mixed bedrock-alluvial conditions in the finite amplitude regime. Their formulation has similarities with that of Nelson and Seminara (2012) but also some major differences that are worth examining.

Inoue *et al.* (2016) employ the shallow water equations to describe the hydrodynamics. Closure for the sediment transport and the formulation of Exner equation are quite similar to those of Nelson and Seminara (2012). However, Inoue *et al.* (2016) do not take into account the effect of the difference between bedrock and sediment roughnesses. Since the theory of Nelson and Seminara (2012) has shown that the latter effect is the only mechanism able to trigger instability in the absence of perturbations of bed elevation, one may reasonably wonder what triggers bar instability in the model of Inoue *et al.* (2016). In order to answer this question one needs to appreciate the second major difference of the model of the latter Authors: they do not decouple the morphodynamic evolution of the channel associated with bar deposition from the incision process driven by bedrock erosion. They describe the latter process through a simple linear relationship between the rate of bedrock erosion and the product between the intensity of bed load transport and the fraction of bed exposure. As a result, simulations carried out with a sediment supply close to transport capacity, show the development of erosion driven perturbations of bed elevation that propagate downstream. It appears that only when such perturbations attain sufficiently large amplitudes, bar deposition occurs. We are then led to the puzzling conclusion that the development of secondary flows needed to drive lateral sediment transport and bar formation in Inoue *et al.* (2016) is a consequence of topographic perturbations associated with bedrock incision.

Results of simulations where sediment supply was much smaller than transport capacity exhibited the development of erosion driven longitudinal grooves.

7.7.5 The effect of macro-roughness

Bedrock channels are often characterized by hydraulically rough bedrock surfaces, with *fluctuations of bedrock elevation large compared to the characteristic size of the clasts constituting the alluvium* (Figure 142a).

These fluctuations are described as *macro-roughness* by Zhang *et al.* (2015) and the length-scale of their amplitude is denoted by L_{MR} (see sketch in Figure 175). Zhang *et al.* (2015) propose a formulation for mixed bedrock-alluvial morphodynamics where the role of macro-roughness adds novel features to the formulation of Nelson and Seminara (2012). The effect of macro-roughness is modeled in terms of a *statistical structure function* (a hypsometric curve for local bedrock topography) analogous to that used in Parker *et al.* (2000) for alluvial beds. With reference to the sketch in Figure 175, the areal fraction f_a of bedrock surface covered with alluvium is assumed to be a function of the ratio χ between the elevation of the alluvial surface e and the macroroughness scale L_{MR} . Hence, within the framework of Zhang *et al.* (2015), the spatial-temporal dependence of f_a is not *free* but *forced* by the spatial-temporal dependence of the elevation e of the alluvial surface.

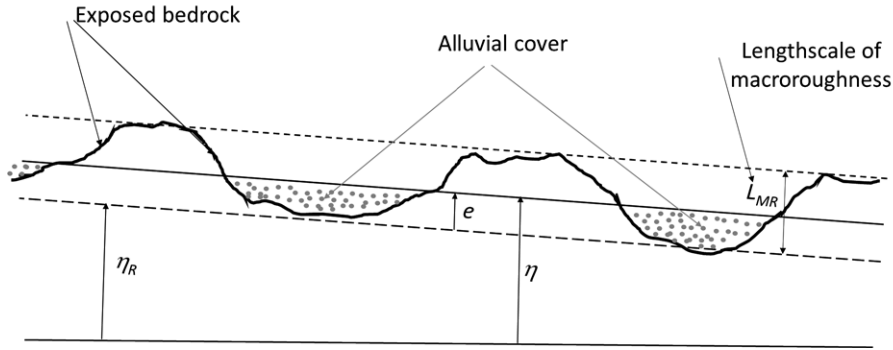


Figure 175. Sketch of the bed profile in a reach of a mixed alluvial-bedrock river and notations.

The 1D form of the Exner equation (600) under mixed bedrock-alluvial conditions and in the presence of macro-roughness then takes the following form:

$$(1 - p) f_a \frac{\partial e}{\partial t} + \frac{\partial}{\partial x} (f_a Q^b) = 0, \quad (603)$$

where $f_a = f_a[e(x, t)]$ is now some *assigned*, statistically defined, hypsometric curve. The reader should note the nonlinear character of (603), which becomes more evident performing some further algebraic manipulations to obtain:

$$\frac{\partial e}{\partial t} + c_A \frac{\partial e}{\partial x} = -\frac{1}{(1 - p)} \frac{\partial Q^b}{\partial x}, \quad (604)$$

Here, c_A is an *alluvial* wavespeed that reads:

$$c_A = \frac{Q^b}{(1 - p) f_a} \frac{df_a}{de} \quad (605)$$

Nonlinearity of (604) arises from the dependence of c_A on the bed elevation e .

Zhang *et al.* (2015) rewrite (604) in the form of an *advective-diffusion equation*, by multiplying and dividing the instantaneous bedload transport capacity Q^b by the instantaneous average slope

$S = -\partial\eta/\partial x = -(\partial e/\partial x + \partial\eta_R/\partial x)$ (Figure 175), and collecting the other terms into a diffusion coefficient. The resulting equation then reads:

$$\frac{\partial e}{\partial t} + c_A \frac{\partial e}{\partial x} + \frac{\partial}{\partial x} [\mathfrak{D}_A \frac{\partial e}{\partial x}] = -\frac{\partial}{\partial x} [\mathfrak{D}_A \frac{\partial \eta_R}{\partial x}], \quad (606)$$

where \mathfrak{D}_A is an *alluvial diffusivity*

$$\mathfrak{D}_A = \frac{1}{(1-p)} \frac{Q^b}{S}. \quad (607)$$

Note, that \mathfrak{D}_A is a nonlinear function of the local and instantaneous value of the Shields stress, which depends on the local and instantaneous value of the slope of the alluvial bed surface.

In conclusion, the Exner equation for mixed bedrock-alluvial channels with macro-roughness takes the form of a nonlinear advection-diffusion equation with a source term arising from the slope of the bedrock surface. Its solution requires closure relationships for the hypsometric curve $f_a = f_a(e)$ and for the bedload transport capacity per unit width Q^b , that allow one to determine the alluvial wave-speed c_A and the alluvial diffusivity \mathfrak{D}_A .

Zhang *et al.* (2015) point out that models that relate the cover to the ratio of sediment supply to capacity transport rate, are unable to interpret transient processes involving spatial-temporal developments of the alluvial cover. They provide some examples (alluvial rarification driven by a drop of sediment supply, development of an alluvial cover over a bare bed in response to increased sediment supply, advection-diffusion of an alluvial pulse over a bare bed) that are successfully treated with the help of (606).

Zhang *et al.* (2015) pursue also the ambitious goal to couple the simulation of processes occurring on the *fast* time scale associated with spatial-temporal developments of the alluvial cover with the process of bedrock incision driven by the saltation-abrasion mechanism, i.e. the very slow process described by a kinematic wave equation with a source term associated with tectonic uplift. The two formulations are linked by a closure relationship for the cover fraction. The reader is referred to the original paper for details of the analysis and some instructive examples.

8. Epilogue

Having completed our journey, it is natural to discuss what this book has hopefully accomplished and what further developments appear to be needed for the near future.

8.1. Achievements and limits of recent developments

In order to appreciate to what extent progress in understanding has been achieved in the last few decades, it may be worth recalling that, before the 1970s, in spite of longstanding efforts of various scientific communities, the variety of fluvial patterns existing in nature had not been systematically observed nor they had been clearly identified. The pioneering works of Leopold and Wolman (1957) and Kinoshita (1961) have essentially provided the observational foundations of large scale river morphodynamics. At the time, however, no satisfactory answer was available to fundamental questions concerning the origin of the observed patterns. This book has presented a rational theoretical framework based on the growth of scientific knowledge, able to explain, at least qualitatively, the mechanisms underlying the origin of most of the large scale fluvial patterns. We feel that the picture emerging from our assessment may be considered reasonably successful, in spite of our yet insufficient knowledge on the Mechanics of sediment transport, which affects our capability to predict the precise conditions for pattern formation and the precise characteristic features of the emerging fluvial patterns.

The main reason which determines our limited ability to analyze large scale morphodynamic processes is that they need sufficiently simple closures for bedload and suspended load. In recent years, as discussed in Chapter 2 and Chapter 3, research developments in the field of *turbulence and sediment transport modeling* have taken advantage from the ever increasing power of computational tools and this has produced a major shift in attitude of researchers, who make a growing use of sophisticated numerical approaches, with the goal to achieve detailed descriptions of turbulent processes. LES techniques have already started to play a role in contexts where the channel geometry does not justify the use of simpler 'slowly varying' type of approaches. DNS techniques are still hard to apply at the large Reynolds numbers that characterize turbulent flows in rivers. Even more so if one wishes to pursue a fully coupled simulation of flow and sediment motion when a large number of sediment particles is involved. Moreover, the complexity of two way coupling increases as sediment particles approach a rough wall and interact with it. One would like to reproduce the details of near wall coherent structures responsible for particle entrainment, as well as of the squeezing flow of the thin fluid layer between the moving particle and the wall, which controls wall-particle interactions. Also, as particle concentration increases, particle-particle hydrodynamic interactions cannot be neglected. This implies a computationally quite heavy task, unlikely to be feasible in the near future for large systems of sediment particles. Progress in this field would also allow a better understanding of the near bed processes occurring when bedload and suspended load coexist at high Shields stresses, conditions that are hard to investigate in detail in the laboratory. This is presently an active area of research, which is likely to be intensified in the future. And, even though fully coupled simulations under realistic conditions are unlike in the near future, however, as discussed in Section 3.3.3, *progress based on simulations for limited numbers of particles is quite useful to substantiate the available physically founded closures of*

sediment transport or suggest better ones.

In particular, the available closures concerning the direction of bedload transport on sloping beds are crucial for morphodynamic modeling but are based on fairly simple models, which assume plane bed conditions with dominant bed load transport. The presence of small scale bedforms as well as the combined effect of bedload and suspended load are not fully understood nor they are accounted for in a satisfactory way. This is a general, albeit insufficiently investigated, area of research that will require both numerical and experimental tools. An instructive experiment would be to let a bedform pattern develop in a straight channel under mobile bed conditions such that dunes coexist with bars. The bed could then be 'frozen' and the dynamics of individual or groups of sediment particles supplied at the entrance and saltating over the fixed dune-bar bottom pattern in clear water could be monitored in detail with the help of suitable visualization techniques. Extensive sets of data would help elucidating the fundamental mechanisms and provide a benchmark for numerical models.

We realize that we are unavoidably approaching the challenging exercise to envisage what new research directions will possibly emerge in the near future. This is a difficult task, as suggested by the famous Niels Bohr's warning: "*Prediction is very difficult, especially if it's about the future*". Hence, we will not engage in the above exercise.

However, for the benefit of young researchers, it may be useful to mention some insufficiently explored areas of research that would be worth addressing in the near future.

One of the major such areas concerns the transport of heterogeneous sediments and, in particular, the mechanism of *vertical sorting*. We have not discussed this process in detail in this book. The reason for this choice was our belief that books should assess fairly well established knowledge and, although various interesting attempts have been proposed, we feel that further analysis will be needed before the process of vertical sorting can be considered as fully understood.

Let us clarify our concerns by formulating a conceptually simple problem. Consider a rectangular, infinitely long channel, with constant slope and cohesionless bed. A given constant fluid discharge per unit width (Q) and an associated constant discharge per unit width (Q_s) of a mixture of sediments with assigned grain size distribution $F_0(\phi)$ are supplied to the channel. Also, suppose that supply equals capacity and hydrodynamic conditions are such that a periodic train of 2D dunes form at the bed interface. With the notations of Figure 176, the bed elevation η of the dune pattern may be written in the form $af(x-ct)$, with x longitudinal coordinate, c dune speed, a dune amplitude and t time. Under the above conditions, an equilibrium stationary solution must exist for the grain size distribution $F(\phi; X, z)$, with z vertical coordinate and $X \equiv (x-ct)$ longitudinal coordinate perceived by an observer translating with the constant speed of the migrating bedform. For dominant bedload, the physical mechanism underlying the establishment of this steady state solution is dominated by gravity and apparently straightforward, at least in principle: front migration leads to the burial of bedload and to the reemergence of previously buried sediments. Yet, a sound deterministic physically based model of this simplest, albeit fundamental, vertical sorting problem is unavailable.

Solving this problem would provide the basic ingredient that might then be incorporated into a more general framework, able to analyze the more complex vertical sorting process associated with the propagation of irregularly distributed bedforms (dunes or bars) in natural rivers.

We may call *stationary free bar conundrum* an insufficiently understood issue in the theory of *free bars*. This is somewhat surprising as the latter theory, presented in Chapter 6, represents one of the most successful achievements of theoretical morphodynamics. In particular, the formation and the characteristics of stationary forced bars are fully justified on theoretical ground. We know that stationary forced bars may arise in a cohesionless channel in response to non uniform boundary conditions (e.g. in a straight channel following a bend) or to geometrical spatial variations of the channel configuration (e.g. channel widening). On the contrary, the linear theory of free bars shows that non migrating features are generally not the most unstable ones (recall Figure 87), thus suggesting that they are not the prevailing perturbations, at least in the initial phase of their growth. We also know that nonlinearity slows bars down in the finite amplitude regime, but not to the extent to let them turn into stationary features (recall Figure 118b). Finally, it is not

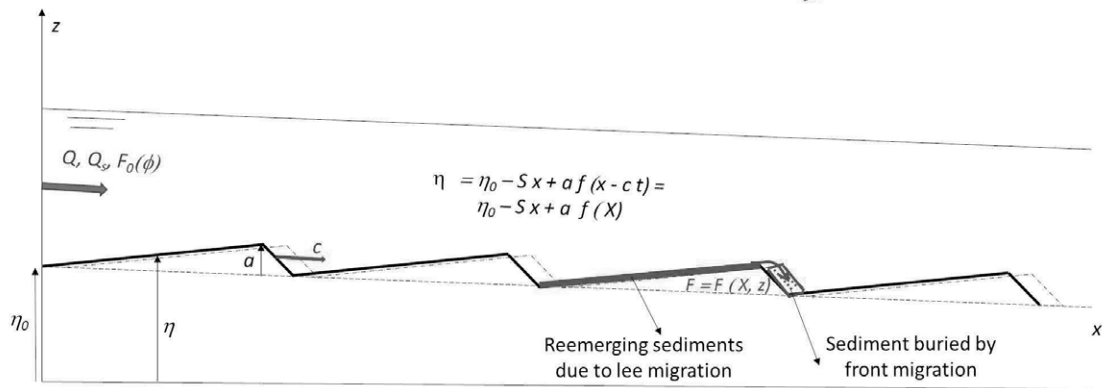


Figure 176. Sketch illustrating a periodic sequence of 2D dunes migrating in a channel with constant slope. Dunes continuously rework their cohesionless bed through vertical mixing of bedload sediments buried at the dune front which reemerge as a result of dune migration.

surprising that, on the contrary, vegetated bars may become steady features as outlined below. With such premises, how can one interpret the recent contributions discussed in Chapter 6, which claim that *free un-vegetated* bars would asymptotically tend to become stationary features? Is there some hidden, as yet unveiled, theoretical feature to be discovered?

The morphodynamics of mixed bedrock-alluvial channels also expects to be fully explored. In particular, in Section 7.7.4 we have outlined a theoretical framework which allowed Nelson and Seminara (2012) to provide a theoretical interpretation of the incipient bar formation observed in the laboratory experiments of Chatanantavet and Parker (2008). The actual soundness of the above theoretical framework needs further substantiation, possibly with the help of DNS simulations of the kind discussed in Section 3.3.3. Once a framework, will have been firmly established, then it will be possible to investigate theoretically the development of free bars in the finite amplitude regime, a process which occurs on the morphodynamic time scale in the absence of significant bedrock erosion. This study would be worth pursuing both theoretically and experimentally as it might disclose the existence of novel patterns in mixed bedrock-alluvial environments or provide a deeper understanding of the origin of patches.

We conclude our journey suggesting a further natural development of morphodynamics. Indeed, the body of research discussed in this book is the outcome of a first change in paradigm occurred in fluvial research about half a century ago, namely *the shift from hydrodynamics to morphodynamics*. More recently, a second change in paradigm has emerged in the ongoing research, namely *the intrusion of ecology into morphodynamics and the birth of eco-morphodynamics*. Indeed, the reasonably coherent theoretical framework for the analysis of large scale fluvial patterns developed in this book includes bio-geomorphic processes only implicitly (e.g. through the erosion properties of the river banks or the effect of riverbed vegetation on flow resistance). Recently, the active role of biogeomorphic processes, i.e. the interaction of biological dynamics with fluvial morphodynamics has increasingly attracted the attention of researchers in the field, motivated by the growing awareness that river management must be 'sustainable'. Various biogeomorphic processes play an active role: the above-ground biomass, besides its passive effect on the flow hydrodynamics, directly affects the morphodynamics inducing sediment trapping; similarly, the below-ground biomass affects the properties of the substrate, modifying its moisture regime and bed erodibility. Also, the role of vegetation undergoes fluctuations associated with its growth cycle, as well as with hydrological perturbations and climate evolution.

Specific contributions have examined the two-way coupling between vegetation and the development of some sedimentary patterns of interest for the present monograph. One example is

sufficient to illustrate this new line of research. Bertoldi *et al.* (2014) showed that bars may shift from an un-vegetated equilibrium state to stable vegetated patterns depending on small variations in water availability or species composition. These ideas were expanded by Serlet (2018) (but see also Serlet *et al.*, 2018), who investigated the coupled evolution of alternate bars and vegetation along a 33 km reach of the Isère River (France), in response to regulation works (straightening, embankments, flow regulation, sediment mining, and vegetation management). It emerged that, over a period of 80 years, bars decreased their density, lengthened and slowed down. Moreover, bars shifted from a bare unvegetated state to a permanent vegetated equilibrium state (Figure 177). Serlet (2018) notes that this is in contrast “with the contemporary evolution of other embanked, regulated river systems such as the Alpine Rhine (see illustration at the bottom of Figure 177) which is located in an analogous geographic setting (bottom of an Alpine valley), has a similar pre-channelization planform morphology (braided – wandering), and has an analogous history of human stressors (gravel mining, complex hydropower regulation, vegetation clearance)”. This suggests that the triggering mechanism of vegetation colonization is as yet unclear, though some interesting attempts to formulate theoretical interpretations have been recently made (Bertagni *et al.*, 2018; Jourdain *et al.*, 2020). They essentially add to the classical governing equations of morphodynamics a ‘vegetation module’, modeling the growth and decay of vegetation in response to local flow conditions. This allows one to formulate a stability analysis of the classical bar type including perturbations of the vegetation cover coupled to perturbations of flow and bed topography.

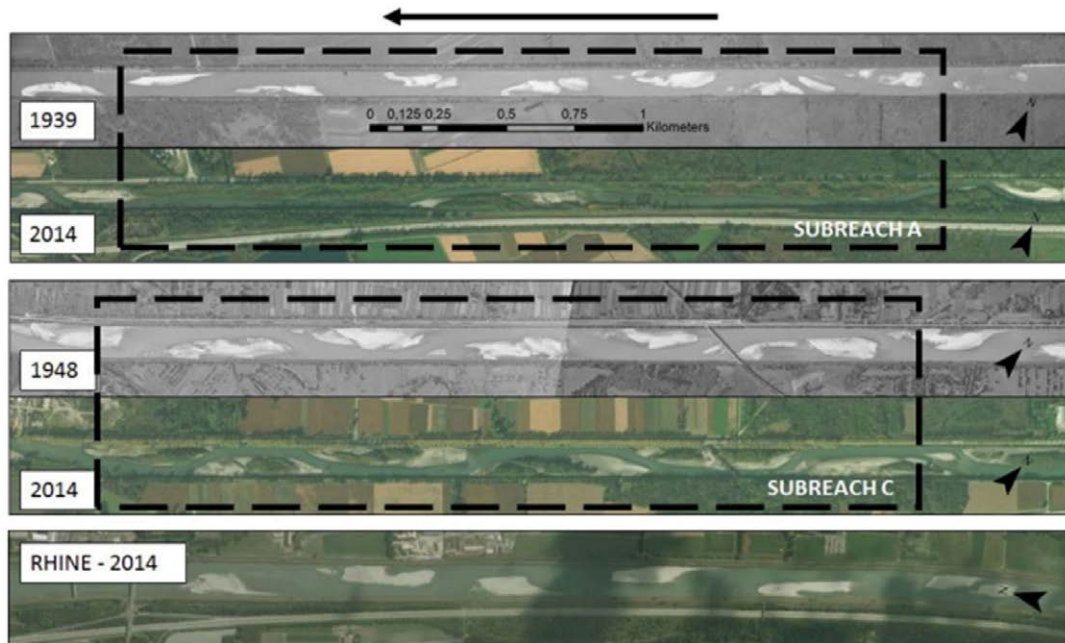


Figure 177. Images of the shift from unvegetated to vegetated bar patterns observed in two sub-reaches of the Isère River near Aiton, France, which have undergone several regulation works in the second half of the last century. Also shown is a similar reach of the embanked Alpine Rhine in 2014. (reproduced from Figure 3.19 of Serlet, 2018).

Without violating Bohr’s axiom, one may reasonably expect a growing interest of the scientific community in the general subject of *bio-morphodynamics*, although the newcomer must be aware that significant progress in the field will not be possible without a close collaboration among ecologists, geomorphologists and hydraulic engineers. Such a progress should involve also the important long term exchanges of water and sediments between the river and the flood plain, mediated through the vegetation dynamics and affecting the planform evolution of rivers.

8.2. Final warning

In his beautiful autobiography, an Italian intellectual (Pintor, 1991) writes: “*Un libro serve a chi lo scrive, raramente a chi lo legge, perciò le biblioteche sono piene di libri inutili*” (A book is useful to the writer, seldom to the reader, this is why shelves are full of useless books). We are aware of the risk pointed out by Pintor but we also encourage the reader to take good notice of the important Voltaire’s aphorism: “*The most useful books are those where the readers themselves make half the work: deepening arguments that are just outlined, correcting what appears to them as flawed, reinforcing with their own thoughts what appears to them to be weak*” (Voltaire, 1765).

9. Mathematical Appendix

The aim of this Chapter is to expose the reader to some basic concepts of *stability theory* (Section 9.3). The present treatment can be followed by readers who know the fundamental notions acquired in the classical lecture courses of Calculus offered in science and engineering schools, including the theory of complex variables and contour integration in the complex plane. We then assume that the reader is familiar with the latter topics and refer to the extensive literature on the subject for deeper understanding. In particular, the application oriented books of Aris (1962); Morse and Feshbach (1953); Carrier *et al.* (2005) and Borisenko and Tarapov (1968) are recommended.

Stability theory does also employ extensively so called *perturbation methods*, which are not usually presented in first courses of Calculus. In Sections 9.1 and 9.2 we then provide some elementary knowledge on the notion of an asymptotic expansion and introduce the reader to few perturbation techniques employed in this Monograph.

9.1. Asymptotic expansions

The material presented below cannot provide an exhaustive treatment of the topic. Our goal is to present the least amount of knowledge required for the applications discussed in the next Sections. Extensive treatments can be found in standard books on the subject (e.g. Kevorkian and Cole, 1981; Nayfeh, 2000).

9.1.1 A simple example of asymptotic representation

In order to introduce the notion of asymptotic series and asymptotic expansions, it is instructive to start with a simple enlightening example. Let us consider the so called *exponential integral function*, that can be defined in the form (Abramowitz and Stegun, 1964, Section 5.1):

$$E_1(z) = \int_z^\infty \frac{e^{-t}}{t} dt, \quad (608)$$

with z complex number such that $|\arg(z)| < \pi$. Hence, z is any complex number defined in the complex plane, with a cut along the negative real axis. Below, we restrict our analysis to real positive values of z ($z = x$). $E_1(x)$ is plotted in Fig. 178. Note that the integrand is singular at the origin. However, for our present purposes, we do not need to care about this singularity as we seek appropriate approximations of the latter integral for large positive values of x .

Also, note that representations of the integral in terms of convergent series are available in the literature (Abramowitz and Stegun, 1964, Sect. 5.1.11, p. 229). However, they are hardly useful as the number of terms they require to provide a reasonable approximation of the function increases rapidly as x increases. Below, we show that a more efficient alternative to convergent series may be obtained through the use of an asymptotic series.

Let us then perform an integration by parts of the integral (608). The reader will readily find

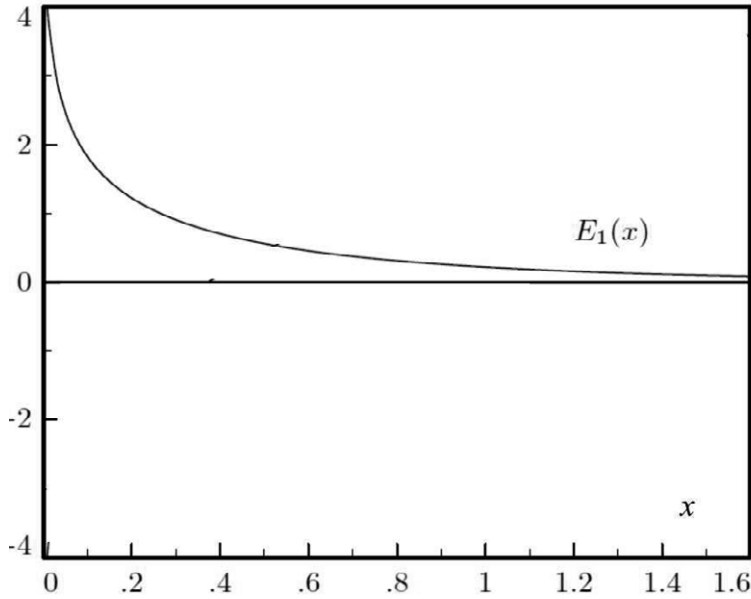


Figure 178. Plot of the exponential integral function.

 Table 1. Modulus of the n -th term of the series (609) for given x .

x	n	$ a_n(x_n, n) $
2	2	$3.38 \cdot 10^{-2}$
	5	$1.01 \cdot 10^{-1}$
	10	$3.99 \cdot 10^1$
	20	$1.57 \cdot 10^{10}$
10	2	$4.54 \cdot 10^{-7}$
	5	$1.09 \cdot 10^{-8}$
	30	$4.01 \cdot 10^{-4}$
	50	$2.76 \cdot 10^8$

the following relationship:

$$E_1(x) = e^{-x} \left[\frac{1}{x} - \frac{1}{x^2} + \frac{2!}{x^3} - \dots + \frac{(-1)^{n+1}(n-1)!}{x^n} \right] + (-1)^n n! \int_x^\infty \frac{e^{-t}}{t^{n+1}} dt. \quad (609)$$

On one hand, this representation suggests that, for given value of the real variable x , the series (609) diverges. Indeed, Table 1 shows that the modulus of the n -th term $a_n(x, n)$ of the series tends to infinity, for given x as $n \rightarrow \infty$.

On the other hand, one may take a different viewpoint. The function $E_1(x)$ can be approximated by the first n -terms of (609) provided the remainder of the latter series (the last term of (609)) can be neglected. A glance at the form of the remainder immediately suggests the following inequality:

$$\left| (-1)^n n! \int_x^\infty \frac{e^{-t}}{t^{n+1}} dt \right| < \frac{n!}{x^{n+1}} \int_x^\infty e^{-t} dt = e^{-x} \frac{n!}{x^{n+1}}. \quad (610)$$

From (610), one readily infers that, for a given number n of retained terms, the remainder tends to vanish as $x \rightarrow \infty$. In other words, for sufficiently large values of x we may obtain a

Table 2. Relative error r of the approximation achieved retaining n terms in the expansion (609).

n	x	$r(\%)$
2	2	100
	5	10
	10	2.22
	100	$2.02 \cdot 10^{-2}$
4	2	600
	5	4.6
	10	0.26
	100	$2.42 \cdot 10^{-5}$

reasonable approximation of $E_1(x)$ retaining a finite number of terms of the divergent series (609). Comparing (609) and (610), the relative error r of this approximation is found from the following relationship:

$$r \leq \frac{\frac{n!}{x^{n+1}}}{\left[\frac{1}{x} - \frac{1}{x^2} + \frac{2!}{x^3} - \dots + \frac{(-1)^{n+1}(n-1)!}{x^n} \right]}. \tag{611}$$

Table 2 shows that, for given n , r tends to vanish as $x \rightarrow \infty$. However, note that increasing n improves the accuracy of the representation only provided x is large enough. Indeed, for $x = 2$, the accuracy obtained retaining four terms is much lower than if one retains only two terms.

9.1.2 Asymptotic expansions

In order to provide some general definitions of asymptotic expansions it is preliminarily convenient to introduce the definition of *order symbols*.

We say that *the function $f(\epsilon)$ is of order $g(\epsilon)$* as $\epsilon \rightarrow 0$ and write:

$$f(\epsilon) \sim \mathcal{O}(g(\epsilon)), \tag{612}$$

provided that

$$\lim_{\epsilon \rightarrow 0} \frac{f(\epsilon)}{g(\epsilon)} = c, \tag{613}$$

with $|c|$ finite.

Similarly, we say that *the function $f(\epsilon)$ tends to its limit faster than the function $g(\epsilon)$* as $\epsilon \rightarrow 0$ and write:

$$f(\epsilon) \sim o(g(\epsilon)), \tag{614}$$

provided that

$$\lim_{\epsilon \rightarrow 0} \frac{f(\epsilon)}{g(\epsilon)} = 0. \tag{615}$$

For example the reader will readily prove that $\sin \epsilon \sim \mathcal{O}(\epsilon)$ and $\sin \epsilon \sim o(\epsilon^{1/n})$ with n any integer larger than one.

We may now define a sequence of gauge functions $g_n(\epsilon)$ ($n=1, 2, \dots$) as *asymptotic* provided that

$$g_n(\epsilon) \sim o[g_{n-1}(\epsilon)], \tag{616}$$

as $\epsilon \rightarrow 0$.

A function $f(\epsilon)$ may be represented in terms of an *asymptotic expansion* as $\epsilon \rightarrow 0$, using the asymptotic sequence $g_n(\epsilon)$ ($n=1, 2, \dots$) in the form:

$$f(\epsilon) = \sum_{n=1}^{\infty} a_n g_n(\epsilon). \tag{617}$$

For any given N , the modulus of the remainder $|f(\epsilon) - \sum_{n=1}^N a_n g_n|$ of the above series is $o[g_n(\epsilon)]$.

Most commonly, the gauge functions are chosen to be powers of the small parameter ϵ , i.e. such that $g_n = \epsilon^n$, although the latter choice may be insufficient in many physical problems.

Asymptotic expansions satisfy a number of properties. In particular:

- provided an asymptotic expansion of the type (617) exists, this expansion is unique and its coefficients are defined by the following relationships:

$$a_0 = \lim_{\epsilon \rightarrow 0} \frac{f(\epsilon)}{g_0(\epsilon)}, \tag{618a}$$

$$a_1 = \lim_{\epsilon \rightarrow 0} \frac{f(\epsilon) - a_0 g_0(\epsilon)}{g_1(\epsilon)}, \tag{618b}$$

..... (618c)

$$a_n = \lim_{\epsilon \rightarrow 0} \frac{f(\epsilon) - \sum_{j=0}^{n-1} a_j g_j(\epsilon)}{g_n(\epsilon)}, \tag{618d}$$

- the same asymptotic expansion may apply to different functions;
- asymptotic expansions are usually, but not necessarily, divergent;
- asymptotic expansions may be subjected to usual operations (linear combinations, multiplication, term by term integration, term by term differentiation).

9.1.3 The asymptotic forms of some integrals: method of steepest descents

An example of asymptotic technique is the *method of steepest descents*, also called *saddle-point method*, which proves quite useful to derive the asymptotic form of integrals of the type:

$$I(t) = \int_{\mathcal{C}} e^{t\gamma(z)} dz, \tag{619}$$

in the limit of $t \rightarrow \infty$. In (619), $z = |z|e^{i\phi}$ is a complex number, t is a real parameter, \mathcal{C} is a contour in the complex plane, $\gamma(z)$ is an analytic function in the domain \mathcal{D} of the complex plane. The basic idea is to seek an approximation for the integral by deforming the contour of integration such that the major contribution to the integral arises from a small portion of the new path, the more so as the parameter t grows. Mathematical problems of this kind are encountered for example when dealing with the long term evolution of unstable wave trains (e.g. free bars, see Section 6.3.3).

Let us briefly illustrate the method. First of all, we note that for a given value of the phase ϕ , large values of $|z|$ result in some very rapid fluctuations of the integrand. Indeed, writing the function $\gamma(z)$ in terms of its real part $f(x, y)$ and imaginary part $g(x, y)$, it is immediately observed that $\exp[itg(x, y)]$ will oscillate rapidly as t increases. The existence of such oscillations makes it difficult to evaluate the integral because of the resultant cancellations of the integrand. To overcome this problem, the integration contour needs to be suitably chosen.

In general the contour should be taken through regions where $t f(x, y)$ is positive and other regions where it is negative. The former regions are more important, since there the integrand function $\exp[t f(x, y)]$ is larger. There, it is important to reduce the oscillations associated with $\exp[itg(x, y)]$. We thus search for a contour along which $t g(x, y)$ is fairly constant and $\exp[t f(x, y)]$ is largest. The considered integral can then be rewritten as:

$$I(t) = \int_{\mathcal{C}} e^{t\gamma(z)} dz = e^{itg(z)} \int_{\mathcal{C}} e^{tf(z)} dz. \tag{620}$$

We now show that the appropriate path leading to (620) consists of the *steepest descent* issuing from a *saddle point* z_0 (Figure 179), i.e. such that

$$\left[\frac{d\gamma}{dz} \right]_{z_0} = 0, \quad \left[\frac{d^2\gamma}{dz^2} \right]_{z_0} \neq 0. \tag{621}$$

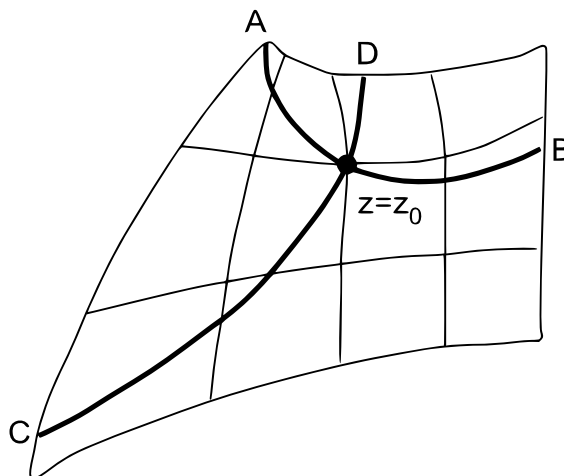


Figure 179. Choice of paths through a saddle point.

Consider the function $f(x, y)$ in a neighborhood of $z_0 = (x_0, y_0)$, geometrically this function represents a surface passing through the point z_0 . The gradient vector $\nabla f|_{z_0}$ allows one to calculate the directional derivative of the function f along the direction of the unit vector \hat{e}_s :

$$\left. \frac{\partial f}{\partial s} \right|_{z_0} = \nabla f|_{z_0} \cdot \hat{e}_s. \quad (622)$$

Hence:

$$\left| \left[\frac{\partial f}{\partial s} \right]_{z_0} \right| = |\nabla f|_{z_0}| \cos \theta, \quad (623)$$

where θ is the angle between the vector $\nabla f|_{z_0} = \left(\frac{\partial f}{\partial x}, \frac{\partial f}{\partial y} \right)$ and \hat{e}_s . This implies that the directional derivative is maximum if $\cos \theta = 1$, i.e. if \hat{e}_s is aligned with the gradient. In other words, *the gradient defines the direction of steepest ascents from $z = z_0$* (line CD in Figure 179). Similarly, the directional derivative is minimum if $\cos \theta = -1$, hence *the vector $-\nabla f|_{z_0}$ defines the direction of steepest descent* (line AB in Figure 179). Finally, if \hat{e}_s is orthogonal to the gradient, then the directional derivative vanishes: hence, the lines orthogonal to ∇f are lines of constant f .

Next, consider the function $g(x, y)$ in a neighborhood of $z_0 = (x_0, y_0)$ and the vector $\nabla g|_{z_0}$. Recalling the Cauchy-Riemann conditions for the complex analytic function $\gamma(z)$, this vector may be written as:

$$\nabla g = (g_{,x}, g_{,y}) = (-f_{,y}, f_{,x}), \quad (624)$$

and is normal to the surface $z = g(x, y)$ in $z_0 = (x_0, y_0)$. Hence, the vectors $\pm(-g_{,y}, g_{,x})$ (orthogonal to ∇g as their scalar product vanishes) are tangent to the surface. Moreover, (624) shows that the latter vectors coincide with $\pm \nabla f$, hence they lie in the direction of steepest ascent-descent through the point z_0 . Finally, the lines of constant g are also orthogonal to $\nabla g|_{z_0}$, hence they also lie in the direction of steepest ascent-descent. These lines are the appropriate integration path issuing from the saddle point z_0 . Indeed, consider the quantity $\delta \gamma = \delta f + i \delta g$. It follows that $|\delta f| \leq |\delta \gamma|$ and the quantity $|\delta f|$ is maximum in z_0 only if δg vanishes, i.e. along the lines of constant g .

The above arguments suggest that the integration path consists of the 'steepest descents' issuing from the saddle point z_0 . At this point of the complex plane, using the Taylor expansion we can write:

$$\gamma(z) = \gamma(z_0) + \frac{1}{2} \left. \frac{d^2 \gamma}{dz^2} \right|_{z_0} (z - z_0)^2 + O(z - z_0)^3 = \gamma(z_0) - \mu^2, \quad (625)$$

and, consequently,

$$I(t) = e^{t\gamma(z_0)} \int_{\mathcal{C}} e^{-t\mu^2} dz. \quad (626)$$

The integration contour \mathcal{C} is now modified such that it passes through the saddle point z_0 and is such that $t f(z)$ is largest at z_0 while $t g(z)$ can be considered equal to the constant $t g(z_0)$ in the neighborhood of z_0 . With these assumptions, the variable μ defined by (625) is real and, as t increases, the integrand in (626) becomes steeper and less of the contour becomes important. We may therefore replace the contour integral by a real integral covering the range from $-\infty$ to ∞ , namely:

$$I(t) = e^{t\gamma(z_0)} \int_{-\infty}^{\infty} e^{-t\mu^2} \frac{dz}{d\mu} d\mu. \quad (627)$$

Neglecting higher order terms and assuming that $[d^2\gamma/dz^2]_{z_0}$ is not small leads to:

$$\frac{dz}{d\mu} = \sqrt{\frac{-2}{[d^2\gamma/dz^2]_{z_0}}}, \quad (628)$$

and, performing the integration, we eventually obtain:

$$\lim_{t \rightarrow \infty} I(t) = e^{t\gamma(z_0)} \sqrt{\frac{-2\pi}{t[d^2\gamma/dz^2]_{z_0}}}. \quad (629)$$

9.2. Elements of perturbation methods

Perturbation methods are employed to derive an asymptotic representation of the solution of mathematical problems involving a small parameter ϵ . In this Monograph, we have used these techniques repeatedly when searching for the solution of the governing equations of fluvial morphodynamics. Most typically, the approach consists of expanding the unknown functions in powers of the small parameter ϵ . This procedure is illustrated in Section 9.2.2. This straightforward approach may turn out to apply to the whole domain of independent variables where the solution is sought: in this case, the perturbation expansion is said to be *uniform*. However, *non-uniformities* are not uncommon and require suitable countermeasures. Various techniques have been developed to remove their effects. In Section 9.2.3 we introduce the reader to one of these techniques, called *Method of multiple scales*, that is widely employed, most notably in the context of stability theory.

We will illustrate the above ideas using the case of a *weakly damped linear oscillator* as instructive example (see Nayfeh, 2000).

9.2.1 Weakly damped linear oscillator: exact solution

Let us consider the following simple ordinary differential problem:

$$\frac{d^2 f}{dt^2} + f = -2\epsilon \frac{df}{dt}, \quad (630a)$$

$$f = 0 \quad (t = 0), \quad (630b)$$

$$\frac{df}{dt} = 1 \quad (t = 0), \quad (630c)$$

with ϵ small parameter.

The above differential system is linear with constant coefficients. Hence, it is readily solved exactly in the form:

$$f(t) = c_1 e^{\lambda_1 t} + c_2 e^{\lambda_2 t}, \quad (631)$$

with c_1 and c_2 constants to be determined and:

$$\lambda_1 = -\epsilon + \sqrt{\epsilon^2 - 1} = -\epsilon + i\sqrt{1 - \epsilon^2}, \quad \lambda_2 = -\epsilon - i\sqrt{1 - \epsilon^2}. \quad (632)$$

Imposing the initial conditions one finds:

$$c_1 = \frac{1}{\lambda_1 - \lambda_2} = -\frac{i}{2\sqrt{1 - \epsilon^2}}, \quad c_2 = -c_1. \quad (633)$$

We leave to the reader the exercise of showing that the above solution can also be expressed in the following clearer form:

$$f(t) = \frac{e^{-\epsilon t}}{\sqrt{1 - \epsilon^2}} \sin(\sqrt{1 - \epsilon^2} t). \quad (634)$$

Figure 180 (black lines) shows a plot of the exact solution (634) for some values of the small parameter.

9.2.2 Perturbation solution based on a straightforward expansion

Let us next check the performance of an asymptotic solution of the same problem derived taking advantage of the presence of the small parameter ϵ . This suggests the possibility to seek a solution in terms of a straightforward expansion of f in powers of the small parameter. We then express f in the form:

$$f = f_0(t) + \epsilon f_1(t) + \mathcal{O}(\epsilon^2). \quad (635)$$

For our present purposes, there is no need to proceed to higher orders of approximation. The solution procedure is as follows.

The expansion (635) is substituted into the differential equation (630a) and its associated initial conditions. Next, one imposes that the equations must be satisfied at each order of approximation: in other words, the governing differential system for f is replaced by N distinct systems obtained equating terms of order $\mathcal{O}(\epsilon^j)$ ($j = 1, 2, \dots, N$) in the governing equation and associated initial conditions. *Note that this step is a consequence of the assumed asymptotic character of the expansion.* Finally, differential systems are solved sequentially, each of them involving the solutions obtained at lower orders of approximation.

Let us apply this procedure to our weakly damped linear oscillator. One readily finds:

$$\left[\frac{d^2 f_0}{dt^2} + f_0 \right] + \epsilon \left[\frac{d^2 f_1}{dt^2} + f_1 + 2 \frac{df_0}{dt} \right] + \mathcal{O}(\epsilon^2) = 0, \quad (636a)$$

$$f_0 + \epsilon f_1 + \mathcal{O}(\epsilon^2) = 0 \quad (t = 0), \quad (636b)$$

$$\frac{df_0}{dt} + \epsilon \frac{df_1}{dt} + \mathcal{O}(\epsilon^2) = 1 \quad (t = 0). \quad (636c)$$

Equating terms $\mathcal{O}(\epsilon^0)$ one ends up with the differential problem governing the leading order approximation of our solution $f_0(t)$:

$$\frac{d^2 f_0}{dt^2} + f_0 = 0, \quad (637a)$$

$$f_0 = 0 \quad (t = 0), \quad (637b)$$

$$\frac{df_0}{dt} = 1 \quad (t = 0), \quad (637c)$$

which is readily solved in the form:

$$f_0 = \sin t. \quad (638)$$

Proceeding to $\mathcal{O}(\epsilon)$ one finds the differential problem governing the first order

$$\frac{d^2 f_1}{dt^2} + f_1 = -2 \frac{df_0}{dt} = -2 \cos t, \quad (639a)$$

$$f_1 = 0 \quad (t = 0), \quad (639b)$$

$$\frac{df_1}{dt} = 0 \quad (t = 0). \quad (639c)$$

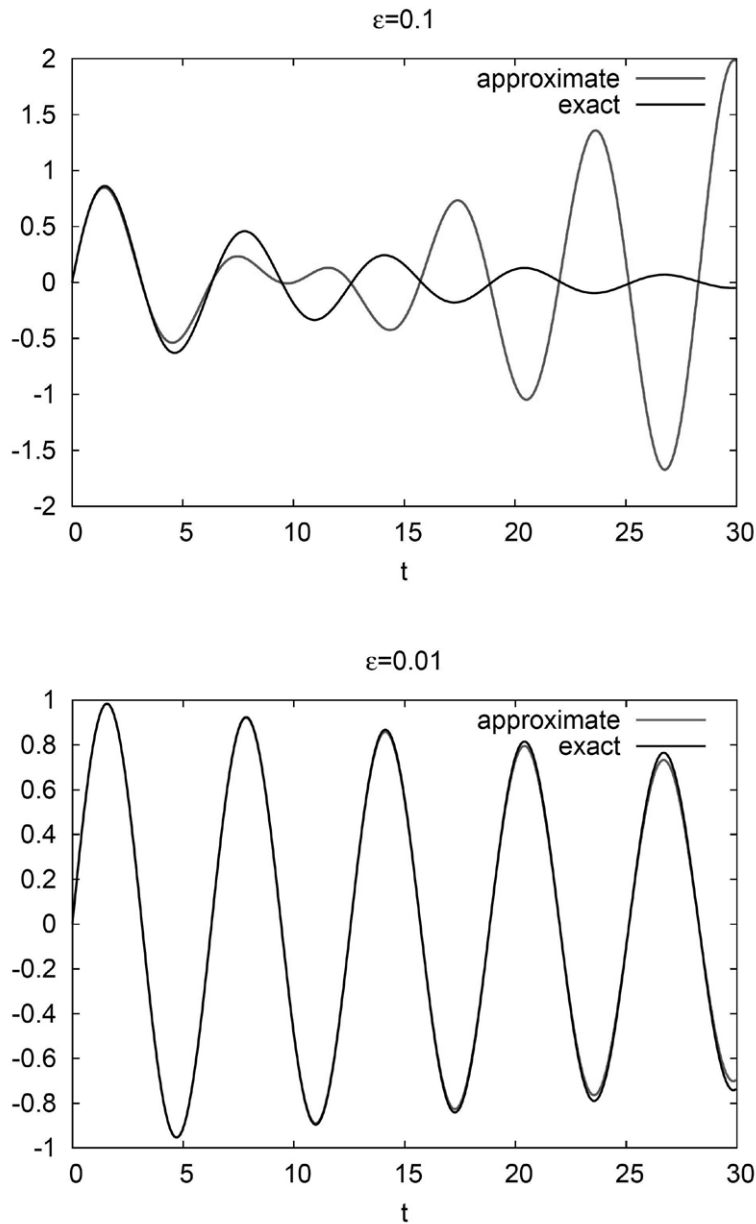


Figure 180. Plot of the exact solution (equation (634), black line) of a weakly damped linear oscillator (630a) for two values of the damping parameter ϵ . Also shown is the approximate solution (641) obtained by a straightforward expansion truncated at $\mathcal{O}(\epsilon)$ (red line).

This is also readily solved to give:

$$f_1 = -t \sin t, \quad (640)$$

and the complete solution up to $\mathcal{O}(\epsilon^2)$ reads:

$$f = \sin t - \epsilon t \sin t + \mathcal{O}(\epsilon^2 t). \quad (641)$$

A glance at (641) immediately suggests that the straightforward expansion leads to a non *uniform* solution. Indeed, the above representation fails, i.e. it loses its asymptotic character, for

large enough values of the independent variable t , such that $\epsilon t \sim O(\epsilon^0)$. Terms proportional to (ϵt) are called *secular terms* as they let the expansion fail for *large time* (seculus is a latin word meaning century and terms of this type occur in astronomical applications where time scales are of the order of centuries). For the expansion to be uniform no secular term must be present. Figure 180 shows a comparison between the exact solution (black lines) and the approximate solution obtained by the straightforward expansion truncated at $\mathcal{O}(\epsilon)$ (red lines). The role of secular terms appears clearly. As the time increases the straightforward expansion starts to fail and this occurs sooner as the small parameter ϵ decreases.

In the next Section we will learn a technique, the method of multiple scales, which replaces the straightforward expansion by a more appropriate perturbation technique which prevents the occurrence of secular terms. However, before we proceed in the latter direction, it is instructive to analyze the origin of secular terms. We achieve this goal expanding the exact solution in Taylor series of the small parameter.

The origin of secular terms.

Expanding (634) in powers of ϵ , one readily finds:

$$e^{-\epsilon t} = \sum_{n=0}^{\infty} \frac{1}{n!} (-\epsilon t)^n, \quad (642a)$$

$$\frac{1}{\sqrt{1-\epsilon^2}} = 1 + \frac{1}{2} \epsilon^2 + \mathcal{O}(\epsilon^4), \quad (642b)$$

$$\sin(\sqrt{1-\epsilon^2} t) = \sin t - \epsilon^2 \frac{t}{2} \cos t + \mathcal{O}(\epsilon^4 t). \quad (642c)$$

It is not surprising that, with the help of (642b, 642c, 642a), the expansion of the exact solution (634) takes a form identical to the solution (641) obtained by the straightforward expansion.

Having established the equivalence of the two approaches, we observe that the secular terms arise from the Taylor expansions of both the functions $\exp(-\epsilon t)$ and $\sin(\sqrt{1-\epsilon^2} t)$. The former series (equation 642a) converges for any value of $(-\epsilon t)$. However, as pointed out by Nayfeh (2000), any approximation of the series obtained retaining a finite number of terms is bound to fail at sufficiently large times (i.e., $t \sim \mathcal{O}(\epsilon^{-1})$). This is clarified in Figure 181a. Similarly, the series (642c) involves terms proportional to $\epsilon^2 t, \epsilon^4 t, \dots$ which imply failure of the expansion for times $t \sim \mathcal{O}(\epsilon^{-2}), t \sim \mathcal{O}(\epsilon^{-4})$, respectively (Figure 181b).

9.2.3 Dealing with non-uniformities: The method of multiple scales

The basic idea underlying the perturbation approaches aimed at removing the non-uniformity of the straightforward expansion arises from the problem noted in the last statement of the previous Section, namely the presence of terms proportional to $\epsilon^j t$ ($j > 0$) in the expansion. The latter observation implies that the unknown function f cannot be simply assumed to depend on the *fast* variable t , but also on *slow* variables $T_j = \epsilon^j t$. The word *slow* indicates that $\mathcal{O}(1)$ variations of the variable T_j occur on very large *fast* time scales $t \sim \mathcal{O}(\epsilon^{-j})$.

We then assume:

$$f = f(t, T_1, T_2, \dots), \quad (643a)$$

$$T_j = \epsilon^j t \quad (j = 1, 2, 3, \dots), \quad (643b)$$

and use the chain rule to evaluate the temporal derivatives of the unknown function f . Hence:

$$\frac{\partial}{\partial t} \rightarrow \frac{\partial}{\partial t} + \epsilon \frac{\partial}{\partial T_1} + \epsilon^2 \frac{\partial}{\partial T_2} + \dots, \quad (644a)$$

$$\frac{\partial^2}{\partial t^2} \rightarrow \left(\frac{\partial}{\partial t} + \epsilon \frac{\partial}{\partial T_1} + \epsilon^2 \frac{\partial}{\partial T_2} + \dots \right) \left(\frac{\partial}{\partial t} + \epsilon \frac{\partial}{\partial T_1} + \epsilon^2 \frac{\partial}{\partial T_2} + \dots \right), \quad (644b)$$

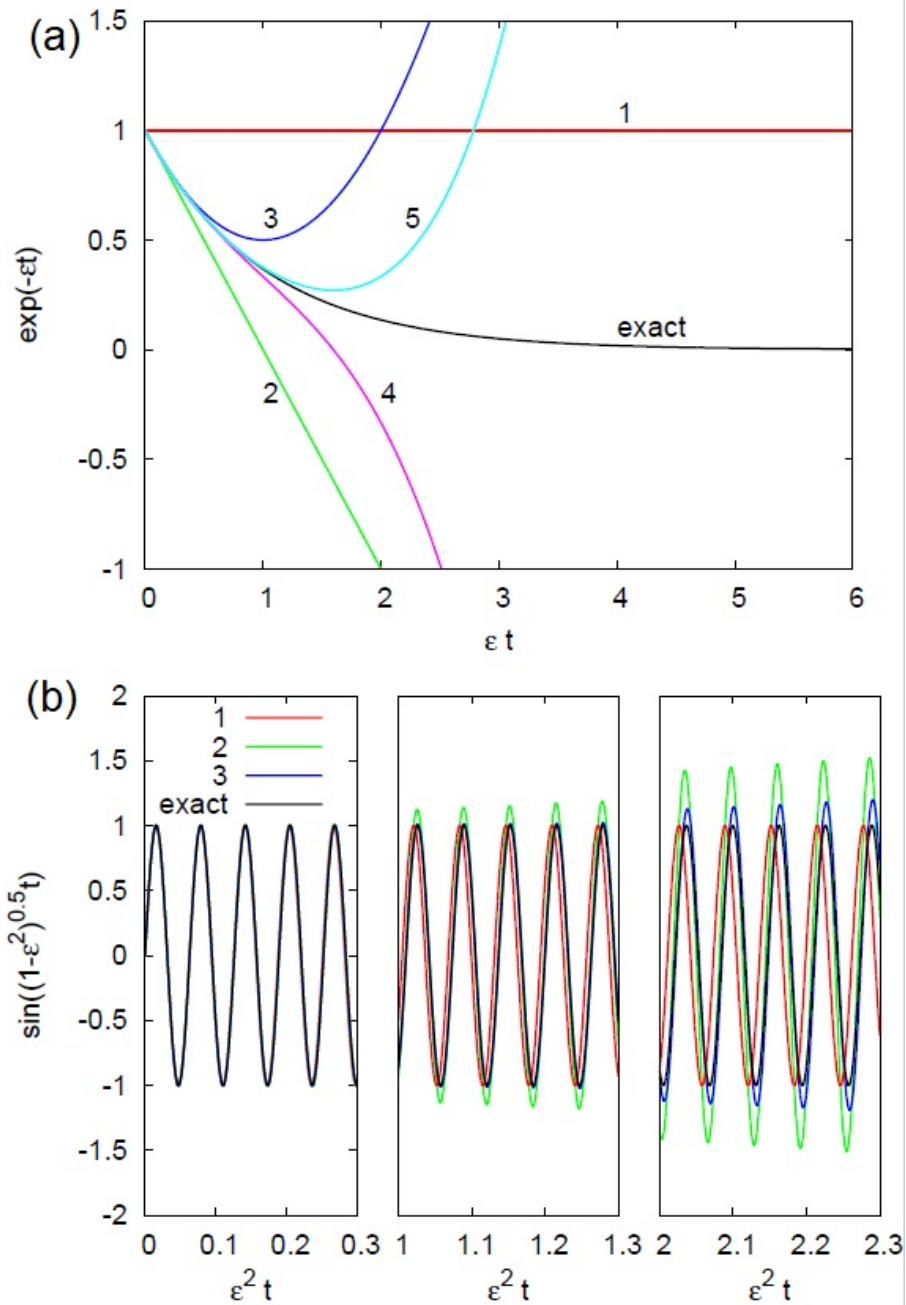


Figure 181. The various approximations to the Taylor series expansions of $\exp(-\epsilon t)$ (a) and $\sin(\sqrt{1-\epsilon^2}t)$ (b) obtained retaining an increasing number of terms in the corresponding series (equations (642a) and (642c), respectively).

i.e.

$$\frac{\partial^2}{\partial t^2} \rightarrow \frac{\partial^2}{\partial t^2} + 2\epsilon \frac{\partial^2}{\partial t \partial T_1} + \epsilon^2 \left[\frac{\partial^2}{\partial T_1^2} + 2 \frac{\partial^2}{\partial t \partial T_2} \right] + \dots \quad (645)$$

Next, we replace the straightforward expansion by the following one:

$$f = f_0(t, T_1, T_2, \dots) + \epsilon f_1(t, T_1, T_2, \dots) + \epsilon^2 f_2(t, T_1, T_2, \dots) + \dots \quad (646)$$

Substituting from (644a,645,646) into the differential system (630a), we find:

$$\begin{aligned} & \frac{\partial^2 f_0}{\partial t^2} + f_0 \\ & + \epsilon \left[\frac{\partial^2 f_1}{\partial t^2} + f_1 + 2 \frac{\partial^2 f_0}{\partial t \partial T_1} + 2 \frac{\partial f_0}{\partial t} \right] \\ & + \epsilon^2 \left[\frac{\partial^2 f_2}{\partial t^2} + f_2 + 2 \frac{\partial f_1}{\partial t} + 2 \frac{\partial f_0}{\partial T_1} + \frac{\partial^2 f_0}{\partial T_1^2} + 2 \frac{\partial^2 f_1}{\partial t \partial T_1} + 2 \frac{\partial^2 f_0}{\partial t \partial T_2} \right] \\ & + \dots = 0. \end{aligned} \quad (647a)$$

The classical procedure, employed for the case of straightforward expansions, consists of equating terms of the same order of magnitude to find a sequence of differential problems at various orders.

$\mathcal{O}(\epsilon^0)$

$$\frac{\partial^2 f_0}{\partial t^2} + f_0 = 0. \quad (648)$$

This equation is readily solved in the form:

$$f_0 = A_0(T_1, T_2) \exp(it) + c.c., \quad (649)$$

where $c.c.$ denotes the complex conjugate and $A_0(T_1, T_2)$ is an amplitude function to be determined, which depends on the slow variables. Below, we restrict our analysis to second order, hence the only slow variables of relevance for our approach are T_1 and T_2 .

$\mathcal{O}(\epsilon)$

$$\frac{\partial^2 f_1}{\partial t^2} + f_1 = -2 \frac{\partial^2 f_0}{\partial t \partial T_1} - 2 \frac{\partial f_0}{\partial t} = -2i \left(\frac{\partial A_0}{\partial T_1} + A_0 \right) \exp(it) + c.c.. \quad (650)$$

This equation is also readily solved in the form:

$$f_1 = A_1(T_1, T_2) \exp(it) - \left(\frac{\partial A_0}{\partial T_1} + A_0 \right) t \exp(it) + c.c., \quad (651)$$

where $A_1(T_1, T_2)$ is a new amplitude function to be determined.

The solution for f_1 contains a secular term (i.e., $\mathcal{O}(\epsilon t)$) that must be suppressed if we wish the expansion to be uniform. We then set:

$$\frac{\partial A_0}{\partial T_1} + A_0 = 0. \quad (652)$$

This is an amplitude equation for A_0 which admits of the simple solution:

$$A_0 = A_{00}(T_2) \exp(-T_1), \quad (653)$$

where $A_{00}(T_2)$ is a new amplitude function that will be determined at the next order.

$\mathcal{O}(\epsilon^2)$

$$\begin{aligned} \frac{\partial^2 f_2}{\partial t^2} + f_2 &= \\ &- 2 \frac{\partial f_1}{\partial t} - 2 \frac{\partial f_0}{\partial T_1} - \frac{\partial^2 f_0}{\partial T_1^2} - 2 \frac{\partial^2 f_1}{\partial t \partial T_1} - 2 \frac{\partial^2 f_0}{\partial t \partial T_2} \\ &= -2ie^{it} \left[\frac{\partial A_1}{\partial T_1} + A_1 + e^{-T_1} \left(\frac{\partial A_{00}}{\partial T_2} + \frac{A_{00}}{2} i \right) \right]. \end{aligned} \quad (654a)$$

This equation is also readily solved in the form:

$$\begin{aligned} f_2 &= A_2(T_1, T_2) e^{it} - \\ &\left[\frac{\partial A_1}{\partial T_1} + A_1 + e^{-T_1} \left(\frac{\partial A_{00}}{\partial T_2} + \frac{A_{00}}{2} i \right) \right] t \exp(it) + c.c., \end{aligned} \quad (655a)$$

where $A_2(T_1, T_2)$ is a new amplitude function to be determined.

The solution for f_2 contains a new secular term that must also be suppressed for uniformity. We then set:

$$\frac{\partial A_1}{\partial T_1} + A_1 = -e^{-T_1} \left(\frac{\partial A_{00}}{\partial T_2} + \frac{i}{2} A_{00} \right). \quad (656)$$

This is an amplitude equation for A_1 which admits of the simple solution:

$$A_1 = A_{10}(T_2) e^{-T_1} - T_1 e^{-T_1} \left(\frac{\partial A_{00}}{\partial T_2} + \frac{i}{2} A_{00} \right), \quad (657)$$

where $A_{10}(T_2)$ is a new amplitude function that could be determined proceeding to the next order.

Note that the solution (657) also includes a secular term that must be suppressed and this leads to a further amplitude equation for A_{00} :

$$\frac{\partial A_{00}}{\partial T_2} + \frac{i}{2} A_{00} = 0, \quad (658)$$

which is readily solved:

$$A_{00} = c_{00} e^{-\frac{i}{2} T_2}, \quad (659)$$

with c_{00} complex constant to be determined imposing the initial conditions.

The analysis can be pursued further, proceedings to higher orders. For our present purposes, it suffices to summarize our findings noting that, using (649), (653) and (659), the multiple scale solution at leading order is found to read:

$$f = c_{00} \exp \left[it - \epsilon t - \frac{i}{2} \epsilon^2 t \right] + c.c.. \quad (660)$$

Imposing the initial conditions (630b) and (630c) at the leading order of approximation one then finds:

$$\begin{aligned} c_{00} + \bar{c}_{00} &= 2 \operatorname{Re}(c_{00}) = 0, \\ i c_{00} - i \bar{c}_{00} &= 1, \quad \Rightarrow \quad \operatorname{Im}(c_{00}) = -\frac{1}{2}, \end{aligned} \quad (661a)$$

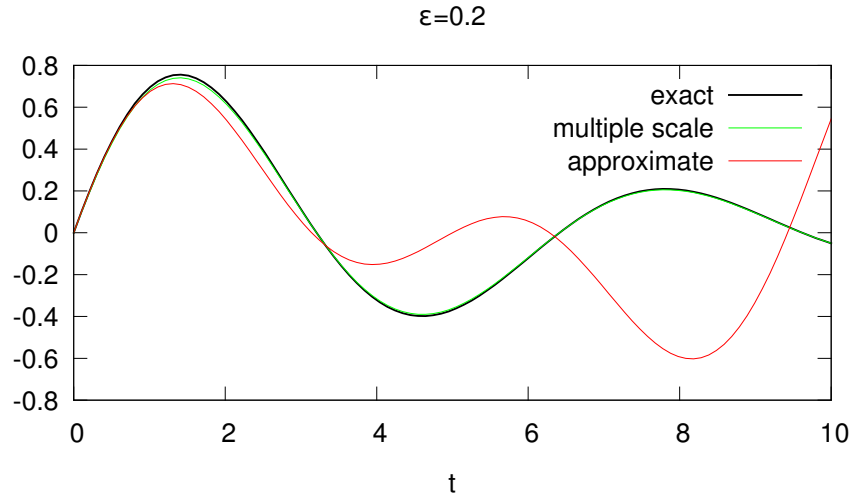


Figure 182. Plot of the exact solution (equation (634), black line) and the multiple scale solution at the leading order (equation (662), green line) of a weakly damped linear oscillator (630a). Also shown is the approximate solution (641) obtained by a straightforward expansion truncated at $\mathcal{O}(\epsilon)$ (red line).

and the final form of the multiple scale solution at leading order becomes:

$$f = e^{-\epsilon t} \sin \left[\left(1 - \frac{1}{2} \epsilon^2 \right) t \right]. \quad (662)$$

Comparison between (662) and the exact solution (634) immediately shows the achievements of the multiple scale technique. The phase of the multiple scale solution at leading order differs from that of the exact solution by terms $\mathcal{O}(\epsilon^4 t)$, hence failure of the expansion is expected for times $\mathcal{O}(\epsilon^{-4})$, much larger than those ($\mathcal{O}(\epsilon^{-1})$) for which failure of the straightforward expansion at leading order is expected. The amplitude of the multiple scale solution at leading order differs from that of the exact solution by terms $\mathcal{O}(\epsilon^2)$ uniformly in time, as the slow time variable $T_1 = \epsilon t$ takes care of the exponential damping exactly.

The Figure 182 provides a visual representation of the comparison between the multiple scale and the exact solutions.

9.3. An introduction to stability theory

9.3.1 The general notion of stability

In very general terms, stability theory has to do with the states a system may take depending on the values of the relevant control parameters.

In order to grasp the basic idea, let us first consider a simple mechanical system, which is definitely familiar to the reader, namely a *pendulum* (Figure 183).

It is well known that a pendulum admits of two vertical equilibrium states, the former (A in Figure 183) pointing downwards, the latter (B in Figure 183) pointing upwards. It is also known that, as a result of small perturbations of the state B, say a small rotation of the system around a horizontal axis, the pendulum will definitely abandon its initial equilibrium state and will start performing oscillations. Due to the damping effects of air resistance and friction experienced at the hinge, oscillations will progressively reduce their amplitudes and lead asymptotically to a new equilibrium state, namely the state A. On the contrary, a pendulum initially in the A state, in response to similar perturbations, will again experience damped oscillations which however will

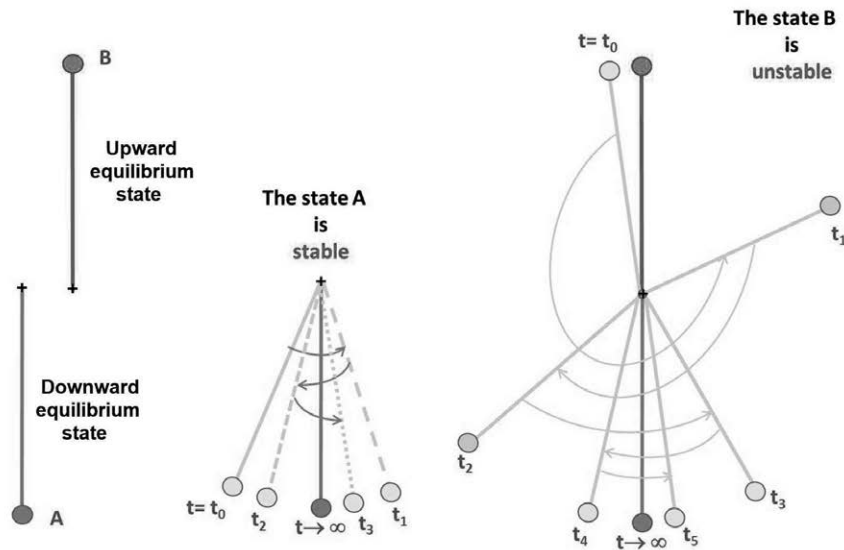


Figure 183. Sketch illustrating the two possible equilibrium states of a pendulum (A and B) and their stabilities

asymptotically lead to restore its initial A state. The very fundamental concept of stability is clear in this simplest example: the state A is stable, the state B is unstable.

In the language of hydrodynamic stability the state whose stability is analyzed is called *base state*. However, the reader should appreciate that the base state is a mathematical idealization. In real systems base states are invariably *perturbed*: no pendulum in the real world will attain a perfectly vertical alignment. This notwithstanding, if the base state is stable, then the observed state is a good approximation of it, as perturbations keep small enough. On the contrary, if the base state is unstable, then perturbations amplify and that state is never observed.

Having grasped the basic concept, the reader should next appreciate that the definition of stability involves a number of further aspects that deserve to be considered.

Some of them concern the *nature of the base state*.

- In the pendulum example, the base states are equilibrium states, i.e. they are *static*. This helps simplifying the picture but is, however, inessential. The notion of stability applies similarly to *dynamic* base states. In the bar instability examined in Chapter 6, the base state is the uniform flow in an open channel in equilibrium with its erodible bed. Instability is thus sought investigating the response of flow and bed topography to spatially and/or temporally varying perturbations of the bed interface.

- Similarly inessential is the *temporal dependence of the base state*. In the bar case the base state will be steady, but similar ideas apply to oscillatory base states, as those encountered in the neighboring fields of coastal and tidal morphodynamics.

- Inessential is also the *spatial dependence of the base state*. In the bar case, the base state will be spatially uniform, but in spatially varying flows, e.g. diverging flows occurring in alluvial fans, similar instabilities are observed.

Other important features to be considered concern the *nature of perturbations experienced by the system*.

- Stability implies that some convenient measure $\mathcal{E}(t)$ of the *energy* of perturbations satisfies the following condition:

$$\lim_{t \rightarrow \infty} \frac{\mathcal{E}(t)}{\mathcal{E}(0)} \rightarrow 0. \quad (663)$$

Mathematicians call the latter condition *asymptotic stability in the mean*. This condition may be satisfied independently of the value of the initial energy of the perturbation $\mathcal{E}(0)$, in which case the base state is said *unconditionally or globally stable*. Alternatively, asymptotic stability may be satisfied only provided $\mathcal{E}(0)$ does not exceed some threshold value, in which case (i.e. when initial perturbations are *sufficiently small*), the base state is said to be *conditionally stable*.

Stability theory has thus developed methods appropriate to investigate the response of systems to infinitesimal perturbations (*linear stability theory*), as well as to perturbations with some finite but *appropriately small size* (*weakly nonlinear stability theories*), or perturbations with size not constrained a priori (*fully nonlinear analysis*).

- Size is not the only characteristic of perturbations which may affect the system stability. Further features that play a role are their *stationary or migrating* character as well as their *spatial-temporal scale*. Different classes of perturbations are referred to as different *modes*. The same system may be unstable to a variety of modes, e.g. ripples, dunes, antidunes and bars are different perturbation modes allowed by fluvial streams. In some cases different modes may even coexist: e.g. ripples are observed superimposed on dunes and both of them may form on the top of bars.

- Finally, the reader familiar with classical hydrodynamic instability should appreciate that *morphodynamic instability is fundamentally distinct from hydrodynamic instability*. The latter deals with the stability of flows. The former concerns instabilities of a free boundary, namely the bed interface.

In conclusion, ascertaining the stable or unstable character of the base state requires an investigation of the response of the system to different classes of perturbations (i.e. different *modes*). The final aim of any stability theory is to determine *stability criteria* identifying the region of the parameter space where the base state is stable to a specific class of perturbations. Moreover, one wishes to determine the characteristics of the new states eventually attained by unstable perturbations. The branch of stability theory dealing with the latter issue is known as *bifurcation theory*.

9.3.2 The toy model

In order to introduce the reader to stability analysis, we consider a model system governed by a single partial differential equation in three independent variables. To retain a language analogy with the physical problem of our interest, we will term x the longitudinal coordinate, y a coordinate orthogonal to the flow direction and t the temporal coordinate. Moreover, we will interpret the dependent variable u as a 'flow speed' and assume the 'flow' to occur in an infinitely wide channel bounded by two parallel plane walls located at $y = 0$ and $y = 1$. The upper wall moves in the longitudinal direction with assigned speed and drives the flow of the fluid within the channel.

Let the model partial differential problem read:

$$\frac{\partial u}{\partial t} - \frac{\partial^2 u}{\partial y^2} + \frac{\partial^4 u}{\partial x^4} + (R - 1) \frac{\partial^2 u}{\partial x^2} + \frac{\partial u}{\partial y} \left(\frac{\partial u}{\partial x} + \frac{\partial^2 u}{\partial x^2} \right) = 0, \quad (664a)$$

$$u = 0 \quad (y = 0), \quad (664b)$$

$$u = 1 \quad (y = 1). \quad (664c)$$

The above problem involves only one control parameter R , say our 'Reynolds number'. The reader will note that both linear and nonlinear terms are included in (664a). The differential problem can then be conveniently rewritten in the form:

$$\frac{\partial u}{\partial t} + Lu + Nu = 0, \quad (665a)$$

$$u = 0 \quad (y = 0), \quad (665b)$$

$$u = 1 \quad (y = 1). \quad (665c)$$

Here, $L(\cdot)$ and $N(\cdot)$ are linear and nonlinear differential operators, respectively, defined as follows:

$$L \equiv -\frac{\partial^2}{\partial y^2} + \frac{\partial^4}{\partial x^4} + (R-1) \frac{\partial^2}{\partial x^2}, \quad (666a)$$

$$N \equiv \frac{\partial}{\partial y} \cdot \left(\frac{\partial}{\partial x} + \frac{\partial^2}{\partial x^2} \right). \quad (666b)$$

9.3.3 The base state

The equation (664a) with the boundary conditions (664b) and (664c) admits of a simplest steady uniform solution $u = u_0(y)$ that satisfies the following ordinary differential problem:

$$\frac{d^2 u_0}{dy^2} = 0, \quad (667a)$$

$$u_0 = 0 \quad (y = 0), \quad (667b)$$

$$u_0 = 1 \quad (y = 1). \quad (667c)$$

Hence:

$$u_0 = y. \quad (668)$$

Below, (668) will be taken as our *base state*. The next step is to investigate its stability.

9.3.4 Linear stability analysis: Temporal normal modes

It is convenient to start with a linear stability analysis, whereby we seek the response of the system to *infinitesimal perturbations* of the steady base solution (668). To pursue this goal we write:

$$u(x, y, t) = u_0(y) + \epsilon u_1(x, y, t) + \mathcal{O}(\epsilon^2), \quad (669)$$

with ϵ an infinitesimal parameter.

The assumption of infinitesimal perturbations allows us to *linearize* the differential problem. Substituting from (669) into (665a-c) and neglecting terms of order ϵ^2 or higher, noting that the base state is steady and independent of x , we obtain^o:

$$\frac{\partial u_1}{\partial t} + L u_1 + \frac{\partial u_1}{\partial x} + \frac{\partial^2 u_1}{\partial x^2} = 0, \quad (670a)$$

$$u_1 = 0 \quad (y = 0), \quad (670b)$$

$$u_1 = 0 \quad (y = 1). \quad (670c)$$

At this stage, it is convenient to restrict the class of perturbations to be considered, noting that (670a) admits of solutions that are exponentially dependent on time. We then separate the temporal dependence of the solution from its spatial dependence and write:

$$u_1(x, y, t) = \hat{u}_1(x, y) \exp(-i\omega t) + c.c., \quad (671)$$

^o Formal substitution from (669) into (665a-c) gives:

$$\begin{aligned} \frac{\partial u_0}{\partial t} + L u_0 + \left(\frac{\partial u_0}{\partial x} + \frac{\partial^2 u_0}{\partial x^2} \right) \frac{\partial u_0}{\partial y} + \epsilon \frac{\partial u_1}{\partial t} + \epsilon L u_1 + \epsilon \left(\frac{\partial u_0}{\partial x} + \frac{\partial^2 u_0}{\partial x^2} \right) \frac{\partial u_1}{\partial y} \\ + \epsilon \left(\frac{\partial^2 u_1}{\partial x^2} + \frac{\partial u_1}{\partial x} \right) \frac{\partial u_0}{\partial y} + \mathcal{O}(\epsilon^2) = 0, \end{aligned}$$

The equation (670a) is then readily obtained noting that $\frac{du_0}{dt} = L u_0 = \frac{\partial u_0}{\partial x} = \frac{\partial^2 u_0}{\partial x^2} = 0$ and $\frac{du_0}{dy} = 1$ (recall eq. 668).

where $i = \sqrt{-1}$ is the imaginary unit, *c.c.* denotes the complex conjugate of a complex number and $\omega = \omega_r + i\omega_i$ is a complex parameter to be determined. It is clear that ω_i represents the temporal growth rate of the perturbation, hence its sign controls the stable ($\omega_i < 0$) or unstable ($\omega_i > 0$) character of the basic state subject to this class of perturbations. The ultimate goal of a linear stability analysis is precisely to derive the dependence of ω on the relevant external parameters (R for our model problem) as well as any further parameter defining the spatial characteristics of perturbations.

Let us then substitute from (682) into (670a-c) to obtain

$$\left(-i\omega + \frac{\partial^4}{\partial x^4} + R \frac{\partial^2}{\partial x^2} + \frac{\partial}{\partial x} - \frac{\partial^2}{\partial y^2}\right) \hat{u}_1 = 0, \quad (672a)$$

$$\hat{u}_1 = 0 \quad (y = 0), \quad (672b)$$

$$\hat{u}_1 = 0 \quad (y = 1). \quad (672c)$$

Hence, we end up with an *eigenvalue problem* for ω , i.e a homogeneous partial differential equation, with homogeneous boundary conditions, defined in a longitudinally unbounded domain. This problem has solutions only provided ω takes appropriate values to be determined. To solve the above eigenvalue problem, noting that the differential equation has constant coefficients, we may rely on the so called *normal mode analysis* whereby u_1 is represented as a Fourier integral of the form:

$$u_1(x, y, t) = \int_{-\infty}^{\infty} f_1(y) \exp[i(\lambda x - \omega t)] d\lambda, \quad (673)$$

where λ is a *real* number denoting the wavenumber of perturbations. In physical terms, we are considering perturbations consisting of a continuous spectrum of waves. Each wave propagates in the x -direction with *wavelength* ($2\pi/\lambda$) and *migration speed* [ω_r/λ]. Moreover, it has a lateral structure described by the function $f_1(y)$ and amplifies (or decays) in time with growth rate ω_i . Each wave may also be written in the form:

$$f_1(y) \exp(\omega_i t) \exp[i(\lambda x - \omega_r t)]. \quad (674)$$

Upon substitution of (673) into (672a-c), we end up with the following ordinary differential eigenvalue problem for ω as a function of the parameters λ and R :

$$\frac{d^2 f_1}{dy^2} - \mu^2 f_1 = 0, \quad (675a)$$

$$f_1 = 0 \quad (y = 0), \quad (675b)$$

$$f_1 = 0 \quad (y = 1), \quad (675c)$$

with

$$\mu^2 = -\lambda^2 R + \lambda^4 - i\omega + i\lambda. \quad (676)$$

The general solution of (675) reads:

$$f_1 = c_1 \exp(\mu y) + c_2 \exp(-\mu y). \quad (677)$$

Recalling the boundary conditions (675b,c), one readily shows that, $c_1 = -c_2$ and, in order for the above solution to be non trivial, the following condition has to be satisfied

$$\exp(\mu) - \exp(-\mu) = 0, \quad (678)$$

which implies that $\mu = im\pi$ with m integer.

Equation (677) thus becomes:

$$f_1(y) = 2i c_1 \sin(m\pi y). \quad (679)$$

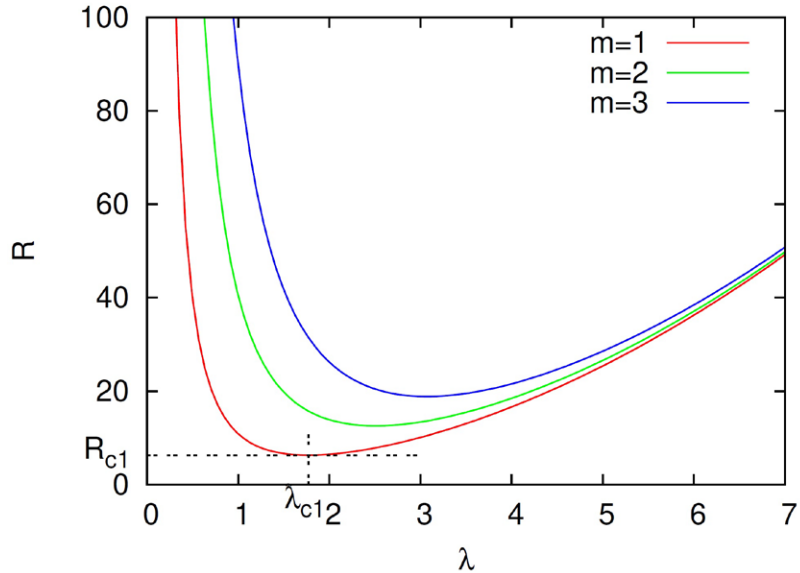


Figure 184. Marginal stability curves are plotted in the plane $\lambda - R$ for the three most unstable modes of our toy model. The absolute minimum of the first and most unstable mode defines the critical values (λ_{c1} and R_{c1}) of the wavenumber and of the control parameter, respectively.

In conclusion, we end up with the following *eigen-relationship* for ω :

$$D(\omega, \lambda; R, m) = -i\omega + i\lambda - \lambda^2 R + m^2 \pi^2 + \lambda^4 = 0. \quad (680)$$

The solution for the linear perturbation u_1 associated with the above eigenrelationship (i.e. the *eigenfunction*) then takes the form:

$$u_1(x, y, t) = a \sin(m \pi y) \int_{-\infty}^{\infty} \exp[i(\lambda x - \omega t)] d\lambda. \quad (681)$$

Here, ω is a function of λ defined by (680) and $a = 2ic_1$ is an arbitrary constant that, in the context of a linear stability theory, remains unspecified. Indeed, linear theories predict an unbounded growth of perturbations. Accounting for nonlinear effects will be needed in order to predict the size asymptotically reached by the amplitude of perturbations.

Let us analyze our results. The eigenrelationship (680) shows that for our toy model, ω is a complex number, namely:

$$\omega = \lambda + i(\lambda^2 R - m^2 \pi^2 - \lambda^4). \quad (682)$$

If we set $\omega_i = 0$ in (682), we determine a discrete set of so called *marginal (or neutral) stability curves* in the plane (λ, R) , one for each mode m . These curves, which separate the region of the plane where the m -th mode is unstable from those where it is stable, are plotted in Figure 184. Moreover, from the eigenrelationship (682) one finds that $\omega_r = \lambda$. Hence, perturbations allowed by the system migrate downstream (i.e. in the positive x -direction) with constant wavespeed $c = \omega_r/\lambda = 1$. If the marginal stability curve associated with mode m exhibits an absolute minimum for values (λ_{cm}, R_{cm}) of the relevant physical parameters, then R_{cm} and λ_{cm} are called *critical value* of the control parameter R and *critical wavenumber* of mode m , respectively. For our model problem, one finds:

$$R_{cm} = 2m\pi, \quad \lambda_{cm} = \sqrt{m\pi}, \quad (683)$$

and the eigenfunction of the problem at criticality reads:

$$u_1 = a \sin(m \pi y) \exp[i \lambda_{cm}(x - t)]. \quad (684)$$

Stability of the base state to infinitesimal perturbation is then ensured by the condition $R < \min(R_{cm})|_{m=1,2,\dots,\infty}$. For our toy model the simple condition $R < 2\pi$ must be satisfied.

This completes our linear stability analysis.

9.3.5 The initial value problem for linear perturbations and the convective-absolute nature of the instability

Temporal stability analyses of the kind presented in the previous Section consider spatially periodic perturbations which amplify in time, i.e. they assume that the perturbation wavenumber λ is real while its frequency ω is complex. Such analyses allow us to distinguish between stable configurations (all the wavenumbers decay in time) and unstable systems (some wavenumbers are amplified). Alternatively, one may conceive a different approach, a so called *spatial stability* analysis, considering perturbations which evolve in space, starting from some initial distribution, i.e. assuming that the perturbation wavenumber is complex and the perturbation frequency is real. When is the latter approach appropriate? In order to answer the latter question, one has to ascertain the nature of the instability.

Indeed, as mentioned in Chapter 6, instability is described as *convective* provided an initial small perturbation localized in space is convected in one direction (say downstream) leaving, as time tends to infinity, the flow domain unperturbed (see Figure 93). On the contrary, instability is described as *absolute* whenever the initial small localized perturbation spreads in all directions (say both upstream and downstream) as time grows, affecting eventually the whole domain. Such a fundamental distinction was originally proposed in the field of plasma physics by Briggs (1964), Bers (1975) and Bers (1983). It has then been applied and developed in hydrodynamic stability by several authors (see the review of Huerre and Monkewitz, 1990).

In order to ascertain the nature of instability, the response of the system to impulsive forcing must be investigated.

For the sake of simplicity, we illustrate the approach removing the dependence of the problem on the y coordinate. To this aim we consider the general transverse mode m and set:

$$u_1(x, y, t) = U_1(x, t) \sin(m \pi y), \quad (685)$$

that obviously satisfies the boundary conditions at $y = 0$ and $y = 1$. The linear response of mode m , starting from some given initial condition, is then obtained as the solution of the following initial-value problem:

$$\left[\frac{\partial}{\partial t} + \frac{\partial^4}{\partial x^4} + R \frac{\partial^2}{\partial x^2} + \frac{\partial}{\partial x} + m^2 \pi^2 \right] U_1 = 0, \quad (686a)$$

$$U_1 = U_{10}(x) \quad (t = 0), \quad (686b)$$

where $U_{10}(x)$ is some arbitrary initial distribution. The approach commonly employed to solve this problem is to determine the Green function $G(x, t)$, i.e. the impulse response of the system. The Green function is the solution of the following differential equation:

$$\left[\frac{\partial}{\partial t} + \frac{\partial^4}{\partial x^4} + R \frac{\partial^2}{\partial x^2} + \frac{\partial}{\partial x} + m^2 \pi^2 \right] G = \delta(x) \delta(t). \quad (687)$$

Here, $\delta(x) \delta(t)$ represents a perturbation that at time $t = 0$ concentrates within an infinitesimally small region close to the origin of the x axis. Indeed, the Dirac distribution $\delta(\xi)$ has the fundamental property that

$$\int_{-\infty}^{+\infty} f(\xi) \delta(\xi - a) d\xi = f(a), \quad (688)$$

and, in particular, $\int_{-\infty}^{+\infty} \delta(\xi) d\xi = 1$. Hence, it may intuitively be thought of as a function that attains an infinite peak at the origin, vanishes elsewhere, and is such that its integral along the ξ axis is finite. The Green function G then describes how the initial localized perturbation evolves into a wave packet. We will seek its asymptotic behavior as $t \rightarrow \infty$ and introduce the following definitions:

- the system is *linearly stable* provided $G(x, t \rightarrow \infty) = 0$ along any ray $x/t = \text{const}$.
- the system is *linearly unstable* provided $G(x, t \rightarrow \infty) \rightarrow \infty$ along at least one ray $x/t = \text{const}$.

In order to determine $G(x, t)$, we note that the perturbation initially located in the origin of the (x, t) plane can be expressed as a mixture of components of all frequencies and wavenumbers through the Fourier transforms:

$$\delta(x) = \frac{1}{2\pi} \int_{-\infty}^{+\infty} e^{i\lambda x} d\lambda, \quad \delta(t) = \frac{1}{2\pi} \int_{-\infty}^{+\infty} e^{-i\omega t} d\omega, \quad (689)$$

where we have used different signs in the Fourier representations of $\delta(x)$ and $\delta(t)$ for the sake of convenience. Similarly, we can map $G(x, t)$ in the $(\lambda - \omega)$ plane by means of the following Fourier transforms:

$$G(x, t) = \frac{1}{2\pi} \int_{\mathcal{C}_\lambda} \hat{G}(\lambda, t) e^{i\lambda x} d\lambda, \quad \hat{G}(\lambda, t) = \frac{1}{2\pi} \int_{\mathcal{C}_\omega} \tilde{G}(\lambda, \omega) e^{-i\omega t} d\omega, \quad (690)$$

where \mathcal{C}_λ and \mathcal{C}_ω are appropriate integration contours in the complex planes λ and ω , respectively. By using (689) and (690), equation (687) leads to:

$$\tilde{G}(\lambda, \omega) = \frac{1}{D(\omega, \lambda; R, m)}, \quad (691)$$

and, applying the inverse Fourier transforms, we eventually obtain

$$G(x, t) = \frac{1}{(2\pi)^2} \int_{\mathcal{C}_\lambda} d\lambda \int_{\mathcal{C}_\omega} \frac{e^{i(\lambda x - \omega t)}}{D(\omega, \lambda; R, m)} d\omega, \quad (692)$$

where $D(\omega, \lambda; R, m)$ is the function defined by the dispersion relationship (680).

The contour \mathcal{C}_ω in the complex ω plane is chosen as a straight line lying above all the singularities $\omega_d(\lambda)$ of the function $D(\omega, \lambda; R, m) = 0$ (continuous line in Figure 185a). When $t < 0$ this straight line is closed at infinity, thus ensuring that $G(x, t)$ vanishes, a condition called *causality*. On the other hand, when $t > 0$ a semicircle is added below the line to close the circuit (dashed line in Figure 185a), such that the residue theorem can be used to compute the integral.

Let $\omega_d(\lambda)$ be any zero of the dispersion relationship (680). Expanding D in Taylor series in a neighborhood of $\omega_d(\lambda)$, the integrand of (692) becomes:

$$\frac{e^{i(\lambda x - \omega t)}}{D(\omega, \lambda; R, m)} = \frac{e^{i(\lambda x - \omega t)}}{(\omega - \omega_d)[\partial D / \partial \omega]_{\omega_d} + O([\omega - \omega_d]^2)}, \quad (693)$$

The residue associated with the integrand of (692) can then be computed according to the relation

$$a_{-1} = \frac{1}{(k-1)!} \lim_{z \rightarrow a} \frac{d^{k-1}}{dz^{k-1}} [(z-a)^k f(z)], \quad (694)$$

yielding the a_{-1} coefficient of the Laurent series about $\omega_d(\lambda)$ for a single pole ($k = 1$). Hence, application the residue theorem to (692), with the help of (693) gives:

$$G(x, t) = \frac{i}{2\pi} \int_{\mathcal{C}_\lambda} \frac{e^{i[\lambda x - \omega_d(\lambda) t]}}{[\partial D / \partial \omega]_{\omega_d}} d\lambda = -\frac{1}{2\pi} \int_{\mathcal{C}_\lambda} e^{it[\lambda x / t - \omega_d]} d\lambda. \quad (695)$$

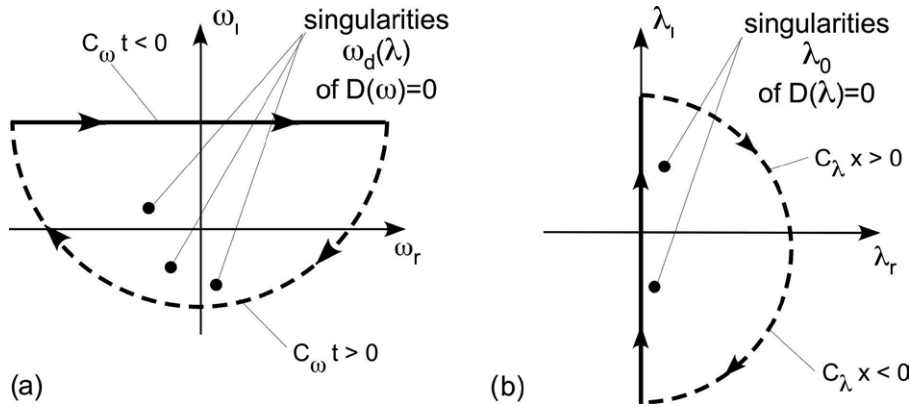


Figure 185. (a) The contour lines C_ω in the complex ω -plane; (b) The contour lines C_λ in the complex λ -plane.

The next step is to perform the integration in the complex λ plane. It is sufficient for our purposes to seek the solution of (695) in the limit $t \rightarrow \infty$. This can be achieved employing the method of steepest descents outlined in Section 9.1.3 and, in particular, the asymptotic relation (629). With the help of (680), we thus set,

$$\gamma(\lambda) = i \left[\lambda \frac{x}{t} - \omega_d(\lambda) \right] = i \lambda \left(\frac{x}{t} - 1 \right) - (\lambda^4 - \lambda^2 R + m^2 \pi^2). \quad (696)$$

The saddle point λ_0 associated with the complex function $\exp(t\gamma)$ is obtained from the condition:

$$\frac{d\gamma}{d\lambda} = i \left(\frac{x}{t} - 1 \right) - 4\lambda^3 + 2\lambda_0 R = 0, \quad (697)$$

implying that

$$\left[\frac{d\omega_d}{d\lambda} \right]_{\lambda_0} = \frac{x}{t}. \quad (698)$$

From (697), with the help of some algebra, one readily finds that λ_{0r} and λ_{0i} are solutions of the following algebraic system:

$$\lambda_{0r} [2\lambda_{0r}^2 - 6\lambda_{0i}^2 - R] = 0, \quad (699)$$

$$4\lambda_{0i}^3 + \lambda_{0i} (-12\lambda_{0r}^2 + 2R) = 1 - \frac{x}{t}. \quad (700)$$

This system has a purely imaginary solution and two complex solutions in general.

Using the relation (629) we finally obtain the following form of the Green function:

$$G(x, \infty) = -\frac{i}{2\sqrt{\pi}} \frac{\exp[it(\lambda_0 x/t - \omega_0)]}{\sqrt{t(R - 6\lambda_0^2)}}, \quad (701)$$

with $\omega_0 = \omega_d(\lambda_0)$. The Green function then takes the form of a wave packet in the (x, t) plane. Among the wavenumbers contained in the impulsive source, the dynamical system selects along each ray $x/t = \text{const}$ the wavenumber given by (698). The group velocity of the wave packet is then real and equal to x/t . On the other hand, the temporal growth rate of the wavenumber λ_0 along the ray is given by:

$$\sigma = \text{Re} \left[it \left(\lambda_0 \frac{x}{t} - \omega_0 \right) \right] = \omega_{0i} - \lambda_{0i} \frac{x}{t}, \quad (702)$$

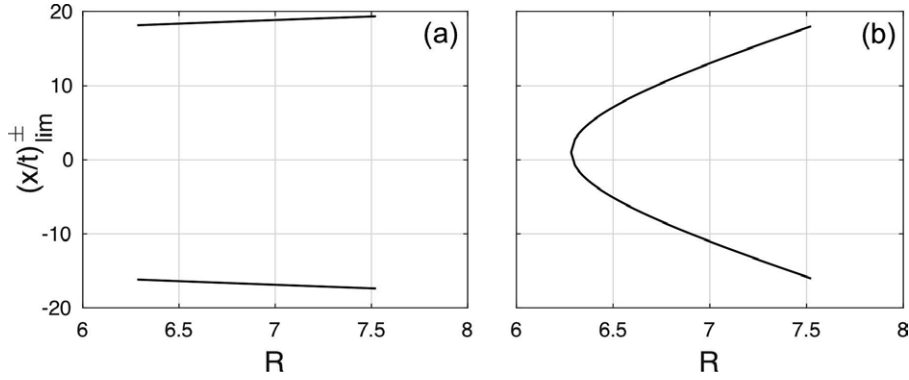


Figure 186. The two rays $(x/t)_{lim}^{\pm}$ bounding the wave packet are plotted as a function of the parameter R for the model problem investigated in this section. (a) Purely imaginary solution (704); (b) complex solution (705).

where ω_{0i} denotes the imaginary part of ω_0 . From (702) one immediately finds that the growth rate of the wave packet vanishes along the rays such that $(x/t)_{lim} = \omega_{0i}/\lambda_{0i}$. With the help of the dispersion relationship, one finds:

$$(x/t)_{lim} = 1 + \frac{R(\lambda_{0r}^2 - \lambda_{0i}^2) + R^2/4 - m^2\pi^2 - [\lambda_{0r}^4 + \lambda_{0i}^4 - 6\lambda_{0r}^2\lambda_{0i}^2]}{\lambda_{0i}}. \quad (703)$$

The reader will readily solve (700) and (710) for λ_{0r} , λ_{0i} and $(x/t)_{lim}$ as functions of R .

A first solution for λ_0 is purely imaginary and such to satisfy the following relationships:

$$\lambda_{01i}^{\pm}|_{\sigma=0} = \pm \sqrt{\frac{R + \sqrt{R^2 + 12m^2\pi^2}}{6}}, \quad (704a)$$

$$1 - (x/t)_{lim} = [4\lambda_{01i}^3 + 2R\lambda_{01i}]_{\sigma=0} \quad (704b)$$

One further solution is complex and reads:

$$\lambda_{02i}^{\pm}|_{\sigma=0} = \pm \sqrt{\frac{-R + \sqrt{7R^2 - 24m^2\pi^2}}{24}}, \quad (705a)$$

$$1 - (x/t)_{lim} = [-32\lambda_{02i}^3 - 4R\lambda_{02i}]_{\sigma=0} \quad (705b)$$

The values of $(x/t)_{lim}^{\pm}$ for the above solutions are plotted in Figure 186. For both solutions the wave packet is confined within a wedge bounded by the two rays $(x/t)_{lim}^{\pm}$. Note also that, except within a narrow range close to critical conditions, one of the rays $(x/t)_{lim}$ invariably lies in the first quadrant while the other one lies in the second quadrant.

The nature of the instability can be assessed by ascertaining where the $x/t = 0$ ray locates with respect to the two limiting rays $(x/t)_{lim}$. The instability is *absolute* if the $x/t = 0$ ray is contained within the wedge region and the associated wavenumber is such that $\omega_{0i} > 0$. Conversely, the instability is *convective* if the $x/t = 0$ ray is outside the wedge region and $\omega_{0i} < 0$. Figure 186 suggests that in both solutions the $x/t = 0$ ray is contained within the wedge region except, for the complex solution, very close to criticality. Let us finally check if the value of ω_{0i} associated with the solutions for $\lambda_0|_{x/t=0}$ is indeed positive.

For our model problem, the solutions for λ_{0r} and λ_{0i} associated with the ray $x/t = 0$ are immediately obtained from (700). Three solutions for λ_{0r} and λ_{0i} are found. They depend only on the control parameter R (Figure 187).

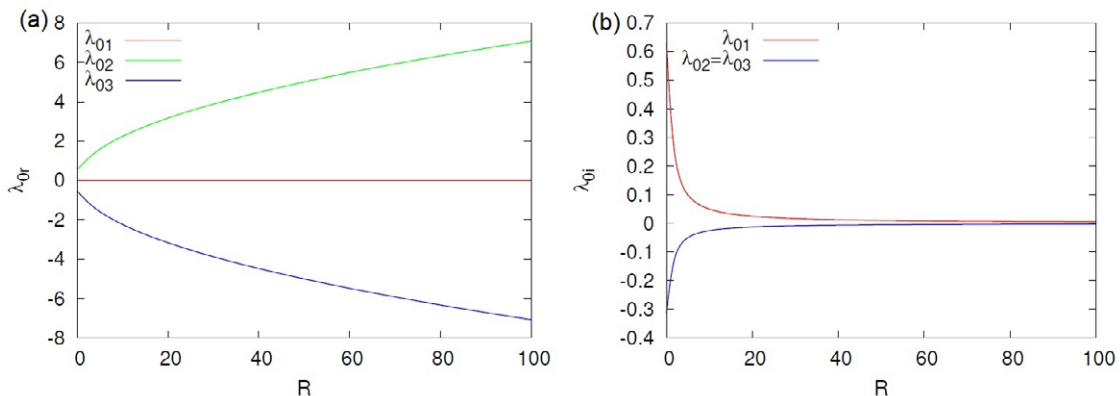


Figure 187. The (a) real and (b) imaginary parts of the three solutions λ_0 associated with the ray $x/t = 0$ are plotted as functions of R .

The first solution is again purely imaginary and reads:

$$\begin{aligned} \lambda_{01r} &= 0, \\ \lambda_{01i} &= \frac{1}{2} \left[\sqrt[3]{1 - \sqrt{1 + \frac{8}{27} R^3}} + \sqrt[3]{1 + \sqrt{1 + \frac{8}{27} R^3}} \right]. \end{aligned} \quad (706)$$

The second and third solutions are complex. Some algebraic work shows that

$$\lambda_{02i} = \lambda_{03i} = -\frac{1}{2} \lambda_{01i}, \quad \lambda_{02,3r} = \pm \sqrt{3 \lambda_{02i}^2 + \frac{R}{2}}, \quad (707)$$

and, hence, $\lambda_{03} = -\bar{\lambda}_{02}$.

The dispersion relationship (682) then allows to evaluate the growth rate $\omega_i|_{\lambda_0}$, which reads:

$$\omega_i|_{\lambda_0} = \lambda_{0i} R (\lambda_{0r}^2 - \lambda_{0i}^2) - m^2 \pi^2 - (\lambda_{0r}^2 - \lambda_{0i}^2)^2 + 4 \lambda_{0r}^2 \lambda_{0i}^2. \quad (708)$$

For the first solution λ_{01} we find that

$$\omega_i|_{\lambda_{01}} = \lambda_{01i} - R \lambda_{01i}^2 - m^2 \pi^2 - \lambda_{01i}^4. \quad (709)$$

As shown in Figure 188, this solution is invariably negative and, hence, describes a wave group that decays asymptotically as $t \rightarrow \infty$.

The other two complex solutions (λ_{02} and λ_{03}) are characterized by the same value of $\omega_i|_{\lambda_0}$, which turns out to be:

$$\omega_i|_{\lambda_{02}} = \omega_i|_{\lambda_{03}} = \lambda_{02i} + 8 \lambda_{02i}^4 + 2 R \lambda_{02i}^2 + \frac{R^2}{4} - m^2 \pi^2. \quad (710)$$

Figure 188 shows that the value of $\omega_i|_{\lambda_{02}}$ is positive for values of the control parameter R larger than R_c . Hence, out of the three solutions (706)-(707), only the two complex solutions (λ_{02} and $-\bar{\lambda}_{02}$) are associated with an absolute instability. Note that the case $R < R_c$ is irrelevant as any initial instability with lateral Fourier mode m decays and the base state is stable.

These findings have been confirmed by the numerical solution of the complete nonlinear problem. In particular, we performed numerical simulations starting from a localized spatial perturbation

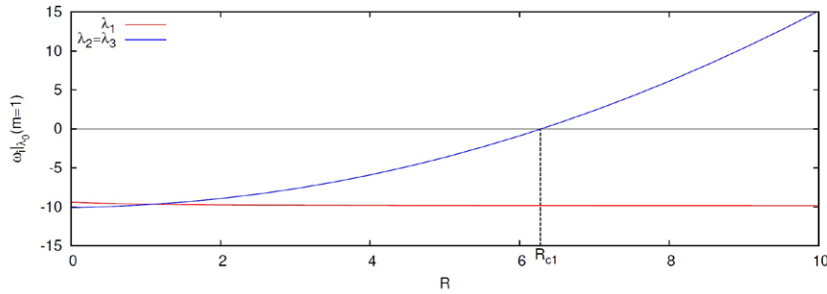


Figure 188. The growth rate $\omega_i(\lambda_0)$ for the three solutions as a function of R for $m = 1$.

of u , namely a bump with an emismetric lateral profile in the middle of the computational domain. Figure 189 shows that the initial perturbation gives rise to the growth of wave groups which migrate both downstream and upstream (Figure 189a) except within a small neighborhood of the critical conditions (Figure 189b), i.e. the nature of instability at a nonlinear level conforms to the behaviour predicted by the linear theory discussed above.

9.3.6 Weakly nonlinear stability analysis

In the previous Section we have shown that, when the control parameter R exceeds a critical value R_c , the basic state is unstable. The linear theory predicts that, under the latter conditions, a spectrum of perturbations will grow exponentially in time and migrate.

However, the linear theory is unable to predict the final fate of perturbations as linearization is a valid approximation only in the initial stage of the process, when the amplitudes of perturbations are infinitesimally small. As perturbations grow, nonlinear interactions among the various linearly unstable components occur, such to prevent their indefinite growth. Although numerical approaches have reached a quite advanced stage that allows to follow the evolution of perturbations from the initial stage to their fully nonlinear state, however it proves extremely instructive to develop a fully analytical theory in what is called the *weakly nonlinear regime*.

The linear form of the perturbation in the weakly nonlinear region

Essentially, nonlinearity is weak provided the control parameter exceeds its critical value only *slightly*. In mathematical terms, this assumption is stated by setting (see Figure 190):

$$R = R_c(1 + r \epsilon^2). \quad (711)$$

Here ϵ is a small parameter and r is a dummy parameter that may take the value 1 (supercritical conditions) or -1 (subcritical conditons).

Let us first analyze the form taken by our linear solution (Section 9.3.4) within a neighborhood of the critical conditions defined by (711) and by allowing some *small* perturbation of λ relative to λ_c . Recalling the dispersion relationship we may expand ω in powers of $(R - R_c)$ and $(\lambda - \lambda_c)$ as follows:

$$\omega = \omega_c + \nu_\lambda(\lambda - \lambda_c) + (\nu_r + i \mu_r)(R - R_c) + \frac{1}{2}(\nu_{\lambda^2} + i \mu_{\lambda^2})(\lambda - \lambda_c)^2 + H.O.T., \quad (712)$$

where ω_c is a real number (the growth rate vanishes at criticality) and

$$\nu_\lambda = \left. \frac{\partial \omega}{\partial \lambda} \right|_{\lambda_c, R_c}, \quad \nu_r + i \mu_r = \left. \frac{\partial \omega}{\partial R} \right|_{\lambda_c, R_c}, \quad \nu_{\lambda^2} + i \mu_{\lambda^2} = \left. \frac{\partial^2 \omega}{\partial \lambda^2} \right|_{\lambda_c, R_c}. \quad (713)$$

The reader will note that the term proportional to $(\lambda - \lambda_c)$ in (712) is purely real as the growth rate $\omega_i(\lambda)$ peaks at criticality. Also, note that the coefficient ν_λ is the group velocity. Applying the

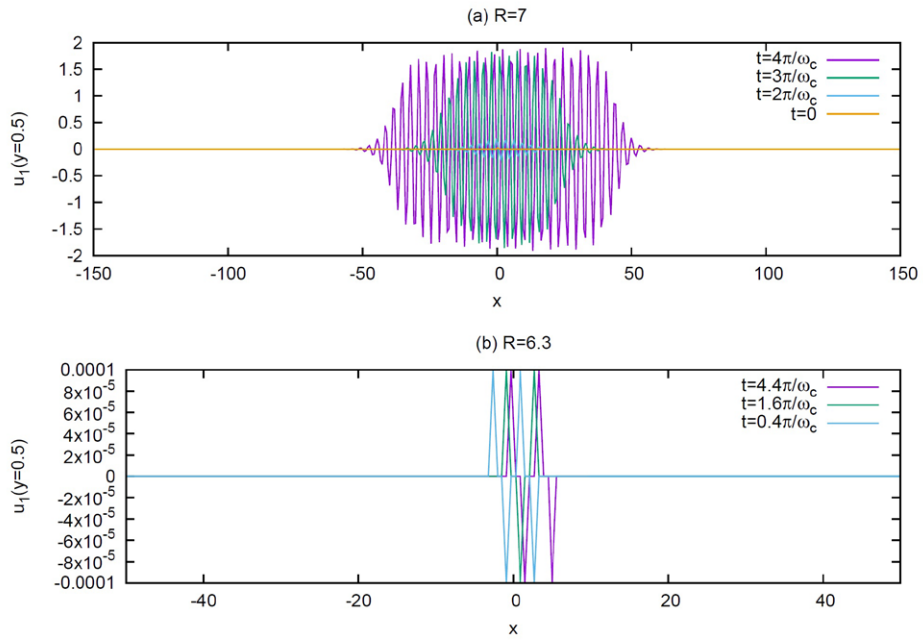


Figure 189. (a) The time evolution of the solution u_1 in $y = 0.5$ at $R = 7$. The initial localized bump in $x = 0$ gives rise to wave groups that grow and migrate both downstream and upstream with time, the instability is absolute (b) Idem at $R = 6.3$: the wave group convects away, the instability is convective.

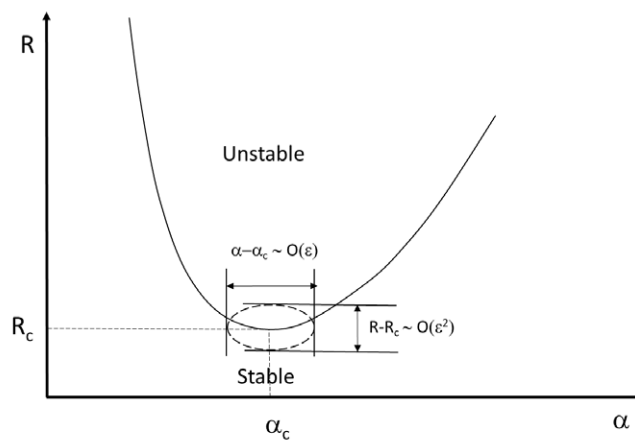


Figure 190. Sketch illustrating the region where the weakly nonlinear theory is developed.

definitions (713) to the dispersion relationship (680), we readily find that, for our model problem with $m = 1$:

$$\nu_\lambda = 1, \quad \nu_r + i\mu_r = i\pi, \quad \nu_{\lambda^2} + i\mu_{\lambda^2} = -8i\pi. \quad (714)$$

Next, it is instructive to substitute from (712) into the linear solution for the first mode of the perturbation, to obtain:

$$\begin{aligned} u_1 &= a \sin(\pi y) \exp[i(\lambda x - \omega t)] \\ &= a \sin(\pi y) \exp[i(\lambda_c x - \omega_c t)] \exp \left[t \left(\mu_r (R - R_c) + \frac{1}{2} \mu_{\lambda^2} (\lambda - \lambda_c)^2 \right) \right] \\ &\quad \exp[i(\lambda - \lambda_c)(x - \nu_\lambda t)] + H.O.T., \end{aligned} \quad (715)$$

with a arbitrary constant. This relationship shows that the growth rate in the neighborhood of critical conditions has two contributions. The former is proportional to $(R - R_c)$, hence, recalling (711), it is of $\mathcal{O}(\epsilon^2)$. The latter is proportional to $(\lambda - \lambda_c)^2$. In order for these two contributions to have the same order, we then require that $(\lambda - \lambda_c) \sim \mathcal{O}(\epsilon)$ and set the following expansion:

$$\lambda = \lambda_c(1 + r_\lambda \epsilon), \quad (716)$$

with r_λ an $\mathcal{O}(1)$ parameter. With the help of (716), we may rearrange (715) in the compact form:

$$u_1 = \sin(\pi y) A(\tau, \xi) \exp[i(\lambda_c x - \omega_c t)], \quad (717)$$

where τ and ξ are the following *slow* variables:

$$\tau = \epsilon^2 t, \quad \xi = \epsilon(x - \nu_\lambda t), \quad (718)$$

and the *amplitude function* $A(\tau, \xi)$ reads:

$$A(\tau, \xi) = a \exp \left[(\mu_r r R_c + \frac{1}{2} \mu_{\lambda^2} \lambda_c^2 r_\lambda^2) \tau \right] \exp [i(\lambda_c r_\lambda \xi)]. \quad (719)$$

The compact form of the linear solution (717) clarifies that the critical wave with wavenumber λ_c and frequency ω_c is modulated through an amplitude function A that describes a *slow* temporal growth and a *slow* migration of the envelope of the wave packet. Growth is described by the *slow* time variable $\epsilon^2 t$, i.e. it occurs on a time scale which is $\mathcal{O}(\epsilon^{-2})$ larger than the characteristic period of the critical wave $2\pi/\omega_c$. The *slow* migration is described by the dependence of A on the slow, moving coordinate, ξ , travelling with the group velocity.

The above analysis clarifies that the main scope of the weakly nonlinear approach is to derive a nonlinear evolution equation for the amplitude function $A(\tau, \xi)$. Moreover, the derivation must be able to take into account the dependence of the process on both the fast scales (x, y, t) and the slow scales (τ, ξ) . This is a perfect context to apply the *method of multiple scales*.

The multiple scale solution

Let us write the solution of our toy model in the form:

$$u = u_0 + \varphi(x, y, t; \tau, \xi), \quad (720)$$

with u_0 basic state and φ perturbation. The dependence of φ on both fast and slow variables suggests the need to reformulate the mathematical problem using the chain rules:

$$\frac{\partial}{\partial t} \rightarrow \frac{\partial}{\partial t} - \epsilon \nu_\lambda \frac{\partial}{\partial \xi} + \epsilon^2 \frac{\partial}{\partial \tau}, \quad \frac{\partial}{\partial x} \rightarrow \frac{\partial}{\partial x} + \epsilon \frac{\partial}{\partial \xi}. \quad (721)$$

Substituting from (711) and (721) into the differential equation (665a) and noting that the repeated application of the chain rule gives:

$$\frac{\partial^2}{\partial x^2} \rightarrow \frac{\partial^2}{\partial x^2} + 2\epsilon \frac{\partial^2}{\partial x \partial \xi} + \epsilon^2 \frac{\partial^2}{\partial \xi^2}, \quad \frac{\partial^4}{\partial x^4} \rightarrow \frac{\partial^4}{\partial x^4} + 4\epsilon \frac{\partial^4}{\partial x^3 \partial \xi} + 6\epsilon^2 \frac{\partial^4}{\partial x^2 \partial \xi^2} + \mathcal{O}(\epsilon^3), \quad (722)$$

with the help of some algebra, one finds:

$$\begin{aligned} \mathcal{L}\varphi &= -\frac{\partial\varphi}{\partial y} \left[\frac{\partial\varphi}{\partial x} + \frac{\partial^2\varphi}{\partial x^2} \right] \\ &+ \epsilon \left[(\nu_\lambda - 1) \frac{\partial\varphi}{\partial \xi} - 2R_c \frac{\partial^2\varphi}{\partial x \partial \xi} - 4 \frac{\partial^4\varphi}{\partial x^3 \partial \xi} - \frac{\partial\varphi}{\partial y} \left(\frac{\partial\varphi}{\partial \xi} + 2 \frac{\partial^2\varphi}{\partial x \partial \xi} \right) \right] \\ &+ \epsilon^2 \left[-\frac{\partial\varphi}{\partial \tau} - r R_c \frac{\partial^2\varphi}{\partial x^2} - (R_c + \frac{\partial\varphi}{\partial y}) \frac{\partial^2\varphi}{\partial \xi^2} - 6 \frac{\partial^4\varphi}{\partial x^2 \partial \xi^2} \right] + \mathcal{O}(\epsilon^3), \end{aligned} \quad (723a)$$

$$\mathcal{L} \equiv \frac{\partial}{\partial t} - \frac{\partial^2}{\partial y^2} + \frac{\partial^4}{\partial x^4} + R_c \frac{\partial^2}{\partial x^2} + \frac{\partial}{\partial x}, \quad (723b)$$

$$\varphi = 0 \quad (y = 0, 1). \quad (723c)$$

We now expand the solution in powers of the small parameter ϵ , assuming that the amplitude of the perturbation at the leading order of approximation is $\mathcal{O}(\epsilon)$. The latter assumption is by no means obvious but it will be clarified below. Let us then write:

$$\varphi = \epsilon u_1 + \epsilon^2 u_2 + \epsilon^3 u_3 + \mathcal{O}(\epsilon^4). \quad (724)$$

Substituting from (724) into (723) and equating likewise powers of ϵ we find the following sequence of differential problems:

$$\boxed{\mathcal{O}(\epsilon)}$$

$$\mathcal{L}u_1 = 0, \quad (725a)$$

$$u_1 = 0 \quad (y = 0, 1). \quad (725b)$$

$$\boxed{\mathcal{O}(\epsilon^2)}$$

$$\mathcal{L}u_2 = -\frac{\partial u_1}{\partial y} \left[\frac{\partial u_1}{\partial x} + \frac{\partial^2 u_1}{\partial x^2} \right] \quad (726a)$$

$$\begin{aligned} &+ (\nu_\lambda - 1) \frac{\partial u_1}{\partial \xi} - 2R_c \frac{\partial^2 u_1}{\partial x \partial \xi} - 4 \frac{\partial^4 u_1}{\partial x^3 \partial \xi}, \\ u_2 &= 0 \quad (y = 0, 1). \end{aligned} \quad (726b)$$

$$\boxed{\mathcal{O}(\epsilon^3)}$$

$$\mathcal{L}u_3 = -\frac{\partial u_1}{\partial y} \left[\frac{\partial u_2}{\partial x} + \frac{\partial^2 u_2}{\partial x^2} \right] - \frac{\partial u_2}{\partial y} \left[\frac{\partial u_1}{\partial x} + \frac{\partial^2 u_1}{\partial x^2} \right] \quad (727a)$$

$$\begin{aligned} &+ (\nu_\lambda - 1) \frac{\partial u_2}{\partial \xi} - 2R_c \frac{\partial^2 u_2}{\partial x \partial \xi} - 4 \frac{\partial^4 u_2}{\partial x^3 \partial \xi} - \frac{\partial u_1}{\partial y} \left[\frac{\partial u_1}{\partial \xi} + 2 \frac{\partial^2 u_1}{\partial x \partial \xi} \right] \\ &- 6 \frac{\partial^4 u_1}{\partial x^2 \partial \xi^2} - \frac{\partial u_1}{\partial \tau} - r R_c \frac{\partial^2 u_1}{\partial x^2} - R_c \frac{\partial^2 u_1}{\partial \xi^2}, \\ u_3 &= 0 \quad (y = 0, 1). \end{aligned} \quad (727b)$$

Hence, at $\mathcal{O}(\epsilon)$ we recover the linear eigenvalue problem. Its solution then reads:

$$u_1 = A(\xi, \tau) S_1 E_1 + c.c., \quad (728)$$

where $A(\xi, \tau)$ is the complex amplitude function to be determined and we have employed the following notation:

$$S_m = \sin(m \pi y), \quad E_m = \exp[i m (\lambda_c x - \omega_c t)]. \quad (729)$$

Proceeding to $\mathcal{O}(\epsilon^2)$, substituting from (728) into the differential system (726), with the help of some algebra, we find:

$$\begin{aligned} \mathcal{L}u_2 = & -\frac{\pi}{2} S_2 [(i \lambda_c - \lambda_c^2) A^2 E_2 + (-i \lambda_c - \lambda_c^2) A \bar{A}] \\ & + S_1 [\nu_\lambda - 1 + i \lambda_c (-2 R_c + 4 \lambda_c^2)] \frac{\partial A}{\partial \xi} E_1 + c.c., \end{aligned} \quad (730)$$

where an overbar denotes, as usual, the complex conjugate of a complex number. The reader should note that the forcing terms on the right hand side of (730) include the effect of nonlinear interactions between the fundamental and itself or its complex conjugate.

Noting that the quantity $[\nu_\lambda - 1 + i \lambda_c (-2 R_c + 4 \lambda_c^2)]$ vanishes, the latter differential system is readily solved in the form:

$$u_2 = S_2 (u_{20} A \bar{A} + u_{22} A^2 E_2) + c.c., \quad (731)$$

with

$$u_{20} = \frac{1}{8} (1 + \frac{1}{\sqrt{\pi}} i), \quad u_{22} = \frac{1}{24} (1 - \frac{1}{\sqrt{\pi}} i). \quad (732)$$

Let us finally proceed to $\mathcal{O}(\epsilon^3)$. Substituting from (728) and (731) into the differential system (727), one finds:

$$\begin{aligned} \mathcal{L}u_3 = & S_1 E_1 \left\{ -\frac{\partial A}{\partial \tau} + (\lambda_c^2 r R_c) A + (6 \lambda_c^2 - R_c) \frac{\partial^2 A}{\partial \xi^2} \right. \\ & + \pi [i \lambda_c (u_{20} + \bar{u}_{20} - u_{22}) - \lambda_c^2 (u_{20} + \bar{u}_{20} + u_{22}) - u_{22} (i \lambda_c - 2 \lambda_c^2)] A^2 \bar{A} \\ & \left. + \text{terms proportional to } S_1 E_3, S_3 E_1, S_3 E_3, S_2 E_0, S_2 E_2, \right. \end{aligned} \quad (733)$$

where we have written explicitly only the terms proportional to $S_1 E_1$ in the right hand side of (733) as they are the only ones needed to derive the sought evolution equation for the amplitude function $A(\tau, \xi)$. Terms proportional to $S_1 E_1$ are *secular* (see Section 9.2.2) and have the same structure of the linear mode. As a result they would lead to an unbounded contribution in the solution for u_3 . The reader will readily appreciate this point noting that, making use of the linear dispersion relationship, the differential problem:

$$\begin{aligned} \mathcal{L}u_3 = & F(A) S_1 E_1 \\ u_3 = & 0 \quad (y = 0, 1), \end{aligned} \quad (734a)$$

is solved in the form:

$$u_3 = x S_1 E_1 \frac{F(A)}{1 + 2 i \lambda_c R_c - 4 i \lambda_c^3}. \quad (735)$$

It is apparent that the latter solution is unbounded as $x \rightarrow \infty$. In order to prevent this behavior we must impose a *solvability condition* that, in the present case, simply consists of constraining the function $F(A)$ to vanish. This leads to the so called Ginzburg-Landau evolution equation of the amplitude function $A(\tau, \xi)$. The name *Ginzburg-Landau* comes from a paper on superconductivity (Ginzburg and Landau, 1950), although in that context the equation is part of a larger system of equations. In general, with the notations employed here, this equation reads:

$$\frac{\partial A}{\partial \tau} = r R_c [\mu_r + i \nu_r] A - \frac{1}{2} [\mu_\lambda^2 + i \nu_\lambda^2] \frac{\partial^2 A}{\partial \xi^2} + [c_r + i c_i] A^2 \bar{A}. \quad (736)$$

For our toy model, recalling (733), some algebra shows that the coefficient $(c_r + ic_i)$ takes the form:

$$c_r + ic_i = -\frac{\pi^2}{24} \left[5 + \frac{2}{\pi} - i \frac{3}{\sqrt{\pi}} \right]. \quad (737)$$

The reader should note that, for more complex differential systems, imposing the solvability condition requires some more sophisticated mathematical argument, referred to as *Fredholm alternative*. It essentially consists of imposing the orthogonality of the secular terms to the solution of the adjoint linear differential problem. Here, we do not present the general approach, which is fairly technical, and refer the reader to specialized books (e.g. Coddington and Levinson, 1955; Nayfeh, 2000).

The particular case of Landau-Stuart equation

The Ginzburg-Landau equation derived above describes the spatial-temporal evolution of the narrow spectrum of waves that becomes unstable near critical conditions. A particular case of the latter equation had been previously proposed by Landau (Landau, 1944) and was derived by Stuart (Stuart, 1958) for the instability of laminar parallel flows. The Landau-Stuart equation (hereafter LS) describes the long-term behaviour of the single most unstable wave and reads:

$$\frac{dA}{d\tau} = rR_c [\mu_r + i\nu_r] A + [c_r + ic_i] A^2 \bar{A}. \quad (738)$$

This equation is readily seen to be obtained from (736) setting $\frac{\partial^2}{\partial \xi^2} \equiv 0$.

It proves quite instructive to examine the solution of the latter equation in some detail. Let us multiply (738) by \bar{A} and sum the resulting equation to that obtained multiplying the complex conjugate of (738) by A , to find the following equation for $|A|^2$:

$$\frac{d|A|^2}{d\tau} = 2rR_c \mu_r |A|^2 + 2c_r |A|^4. \quad (739)$$

This equation is readily solved⁽⁰⁾ in the following closed form:

$$|A|^2 = \frac{rR_c \mu_r |A_0|^2 \exp(2rR_c \mu_r \tau)}{rR_c \mu_r + c_r |A_0|^2 [1 - \exp(2rR_c \mu_r \tau)]}, \quad (740)$$

having denoted by $|A_0|$ the value of $|A|$ at $\tau = 0$.

In order to clarify the behavior of the solution (745), we must distinguish between two fundamentally different cases.

The first case is described as *supercritical instability*. It occurs when the coefficient c_r is negative with $r = 1$. Under these conditions perturbations tend to an equilibrium solution, asymptotically reached as $\tau \rightarrow \infty$, such that:

$$|A_e|^2 = -\frac{R_c \mu_r}{c_r}. \quad (744)$$

⁰ Solution is obtained by separating the variables and noting that the equation

$$\frac{df}{d\tau} = af + bf^2, \quad (741)$$

may be rewritten in the form:

$$\frac{df}{af + bf^2} = \frac{df}{a} \left[\frac{1}{f} - \frac{b}{a + bf} \right] = d\tau, \quad (742)$$

which is immediately integrated between 0 and τ to obtain:

$$f = \frac{af_0 e^{a\tau}}{a + bf_0(1 - e^{a\tau})}. \quad (743)$$

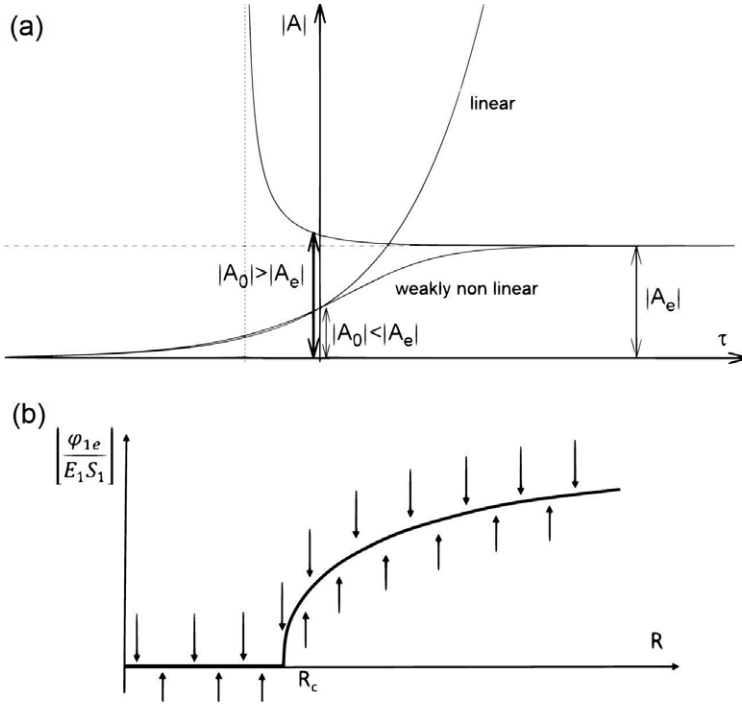


Figure 191. Sketch illustrating the solution of Landau-Stuart equation in the supercritical case. (a) Temporal dependence (b) Bifurcation diagram

Solution (745) can be thus rewritten as:

$$|A|^2 = \frac{|A_0|^2}{|A_0|^2/|A_e|^2 + (1 - |A_0|^2/|A_e|^2) \exp(2c_r|A_e|^2\tau)}. \quad (745)$$

The solution is plotted in Figure 191a. Note that it shows that perturbations with an initial amplitude $|A_0| < |A_e|$ grow leaving the linear exponential regime and tend asymptotically to the finite equilibrium amplitude $|A_e|$. On the other hand, the perturbations with an initial amplitude $|A_0|$ larger than $|A_e|$ decay asymptotically to the finite equilibrium amplitude $|A_e|$. The above equilibrium solution is stable. This is readily shown by perturbing the equilibrium solution in the form:

$$|A|^2 = |A_e|^2 + \delta \hat{a}, \quad (746)$$

with δ infinitesimal. Substituting from (746) into LS equation and retaining only terms linear in δ , one finds the following differential equation for the perturbation \hat{a} :

$$\frac{d\hat{a}}{d\tau} = [2R_c\mu_r + 4c_r|A_e|^2]\hat{a} = 2c_r|A_e|^2\hat{a}. \quad (747)$$

Since c_r is negative (747) admits of exponentially decaying solution, showing the stable character of the supercritical equilibria. This is also illustrated in the bifurcation diagram of Figure 191b. Note that the direction of arrows indicates whether perturbations let the solution depart from the equilibrium state, which is said to bifurcate from the null solution as R exceeds R_c .

The second case is described as *subcritical instability*. It occurs when the coefficient c_r is positive. Under these conditions an equilibrium amplitude of the perturbation is asymptotically reached as $\tau \rightarrow -\infty$ in the subcritical regime ($R < R_c$), the dummy parameter r being equal to -1 .

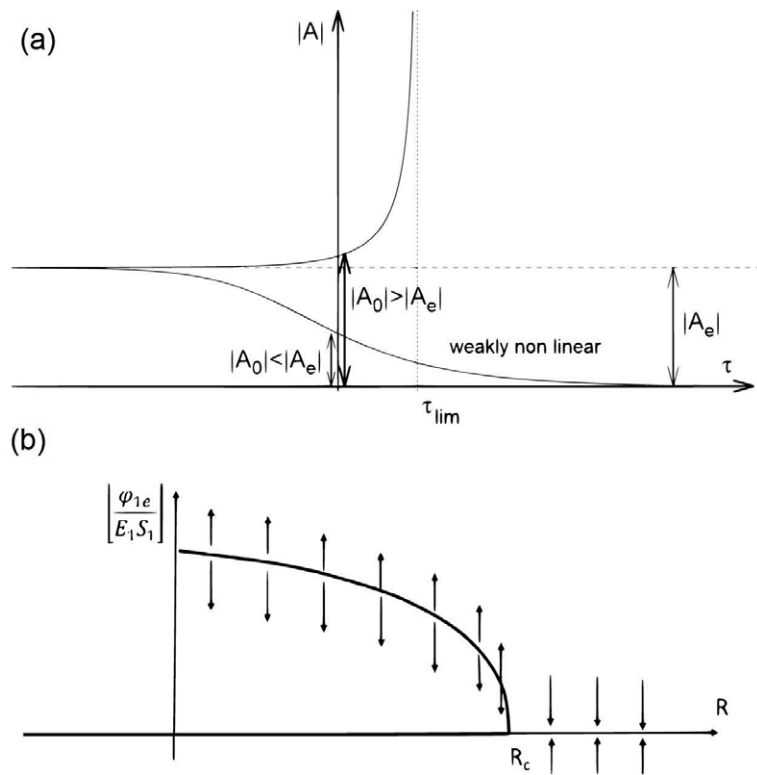


Figure 192. Sketch illustrating the solution of Landau-Stuart equation in the subcritical case. (a) Temporal dependence (b) Bifurcation diagram.

This equilibrium solution sets a *threshold amplitude for the perturbation*. The linear stability of the equilibrium solution shows that, in this case, perturbations exceeding the threshold amplitude are able to destabilize the system that is stable to infinitesimal perturbations. On the contrary, *finite* amplitude perturbations that do not exceed the threshold are stable. This is illustrated in Figure 192 which also shows that the amplitude of unstable perturbations tend to infinity at the finite $\tau_{lim} = \ln [|A_0|^2 / (|A_0|^2 - |A_e|^2)] / c_r |A_e|^2$.

Let us conclude this analysis noting that, in our toy model, the bifurcation is supercritical and the amplitude predicted by the LS equation reads:

$$|A_e| = \frac{1}{\epsilon} \sqrt{\frac{24(R - R_c)}{\pi}} = \sqrt{\frac{48\pi}{5\pi + 2}}. \quad (748)$$

Solutions of the Ginzburg-Landau equation

The properties of the solutions of the Ginzburg-Landau equation (736) have been analyzed in depth by several Authors. Here, we restrict ourselves to few fundamental results that are relevant to our morphodynamic problems.

Following Schielen *et al.* (1993) we first seek periodic solutions of (736) and set:

$$A(\xi, \tau) = \mathcal{A} \exp i(K\xi - \Omega\tau), \quad (749)$$

with \mathcal{A} , K and Ω real quantities.

Substituting into (736), the real and imaginary parts of the equation lead to the following algebraic constraints:

$$\Omega = -rR_c\nu_r - \frac{1}{2}K^2\nu_{\lambda^2} - c_i\mathcal{A}^2, \quad (750)$$

$$0 = rR_c\mu_r + \frac{1}{2}K^2\mu_{\lambda^2} + c_r\mathcal{A}^2. \quad (751)$$

From (751), assuming supercritical conditions ($r=1$), we derive the following relationship for the amplitude \mathcal{A} :

$$\mathcal{A}^2 = |A_e|_{LS}^2 - \frac{1}{2} \frac{\mu_{\lambda^2}}{c_r} K^2. \quad (752)$$

Since, for our toy model, both c_r and the coefficient μ_{λ^2} (see equation (714)) are negative, the amplitude predicted by the Ginzburg-Landau equation peaks and coincides with that predicted by the LS equation for $K = 0$, i.e. for the critical value of the perturbation wavenumber. This solution is called a *Stokes wave*. It has an amplitude that decreases from its maximum $|A_e|_{LS}$ at $K = 0$, to zero at $|K| = K_M = \sqrt{-2R_c\mu_r/\mu_{\lambda^2}}$. For $|K| > K_M$ the Stokes wave does no longer exist. For our toy model, one readily find that $|K_M| = \sqrt{(R - R_c)}/2\epsilon$. The region of the (λ, R) plane, where periodic solutions of the Ginzburg-Landau equation exist, is plotted in Figure 193. Here, *the dashed line ($|K|=K_M$) may be considered as the second order approximation of the marginal stability curve*.

The algebraic constraints (750) is essentially a nonlinear dispersion relationship, which predicts that the frequency Ω , besides depending on the wavenumber as in linear systems, is also affected by the perturbation amplitude. In our toy model, the coefficient c_i is found to be positive, hence the frequency Ω and the speed of perturbations $(\omega_c + \epsilon\nu_{\lambda}K + \Omega\epsilon^2)/(\lambda_c + \epsilon K)$ decrease as the amplitude increases. Let us finally write the complete solution at leading order. Recalling (718), (728) and (749) we write:

$$u_1 = \mathcal{A}S_1 \exp [i(\lambda_c + \epsilon K)x - i(\omega_c + \epsilon\nu_{\lambda}K + \Omega\epsilon^2)t]. \quad (753)$$

This shows that *nonlinearity affects the frequency and the speed of perturbations which decrease as the amplitude increases*. This property is common to the so called *anormal dispersive waves*.

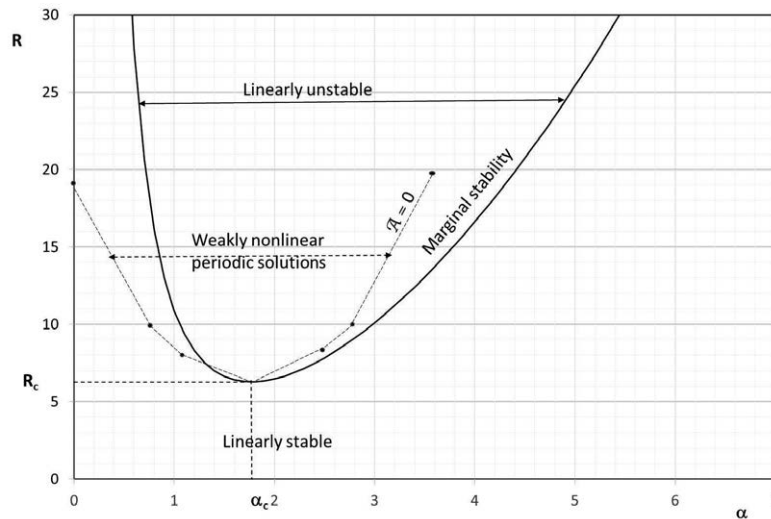


Figure 193. Sketch illustrating the region of the (λ, R) plane where nonlinear periodic solutions of the Ginzburg-Landau equation exists for our toy model, compared with the marginal stability curve of linear theory

One further feature of the Ginzburg-Landau equation is that it allows to ascertain the stable-unstable character of the periodic solutions derived above. Instability may arise from interactions between the various components of the wave group and could not be detected in the context of the LS approach, which considers the nonlinear development of a single harmonic. An application of the analysis to the nonlinear instability of free fluvial bars was presented by Schielen *et al.* (1993). We will not discuss this issue in detail as the reader should at this stage be able to carry on the linear stability analysis by himself. It suffices here to show the main result of the analysis, which is depicted in Figure 193. In the region of the (λ, R) plane bounded by the nonlinear marginal stability curve, two subregions can be defined. In the inner region periodic solutions are stable, whilst they are unstable in the outer region.

In order to determine the structure of the solution in the latter regions, one may employ numerical tools. Extensive numerical analysis was carried on by Keefe (1985) and Doelman (1991). Various types of solution emerged depending on the values of the coefficients of the equation. Solutions may converge to a stable *periodic* Stokes wave, or to a so called *quasi-periodic* pattern (such that all frequencies of the solution are integer combinations of two fundamental frequencies which are mutually irrational) or even to *chaotic* patterns. These results have conceptual relevance, but practical implications in morphodynamic problems have never been demonstrated.

10. Bibliography

- Abbott, J.E. and Francis, R.D. (1977) Saltation and suspension Trajectories of solid grains in a water stream *Philos. Trans. R. Soc. London A.*, 284: 225-254.
- Abramowitz, M. and I. Stegun (1964). Handbook of Mathematical Functions with Formulas, Graphs, and Mathematical Tables (Abramowitz and Stegun. New York: Dover. ISBN 978-0-486-61272-0.), Chapter 5.
- Adachi, S. (1967) A theory of stability of streams. *Proc. 12th Congr. IAHR, Fort Collins, Colorado*, 1:338-343.
- Adami, L. (2016) Multi-decadal morphodynamics of alternate bars in channelized rivers: a multiple perspective. *Thesis submitted in partial fulfillment of the requirements for the degree of Doctor of Philosophy in Hydrodynamics and Environmental Modeling*. University of Trent.
- Adami, L., W. Bertoldi, and G. Zolezzi (2016). Multidecadal dynamics of alternate bars in the Alpine Rhine River, *Water Resour. Res.*, 52, 8938-8955, doi:10.1002/2015WR018228.
- Allen, J.R.L., (1971a), Transverse erosional marks of mud and rock: Their physical basis and geological significance. *Sedimentary Geology*, 5, 167-385.
- Allen, J.R.L., (1971b), Bed forms due to mass transfer in turbulent flows: A kaleidoscope of phenomena. *Journal of Fluid Mechanics*, 49, 49-63.
- Amsler, M. A., and García, M. H. (1997). Discussion of sand dune geometry of large rivers during floods by P. Y. Julien and G. J. Klaassen, *Journal of Hydraulic Engineering, ASCE*, 123(6), 582-584.
- Amsler, M. L., and Schreider, M. I. (1999). Dune height prediction at floods in the Paraná River, Argentina. *River Sedimentation: theory and applications*, A. W. Jayewardena, J.H.W. Lee and Z. Y. Wang, eds., A. A. Balkema. Rotterdam, pp. 615-620.
- Ancey, C., Davison, A. C., Bohm, T., Jodeau, M., and Frey, P. (2008). Entrainment and motion of coarse particles in a shallow water stream down a steep slope. *Journal of Fluid Mechanics*, 595, 83-114. doi:10.1017/S0022112007008774
- Ancey, C. (2020a). Bedload transport: a walk between randomness and determinism. Part 1. The state of the art. *Journal of Hydraulic Research*, 58(1), 1-17. doi:10.1080/00221686.2019.1702594.
- Ancey, C. (2020b). Bedload transport : a walk between randomness and determinism. Part 2. Challenges and prospects. *Journal of Hydraulic Research*, 58(1), 18-33. doi:10.1080/00221686.2019.1702595
- Anderson, R.S. and Haff, P.K. (1988) Simulation of eolian saltation *Science*, 241, 820-823.
- Andrews, E. D. (1980). Effective and bankfull discharges of streams in the Yampa river basin, Colorado and Wyoming. *Journal of Hydrology*, 46(34):311-330.
- Aris, R. (1962), *Vector, Tensors, and the Basic Equations of Fluid Mechanics*, Dover Publications Inc., New York, 300 pp.

- Armanini, A. (1995). Non-uniform sediment transport. Dynamics of the active layer. *J. Hydr. Res.*, 33(5), 611-622, Delft, The Netherlands,.
- Armanini, A., and G. Di Silvio (1988). A one-dimensional model for the transport of a sediment mixture in non-equilibrium conditions, *J. Hydr. Res.*, 26(3), 275-292.
- Armanini, A. and Di Silvio, G. (1988). A one-dimensional model for the transport of sediment mixture in non-equilibrium condition. *J. Hydr. Res.*, 26(3), 275-292.
- ASCE Task Committee on Hydraulics, Bank Mechanics, and Modeling of River Width Adjustment (1998), River Width Adjustment. I: Processes and Mechanics, *Journal of Hydraulic Engineering* (ASCE), 124(9), 881-899
- Ashida, K. and Michiue, M. (1972) Study on hydraulic resistance and bedload transport rate in alluvial streams *Trans., Japanese Society of Civil Engineering*, 206, 59-69.
- Ashida, K. and Shiomi, Y., (1966) Study on the hydraulic behaviours of meander in channels. *Disaster Prevention Research Institute Annals, Kyoto Univ.*, 9:457-477.
- Ashmore, P. E. (1982) Laboratory modelling of gravel bed stream morphology. *Earth Surf. Proc. Landforms* 7, 201-225.
- Ashmore, P. E. (1991) How do gravel-bed rivers braid? *Can. J. Sci.* 28, 326-341.
- Aubert G., V. J. Langlois and P. Allemand (2016), Bedrock incision by bedload: insights from direct numerical simulations, *Earth Surf. Dynam.*, 4, 327-342. doi:10.5194/esurf-4-327-2016
- Auton, T. R. (1987) The lift force on a spherical body in a rotational flow. *J. Fluid Mech.* 183:199
- Baar, A. W., de Smit, J., Uijttewaal, W. S. J., and Kleinham, M. G. (2018). Bed Slopes in Rotating Annular Flume Experiments. *Water Resources Research*, 54, 19-45. doi:10.1002/2017WR020604.
- Bagchi, P. and S. Balachandar (2002). Effect of free rotation on the motion of a solid sphere at moderate Re. *Phys. Fluids*, 14:2719-2737
- Bagnold, R.A. (1941) *Physics of blown sand* (Reprinted 1954) London: Methuen.
- Bagnold, R.A. (1956) The flow of cohesionless grains in fluids *Phil. Trans. Roy. Soc. Lond.* A225: 49-63.
- Bagnold, R. A. (1966) An approach to the sediment transport problem from general physics. *Prof. Paper 422-1, U. S. Geol. Surv.*
- Bagnold, R.A. (1973) The nature of saltation and of 'bed-load' transport in water *Proc. R. Soc. London A*, 332, 473-504.
- Balachandar, S. (2009). A scaling analysis for point-particle approaches to turbulent multiphase flows. *Int. J. Multiphase Flow* 35:801-10
- Balachandar, S. and J. K. Eaton (2010). Turbulent Dispersed Multiphase Flow. *Annu. Rev. Fluid Mech.*, 42, 111-33
- Bankert, A. R. and Nelson, P. A. (2018) Alternate bar dynamics in response to increases and decreases of sediment supply, *Sedimentology* 65, 702-720. doi:10.1111/sed.12399
- Basset, A. B. (1888). A Treatise on Hydrodynamics, Vol. 2, Ch. 22, Deighton, Bell and Co., Cambridge, England.
- Batchelor G. K. (1967) An Introduction to Fluid Dynamics. Cambridge, UK: Cambridge Univ. Press
- Batchelor, G. K. (1970). An Introduction to Fluid Dynamics, Cambridge, University Press, Massachusetts.
- Batchelor, G. K. (1988) A new theory of the instability of a uniform fluidized bed. *J. Fluid Mech.* 193, 75-110.
- Beer, A. R. and J. M. Turowski (2015) Bedload transport controls bedrock erosion under sediment-starved conditions, *Earth Surf. Dynam.*, 3, 291-309.
- Bers, A. (1975). Linear waves and instabilities. In *Physique des Plasmas*, ed. C DeWitt, J. Peyraud, pp. 117-215. New York: Gordon & Breach

- Bers, A. (1983). Space-time evolution of plasma instabilities-absolute and convective. In *Handbook of Plasma Physics*, ed. M. N. Rosenbluth, R. Z. Sagdeev, I : 451-517. Amsterdam: North-Holland
- Bertagni, M. B. and C. Camporeale (2018) Finite Amplitude of Free Alternate Bars With Suspended Load, *Water Resources Research*, 54, 9759-9773, doi:10.1029/2018WR022819.
- Bertagni M. B., Perona P., Camporeale C. (2018) Parametric transitions between bare and vegetated states in water-driven patterns. *Proceedings of the National Academy of Sciences* 115(32): 8125-8130, doi:10.1073/pnas.1721765115.
- Bertoldi, W., A. Siviglia, S. Tettamanti, M. Toffolon, D. Vetsch, and S. Francalanci (2014), Modeling vegetation controls on fluvial morphological trajectories, *Geophys. Res. Lett.*, 41, 7167-7175, doi:10.1002/2014GL061666.
- Best, J. (2005). The fluid dynamics of river dunes : A review and some future research directions. *Journal of Geophysical Research*, 110(F04S02), 1-21. doi:10.1029/2004JF000218
- Bitter, J. G. A. (1963), A study of erosion phenomena, part 1, *Wear*, 6, 5-21.
- Bittner, L. (1994) River bed response to channel width variation: Theory and experiments. *Thesis submitted in partial fulfillment of the requirements of the degree of Master of Science. Graduate School of Civil Engineering.* University of Illinois at Urbana-Champaign.
- Blom, A., J. S. Ribberink, and G. Parker (2008), Vertical sorting and the morphodynamics of bed form-dominated rivers: A sorting evolution model, *J. Geophys. Res.*, 113, F01019, doi:10.1029/2006JF000618.
- Blondeaux, P. and Seminara, G. (1983) Bed topography and instabilities in sinuous channels. In *Proc. ASCE Rivers '83*, New Orleans, pp. 747-758.
- Blondeaux, P., and G. Seminara (1985), A unified bar-bend theory of river meanders, *J. Fluid Mech.*, 157:449-479.
- Blondeaux, P. and G. Vittori, (2023), Sea waves and small scale bedforms, *Monograph Series on Morphodynamics of Sedimentary Patterns*, Ed. Genova University Press.
- Blondeaux, P., Colombini, M., Seminara, G. and G. Vittori, (2018), Introduction to Morphodynamics of Sedimentary Patterns, *Monograph Series on Morphodynamics of Sedimentary Patterns*, Ed. Genova University Press.
- Blondeaux, P., Brocchini, M. and G. Vittori, (2023), Waves, currents and bedforms in the nearshore region, *Monograph Series on Morphodynamics of Sedimentary Patterns*, Ed. Genova University Press.
- Blumberg, P. N. and R. L. Curl (1974), Experimental and theoretical studies of dissolution roughness. *Journal of Fluid Mechanics*, 5, 735-742.
- Bohorquez, P., and Ancy, C. (2015). Stochastic-deterministic modeling of bed load transport in shallow water flow over erodible slope: Linear stability analysis and numerical simulation. *Advances in Water Resources*, 83, 36-54.
- Bolla Pittaluga, M., and G. Seminara (2003), Depth-integrated modelling of suspended sediment transport, *Water Resour. Res.*, 39(5), 1137, doi:10.1029/2002WR001306.
- Bolla Pittaluga M., Luchi R., Seminara G. (2014a) On the equilibrium profile of river beds. *J. Geophys. Res. Earth Surf.*, 119(2), 317-32, doi:10.1002/2013JF002806.
- Bolla Pittaluga M., Tambroni N., Canestrelli A., Slingerland R., Lanzoni S., Seminara G. (2014b) Where river and tide meet: The morphodynamic equilibrium of alluvial estuaries. *J. Geophys. Res. Earth Surf.*, 120, 75-94, doi:10.1002/2014JF003233.
- Bonnefille, R. (1963). Essais de synthese des lois de debut d'entrainement des sediments sous l'action d'un courant en regime uniform. *Bulletin du Centre de Recherche et d'Essais de Chatou*, 5, France (in French).
- Borisenko, A.I., Tarapov, I.E. (1968), *Vector and Tensors Analysis With Applications*, Dover Publications Inc., New York, 257 pp.
- Bourke, M. and H. Viles (2007) A Photographic Atlas of Rock Breakdown Features in Geomorphic Environments, Edited by Mary Bourke and Heather Viles, Planetary Science Institute.

- Boussinesq, V. J. (1885). Sur la resistance qu'oppose un liquide indéfini en repos sans pesanteur, au mouvement varié d'une sphère solide qu'il mouille sur toute sa surface, quand les vitesses restent bien continues et assez faibles pour que leurs carrés et produits soient négligeables., *Comptes Rendu, Acad. Sci.*, 100:935-937
- Boussinesq, V. J. (1877) Essai sur la théorie des eaux courantes (Treatise on the theory of flowing water), Mémoires présentés par divers savants à l'Académie des sciences 23 (1877) 1-660 (in French).
- Bowen, R. M. (1971) Continuum Physics II, A. C. Eringen, Ed. Academic Press, NY.
- Brice, J. C. (1984), Planform properties of meandering rivers, Keynote paper, in *River Meandering, Proceedings of the Conference Rivers, '83 New Orleans, LA*, 24-26 October 1983, edited by C. M. Elliott, pp. 1-15, American Society of Civil Engineers, N. Y.
- Bridge J. S. and Dominic D. F. (1984) Bed Load Grain Velocities and Sediment Transport Rates, *Water Resources Research* 20(4):476-490, doi:10.1029/WR020i004p00476.
- Briggs, R. J. (1964). Electron-Stream Interaction With Plasmas. *Cambridge, Mass: MIT Press*
- Brownlie, W.R., (1981) Prediction of flow depth and sediment discharge in open channel. *W.M. Laboratory Report No KH-R-43A*.
- Brownlie, W. R. (1983). Flow depth in sand-bed channels. *Journal of Hydraulic Engineering*, 109(7), 959-990.
- Buffington, J. M. (1999). The legend of A. F. Shields. *Journal of Hydraulic Engineering ASCE*, 125(4): 376-387 ISSN 0733-9429/99/0004-0376-0387
- Callander, R. A. (1969) Instability and river channels. *J. Fluid Mech.* 36:465.
- Carling, P. A., Williams, J. J., Golz, E., and Kesley, A. D. (2000). The morphodynamics of fluvial sand dunes in the River Rhine, near Mainz , Germany. II. Hydrodynamics and sediment transport. *Sedimentology*, 47, 253-278.
- Carling, P. A., J. Herget, J. K. Lanz, K. Richardson and A. Pacifici (2009) Channel-scale erosional bedforms in loose granular material and in bedrock: character, processes and implications. In: *Megaflooding on Earth and Mars*, ed. Devon M. Burr, Paul A. Carling and Victor R. Baker. Cambridge University Press.
- Carrier GF. (1958). Shock waves in a dusty gas. *J. Fluid Mech.* 4:376-82
- Carrier, G. F., Krook M. and C. E. Pearson (2005) Functions of a Complex Variable: Theory and Technique, *SIAM*
- Celik, I. and Rodi, W. (1984). Simulation of free-surface effects in turbulent channel flows. *Physicochemical Hydrodynamics*, 5, 217-227.
- Celik, I., and Rodi, W. (1988). Modeling suspended sediment transport in non-equilibrium situations. *J. Hydr. Engrg., ASCE*, 114(10), 1157-1191.
- Chang H., Simons, B. D. and Woolhiser, D. A. (1971) Flume experiments on alternate bar formation. *J. Waterways, Proc. A.S.C.E.* 97 (WW 1), 155.
- Charru, F. (2006) Selection of the ripple length on a granular bed sheared by a liquid flow. *Phys. Fluids*, 18 (12), 121508.
- Charru, F., Andreotti, B. and Claudin, P. (2013) Sand ripples and dunes. *Annu. Rev. Fluid Mech.* 45 (1), 469-493.
- Chatanantavet, P., and G. Parker (2008), Experimental study of bedrock channel alluviation under varied sediment supply and hydraulic conditions, *Water Resour. Res.*, 44, W12446, doi:10.1029/2007WR006581.
- Chatanantavet, P., and G. Parker (2009), Physically based modeling of bedrock incision by abrasion, plucking, and macroabrasion, *J. Geophys. Res.*, 114, F04018, doi:10.1029/2008JF001044.
- Chatanantavet, P., K. X. Whipple, M. Adams, and M. P. Lamb (2013), Experimental study on coarse grain saltation dynamics in bedrock channels, *J. Geophys. Res. Earth Surf.*, 118, 1161-1176, doi:10.1002/jgrf.20053.

- Chavarrías, V., Schielen, R., Ottevanger, W. and A. Blom (2019) Ill posedness in modelling two-dimensional morphodynamic problems: effects of bed slope and secondary flow, *J. Fluid Mech.*, 868, 461-500, doi:10.1017/jfm.2019.166
- Chézy, A. (1776). Formule pour trouver la vitesse de l'eau conduit dans une rigole donnée. Dossier 847(MS 1915) of the manuscript collection of the École National des Ponts et Chaussées, Paris. Reproduced in: Mouret, G. (1921). Antoine Chézy: histoire d'une formule d'hydraulique. *Annales des Ponts et Chaussées* 61,165-269.
- Choi, H., Moin, P., and Kim, J. (1993). Direct numerical simulation of turbulent flow over riblets. *Journal of Fluid Mechanics*, 255, 503-539. doi:10.1017/S0022112093002575.
- Church, M., and S. P. Rice (2009), Form and growth of bars in a wandering gravel-bed river, *Earth Surf. Processes Landforms*, 34(10), 1422-1432, doi:10.1002/esp.1831.
- Clift, R., Grace, J. R. and M. E. Weber (1978). *Bubbles, Drops and Particles*. Academic, New York.
- Coddington, E. A. and Levinson, N. (1955) *Theory of Ordinary Differential Equations*. McGraw-Hill.
- Coleman N. L. (1967) A theoretical and experimental study of drag and lift forces acting on a sphere resting on a hypothetical stream bed. *Proceedings of 12th IAHR Congress, vol 3. Fort Collins*, 185-192
- Coleman, N. L. (1969). A new examination of sediment suspension in open channels. *J. Hydr. Res.*, 7(1), 67-82.
- Coles, D. (1956). The law of the wake in the turbulent boundary layer. *J. Fluid Mech.* 1, 191-226.
- Colombini, M. (1993), Turbulence driven secondary flows and the formation of sand ridges, *J. Fluid Mech.*, 254, 701-719, doi:10.1017/S0022112093002319.
- Colombini, M. (2004), Revisiting the linear theory of sand dune formation, *J. Fluid Mech.* vol. 502, pp. 1-16.
- Colombini, M and Parker, G. (1995), Longitudinal streaks, *J. Fluid Mech.* (1995), 304, 161-183.
- Colombini, M., and M. Tubino, (1991) Finite-amplitude free bars: A fully nonlinear spectral solution, in *Sand Transport in Rivers, Estuaries and the Sea*, edited by R. Soulsby and R. Bettess, pp. 163-169, A. A. Balkema, Brookfield.
- Colombini, M., G. Seminara, and M. Tubino (1987), Finite-amplitude alternate bars, *J. Fluid Mech.*, 181:213-232.
- Copeland, R. R., Biedenharn, D. S., and C., F. J. (2000), Channel forming discharge. Technical Note ERDC/CHL CHETN-VIII-5, U.S. Army Corps of Engineers, Washington D.C., USA.
- Cordier, F., P. Tassi, N. Claude, A. Crosato, S. Rodrigues, D. Pham Van Bang (2019), Numerical study of alternate bars in alluvial channels with nonuniform sediment, *Water Resources Research*, 55 (4), 2976-3003, doi: 10.1029/2017WR022420.
- Crosato, A., E. Mosselman, F. Beidmariam Desta, and W. S. J. Uijttewaal (2011), Experimental and numerical evidence for intrinsic nonmigrating bars in alluvial channels, *Water Resour. Res.*, 47, W03511, doi:10.1029/2010WR009714.
- Crosato, A., F. B. Desta, J. Cornelisse, F. Schuurman, and W. S. J. Uijttewaal (2012), Experimental and numerical findings on the long-term evolution of migrating alternate bars in alluvial channels, *Water Resour. Res.*, 48, W06524, doi:10.1029/2011WR011320.
- Crosby, B. T. (2006) The Transient Response of Bedrock River Networks to Sudden Base Level Fall Submitted to the Department of Earth, Planetary Sciences in partial fulfillment of the requirements for the degree of Doctor of Philosophy in Geology at the Massachusetts Institute of Technology.
- Crosby B. and K. X. Whipple (2006). Knickpoint initiation and distribution within fluvial networks: 236 waterfalls in the Waipaoa River, North Island, New Zealand. *Geomorphology*, 82, 16-38, doi: 10.1016/j.geomorph.2005.08.023
- Crosby, B. T., K. X. Whipple, N. M. Gasparini, and C. W. Wobus (2007) Formation of fluvial hanging valleys: Theory and simulation, *J. Geophys. Res.*, 112, F03S10, doi:10.1029/2006JF000566.

- Crowe C., Sommerfeld M. and Y. Tsuji (2012) *Multiphase Flows with Droplets and Particles*. Boca Raton, FL: CRC Press
- Curl, R.L., (1966), Scallops and flutes. *Cave Research Group of Great Britain Transactions*, 7, 121-160.
- Darby, S. E., H. Q. Trieu, P. A. Carling, J. Sarkkula, J. Koponen, M. Kumm, I. Conlan, and J. Leyland (2010) A physically based model to predict hydraulic erosion of fine-grained riverbanks: The role of form roughness in limiting erosion, *J. Geophys. Res.*, 115, F04003, doi:10.1029/2010JF001708.
- Dean, R. B. (1974) *Aero Rept. 74-11, Imperial College, London*.
- Dean, R. B. (1978). Reynolds number dependence of skin friction and other bulk flow variables in two-dimensional rectangular duct flow. *J. Fluids Eng. Trans.* ASME 100, 215-223.
- Defina, A. (2003) Numerical experiments on bar growth. *Water Resour. Res.* 39, art. no. 1092.
- Demeter, G. I., L. S. Sklar, and J. R. Davis (2005), The influence of variable sediment supply and bed roughness on the spatial distribution of incision in a laboratory bedrock channel, *Eos Trans. AGU*, Fall Meet. Suppl., H53D-0519.
- de Saint-Venant, A. J. C. B. (1871) Théorie du mouvement non-permanent des eaux avec application aux crues des rivières et à l'introduction des marées dans leur lit (Theory of unsteady water flow, with application to river floods and tidal propagation in rivers), *C. r. hebdomadaire des séances Acad. sci.* 73, 148-154; 73, 237-240 (in French).
- Dey, S. (2001). Bank profile of threshold channels: a simplified approach. *Journal of Irrigation and Drainage Engineering*, 127(3), 184-187.
- Dietrich, W. E., (1982) Settling Velocity of Natural Particles, *Water Resour. Res.*, 18(6) 1615-1626
- Dietrich, W. E., J. W. Kirchner, H. Ikeda, and F. Iseya (1989), Sediment supply and the development of the coarse surface layer in gravel-bedded rivers, *Nature*, 340, 215-217, doi:10.1038/340215a0.
- Dietrich, W. E., P. A. Nelson, E. Yager, J. G. Venditti, M. P. Lamb, and L. Collins (2005), Sediment patches, sediment supply, and channel morphology, in *River, Coastal and Estuarine Morphodynamics: RCEM 2005*, edited by G. Parker and M. H. Garcia, pp. 79-90, Taylor and Francis, London.
- Dinehart, R. L. (1989). Dune migration in a steep, coarse-bedded stream. *Water Resources Research*, 25(5), 911-923.
- Diplas, P. and G. Vigilar (1992) Hydraulic Geometry of Threshold Channels, *Journal of Hydraulic Engineering*, 118(4), 597-614.
- Doelman A. (1991) Finite dimensional models of the Ginzburg-Landau equation. *Nonlinearity* 4, 231-250
- Drake, T.G., Shreve, R.L., Dietrich, W.E., Whiting, P.J. and Leopold, L.B. (1988) Bedload transport of fine gravel observed by motionpicture photography *J. Fluid Mech.*, 192, 193-217.
- Drew, D.A., (1983). Mathematical modeling of two-phase flow. *Annual Review of Fluid Mechanics*, 15. Annual Reviews, Inc., pp. 261-291.
- Dunne, K. B. J. and Jerolmack, D. J. (2020). What sets river width? *Science Advances*, 6(41), 1-9. doi: 10.1126/sciadv.abc1505
- Duran, O., Andreotti, B., and Claudin, P. (2012) Numerical simulation of turbulent sediment transport, from bed load to saltation, *Phys. Fluids*, 24, 103306, doi:10.1063/1.4757662.
- Durbin, P.A. and Petterson Reif, B.A. (2011) *Statistical theory and modeling for turbulent flows*. 2nd Edition.
- Eckelmann, H. (1974) The structure of the viscous sublayer and the adjacent wall region in a turbulent channel flow. *J. Fluid Mech.* 65, 439.
- Eekhout, J. P. C. (2014) *Morphological Processes in Lowland Streams. Implications for Stream Restoration*, Thesis submitted in fulfillment of the requirements for the degree of doctor at Wageningen University, the Netherlands.

- Eekhout, J. P. C., A. J. F. Hoitink, and E. Mosselman (2013), Field experiment on alternate bar development in a straight sand-bed stream, *Water Resour. Res.*, 49, 8357-8369, doi:10.1002/2013WR014259.
- Egiazaroff, I. V. (1965) Calculation of nonuniform sediment concentrations, *Journal of Hydraulic Engineering*, 91(4), 225-247
- Einstein, A. (1926). Die Ursache der Mäanderbildung der Flussläufe und des sogenannten Baerschen Gesetzes Die Naturwissenschaften, 14 (11), 223-224 doi: 10.1007/BF01510300
- Einstein, H. (1937). Der Geschiebetrieb als Wahrscheinlichkeit problem (Bedload transport as a probability problem) (English translation by W.W. Sayre, in Sedimentation (Symposium to honor H. A. Einstein), edited by H. W. Shen, Fort Collins, Colorado, 1972, C1-C105). Zurich: ETHZ.
- Einstein, H. A. (1950). The Bedload function for sediment transportation in open channel flows. *Technical Bulletin 1026, U.S. Dept. of the Army, Soil Conservation Service*, 1-71.
- Einstein, H. A., and Chien, N. (1955). Effects of heavy sediment concentration near the bed on velocity and sediment distribution. *MRD Series No. 8, Univ. of California/Missouri River Div., Corps of Engrs., Omaha, Neb.*
- Elghobashi, S. (1991). Particle-laden turbulent flows: direct simulation and closure models. *Appl. Sci. Res.* 48:301-14
- Elghobashi, S. (1994). On predicting particle-laden turbulent flows. *Appl. Sci. Res.* 52:309-29
- Elghobashi S. and Truesdell G.C. (1993). On the two-way interaction between homogeneous turbulence and dispersed solid particles. I: Turbulence modification. *Phys. Fluids A* 5:1790-801
- Engelund, F. (1964). A practical approach to self-preserving turbulent flows. *Acta Polytechnica Scandinavica*.
- Engelund, F. (1974), Flow and bed topography in channel bends, *J. Hydraul. Div.*, 574 100 (11), 1631-1648.
- Engelund, F. and Fredsøe, J. (1976) A Sediment Transport Model for Straight Alluvial Channels, *Nordic Hydrology*, 7: 293-306
- Engelund F. and Fredsøe J. (1982). Sediment ripples and dunes. *Annu. Rev. Fluid Mech.* 14:13-37
- Engelund, F. and Hansen, E. (1966). Hydraulic resistance in alluvial streams, *Acta Polytechnica Scandinavica*, V. Ci-35.
- Engelund, F., and Hansen, E. (1967). A Monograph on Sediment Transport in Alluvial Streams. *Teknisk Vorlag*, Copenhagen, Denmark.
- Engelund, F. and Skovgaard, O. (1973) On the origin of meandering and braiding in alluvial streams. *J. Fluid Mech.* 57, 289.
- Engle, P. A. (1978), *Impact Wear of Materials*, Elsevier Sci., New York.
- Exner, F. M. (1925) Über die Wechselwirkung zwischen Wasser und geschiebe in Flüssen. *Sitzer Akad. Wiss. Wien* 165-180.
- Fadlun, E., Verzicco, R., Orlandi, P., Mohd-Yusof, J. (2000) Combined immersed-boundary finite-difference methods for threedimensional complex flow simulations, *J. Comput. Phys.* 161, 35-60.
- Federici, B., and G. Seminara (2003), On the convective nature of bar instability, *J. Fluid Mech.*, 487, 125-145.
- Federici, B., and G. Seminara (2006), Effect of suspended load on sandbar instability, *Water Resour. Res.*, 42, W07407, doi:10.1029/2005WR004399.
- Fenton, J.D. and Abbott, J.E. (1977) Initial movement of grains on a stream bed: the effect of relative protrusion *Proc. Roy. Soc. London.A* 352: 523-537.
- Ferguson, R.I., Prestegard, K. and Ashworth, P.J. (1989) Influence of sand on hydraulics and gravel transport in a braided, gravel-bed river. *Water Resources Research* 25, 635-43.

- Fernandez Luque, R., and R. van Beek (1976), Erosion and transport of bed-load sediment, *J. Hydraul. Res.*, 14, 127-144.
- Ferrante A, Elghobashi S. (2003) On the physical mechanism of two-way coupling in particle-laden isotropic turbulence. *Phys. Fluids* 15:315-29
- Ferry J, Rani SL, Balachandar S. (2003). A locally implicit improvement of the equilibrium Eulerian method. *Int. J. Multiphase Flow* 29:869-91
- Ferry, J. and S. Balachandar (2001). A fast Eulerian method for disperse two-phase flow. *Int. J. Multiphase Flow* 27:1199-1226.
- Fick, A. (1855) *Ann. der Phys.* 94: 59.
- Finnegan N. J. (2007) Channel morphology and bedrock river incision: Theory, experiments, and application to the eastern Himalaya, Ph D Dissertation, University of Washington, USA.
- Finnegan, N. J., Roe, G., Montgomery, D. R., and Hallet, B. (2005). Controls on the channel width of rivers: Implications for modeling fluvial incision of bedrock. *Geology*, 33(3), 229-232, doi: 10.1130/G21171.1
- Finnegan, N. J., L. S. Sklar, and T. K. Fuller (2007), Interplay of sediment supply, river incision, and channel morphology revealed by the transient evolution of an experimental bedrock channel, *J. Geophys. Res.*, 112, F03S11, doi:10.1029/2006JF000569.
- Fischer, H. B., List, E. J., Koh, R. C. Y., Imberger, J., and Brooks, N. H. (1979). *Mixing in Inland and Coastal Waters*. New York: Academic Press.
- Fletcher, C. A. J. (1991). *Computational Techniques for Fluid Dynamics. 1*, CSpringer-Verlag, Berlin, Heidelberg.
- Francalanci S. (2005) Sediment transport processes and local scale effects on river morphodynamic. Thesis submitted in partial fulfillment of the requirements for the degree of Doctor of Philosophy in in Hydrodynamics and Environmental Modeling. University of Florence
- Francalanci, S., and Solari, L. (2007). Gravitational effects on bed load transport at low shields stress: Experimental observations, *Water Resour. Res.*, 43, W03424.
- Francalanci, S., and Solari, L. (2008). Bed-Load Transport Equation on Arbitrarily Sloping Beds. *Journal of Hydraulic Engineering*, 134(1), ISSN 0733-9429/2008/1-110-115
- Francalanci, S., Lanzoni, S., Solari, L. and Papanicolaou, A. N. (2020). Equilibrium cross section of river channels with cohesive erodible banks. *Journal of Geophysical Research: Earth Surface*, 125, e2019JF005286. doi:10.1029/2019JF005286
- Francis, J.R.D. (1973) Experiments on the motion of solitary grains along the bed of a water stream. *Proc. R. Soc. London A*, 332, 443-471.
- Fredsøe, J. (1978) Meandering and braiding of rivers. *J. Fluid Mech.* 84, 609-624.
- Fredsøe, J. (1982). Shape and dimensions of stationary dunes in rivers. *Journal of the Hydraulics Division*, ASCE, 108(8), 932-947.
- Fredsøe, J., and R. Deigaard (1992). *Mechanics of Coastal Sediment Transport*. World Scientific.
- Frisch, U. (1995) *Turbulence: The Legacy of A. N. Kolmogorov*. Cambridge University Press.
- Fujita, Y. and Y. Muramoto (1982) Experimental study on stream channel processes in alluvial rivers, *Bull., Disast. Prev. Res. Inst., Kyoto Univ.*, 32(1), 49-96.
- Fujita, Y., and Y. Muramoto, (1985) Studies on the process of development of alternate bars, *Bull. Disaster Prev. Res. Inst. Kyoto Univ.*, 35: 55-86.
- Furbish, D. J., Haff, P. K., Roseberry, J. C., and Schmeeckle, M. W. (2012). A probabilistic description of the bed load sediment flux: 1. Theory. *Journal of Geophysical Research*, 117(F03031) doi:10.1029/2012JF002352.
- Furbish, D. J., Fathel, S. L., Schmeeckle, M. W., Jerolmack, D. J., and Schumer, R. (2017). The elements and richness of particle diffusion during sediment transport at small timescales. *Earth Surface Processes and Landforms*, 42, 214-237. doi:10.1002/esp.4084
- Galappatti, R., (1983) A depth-integrated model for suspended transport, *Delft University of Technology, Faculty of Civil Eng.*, Report No.83-7.

- Galappatti, R. and Vreugdenhil, C.B. (1985) A depth-integrated model for suspended sediment transport, *J. Hydr. Res.*, 23(4):359-377.
- Garcia, M.H. (2008) Sedimentation engineering: processes, measurements, modeling and practice, *ASCE manuals and reports on engineering practice*, 110. ASCE: Reston. ISBN: 978-0-7844-0814-8. xx, 1132.
- Garcia, M. H. and G. Parker, (1991) Entrainment of Bed Sediment Into Suspension. *Journal of Hydraulic Engineering*, 117(4), 414-435.
- Gatignol R. (1983). The Faxén formulae for a rigid particle in an unsteady non-uniform Stokes flow. *J Mecanique Theorique et Appliquè* 1(2):143-160.
- Gelfenbaum, G., and J. D. Smith (1986), Experimental evaluation of a generalized suspended-sediment transport theory, in *Shelf Sands and Sandstones*, edited by R. J. Knight and J. R. Mclean, pp. 133-144, Canadian Society of Petroleum Geologists Memoir II, Calgary, Alberta, Canada.
- Gilbert, G. K. (1877), *Report on the Geology of the Henry Mountains: Geographical and Geological Survey of the Rocky Mountain Region*, 160 pp., U.S. Gov. Print. Off., Washington, D. C.
- Gilbert, G.K., (1914a) Transportation of Debris by Running Water *Professional Paper* No. 86, United States Geological Survey.
- Gilbert, G. K. (1914b), The transport of debris by running water, *U.S. Geol. Survey Prof. Paper* 86, 263 p.
- Ginzburg, V.L. and L.D. Landau, (1950) On the theory of superconductivity, *Zh. Eksper. Teor. Fiz.*, 20, 1064-1082 (In Russian) (English transl.: *Men of Physics: L.D. Landau (D. ter Haar, ed.)*, Pergamon, 1965,138-167)
- Glover, R. E. and Q. L. Florey (1951) Stable channel profiles, *Bureau of Reclamation Hydraulic Lab. Rep.*, n. 325
- Goldstein, D., Handler, R. and Sirovich, L. (1993) Modeling a no-slip boundary with an external force field, *J. Comput. Phys.* 105, 354–366.
- Gomez, B., R. L. Naff, and D. W. Hubbell (1989), Temporal variations in bedload transport rates associated with the migration of bedforms, *Earth Surf. Processes Landforms*, 14, 135-156, doi:10.1002/esp.3290140205.
- Graf, W. H. (1971). Hydraulics of sediment transport. McGraw-Hill Book Co., Inc., New York, N.Y.
- Green, M. A., Rowley, C. W. and Haller, G. (2007) Detection of Lagrangian coherent structures in three-dimensional turbulence, *Journal of Fluid Mechanics*, 572, 111-120.
- Gresho, P. M. (1991). Incompressible Fluid Dynamics: Some Fundamental Formulation Issues, *Annu. Rev. Fluid Mech.*, 23, 413-453.
- Griffiths, G. A. (1981) Stable-channel design in gravel-bed rivers *Journal of Hydrology*, 52(3-4), 291-305.
- Guy, H.P., Simmons, D.B and Richardson, E.V. (1966) Summary of Alluvial Channel Data from Fume Experiments, 1956-61 *Professional Paper* 462-I, United States Geological Survey.
- Hack J. T. (1957). Studies of longitudinal stream profiles in Virginia Maryland. *U.S. Geol. Surv. Prof. Pap.*, 294-B:97.
- Hadamard, J. S. (1923) Lectures on Cauchy's Problem in Linear Partial Differential Equations, *Yale University Press*.
- Hager, W. H., and Castro-Orgaz, O. and Hutter, K. (2019) Correspondence between de Saint-Venant and Boussinesq. 1: Birth of the Shallow Water Equations, *Comptes Rendus Mécanique* 347 (9), 632-662
- Hall, P. (2007) A note on bar instabilities in very wide rivers. *Int. J. of Computing Science and Mathematics* 1, 147-156.
- Hansen, E. (1967) The formation of meanders as a stability problem. *Hydraul. Lab., Tech. Univ. Denmark Basic Res. Prog. Rep. no. 13*.

- Happel, J. and H. Brenner (1965). Low Reynolds number hydrodynamics: With special applications to particulate media. *Prentice-Hall (Englewood Cliffs, N.J.)*
- Hasegawa, K. (1981) Bank-erosion discharge based on a non-equilibrium theory (in Japanese), *Trans. Jpn. Soc. Civil Eng.*, 316, 37-52.
- Hashin, Z. (1964) Theory of mechanical behaviour of heterogeneous media. *Appl. Mech. Rev.* 17, 1-9
- Hassan, M. A., and Church, M. (1994). Vertical mixing of coarse particles in gravel-bed rivers: A kinematic model, *Water Resour. Res.*, 30(4), 1173-1185.
- Hayashi, T. (1971) Study on the cause of meandering of rivers. *Trans. JSCE* 2:235.
- Hayashi, T. and Ozaki, S. (1980) Alluvial bed form analysis - formation of alternating bars and braids. In *Application of Stochastic Processes in Sediment Transport (ed. T. Kishi & M. Kuroki) Water Resources Publ., Littleton, Colorado*, pp. 7.1-7.40.
- Head, M. R. and Bandyopadhyay, P. (1981) New aspects of turbulent boundary-layer structure. *J. Fluid Mech.* 107, 297-337.
- Head, W. J., and M. E. Harr (1970), The development of a model to predict the erosion of materials by natural contaminants, *Wear*, 15, 1-46.
- Heathershaw, A.D. and Thorne, P.D. (1985) Sea-bed noises reveal role of turbulent bursting phenomenon in sediment transport by tidal currents. *Nature* 316, 339-432.
- Henshaw, A. J., A. M. Gurnell, W. Bertoldi, and N. A. Drake (2013), An assessment of the degree to which Landsat TM data can support the assessment of fluvial dynamics, as revealed by changes in vegetation extent and channel position, along a large river, *Geomorphology*, 202, 74-85, doi:10.1016/j.geomorph.2013.01.011.
- Hersen, P. (2005), Flow effects on the morphology and dynamics of aeolian and subaqueous barchan dunes, *J. Geophys. Res.*, 110, F04S07, doi:10.1029/2004JF000185.
- Hey, R. and Thorne, C. (1986) Stable Channels with Mobile Gravel Beds, *Journal of Hydraulic Engineering*, 112(8), 671-689.
- Heywood, J. G., Rannacher, R., Turek, S. (1994). Artificial boundaries and flux and pressure conditions for Navier-Stokes Equations *Int. J. Comput. Fluid Mech.*, 22, 325-352.
- Hibma, A., Schuttelaars, H. M., and Wang, Z. B. (2003). Comparison of longitudinal equilibrium profiles of estuaries in idealized and process-based models. *Ocean Dynamics*, 53, 252-269, doi:10.1007/s10236-003-0046-7
- Hirano, M. (1971), River bed degradation with armouring (in Japanese), *Trans. Jpn. Soc. Civ. Eng.*, 3, 194-195.
- Hirano, M. (1973), River-bed variation with bank-erosion, *Trans. Jpn. Soc. Civ. Eng.*, 210:13-20 (in Japanese).
- Hirsch, C. (2007). Numerical Computation of Internal and External Flows, 2nd Edition *Butterworth-Heinemann, Elsevier, Oxford*. ISBN: 978-0-7506-6594-0
- Hodge, R. A., and T. B. Hoey (2012), Upscaling from grain-scale processes to alluviation in bedrock channels using a cellular automaton model, *J. Geophys. Res.*, 117, F01017, doi:10.1029/2011JF002145.
- Hodge, R. A., T. B. Hoey, and L. S. Sklar (2011), Bed load transport in bedrock rivers: The role of sediment cover in grain entrainment, translation, and deposition, *J. Geophys. Res.*, 116, F04028, doi:10.1029/2011JF002032.
- Hodge, R., T. Hoey, G. Maniatis and E. Leprêtre (2016) Formation and erosion of sediment cover in an experimental bedrock-alluvial channel *Earth Surf. Process. Landforms*, doi:10.1002/esp.3924
- Hopson, T. M. (1999), The form drag of large natural vegetation along the banks of open channels, *M. S. thesis, 114 pp., Univ. of Colorado at Boulder*.
- Houjou, K., Shimizu, Y., and Ishii, C. (1990). Calculation of boundary shear stress in open channel flow. *J. Hydrosoci. Hydr. Eng.*, 8, 21-37.

- Howard, A. D. (1980), Thresholds in five regimes, in *Thresholds in Geomorphology* edited by D.R. Coates and J.D. Vitek, pp. 227-258, Allen and Unwin, Winchester, Mass., 1980.
- Howard, A. D. (1987), Modelling fluvial systems: Rock, gravel and sand bed channels, in *River Channels*, edited by K. S. Richards, pp. 69-94, Basil Blackwell, Oxford.
- Howard A. D. and G. Kerby (1983). Channel changes in badlands. *Geological Society of America Bulletin*, 94, 739-752.
- Howard, A. D., W. E. Dietrich, and M. A. Seidl (1994), Modeling fluvial erosion on regional to continental scales, *J. Geophys. Res.*, 99, 13, 971-13,986.
- Huda, S. A. (2013) Modeling the Effects of Bed Topography on Fluvial Erosion by Saltating Bed Load, A thesis submitted to the Faculty of the Graduate School of the University of Colorado in partial fulfillment of the requirements for the degree of Master of Science.
- Huda, S. A. and Small, E. E. (2014) Modeling the Effects of Bed Topography on Fluvial Bedrock Erosion by Saltating Bed Load, *J. Geophys. Res. Earth*, 119, 1222-1239, doi:10.1002/2013JF002872.
- Huerre, P. and P. Monkewitz (1990) Local and global instabilities in spatially developing flows, *Annual Review of Fluid Mechanics* 22, 473-537
- Hunziker, R. P. and Jäggi, M. N. R. (2002). Grain sorting processes. *J. Hydraul. Eng., ASCE*, 128(12): 1060-1068
- Ikeda, S. (1971) Some studies on the mechanics of bed load transport. *Proc. of JSCE*, 185: 61-69
- Ikeda, S. (1982a) Incipient motion of sand particles on side slopes *Hydraul. Div. Am. Soc. Civ. Eng.*, 108(HY1), 95-114.
- Ikeda, S. (1982b) Prediction of alternate bar wavelength and height. *Rep. Dept. Found. Engng and Const. Engng, Saitama Univ.*, 12:23-45.
- Ikeda, S. and N. Izumi (1991) Stable Channel Cross Sections of Straight Sand Rivers, *Water Resources Research*, 27(9), 2429-2438, doi: 10.1029/91WR01220
- Ikeda S, Parker G, Sawai K. (1981). Bend theory of river meanders. Part 1. Linear development. *J. Fluid Mech.*, 112:363-77
- Jaeggi, M. (1983) Alternierende Kiesbänke. *Mitteilungen der Versuchsanstalt für Wasserbau, Hydrologie und Glaziologie. Zurich: E.T.H.*
- Jaeggi, M. (1984) Formation and effects of alternate bars. *J. Hydraul. Eng., ASCE* 110:142-156.
- Jimenez, J. (2004). Turbulent flows over rough walls. *Annu. Rev. Fluid Mech.* Vol. 36:173-196 doi:10.1146/annurev.fluid.36.050802.122103
- Inoue, T., and Nelson, J. M. (2020). An experimental study of longitudinal incisional grooves in a mixed bedrock-alluvial channel. *Water Resources Research*, 56, e2019WR025410, doi:10.1029/2019WR025410.
- Inoue, T., Izumi, N., Shimizu, Y., Parker, G., (2014). Interaction among alluvial cover, bed roughness and incision rate in purely bedrock and alluvial-bedrock channel. *J. Geophys. Res. Earth Surf.*, 119, 2123-2146, doi:10.1002/2014JF003133.
- Inoue, T., Iwasaki, T., Parker, G., Shimizu, Y., Izumi, N., Stark, C. P., and Funaki, J. (2016). Numerical simulation of effects of sediment supply on bedrock channel morphology, *J. Hydr. Eng.*, 142, 04016014.
- Inoue, T., S. Yamaguchi and J. M. Nelson (2017), The effect of wet-dry weathering on the rate of bedrock river channel erosion by saltating gravel, *Geomorphology*, doi:10.1016/j.geomorph.2017.02.018
- Izumi, N., Yokokawa, M. and Parker, G. (2017) Incisional cyclic steps of permanent form in mixed bedrock-alluvial rivers, *J. Geophys. Res. Earth Surf.*, 122, 130-152.
- John, V. (2016) Finite Element Methods for Incompressible Flow Problems. Springer Series in Computational Mathematics. Springer International Publishing.
- Johnson, J. P. L., and K. X. Whipple (2010), Evaluating the controls of shear stress, sediment supply, alluvial cover, and channel morphology on experimental bedrock incision rate, *J. Geophys. Res.*, 115, F02018, doi:10.1029/2009JF001335.

- Johnson, J. P., and K. X. Whipple (2007), Feedbacks between erosion and sediment transport in experimental bedrock channels, *Earth Surf. Processes Landforms*, 32, 1048-1062.
- Johnson, J. P. L., K. X. Whipple, L. S. Sklar, and T. C. Hanks (2009), Transport slopes, sediment cover, and bedrock channel incision in the Henry Mountains, Utah, *J. Geophys. Res.*, 114, F02014, doi:10.1029/2007JF000862.
- Joseph, G. G., and M. L. Hunt (2004), Oblique particle-wall collisions in a liquid, *J. Fluid Mech.*, 510, 71-93, doi:10.1017/S002211200400919X
- Joseph, D. D. and Lundgren, T. S. (1990) Ensemble averaged and mixture theory equations for incompressible fluid-particle suspensions. *Int. J. Multiphase Flow* 16, 3542.
- Jourdain, C., Claude, N., Tassi, P., Cordier, F. and Germain A. (2020) Morphodynamics of alternate bars in the presence of riparian vegetation, *Earth Surf. Process. Landforms* 45, 1100-1122
- Julien, P. Y. and Klaassen, G. J. (1995). Sand-dune geometry of large rivers during floods. *Journal of Hydraulic Engineering, ASCE*, 121, 657-663.
- Kean, J. W. (2003) Computation of flow and boundary shear stress near the banks of streams and rivers. A thesis submitted to the Faculty of the Graduate School of the University of Colorado in partial fulfillment of the requirement for the degree of Doctor of Philosophy.
- Kean, J. W., and Smith, J. D. (2004). Flow and boundary shear stress in channels with woody bank vegetation. *Riparian vegetation and fluvial geomorphology*, AGU Water Science and Application Series 8, S. J. Bennett and A. Simon, eds., AGU, Washington, D.C., 237-252.
- Kean, J. W., and J. D. Smith (2006a), Form drag in rivers due to small-scale natural topographic features: 1. Regular sequences, *J. Geophys. Res.*, 111, F04009, doi:10.1029/2006JF000467.
- Kean, J. W., and J. D. Smith (2006b), Form drag in rivers due to small-scale natural topographic features: 2. Irregular sequences, *J. Geophys. Res.*, 111, F04010, doi:10.1029/2006JF000490.
- Kean, J. W., Kuhnle, R. A., Dungan Smith, J., Alonso, C. V. and Langendoen, E. J. (2009) Test of a Method to Calculate Near-Bank Velocity and Boundary Shear Stress *Journal of Hydraulic Engineering*, 135(7), ASCE, ISSN 0733-9429/2009/7-588-601.
- Keefe L. R. (1985) Dynamics of perturbed wavetrain solutions to the Ginzburg-Landau equation. *Stud. Appl. Maths.* 73, 91-153.
- Kennedy, J. F. (1995). The Albert Shields story. *J. Hydr. Engrg., ASCE*, 121(11): 766-772.
- Kevorkian, J. and Cole, J. D. (1981) *Perturbation Methods in Applied Mathematics*. Springer.
- Keylock, C.J., Constantinescu, G. and Hardy, R.J. (2012) The application of computational fluid dynamics to natural river channels: Eddy resolving versus mean flow approaches. *Geomorphology*, 179. 1-20. ISSN 0169-555X.
- Kidanemariam A. G. and Uhlmann, M. (2014a) Direct numerical simulation of pattern formation in subaqueous sediment. *J. Fluid Mech.* 750, R2.
- Kidanemariam A. G. and Uhlmann, M. (2014b) Interface-resolved direct numerical simulation of the erosion of a sediment bed sheared by laminar channel flow. *Intl J. Multiphase Flow* 1-27.
- Kidanemariam A. G. and Uhlmann, M. (2017) Formation of sediment patterns in channel flow: minimal unstable systems and their temporal evolution. *J. Fluid Mech.*, vol. 818, pp. 716-743.
- Kidanemariam A. G., Scherer, M. and Uhlmann, M. (2022) Open-channel flow over evolving subaqueous ripples *J. Fluid Mech.*, vol. 937, A26, doi:10.1017/jfm.2022.113
- Kim, J., Kline, S. J. and Reynolds, W. C. (1971). The production of turbulence near a smooth wall in a turbulent boundary layer. *J. Fluid Mech.* 50, 133.
- Kim, J., Moin, P. & Moser, R. (1987) Turbulence statistics in fully developed channel flow at low Reynolds number. *J. Fluid Mech.* 177, pp. 133-166.
- Kinoshita, R. (1961) An investigation of channel deformation of the Ishikari River. *Tech. Rep., Natural Resources Division, Ministry of Science and Technology of Japan, Tokyo, 36*, pp. 1-174

- Kinoshita, R. and Miwa, H. (1974). River channel formation which prevents downstream translation of transverse bars, *Shinsabo* 94, 12-17 (in Japanese).
- Kirchner, J.W., W. E. Dietrich, F. Iseya, and H. Ikeda (1990), The variability of critical shear stress, friction angle, and grain protrusion in water-worked sediments, *Sedimentology*, 37(4), 647-672, doi:10.1111/j.1365-3091.1990.tb00627.x.
- Kline, S. J., Reynolds, W. C., Schraub F. A. and Runstadler P. W. (1967). The structure of turbulent boundary layers. *J. Fluid Mech.* 30(4):741-773
- Kline, S. J. and Runstadler, W. (1959) *J. Appl. Mech. Trans. ASME*, 26 (Ser. E), no. 2, 166.
- Kolmogorov, A. N. (1941) Dokl. Akad. Nauk. SSSR. 30, 3201. (English translation, Kolmogorov, A. N. 1991. The local structure of turbulence in incompressible viscous fluid for very large Reynolds number. *Proc. R. Soc. Lond.* 434:9-13).
- Kolmogorov, A.N. (1942) Equations of turbulent motion in an incompressible fluid. *Izv. Akad. Nauk. SSSR ser. Fiz.* 6, 56-58.
- Komar, P.D. and Li, Z. (1986): Pivoting analyses of the selective entrainment of sediments by shape and size with application to the gravel threshold, *Sedimentology* 33, 425-36.
- Kovacs, A., and G. Parker, (1994) A new vectorial bedload formulation and its application to the time evolution of straight river channels, *J. Fluid Mech.*, 267, 153- 183.
- Lague, D., N. Hovius, and P. Davy (2005), Discharge, discharge variability, and the bedrock channel profile, *J. Geophys. Res.*, 110, F04006, doi:10.1029/2004JF000259.
- Lajeunesse, E., Malverti, L., and Charru, F. (2010). Bed load transport in turbulent flow at the grain scale : Experiments and modeling. *Journal of Geophysical Research*, 115(F04001), 1-16. doi:10.1029/2009JF001628.
- Lamb, M. P. (2008) Formation of Amphitheater-Headed Canyons A dissertation submitted in partial satisfaction of the requirements for the degree of Doctor of Philosophy in Earth Planetary Science, University of California at Berkeley
- Lamb, M. P., W. E. Dietrich, and L. S. Sklar (2008), A model for fluvial bedrock incision by impacting suspended and bedload sediment, *J. Geophys. Res.*, 113, F03025, doi:10.1029/2007JF000915.
- Lamb, M. P., Finnegan, N. J., Scheingross, J. S., and Sklar, L. S. (2015). New insights into the mechanics of fluvial bedrock erosion through flume experiments and theory. *Geomorphology*, 244(33-55), doi:10.1016/j.geomorph.2015.03.003
- Landau, L. D. (1944). On the problem of turbulence. In *Dokl. Akad. Nauk SSSR*, Vol. 44, No. 8, pp. 339-349.
- Lanzoni, S. (1995). Experiments on free and forced bar formation in a straight flume. Vol. I: Uniform sediment. *Delft Hydraulics Res. Report Q1774*.
- Lanzoni, S., (2000a). Experiments on bar formation in a straight flume: 1. Uniform sediment, *Water Resour. Res.*, 36, 3337-3349.
- Lanzoni, S., (2000b). Experiments on bar formation in a straight flume: 2. Graded sediment, *Water Resour. Res.*, 36, 3351-3363.
- 0 Lanzoni, S. and G. Seminara (2002). Long-term evolution and morphodynamic equilibrium of tidal channels, *Journal of Geophysical Research*, 107(C1), 3001, 10.1029/2000JC000468
- Lanzoni, S., and M. Tubino (1999), Grain sorting and bar instability, *J. Fluid Mech.*, 393, 149-174.
- Lanzoni, S., Tubino, M. and Bruno, S. (1994) Formazione di barre alternate in alvei incoerenti a granulometria non uniforme. *XXIII Convegno di Idraulica e Costruzioni Idrauliche, Napoli*, II, T4/pp. 171-181 (in Italian).
- Lanzoni, S., Bolla Pittaluga, M. and Luchi R. (2015). Modeling the morphodynamic equilibrium of an intermediate reach of the Po River (Italy). *Adv. Water. Resour.* doi:10.1016/j.adwatres.2014.11.004.
- Lauder, E. and Spalding, B. (1974) The numerical computation of turbulent flow. *Comp. Meth. Appl. Mech. & Engng* 3, 269-289.

- Leclair, S. F. (1999). Preservation of cross-strata due to migration of subaqueous dunes. *PhD thesis*, Binghamton University, New York.
- Leighly, J. B. (1932). Toward a theory of the morphologic significance of turbulence in the flow of water in streams. *Univ. Calif. Publ. Geogr.*, 6(1), 1-22.
- Leopold, L. B. (1994), A View of the River, 298 pp., Harvard Univ. Press, Cambridge, Mass.
- Leopold, L. B. and Maddock, T. Jr. (1953) The hydraulic geometry of stream channels and some physiographic implications. *Prof. Paper 252, U. S. Geol. Survey, 57*
- Leopold L. and Wolman M. (1957). River channel patterns: braided, meandering and straight. *Geological Survey professional paper 282-B. US Government Printing Office, Washington, DC.*
- Leopold, L. B., and M. G. Wolman (1960), River Meanders, *Geol. Soc. Am. Bull.*, 71(6), 769-793.
- Lesieur, M. (1997), *Turbulence in Fluids*, Kluwer Academic Publishers, Dordrecht, The Netherlands.
- Lesieur M. and O. Metais (1996) New Trends in Large-Eddy Simulations of Turbulence, *Annu. Rev. Fluid Mech.* 28, 45-82. doi:10.1146/annurev.fl.28.010196.000401
- Lesser, G. R., Roelvink, J. A., Kester, J. A. T. M. Van, and Stelling, G. S. (2004). Development and validation of a three-dimensional morphological model, *Coastal Engineering*, 51, 883-915. doi:10.1016/j.coastaleng.2004.07.014.
- Lewin, J. (1976), Initiation of bedforms and meanders in coarse grained sediment, *Bull. Geol. Soc. Am.*, 87(2), 281-285.
- Lisle, T. (1982), Effects of Aggradation and Degradation on Riffle-Pool Morphology in Natural Gravel Channels, Northwestern California, *Water Resour. Res.*, 18(6), 1643-1651.
- Lisle, T. E., H. Ikeda, and F. Iseya, (1991) Formation of stationary alternate bars in a steep channel with mixed-size sediment: A flume experiment, *Earth Surf. Processes Landforms*, 16, 463-469.
- Lisle, T.E., Iseya, F. and Ikeda, H. (1993) Response of a channel with alternate bars to a decrease in supply of mixed-size bed load: a flume experiment. *Water Resour. Res.*, 29(11), 3623-3629.
- Liu, H. K. (1957) Mechanics of sediment-ripple formation. *J. Hydraul. Div.* 83(2):1-23
- Luchi, R., J. M. Hooke, G. Zolezzi, and W. Bertoldi (2010), Width variations and mid-channel bar inception in meanders: River Bollin (UK), *Geomorphology*, 119(1-2), 1-8, doi:10.1016/j.geomorph.2010.01.010.
- Luchi, R., M. Bolla Pittaluga, and G. Seminara (2012), Spatial width oscillations in meandering rivers at equilibrium, *Water Resour. Res.*, 48, W05551, doi:10.1029/2011WR011117.
- Lumley, J.L. (1978) Computational modeling of turbulence flows. *Adv. Appl. Mech.* 18, 123-177.
- Lumley, J.L. (1970) Toward a turbulent constitutive equation. *J. Fluid Mech.* 41, 413-434.
- Lundgren, T. S. (1972) Slow flow through stationary random beds and suspensions of spheres. *J. Fluid Mech.* 51, 273-299.
- Luque, F. R. and Van Beek, R. (1976) Erosion and transport of bed sediment *J. Hydraul. Res.*, 14(2): 127-144.
- Luu, L. X., Egashira, S., & Takebayashi, H. (2004). Investigation of Tan Chau reach in lower Mekong using field data and numerical simulation, *Annual Journal of Hydraulic Engineering, JSCE*, 48, 1057-1062.
- Lysne, D. K. (1969). Movement of sand in tunnels. *J. Hydraul. Div. Am. Soc. Civil Eng.*, 95(HY6),1835-46
- Magnaudet, J. and I. Eames (2000). The motion of high-Reynolds-number bubbles in inhomogeneous flows. *Annu. Rev. Fluid Mech.* 32:659-708.
- Mantz, P.A. (1980) Low Sediment Transport Rates over Flat Beds *Journal of the Hydraulic Division, Proc. ASCE*, 106(HY7): 1173-1190.
- Marble FE. (1970). Dynamics of dusty gases. *Annu. Rev. Fluid Mech.* 2:397-446
- Maxey, M. R. (1987). The gravitational settling of aerosol particles in homogeneous turbulence and random flow fields. *J. Fluid Mech.* 174: 441-465

- Maxey, M. R. and J. J. Riley (1983). Equation of motion for a small rigid sphere in a nonuniform flow, *Phys. Fluids* 26, 883- 1983.
- Mazzuoli, M., Kidanemariam, A. G., Blondeaux, P., Vittori, G. and Uhlmann, M. (2016) On the formation of sediment chains in an oscillatory boundary layer. *J. Fluid Mech.* 789, 461–480.
- Mazzuoli, M., Kidanemariam, A., and Uhlmann, M. (2019). Direct numerical simulations of ripples in an oscillatory flow. *J. Fluid Mech.* 863, 572-600.
- Mazzuoli, M., Blondeaux, P., Vittori, G., Uhlmann, M., Simeonov, J. and J. Calantoni (2020) Interface-resolved direct numerical simulations of sediment transport in a turbulent oscillatory boundary layer, *J. Fluid Mech.*, vol. 885, A28.
- McTigue, D. F. (1981). Mixture theory for suspended sediment transport. *J. Hydr. Div. ASCE*, 107, 659-673.
- Metais, E. (2002). Large-eddy simulations of turbulence. In: *New Trends in Turbulence*, Edited by Lesier, M., Yaglom, A., David, F., Springer, Berlin.
- Meyer-Peter, E. and Müller, R. (1948) Formulas for bedload transport, *2nd IAHR Congress, Int Assoc. for Hydraul. Res.*, Stockholm.
- Michaelides, E. E. (2006). Particles, Bubbles and Drops. Their Motion, Heat and Mass transfer. *World Scientific Publishers, New Jersey*
- Milhous, R. T., (1973), Sediment transport in a gravel-bottomed stream, *Ph.D. thesis*, Dept. of Civil Engineering, Oregon State University, U.S.A., 232 p.
- Mishra, J., and T., Inoue (2020) State of the Art Study of Influence of Bed Roughness and Alluvial Cover on Bedrock Channels and Comparisons of Existing Models with Laboratory Scale Experiments, *Earth Surf. Dynam. Discussions*, doi:10.5194/esurf-2019-78
- Moin, P. and Kim, J. (1982). Numerical investigation of turbulent channel flow. *J. Fluid Mech.*, 118, 341-377. doi:10.1017/S0022112082001116.
- Moin, P., Mahesh, K. (1998), Direct Numerical Simulation: A Tool in Turbulence Research. *Annu. Rev. Fluid Mech.*, 1998. 30:539-78
- Monin, A.S. and Yaglom, A.M. (1971) *Statistical fluid mechanics*, vol.1, MIT Press.
- Morse, P. M. and Feshback, H. (1953). *Methods of Theoretical Physics*, McGraw-Hill, New York.
- Mosley, M. P. (1976) An experimental study of channel confluences. *J. Geol.* 4, 535-562.
- Muramoto, Y. and Fujita, Y. (1978) The classification of meso-scale river bed configuration and the criterion of its formation. *Proc. 22nd Japanese Conf. on Hydraulics*, 275-282. JSCE.
- Nakagawa, H. and Tsujimoto, T. (1980) Sand bed instability due to bed load motion. *J. Hydraul. Div.*, ASCE, 106, 12.
- Nayfeh A. H. (2000). *Perturbation methods*. John Wiley & Sons.
- Nayfeh, A. H. (2011) *Introduction to Perturbation Techniques*. John Wiley & Sons.
- Nelson, P. A., and G. Seminara (2011), Modeling the evolution of bedrock channel shape with erosion from saltating bed load, *Geophys. Res. Lett.*, 38, L17406, doi:10.1029/2011GL048628.
- Nelson, P. A., and G. Seminara (2012), A theoretical framework for the morphodynamics of bedrock channels, *Geophys. Res. Lett.*, 39, L06408, doi:10.1029/2011GL050806.
- Nelson, J. M., and J. D. Smith, (1989). Flow in meandering channels with natural topography, in *River Meandering, Water Resour. Monogr.*, vol. 12, edited by S. Ikeda and G. Parker, pp 69-102, AGU, Washington, D. C.
- Nelson, J.M., Shreve, R.L., McLean, S.R. & Drake, T.G. (1995) Role of near-bed turbulence structure in bed load transport and bed form mechanics. *Water Resources Research*, 31(8): 2071-2086.
- Nelson, P. A., J. G. Venditti, W. E. Dietrich, J. W. Kirchner, H. Ikeda, F. Iseya, and L. S. Sklar (2009), Response of bed surface patchiness to reductions in sediment supply, *J. Geophys. Res.*, 114, F02005, doi:10.1029/2008JF001144.
- Nezu, I. and Nakagawa, H. (1993). *Turbulence in open-channel flows*. Balkema, Rotterdam NL.

- Nikuradse J. (1933). Strömungsgesetze in Rauhen Rohren, *VDI-Forsch. 361* (Engl. transl. 1950. Laws of flow in rough pipes. *NACA TM 1292*)
- Niño, Y. (1995) Particle motion in the near bed region of a turbulent open channel flow: implications for bedload transport by saltation and sediment entrainment in suspension. *Thesis* submitted in partial fulfillment of the requirements of the degree of Philosophy Doctor. Graduate School of Civil Engineering. University of Illinois at Urbana-Champaign.
- Niño, Y. and Garcia, M. H. (1994) Gravel saltation Modelling *Water Resources Research*, 30(6): 1915-1924.
- Niño, Y. and Garcia, M. H. (1996) Experiments on particle turbulent interactions in the near wall region of an open channel flow: implications for sediment transport. *J. Fluid Mech.*, 326: 285-319.
- Niño, Y., Lopez F. and Garcia, M. (2003) Threshold for particle entrainment into suspension *Sedimentology* 50: 247-263
- Nittrouer, J. A. (2010) Sediment Transport Dynamics in the lower Mississippi river: non-uniform flow and its effects on river channel morphology. *Dissertation* Presented to the Faculty of the Graduate School of The University of Texas at Austin in Partial Fulfillment of the Requirements for the Degree of Doctor of Philosophy.
- Nittrouer, J. A., D. Mohrig, M. A. Allison and A-P. B. Peyret (2011) *Sedimentology* 58, 1914-1934, doi: 10.1111/j.1365-3091.2011.01245.x
- Olesen, K. W. (1984), Alternate bars in and meandering of alluvial rivers, in *River Meandering, Proceedings of the Conference Rivers 1983*, edited by C. M. Elliott, pp. 873-884, American Society of Civil Engineers, New York.
- Owen, P.R. (1964) Saltation of uniform grains in air. *J. Fluid Mech.*, 20: 225-242.
- Panton, R. L. (2001) Overview of the self-sustaining mechanisms of wall turbulence. *Progress in Aerospace Sciences* 37, 341-383
- Parker G. (1975) Sediment inertia as cause of river antidunes *J. Hydraul. Div.*, ASCE 101, 211-221.
- Parker G. (1976) On the cause and characteristic scales of meandering and braiding in rivers. *J. Fluid Mech.* 76, 457.
- Parker, G. (1978a). Self-formed straight rivers with equilibrium banks and mobile bed. Part 1. The sand-silt river. *J. Fluid Mech.*, 89:109-125.
- Parker, G. (1978b), Self-formed straight rivers with equilibrium banks and mobile bed. Part 2. The gravel river, *J. Fluid Mech.*, 89:127-146
- Parker, G. (1979), Hydraulic geometry of active gravel rivers, *Journal of the Hydraulic Division (ASCE)*, 105(9), 1185-1201
- Parker G. (1984). Lateral bed load transport on side slopes. *J. Hydraul. Eng. ASCE* 110(HY2):197-99
- Parker, G. 1990: Surface-based bedload transport relation for gravel rivers, *Journal of Hydraulic Research*, 28, 417-36.
- Parker, G. (1992), Some random notes on grain sorting, *Proceedings, International Seminar on Grain Sorting, Ascona, Switzerland*, 19-76.
- Parker G. (2008). Transport of Gravel and Sediment Mixtures, Ch. 3 in *Sedimentation Engineering (Manual 110) Processes, Measurements, Modeling, and Practice*, M. Garcia Ed., 1132 pp.
- Parker, G., and E. D. Andrews, (1985) Sorting of bed load sediment by flow in meander bends, *Water Resources Reserach*, 21(9), 1361-1373.
- Parker, G., and N. Izumi (2000). Purely erosional cyclic and solitary steps created by flow over a cohesive bed, *J. Fluid Mech.*, 419, 203-238.
- Parker, G. and Klingeman, P.C. (1982). On why gravel bed streams are paved, *Water Resources Research*, 18, 1409-23.
- Parker, G., and Toro-Escobar, C. M. (2002). Equal mobility of gravel in streams: The remains of the day, *Water Resour. Res.*, 38(11), 1264, doi:10.1029/2001WR000669.

- Parker, G., Dhamotharan, S. and Stefan, H. (1982a): Model experiments on mobile, paved gravel-bed streams. *Water Resources Research* 18, 1395-408.
- Parker, G., Klingeman, P.C. and McLean, D.C. (1982b): Bedload and size distribution in paved, gravel-bed streams. *Proceedings of the American Society of Civil Engineers, Journal of the Hydraulics Division* 108, 544-71.
- Parker, G., C. Paola, and S. F. Leclair (2000), Probabilistic Exner sediment continuity equation for mixtures with no active layer, *J. Hydraul. Eng.*, 126(11), 818-826.
- Parker, G., G. Seminara, and L. Solari (2003), Bed load at low Shields stress on arbitrarily sloping beds: Alternative entrainment formulation, *Water Resour. Res.*, 39(7), 1183, doi:10.1029/2001WR001253.
- Parker, G., P. R. Wilcock, C. Paola, W. E. Dietrich, and J. Pitlick (2007), Physical basis for quasi-universal relations describing bankfull hydraulic geometry of single-thread gravel bed rivers, *J. Geophys. Res.*, 112, F04005, doi:10.1029/2006JF000549.
- Passman, S. L., Nunziato, J. W., and Walsh, E. K. (1984) A theory for multiphase mixtures. In *Rational Thermodynamics*, ed. C. Truesdell (second editor). Springer, NY. 286-325
- Perry, A.E., Lim, T.T. and Teh, E.W. (1981), A visual study of turbulent spots, *J. Fluid Mech.*, 104, 387-405.
- Peskin C., (2002), The immersed boundary method, *Acta Numerica* 11, 1-39.
- Perry, A.E., Lim, T.T. and Teh, E.W. (1981), A visual study of turbulent spots, *J. Fluid Mech.*, 104, 387-405.
- Picano, F., W. Breugem, and L. Brandt (2005) Turbulent channel flow of dense suspensions of neutrally buoyant spheres. *J. Fluid Mech.*, 764, 463-487. doi:10.1017/jfm.2014.704.
- Pintor, L. (1991) Servabo (memoria di fine secolo) Bollati Boringhieri ed., 95 p. (in Italian)
- Piomelli, U., and Balaras, E. (2002). Wall-layer models for large-eddy simulations, *Annual Review of Fluid Mechanics*, 34, 349-74.
- Pope, S. B. (2000) Turbulent Flows. Cambridge University Press.
- Posada-García, L. (1995). Transport of sands in deep rivers. *Ph.D. Dissertation, Department of Civil Engineering, Colorado State University, Fort Collins, Colorado.*
- Powell, D. M. (1998). Patterns and processes of sediment sorting in gravel-bed rivers, *Progress in Physical Geography*, 22(1), 1-32.
- Powell, D. M., Reid, I. and Laronne, J. B., (2001), Evolution of bedload grain-size distribution with increasing flow strength and the effect of flow duration on the caliber of bedload sediment yield in ephemeral gravel-bed rivers, *Water Resources Research*, 37(5), 1463-1474.
- Prandtl, L. (1925). Über die ausgebildete turbulenz. *ZAMM* 5, p. 136.
- Prandtl, L. (1927), Turbulent Flow, *NACA-TM-435, Washington, USA*
- Prandtl, L. (1945) Über ein neues formelsystem für die ausgebildete turbulenz. *Nachr. Akad. Wiss., Göttingen, Math.-Phys. Klasse, p. 6.*
- Press, W. H., Teukolsky, S. A., Vetterling, W. T., Flannery, B. P. (2007). *Numerical Recipes: The Art of Scientific Computing (3rd ed.): Section 18.1* New York: Cambridge University Press. ISBN 978-0-521-88068-8.
- Prosperetti, A. and Jones, A. V. (1984) Pressure forces in disperse two-phase flows. *Int. J. Multiphase Flow* 10, 425-440.
- Ramette, M. and Heuzel, M, (1962), A study of pebble movements in the Rhone by means of tracers, *La Houille Blanche, Spécial A*, 389-398 (in French).
- Rattray, M. and Mitsuda, E. (1974) Theoretical Analysis of Conditions in a Salt Wedge, *Estuarine and Coastal Marine Science* 2, 375-394
- Raudkivi, A. J. (1990). Loose Boundary Hydraulics, 3rd ed., Pergamon Press, New York.
- Recking, A., Liebault, F., Peteuil, C., and Jolimet, T. (2012). Testing bedload transport equations with consideration of time scales. *Earth Surface Processes and Landforms*, 37, 774-789. doi: <http://doi.org/10.1002/esp.3213>

- Repetto, R. (2000). Unit processes in braided rivers, *Thesis* submitted in partial fulfillment of the requirements for the degree of Doctor of Philosophy in Hydrodynamics and Environmental Modeling. Univ. of Padua.
- Repetto, R., and M. Tubino, (1999a) Topographic expressions of bars in channels with variable width. *XXIV EGS General Assembly*, The Hague, The Netherlands.
- Repetto, R., and M. Tubino, (1999b) Transition from migrating alternate bars to steady central bars in channels with variable width, *Proc. of first IAHR-RCEM Symposium*, Int. Assoc. for Hydraul. Res., Genoa, Italy, 6-10 Sept.
- Repetto, R., M. Tubino, and C. Paola (2002), Planimetric instability of channels with variable width, *J. Fluid Mech.*, 457, 79-109.
- Reynolds, O. (1895) On the dynamical theory of incompressible viscous fluids and the determination of the criterion. *Phil. Trans. Soc.*, pp. 123-164.
- Ribberink, J. S. (1987). Mathematical modelling of one-dimensional morphological changes in rivers with non-uniform sediment, *Ph.D. thesis*, Delft Univ. of Technol., Delft, Netherlands.
- Richards, K. (1976), Channel width and the riffle-pool sequence, *Geol. Soc. Am. Bull.*, 87, 883-890.
- Richardson, L.F. (1922), *Weather prediction by numerical process*, Cambridge University Press, OCLC 3494280
- Richardson, K., and Carling, P.A. (2005), A typology of sculpted forms in open bedrock channels: *Geological Society of America*, Special Paper 392, 108 p., doi:10.1130/2005.2392.
- Rodi, W. and N. N. Mansour (1993). Low Reynolds number $\mathcal{K} - \epsilon$ modelling with the aid of direct numerical simulation data. *J. Fluid Mech.*, 250, 509-529.
- Rodriguez-Iturbe, I. and Rinaldo, A., (2010). *Fractal River Basins. Chance and Selforganization*, Cambridge University Press, 564 pp.
- Roelvink, J.A. (2006), Coastal morphodynamic evolution techniques, *Coastal Engineering*, 53, 2, 277 - 287.
- Rosenbloom, A., and R. S. Anderson, (1994) Evolution of the marine terraced landscape Santa Cruz, California, *J. Geophys. Res.*, 99, 14,013-14,030
- Rouse, H., (1937). Modern conceptions of the mechanics of fluid turbulence. *Trans. A.S.C.E.*, 102, 463-543.
- Rouse, H. (1939). An analysis of sediment transportation in light of fluid turbulence. *Rep. No. SCS-TP-25, Sediment Division, U.S. Dept. of Agr., Soil Conservation Service, Washington, D.C.*
- Saffman P.G. (1970). A model for inhomogeneous turbulent flow. *Proc. Roy. Soc. Lond. A* 317, 417-433
- Saffman, P. (1971) On the boundary condition at the surface of a porous medium. *Studies in Appl. Math.*, 93.
- Saffman, P. G. and Wilcox, D. C. (1974). Turbulence-model predictions for turbulent boundary layers. *AIAA J.* 12: 541-46
- Sani, R. L., Gresho, P. M. (1994), Rešumé and remarks on the Open Boundary Condition Minisymposium, *International Journal for Numerical Methods in Fluids*, 18, 983-1008.
- Scheingross, J. S. (2016) Mechanics of sediment transport and bedrock erosion in steep landscapes, *Dissertation In Partial Fulfillment of the Requirements for the Degree of Doctor of Philosophy California Institute of Technology*, Pasadena, California
- Scheingross, J. S. and Lamb, M. P. (2017). A mechanistic model of waterfall plunge pool erosion into bedrock. *Journal of Geophysical Research: Earth Surface*, 122, 2079-2104, doi:<https://doi.org/10.1002/2017JF004195>.
- Scheingross, J. S., Brun, F., Lo, D. Y., Omerdin, K., & Lamb, M. P. (2014). Experimental evidence for fluvial bedrock incision by suspended and bedload sediment. *Geology*, 42(6), 523-526. doi:<https://doi.org/10.1130/G35432.1>.

- Scheingross, J. S., Lamb, M. P. and Fuller, B. M. (2019). Self-formed bedrock waterfalls. *Nature*, 567(7747), 229-233, doi: <https://doi.org/10.1038/s41586-019-0991-z>
- Scheingross, J. S., Limaye, A. B., McCoy, S. W. and Whittaker, A. C. (2020). The shaping of erosional landscapes by internal dynamics. *Nature Reviews Earth and Environment*, 1(12), 661-676, doi: <https://doi.org/10.1038/s43017-020-0096-0>.
- Scherer, M., Kidanemariam A. G. and Uhlmann, M. (2020) On the scaling of the instability of a flat sediment bed with respect to ripple-like patterns. *J. Fluid Mech.* 900, A1.
- Scherer, M., Uhlmann, M., Kidanemariam A. G., and M. Kraymer (2022) On the role of turbulent large-scale streaks in generating sediment ridges, *J. Fluid Mech.*, vol. 930, A11, doi:10.1017/jfm.2021.891.
- Schielen, R. M. J., (1995) Nonlinear Stability Analysis and Pattern Formation in Morphological Models, *Phd Thesis*.
- Schielen R, Doelman A, de Swart HE. (1993). On the nonlinear dynamics of free bars in straight channels. *J. Fluid Mech.* 252:325-56
- Schiller, L. and A. Neumann (1933). Über die grundlegenden Berechnungen bei der Schwerkraftaufbereitung. *Ver. Deutt. Ing.* 77:318.
- Schmeeckle, M. W. (2014). Numerical simulation of turbulence and sediment transport of medium sand, *Journal of Geophysical Research: Earth Surface*, 119, 1240-1262. doi:<http://doi.org/10.1002/2013JF002911.1>
- Schumm, S. A., (1960) The shape of alluvial channels in relation to sediment type, *Geological survey professional paper*, n. 352-B, 17-30
- Sekine, M., and H. Kikkawa (1992) Mechanics of saltating grains, *J. Hydraul. Eng.*, 118(4), 536-558.
- Sekine, M., and G. Parker (1992), Bed-load transport on transverse slope. I, *Journal of Engineering*, ASCE, 118 (4), 513-535.
- Seminara, G. (1995), Effect of grain sorting on the formation of bedforms, *Applied Mechanics Reviews*, 48: 549-563.
- Seminara, G. (2010) Fluvial Sedimentary Patterns, *Annu. Rev. Fluid Mech.* 42:43-66
- Seminara G. and Tubino M. (1989). Alternate bars and meandering: free, forced and mixed interactions. In *River Meandering* (ed. S. Ikeda & G. Parker). *AGU Water Resour. Monograph*, 12, pp. 267-320.
- Seminara G. and Tubino M. (1992) Weakly nonlinear theory of regular meanders. *J. Fluid Mech.* 244:257-88
- Seminara, G., Colombini, M. and Parker, G. (1996). Nearly pure sorting waves and formation of bedload sheets, *J. Fluid Mech.*, 312, 253-278.
- Seminara, G., Solari, L., Parker G. (2000) Trasporto solido a bassi Shields e non validita' dell'ipotesi di Bagnold, *XXVII Convegno di Idraulica e Costruzioni Idrauliche*, 349-356.
- Seminara, G., Zolezzi, G., Tubino, M. and Zardi, D. (2001a) Downstream and upstream influence in river meandering. Part 2. Planimetric development. *J. Fluid Mech.*, 438, 213-230.
- Seminara, G., L. Solari, and G. Parker, (2001b) Bed-load transport on arbitrarily sloping beds at low Shields stress and validity of Bagnold's hypothesis. *2nd IAHR Symposium on River, Coastal and Estuarine Morphodynamics, RCEM 2001*, 10-14 September 2001, Obihiro Japan.
- Seminara, G., L. Solari, and G. Parker, (2002) Bed load at low Shields stress on arbitrarily sloping beds: Failure of the Bagnold hypothesis, *Water Resour. Res.*, 38(11), 1249, doi:10.1029/2001WR000681.
- Seminara, G., Bolla Pittaluga, M., and Luchi, R. (2011). Valutazione dell'efficacia di interventi di dragaggio del tratto terminale del Fiume Magra ai fini della riduzione delle condizioni di rischio idraulico. *Technical Report, Department of Civil, Chemical and Environmental Engineering, University of Genova, Italy*.

- Seminara, G., Bolla Pittaluga, M., and Luchi, R. (2012). Attività di studio della morfodinamica del Fiume Magra e degli affluenti principali in relazione all'evento alluvionale del 25/10/2011 e definizione delle azioni e degli interventi di messa in sicurezza. *Technical Report, Department of Civil, Chemical and Environmental Engineering, University of Genova, Italy.*
- Seminara G. and S. Lanzoni and N. Tambroni (2023) Theoretical Morphodynamics: River Meandering, *Firenze University Press.*
- Serlet, A. (2018) Biomorphodynamics of river bars in channelized, hydropower-regulated rivers. *Thesis* submitted in partial fulfillment of the requirements for the degree of Doctor of Philosophy. Erasmus Mundus Joint Doctorate School in Science for Management of Rivers and their Tidal System. University of Trent, Queen Mary University of London.
- Serlet A. J., Gurnell A. M., Zolezzi G., Wharton G., Belleudy P., Jourdain C. (2018). Biomorphodynamics of alternate bars in a channelized, regulated river: an integrated historical and modelling analysis. *Earth Surface Processes and Landforms* 43: 1739-1756, doi: <https://doi.org/10.1002/esp.4349>.
- Shields, A. (1936) Application of similarity principles and turbulence research to bed-load movement. *Mitteilungen der Preussischen Versuchsanstalt fur Wasserbau und Schiffbau*, Berlin. In: Ott, W.P. & van Uchelen, J.C. (translators), California Inst. Tech., W.M. Keck Lab. of Hydraulics and Water Resources, Rept. No. 167.
- Shimizu, Y., and T. Itakura, (1989) Calculation of bed variation in alluvial channels, *J. Hydraul. Div. Am. Soc. Civ. Eng.*, 115(HY3), 367-384.
- Simons, D. B. and Richardson, E. V. (1961) Forms of bed roughness in alluvial channels, *Journal of the Hydraulics Division*, ASCE, 87 (3), 87-105
- Simons, D. B. and Richardson, E. V. (1966) Resistance to Flow in Alluvial Channels, *U.S. Geol. Survey Prof. Paper 422J*, 70 p.
- Sinha S. K. and G. Parker (1996) Causes of concavity in longitudinal profiles of rivers, *Water Resources Research*, 32(5): 1417-1428.
- Siviglia A., Stecca G., Vanzo D., Zolezzi G., E.F. Toro and M. Tubino (2013) Numerical modelling of two-dimensional morphodynamics with applications to river bars and bifurcations *Advances in Water Resources*, 52: 243-260, doi:<https://doi.org/10.1016/j.advwatres.2012.11.010>.
- Sklar, L. S., and W. E. Dietrich (2001), Sediment and rock strength controls on river incision into bedrock, *Geology*, 29, 1087-1090.
- Sklar, L. S., and W. E. Dietrich (2002), Thresholds of alluviation in an experimental bedrock channel and controls on river incision into bedrock, *Eos Trans. AGU*, 83(47), Fall Meet. Suppl., Abstract H12F-09.
- Sklar, L. S., and W. E. Dietrich (2004), A mechanistic model for river incision into bedrock by saltating bed load, *Water Resour. Res.*, 40, W06301, doi:10.1029/2003WR002496.
- Sklar, L. S., and W. E. Dietrich (2006), The role of sediment in controlling bedrock channel slope: Implications of the saltation-abrasion incision model, *Geomorphology*, 82, 58-83, doi:10.1016/j.geomorph.2005.08.019.
- Sklar, L. S., and W. E. Dietrich (2008) Implications of the Saltation-Abrasion Bedrock Incision Model for Steady-State River Longitudinal Profile Relief and Concavity. *Earth Surf. Process. Landforms* 33, 1129-1151, doi:10.1002/esp.1689.
- Smagorinsky, J. (1963). General circulation experiments with the primitive equations: I. The basic equations. *Mon. Weather Rev.* 91, 9S164.
- Smith, J. D., and McLean S. R. (1977). Spatially averaged flow over a wavy surface. *Journal of Geophysical Research*, 83, 1735-1746.
- Sotiropoulos, F. (2019) Hydraulic Engineering in the Era of Big Data and Extreme Computing: Can Computers Simulate River Turbulence?, *J. Hydraul. Eng.*, 145(6): 02519002, doi: [https://doi.org/10.1061/\(ASCE\)HY.1943-7900.0001594](https://doi.org/10.1061/(ASCE)HY.1943-7900.0001594)
- Spalart, P. R. (2009), Detached eddy-simulation, *Annu. Rev. Fluid Mech.*, 41, 181-202.

- Speziale, C.G. (1985) Modeling the pressure gradient-velocity correlation of turbulence. *Phys. Fluids* 28, pp. 69-71.
- Speziale, C.G., (1987) On nonlinear $K - l$ and $K - \epsilon$ models of turbulence. *J. Fluid Mech.* 178, pp. 459-4675.
- Speziale, C.G. (1991) Analytical methods for the development of Reynolds-stress closures in turbulence. *Ann. Rev. Fluid Mech.* 23, pp. 107-157.
- Springer, G.S., and E.E. Wohl, (2002), Empirical and theoretical investigations of sculpted forms in Buckeye Creek, west Virginia. *Journal of Geology*, 110, 469-481.
- Stark, C. P. (2006), A self-regulating model of bedrock river channel geometry, *Geophys. Res. Lett.*, 33, L04402, doi:10.1029/2005GL023193.
- Stecca, G. (2012) Numerical modelling of gravel-bed river morphodynamics. *Thesis* submitted in partial fulfillment of the requirements for the degree of Doctor of Philosophy in Hydrodynamics and Environmental Modeling, University of Trent.
- Stecca, G., A. Siviglia and A. Blom, (2014). Mathematical analysis of the Saint-Venant-Hirano model for mixed-sediment morphodynamics, *Water Resour. Res.*, 50, doi:10.1002/2014WR015251.
- Stecca, G., A. Siviglia and A. Blom, (2016). An accurate numerical solution to the Saint-Venant-Hirano model for mixed-sediment morphodynamics in rivers, *Advances in Water Resources*, 93, 39-61, doi:<https://doi.org/10.1016/j.advwatres.2015.05.022>.
- Stefan, S. J. (1871) *Sber. Akad. Wise. Wien.* 63: 63
- Stock J. D. and W. E. Dietrich (2003). Valley incision by debris flows: evidence of a topographic signature. *Water Resources Research*, 39, 1089, doi:10.1029/2001wr001057.
- Stoesser, T. (2014) Large-eddy simulation in hydraulics: Quo Vadis?, *Journal of Hydraulic Research*, 52:4, 441-452
- Struiksma, N. and A. Crosato, (1989) Analysis of a 2-D bed topography model for rivers, in *River Meandering Water Resour. Monogr.*, vol. 12, edited by S. Ikeda and G. Parker, pp. 153-180, AGU, Washington, D.C.
- Struiksma, N., K. W. Olesen, C. Flokstra, and H. J. de Vriend (1985) Bed deformation in a curved alluvial channel, *J. Hydraul. Res.*, 23(1), 57- 79.
- Stuart, J. T. (1958). On the non-linear mechanics of hydrodynamic stability. *Journal of Fluid Mechanics*, 4(1), 1-21.
- Sukegawa, M., (1971) Study on meandering of streams in straight channels. *Rep. Bureau of Resources, Dept. Science and Technology, Japan*, 335-363.
- Surian, N. and Rinaldi, M. (2003). Morphological response to river engineering and management in alluvial channels in Italy. *Geomorphology*, 50(4):307-326.
- Sutherland, A.J. (1967) Proposed mechanism for sediment entrainment by turbulent flows. *J. geophys. Res.*, 72, 6183-6194.
- Taki, K. and Parker, G. (2005). Transportational cyclic steps created by flow over an erodible bed. Part 1. Experiments, *Journal of Hydraulic Research*, 43, 488-501.
- Talmon, A. M. (1992). Bed topography of river bends with suspended sediment transport, *Communications on Hydraulics and geotechnical Engineering, Delft University of technology*, n. 92-5
- Talmon, A. M., M. C. L. M. Mierlo, and N. Van Struiskma (1995), Laboratory measurements of the direction of sediment transport on transverse alluvial-bed slopes., *J. Hydraul. Res.*, 33, 495-517.
- Tambroni, N., Seminara, G. and C. Paola (2019), On the incipient formation of bars and channels on alluvial fans. *Earth Surf. Process. Landforms*, 44, 2479-2493
- Taylor, B.D. (1971) Temperature Effects in Alluvial Streams. *Report No. KH-R-27, W.M. Keck Laboratory of Hydraulics and Water Resources, California Institute of Technology, Pasadena, California.*
- Tennekes, H. and J. L. Lumley (1972). A first course in turbulence. MIT Press.

- Theodorsen, T. (1952), Mechanism of turbulence, *Proceedings of the Second Midwestern Conference on Fluid Mechanics, Ohio State University*, 1-18.
- Thorne, P.D., Williams, J.J. and Heathershaw, A.D. (1989) In situ acoustic measurements of marine gravel threshold and transport. *Sedimentology* 36, 61-74.
- Tjerry, S., and J. Fredsøe (2005), Calculation of dune morphology, *J. Geophys. Res.*, 110, F04013, doi:10.1029/2004JF000171.
- Toffolon, M., and G. Vignoli (2007), Suspended sediment concentration profiles in nonuniform flows: Is the classical perturbative approach suitable for depth-averaged closures?, *Water Resour. Res.*, 43, W04432, doi:10.1029/2006WR005183.
- Toro-Escobar, C. M., Parker G. and Paola, C. (1996). Transfer function for the deposition of poorly sorted gravel in response to streambed aggradation. *Journal of Hydraulic Research*, 34(1), 35-53.
- Townsend, A.A. (1976) *The structure of turbulent shear flow*. (2nd ed.), Cambridge University Press.
- Truesdell, C. (1957) *Atti Accad. naz. Lincei Re. Ser.* 8 22 33, 158. (Also translation by the author in *Continuum Mechanics H. The Rational Mechanics of Materials* p. 295 (Ed. C. Truesdell) Gordon and Breach, New York, 1965.)
- Tubino, M. (1991). Growth of alternate bars in unsteady flow, *Water Resources Research*, 27, 37-52.
- Tubino, M. (1992) Il campo di moto e la forma di equilibrio della sezione in correnti a fondo mobile e curvatura costante, *Proceedings of 23rd Convegno di Idraulica e Costruzioni Idrauliche* (in Italian), D447-D458
- Tubino, M. and M. Colombini (1992) Correnti uniformi a superficie libera e sezione lentamente variabile, *Proceedings of 23rd Convegno di Idraulica e Costruzioni Idrauliche* (in Italian), D375-D386
- Tubino, M. and G. Seminara (1987) Unsteady alternate bars. Seminario su Leggi morfologiche e loro verifica di campo - Cosenza 25/26 giugno 1987 Editoriale Bios. ISBN 8877400730 (In Italian)
- Tubino, M., R. Repetto, and G. Zolezzi (1999), Free bars in rivers, *J. Hydraul. Res.*, 37:759-775.
- Turowski, J. M. and Bloem, J.-P. (2015) The influence of sediment thickness on energy delivery to the bed by bedload impacts, *Geodin. Acta*, 28, 1-10, doi:10.1080/09853111.2015.1047195.
- Turowski, J. M. and Hodge, R. (2017) A probabilistic framework for the cover effect in bedrock erosion, *Earth Surf. Dynam.*, 5, 311-330.
- Turowski, J. M., D. Lague, and N. Hovius (2007), Cover effect in bedrock abrasion: A new derivation and its implications for the modeling of bedrock channel morphology, *J. Geophys. Res.*, 112, F04006, doi:10.1029/2006JF000697.
- Turowski, J. M., D. Lague, and N. Hovius (2009), Response of bedrock channel width to tectonic forcing: Insights from a numerical model, theoretical considerations, and comparison with field data, *J. Geophys. Res.*, 114, F03016, doi:10.1029/2008JF001133.
- Uhlmann, M. (2005) An immersed boundary method with direct forcing for the simulation of particulate flows. *J. Comput. Phys.*, 209(2):448-476.
- Urushihara T., Meinhart C. D. and Adrian R. J. (1993) Investigation of the logarithmic layer in pipe flow using particle image velocimetry, *Near-Wall Turbulent Flows* ed. R So et al. (New York Elsevier) 433-46.
- Van Driest, E. R. (1956). On turbulent flow near a wall, *Journal of the Aeronautical Sciences*, 23, 1007.
- Vanoni, V. A. ed., (1975) Sedimentation Engineering, *ASCE Manual n. 54*
- van Rijn, L.C. (1984a) Sediment transport, I, Bed load transport, *J. Hydraul. Eng. Am. Soc. Civ. Eng.*, 110(10): 1431-1456.
- van Rijn, L. C. (1984b). Sediment transport, Part II: Suspended load transport. *J. Hydr. Engrg.*, 110(11), 1613-1641.

- van Rijn, L. C. (1984c). Sediment transport, part III: Bed forms and alluvial roughness. *Journal of Hydraulic Engineering, ASCE*, 110(12), 1733-1754.
- van Rijn, L. C. (1993). Principles of sediment transport in rivers, estuaries, and coastal areas. *Aqua Publications, Amsterdam, The Netherlands*.
- van Rijn, L. C. (1996). Combining laboratory, field, and mathematical modeling research for bed forms, hydraulic roughness, and sediment transport during floods. *Issues and Directions in Hydraulics*, T. Nakato and R. Ettema, eds., Balkema, Rotterdam, 55-73.
- Venditti, J. G., P. A. Nelson, J. T. Minear, J. Wooster, and W. E. Dietrich (2012). Alternate bar response to sediment supply termination, *J. Geophys. Res.*, 117, F02039, doi:10.1029/2011JF002254.
- Vetsch D., Siviglia A., Caponi F., Ehrbar D., Gerke E., Kammerer S., Koch A., Peter S., Vanzo D., Vonwiller L., Facchini M., Gerber M., Volz C., Farshi D., Mueller R., Rousselot P., Veprek R., Faeh R. (2018). *System Manuals of BASEMENT, Version 2.8*. Laboratory of Hydraulics, Glaciology and Hydrology (VAW). ETH Zurich. Available from <http://www.basement.ethz.ch>.
- Villaret, C., Hervouet, J.-M., Kopmann, R., Merkel, U., and Davies, A. G. (2013). Morphodynamic modeling using the Telemac finite-element system. *Computers and Geosciences*, 53, 105-113, doi:<http://doi.org/10.1016/j.cageo.2011.10.004>.
- Voltaire (1765) Preface to the Varberg edition of *Dictionnaire philosophique portatif*, London, 1765
- Vreugdenhil, C. B. (1994). *Numerical Methods for Shallow-Water flow*, Kluwer Academic Publishers, Dordrecht, The Netherlands.
- Wallace J.M. (1985). The vortical structure of bounded turbulent shear flow. In: Meier G.E.A., Obermeier F. (eds) *Flow of Real Fluids. Lecture Notes in Physics, vol 235*. Springer, Berlin, Heidelberg
- Wang, Z. B. (1989). Mathematical modelling of morphological processes in estuaries, Ph.D. thesis, *Communications on Hydraulic and Geotechnical Engineering*, Report n. 89-1, Delft University of Technology, Netherlands, ISSN 0169-6548.
- Wang, Z. B. (1992). Theoretical analysis on depth-integrated modelling of suspended sediment transport, *J. Hydraul. Res.*, 30(3):403-421.
- Warner, J. C., Sherwood, C. R., Arango, H. G., and Signell, R. P. (2005). Performance of four turbulence closure models implemented using a generic length scale method, *Ocean Modelling*, 8, 81-113. doi:<http://doi.org/10.1016/j.ocemod.2003.12.003>.
- Welford, M. R. (1994), A field test of Tubino's (1991) model of alternate bar formation, *Earth Surf. Processes Landforms*, 19(4), 287-297, doi:10.1002/esp.3290190402.
- Well, M.R. and Stock, D. E. (1983) The effects of crossing trajectories on the dispersion of particles in a turbulent flow, *J. Fluid Mech.* 136: 31-62
- Whipple, K. X. (2004). Bedrock rivers and the geomorphology of active orogens, *Ann. Rev. Earth Pl. Sci.*, 32, 151-185.
- Whipple, K. X. and Tucker, G. E. (1999). Dynamics of the stream-power river incision model: implications for height limits of mountain ranges, landscape response timescales, and research needs, *J. Geophys. Res.*, 104, 17661-17674.
- Whipple, K.X., Hancock, G.S., and Anderson, R.S., (2000). River incision into bedrock: Mechanics and relative efficacy of plucking, abrasion and cavitation. *Geological Society of America Bulletin*, 112, 490-503, doi:10.1130/0016-7606(2000)1122.3.CO;2.
- Whiting, P. J., Dietrich W. E., Leopold L. B., Drake T. G. and Shreve R. L. (1988). Bedload sheets in heterogeneous sediment, *Geology*, 16, 105-109.
- Wiberg, P. L. and Smith J. D. (1985) A theoretical model for saltating grains in water, *Journal of Geophysical Research Atmospheres* 90(NC4):7341-7354, doi:10.1029/JC090iC04p07341.
- Wiberg, P.L. and Smith, J.D. (1987). Calculations of the critical shear stress for motion of uniform and heterogeneous sediments, *Water Resources Research*, 23, 1471-80.

- Wiggins, S. (2003). Introduction to applied nonlinear dynamical systems and chaos (Vol. 2). *Berlin, Heidelberg: Springer Science & Business Media.*
- Wilcock, P. R. (1993), Critical shear stress of natural sediments, *Journal of Hydraulic Engineering*, 119, 491-505.
- Wilcock, P. R., and J. C. Crowe (2003), A surface-based transport model for sand and gravel, *Journal of Hydraulic Engineering*, 29, 120- 128.
- Wilcox, D.C. (1993), Turbulence modelling for CFD, DCW Industries Inc., La Cañada, California.
- Wilcox, D. C. (1994). Simulation of transition with a two-equation turbulence model. *AIAA J.*, 42(2), 247-255.
- Wilcox, D. C. (2006) Turbulence modeling for CFD. DCW Industries, Inc. La Cañada, California
- Wilcox, D. C. (2008). Formulation of the $\mathcal{K} - \omega$ Turbulence Model Revisited. *AIAA JOURNAL*, 46(11):2823-2838.
- Wilkerson, G.V. and G. Parker (2011) Physical Basis for Quasi-Universal Relationships Describing Bankfull Hydraulic Geometry of Sand-Bed Rivers, *Journal of Hydraulic Engineering*, 137(7).
- Wilkinson, C., Harbor, D.J., Helgans, E., and Kuehner, J.P., (2018). Plucking phenomena in nonuniform flow, *Geosphere*, 14 (5), 2157-2170.
- Williams, P.G. (1970) Flume Width and Water Dept Effects in Sediment Transport Experiments, *U.S. Geological Survey, Professional Paper 562-H*
- Williams, G. P. (1978). Bank-full discharge of rivers. *Water Resources Research*, 14(6):1141-1154.
- Whitham, G.B. (1974) Linear and Non-Linear Waves, *John Wiley, New York*, 636 pp..
- Wohl, E., and G. C. L. David (2008). Consistency of scaling relations among bedrock and alluvial channels, *J. Geophys. Res.*, 113, F04013, doi:10.1029/2008JF000989.
- Wolman, M. G. and Miller, J. P. (1960). Magnitude and frequency of forces in geomorphic processes. *The Journal of Geology*, 68(1):54-74.
- Wong, M. and Parker, G. (2006) Reanalysis and Correction of Bed-Load Relation of Meyer-Peter and Müller Using Their Own Database. *Journal of Hydraulic Engineering, ASCE* 132(11): 1159-1168.
- Wright, S.A., (2003), Density stratification, suspended-sediment transport, and downstream fining in large, low-slope, sand-bed rivers. *Ph.D. Thesis*, University of Minnesota.
- Wright, S., and Parker, P. (2004a). Density stratification effects in sand-bed rivers. *Journal of Hydraulic Engineering*, 130(8), 783-795
- Wright, S., and Parker, P. (2004b). Flow Resistance and Suspended Load in Sand-Bed Rivers: Simplified Stratification Model Density. *Journal of Hydraulic Engineering*, 130(8), 796-805.
- Wobus, C. W., G. E. Tucker, and R. S. Anderson (2006). Self-formed bedrock channels, *Geophys. Res. Lett.*, 33, L18408, doi:10.1029/2006GL027182.
- Wobus, C. W., J. W. Kean, G. E. Tucker, and R. S. Anderson (2008). Modeling the evolution of channel shape: Balancing computational efficiency with hydraulic fidelity, *J. Geophys. Res.*, 113 , F02004, doi:10.1029/2007JF000914.
- Wu, F.-C., Yeh, T.-H. (2005). Forced bars induced by variations of channel width: Implications for incipient bifurcation, *Journal of Geophysical Research: Earth Surface*, 110(2), F02009.
- Wu, W., and Wang, S. S. Y. (2008). One-dimensional explicit finite-volume model for sediment transport with transient flows over movable beds, *Journal of Hydraulic Research*, 46(1), 87-98.
- Wu, F. -C., Y.-C. Shao, and Y.-C. Chen (2011), Quantifying the forcing effect of channel width variations on free bars: Morphodynamic modeling based on characteristic dissipative Galerkin scheme, *J. Geophys. Res.*, 116, F03023, doi:10.1029/2010JF001941.
- Yalin, M. S. (1964) Geometrical properties of sand waves, *Journal of the Hydraulics Division, ASCE*, 90, HY5.
- Yalin, M. S. (1972) *Mechanics of Sediment Transport*, Pergamon Press, London, England.

- Yamamoto, Y., Potthoff M, Tanaka T, Kajishima T and Y. Tsuji (2001). Large eddy simulation of turbulent gas-particle flow in a vertical channel: effect of considering interparticle collisions. *J. Fluid Mech.* 442:303-34
- Yamasaka, M., and S. Ikeda (1988), Lateral sediment transport of heterogeneous bed materials, in *Proceedings, IAHR, 6th Congress Asian and Pacific Regional Division*, Kyoto, Japan.
- Yang, S. Q., S. K. Tan, and X. K. Wang (2012), Mechanism of secondary currents in open channel flows, *J. Geophys. Res.*, 117, F04014, doi:10.1029/2012JF002510.
- Zhang, Z. and Prosperetti, A. (2003) A method for particle simulation, *J. Appl. Mech.*, 70, 64–74.
- Zhang, Z. and Prosperetti, A. (2005) A second-order method for three-dimensional particle simulation, *Journal of Computational Physics*, 210, 292–324
- Zhang, L., Parker, G., Stark, C. P., Inoue, T., Viparelli, E. , Fu, X., and Izumi, N. (2015). Macro-roughness model of bedrock-alluvial river morphodynamics, *Earth Surf. Dynam.*, 3, 113-138, doi:10.5194/esurf-3-113-2015.
- Zhong, D., Wang, G., and Sun, Q. (2011). Transport Equation for Suspended Sediment Based on Two-Fluid Model of Solid/Liquid Two-Phase Flows. *J. Hydraul. Eng.*, 137(5), 530-542. doi:10.1061/(ASCE)HY.1943-7900.0000331.
- Zolezzi, G., and G. Seminara (2001), Downstream and upstream influence in river meandering. Part 1. General theory and application to overdeepening, *J. Fluid Mech.*, 438, 183-211.
- Zolezzi G, Guala M, Seminara G, Termini D. (2005) Experimental observations of upstream overdeepening. *J. Fluid Mech.* 531:191-219

11. Notations

- f

f any scalar, vectorial or tensorial quantity

\tilde{f} dimensionless form of f

$\langle f \rangle$ large scale turbulent flow (macroscopic) average of f

f' fluctuations of f

\overline{f}

\overline{f} overbar is used for the instantaneous and local value of the volume (spatial) average of f (microscopic average) and to denote the conjugate of a complex number

∇_h two dimensional gradient operator ($\partial/\partial x, \partial/\partial y$)

$|\mathbf{f}|$ modulus of the vector \mathbf{f}

- a

a reference level for concentration

a_p amplitude of bank undulations

a_{reg} amplitude of an equivalent regular sequence of bumps surrogating the actual distribution of bank undulations

A cross sectional area in 5

A_d dune height

\mathcal{A} dimensionless function for the particle velocity

- b

b_1 dimensional unit width

b_d dune width

B half width of the free surface

B_b half width of the bottom

$B_{R/L}$ lateral coordinates of the intersection between the free surface and the left/right bank

B_0 scale for the channel width

$B_{bR/L}$ lateral coordinates of the intersection between the channel bottom and the left/right bank

- c

c local, instantaneous volumetric concentration of the solid phase

c also dimensionless wavespeed in Chapter I.1.

c_D drag coefficient

c_{Db} drag coefficient associated to F_{Db}

c_L average lift coefficient

c_a added mass coefficient

c_a also mean concentration at some reference level a

C_a average areal concentration of bedload particles

c_M volumetric concentration of the granular medium
 C depth averaged value of the Reynolds averaged local sediment concentration
 C_u depth averaged value of the sediment concentration associated with the uniform flow
 C_f friction coefficient
 C_{fu} friction coefficient associated with the uniform flow
 C_{fw} friction coefficient associated with the wind action on the free surface
 \bar{C}_f cross sectionally averaged friction coefficient
 \bar{C}_{fw} free surface averaged wind friction coefficient
 C_{fg} friction coefficient associated with the grain roughness
 \bar{C} cross sectionally averaged concentration

- d

d sediment particle diameter
 d_g geometric mean grain size of a sediment mixture
 d_s relative roughness d/D_u
 d_0 average grain size in the upstream reach
 d_{50} average grain size
 d_{90} sediment size such that 90% percent of the sample is finer
 $D(x, y, t)$ local instantaneous flow depth
 D^* Bonnefille dimensionless particle diameter
 D_0 scale for the flow depth
 D_m depth in the center of the channel
 D_u uniform flow depth
 D_{ug} uniform flow depth that would occur in absence of bedforms
 D_b flow depth at the bank
 \mathcal{D} cross sectionally averaged flow depth
 \mathcal{D}_e equilibrium flow depth
 \mathcal{D}_{e0} equilibrium flow depth in the upstream reach
 \mathfrak{D}_P particle diffusivity
 \mathfrak{D} molecular diffusivity
 \mathfrak{D}_t thermal diffusivity for heat transport
 \mathfrak{D}_j j -th-component of the *turbulent diffusivity* vector

- e

e dimensionless parameter measuring the degree of particle exposure
 e_s absolute bed roughness
 e_s^{bank} absolute roughness at the banks
 \mathcal{E} entrainment function in Chapters 3 and 4
 $\mathcal{E} (\equiv L T^{-1})$ absolute bedrock *erosion rate* in Chapter I.1.

- f

$f_0(d)$ grain size density distribution
 f_a probability density function of the active layer also the areal fraction of bedrock surface covered with alluvium in Chapter I.1. f_s probability density function of the substrate

 f_G dimensionless function accounting for bed slope in the bedload sediment transport flux
 \mathbf{F}_D drag force exerted on one particle
 F_{Dd} intensity of the average drag force over one bedform wavelength
 F_{Db} form drag acting on an individual element of bank ondulation
 F_{Dg} grain roughness component of the drag force
 F_{Df} form component of the drag force

- F_G submerged gravity
 F_L lift force
 F_μ static friction force
 F hydrodynamic force on sediment particle
 F_{St} Stokes drag
 F^0 force that the ambient flow would exert on a fluid sphere instantaneously coincident with the solid sphere
 F^1 perturbation force on sediment particle associated with the modification of the undisturbed ambient flow due to the presence of the particle.
 \mathcal{F}_0 shape function for the logarithmic vertical velocity profile
 F_r Froude number
 F_{r0} typical value of the Froude number
 F_{ru} uniform flow Froude number
- g
- g gravity vector
 \mathcal{G} (2×2) tensor accounting for bed slope in the bedload flux in weakly sloping beds
- h
- h_b thickness of the layer containing sediment particles in motion
 h_p metric coefficient of the lateral curvilinear coordinate
 $H(x, y, t)$ local, instantaneous free surface elevation
 H_0 free surface elevation at the initial cross section
 H_b bar height
 H_{be} equilibrium bar height
 $\bar{H}(x)$ laterally averaged free surface elevation
 \mathcal{H} total head
- i
- I unit tensor
 I parameter for the volumetric discharge of suspended sediments per unit width
 I_i ($i = 1, 2$) Einstein integrals for the volumetric discharge of suspended sediments per unit width
 i interactive specific force for the fluid phase
- j
- J energy slope
- k
- k von Karman constant
 k_x longitudinal mixing coefficient
 k_y transversal mixing coefficient
 \mathcal{K} turbulent kinetic energy per unit mass
 k_s Strickler parameter
- l
- l thickness of the sediment layer
 L macroscale scale measuring the distance over which significant variations of the average

properties of the mixture are experienced also wavelegth in Chapter I.1.

L_0 scale of spatial variations of the ambient flow

L_a thickness of the active layer

L_b bar wavelength

L_B channel convergence length

L_{be} equilibrium bar wavelength

L_d dune wavelength

L_p wavelength of bank undulations

L_r reach length

L_s particle saltation length

ℓ characteristics length scale of the flow (e.g. flow depth) also scale for the average properties of the mixture

ℓ_k spatial Kolmogorov microscale

ℓ_i scale of eddies in the inertial subrange

- m

m empirical exponent in the general relationship for transport capacity

- n

n empirical constant in the general relationship for transport capacity

\mathcal{N} shape function for eddy viscosity

$\hat{\mathbf{n}}$ unit vector normal to the element, oriented in the outward direction

$\hat{\mathbf{n}}_f$ unit vector locally normal to the surface f

N_P number of grains which crosses the unit width of the stream in the interval Δt

- p

$p(\mathbf{x}, t)$ pressure

p sediment porosity also curvilinear coordinate defined along the wetted perimeter in Section 2

$p(v_j)$ probability density function of the variable v_j

P Reynolds averaged pressure

\mathcal{P}_w the wetted perimeter

- q

q_s local total sediment flux per unit width

$q_s^{b,s}$ local (b bedload; s suspended) sediment flux per unit width

\hat{Q} local fluid discharge per unit width

Q (modulus of the) local fluid discharge per unit width

\hat{Q} flow discharge

Q_0 value of the fluid discharge per unit width in the upstream reach

Q_0^b sediment supply per unit width of the reference uniform state

Q_s local depth integrated total sediment flux per unit width

$Q_s^{b,s}$ local depth integrated (b bedload; s suspended) sediment flux per unit width

Q_s modulus of the depth integrated total sediment flux per unit width

Q_{s0} upstream reach value of the depth integrated sediment flux per unit width

$Q_s^{b,s}$ modulus of the depth integrated (b bedload; s suspended) sediment flux per unit width

\hat{Q}_s^b dimensionless modulus of the depth integrated bedload sediment flux per unit width (it coincides with Φ^b in plane bed conditions)

$Q_s[L^3T^{-1}]$ total longitudinal sediment flux transported in the cross section $Q_s^i[L^3T^{-1}]$ ($i=b$)

bedload; $i=s$ suspended) sediment flux transported in the cross section

- r

R_ℓ Reynolds number of the flow
 R_e relative Reynolds number of particle motion
 R_k shear Reynolds number
 R_Ω rotational Reynolds number
 R_p particle Reynolds number
 R_τ particle Reynolds number based on the friction velocity
 R_h hydraulic radius

- s

s is the relative particle density
 s also longitudinal curvilinear coordinate in Section 2
 s also microscale of the order of the average interparticle distance
 S channel slope
 S_e equilibrium slope
 S_{e0} equilibrium slope in the upstream reach
 S_t Stokes number
 S_f fluid portion of the boundary of \mathcal{V}
 S_i boundary of the portions of solid particles contained in \mathcal{V}
 S_s solid portion of the boundary of \mathcal{V}

- t

t time
 $\mathbf{t}(\mathbf{x}, t; \hat{\mathbf{n}})$ instantaneous stress vector acting on a surface element of fluid located at \mathbf{x} and characterised by unit normal $\hat{\mathbf{n}}$
 $\mathbf{T}(\mathbf{x}, t)$ fluid stress tensor
 \mathbf{T}_k^{tot} total stress tensor of the k phase ($k = s, f$)
 \mathbf{T}_k^t Reynolds stress tensor of the k phase ($k = s, f$)
 \mathbf{T}^t Reynolds stress tensor
 \mathbf{T}^{tM} macroscopic Reynolds stress tensor
 T transport stage parameter in Chapter I.1.
 T also period of the bar wave in Chapter I.1.
 \mathcal{T} depth averaged Reynolds stress tensor
 $\mathcal{T}^{(disp)}$ dispersive stress tensor
 \mathcal{T} cross sectionally averaged value of the Reynolds stress T_{xx}

- u

u_τ friction velocity
 $u_{\tau u}$ friction velocity of the uniform flow
 $u_{\tau 0}$ friction velocity scale
 u longitudinal velocity scale
 u_{ref} reference velocity for the study of bank undulations
 $\mathbf{u} = (u, v, w)$ Reynolds averaged fluid velocity
 $\mathbf{u}' = (u'_x, u'_y, u'_z)$ velocity fluctuations
 u_p slip velocity
 U_u depth averaged uniform flow velocity
 U depth averaged longitudinal velocity
 U_0 scale of fluid velocity

U_w longitudinal component of the wind velocity
 \mathcal{U} cross sectionally averaged flow speed
 U_1 cross sectionally averaged flow speed at the dune top
 U_2 cross-sectional averaged flow speed at the dune toe
 \mathcal{U}_t ($\equiv LT^{-1}$) rate of tectonic uplift

- v

$\mathbf{v}(\mathbf{x}, t)$ local instantaneous fluid velocity
 \mathbf{v}_0 initial conditions consisting of a divergence free flow
 $\mathbf{v}_s(\mathbf{x}, t)$ instantaneous value of the velocity of the solid phase
 $\mathbf{v}_P(t)$ velocity of sediment particle
 v_k Kolmogorov velocity microscale
 V lateral component of the depth averaged velocity
 V_0 scale of the lateral component of velocity
 V_b volume of sediment transported in the bedload layer
 V_p average speed of saltating particles
 V_P scale of the particle velocity
 V_H velocity of the free surface
 V_w lateral component of the wind velocity
 \mathcal{V} volume of linear scale ℓ contained in the region instantaneously occupied by the sediment mixture in a neighborhood of \mathbf{x}
 \mathcal{V}_f portion of \mathcal{V} occupied by the fluid phase
 \mathcal{V}_s portion of \mathcal{V} occupied by the solid phase
 \mathcal{V}_P volume of sediment particle
 ∇ flow domain

- w

\mathbf{w}_P velocity of the particle relative to the ambient component of the fluid velocity
 w_s asymptotic steady value of the sediment settling speed
 w_f wake correction
 W_f wake function
 W_0 scale of the vertical velocity component

- x

$\mathbf{x}_0(t)$ location of the centre of the sediment particle at time t
 \mathbf{x} point vector
 \mathbf{x} also position
 x_3 axis aligned with the vertical direction and pointing upwards
 $x_j, j = 1, 2, 3$ Cartesian coordinate system

- z

z axis orthogonal to the channel axis
 z^+ z variable scaled by the viscous length scale
 $\hat{\mathbf{z}}$ unit vector
 ζ normalized vertical coordinate
 \mathcal{Z} Rouse parameter
 \mathcal{Z}_0 reference Rouse parameter
 z_0 elevation where no-slip is imposed at the wall
 z_P conventional distance from the bed to estimate the average particle drag

- α
 - α_x stream-wise inclination angle of the bottom
 - α_y transverse inclination angle of the bottom

- β
 - β aspect ratio of the channel cross-section defined as half width over depth
 - β_{cor} correction coefficient in the 1D momentum equation

- γ
 - Γ_η solid-liquid interface
 - Γ_H free surface
 - Γ_{in} inflow part of the flow boundary
 - Γ_{out} outflow part of the flow boundary

- δ
 - δ dimensionless parameter of the advection-diffusion equation for sediment concentration also a parameter measuring the degree of channel narrowing/widening in Chapter I.1.
 - δ_ν viscous length scale
 - $\delta_i (i = 1, 4)$ dimensionless parameters of the advection-diffusion equation for sediment concentration
 - δ_{ij} Kronecker index
 - δ_{ijk} Ricci tensor
 - δ_P is the phase lag of the property P relative to bottom elevation
 - Δ parameter accounting for the lift force effects in the critical Shields stress

- ϵ
 - ϵ rate of energy dissipation per unit mass
 - ϵ_M ratio between the morphological and hydrodynamic time scales

- ζ
 - ζ dimensionless version of the z coordinate
 - ζ also coordinate normal to the boundary in Section 2
 - ζ_a dimensionless reference level for the mean concentration
 - ζ_0 dimensionless elevation where no-slip is imposed at the wall

- η
 - η elevation of the bed interface
 - η_a elevation of the channel axis
 - $\bar{\eta}$ cross sectionally averaged bottom elevation

- θ
 - θ inclination angle of the bed

- λ
 - λ longitudinal wavenumber of bars

- μ

μ dynamic viscosity
 μ_s static friction coefficient
 μ_d dynamic friction coefficient

- ν

ν viscosity
 ν_T eddy viscosity

- ϕ

ϕ angle of repose of the granular medium
 ϕ also phase lag of free surface elevation relative to flow depth in Chapter I.1.
 ϕ also geologic scale for the grain size in Chapter 7
 ϕ_g average grain size
 ϕ_0 function describing the Rouse concentration distribution
 Φ_{0d} dimensionless bedload transport capacity of homogeneous sediments in a uniform stream
 Φ^b dimensionless depth integrated bedload sediment flux per unit width under plane bed conditions
 Φ^s dimensionless depth integrated suspended sediment flux per unit width

- χ

χ flow conductance
 χ also angle that the bottom stress forms with the longitudinal axis
 χ_u *flow conductance* of uniform flows

- ψ

ψ angle that the velocity of the bedload particles forms with the bottom shear stress vector
 τ

- ρ

ρ water density
 ρ_s density of sediment particles
 ρ_a air density

- σ

σ standard deviation of the grain size distribution
 σ_g geometric standard deviation of the grain size distribution
 σ_s standard deviation of the grain size distribution of the surface layer

- τ

τ flow shear stress
 τ_k temporal Kolmogorov microscale
 τ_u bottom value of the uniform shear stress
 τ_0 mean shear stress at the bed-fluid interface
 $\bar{\tau}_0$ longitudinal bottom shear stress τ_x^η averaged along the wetted perimeter
 $\bar{\tau}_{0g}$ longitudinal bottom shear stress associated with the grain roughness component of drag averaged over a dune wavelength

$\bar{\tau}_{0f}$ longitudinal bottom shear stress associated with the form component of drag averaged over a dune wavelength
 τ_c threshold shear stress for incipient sediment motion
 τ_r residual bottom stress
 τ_s threshold shear stress for incipient transport in suspension
 τ_{sd} threshold shear stress for transition to sheet-debris mode
 τ_T total bottom shear stress
 τ_{sf} average component of τ_T associated with skin friction
 τ_D average component of τ_T associated with form drag generated by the boundary irregularities
 τ_m average bottom stress in an equivalent wide channel with flow depth equal to the flow depth at the center of the channel
 $\hat{\tau}_1, \hat{\tau}_2$ unit vectors in the plane locally tangent to the free surface
 $\hat{\tau}$ unit vector tangential to the bottom
 \mathcal{T}_H , air stress acting on the free surface
 $\mathcal{T}_\eta, \mathcal{T}$ stress on the bed interface

$\bar{\tau}_w$ shear stress at the free surface τ_x^H averaged across the water surface

τ_* local value of the dimensionless Shields stress
 τ'_* Shields stress associated with the grain roughness
 $\bar{\tau}_*$ laterally averaged value of the dimensionless Shields stress
 τ_{*c} critical value of the Shields stress for incipient motion
 τ_{*c0} critical value of the Shields stress for incipient motion under conditions of nearly vanishing bed slope
 τ_{*c1} dynamic critical Shields stress
 τ_{*e} equilibrium Shields stress
 τ_{*e0} equilibrium Shields stress in the upstream reach
 τ_{*g} Shields stress associated with the geometric mean size of the sediments in the surface layer
 τ_{*r} residual Shields stress
 τ_{*u} dimensionless Shields stress of the uniform flow
 $\bar{\tau}_{*f}$ form component of the Shields stress

- ω

ω inverse of the characteristic temporal scale of the flow in Chapter I.1.
 ω also growth rate in Chapter I.1.
 ω vorticity
 Ω mean vorticity, averaged over turbulence
 Ω_P angular velocity of sediment particles
 Ω cross sectional area
 Ω_1 cross-sectional area at the dune top
 Ω_2 cross-sectional area at the dune toe

STUDIES IN SCIENCES AND TECHNOLOGY

TITOLI PUBBLICATI

1. Giovanni Seminara, Stefano Lanzoni, Nicoletta Tambroni, *Theoretical Morphodynamics: Straight Channels*, 2023

Studies in Sciences and Technology

1

This monograph presents the mechanistic foundations of the theory of Morphodynamics, a discipline that investigates the shape of the erodible boundary of natural water bodies. We focus on the fluvial Morphodynamics of straight erodible channels, providing the basis for subsequent extensions to meandering rivers (treated in the companion monograph 2 of this series) and braided rivers. We present basic notions on the Mechanics of Turbulent Flows and Sediment Transport in straight open channels with mobile beds. We then investigate their morphodynamic equilibrium and its instability, that leads to the formation of a variety of bedforms observed in natural rivers. In particular, fluvial bars will deserve special attention as the fundamental building block of large scale fluvial patterns.

GIOVANNI SEMINARA, Master in Civil Engineering (University of Genoa), PhD in Applied Math (Imperial College, London), Professor Emeritus at the University of Genoa and Socio Nazionale of Accademia Nazionale dei Lincei.

STEFANO LANZONI, Master in Hydraulic Engineering (University of Padua), PhD in Hydrodynamics (joint program, Universities of Genoa, Florence, Padua and Trent), Professor of Fluid Mechanics at the University of Padua.

NICOLETTA TAMBRONI, Master in Civil Engineering (University of Genoa), PhD in Fluid dynamics and Environmental Processes in Engineering (University of Genoa), Associate Professor of Fluid Mechanics at the University of Genoa.

ISBN 979-12-215-0212-1 (Print)
ISBN 979-12-215-0213-8 (PDF)
ISBN 979-12-215-0214-5 (XML)
DOI 10.36253/979-12-215-0213-8

www.fupress.com